

SL.LACW.CB.V0.1



Latin American CubeSat Workshop: CubeSat-Based Satellites and Their Applications

Companion Book v0.1

SpaceLab, Federal University of Santa Catarina, Salvador - Brazil






October 2024



Both logomarks were conceived and designed by Victor Freitas Caraméz <vfcaramez@gmail.com> on the occasion of the Latin American Cubesat Workshop, held from 21 to 24 October 2024.




INSTITUTIONAL AND FINANCIAL SUPPORT

The success of this event was made possible through the support and collaboration of our sponsors and partners, listed below:

Institution	Type of Support
	Institutional Support
	Institutional Support
	Institutional Support
 PELO FUTURO DA INOVAÇÃO	Institutional Support
	Institutional Support

(Continued on next page)

INSTITUTIONAL AND FINANCIAL SUPPORT

Institution	Type of Support
	Institutional Support
	Financial Support
 VISIONA Tecnologia Espacial	Financial Support

KEYNOTE SPEAKERS

We extend our appreciation to the keynote speakers, whose insights and expertise contributed significantly to the success of this event, listed below:

Name	Contact	Affiliation
Dr. Rodrigo Leonardi	TODO	Director of Portfolio Management at the Brazilian Space Agency (AEB)
Dr. Viyas Gupta	TODO	Researcher at the European Space Agency (ESA), with expertise in radiation effects.
Dr. Victor Hugo Schulz	TODO	Researcher at Laboratory of Lean Satellite Enterprises and In-Orbit Experiments, KYUTECH

EDITORIAL BOARD

We would like to acknowledge the dedicated efforts of the editorial team, whose contributions were instrumental in bringing this proceedings to fruition. The individuals involved are listed below:

Name	Contact	Position
Eng. João Cláudio Elsen Barcellos	TODO	Editor
Mr. Gabriel Mariano Marcelino	TODO	Associate Editor
Dr. Eduardo Augusto Bezerra	TODO	Senior Advisor
Lucas Ryan	TODO	Reviewer
Eng. Miguel Boing	TODO	Reviewer

ORGANIZING COMMITTEE

The organization of this event was led by the dedicated efforts of the organizing committee, listed below:

Name	Contact	Role
Caique Miranda Sales	kiqsmg@gmail.com	Communication support
Eng. Felipe Costa Juliano	felipecostajuliano@live.com	Chair support
Fernanda Paiva de Moraes	Fernandapaivamorais@gmail.com	Financial Organization
Gabriel Cabral Marcilio	gabrielcabralmarcilio989@gmail.com	Design and media
Eng. João Claudio Barcellos	joaoclaudiobarcellos@gmail.com	Chair support
Eng. Miguel Boing	miguelboing13@gmail.com	Chair support
Maria Eduarda Rezende	dudarezende14@gmail.com	Chair support
Eng. Ramon de Araujo Borba	ramonborba97@gmail.com	Chair support
Rebeca Quintino do Ó	rebeccaquintino@gmail.com	Financial Organization
Dr. Rafael Giovani Venuto	rafael.vnt@gmail.com	Design and media
Sheila Costa	contact.sheilacosta@gmail.com	Financial Organization
Eng. Yuniór Alcantara Guevara	yuniór.alcantara@posgrad.ufsc.br	Chair support
Dr. Anderson Wedderhoff Spengler	TODO	Peer reviewer
Dr. André Pierre Mattei	TODO	Peer reviewer
Dr. Antônio Carlos de Oliveira Pereira Junior	TODO	Peer reviewer

(Continued on next page)

ORGANIZING COMMITTEE

Name	Contact	Role
Dr. Antônio Fernando Bertachini	TODO	Peer reviewer
Dr. Carlos Alberto Rios Brito Jr.	TODO	Peer reviewer
Dr. Cesar Augusto Missio Marcon	TODO	Peer reviewer
Dr. Cezar Rigo	TODO	Peer reviewer
Dr. Edemar Morsch Filho	TODO	Peer reviewer
Dr. Ediz Cetin	TODO	Peer reviewer
Dr. Eduardo Escobar Burger	TODO	Peer reviewer
Dr. Fabian Luis Vargas	TODO	Peer reviewer
Dr. Fábio Armelin	TODO	Peer reviewer
Dr. Fabrício Kucinskis	TODO	Peer reviewer
Dr. Felipe Viel	TODO	Peer reviewer
Dr. Geilson Loureiro	TODO	Peer reviewer
Dr. Geraldo Magela Couto Oliveira	TODO	Peer reviewer
Mr. Gabriel Mariano Marcelino	TODO	Peer reviewer
Dr. Jarbas Aryel Nunes da Silveira	TODO	Peer reviewer
Dr. João Baptista dos Santos Martins	TODO	Peer reviewer
Dr. Laio Oriel Seman	TODO	Peer reviewer
Dr. Luís Eduardo Vergueiro Loures da Costa	TODO	Peer reviewer
Dr. Manoel Jozeane Mafra de Carvalho	TODO	Peer reviewer
Dr. Marcelo Tosin	TODO	Peer reviewer
Dra. Marcia Alvarenga dos Santos	TODO	Peer reviewer
Dra. Maria Cecilia P. Faria	TODO	Peer reviewer
Dr. Moisés Cirilo de Brito Souto	TODO	Peer reviewer

(Continued on next page)

Name	Contact	Role
Dr. Otavio Santos Cupertino Durão	TODO	Peer reviewer
Dr. Paolo Gessini	TODO	Peer reviewer
Dr. Paulo Ricardo Cechelero Villa	TODO	Peer reviewer
Dr. Renato Alves Borges	TODO	Peer reviewer
Dr. Rodrigo Leonardi	TODO	Peer reviewer
Dr. Ronnie Nader	TODO	Peer reviewer
Dra. Rosa Ma. Del Refugio Ramírez De Arellano Y Haro	TODO	Peer reviewer
Dr. Rui Policarpo Duarte	TODO	Peer reviewer
Dra. Tatiana Ribeiro Viana	TODO	Peer reviewer
Dr. Victor Hugo Schulz	TODO	Peer reviewer
Dr. Walter Abrahão dos Santos	TODO	Peer reviewer
Dr. Xisto Lucas Travassos Junior	TODO	Peer reviewer

MESSAGE FROM THE CHAIRS

TODO

PREFACE

We are pleased to present the proceedings of the Latin American CubeSat Workshop (LACW) 2024. This biennial event brings together engineers from the industry, researchers from various fields, and enthusiasts to discuss trends and innovations in the use of CubeSat-based satellites.

The CubeSat standard was introduced in 1999 by Prof. Jordi Puig-Suari and Prof. Bob Twiggs, and has since been widely adopted for its cost-effectiveness and rapid implementation. This standard has democratized access to space, enabling universities around the world to conduct scientific research. Additionally, it provides valuable first contact for undergraduate and graduate students. Today, these satellites are utilized in critical applications, such as Earth observation and remote sensing, demonstrating their versatility and importance in the sector.

At SpaceLab, we are excited to be part of this field and to participate in a significant event like the LACW. We are proud to contribute not only to the organization of the workshop but also by presenting the research we conduct daily in our laboratory, as well as exploring the work being done by other teams and institutions around the world, particularly in Latin America.

We sincerely thank all the experts and enthusiasts who attended the event and shared their experiences, discoveries, and questions. Open dialogue and constructive criticism are essential for advancing this sector, which is poised to grow and evolve in the coming years.

In this volume, you will find a compilation of the works presented during the days of October 22 to 24, 2024, in both poster and oral presentation formats. We have made great efforts to provide you, the reader, with an enriching experience, and we hope you enjoy the content we have prepared!

REVIEW PROCESS

Authors initially submitted extended abstracts for preliminary analysis by peer reviewers. Some of these abstracts were provisionally accepted, allowing authors to submit their full papers for further evaluation. The full papers could be either rejected or accepted at various levels (such as for poster presentation or oral presentation). Regardless of the acceptance type, all full papers were included in the proceedings.

CONTENTS

	INSTITUTIONAL AND FINANCIAL SUPPORT	
	KEYNOTE SPEAKERS	
	EDITORIAL BOARD	
	ORGANIZING COMMITTEE.....	
	MESSAGE FROM THE CHAIRS	
	PREFACE	
	REVIEW PROCESS.....	
1	PRELIMINARY FULL PAPERS.....	1
1.1	PROPOSED PAPER'S MODEL FOR THE PROCEEDINGS.....	2
1.2	FLORIPASAT-3: PLATFORM DESIGN METHODOLOGY AND PRELIMINAR ANALYSIS	6
1.3	ORBIT ANALYSIS AND DESIGN FOR AN ACADEMIC SATEL- LITE.....	14
1.4	GEOMETRIC DESIGN, CONSTRUCTION AND CHARACTERI- ZATION OF A PROTOTYPE STRUCTURE FOR A 3U CUBESAT SATELLITE	16
1.5	PROGRESS REPORT: FLATSAT PLATFORM FOR GOLDS-UFSC AND FUTURE MISSIONS	18
1.6	THE NASCERR MISSION – AN UNIVERSITY/PRIVATE SECTOR COOPERATION WITH CUBESAT	24
1.7	ON-BOARD IMAGE PROCESSING INSIDE THE RAIOSAT EX- PERIMENT MISSION – EARLY RESULTS AND SUITABILITY TESTS	31
1.8	ALCÂNTARA IN ORBIT	37
1.9	ORBIT SENSITIVITY ANALYSIS FOR CATARINA CONSTELLA- TION.....	39
1.10	ADVANCEMENTS IN GNSS RADIO OCCULTATION TECHNIQUES: OPPORTUNITIES AND CHALLENGES IN CUBESAT PLAT- FORMS.....	45
1.11	THE NANOMIRAX-1 MISSION – THE FIRST BRAZILIAN AS- TROPHYSICS SPACE MISSION	55

CONTENTS

1.12	PRELIMINARY DESIGN OF THE COMMUNICATIONS SUBSYSTEM FOR THE CHASQUI II CUBESAT MISSION.....	61
1.13	PERSISTENT-1: THE PRELIMINARY DESIGN OVERVIEW.....	63
1.14	SATELLITE OPERATIONS SERVICE - DATASAT: A STUDY ON NOISE MITIGATION SYSTEMS WITHIN THE ADA FRAMEWORK	71
1.15	PROPOSAL AND REVIEW OF A GROUND SENSOR TERMINAL (GST) DESIGN FOR ENVIRONMENTAL DATA COLLECTION AND LORA BASED CUBESAT MISSIONS	78
1.16	DEVELOPMENT OF AN AUTOMATED APPLICATION TO COLLECT AND FILTER CUBESAT'S DATA.....	85
1.17	A BASE MODEL ARCHITECTURE SYSTEM FOR CUBESAT DEVELOPMENT	92
1.18	INVESTIGATING THE IMPACT OF CUBESAT SIZE ON POWER GENERATION.....	99
1.19	EPS CONTROL FOR A CUBESAT	105
1.20	AN ENDURED ON-BOARD COMPUTER FOR SMALL SATELLITES, USING LOW COST COTS COMBINED WITH RAD-HARD DEVICES AND FAULT-TOLERANCE STRATEGIES.....	113
1.21	MAXIMIZING POWER POTENTIAL: DESIGNING AN ALGORITHMICALLY OPTIMIZED SOLAR CELL ARRAY DESIGN FOR THE PERUVIAN 3U CUBESAT CHASQUI II	120
1.22	THE INFLUENCE OF DIFFERENT SCENARIOS ON THE TEMPERATURE RESPONSE OF CUBESAT'S BATTERY.....	122
1.23	ANALYSIS OF THE COLLIMATION OF AN ELECTRON BEAM IN A MAGNETIC MIRROR FOR POSSIBLE PLASMA THRUSTER APPLICATIONS.....	129
1.24	INITIAL DEVELOPMENT OF A GAS-FED PULSED PLASMA THRUSTER FOR NANO AND PICO SATELLITES.....	135
1.25	DEVELOPMENT OF A RADIOFREQUENCY CATHODE FOR HALL THRUSTERS	142
1.26	COMPARATIVE STUDY OF PROPELLANT INJECTION MODES IN A LOW POWER HELICON THRUSTER.....	146
1.27	DESIGN AND PRELIMINARY CHARACTERIZATION OF A HELICON PLASMA DEVICE FOR AEROSPACE PROPULSION	152
1.28	EVALUATION OF THE EFFECTS OF DISTURBANCES CAPABLE OF ALTERING THE ORBIT OF THE BIOMESAT SATELLITE.....	157

1.29	3U CUBESAT DETUMBLING AND ATTITUDE CONTROL WITH MAGNETORQUERS.....	163
1.30	HARDWARE-IN-THE-LOOP (HIL) AND SOFTWARE-IN-THE-LOOP (SIL) SYSTEM FOR CUBESAT ADCS TESTING.....	165
1.31	DEVELOPMENT AND PERFORMANCE ANALYSIS OF AN ATTITUDE AND ORBIT SIMULATOR FOR CUBESAT	173
1.32	ANALYSIS OF FUEL CONSUMPTION FOR ORBITAL CORRECTION MANEUVERS TO MITIGATE INJECTION ERRORS AFTER LAUNCH.....	175
1.33	MANAGEMENT THEORY AND DOCUMENTATION STANDARDS INTEGRATED WITH GRAPH-BASED PROJECT ORGANIZATION: A CASE STUDY FOR PDQSAT CUBESAT PROJECT 180	
1.34	SYSTEMS ENGINEERING OF A BRAZILIAN AMAZON IMAGING CUBESAT CONSTELLATION: FRITZSAT MISSION	190
1.35	FEA-BASED VIBRATION ANALYSIS OF CUBESAT BATTERY STRUCTURES.....	200
1.36	DESIGN OF A LOW-COST SOLAR SIMULATOR FOR CUBESATS	205
1.37	STRATOSPHERIC BALLOONS AS A MULTI MISSION PLATFORM TESTBED FOR SCIENTIFIC AND TECHNOLOGICAL APPLICATIONS.....	211
1.38	CYBER ATTACK TREE ANALYSIS ON NATAL MULTI-MISSION STATION FOR SATELLITE TT&C: SYSTEMATIC LITERATURE REVIEW	218
1.39	REVIEW OF THE APPLICATION OF CCSDS TELEMETRY AND TELECOMMAND RECOMMENDATIONS IN CUBESAT MISSIONS.....	226
1.40	QUADRUPOLE ANTENNAS FOR CUBESATS: RADIATION CHARACTERISTICS IN DIFFERENT CONFIGURATIONS AND INITIAL RESULTS	234
1.41	ANALYSIS OF DIELECTRIC MATERIAL FOR S-BAND MICROSTRIP ANTENNA AIMED AT SPACE APPLICATIONS	240
1.42	ROCUS-1: THE PRELIMINARY DESIGN OVERVIEW	246

CHAPTER 1

PRELIMINARY FULL PAPERS

The following presents all the accepted works in their preliminary form for presentations, whether in oral format or as posters. Please note that this initial version, referred to as the *Companion Book v0.1*, may not reflect the most updated versions of the works. In the next version, the official proceedings of the event, these works may be formatted differently and may contain slight updates or modifications in their content. Some of the submissions are presented as abstracts because the full papers were not submitted in time.



LATIN AMERICAN CUBESAT WORKSHOP SALVADOR, BR

DOI: 10.1234/example-doi-1

Testing and idea for the proceedings

Your Name

Abstract

Lorem ipsum dolor sit amet, consectetur adipiscing elit. Ut purus elit, vestibulum ut, placerat ac, adipiscing vitae, felis. Curabitur dictum gravida mauris. Nam arcu libero, nonummy eget, consectetur id, vulputate a, magna. Donec vehicula augue eu neque. Pellentesque habitant morbi tristique senectus et netus et malesuada fames ac turpis egestas. Mauris ut leo. Cras viverra metus rhoncus sem. Nulla et lectus vestibulum urna fringilla ultrices. Phasellus eu tellus sit amet tortor gravida placerat. Integer sapien est, iaculis in, pretium quis, viverra ac, nunc. Praesent eget sem vel leo ultrices bibendum. Aenean faucibus. Morbi dolor nulla, malesuada eu, pulvinar at, mollis ac, nulla. Curabitur auctor semper nulla. Donec varius orci eget risus. Duis nibh mi, congue eu, accumsan eleifend, sagittis quis, diam. Duis eget orci sit amet orci dignissim rutrum.

Nam dui ligula, fringilla a, euismod sodales, sollicitudin vel, wisi. Morbi auctor lorem non justo. Nam lacus libero, pretium at, lobortis vitae, ultricies et, tellus. Donec aliquet, tortor sed accumsan bibendum, erat ligula aliquet magna, vitae ornare odio metus a mi. Morbi ac orci et nisl hendrerit mollis. Suspendisse ut

massa. Cras nec ante. Pellentesque a nulla. Cum sociis natoque penatibus et magnis dis parturient montes, nascetur ridiculus mus. Aliquam tincidunt urna. Nulla ullamcorper vestibulum turpis. Pellentesque cursus luctus mauris..

1 Introduction

Lorem ipsum dolor sit amet, consectetur adipiscing elit. Ut purus elit, vestibulum ut, placerat ac, adipiscing vitae, felis. Curabitur dictum gravida mauris. Nam arcu libero, nonummy eget, consectetur id, vulputate a, magna. Donec vehicula augue eu neque. Pellentesque habitant morbi tristique senectus et netus et malesuada fames ac turpis egestas. Mauris ut leo. Cras viverra metus rhoncus sem. Nulla et lectus vestibulum urna fringilla ultrices. Phasellus eu tellus sit amet tortor gravida placerat. Integer sapien est, iaculis in, pretium quis, viverra ac, nunc. Praesent eget sem vel leo ultrices bibendum. Aenean faucibus. Morbi dolor nulla, malesuada eu, pulvinar at, mollis ac, nulla. Curabitur auctor semper nulla. Donec varius orci eget risus. Duis nibh mi, congue eu, accumsan eleifend, sagittis quis, diam. Duis eget orci sit amet orci dignissim

rutrum.

Nam dui ligula, fringilla a, euismod sodales, sollicitudin vel, wisi. Morbi auctor lorem non justo. Nam lacus libero, pretium at, lobortis vitae, ultricies et, tellus. Donec aliquet, tortor sed accumsan bibendum, erat ligula aliquet magna, vitae ornare odio metus a mi. Morbi ac orci et nisl hendrerit mollis. Suspendisse ut massa. Cras nec ante. Pellentesque a nulla. Cum sociis natoque penatibus et magnis dis parturient montes, nascetur ridiculus mus. Aliquam tincidunt urna. Nulla ullamcorper vestibulum turpis. Pellentesque cursus luctus mauris. [1].

2 Methodology

Lorem ipsum dolor sit amet, consectetur adipiscing elit. Ut purus elit, vestibulum ut, placerat ac, adipiscing vitae, felis. Curabitur dictum gravida mauris. Nam arcu libero, nonummy eget, consectetur id, vulputate a, magna. Donec vehicula augue eu neque. Pellentesque habitant morbi tristique senectus et netus et malesuada fames ac turpis egestas. Mauris ut leo. Cras viverra metus rhoncus sem. Nulla et lectus vestibulum urna fringilla ultrices. Phasellus eu tellus sit amet tortor gravida placerat. Integer sapien est, iaculis in, pretium quis, viverra ac, nunc. Praesent eget sem vel leo ultrices bibendum. Aenean faucibus. Morbi dolor nulla, malesuada eu, pulvinar at, mollis ac, nulla. Curabitur auctor semper nulla. Donec varius orci eget risus. Duis nibh mi, congue eu, accumsan eleifend, sagittis quis, diam. Duis eget orci sit amet orci dignissim rutrum.

Nam dui ligula, fringilla a, euismod sodales, sollicitudin vel, wisi. Morbi auctor lorem non justo. Nam lacus libero, pretium at, lobortis

vitae, ultricies et, tellus. Donec aliquet, tortor sed accumsan bibendum, erat ligula aliquet magna, vitae ornare odio metus a mi. Morbi ac orci et nisl hendrerit mollis. Suspendisse ut massa. Cras nec ante. Pellentesque a nulla. Cum sociis natoque penatibus et magnis dis parturient montes, nascetur ridiculus mus. Aliquam tincidunt urna. Nulla ullamcorper vestibulum turpis. Pellentesque cursus luctus mauris..

3 Results

Lorem ipsum dolor sit amet, consectetur adipiscing elit. Ut purus elit, vestibulum ut, placerat ac, adipiscing vitae, felis. Curabitur dictum gravida mauris. Nam arcu libero, nonummy eget, consectetur id, vulputate a, magna. Donec vehicula augue eu neque. Pellentesque habitant morbi tristique senectus et netus et malesuada fames ac turpis egestas. Mauris ut leo. Cras viverra metus rhoncus sem. Nulla et lectus vestibulum urna fringilla ultrices. Phasellus eu tellus sit amet tortor gravida placerat. Integer sapien est, iaculis in, pretium quis, viverra ac, nunc. Praesent eget sem vel leo ultrices bibendum. Aenean faucibus. Morbi dolor nulla, malesuada eu, pulvinar at, mollis ac, nulla. Curabitur auctor semper nulla. Donec varius orci eget risus. Duis nibh mi, congue eu, accumsan eleifend, sagittis quis, diam. Duis eget orci sit amet orci dignissim rutrum.

Nam dui ligula, fringilla a, euismod sodales, sollicitudin vel, wisi. Morbi auctor lorem non justo. Nam lacus libero, pretium at, lobortis vitae, ultricies et, tellus. Donec aliquet, tortor sed accumsan bibendum, erat ligula aliquet magna, vitae ornare odio metus a mi. Morbi ac orci et nisl hendrerit mollis. Suspendisse ut

massa. Cras nec ante. Pellentesque a nulla. Cum sociis natoque penatibus et magnis dis parturient montes, nascetur ridiculus mus. Aliquam tincidunt urna. Nulla ullamcorper vestibulum turpis. Pellentesque cursus luctus mauris..

4 Discussion

Lorem ipsum dolor sit amet, consectetur adipiscing elit. Ut purus elit, vestibulum ut, placerat ac, adipiscing vitae, felis. Curabitur dictum gravida mauris. Nam arcu libero, nonummy eget, consectetur id, vulputate a, magna. Donec vehicula augue eu neque. Pellentesque habitant morbi tristique senectus et netus et malesuada fames ac turpis egestas. Mauris ut leo. Cras viverra metus rhoncus sem. Nulla et lectus vestibulum urna fringilla ultrices. Phasellus eu tellus sit amet tortor gravida placerat. Integer sapien est, iaculis in, pretium quis, viverra ac, nunc. Praesent eget sem vel leo ultrices bibendum. Aenean faucibus. Morbi dolor nulla, malesuada eu, pulvinar at, mollis ac, nulla. Curabitur auctor semper nulla. Donec varius orci eget risus. Duis nibh mi, congue eu, accumsan eleifend, sagittis quis, diam. Duis eget orci sit amet orci dignissim rutrum.

Nam dui ligula, fringilla a, euismod sodales, sollicitudin vel, wisi. Morbi auctor lorem non justo. Nam lacus libero, pretium at, lobortis vitae, ultricies et, tellus. Donec aliquet, tortor sed accumsan bibendum, erat ligula aliquet magna, vitae ornare odio metus a mi. Morbi ac orci et nisl hendrerit mollis. Suspendisse ut massa. Cras nec ante. Pellentesque a nulla. Cum sociis natoque penatibus et magnis dis parturient montes, nascetur ridiculus mus. Aliquam tincidunt urna. Nulla ullamcorper ve-

stibulum turpis. Pellentesque cursus luctus mauris..

5 Conclusion

Lorem ipsum dolor sit amet, consectetur adipiscing elit. Ut purus elit, vestibulum ut, placerat ac, adipiscing vitae, felis. Curabitur dictum gravida mauris. Nam arcu libero, nonummy eget, consectetur id, vulputate a, magna. Donec vehicula augue eu neque. Pellentesque habitant morbi tristique senectus et netus et malesuada fames ac turpis egestas. Mauris ut leo. Cras viverra metus rhoncus sem. Nulla et lectus vestibulum urna fringilla ultrices. Phasellus eu tellus sit amet tortor gravida placerat. Integer sapien est, iaculis in, pretium quis, viverra ac, nunc. Praesent eget sem vel leo ultrices bibendum. Aenean faucibus. Morbi dolor nulla, malesuada eu, pulvinar at, mollis ac, nulla. Curabitur auctor semper nulla. Donec varius orci eget risus. Duis nibh mi, congue eu, accumsan eleifend, sagittis quis, diam. Duis eget orci sit amet orci dignissim rutrum.

Nam dui ligula, fringilla a, euismod sodales, sollicitudin vel, wisi. Morbi auctor lorem non justo. Nam lacus libero, pretium at, lobortis vitae, ultricies et, tellus. Donec aliquet, tortor sed accumsan bibendum, erat ligula aliquet magna, vitae ornare odio metus a mi. Morbi ac orci et nisl hendrerit mollis. Suspendisse ut massa. Cras nec ante. Pellentesque a nulla. Cum sociis natoque penatibus et magnis dis parturient montes, nascetur ridiculus mus. Aliquam tincidunt urna. Nulla ullamcorper vestibulum turpis. Pellentesque cursus luctus mauris..

References

- [1] J. Doe, "Sample article title," *Sample Journal*, vol. 1, pp. 1–10, 2024.

FloripaSat-3: Platform Design Methodology and Preliminar Analysis

Vitória B. Bianchin¹, Gabriel C. Marcílio², Fernanda P. de Moraes³, Rebecca Q. do Ó⁴, João Cláudio E. Barcellos⁵, Gabriel M. Marcelino⁶ and Eduardo A. Bezerra⁷

Abstract—This paper details the development of the third version of the FloripaSat CubeSat platform, focusing on enhanced reliability and robustness. CubeSats have gained popularity due to their low cost and rapid development cycle, yet the affordability of commercial platforms remains a barrier for many educational and research institutions. The SpaceLab team at UFSC aims to address this issue by creating an open-source, robust satellite platform. The FloripaSat-3 platform improves upon its predecessors, FloripaSat-1 and 2, by introducing a systematic design methodology for key subsystems such as On-Board Data Handling (OBDH), Telemetry and Telecommand (TMTC), and the Electrical Power System (EPS). The design process is based on ECSS guidelines and divided into four stages: requirement analysis, schematic and layout design, preliminary testing, and final adjustments with full subsystem integration. The primary goal is to create a reliable platform that can be reused for various missions, addressing the limitations encountered in earlier versions, particularly those related to scalability and processing power. Additionally, the paper emphasizes the open-source nature of the project, providing detailed documentation, schematics, and block diagrams, which can be further developed by other teams. FloripaSat-3 is expected to serve as a foundation for more ambitious space projects, making space technology more accessible to a broader range of users and contributing to the evolution of small satellite platforms.

Index Terms—Embedded Systems, Satellite, CubeSat, Subsystems.

I. INTRODUCTION

In June 2003, the first CubeSat, XI-IV, was launched by the team at the Intelligent Space Systems Laboratory (ISSL) of the University of Tokyo. This satellite not only made history by remaining operational for over 15 years [1], but it also marked the beginning of a new era in satellite development and launch. This era is characterized by the development and mass launch of miniaturized satellites following a well-defined standard [2].

This standard was conceived in 1999 by researchers from California Polytechnic State University and Stanford University, with the goal of democratizing access to the space environment. Initially, most CubeSat missions were conducted by students and researchers at universities, focusing on hands-on learning and scientific/technological research [3]. Currently,

they are being used for Earth observation [4], remote sensing [5] and even deep-space applications [6].

Despite their diverse applications, all CubeSats share a common architecture, comprising of a service module and one or more payloads. Payloads are the satellite's equipment or instruments that enable the mission, such as a camera for Earth observation applications. The service module, on the other hand, ensures the satellite's overall functionality throughout the mission and typically consists of three main subsystems: Electrical Power System (EPS), On-Board Data Handling (OBDH), and Telemetry and Telecommand (TMTC).

Given the importance of the satellite's service module, it is common to either purchase COTS platforms from well-known companies, like EnduroSat, GomSpace, or ISISpace, or to develop a custom, reusable platform, which can be more cost-effective. The SpaceLab team opted for the latter to promote hands-on learning and to create a more economical and adaptable platform for both current and future missions.

The FloripaSat-1 [7] was SpaceLab's first platform, successfully used in the satellite of the same name launched in 2019. It was subsequently improved through hardware modifications and firmware restructuring, leading to the development of the FloripaSat-2 platform [8]. This platform is closer to a multi-mission design and is currently used in several missions, including GOLDS-UFSC [9], Catarina-A1 and A3¹, Aldebaran-1², CIMATELITE [10], and others. However, the MSP430 microcontrollers used in previous platforms present several limitations, and other constraints have been observed that impact its scalability.

To overcome the limitations of previous platforms, we aim to develop FloripaSat-3, a new platform that prioritizes flexibility, reliability, and robustness without compromising practicality. The development methodology for FloripaSat-3 entails a comprehensive analysis of existing platforms (both commercial and custom-built), followed by an assessment of requirements and evaluation of various components. This systematic approach will inform the design of the new platform, ensuring it addresses the shortcomings of its predecessors. This article focuses on the development methodology, emphasizing the lessons learned from previous platforms to achieve continuous improvement and enhanced accessibility.

The remainder of this work is organized as follows: In Section II, we present the development methodology for a

Vitória B. Bianchin, UFSC, Brazil, (vitoria.bianchin@spacelab.ufsc.br).
 Gabriel C. Marcílio, UFSC, Brazil, (gabrielcabralemarcilio989@gmail.com).
 Fernanda P. de Moraes, UFSC, Brazil, (Fernandapaivamorais@gmail.com).
 Rebecca Q. Do Ó, UFSC, Brazil, (rebecca.quintino@spacelab.ufsc.br)
 João C. E. Barcellos, UFSC, Brazil, (joaoclaudiobarcellos@gmail.com).
 Gabriel M. Marcelino, UFSC, Brazil, (gabriel.marcelino@spacelab.ufsc.br).
 Eduardo A. Bezerra, UFSC, Brazil, (eduardo.bezerra@ufsc.br).

¹<https://www.gov.br/aeb/pt-br/acoes-e-programas/desenvolvimento-tecnologico/constelacao-catarina>

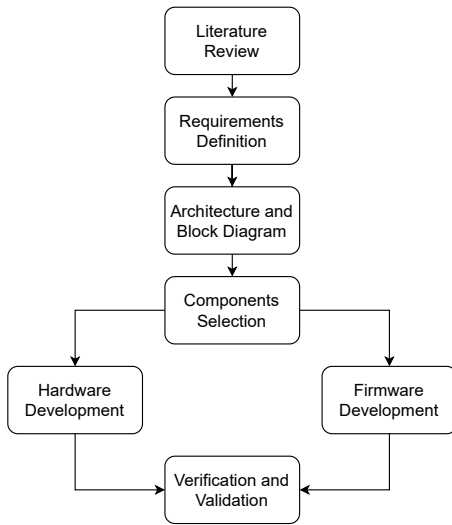
²<https://www.gov.br/aeb/pt-br/centrais-de-conteudo/publicacoes/instagram-do-periodo-de-defeso-eleitoral-2022/missao-aldebaran-i>

CubeSat platform, outlining the step-by-step process used to develop SpaceLab’s new platform. Also in this section, specific aspects of developing each subsystem of the platform are presented. Section IV addresses the next steps in the development process. Finally, Section V presents the conclusions drawn from this study.

II. METHODOLOGY

The methodology adopted for the development of the FloripaSat-3 platform is structured into several key stages: 1) a comprehensive literature review, 2) definition of baseline requirements, 3) block diagram creation, 4) components selection, 5) hardware and firmware development, and 6) verification and validation of the platform. So far, the SpaceLab team has completed the initial stages, including the literature review, requirements definition, and component selection, along with the creation of an initial block diagram. These foundational steps set the stage for the subsequent development phases, which will involve detailed hardware and firmware work. For a clearer understanding of the entire process, Fig. 1 provides a flowgraph of the proposed approach.

Fig. 1: Flowgraph of the development and design methodology proposed for the FloripaSat-3.



Initially, an extensive literature review was conducted on existing projects at other institutions to identify best practices, innovations, and challenges faced in similar developments. The predecessor platforms developed by the laboratory, FloripaSat-1 [7] and FloripaSat-2 [9], played a crucial role in shaping the decisions for the current system. The experience gained from these earlier projects provided valuable insights into key design choices, such as in component selection, system architecture, and mission requirements. This foundation ensures that lessons learned from previous modules, commercial and non-commercial, were incorporated to enhance performance and reliability.

Clear and well-defined requirements are essential to align each module to the mission objectives and guide design and testing. For this project, the European Cooperation for Space Standardization (ECSS) recommendations were used as a foundation [11] [12], covering aspects like performance, reliability, and verification. Insights gained from previous missions, including FloripaSat-1 and GOLDS-UFSC, also influenced these criteria. Requirements were classified by type, verification method, and system level following IEEE standards [13]. Additionally, the laboratory introduced its own nomenclature for the requirements: SLB-SYS-REQ-XYZ, where SLB refers to SpaceLab, SYS represents the name of the system module, REQ stands for requirements, and XYZ is the requirement code. The first digit indicates the type of requirement, while the last digit indicates its specific order (e.g., first, second, etc.).

Next, the overall architecture of the module was defined based on those requirements, depicted on a detailed block diagram. It included all main components and their interconnections, serving as a guide for subsequent project stages. With the architecture in place, specific electronic components were selected to meet the established requirements. The component selection considered factors such as availability, cost, performance and reliability. Selecting preferably automotive components due to its temperature range and extreme conditions resilience, improving its reliability.

In the hardware development phase, detailed schematics for the functional blocks will be created and reviewed. Once approved, circuit board layouts must be designed. For its development, the methodology of [14] is used. Even without a specific mission, parallel development of firmware is feasible once components are selected, as development kits for the ICs can be utilized and the base code can be written. This allows for early firmware development and testing alongside hardware design.

The board for each module is then fabricated and subjected to bench tests, including visual inspection, electrical checks, performance tests, and reliability analyses, to ensure that each part of the subsystem operates according to the established requirements [15].

Based on the results of bench tests and firmware development, final adjustments are made to the schematics and layouts. These modifications aim to correct any faults, improve efficiency, and ensure seamless integration between all components. After adjustments, the final module board can be fabricated, integrating all the previously developed and tested functional blocks. The complete board undergoes another round of bench tests, verifying the interaction between all components and the combined operation of hardware and firmware.

Furthermore, the project adheres to open-source principles, utilizing the CERN-OHL-S license for hardware, GPLv3 for software, and Creative Commons BY-SA 4.0 for documentation. This commitment to open-source philosophy ensures the project’s accessibility to other research groups and external contributions. For instance, the hardware development for the FloripaSat-3 platform is being carried out entirely using KiCad EDA software, rather than the proprietary Altium Designer

used in previous generations.

Throughout the entire process, documentation shall continuously updated to reflect any changes or improvements. This documentation may include all technical specifications, schematics, layouts, test results, and firmware utilization, ensuring traceability and compliance with the initial requirements.

III. PRELIMINARY ANALYSIS AND DEFINITIONS

In this section, it is presented a preliminary analysis and initial definitions so far for the three main subsystems of FloripaSat-3 platform: TMTC, OBDH and EPS.

A. TMTC

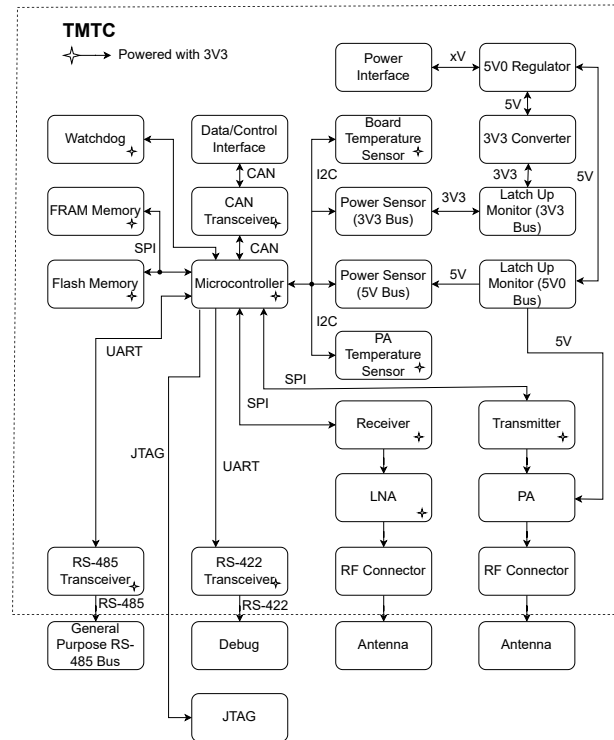
Designing a robust telemetry and telecommand module requires a detailed analysis of the state of the art. In this context, the review began with the analysis of the TTC 2.0, the telemetry and telecommand module from SpaceLab's FloripaSat-2. This module uses GFSK/GMSK modulation, operates at VHF and/or UHF bands, and follows the NGHam protocol, with UART, I²C, and SPI interfaces. This previous telecommunication module influenced several decisions regarding the current TMTC. Additionally, a review was conducted of commercial modules from EnduroSat [16], ISISpace [17] and GomSpace [18], focusing on UHF modules and comparing their characteristics, as shown in TABLE I.

After conducting a thorough review of the state of the art, the requirements for the TMTC module were developed and refined according to the proposed methodology. These requirements encompass both the specific functionalities of the module and its integration with the rest of the satellite system. An example of TMTC requirement is that the TMTC module shall operate correctly between -40 and 85 °C, in order to perform a safe operation in LEO environment. This type of requirement led the team to select components such as RS-422/RS-485 transceiver MAX3362AKA+T, MMZ09332B power amplifier and also the LTC4361ITS8-2 overvoltage/overcurrent protection controller, for example.

With the requirements clearly defined, the architecture of the module was determined. The corresponding block diagram in Fig. 2 illustrates the design and functional components of the module. It describes the architecture and data flow of the TMTC module, focusing on the core components and their functions. The microcontroller is central to the module's operations, communicating with other subsystems via buses like RS-485 and/or CAN, and managing the internal peripherals of the module, such as the radio ICs and sensors.

Key components include the CAN transceiver, which enables communication with other systems on the CAN bus, and the power interface, responsible for converting input power to required voltage levels using a 5 V regulator and a 3.3 V converter. Latch-up monitors protect the system from latch-up events, while power sensors track power consumption for health monitoring. Temperature sensors monitor both the Power Amplifier (PA) and the board temperature. Memory components, including NOR flash and FRAM, provide reliable

Fig. 2: Block diagram of TMTC.



storage, while a watchdog timer enhances system safety by resetting the system during malfunctions.

The module also handles RF signals through its receiver and transmitter units. The use of a PA in the transmitter, and a Low-Noise Amplifier in the receiver, ensures the appropriate power level for incoming and transmitted packets. For debugging and programming, a JTAG interface is included, together with a RS-422 bus for transmitting log messages.

A significant change was made to the key component of the radio compared to its predecessor: the entire RF circuit chain was designed from the ground up by the laboratory. Only off-the-shelf integrated circuits were selected for the PA, LNA, transmitter and receiver IC. This approach was adopted to provide greater flexibility in the design, allowing the team to tailor the system to specific requirements, such as the desired frequency range, avoid dependency on specific manufacturers, and maintain full control over the quality of the components used within the radio. Alongside, this subsystem is designed for full-duplex communication, enabling simultaneous data transmission and reception, in contrast to its previous generation that was half-duplex.

The module will incorporate an aluminum shield to mitigate radiation [19] effects, and electromagnetic interference (EMI) to and/or from other subsystems within the satellite. The choice of aluminum is driven by its effective EMI shielding properties, alongside providing good protection against radiation effects, considering its lighter density compared to other metals.

Parameter	Manufacturer				
	EnduroSat	GomSpace	ISISpace	SpaceLab	SpaceLab
Model	UHF TRANSCIEVER II	AX100	TRXVU	TTC 2.0	TMTC
Frequency range	400-403/430-440 MHz	395-405/430-440	145.8-146/148- 150.05 MHz (RX), 400.15-402/435-438 MHz (TX)	145-146/400- 402/435-438/468-469	400-402 (RX), 468-469 MHz (TX)
Modulation	OOK, (G)FSK, (G)MSK, 4(G)FSK	FSK, MSK, (G)FSK, (G)MSK	BPSK/(G)MSK	(G)FSK, (G)MSK	(G)FSK, (G)MSK
Protocol	AX.25	CSP + RS	AX.25/HDLC	NGHam	NGHam
TX power	30 dBm	24-30 dBm	27 dBm	30 dBm	30 dBm
Power consumption	0.12 W (RX)/2.7 W (TX)	1 W	0.48 W (RX)/4 W (TX)	0.16 W (RX)/2.8 W (TX)	≤ 0.3 W (RX)/3 W (TX)
Data transmission mode	Half-Duplex	Half-Duplex	Full-Duplex	Half-Duplex	Full-Duplex
Frequency stability	2.5 ppm	Unknown	3.5 kHz	10 ppm	1 ppm
Data rate	up to 19200 bps	up to 19200 bps	1200-9600 bps	1200-9600 bps	1200-9600 bps
Sensitivity	down to -121 dBm	down to -137 dBm	down to -104 dBm	down to -126 dBm	down to -126 dBm
Interfaces	RS-485, UART, I ² C, USB	I ² C, UART, CAN	I ² C	UART, SPI	RS-485, RS-422, CAN
Dimensions	88.3 × 95 × 23.2 mm	65 × 40 × 7.2 mm	90 × 96 × 15 mm	89.15 × 92.13 × 15 mm	≤ 90 × 95 × 20 mm
Mass	94 g	24.5 g	75 g	73 g	≤ 100 g

TABLE I: Commercial TMTC board comparison.

B. OBDH

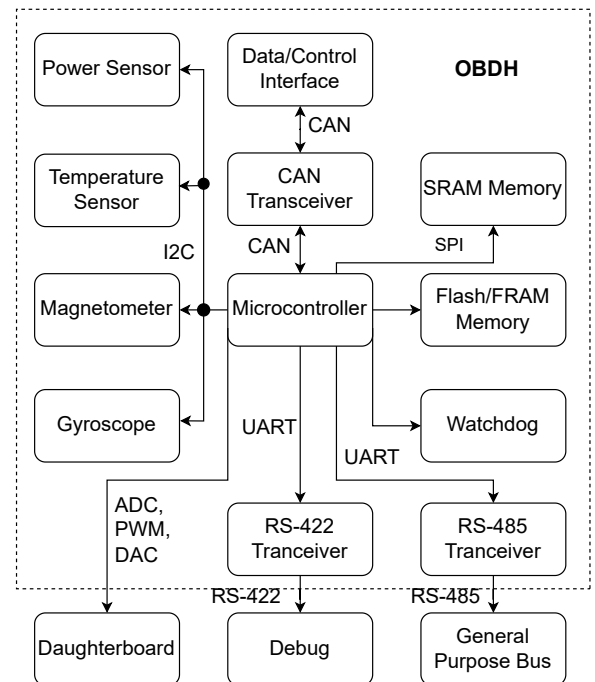
The On-Board Data Handling (OBDH) module centralizes data management and communication across the satellite's subsystems. To enhance the FloripaSat-3 platform, a new OBDH module was developed following an analysis of SpaceLab's OBDH 2.0. This module uses a Texas Instruments MSP430F6659 microcontroller and supports various interfaces, including I²C, SPI, UART, JTAG, PC-104, and a daughterboard connector for expansion. It also features non-volatile memory, an external watchdog timer, voltage and current sensors, I²C buffers, and an RS-485 transceiver. Additionally, other commercial modules were reviewed, as shown in TABLE II, including the OBC [20] from EnduroSat, the Kryten M3 [21] from AAC Clyde Space, and the NanoMind A3200 [22] from GomSpace.

Another point is that the OBDH 2.0 is based on the MSP430F6659 microcontroller, which does not support the CAN protocol. As already mentioned, CAN is one of the most suitable protocols when developing projects for space applications [23]. That condition led to a search for different microcontrollers. From the analysis of the TABLE II, it can be inferred that both the Kryten M3 and the NanoMind A3200 are CAN compatible. The analysis also shows that all the modules have ARM-based processors and offer various communication interfaces. In detail, they differ in memory capacity, power consumption and functionality. The Kryten M3 and EnduroSat OBC have better radiation tolerance, an essential feature for space [24] [25]. In addition, the NanoMind A3200 has a very low mass, which is valuable in CubeSats with strictly limited mass budgets. Other differences in the sensors onboard each module are notable, as the NanoMind A3200 has sensors such as magnetometers, accelerometers, and gyroscopes, which are essential for determining attitude in space, while the EnduroSat OBC offers fewer sensor capabilities. The inclusion of these sensors on a new version of the OBDH board is an important factor in meeting mission requirements, as they increase

the satellite's ability to determine its attitude in space, thus enabling active attitude control.

These preliminary analyses have produced a first draft of the OBDH block diagram, as can be seen in Fig. 3. This diagram outlines the structure of the new board, including the addition of sensors, and thus forms a starting point for further design and refinement.

Fig. 3: Block diagram of OBDH.



Parameter	Manufacturer				
	EnduroSat	AAC Clyde	GomSpace	SpaceLab	SpaceLab
<i>Model</i>	Onboard Computer	Kryten M3	NanoMind A3200	OBDH 2.0	OBDH 3.0
<i>Processor</i>	ARM Cortex M7	SmartFusion2 ARM Cortex-M3 based SoC FPGA	AT32UC3C	MPS430F6659	SmartFusion2 ARM Cortex-M3 based SoC FPGA
<i>Clock</i>	Unknown	50 MHz	8 to 64 MHz	32 MHz	166 MHz
<i>Memory (RAM)</i>	SRAM: 1 MB	SDRAM: 64 MB	SDRAM: 32 MB	SRAM: 64 kB	SRAM: ≥ 1 MB
<i>Memory (non-volatile)</i>	FRAM: 8 MBit	MRAM: 16MB	FRAM: 32 kB, NOR Flash: 128 MB	FRAM: 2 MBit, NOR Flash: 128 MB	FRAM: ≥ 2 MBit, Flash: ≥ 256 MB
<i>Power consumption</i>	Unknown	Typ.: 400 mW, Max.: 1W	0.9 W	0.66 W	≤ 1 W
<i>Interfaces</i>	4xRS-485, 2xRS-422, 3xUART, 2xI ² C, SPI, USB, CAN	8xUART, 2xI ² C, 1xSPI, 1xCAN, 1xRS-422, 1xDTM, 1xLVDS, 3xQSPI, 17xGPIO	SPI, I ² C, UART, CAN	UART, I ² C, SPI, GPIO, PWM, ADC, DAC and RS-485	CAN, UART, I ² C, SPI, GPIO, PWM, ADC, DAC, RS-422 and RS-485
<i>Sensors</i>	Magnetometer	Unknown	Magnetometer, Gyroscope, Temperature	Voltage, Current, Temperature	Magnetometer, Gyroscope, Temperature, Power
<i>Dimensions</i>	95.89 × 90.17 × 5.51 mm	95.89 × 90.17 × 5.51 mm	65 × 40 × 7.1 mm	89.15 × 92.13 × 15 mm	$\leq 90 \times 95 \times 20$ mm
<i>Mass</i>	130 g	61.9 g	24 g	53 g	≤ 100 g

TABLE II: Comparison of commercial OBDH boards.

The block diagram of the OBDH module outlines its basic structure and main components. The microcontroller is the centerpiece of such a system and has many design considerations, including the kind of communication interfaces and memory that will be implemented. Communication interfaces, including CAN, I²C, and SPI, are incorporated according to the protocols mandated by the sensors and subsystems. Furthermore, the module facilitates ADC, PWM, and DAC capabilities to enable external communication via a daughterboard. In this context, the OBDH is equipped with sensors such as a power sensor for monitoring power usage, a temperature sensor for evaluating internal environmental conditions, a magnetometer for collecting information about the satellite's orientation, and a gyroscope for measuring the angular motion of the satellite. All of these shall respect precision requirements. The satellite must also have internal communication with all the modules, for which the CAN bus and/or RS-485 will be used. Moreover, the system must have externally accessible interfaces for programming the microcontroller, for this a JTAG will be available. Other memory options such as SRAM and Flash/FRAM are selected based on the capability of the microcontroller for internal storage. If internal memory is not sufficient in the microcontroller, more external memory can also be added to handle the data efficiently. Finally, a watchdog timer is added to enhance the system's reliability and security against robust operations over the entire mission, according to the system's requirements.

As mentioned above, the selection of a microcontroller depends on the requirements of the module and the mission, which demands a balance between processing capacity, flexibility and robustness. One of the requirements mentioned is that the processor has a 32-bit architecture, in this view, some processors used in commercial OBDHs and CubeSat missions have been compared that have this architecture. All content are detailed in TABLE III.

This process has shown that the cheapest version of the SmartFusion2 model was chosen to save costs, provided it meets the required specifications. SmartFusion2 M2S005 combines an Field-Programmable Gate Array (FPGA) with a

32-bit ARM Cortex-M3 processor. This combination provides a great deal of flexibility in terms of hardware customization.

In contrast, the STM32H747/757 delivers enhanced computational capabilities owing to its dual-core design, which incorporates both a Cortex-M7 core and a Cortex-M4 core. The TMS570LS3137 Hercules is distinguished by its notable characteristics, including a dual lockstep processor and supplementary security features; however, it is characterized by a higher power consumption [27].

C. EPS

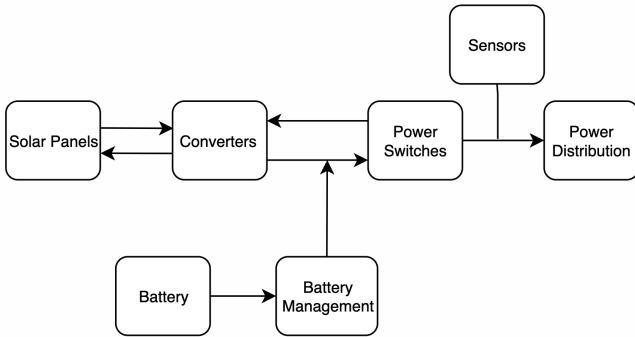
The Electrical Power System (EPS) function is the heart of a CubeSat. It is the module responsible for channeling the energy generated by the solar panels to the payloads that operate the satellite. However, this process involves several stages. Starting with the energy received by the panels, there are methods that can be employed to redistribute this energy with the highest possible efficiency, thus ensuring the proper functioning of the CubeSat. Once this is established, the power module also requires protection, both for the battery and for itself and the payloads.

The use of components that safeguard our system against overcurrent, overvoltage, and overload is indispensable for any project related to this subsystem. For the system's charging, components are required to manage the battery charging process, from monitoring its state to controlling the energy flow from the supplying source and regulating voltage and current based on the monitoring performed. For the interaction of the energy generated by the panels with the subsystems connected to the EPS, the voltage applied to them must be regulated. To achieve this, DC-DC converters must be selected to fulfill this task. With all this in mind, system telemetry must also be implemented to monitor the magnitude of the current and voltage data in the battery regulation system and the subsystem regulator. This data will be read by a processing center that may or may not be located within the EPS. If it is within the EPS, it becomes necessary to choose a microprocessor that will handle communication with each of the sensors. A figure of a base EPS block diagram can be seen on Fig. 4.

Processor	SmartFusion2 M2S005	TMS570LS3137 Hercules	STM32H747/757
Manufacturer	Microchip Technology	Texas Instruments	STMicroelectronics
Architecture	Hard 166-MHz 32-Bit ARM Cortex-M3 based SoC FPGA ~60 mW	ARM Cortex-R4F 32-Bit RISC CPU	480 MHz fCPU on the Cortex-M7 and 240 MHz on the Cortex-M4
Power consumption		700 mA	Unknown
Interfaces	CAN, 2xSPI, 2xI ² C, UART, USB, Ethernet	CAN, I ² C, UART, Ethernet	2xCAN, 6xSPI, 4xI ² C, 4xUART, 2xUSB, Ethernet
Memory	128 KB eNVM, 64 KB eSRAM, Total RAM 191Kbit	3MB Flash, 256KB RAM, 64KB Flash for Emulated EEPROM	1 to 2 Mbytes of Flash memory; 1 Mbyte of user SRAM; 192 Kbytes TCM RAM; 864 Kbytes of Backup SRAM and 4 Kbytes of Backup SRAM
Operating temperature	-40 to 125 °C	-40 to 125 °C	-40 to 125 °C
CubeSat missions use	IDEASSat, ArcticSat	Aalto-1, CubeBug-1 and -2	Unknown
Commercial OBDH use	Kryten-M3 [21]	UNISAT-7 [26]	EnduroSat OBC [20]

TABLE III: Comparison of the selected microcontrollers.

Fig. 4: Simplified EPS diagram.

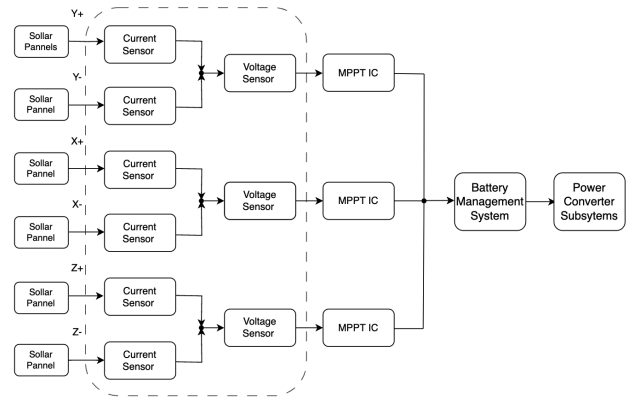


The third-generation of the EPS for FloripaSat platform is in its initial design phase, with a focus on defining its architecture. As part of this, the power management system is being conceptualized, requiring a decision on the power distribution method for the satellite. The chosen power regulation method is Maximum Power Point Tracking (MPPT), known for its reliability in CubeSats where solar panels and batteries might not be ideally matched. This is often the case as solar panel size is typically constrained by the satellite's dimensions [28]. With the power regulation method established, the next step involves selecting the components that will form the interface between the solar panels and the battery. In the pursuit of components to implement MPPT, options include custom-designed converters (as in the FloripaSat-2 platform), commercial converters, or dedicated MPPT-capable ICs.

With the aim of improving reliability and performance, a comparative study was made, and for the new platform, two possible MPPT-capable ICs were quoted: SPV1040 and LT3652. SPV1040 is a charge module with a 3×4 mm footprint that operates in a range of 0.3-5.5 V, with an MPPT algorithm and a PWM frequency of 100 kHz. It protects itself and the other circuit components from overcurrent and overvoltage, but it does not have protection for undervoltage, which is a problem when the panels are connected in parallel, as pointed out by the ESTCube-1 mission [29]. This problem can be avoided by an ideal diode system. The other option, LT3652, is a more feature-rich integrated circuit. It has

temperature sensing, overvoltage, and overcurrent protection, just like the SPV1040, but it also includes native undervoltage protection and has a 3×3 mm footprint [30]. An IC MPPT system is represented in the Fig. 5.

Fig. 5: MPPT circuit diagram.



The same way that the system's input converters are important, the output converters are equally vital, as they are responsible for supplying power to the other CubeSat modules. The EPS 2.0 incorporated several output converters from the TPS family, for example the TPS5420QDRQ1. The TPS converters utilized in the EPS 2.0 employ an asynchronous architecture, which while offering cost and implementation advantages, may exhibit lower efficiency compared to synchronous alternatives such as the LTC3833 step-down controller. Furthermore, the LTC3833 controller features radiation tolerance [31] [32], a notable characteristic for components destined for integration into a CubeSat. A significant departure from the previous platform to the new one lies in the battery monitoring circuitry. Previously, this circuit resided on the EPS 2.0 board, managed by a DS2777G+. In the new platform, battery monitoring will be integrated directly onto the system's battery board itself.

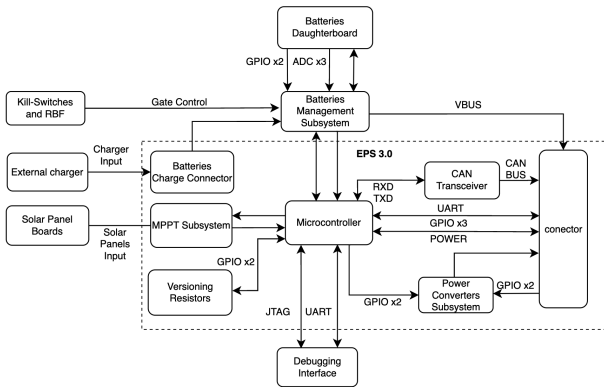
This reallocation potentially frees up valuable space on the EPS board for other components or functionalities. In the development of the next-generation EPS platform, a key decision was made to upgrade the microcontroller from the legacy MSP430 to a modern Cortex-M0 architecture. This transition

aims to enhance the EPS's capabilities in terms of processing power, energy efficiency, and peripheral integration. While the MSP430 has served reliably in previous EPS iterations, its limitations in processing power and peripheral integration presented challenges in meeting the complex requirements of modern satellite missions.

The Cortex-M0, with its 32-bit architecture and higher clock speeds, offers significantly enhanced processing capabilities, enabling faster execution of power management algorithms and real-time data processing [33]. Moreover, the Cortex-M0's power management features and sleep modes translate to improved energy efficiency, crucial for extending the satellite's operational lifetime. Additionally, the Cortex-M0's peripheral set, including high-resolution ADCs, timers, and communication interfaces such as CAN, simplifies the EPS. The ability to communicate via CAN is particularly crucial as it is a requirement for all modules in this platform, ensuring seamless integration and data exchange. This upgrade to the Cortex-M0 microcontroller in the EPS platform represents a significant step forward, enabling the EPS to meet the increasingly demanding requirements of modern satellite missions, ensuring reliable power management, and contributing to the overall success of the mission.

The preliminary block diagram of the EPS module can be verified in Fig. 6.

Fig. 6: Block diagram of EPS.



IV. DISCUSSION: TRENDS AND DIRECTIONS

A key aspect of FloripaSat-3's evolution was reassessing the technologies and standards used in previous missions, particularly FloripaSat-2. This transition reflects a clear trend towards adopting more advanced and reliable components. The replacement of outdated elements with newer, more robust technologies demonstrates a shift in focus towards enhancing the overall performance and longevity of the platform.

One of the main changes was the introduction of the CAN protocol for communication between subsystems. This decision was driven by the need for more robust and fault-tolerant communication compared to I²C, which was identified as a vulnerability in high-interference environments.

Another crucial adaptation was the change in connection standards. The use of RS-485 and RS-422 buses, replacing

previous options (UART), will provide greater resistance to noise and improved signal integrity. This choice was based on performance analyses in adverse conditions, showing significant improvements in the reliability of internal satellite communications.

Additionally, an important change was the replacement of the PC-104 interface, widely used in previous versions like FloripaSat-2. The PC-104 interface had several disadvantages, including limited expansion capacity and compatibility issues with new modules. Its rigid architecture and reliance on a specific stack of modules made system reconfiguration challenging for different missions, limiting the flexibility needed for new experiments and technologies. In response, FloripaSat-3 adopted a more modular and flexible approach using dedicated connectors for each interface, allowing easy integration of new components and system customization according to mission requirements.

An additional innovation in FloripaSat-3 is the development of an in-house designed RF chain. While the overall design and architecture are developed by the team, the project leverages commercial components, such as the PA, LNA, and transceivers. This approach allows for a custom optimization tailored to specific mission needs while benefiting from the proven reliability and performance of off-the-shelf components. The internally designed RF circuit offers the flexibility to adjust specifications and functionalities as required, ensuring efficient and high-quality performance.

Moreover, the design methodologies discussed underscore the growing need for modularity and flexibility in satellite projects. The trend towards developing modular systems that can be easily adapted or upgraded in response to technological advancements or mission requirements is indicative of the industry's future direction. This approach not only addresses current trends but also paves the way for innovations like the potential reuse of components in different missions or in-orbit upgrades.

Ultimately, the FloripaSat-3 development team actively sought to incorporate open standards and best industry practices, including guidelines such as ECSS, to ensure that the platform meets mission requirements while contributing to the broader advancement of CubeSat technology. In line with them, the selection of components prioritizes automotive-grade parts, whenever possible with flight heritage and radiation resistance. This focus ensures that the components used in FloripaSat-3 can withstand the harsh conditions of space, contributing to the overall reliability and longevity of the satellite.

V. CONCLUSION

FloripaSat-3 introduces a systematic design approach aimed at improving the reliability and robustness of its predecessor FloripaSat-2. The modular architecture of FloripaSat-3 allows for easier integration of new technologies and components, providing adaptability for future missions. Through its open-source framework and adherence to industry standards, the platform promotes wider accessibility and collaboration within the CubeSat community, supporting both educational and research-driven projects.

The transition from the previous FloripaSat-2 platform to FloripaSat-3 involves several key upgrades aimed at improving performance and reliability. The new platform replaces outdated communication protocols with the CAN protocol. It also moves from a rigid PC-104 interface to a modular system with dedicated connectors, enhancing flexibility and integration. These changes, along with the adoption of custom RF circuits and the use of modern standards and components, collectively advance the platform's capabilities and operational efficiency.

ACKNOWLEDGEMENTS

To all students, researchers, professionals and institutions that directly or indirectly collaborated with this work: Brazilian Space Agency (AEB), National Council for Scientific and Technological Development (CNPq) and Coordination for the Improvement of Higher Education Personnel (CAPES).

REFERENCES

- [1] R. Funase, S. Ikari, R. Suzumoto, N. Sako, M. Sanada, and S. Nakasuka, "On-orbit operation results of the world's first cubesat xi-iv—lessons learned from its successful 15-years space flight," in *Proceedings of the 33rd Annual AIAA/USU Small Satellite Conference*, 2019.
- [2] The CubeSat Program, *CubeSat Design Specification*. California Polytechnic State University, San Luis Obispo, CA - EUA, rev 14 ed., July 2020. Available at: <<http://www.cubesat.org/>>.
- [3] J. Bouwmeester and J. Guo, "Survey of Worldwide Pico- and Nanosatellite Missions, Distributions and Subsystem Technology," *Acta Astronautica*, vol. 67, pp. 854–862, 2010.
- [4] S. Wu, W. Chen, C. Cao, C. Zhang, and Z. Mu, "A multiple-CubeSat constellation for integrated earth observation and marine/air traffic monitoring," *Advances in Space Research*, vol. 67, no. 11, pp. 3712–3724, 2021. Satellite Constellations and Formation Flying.
- [5] M. E. Grøtte, R. Birkeland, E. Honoré-Livermore, S. Bakken, J. L. Garrett, E. F. Prentice, F. Sigernes, M. Orlandić, J. T. Gravadahl, and T. A. Johansen, "Ocean Color Hyperspectral Remote Sensing With High Resolution and Low Latency—The HYPPO-1 CubeSat Mission," *IEEE Transactions on Geoscience and Remote Sensing*, vol. 60, pp. 1–19, 2022.
- [6] J. Schoolcraft, A. Klesh, and T. Werne, *MarCO: Interplanetary Mission Development on a CubeSat Scale*, pp. 221–231. Cham: Springer International Publishing, 2017.
- [7] G. M. Marcelino, S. Vega-Martinez, L. O. Seman, L. Kessler Slongo, and E. A. Bezerra, "A critical embedded system challenge: The floripasat-1 mission," *IEEE Latin America Transactions*, vol. 18, no. 02, pp. 249–256, 2020.
- [8] G. M. Marcelino, A. M. P. de Mattos, J. C. E. Barcellos, B. F. Ribeiro, L. O. Seman, E. M. Filho, and E. A. Bezerra, "Floripasat-2: An open-source platform for cubesats," *IEEE Embedded Systems Letters*, vol. 16, no. 1, pp. 77–80, 2024.
- [9] Space Technology Research Laboratory (SpaceLab), *FloripaSat-II Documentation*, 2023. Available at <<https://github.com/spacelab-ufsc/floripasat2-doc>>.
- [10] Y. M. d. Silva, "DESENVOLVIMENTO DE UMA METODOLOGIA INTEGRADA DE PROJETO PARA CUBESAT: UM ESTUDO DE CASO DO PROJETO CIMATELITE," B.S. thesis, Federal University of Santa Catarina, Joinville, SC, Brazil, 2024.
- [11] E. C. for Space Standardization (ECSS), "Space engineering - technical requirements specification," Tech. Rep. ECSS-E-ST-10-06C, European Cooperation for Space Standardization, July 2009.
- [12] E. C. for Space Standardization (ECSS), "Space engineering - system engineering general requirements," Tech. Rep. ECSS-E-ST-10C, European Cooperation for Space Standardization, March 2009.
- [13] "Ieee standard for system, software, and hardware verification and validation," *IEEE Std 1012-2016 (Revision of IEEE Std 1012-2012/ Incorporates IEEE Std 1012-2016/Cor1-2017)*, pp. 1–260, 2017.
- [14] C. A. Rigo, L. O. Seman, M. D. Berejuck, and E. A. Bezerra, "Printed circuit board design methodology for embedded systems targeting space applications," *IEEE Latin America Transactions*, vol. 18, no. 02, pp. 257–264, 2020.
- [15] J. Praks, M. R. Mughal, R. Vainio, P. Janhunen, J. Envall, P. Oleynik, A. Näsilä, H. Leppinen, P. Niemelä, A. Slavinskis, J. Gieseler, P. Toivanen, T. Tikka, T. Peltola, A. Bossler, G. Schwarzkopf, N. Jovanovic, B. Riwanto, A. Kestilä, A. Punkkinen, R. Punkkinen, H.-P. Hedman, T. Sääntti, J.-O. Lill, J. Slotte, H. Kettunen, and A. Virtanen, "Aalto-1, multi-payload cubesat: Design, integration and launch," *Acta Astronautica*, vol. 187, pp. 370–383, 2021.
- [16] EnduroSat, "Uhf transceiver ii," <https://www.endurosat.com/products/uhf-transceiver-ii/>, 2024.
- [17] ISISPACE, "Isis uhf downlink vhf uplink full duplex transceiver," <https://www.isispace.nl/product/isis-uhf-downlink-vhf-uplink-full-duplex-transceiver/>, 2024.
- [18] GomSpace, "Nanocom ax100," <https://gomspace.com/shop/subsystems/communication-systems/nanocom-ax100.aspx>, 2024.
- [19] D. L. Thomsen III, T. M. Jordan, L. Milic, and W. Girard, "Shielding considerations for cubesat structures during solar maximum," in *37th Annual Small Satellite Conference*, 2023.
- [20] EnduroSat, "Onboarding computer," <https://www.endurosat.com/products/onboard-computer/>, 2024.
- [21] "Kryten-m3," <https://www.aac-clyde.space/what-we-do/space-products-components/command-data-handling/kryten-m3>, 2021.
- [22] GOMSpace, "Nanomind a3200," <https://gomspace.com/shop/subsystems/command-and-data-handling/nanomind-a3200.aspx>, 2024.
- [23] A. Scholz, J.-N. Juang, P. Mader, J. Schlegel, and M. Starcik, "Spacecan - a low-cost, reliable and robust control and monitoring bus for small satellites," *Acta Astronautica*, vol. 161, pp. 1–11, 2019.
- [24] F. C. Bruhn, N. Tsog, F. Kunkel, *et al.*, "Enabling radiation tolerant heterogeneous gpu-based onboard data processing in space," *CEAS Space Journal*, vol. 12, pp. 551–564, 2020.
- [25] F. Bruhn, K. Brunberg, J. Hines, L. Asplund, and M. Norgren, "Introducing radiation tolerant heterogeneous computers for small satellites," in *2015 IEEE Aerospace Conference*, (Big Sky, MT, USA), pp. 1–10, IEEE, 2015.
- [26] Gauss, *UNISAT-7*, 2021. Available at <<https://www.gaussteam.com/products/onboard-computer/hercules/>>.
- [27] S. Vartanian, G. R. Allen, F. Irom, A. Daniel, and S. Zajac, "Single event effects results for cots microcontrollers and microprocessors," *2023 IEEE Radiation Effects Data Workshop (REDW) (in conjunction with 2023 NSREC)*, 2023.
- [28] J. Campbell and F. Udrea, "Mppt techniques for cubesat electrical power systems," 2013.
- [29] M. Ustav, M. Pajusalu, M. Klevtis, J. Praks, R. Kuuste, T. Eenmäe, and I. Koppel, "Design and pre-flight testing of the electrical power system for the estcube-1 nanosatellite," *Proceedings of the Estonian Academy of Sciences*, vol. 64, no. 2S, pp. 201–210, 2015.
- [30] S. A. Kimura, H. Wijanto, Edwar, F. F. A. Rafsanjani, H. Prananditiya, and A. A. Ichwan, "Development of the electronic power subsystem design for tel-usat," 2019.
- [31] D. Figueiredo, "Reliability enhanced electrical power system for nanosatellites," Master's thesis, Federal University of Santa Catarina (UFSC), Florianópolis, SC, Brazil, 2023.
- [32] T. Cook, N. Franconi, B. Shea, C. Wilson, B. M. Grainger, and A. D. George, "Radiation-tolerant, gan-based point of load converters for small spacecraft missions," in *Small Satellite Conference*, 2018. Accessed: 2024-09-14.
- [33] K. V. C. K. de Souza, Y. Bouslimani, M. Ghribi, and T. Boutot, "On-board computer and testing platform for cubesat development," *IEEE Journal on Miniaturization for Air and Space Systems*, vol. 4, no. 2, pp. 199–211, 2023.



LATIN AMERICAN CUBESAT WORKSHOP SALVADOR, BR

DOI: 10.1234/example-doi-01

Orbit analysis and design for an academic satellite

Raphael Bolsonaro Guilherme¹ and Maria Cecilia Pereira¹

¹UFMG

Abstract

Meticulous orbit design is one of the critical success criteria for CubeSat missions, particularly for PdQSat, which aims to validate a commercial Li-S battery and an academia-developed supercapacitor through in-flight testing. This research identifies and analyzes suitable operational orbits for PdQSat, considering critical factors such as orbital decay time, data transmission capacity, and power budget from solar panel energy generation. The Systems Tool Kit® software enables a comprehensive analysis of various orbital scenarios to determine the effects of orbit altitude and inclination angle on selected mission parameters. The extensive simulations and analyses provide a summary of key findings that demonstrate the feasibility and effectiveness of different orbit configurations for PdQSat. It is evident that orbits ranging from 400 to 700 km in altitude, with varying inclinations, offer favorable conditions for the mission's objectives. These orbits strikingly balance mission duration, communication capabilities, and energy viability, thus ensuring the necessary flexibility in selecting a suitable launch vehicle to meet the mission requirements. Moreover, the validation of mission parameters is a crucial step in the study. The study defines protocols for assessing orbital decay, data and link budgets, as well as solar panel power generation, which are robust enough to verify the performance and viability of the mission. These validation procedures not only confirm the initial mission design but also allow for ongoing assessment and refinement throughout the project's progress. The study, by identifying optimal operating orbits and establishing validation procedures for mission parameters, lays a solid foundation for the success of the PdQSat mission. The results of this research not only promise

very likely success but also provide valuable insights and guidelines for future CubeSat missions, offering a more systematic approach to orbit design and mission validation. Consequently, the mission parameters and procedures established and validated in this study become invaluable tools for ensuring that the PdQSat mission is conducted efficiently and effectively. Implementing these findings enables mission planners to make informed decisions regarding orbit selection, launch vehicle compatibility, and mission duration, maximizing the likelihood of mission success. In conclusion, the objectives set for this study have been affirmatively met.



LATIN AMERICAN CUBESAT WORKSHOP SALVADOR, BR

DOI: 10.1234/example-doi-02

Geometric Design, construction and characterization of a prototype structure for a 3U CubeSat satellite

Sarah Rodi Thomaz¹, Natasha Caroline Santos de Souza¹, Marcelo Greco¹, Maria Lúcia Machado Duarte¹, and Maria Cecilia Pereira¹

¹UFMG

Abstract

In this research, we explore the design and analysis of a basic structure for a 3U Cubesat. Currently, structures with comparable specifications are often imported at costs that can be prohibitive for public universities. As an alternative, we consider the internal development of these structures. The primary goal of this study is to create an affordable structure, utilizing joints and screws, to lower manufacturing costs and enhance accessibility for academic institutions. Our focus is on PdQSat, a 3U Cubesat under development at the Federal University of Minas Gerais. The design proposed here is flexible and can be easily adapted for Cubesats of different sizes, including 2U and 1U. Our work includes three-dimensional structural design, static structural analysis, buckling analysis, evaluation of natural resonance frequencies, and the creation of technical drawings for manufacturing. We conducted structural analyses using various aluminum alloys, namely 7075-T6, 6063-T5, and 6061-T6, each providing satisfactory results. After considering the budget and prioritizing manufacturing cost and reliability, we chose a combination of aluminum 7075-T6 and 6063-T5 to construct an initial prototype for testing. We assessed the natural resonance frequencies through various tests to gather more information about the structure. These tests included random vibration testing, vibration tests at 200 Hz—simulating the likely launch frequency—and 20 Hz, as well as tests using an impact hammer. It is important to note that the manufacturing cost of the proposed structure

is up to six times lower than that of commercially available counterparts with similar specifications. This significant cost reduction underscores the viability and economic benefits of internal development for academic institutions engaged in Cubesat projects. The designed structure meets the launch and operational requirements set by Cubesat Design Requirements, Rev. 14, and aligns with the specifications of the PdQSat project.

Progress Report: FlatSat Platform for GOLDS-UFSC and Future Missions

Carlos Augusto Porto Freitas[✉],
 Eduardo Dutra Bitencourt[✉],
 João Cláudio Elsen Barcellos[✉],
 Gabriel Mariano Marcelino[✉], and Eduardo Augusto Bezerra[✉]

Abstract

CubeSats are small satellites, known as "nanosatellites," that are used for Earth observation, scientific research, and remote sensing applications. Despite their growing popularity, CubeSat missions usually suffer from a significantly high failure rate. To address the issues encountered in CubeSats, a more rigorous verification and validation (V&V) process of the system can be adopted, using a FlatSat. A FlatSat is an electrical model of the satellite with the subsystems mounted side by side on a workbench. This approach is gaining popularity in small satellite applications due to its ability to integrate and test systems at a level that would otherwise be complex and error-prone. An example of a FlatSat platform is the one developed at SpaceLab/UFSC for testing the FloripaSat family of satellite platforms. This FlatSat was designed to be highly configurable, capable of testing and monitoring CubeSat subsystems, reading operation data, and injecting faults into communication buses. However, the FlatSat platform itself has not yet been fully tested, and no full satellite mission has been developed using it. This paper presents the initial exploration of the platform, starting with basic electrical testing and progressing to reading real data from a CubeSat subsystem. The tests are divided into three parts: (i) first, electrical and power tests are performed to validate the physical structure of the FlatSat board; (ii) then, the MicroZed is attached for initial design validation and on board sensor tests; (iii) finally, satellite's subsystems are connected to conduct temperature and current reading tests, as well as interface with a subsystem simulation application running on MicroZed. To carry out these tests, embedded Linux and the MicroZed's programmable logic are used, providing a highly reconfigurable and versatile platform for testing and data acquisition. This configuration allows for future expansion of FlatSat functionality, including more complex applications than those initially envisioned. The first part of the tests aims to create a validated and secure environment for implementing the MicroZed and satellite modules, as well as conducting their tests. These tests are designed to simulate CubeSat operational conditions, and the results aim to validate the basic use of FlatSat, paving the way for future applications.

Index Terms

Embedded Systems, CubeSats, FloripaSat-2, Verification and Validation (V&V), FlatSat.

I. INTRODUCTION

The space industry's small satellite development has grown explosively over the years, in particular CubeSats, which are nanosatellites, with lower cost and complexity, played a important role in it [1]. Because of these characteristics, CubeSats have shown great importance in the area of technology demonstration and in-orbit validation [1]. In addition, these satellites are widely used in student-driver missions, contributing to student training while fostering technological and scientific development [2].

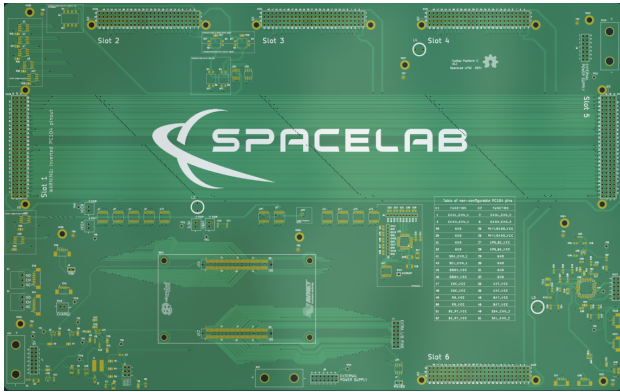
Even though these satellites can be developed relatively fast and inexpensively, numerous issues can arise both during development and throughout their mission. For instance, launch-related mechanical failures, software bugs, and radiation-induced faults are just a few of the potential complications. To mitigate these, an extensive Verification and Validation (V&V) campaign can be used [3], which employs various methods to validate the system against likely and unlikely scenarios, observing its behavior in a way to identify vulnerabilities.

One valid option for the V&V campaign is the usage of a FlatSat, which is an electrical model of the satellite, where the satellite's subsystems are assembled and connected side by side over a workbench [4]. Such platforms, according to [4], have grown in popularity among small satellite applications. FlatSats provide a broad view of the system operability,

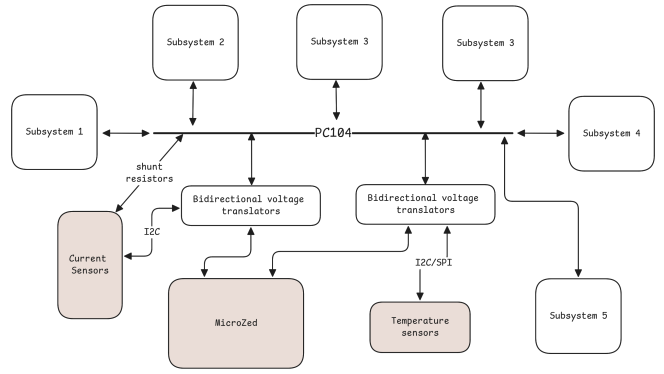
easing the V&V process from both the hardware and software perspective, they allow the early detection of some of the problems mentioned previously, as seen in [5], [6]. For instance, software bugs and system-level integration testing can be quite complex and error prone without proper testing instrumentation, especially if the team lacks experience, as it happened in FloripaSat-1 [7] V&V campaign.

During Latin American CubeSat Workshop (LACW) 2022, a FlatSat was proposed at [8] with the aim of aiding the development of satellites at the SpaceLab laboratory at the Federal University of Santa Catarina. The project support up to six subsystems, including service modules and payloads, interfacing with a MicroZed [9] and build-in circuits for sensing, monitoring and controlling the system. The aim of the MicroZed is to make it possible to simulate the inputs and outputs of satellite modules in order to observe the response of a dispositive under test. Figure 1 describes how the project is architected.

In order to utilize the FlatSat implementation proposed by [8] to its full potential, with similar functionality to an Electrical Ground Support Equipment (EGSE), there is a need to validate the platform itself. This first step aims to create a validated and secure environment to actually conduct tests and is composed of the basic electrical validation of the Printed Circuit Board (PCB), which includes checking for design and



(a) FlatSat2 Platform



(b) Architecture diagram

Fig. 1: FlatSat Architecture

fabrication flaws, checking the power circuitry operation and evaluate the built-in sensors of the board.

Following the platform validation, the plan is to attach a satellite subsystem to collect real operation data, specifically ambient temperature and current measurements. Naturally, a subsystem will need to communicate with other subsystems, which will be simulated by the MicroZed. The MicroZed will also collect data from the onboard sensors and store it to further processing and analysis. Additionally, subsystem data obtained from the simulated communication the MicroZed will also be presented.

As said previously the platform has yet to be tested and, currently, there is no application developed for it, thus conducting this initial exploration is necessary to validate the basic functionality of the proposed FlatSat. This study paves the way for more complex applications, including EGSE-like operation, furthermore, it also allows the platform usage for testing GOLDS-UFSC and future missions, enhancing their V&V campaigns.

The remaining of this work is organized as follows. In Section II, the methodology used to validate and collect data of the FlatSat is described. The process of testing, validating and collecting operational data of the platform are described in detail in Section III. Additionally, obtained results are also discussed in Section III. Further discussions and directions are shown in Section IV. Finally, in Section V, conclusions are presented.

II. METHODOLOGY

Taking in account the aforementioned objectives, a test flowchart becomes necessary, mainly to ensure result validity for each test and to provide an overall test suite organization. In addition, it also helps to avoid possible unrelated sources of error interfering with the results. The flowchart can be seen at Figure 2. The tests follow the SpaceLab's methodology for initial subsystem testing, which can be seen at [10], [11], additionally they also follow the European Cooperation for Space Standardization (ECSS) testing standard [12] when applicable.

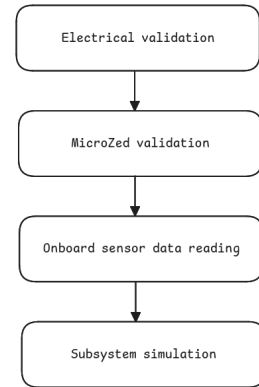


Fig. 2: Tests flowchart

A. Electrical validation

The electrical validation process of the PCB is essential for identifying manufacturing and assembly errors, such as short circuits, open circuits, poor soldering and missing components. It also helps uncover design flaws that could lead to permanent damage to connected modules or cause malfunctions. Initially, considering the need to guarantee this safety, continuity and connection inspection tests were carried out in order to validate the design and manufacture of the board [12]. To do this, all the connections on the board were tested using a multimeter, along with the design schematic (in order to check that the connection is consistent with what was planned). After this first stage, it was possible to carry out power and signal tests along the board, i.e. to ensure that the power supply and the signal applied to the FlatSat are able to reach all the expected points [12]. To carry out this experiment, stimuli was applied via the power supply bench and then the voltages at the expected points were measured using a multimeter and an oscilloscope.

B. MicroZed validation

As mentioned earlier, the FlatSat has a MicroZed embedded in its design, this addition extends quite a lot the functionality of the platform. However, the System on Module (SOM) has to

be tested before the integration with the board, as to eliminate any possibility of hardware failures unrelated to the FlatSat. Testing it also involves booting the SOM with an embedded linux operating system as well as the Zynq's Programmable Logic (PL) design. Those were used for all operations of the MicroZed, such as simulating subsystems or collection sensor data.

Choosing Linux as its operating system was done mainly for future use, as Linux provides a highly customizable system with a very large ecosystem of libraries, device drivers and packages. By using it, development time is reduced, especially as application complexity grows towards an EGSE-like functionality.

Next, the MicroZed was integrated into the platform, and its operation reevaluated to identify any errors introduced by the FlatSat design. Once any present errors are addressed, the test suite can progress to collecting data from the onboard sensors. This next step intends to only verify the basic functionality of the sensors and its communication with the MicroZed, since a more thorough test is done later in a real operation setting, with satellite subsystems integrated to the FlatSat.

C. Functional tests with real subsystems

Following the test suite, the GOLDS-UFSC mission's Electrical Power System (EPS), named as EPS 2.0, was connected to the FlatSat as a representative subsystem. Being part of the FloripaSat-2 platform, proposed in [13], this subsystem has been thoroughly tested in the previous FlatSat version and during integration tests with the Engineering Qualification Model (EQM) of GOLDS-UFSC satellite.

As a well known module, the usage of it as a testing reference facilitates the validation of the FlatSat, since its usual behavior is already documented.

After the EPS validation step, it was possible to test the sensors in a real setting. In this sense, the Environmental Data Collector (EDC), proposed in [14], was used as a payload. As is the case with EPS, EDC has been thoroughly tested and has a well known behavior, since it is the main payload for the GOLDS-UFSC mission [13] and was also tested with the EQM.

The test aims to collect readings from the built-in sensors and verify its accuracy and feasibility. In it, there were two measurements being collected concurrently, one being ambient temperature readings by the TMP112 [15] sensor and the other one being EDC current consumption readings using the INA219 [16]. Measurements of the EDC current were also made using a Keithley DMM6500 digital multimeter [17] to serve as a reference.

Lastly, the test suite's final test aims to collect real operation data from the EPS, by simulating the FloripaSat-2 platform OnBoard Data Handling (OBDH) module [13] through the MicroZed. During simulation, the SOM gathered the available telemetry data obtained by mimicking OBDH commands in the EPS's Inter Integrated Communication (I2C) interface.

The OBDH simulation was running simultaneously with the measurements from the previous test, so that the EPS telemetry data could be compared with the platform's built-in sensors data. Performing both tests concurrently served

to assess MicroZed's ability to handle multiple applications running simultaneously, which will be used extensively in future works.

Furthermore, having access to the satellite communication busses allows the FlatSat's usage for communication and fault injection analysis as done in [18], as well as to do a performance characterization of the bus like the one made in [5]. Therefore, the proposed test also serves to evaluate the feasibility of conducting these intricate tests and analysis.

III. IMPLEMENTATION & RESULTS

In order to test a system, in this case the FlatSat platform, it is imperative to build a sequence of operations that are consistent with the system and the related objective. For this article, the test flow described at Figure 2 was followed.

A. Electrical Tests

With a view to electrical validation and the safety of the other devices, the first step was to ensure that there were no short circuits within the power systems and then to investigate the signal connections on the board. To carry out both steps, an inspection was carried out using a multimeter and the original schematic of the board. As a result, it was possible to find several short circuits in the voltage translators, as well as one between one of the input voltages and ground. These problems were caused during the soldering stage of the FlatSat components, making it necessary to remove excess solder flux and replace some of the voltage translators.

After ensuring that FlatSat was electrically coherent with what had been developed, it was necessary to check the routing on the board, so that it would be possible to understand and analyze how it worked. An inconsistency was found in relation to the board's purpose: the pinouts related to the communication protocols were not consistent with those found on Zynq's available peripheral controllers for the Processing System (PS), making it impossible to use the board for these protocols via PS. In order to continue testing the rest of the board, access via PL was used.

Finally, with regard to the system's power system, there were two problems in the circuit, one relating to the Power_Enable power input, making it necessary to use an external source to supply 3.3V directly. While the other one was a misdirection of the Zynq's IO banks enable pin, which is an output signal generated by the SOM, however, the FlatSat circuitry considered this signal to be an input, therefore, to avoid any issues, this part of the power circuitry was not populated.

B. MicroZed Setup

After making sure that the platform's power circuitry and the SOM itself work as intended the next step is to create a custom embedded linux image and hardware design. For that, it was used Xilinx's Petalinux and Vivado Design Suite tools. Using Vivado, a simple hardware design was made, which basically routes the relevant peripherals, like the I2C controllers, to the sensors and subsystems interfaces.

For the Programming System (PS) side of Zynq, a custom embedded linux was made, which includes essential libraries,

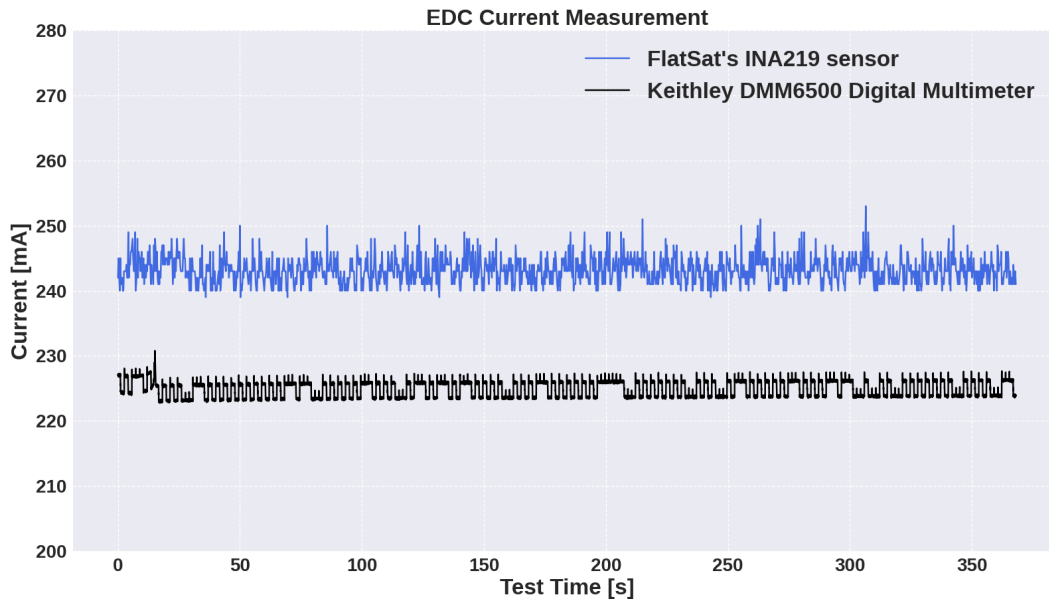


Fig. 3: EDC current test readings.

device drivers for the FlatSat sensors, custom services and user applications. The image includes a sensor reading service, which provide a simple interface to enable specific sensor readings, manage log files, etc. Furthermore, it also have a application for OBDDH simulation that communicates with EPS, requesting its telemetry periodically.

With the SOM configured and working individually, it was attached to the FlatSat aiming to test the software applications, also serving as a preliminary test for the onboard sensors. To assess the INA219 functionality and the sensor reading service, resistors and one light emitting diode (LED) were connected to the power busses of the platform, which were powered by a digital power analyzer. Additional resistors were added in 30 second intervals, as to change the current drawn by the LED and test the responsiveness of the current sensor.

The results came in as expected, the service was able to read data from the onboard sensors, which includes temperature measurements from the TMP112 and current, bus voltage, shunt voltage and power measurements from the INA219. At this stage, it was discovered an issue regarding current readings, which had a greater inaccuracy as the drawn current gets smaller, particularly when the current is less than 10 milliamperes (mA). This happens mainly due to the device driver resolution, which only provides measurements that are integer multiples of milliamperes, therefore changes on current of less than 1 mA will most likely be unnoticed. More discussions about measurement adequacy are made at subsection III-C.

C. Functional Tests

As per the test suite, a test setup was made to allow the execution of functional tests with real subsystems, these will involve mainly the EDC and EPS subsystems, both having well documented behaviors, which aids the validation process of the FlatSat. A diagram describing the setup can be seen at Figure 4, for simplicity the diagram does not include the power

connections besides the 5V payload bus, which is produced by EPS.

Both EPS and EDC were powered by a lithium-ion battery, being the same as the one used in the GOLDS-UFSC mission satellite. As for the MicroZed and the onboard sensors, they were powered by a digital power analyzer connected to FlatSat's power circuitry, which had to be adapted due to the problems described at subsection III-A.

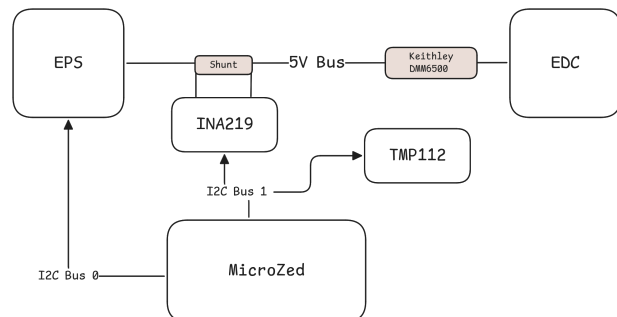


Fig. 4: Test setup diagram.

As stated in Section II this setup is used for two tests to run simultaneously, where the first one is composed of current measurements to monitor EDC power consumption, taken in 250 millisecond intervals by both the INA219 and DMM6500, and the second consists of reading EPS telemetry and TMP112 data every three seconds.

The EDC consumption results can be seen at Figure 3. The consumption itself is in line with EDC's datasheet [19] and the one observed during tests of GOLDS-UFSC mission. By looking at the chart it becomes clear that the INA219 readings, represented by the blue curve, have quite a bit of deviation from DMM6500's reference readings, with the largest sample to sample deviation being of, approximately, 27

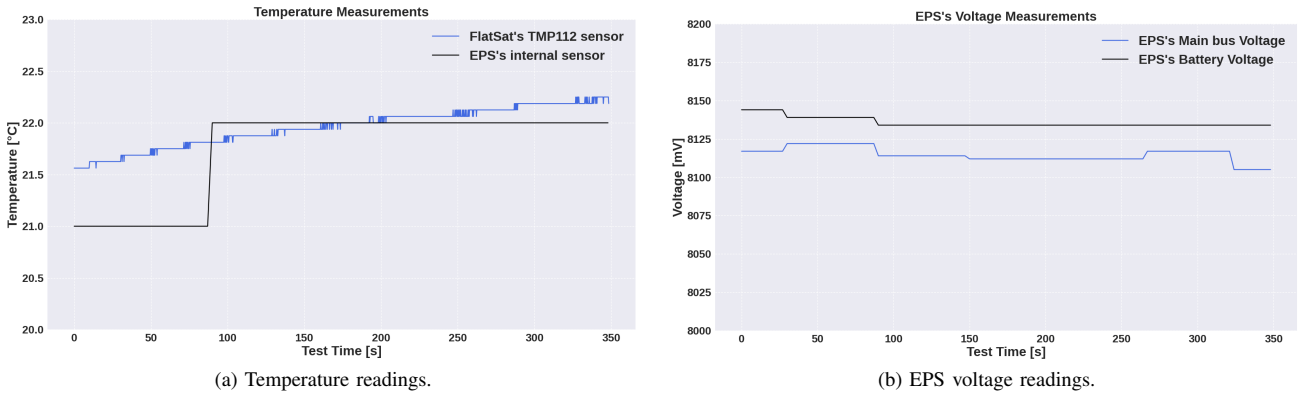


Fig. 5: Subsystem simulation readings.

mA, the lowest 13 mA and the average 18 mA, which represent 10.81%, 5.37% and 7.51% of relative error, respectively.

This difference can be explained by driver details and overall precision difference between the devices. As discussed previously, the INA219 driver used, which is the linux kernel device driver for INA2xx devices [20], can only provide integer multiples of milliamperes, moreover, it also sets a default calibration configuration on the sensor, those two factors can explain the deviation seen at Figure 3.

To mitigate this, a custom device driver can be made to provide a runtime calibration configuration and microampere reading resolution. However, that would be quite time consuming and would require a specific analysis to determine whether it is justified. After all, if a highly precise reading is imperative to the test, using the DMM6500 or a similar device directly would be a preferred approach.

Concurrently to the EDC consumption test, the MicroZed had a running application that simulates OBDH data requests to EPS and was collecting ambient temperature readings. The application simulates OBDH data requests using its own firmware drivers and tasks [21] developed to communicate with EPS, minor modifications had to be done at the low level interfaces due to OBDH running FreeRTOS as an operating system, as opposed to the MicroZed running embedded linux. The data requests were composed of battery voltage, main bus voltage and temperature, all accessible in the EPS parameter table [11] through its I2C interface.

A graphic containing both the ambient temperature from TMP112 and EPS microcontroller temperature measurements can be seen at Figure 5a. The purpose of the comparison is to quantify the difference of temperature experienced by EPS and the actual ambient temperature. This difference is relevant not only to understand the heat produced by the board, but also to verify the behavior of the subsystem, since it takes in to account the current temperature to enable specific modules. By looking at the Figure 5a, it becomes clear that the exposed temperature parameter is an integer value, nevertheless, it still allows for a rough estimate of its behavior, which, in this case, resembles very much the ambient temperature readings from TMP112.

As for the voltage parameters from Figure 5b, both mea-

surements are obtained directly from EPS and represent the FlatSat's capability to track the system's parameters and facilitate behavioral analysis of all available data, which can be used to perform more sophisticated tests, as described in subsection II-C. The readings themselves are not that interesting, since the test time was about 6 minutes and, for a good understanding of the battery behavior over time, much more time would be needed, moreover, charge measurements would be better for that type of test as opposed to voltage ones. An interesting result taken from the Figure 5b is to observe the power loss due to the EPS circuitry, which manifests in the voltage drop between battery voltage and main bus voltage.

IV. DISCUSSIONS AND DIRECTIONS

This article developed a test suite in order to do a follow up of the work presented at LACW 2022 [8], in particular, it aims to perform the initial validation of the proposed FlatSat.

As the test suite was carried out, the validation importance became apparent, specially the electrical validation, which, if had not been done, would result in several functional issues and could cause permanent damage to the platform components. In addition, the schematic reassessment was also critical to the tests, since it unveiled routing issues that would hinder MicroZed's ability to communicate with the subsystems.

For the validation's software side, the decision to start with embedded linux has facilitated considerably the application and service development, it also eased testing them. Furthermore, the flexibility that a linux based operating system brings has allowed the applications and services to be integrated in a much simpler way, which will be crucial to the platform as new tests and services get added.

Moreover, effort on developing these new features are already being made. Examples of them are: adding an internal database to MicroZed, as well as a cloud based one, to organize test data, extending the simulation application to replicate more subsystems, adding support to other sensors, MicroZed remote access through Secure Shell (SSH), among other software applications. Extending hardware capabilities of the platform through daughter boards is also planned, with a major example being a board to interface other connector types with the PC104.

V. CONCLUSION

This article presented the beginning of the V&V process of the FlatSat platform proposed by [8]. In addition, applications and services were developed to utilize the platform's built-in features.

A overall design revision was made, including a schematic review, in which both problems and improvement points were found. For instance, the MicroZed routing and FlatSat's power circuitry will have to be corrected in the next version of the platform.

Moreover, an effort to test and validate the platform's onboard capabilities, specially the MicroZed and sensor integration, was carried. It covered both the hardware and software side, starting with electrical tests of the platform, passing to basic software applications embedded in the SOM, to, finally, collecting real operation data from both onboard sensors and real CubeSat subsystems.

From obtained results, it was possible to see that the addition of onboard sensors and the MicroZed provides much more data retrieving capabilities to the platform, which eliminate the need to rely on the subsystem's sensors to monitor the whole system's behavior. Even though the sensors accuracy have some caveats, like in the INA219 case, it, nevertheless, can be useful for estimates and overall monitoring. In addition, MicroZed's presence provide a wide range of possibilities, including test automation and subsystem simulations, which will be explored in order to enhance V&V campaigns for future missions.

Finally, lessons learned and future directions were discussed. As addressed throughout this work, the FlatSat has a great potential for aiding V&V campaigns, however, there still much effort to be done to realize that potential, for that, possible additional features to be developed were presented. Furthermore, the project of the platform is open source and can be found at: <https://github.com/spacelab-ufsc/flatsat-platform2>.

ACKNOWLEDGEMENTS

The authors want to acknowledge that this work was supported by CNPq/Brazil (National Council for Scientific and Technological Development - <http://www.cnpq.br>), and by AEB (Brazilian Space Agency - <http://www.aeb.gov.br>).

REFERENCES

- [1] A. Poghosyan and A. Golkar, "Cubesat evolution: Analyzing cubesat capabilities for conducting science missions," *Progress in Aerospace Sciences*, vol. 88, pp. 59–83, 2017.
- [2] R. M. Millan, R. von Steiger, M. Ariel, S. Bartalev, M. Borgeaud, S. Campagnola, J. C. Castillo-Rogez, R. Fléron, V. Gass, A. Gregorio, D. M. Klumpar, B. Lal, M. Macdonald, J. U. Park, V. Sambasiva Rao, K. Schilling, G. Stephens, A. M. Title, and J. Wu, "Small Satellites for Space Science: A Cospar Scientific Roadmap," *Advances in Space Research*, vol. 64, pp. 1466–1517, 2019.
- [3] J. Bouwmeester, A. Menicucci, and E. Gill, "Improving CubeSat reliability: Subsystem redundancy or improved testing?," *Reliability Engineering & System Safety*, vol. 220, p. 108288, 2022.
- [4] J. C. E. Barcellos, A. W. Spengler, L. O. Seman, R. D. C. e Silva, H. P. Roldán, and E. A. Bezerra, "Flatsat platforms for small satellites: A systematic mapping and classification," *IEEE Journal on Miniaturization for Air and Space Systems*, 2023.
- [5] J. P. Monteiro, R. M. Rocha, A. Silva, R. Afonso, and N. Ramos, "Integration and Verification Approach Of ISTRSat-1 CubeSat," *Aerospace*, vol. 6, p. 131, 2019.
- [6] J. Praks, M. R. Mughal, R. Vainio, P. Janhunen, J. Envall, P. Oleynik, A. Näsilä, H. Leppinen, P. Niemelä, A. Slavinskis, *et al.*, "Aalto-1, Multi-Payload CubeSat: Design, Integration and Launch," *Acta Astronautica*, vol. 187, pp. 370–383, 2021.
- [7] M. G. Mariano, F. E. Morsch, M. S. Vega, D. M. A. M. Pio, S. L. Oriol, S. L. Kessler, and B. E. Augusto, "Qualification and Validation Test Methodology of the Open-Source CubeSat FloripaSat-I," *Journal of Systems Engineering and Electronics*, vol. 31, pp. 1230–1244, 2020.
- [8] J. C. E. Barcellos, B. F. Ribeiro, A. W. Spengler, L. O. Seman, and E. A. Bezerra, "Development of a flatsat platform for golds-ufsc and future missions," in *Companion Book of the IAA Latin American CubeSat Workshop*, 2022.
- [9] MicroZed, *FY23_800_MicroZed_Product_Brief_r2*. Avnet, 2022. Available in: https://www.avnet.com/opasdata/d120001/medias/docus/209/FY23_800_MicroZed_Product_Brief_r2.pdf.
- [10] SpaceLab, "OBDH2 User Manual." https://github.com/spacelab-ufsc/obdh2/blob/master/doc/user_manual/slb-obdh2-doc-v0.10.pdf, 2022.
- [11] SpaceLab, "EPS2 User Manual." <https://github.com/spacelab-ufsc/eps2/blob/master/doc/slb-eps2-doc-v0.4.pdf>, 2023.
- [12] ECSS Secretariat, "ECSS-E-ST-10-03C – Testing," Technical Report TBD, ECSS-ESTEC, May 2022.
- [13] G. M. Marcellino, A. M. P. de Mattos, J. C. E. Barcellos, B. F. Ribeiro, L. O. Seman, E. Morsch Filho, and E. A. Bezerra, "Floripasat-2: An open-source platform for cubesats," *IEEE Embedded Systems Letters*, 2023.
- [14] K. Queiroz, S. Dias, J. Duarte, and M. Carvalho, "Uma solução para o sistema brasileiro de coleta de dados ambientais baseada em nanosatÉlites," *HOLOS*, vol. 7, pp. 132–142, 12 2018.
- [15] TMP112, *TMP112x High-Accuracy, Low-Power, Digital Temperature Sensors With SMBus and Two-Wire Serial Interface in SOT563 (Rev. I)*. Texas Instruments, 2018. Available in: <https://www.ti.com/lit/ds/symlink/tmp112.pdf>.
- [16] INA219, *INA219 Zero-Drift, Bidirectional Current/Power Monitor With I2C Interface (Rev. G)*. Texas Instruments, 2015. Available in: <https://www.ti.com/lit/ds/symlink/ina219.pdf>.
- [17] DMM6500, *DMM6500 6½-Digit Bench/System Digital Multimeter*. Keithley, 2022. Available in: https://download.tek.com/datasheet/1KW-61315-1_DMM6500_Datasheet_050924.pdf.
- [18] C. A. Conceicao, F. Mattiello-Francisco, and C. L. Batista, "Dependability verification of nanosatellite embedded software supported by a reusable test system," in *2016 Seventh Latin-American Symposium on Dependable Computing (LADC)*, pp. 157–163, 2016.
- [19] E. D. Team, "doc." https://gitlab.com/edc_team/doc, 2022.
- [20] L. Felten, *Kernel driver ina2xx*, 2024. Available in: <https://docs.kernel.org/hwmon/ina2xx.html>.
- [21] SpaceLab, "obdh2." <https://github.com/spacelab-ufsc/obdh2>, 2024.


The NASCERR Mission – An University/Private Sector Cooperation with Cubesat

1st Jarbas Silveira 

Dept. of Teleinformatics Engineering
Federal University of Ceara
Fortaleza, Brazil
jarbas@lesc.ufc.br

2nd Otavio Durão

CRON – Sistemas e Tecnologias Ltd
São José dos Campos, Brazil
otavio@cronsistec.com.br

3rd Edilson Filho 

Dept. of Teleinformatics Engineering
Federal University of Ceara
Fortaleza, Brazil
edilsonfilho@lesc.ufc.br

4th Alexandre Almeida

Dept. of Teleinformatics Engineering
Federal University of Ceara
Fortaleza, Brazil
alexandre.almeida@lesc.ufc.br

5th Nicolas Araújo

Dept. of Teleinformatics Engineering
Federal University of Ceara
Fortaleza, Brazil
nicolas@ufc.br

6th João Baptista

Federal University of Santa Maria
Santa Maria, Brazil
batista@inf.ufsm.br

7th Valter Schad

Horuseye Tech
São José dos Campos, Brazil
horuseye@horuseye.com.br

8th Luiz Henrique Laurini

Université Grenoble Alpes (UGA)
Grenoble, France

9th Rodrigo Possamai

Université Grenoble Alpes (UGA)
Grenoble, France

Abstract—NASCERR stands for Radiation Hard Electronics Nanosatellite (Nanosatélite Com Eletrônica Robusta à Radiação, in Portuguese). It was proposed and accepted in a call issued by the Brazilian National Research Council – CNPq for Brazilian universities and public research institutes for the development of CubeSats and their equipment/subsystems. One of the requirements of the call was the mandatory participation of private companies in the proposal and development of the CubeSat. Qualification testing at these levels will be performed at the Integration and Testing Lab (LIT) of the National Institute for Space Research (INPE). The CubeSat will communicate with ram frequencies and its coordination is being requested by IARU. It is a 2U cubesat where 1U holds the bus and the other U is for the payloads. NASCERR, as required by the CNPq call, is a cooperation between the university and Brazilian companies. The attitude determination and control subsystem, the solar panels, the electronic power subsystem, the structure, and the onboard and ground software were developed by these companies, while the onboard computer, the transceiver, and the onboard antenna set were imported. All the subsystems were already either delivered or contracted with delivery within the coming six months. Students from UFC and UFSM participate in the project with scholarships from its budget. Only a proto-flight model will be developed. Qualification testing at these levels will be performed at the Integration and Testing Lab (LIT) of the National Institute for Space Research (INPE). The CubeSat will communicate with ham frequencies and its coordination is being requested to IARU. This is the first CubeSat mission managed and developed by UFC. The mission was presented to the Brazilian Space Agency and its Space Mission Selection and Acceptance Process – ProSAME for habilitation in the official space mission portfolio of the country. The schedule of the call

requests the cubesat be ready for delivery to launch by the end of 2025. Launching and ground station and operation are not included in the CNPq provided budget. The NASCERR launch is planned to 2026. This is the first CubeSat mission managed and developed by UFC. The paper presents the CubeSat's operating range, electrical schematics, and other technical details.

Index Terms—radiation hardening, public/private cooperation, cubesat use, experiments.

I. INTRODUCTION

This project results from a public call (CNPq/MCTI/FNDCT N° 19/2022) from the National Council for Research - CNPq to develop cubesat space missions. It required that Brazilian research groups team up with Brazilian companies for its development. The proposal put together different research and experienced groups in electronics and computer systems applied to space, with new technological companies dedicated mostly to space projects. It involved three states in Brazil distant hundreds of kilometers from each other in the country's South, Southeast, and Northeast. And one French group associated with the two research groups. NASCERR (Radhard Electronic Nanosatellite) [1] is a 2U technological Cubesat with 1U dedicated to the platform and the other U to the experiments. The platform is modular and used in the nanoMIRAX mission¹, from the National Institute for Space Research – INPE like LECX[2] mission.

The NASCERR mission is the continuation of the work done by these research groups in other Brazilian CubeSats

Acknowledgment: This study was financed in part by CNPq and partially supported by Fundação Cearense de Apoio ao Desenvolvimento Científico e Tecnológico (FUNCAP) under grant ITR-0214-00041.01.00/23.

¹http://www.das.inpe.br/publicacoes/pdfs/braga_mirax.pdf

and an opportunity to test in space other components and equipment developed by them with radiation hardening to improve the reliability of CubeSats and their useful life in space.

II. PAYLOADS

The NASCERR project consists of four experiments: (i) ROBOC – Robust On-Board Computer; (ii) Radiation Hard Error-Correcting Code; (iii) Implementations of Machine Learning (ML) Algorithms; and (iv) an amateur point-to-point radio communication software, now in its third version, after the first two flew in other Brazilian cubesats. Of the four experiments, the first three involve hardware and software integration, while the last is predominantly a software experiment. The overall architecture of Nascerr can be seen in Figure 1

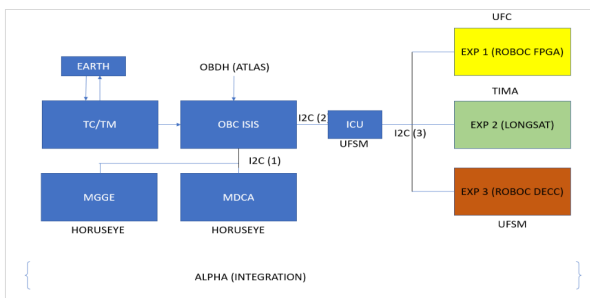


Fig. 1. NASCERR Architecture.

A. ROBOC – Robust On-Board Computer

ROBOC aims to study and validate dynamic error correction code (ECC) algorithms for protecting data in external memory. The NASCERR implementation uses a SmartFusion2 025 FPGA from Microsemi. An RTL was developed in SystemVerilog to implement the described ECC models, ensuring that all operations requested by the processor to the memory are handled transparently. This means that, when reading from or writing to memory, the processor is unaware that the data is passing through the FPGA, which acts as a "Man-in-the-Middle." The entire communication process happens invisibly to the processor, maintaining system performance without any interference.

As illustrated in Figure 2, the FPGA intermediates the communication between the main processor and the SRAM. Every time the processor writes data, the FPGA encodes it using an ECC, generating redundant bits. The DATA + redundancy set is then stored in the SRAM. When the data is read again, the FPGA reads the set, decodes the data using the ECC, corrects any detected errors, and then passes the corrected data back to the processor. This process occurs without introducing additional latency, as the operation is conducted using only combinational circuits, ensuring that the MATM (Man-in-the-Middle) block does not degrade the read and write performance to external memory. The ECC mechanism implemented in NASCERR is not only responsible for detecting errors but also for correcting them, working to

prevent information loss by correcting errors according to the capabilities of each ECC algorithm.

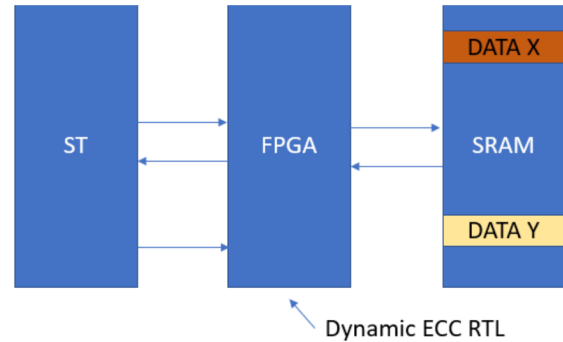


Fig. 2. Dynamic ECC protection in SRAM

The MATM block implemented on the FPGA supports up to four modes of operation: (i) without ECC; (ii) MRSC; (iii) eMRSC; and (iv) TBEC-RSC.

- The MRSC (Matrix Region Selection Code) is an efficient and low-cost error correction code (ECC) for microcontroller units (MCUs) that uses a 2-D parity encoding scheme. It divides data bits into regions and utilizes logic equations to pinpoint error locations, implementing a region selection algorithm (RSA). This code corrects up to two-bit errors per data word and handles several adjacent error patterns with lower synthesis costs compared to other robust ECCs.
- The eMRSC (Extended MRSC) extends the original 16-bit version of the MRSC to a new 32-bit format. It offers two code versions: one with a lower increase in redundancy and another with higher correction capability. The eMRSC introduces a new data matrix region scheme that reduces the number of redundant bits generated, providing a tradeoff between area, power overhead, and reliability.
- The TBEC-RSC (Triple Burst Error Corrector based on Region Selection Code) is a 2-D ECC scheme mapped onto a 1-D physical structure. It builds on the MRSC algorithm but with modifications to enhance its error correction efficacy, particularly for burst errors. The TBEC-RSC is designed to correct 100% of triple burst errors and more than 40% of eight-bit burst errors. The code has been tested with 16-bit data, but it can be easily extended to larger base-2 data words, such as 64 bits.

Each of the four modes of operation of the MATM block can function either in a static or dynamic manner. In static mode, the experiment's software, running on the main processor (ST Processor), selects the protection mode to be used. In dynamic mode, the MATM block automatically chooses the most ap-

appropriate mode based on pre-set criteria. For instance, if the number of errors within a given time window exceeds a certain threshold, the algorithm with the highest correction capability will be selected. Otherwise, an algorithm with lower correction capability, which uses less redundancy, will be chosen. It is important to note that algorithms with higher correction capacity require more redundant bits, which increases data overhead in the SRAM. Therefore, memory efficiency criteria can also be selected, resulting in data protection that is tailored to system needs.

B. Radiation Hard Error-Correcting Code

1) *Radiation Problem in Integrated Circuits:* Over the past decade, TID² radiation [3] hardening in commercial CMOS technology [4] [5] has been evolving rapidly due to the continuous reduction of gate oxide thickness. However, there is no guarantee that the same level of radiation tolerance among different manufacturers will work for the same technology node, since radiation hardening is not a factory-monitored parameter. In addition, TID effects for a given CMOS technology are closely linked to the exact gate oxide thickness, the imperfection levels in the SiO₂ insulation region, etc. Unfortunately, these parameters are usually not modeled in CMOS devices, which makes predicting the radiation impact of a CMOS circuit very difficult. They are often not disclosed by the manufacturer, which complicates the modeling of radiation effects at the semiconductor level. Therefore, in addition to choosing a more advanced CMOS technology for radiation-hardened designs, RHBD techniques [6] are also required in the circuit to ensure its reliability and performance even under extreme radiation levels. RHBD techniques can be used throughout the design phase of a CMOS chip. In general, they can be separated into four hierarchical levels: system level, circuit level, device level, and layout level. See Figure 3.

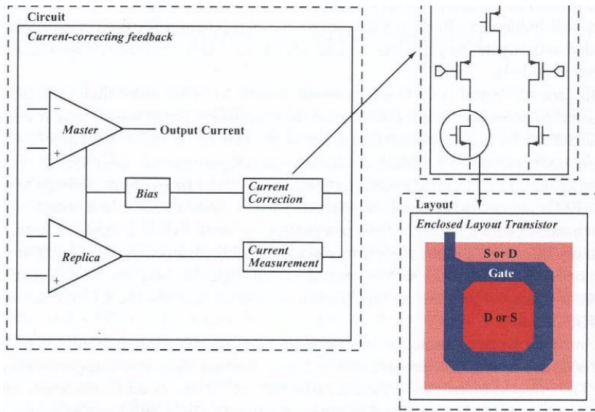


Fig. 3. Dynamic ECC protection in SRAM

A) System Level

²TID (Total Ionizing Dose) effects refer to the cumulative damage caused to electronic devices by prolonged exposure to ionizing radiation, impacting their performance and reliability over time.

RHBD at the system level is the most effective way to ensure radiation hardening of an electronic device. When an electronic system is required to perform certain functions in a radiation environment, the first consideration should be to choose a system structure that provides the highest radiation tolerance. A good example is the selection of an analog-to-digital converter (ADC) suitable for radiation-tolerant applications [7]. ADCs have various architectures, such as flash, pipeline, successive approximation (SAR), dual-slope integration, and Sigma-Delta. For a given specification in terms of resolution, power consumption, and dynamic range, all these types of ADCs may be suitable. However, they have different radiation tolerance levels. Commercial ADCs from different manufacturers were compared to verify their performance against gamma radiation. Interestingly, a tested Sigma-Delta ADC (ADS 1210) showed a higher level of radiation tolerance (about 25 kGy) when an external reference voltage is used for it (if the internal bandgap circuit is used to provide a reference voltage, the converter will fail after reaching 200Gy). Flash ADCs are more vulnerable to the TID effect.

b) Circuit Level

Although there is adequate radiation tolerance at the system architecture level, radiation-induced failures can occur at the circuit level, as in the case of the bandgap circuit of the Sigma-Delta ADC. Therefore, radiation-sensitive components throughout the system must be identified and ensured that they can achieve the required radiation tolerance level. Due to this, RHBD techniques must be applied at the circuit level. As an example, an RHBD approach is presented at the circuit level to improve the radiation hardening of a CMOS VCSEL driver. The driver is implemented in 0.7 μ m CMOS technology. Radiation induces changes in the threshold voltage of the MOS transistor in the driver, causing a change in the VCSEL current. This is addressed with a current feedback mechanism for correction, as shown in Figure 4. The purpose of this feedback circuit is to maintain a constant current through the VCSEL. An extra replica of the driver is employed to reproduce the same current. The replica and main drivers are identical devices, so any performance changes in the main driver due to the effects of TID will be reflected in the replica device as well. A control loop continuously monitors this process to keep the output current constant.

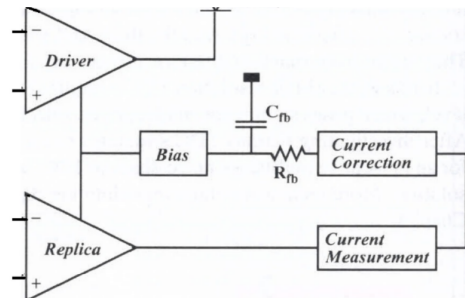


Fig. 4. ELT transistor and its geometric parameters

c) Device Level

RHBD at the device level addresses radiation hardening issues by choosing appropriate transistor types and geometries (width and length) in the implementation of CMOS circuits. For example, in older CMOS technologies, PMOS transistors are preferred for radiation-tolerant designs, since varying the threshold voltage causes only performance changes rather than functional failures. Furthermore, TID effects in a transistor have dependencies on the geometry in which it is designed.

d) Layout Level

RHBD techniques at the layout level have proven to be very effective in eliminating the latch-up effect and preventing radiation-induced leakage currents. One example is the Enclosed Layout Transistor (ELT) technique for very high radiation hardening applications. An ELT has a closed gate design, which separates the drain and source regions of a CMOS transistor. An ELT is shown in Fig 5. This design eliminates the parasitic transistors that were originally located on two edges of a conventional CMOS device. The radiation-induced leakage current of the MOS transistor is greatly reduced. The main drawbacks of the ELT transistor are increased area and greater difficulty in electrical modeling.

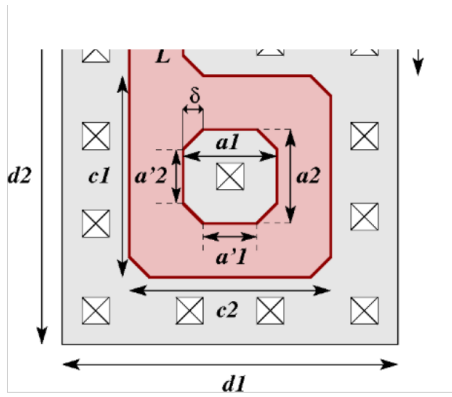


Fig. 5. ELT transistor and its geometric parameters

2) Radiation Hard Cell Library: The Santa Maria Design House (SMDH) project linked to the Federal University of Santa Maria has developed a radiation hard digital cell library (SMDH-RH) using RHBD techniques for the standard 180nm XFAB CMOS technology. The library is presented in 5 types with 24 cells for each library type, as shown below. RH (Radiation Hard) library type with 24 cells each:

- library typical voltage: 1.8v; temperature: 25c;
- slow library with voltage: 1.62v; temperature: -55c;
- slow library with voltage: 1.62v; temperature: 125c;
- fast library with voltage: 1.98v; temperature: -55c;
- fast library with voltage: 1.8v; temperature: 125c

Cells contained in the libraries are the following: ANTEN-NACELLRH3: "protection cell against antenna effects (net charge) at manufacture, PIMP diode in NWELL", see Table I and Figure 6.

TABLE I
CODE PIN ANTENNA

BURHX1: "Buffer X1"	BURHX2: "Buffer X2"
BURHX4: "Buffer X4"	DECAPRH3: "DECAP cell"
DFFRHRSX1: "negedge D-Flip-Flop with Reset and Set"	DFRRHX1: "posedge D-Flip-Flop"
DLHRHX1: "high active transparent D-latch"	DLYRH2X1: "Delay cell, typical 1ns"
EORH2X1: "2-Input XOR"	FEEDRH1: "FEED cell"
INRHX1: "Invert"	INRHX2: "Invert"
INRHX4: "Invert"	LOGIC0RH: "Constant logic 0"
LOGIC1RH: "Constant logic 1"	MAJRH3X1: "3-Inputs Majority cell"
MURH2X1: "2:1 Multiplexer"	NARH2X1: "2-Input NAND"
NARH3X1: "3-Input NAND"	NORH2X1: "2-Input NOR"
NORH3X1: "3-Input NOR";	SDFRRHX1: "posedge D-Flip-Flop with Scan"
XDLHRHX1: "SEE hardened high active transparent D-latch"	

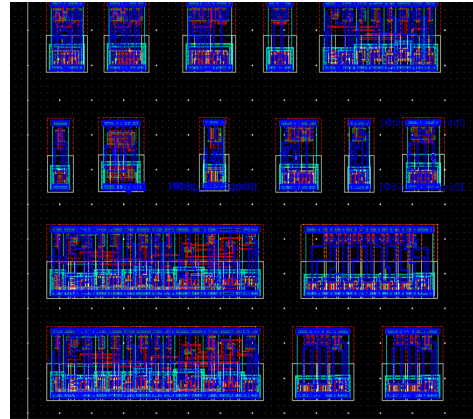


Fig. 6. Cell Design (XFAB 180nm Technology)

3) Error Correction Code (ECC) : In computing, telecommunications, information theory, and coding theory, an Error Correction Code (ECC) is a software-implemented technique used to control data errors in unreliable or noisy communication channels. This technique can be successfully used in the space environment. It is important to consider that systems need to be prepared for errors arising from radiation effects in the environment. The disturbances that occur can be detected and even corrected by ECCs depending on how they occur. The inversion of one or more bits can occur during transmission or storage within the memory. If the error is detected during transmission, but there is no way to correct it, simply retransmit. However, if data inconsistency is detected during memory reading, there is a need for correction, since there is no way to extract the information again from its source. One of the techniques used to protect memories applied in satellite OBCs is the use of ECC. The integrated circuit that performs the interface between the onboard computer and the memory can be an FPGA or a specific circuit prototyped for this purpose. An ECC is the circuit to be analyzed aiming at the development of a specific integrated circuit (ASIC) and robust to radiation since radiation-tolerant FPGAs are not used

in nanosatellites. Radiation-robust FPGAs have a very high cost.

C. Implementations of ML Algorithms

In the advent of new generations of electric self-driving cars, autonomous drones, airplanes, and satellites, artificial intelligence (AI) applications, and machine learning (ML) algorithms have been rising in popularity thanks to the constant technological evolution of electronic computing systems, autonomous taking decisions in situations that are usually of high risk in case of failure. Those applications necessarily face harsh environmental conditions, being considered safety-critical because unexpected failures in their systems may lead them to catastrophic situations such as a loss of navigation control, harming users and people around. Hence, computing systems and their sensors in safety-critical applications must safely and reliably operate under environmental perturbations by mitigating their harmful effects and minimizing risks for human beings and related surroundings, even under simple impacts of single subatomic particles released by radiation effects of cosmic rays coming from space to ground levels. In this context, several scientific challenges are raised. For instance, how reliable to radiation effects are the more and more complex firmware embedded in applications such as nanosatellites that usually are built with low-cost commercial-off-the-shelf (COTS) components? The Université Grenoble Alpes (UGA/TIMA) will design, implement, and test a nanosatellite payload board based on COTS components. The scientific goals of the UGA payload board are to assess the reliability of ML algorithms as well as attitude estimation (AE) algorithms facing low Earth orbit (LEO) radiation effects, correlating spaceflight-level results with data collected in ground-level accelerated radiation tests.

The actions for specifying, designing, implementing, testing, and reporting the UGA payload board were organized into 17 milestones/deliverables. The UGA payload board will be integrated into the Brazilian nanosatellite "NASCERR" planned to be launched by our international partners in 2026. The actions will be executed by 4 interns, 3 PhD students, a senior engineer, and a professor. The procedures for performing the UGA payload board's scientific experiments and transmitting data from space to ground will be aligned with the University of Santa Maria (UFSM) team. Essentially, the on-board computing systems will be composed of software (firmware), ML and AE algorithms, and COTS components. One of the deliverables will be an interface control document (ICD) following the standards of space agencies.

D. Amateur point-to-point radio communication software

This is a point-to-point amateur radio communication software. It is an advanced version of the previous one that flew in ITASAT-1. The experiment consists of reception, storage, and retransmission of short (64 bytes maximum) text messages following the format: Origin—Locator—Destiny—Message, where the character "—" separates each field, and:

- Origin: Callsign of transmitter station (6 characters maximum);
- Locator: QTH Locator (6 characters maximum);
- Destiny: Callsign of receiver station (6 characters maximum).

To store a message, the satellite includes a date-hour field with the satellite hour such as: *Date-hour—Origin—Locator—Destiny—Message*. A station can request the last 20 messages for a certain destiny. The messages are stored in the memory of the satellite during a time interval and are deleted after this period. The experiment does not require any additional hardware to the platform or the other payloads.

III. PLATAFORM

The platform for the NASCERR cubesat will have a 2U structure (10cm x 10cm x 20cm) with 1U made available for the payloads described in the previous item and 1U made available for the service subsystems. Among these, five are developments made by national companies in the country for the project, and three are imported from companies that produce them abroad. Two of these can also be developed by national companies, but to mitigate further risks to the mission, they will be imported from companies that already produce them with significant space heritage.

A. Power Subsystem (MGGE)

Performs the following functions:

- Optimizes the transfer of the energy captured by the solar panels;
- Controls the distribution of energy to the system;
- Manages the generation, storage, and consumption of energy by the system;
- Makes all information available for processing by the main on-board system;
- Performs battery protection (voltage and current) by hardware and software;
- Allows the configuration of parameters inherent to battery charging and energy distribution;
- Controls the temperature of batteries by hardware and software.

The energy conversion of the solar panels is carried out by BOOST converters (voltage lifters) with MPPT (Maximum Power Point Tracking) operating mode. Each converter with two inputs for solar panels. It uses the MPPT operation to maximize the use of the energy that the panels can generate when the system needs to recharge the batteries and does not consume the full capacity of the panels. In this case, all excess consumption is directed to storage. The circuit operates in two MPPT modes: constant voltage and maximum power

Batteries are Lithium-ion with a total supply of 7.56 +/-0.2V and operating temperature between -20 and + 50 degrees Celsius. The circuit allows the change of the working voltage of the panel, around a default value, so that, according to previous configuration, it can operate in any mode. The working voltage value can be changed to constant voltage mode (microcontrol

dependent) by software. When there is no destination for the surplus energy that the panels can generate, the converter operates in constant voltage output mode, extracting from the panels only what the system needs.

Control is made with an Atmel microcontroller, ARM 32bits, M4, from the SAMG55 family, supported by several external function blocks, with high performance and low consumption. Operating frequency around 24MHz for minimum consumption, with external crystal for clock stability. Internal RTC for "time stamping" of operational analysis and availability of last event window with occurrence accuracy. External flash memory (IC2) with a capacity of 128kbytes, with an SPI interface.

B. Attitude Determination and Control Subsystem (MDCA)

It uses an Atmel microcontroller, ARM 32bits, M7, from the SAME70 family, supported by several external functional blocks, high performance with moderate consumption, being able to operate up to 300MHz of internal clock (use of the lowest allowable clock for processing for minimum consumption). It can completely turn off the microcontroller without loss of the onboard time reference. Memory capacity for internal flash code with at least 2 Mbytes and for work (internal RAM) at least 384 kbytes. Forecast for NOR flash with a capacity of 16 Mbytes and for two units of FRAM memories (SPI interface) with a capacity of 512 kBytes each, totaling 1 Mbyte of resource (IC2 and IC3). Interface for SD Card available on the microcontroller using external 8 kbyte E2prom (I2C interface). It communicates with the subsystem's internal attitude-sensing devices, through an SPI bus with several selector lines and an I2C Master bus, and with external devices or systems via I2C Slave bus, SPI bus, two asynchronous serial interfaces, one USB interface, and one CAN interface. Firmware load is done via the JTAG interface, accessed by JTAG connector.

It uses as attitude sensors a three-axis magnetometer and gyroscopes, both of the MEMS type (for reading in eclipse), and solar sensors, these placed in the CubeSat panels. As actuators, three torque coils, one air core, and two ferrous cores, are arranged on the two sides of the subsystem board. The air core coil and the ferrous core coils are mounted on opposite faces on the subsystem board, completing the control trihedron. The electronics are assembled in the space enclosed by the torque coils on the board. Configuration does not require the solar panels to have magnetic actuators and allows the determination of the attitude throughout the entire orbit.

It has a GPS receiver for onboard orbit determination. GPS antenna placed on the top face of the CubeSat. Orbit is obtained autonomously on board, without the need, for this definition, to receive the TLEs (two lines elements) obtained by the earth station via the internet through NORAD. The data read on board, from the platform and the payload, can be associated on board with the point in the orbit at which it was obtained and transmitted to the ground with this identification.

C. Transceiver, onboard computer and onboard antenna set

These three subsystems were imported from ISISpace for the reasons explained above. The transceptor was imported from ISISpace. It is a VHF uplink/UHF downlink full duplex transceiver that can operate in commercial amateur radio bands in the VHF/UHF frequency spectrum with flexibility of transmit rate and frequency change during flight. TMTC and Beacon are on the same board.

The data management module (OBDH) has an MSP430 20MHz ultra-low power microcontroller with I2C, UART, and SPI interfaces. With antenna release control and 2G bytes flash memory. It performs housekeeping operations and allows the management of payloads. Electronic components with flight heritage and with communication with the other modules. Includes the operating software and library.

The antenna system contains four ribbon spring antennas up to 55 cm long. The system has a thermal knife composed of a wire and two redundant heating elements per tape. RF phasing/BalUn circuits join the antennas in a spool configuration. Depending on the configuration, one or two radios in the CubeSat can connect to the antenna system via miniature RF connectors. The top face of the antenna system can accommodate a two-cell solar panel and can be customized to accommodate sensors or other systems that protrude outward. The antenna is compatible with any UHF and/or VHF radio system. It can be mounted on all the frames of the main suppliers of CubeSats frames on the market. For custom-made structures, that follow the standard CubeSat mechanical envelope, assembly is also possible.

D. Structure

2U aerospace aluminum alloy structure in 7075-T6 alloy with qualified corrosion protection for the environmental conditions of space and vibration at launch. Surface treatment (black sulfuric anodizing 16 to 20 microns); Worm shafts and screws in 304 stainless steel. Kill switch mechanisms to activate the opening of the on-board antennas in stainless steel 316 and aerospace aluminum 7075-T6. External dimensions (width X length X height) of 100 X 100 X 227 millimeters. Weight up to 400 grams.

E. Software

- Management of onboard data for the NASCERR flight model platform and communication with the platform's subsystems and payloads.
- Mission application software for acquiring and processing telemetry from the satellite and for formatting and sending telecommands to the satellite
- Integration of onboard software and mission application software.
- On-board computer interfaces and platform subsystems.
- On-board management software in binary format (installable).

F. Solar panels

Solar Panels for 2U Cubesat, in +-X, Y and Z with temperature sensor and solar with four solar cells assembly (SCA), except in Z where there are 2 SCA in each. Triple-junction solar cells, InGaP/GaAs/Ge, with spatial qualification by ECSS E ST20-08C standard for low orbit, mass between 80-90 mg/cm² and area between 26 and 27 cm². Efficiency greater than 29%, external by-pass protection diode and high radiation resistance.

IV. COORDINATION OF ATTENDANCE, LAUNCH AND OPERATION

The CubeSat will operate with amateur radio frequency in VHF (145.9 MHz) for uplink and UHF (436.5 MHz) for downlink. The main ground station will be in the campus of the University of Ceará – UFC. The auxiliary ground station will be located at the National Space Research Northeast Regional Center – INPE/CRN, in the city of Natal, RN. Both stations will be able both to send commands and receive telemetry from NASCERR, from the payloads and the platform performance data. Amateur radio stations around the globe will also be able to receive telemetry data and so track the CubeSat in its entire orbit. Therefore being an important auxiliary element to provide information about its health, performance, and operation planning.

The launch will be piggyback, All the experiments on board are independent of the orbital plane inclination angle. Thus, NASCERR may be suited to be launched from the Alcantara Launching Center, in Brazil, in low-inclination planes, if this launch site is available.

V. CONCLUSION

All the subsystems for the NASCERR platform are done and delivered. Those developed in Brazil were qualified at the Integration and Testing Laboratory of the National Institute for Space Research – LIT/INPE. Those imported have many hours in space. The payloads are being developed and are continuation or spin-offs from other projects and research. Due to their different requirements and complexities, they have different conclusion schedules but all are feasible within the mission schedule. This is mostly due to the foundry process of the hardware and the very tight schedule and lead time of the companies abroad that will be hired to do this process. Also, two payloads are interdependent and have to be developed partially in sequence. The mission software, both for on board and for the ground station are being developed with the participation of students from the Federal University of Ceará (UFC). The project sponsors these students. There are different options for the ground station at the UFC campus that are being studied.

NASCERR will be delivered for launch in 2025. Its launch is forecasted to 2026.

REFERENCES

- [1] Edilson Silva et al. “NASCERR: Nanosatellite with Electronics Radiation Robust”. In: *2024 International Conference on Global Aeronautical Engineering and Satellite Technology (GAST)*. IEEE. 2024, pp. 1–6.
- [2] João Braga et al. “LECX: a cubesat experiment to detect and localize cosmic explosions in hard X-rays”. In: *Monthly Notices of the Royal Astronomical Society* 493.4 (2020), pp. 4852–4860.
- [3] Federico Faccio et al. “TID and displacement damage effects in vertical and lateral power MOSFETs for integrated DC-DC converters”. In: *2009 European Conference on Radiation and Its Effects on Components and Systems*. IEEE. 2009, pp. 46–53.
- [4] Josua Florczak et al. “Radiation monitor extension for CMOS imaging instruments in nanosatellites”. In: *IEEE transactions on nuclear science* 69.7 (2022), pp. 1651–1658.
- [5] PE Dodd et al. “Current and future challenges in radiation effects on CMOS electronics”. In: *IEEE Transactions on Nuclear Science* 57.4 (2010), pp. 1747–1763.
- [6] A Balasubramanian et al. “RHBD techniques for mitigating effects of single-event hits using guard-gates”. In: *IEEE Transactions on Nuclear Science* 52.6 (2005), pp. 2531–2535.
- [7] Kai Chen et al. “Evaluation of commercial ADC radiation tolerance for accelerator experiments”. In: *Journal of Instrumentation* 10.08 (2015), P08009.

On-Board Image Processing inside the RaioSat Experiment Mission – Early Results and Suitability Tests

Jan Zurawski
Dept. Elec.Eng. and Info.Technology
University of Applied Sciences
Jena, Germany
jan.zurawski@stud.eah-jena.de

Sebastian Thaut
Dept. Elec.Eng. and Info.Technology
University of Applied Sciences
Jena, Germany
sebastian.thaut@stud.eah-jena.de

Lazaro Aparecido Pires Camargo
SmallSats Division
National Institute for Space Research
São José dos Campos, Brazil
lazaro.camargo@inpe.br

Antonio Cassiano Julio Filho
SmallSats Division
National Institute for Space Research
São José dos Campos, Brazil
cassiano.filho@inpe.br

Kleber Pinheiro. Naccarato
Meteorological Satellite and Sensor
Division
National Institute for Space Research
São José dos Campos, Brazil
kleber.naccarato@inpe.br

Walter Abrahão dos Santos
SmallSats Division
National Institute for Space Research
São José dos Campos, Brazil
walter.abrahao@inpe.br

Abstract— The RaioSat Experiment mission, coordinated by the Earth Science Coordination at the National Institute for Space Research (INPE) in Brazil, aims to monitor atmospheric discharges, also known as lightning flashes, using either a 6U CubeSat configuration or a piggyback configuration on a larger satellite. This mission will collect valuable data over the Brazilian territory, aiding in the analysis of correlations between lightning activity and extreme weather events. A critical component of this mission is the development and validation of an onboard computer (OBC) integrated with a CCD sensor for detecting and processing lightning flashes. The iOBC from ISISpace has been tested on this task.

In order to ensure the iOBC's suitability for the RaioSat mission, extensive testing is required, focusing on its processing speed and ability to handle the detection of lightning events using static images. This abstract outlines the methodology and results of these tests. The tests simulate the real-time conditions the iOBC will encounter in orbit, focusing on the processing of example pictures containing randomly generated lightning events.

The testing procedure involves generating synthetic images with varying densities and patterns of lightning events, reflecting potential in-orbit scenarios. The iOBC's processing capabilities are evaluated based on its ability to accurately detect and process these lightning events within the images. Key performance metrics include the processing time per image, latency, and accuracy of lightning detection.

Initial results indicate that the iOBC demonstrates very good accuracy and processing speed suitable for night-time detection of lightning events. However, during the day, the background noise is too heavy for effective real-life detection. To address this, an increase in processing speed is necessary for daytime operations. The current performance suggests that the iOBC may have the potential for further optimization to handle these conditions and contribute to a better understanding of extreme weather patterns in Brazil.

Keywords— *Cubesats, Lighting detection, On-board computing, Performance evaluation*

I. INTRODUCTION

The ability to predict and understand severe weather events has become an important task to monitor climate change and study earth system processes [1]. This task can be partly achieved by observations from space and by monitoring

lightning, which is associated with climatic events, such as storms and floods.

The RaioSat project intends to detect intra-cloud and cloud-to-ground lightning flashes simultaneously, the so-called total lightning data, using an optical sensor and a VHF antenna onboard a CubeSat platform [2]. This shows how lightning could be detected and monitored from space and is therefore an important part of climate change studies.

The project is an international research collaboration to assist in the development of the RaioSat satellite. Particularly, the aim is a performance evaluation of a compute platform for lightning detection in a CubeSat. Henceforth, this paper objective is to evaluate the usability of the on-board computer (OBC) iOBC by ISISpace for the project's image processing. This includes assessing the processing power of the OBC and the processing time needed for lightning detection. The images used for this will not be provided by an optical sensor, as intended in the project. For better replicability of the results jpg files are the chosen.

In order to determine this intention, a background subtraction and event detection algorithm will be implemented on the iOBC, as they will be crucial for the image processing of the RaioSat project. Determining whether the iOBC is usable for the mission or not, it is split into two steps as follows:

- Determining the best coding strategies on the iOBC: To determine the most efficient way to use the board, the most fitting coding strategy must be found out. For this purpose, the image processing algorithms will be measured in their processing time and optimised in their code. The optimal code then generates the best possible framerate as is the objective.
- Correlation of framerate and resolution: After finding the best available code for the image processing algorithms, the code can be measured on its processing time with different image resolutions. A higher resolution should correspond to longer processing times, giving an idea of which resolution corresponds to a framerate. As the camera and its resolution are yet to be determined, knowing this correlation can help with the selection process of the camera itself.

This document is organized as follows: section II presents the fundamental concepts; section III describes the approach and implementation; section IV outlines the measurements and evaluation; section V presents a project outlook, and section VI the conclusions.

II. FUNDAMENTAL CONCEPTS

This section will give a brief overview of existing technologies for lightning detection in space, as well as putting them into context with the RaioSat mission.

Previous technologies to detect lightning from space, GLM [3], LIS [4], LMI [5], used real-time event processing (RTEP), similar to the RaioSat mission. The difference is that the processing technologies' power consumption is bigger than those available for a CubeSat platform. Currently, there are no proven solutions for lightning detection in a CubeSat using commercial off-the-shelf components, justifying the objective of this work. In addition to RaioSat, the concept mission "CubeSpark", a 3D lightning mapper that uses multiple CubeSats, is currently under development at NASA Marshall Space Flight Center and Los Alamos National Laboratory [6].

A. Optical basics of lightning

To determine the hardware's useability, a target processing time and therefore a target framerate must be set. This chapter focuses on the critical timing of lightning in the context of its optical detectability, giving an idea for possible framerates. A lot of different factors weigh in the mentioned framerate. The time resolve desired by the research team for further analysis, which is not yet determined, and the resolve to differentiate between several kinds of lightning. One of the lightning types, Cloud-to-Ground-flashes (CG), has the most crucial characteristics for the time resolve, depending on the desired results. A CG-flash consists on an average of 4.6 pulses [7] with an amplitude high enough for optical detection. Each of those pulses last between $20 \mu\text{s}$ and 1.2 ms with an average of $422 \mu\text{s}$ [10]. In 95% of all flashes the interstroke time exceeds 13 ms [7].

A target framerate can only be given by requirements for lightning analysis and the other factors weighing into it, such as the requirements of other sensors or the expected background noise. To get examples of framerates only the described lightning characteristics were used in the following.

If the flash should be seen as a blinking event, the framerate must match the interstroke time twice to get a frame without pulse between two pulses. This would mean a resolve of $6,5 \text{ ms}$ or a framerate of 154 fps . A resolve for every pulse would mean to match the interstroke time with 13 ms and a framerate of 77 fps . to only resolve the whole flash with all pulses in one frame, the framerate can be set to approximately 26 fps . A simplified example of a possible CG-flash and the correlation with the framerates can be seen in Figure 1.

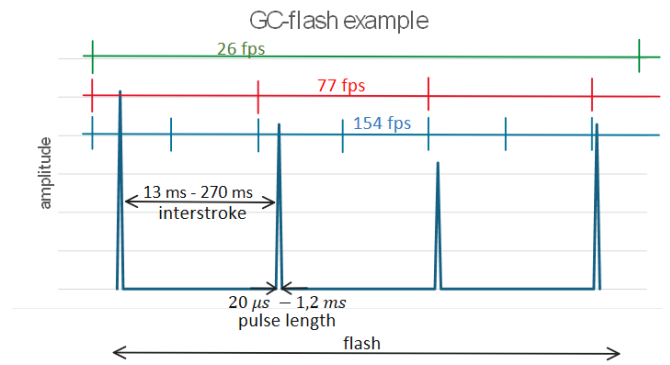


Fig. 1. CG-flash exemplary explanation on time resolve.

B. Background subtraction

Basic background subtraction is a method used to make changes visible in different pictures [8]. As the images are stored as single-pixel values, an iteration over every pixel can be performed, while each pixel will be subtracted from the background. Each pixel not subtracted to zero is a change in the picture. A simple example can be seen in Figure 2.

Image			Background			Mask		
33	33	33	33	33	33	0	0	0
33	150	33	33	33	33	0	117	0
33	150	33	33	33	33	0	117	0
33	33	33	33	33	33	0	0	0

Figure 2: Exemplary execution of a background subtraction.

The background image must be calculated dynamically to account for a moving camera and therefore a changing background. A computation structure similar to an IIR filter is implemented. Figure 3 shows that an incoming image is weighted and added to the weighted background from the last iteration. This sum is then subtracted from the incoming image to calculate the mask, which shows all the changes in the image.

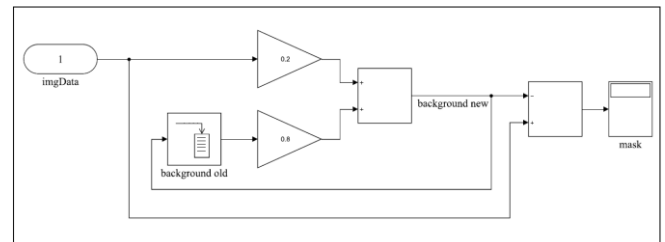


Figure 3: Functionality of dynamic background subtraction [8].

C. Connected component labelling

The connected component labelling algorithm is a method to detect multiple pixels in a two-dimensional array, which are adjacent with a specific value. The algorithm consists of initialisation and two passes to determine the so-called "blobs" of pixels. The algorithm is a three-step process described as follows.

The initialisation creates an array for the labels the same size as the image.

Afterwards the first pass is labelling, where every pixel is checked for its value, for example, in a binary image, whether it is 1 or 0. When searching for blobs of value one, every pixel with the value 1 will trigger a check of the neighbours. For this

check, two basic variants exist. Either check only horizontal and vertical adjacent pixels, the 4-neighbour check, or also check diagonally adjacent pixels, an 8-neighbour check. An explanatory graphic of these two variants can be seen in Figure 4.

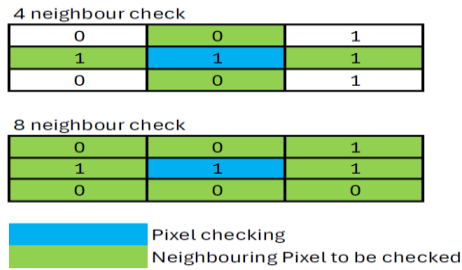


Figure 4: Graphic description of 4- and 8-neighbour check of the CCL algorithm

The initial pixel with the value of 1 will now be labelled based on the number of blobs detected. This label will be saved in the label array at the exact position the pixel is found if it is the first pixel of this value label 1, the second label 2, and so on. All the adjacent pixels with the value 1 will also receive the same one. If any of the neighbouring pixels already have a label the initial pixel and all its neighbours will receive this label instead. At the end of the first pass now exists an array the same size as the image, filled with label values for each blob detected in this pass.

At last, the second pass, which extracts the properties of the blobs from the label array. These consist of the size of the blob, how many pixels of each label exist, and the blob's position. Most of the time, the centroid of all the same labelled pixels is chosen for the position. For these properties, simple math operations, as well as counting the labels are sufficient, as we already know the exact position of every labelled pixel. After both passes, the properties of the blobs can be returned for further use.

III. APPROACH AND IMPLEMENTATION

The following section aims to describe the setup used for this approach, focussing on the two essential parts: First looking into the hardware setup and further taking a view at the software setup used for this paper.

A. Hardware setup

The Hardware used is the ISISpace iOBC development board with a 400 MHz 32 bit ARM9 processor and 64 MB of RAM [9]. This off-the-shelf on-board computer is already tested and proven for satellite use. It is powered by a 3.3V power supply. For programming and testing, the board is connected via the programming adapter delivered with the iOBC from ISISpace. As input and output the adapter and computer are serial connected via USB. Also, the adapter connects to a J-Tag programmer by SEGGER, which makes programming and debugging easier.

B. Software setup

As programming software, the Eclipse IDE, delivered in the Software Development Kit (SDK) from ISISpace is used, as well as the delivered program PUTTY for serial input and output. The SDK also provides a FREERTOS operating system already set up for the iOBC.

The Stbi_image library is used to decode jpg files; it serves no other purpose. Already implemented algorithms include a decode function to decode the jpg files from 3-channel RGB

images into a greyscale value image decoded in pixel values. This function imitates the optical sensor and will not be discussed in this work.

Further, a dynamic background subtraction algorithm is implemented in two functions, which will be discussed separately, as well as an event detection algorithm based on a connected component labelling algorithm. These algorithms work to detect lightning events in the example images. Their accuracy will not be discussed, as it is outside the scope of this work.

C. Determining the best coding strategies on the iOBC

This chapter is going to explain the methodology to determine the best possible processing time using the 150-pixel example images. The image processing functions were measured on their processing time using an oscilloscope and toggling a GPIO-pin before and after the function call. After an initial measurement, the functions were optimised using different coding strategies to improve the processing time. All optimisations were tested on their accuracy and functionality in achieving the core goal of detecting lightning events. This approach mentions only optimisations that didn't change the working detection.

A total of three image-processing functions were implemented and called after each other in the main function, as they depend on the one before them. The first call is the dynamic background calculation function, the first function of the background subtraction. In this function, each pixel of the last iteration's background and the current iteration's image is weighed and added, calculating the current iteration's background. This background is used in the second background subtraction function, the mask calculation. In this calculation, each pixel of the calculated background is subtracted from the corresponding image pixel calculating the mask. The following and last image-processing function is the detection, using the mask calculated before. The detection function is an implementation of the formerly explained connected component labelling algorithm, which is specified for the detection of lightning.

Optimisations concerning all three functions were tested first to build function-specific ones later. The only optimisation that concerned all three functions was the change from one-dimensional arrays to two-dimensional arrays for storing all pixel values.

D. Mask calculation

As the mask is a very simple operation of only subtracting pixel values from each other, the options for optimisations are limited. The best option for simple and fast calculation would be single-instruction-multiple-data (SIMD) operations, in which four variables can be subtracted simultaneously in one iteration, with the problem that these are not available on the used processor.

Trying to imitate the SIMD operation, an unrolled loop and a SIMD-like operation are implemented. The unrolled loop contains an extra loop, which incremented by 4 and calculated the pixel in a shorter loop. The SIMD-like operation calculated 4 pixels in one loop and incremented the second loop by 4 instead of 1. Another approach was to shift bitwise instead of calculating the subtraction, trying to save processing time of calculation operations inside the processor. Finally, the built-in QSUB subtraction was used to saturate the values inside the calculation instead of checking them

afterwards. All these functions did not reduce the number of calculations or iterations in total.

E. Dynamic background calculation

As the dynamic background calculation is similar to the mask calculation, the algorithms already tried were not tested again, as they didn't improve the processing time before. The only option to improve the processing time for this function was to change the datatypes. The decimal numbers are essential for the function, as explained in the background subtraction basics.

By changing the datatype for the weights from float to integer the processing time decreases. When using integer types a decimal number could not be used by assigning it the desired value, but by calculating it. The simple calculation generates the decimal number desired for the weights by assigning a number that could be used by integer to it, in this case the weights times 10 was sufficient to get an integer usable value. After the background calculation, the result is divided by 10 to get the originally desired result. This extra step in the calculation is necessary to get the same results as the float variables would, but improved processing time none the less.

F. Detect function

The connected component labelling algorithm was chosen to detect lightning events. It is implemented as explained in chapter 2.4, but instead of checking a binary image, the ones in use are 8-bit grayscale images. To label a pixel, a threshold, that has proven effective in detecting flashes in the images, was used to determine an event. The calculation of the position, initially a one-dimensional array, was measured. After the change of one-dimensional arrays to two-dimensional arrays, the question of the fastest detection algorithm was between a 4-neighbour or 8-neighbour check. For this purpose, both algorithms were implemented and tested. As for accuracy, both algorithm versions turn out to have the same results, so the 4-neighbor check didn't overlook any pixels connected to the event.

Furthermore, time-intensive parts were checked on their necessity of time needed to improve the algorithm further. The label merging step ran a loop over the whole picture, finding connected pixels with different labels every time a new pixel was found. This proved to be very time-consuming for pictures with high pixel counts above the threshold. A different approach was tested to ensure that only pixels connected to the newly located pixel would be searched for a similar label. So, instead of iterating over the whole picture, only the neighbours of the freshly found pixel are checked for different labels. As the blobs of the examples grew with increasing resolution, the checked neighbours also had to be different. For all resolutions up to 300 pixels, a neighbour check of only the direct adjacent pixel proved sufficient. A larger label merging area had to be implemented only for the 500-pixel resolution. An area of 5 pixels in each direction ensured a stable merging with the best results in time measurements. This ensures accuracy and can be changed depending on the expected event size.

G. Correlation of framerate and resolution

After determining the best image processing code, different image resolutions are measured in their processing time. For this purpose and comparability, the same scenes as used in the first objective, merely downscaled or upscaled

from the starting 150x150 pixel resolution, were used. Four different resolutions have got tested: 100, 150, 300, and 500 pixels squared. With these resolutions, which should represent the most realistic values for a CubeSat mission, a function and correlation of framerate to resolution can be determined

IV. MEASUREMENTS AND EVALUATION

The following section describes the measurements and their evaluation for objective one, to determine the best coding strategy and objective two, finding the correlation between framerate and image resolution. All measurements are the time a process needs to complete, realized by toggling a GPIO high before a function call and low after one. This high time was then measured with an oscilloscope.

A. Measurements and evaluation for iOBC best coding strategies

Except for the change from one-dimensional arrays of the initial implementation to two-dimensional arrays. This change had a coding effect on all functions but only changed the processing time of the detect algorithm, which will be shown later, the detect algorithm changes.

1. MASK CALCULATION

The five modifications to the mask function as described earlier, were tested on their processing time. Figure 5 shows that no change could improve the time needed for the mask calculations. The critical observation to make is that the two-dimensional array did not affect the time, being important as either all functions are in the two-dimensional format or none. As it has no impact, two-dimensional arrays are the version used for an optimal code.

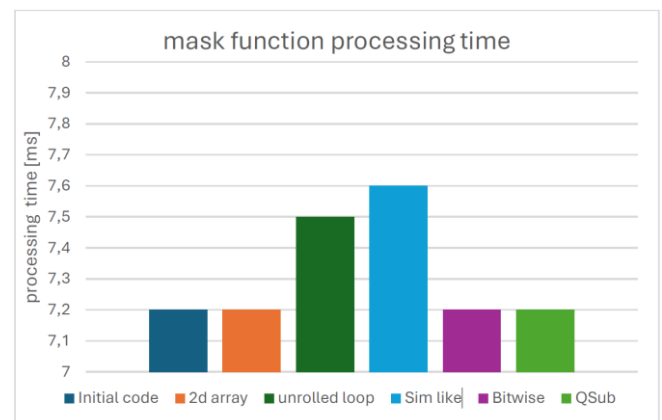


Figure 5: Mask function processing time comparison

The measured times show that no change in the mask function is necessary except for the two-dimensional array format.

2. DYNAMIC BACKGROUND CALCULATION

As described, the only change made to the background calculation is changing the data type of the weight values from float to integer. This improved the processing time significantly from 25,6 ms to 6,4 ms, despite the extra calculation step needed. This effect originates from the simplicity of integer calculations. The hardware structure of most micro-controllers allows integer calculations to be done in one or a few clock cycles, as they are represented directly as a binary number. A float calculation is more complicated, with steps as aligning exponents, calculating the mantissas and normalizing by shifting the mantissas. These extra steps are

the reason for more clock cycles in float calculations. This problem is solved in most microcontrollers with a Floating Point Unit (FPU), but the used hardware does not have one. As the calculation is very simple, the change from float to integer is sufficient for desired processing time improvement.

3. DETECT FUNCTION

Three changes of the detect function to improve the processing time were tested consecutively building on each other, beginning with the shift from one-dimensional to two-dimensional arrays as step one. In step two measurements on the 4-neighbour and 8-neighbour were performed. Lastly, a new label merging process to eliminate time inconsistencies was implemented for step three. These three steps can be seen in Figure 6 with their worst-case and best-case times. All steps except the 4-neighbour check already use the 8-neighbour check.

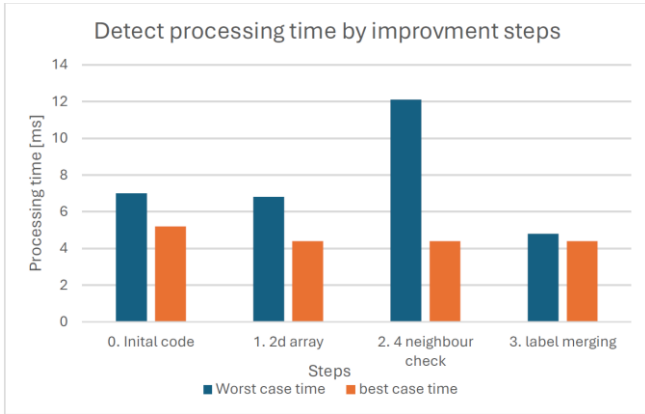


Figure 7: Detect functions processing time comparison.

Step three shows the best results, with the changes implemented, having the same best-case time as the previous changes but a significantly shorter worst-case time, proving to be the code for further use.

4. iOBC BEST CODING STRATEGY EVALUATION

The measurements dictate the optimal code for objective II. The most straightforward mask calculation, a background calculation using integer arithmetic and a detect function with the CCL algorithm, an 8-neighbour check and small-scale label merging are the best coding strategy. All functions using a two-dimensional array as the image memory. With this optimal code the objective II is measured and evaluated.

B. Measurements and evaluation of framerate and resolution correlation

Now the measurements and their evaluation for the correlation of framerate and image resolution, using the optimal code just determined.

1. iOBC BEST CODING MEASUREMENTS

In order to find the correlation between the resolution and the possible framerate, the processing times of each function were added to gain a total processing time for each resolution. The data in Figure 7 shows the correlation of the gathered processing time to the resolution squared. The graph represents the worst-case times measured for each resolution, but using the optimal code from objective I, the difference between best and worst-case time was not significantly large.

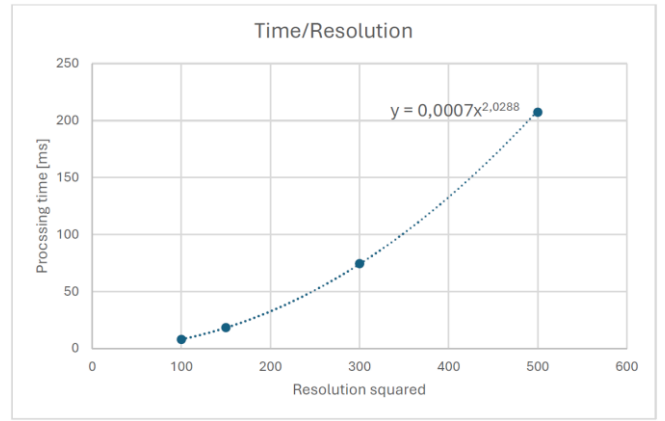


Figure 7: Correlation of processing time and image resolution.

As the function from this graph shows, the correlation between framerate and resolution can be generated by inverting the function and factoring it by a 1000 because the 1 fps corresponds to 1000/1ms. This calculates the function of the framerate over different resolutions, as shown in Figure 8. This function can now be used to calculate a framerate to a corresponding resolution.

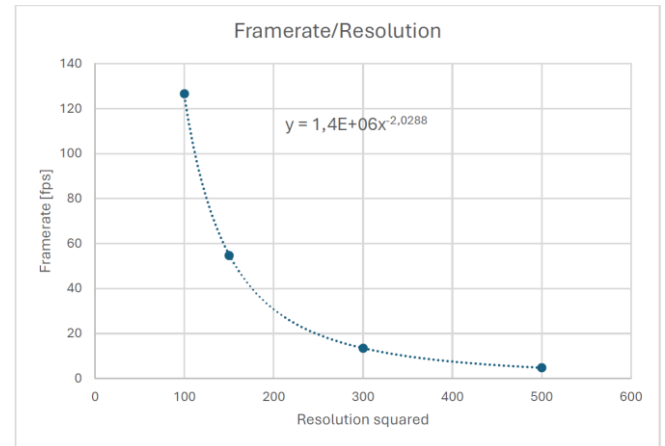


Figure 9: Correlation of framerate and image resolution.

2. iOBC BEST CODING EVALUATION

The function resulting from the measurements and seen in Figure 8, can now calculate a corresponding framerate for every resolution. This method is used for the mission target of lightning detection as follows. Extracting the formula with f for the framerate and x for the resolution and transposing for the resolution.

$$f = 1,4 * 10^6 x^{-2,0288} \quad (1)$$

$$x = \sqrt[-2,0288]{\frac{f}{1,4 * 10^6}} \quad (2)$$

A framerate must be chosen to calculate a corresponding resolution. As an example, and the purpose of proving the extracted formula, the framerate, discussed in the section 2, is chosen to be of 77 fps which results into $x = 125,77$.

This calculates the resolutions squared, concluding that the resolution corresponding to at least 77 fps is 125x125 pixels or 15625 pixels in total with any other aspect ratio.

By testing this resolution to prove the formula, the corresponding framerate to the 125x125 pixels resolution is 76,34 fps. This framerate is not even 1 fps lower than expected, which can be explained by measuring inaccuracies throughout the whole process. This result proves the calculation process and formula, but a lower resolution should be chosen to ensure that the required framerate can be accomplished.

The calculated resolution is slightly lower than the LIS-system's one, which is not a CubeSat-compatible technology. The objective is successful, as the correlation of resolution and framerate for the iOBC can be calculated.

V. RAIOSAT PROJECT OUTLOOK

In order to further prove the iOBC suitability for the mission, a hardware test with a camera will be necessary to test the data transfer of the image sensor interface, as well as the processing time of the image processing. A camera with an adjustable framerate would be preferable to test different framerates.

Moreover, improvements could be tested on the software part. Different event detection algorithms could be tested besides the CCL, to see if they improve the processing time. Also, the hardcoded variables need to be looked at, such as the weights of the dynamic background subtraction, which should have a calculation based on the background. Important is also that the threshold for the event detection must be different for different circumstances of the image, such as lighting of the background and weather.

By adjusting these issues, the accuracy could improve for different background circumstances, but also impact the processing time and, ultimately, the framerate. The usage of different examples, with simulations of IC- and CG-flashes should be implemented and an algorithm to differentiate these two. These more in-depth tests could show their impact on processing time and if it is better to do this on board or on the ground.

VI. CONCLUSIONS

To conclude this work, placing the evaluations obtained in this paper into context is necessary. The first target which had the goal of finding the best coding strategy evaluates to the mentioned code and is in its essence to keep the code as simple as possible, including calculations and datatypes. Placing that evaluation into context of not only the RaioSat mission but the iOBC as an on-board computer in general, it concludes that the iOBC can be considered as an image processing unit on different CubeSat missions.

The goal of finding the correlation of framerate and image resolution of Objective II can be considered a success. Either of these two variables can now be calculated for the mission target and help with the camera selection process. Further does the iOBC show, that it is capable of a comparable resolution to existing lightning detection technology, which is why it should be considered being part of the RaioSat mission.

The framerate correlating to this resolution is in simplified terms sufficient for lightning detection but are going to be

ultimately set by the research team and their analysis requirements on time resolve. To be part in the RaioSat mission, this iOBC must face more in-depth testing. None the less can these conclusions help in the beginning process of selecting the image processing unit and the camera.

ACKNOWLEDGMENT

The authors would like to thank the German DAAD for providing the scholarships as well as Brazilian CAPES for the PrInt Program.

REFERENCES

The template will number citations consecutively within brackets [1]. The sentence punctuation follows the bracket [2]. Refer simply to the reference number, as in [3]—do not use “Ref. [3]” or “reference [3]” except at the beginning of a sentence: “Reference [3] was the first ...”

Number footnotes separately in superscripts. Place the actual footnote at the bottom of the column in which it was cited. Do not put footnotes in the abstract or reference list. Use letters for table footnotes.

Unless there are six authors or more give all authors' names; do not use “et al.”. Papers that have not been published, even if they have been submitted for publication, should be cited as “unpublished” [4]. Papers that have been accepted for publication should be cited as “in press” [5]. Capitalize only the first word in a paper title, except for proper nouns and element symbols.

For papers published in translation journals, please give the English citation first, followed by the original foreign-language citation [6].

- [1] Naccarato, et al. (2018). Advances in the RaioSat project: detecting lightning from space using a nanosatellite. International Lightning Detection Conference.
- [2] Naccarato, et al. (2016). Total Lightning Flash Detection From Space, A CubeSat Approach. 24th International Lightning Detection Conference.
- [3] S. J. Goodman, R. B. (2013). The GOES-R Geostationary Lightning Mapper (GLM). Elsevier B.V.
- [4] H. J. Christian, R. B. (2000). Algorithm theoretical basis document (ATBD) for the Lightning Imaging Sensor (LIS). NASA George C. Marshall Space Flight Center.
- [5] Remote Sensing (2021). Lightning Activity observed by the FengYun-4A Lightning Mapping Imager (LMI). July 31, 2021.
- [6] S. Behnke et al. (2024). Cubespark-RF: Designing the Radio Frequency Payload for Space-borne 3-D Observations of Lightning. European Geosciences Union General Assembly 2024 (EGU24), held 14-19 April, 2024 in Vienna, Austria.
- [7] M. G. Ballarotti (2012). Frequency distributions of some parameters of negative downward lightning flashes based on accurate-stroke-count studies.
- [8] J. Zecherle (2021). Embedded GPU powered image processing for nanosatellite-based optical lightning detection
- [9] ISISpace (2023). ISISpace iOBC Quick Start Guide. Version 1.0, delivered with software development kit.
- [10] S. J. Goodman, H. C. (1988). A Comparison of the Optical Pulse Characteristics of Intra-cloud and Cloud-to-Ground Lightning as Observed above Clouds. Journal of Applied.



LATIN AMERICAN CUBESAT WORKSHOP SALVADOR, BR

DOI: 10.1234/example-doi-03

Alcântara in Orbit

Aline Rebeca Araújo Barroso¹, Ronaldy Lima França¹, João Victor Alberto Cancissu¹, Gabrielle Ribeiro Silva¹, Pedro Henrique Pereira da Silva¹, Luis Claudio de Oliveira Silva¹, and Carlos Alberto Rios Brito Junior¹

¹UFMA

Abstract

This work describes the process of construction and launch of an educational nanosatellite model Cubesat 1U. This is a proof concept in which the model should read and store payload and telemetry data. The mission "Alcântara em Órbita" was born from a high school students project of Tiradentes Military College I with the initial objective of environmental monitoring in the northern region of Maranhão, with the aim of participate in the 2nd Brazilian Satellite Olympiad (OBSAT) MCTI in the year 2023. The students designed, integrated all components, programmed, and assembled everything with structure based on 3D printing, in order to attend and perform all subsystems for the success of the mission. Throughout the Northwest Regional Event, the OBSAT organization required robustness in all subsystems to validate the flight model, making thermal, magnetic and vibration tests. As a result, it passed in all of them, qualifying the artifact for flight through a stratospheric balloon (reaching a maximum altitude of 26.7 km) at the Barreira do Inferno Launch Center (CLBI). During the mission, the satellite successfully collected payload and telemetry data, storing the data in a microSD card. After the rescue, the collected data were processed and organized using Pandas data visualization module in Python3 to make it easier for all community to understand the mission's outcome. Now, after the educational olympiad, the project is going to proceed as research academic work, with support of the Aerospace Engineering Coordination of Federal University of Maranhão (UFMA) through its Laboratory of Electronics and Embedded Space

Systems (LABESEE). The main proposal is to build a standard nanosatellite model CubeSat 1U to be launched into Low Earth Orbit (LEO) and Data Collection Platforms (PCDs) to be installed around the city of Alcântara, both with more advanced technical parameters, for the collection of environmental data from the region by remote sensing, thus contributing to the development of the city, communities and Alcantara Space center (CEA), also making the mission results accessible to the population.

Orbit Sensitivity Analysis for Catarina Constellation

1st Guilherme Peinador Gomes

Joinville Technology Center
Federal University of Santa Catarina
Joinville, Brazil
guilherme.peinador@grad.ufsc.br

2nd Rafael Gigena Cuenca

Joinville Technology Center
Federal University of Santa Catarina
Joinville, Brazil
rafael.cuenca@ufsc.br

3rd Damylle Cristina Xavier Donati

Joinville Technology Center
Federal University of Santa Catarina
Joinville, Brazil
damylle.xavier@t2f.ufsc.br

4th Rodrigo da Silva Cardozo

Joinville Technology Center
Federal University of Santa Catarina
Joinville, Brazil
rodrigo.cardozo@t2f.ufsc.br

5th Talita Sauter Possamai

Joinville Technology Center
Federal University of Santa Catarina
Joinville, Brazil
talita.possamai@ufsc.br

Abstract—The Brazilian Data Collection System (SBCD) currently relies on geostationary satellites to gather environmental data and provide climate and defense analyses in Brazilian territory. However, due to the high costs associated with large satellite missions, the development of CubeSats - small, cost-effective satellites - has become a more attractive option for both companies and universities. As a result, the Catarina Constellation project was established to create a constellation of nanosatellites that would significantly improve remote sensing capabilities, stimulate the growth of the space industry in Santa Catarina, and foster collaboration between industry, government, and universities. To ensure the success of the Catarina Constellation project and due to launch uncertainties, a sensitivity analysis was conducted on the inclination, altitude, and right ascension of the ascending node of the orbit. This analysis aimed to determine the impact of these variations on specific mission parameters, including the number of times communication is established, the time the communication between the nanosatellite and the ground station, and the evaluation of days when communication is established. Using an orbital propagation code developed by the authors, a series of simulations were conducted to perturb the orbital parameters within a margin of error of +/- 25 km ($\pm 0.4\%$) for the semi-major axis, +/- 5 degrees ($\pm 5\%$) for the inclination, and +/- 10 degrees ($\pm 5\%$) for the right ascension of the ascending node. From this data the results in a variation of 25% in the contact time and the average communication time, and a variation of 20% in the number of passes.

Index Terms—Catarina Constellation, nanosatellite, orbital mechanics, sensitivity analysis, communication optimization

I. INTRODUCTION

The miniaturization of digital circuits has promoted the popularization of nanosatellites, mainly due to the lower costs of developing, launching, and maintaining these devices [10]. These advances have made nanosatellites more accessible to private companies and universities, allowing space missions and research to be conducted at a lower cost [1], [7], [9], [17].

Along with miniaturization, satellite constellations consisting of multiple satellites working together have become an essential tool for a wide range of technological and scientific applications. These systems offer enhanced communication

[8], navigation [4], [6], [14], environmental monitoring [16] and Earth observation capabilities [12], [13].

In this context, the Catarina Constellation mission was born with the aim of launching a constellation of nanosatellites with missions ranging from data collection to Earth imaging. The Catarina Constellation, specifically Fleet A, consists of three CubeSats and its main mission is data collection. It is being developed by the Federal University of Santa Catarina (UFSC) and the SENAI Institute for Innovation in Embedded Systems (ISI-SE), with the support of the Brazilian Space Agency (AEB) and the National Institute of Space Research (INPE). The overall objective of this constellation is to promote the aerospace industry in the state of Santa Catarina and to train qualified human resources, taking advantage of the strategic collaboration between AEB, UFSC and ISI-SENAI [3]. In addition, Catarina Constellation seeks to provide services that contribute to the Brazilian Data Collection System (SBCD).

For a comprehensive analysis of the potential launch of the Catarina Constellation mission, with orbital parameters defined by a semi-major axis of 6896 km, an inclination of 98° , and three satellites, distributed in a triangular formation, with Right Ascension of Ascending Node (RAAN) angles of 10° , 130° , and 250° , according to [5], the initial optimization for this mission showed that the angular separation between the satellites should be at least 40° to avoid interference during communication with the ground station.

The sensitivity analysis is a fundamental tool in various fields, including engineering and economics. It allows to assess how variations in input parameters influence the outcomes of a model, this process is crucial for understanding the robustness and reliability of predictions and decisions. In this context, the Latin Hypercube Sampling method was chosen because of its ability to provide robust and efficient results [11], [15].

In this article, a sensitivity analysis was performed on the initial parameters of semi-major axis, inclination, and longitude of the ascending node predicted for the launch of the Catarina Constellation mission.

II. SENSITIVITY ANALYSIS FORMULATION

In order to calculate the orbital propagation of the CubeSat, a Python code was developed which makes use of the Gauss equations as outlined by Curtis in its book [2].

$$\frac{dh}{dt} = rp_s \quad (1)$$

$$\frac{de}{dt} = \frac{h}{\mu} \sin \theta p_r + \frac{1}{\mu h} [(h^2 + \mu r) \cos \theta + \mu e r] p_r \quad (2)$$

$$\frac{d\theta}{dt} = \frac{h}{r^2} + \frac{1}{eh} \left[\frac{h^2}{\mu} \cos \theta p_r - \left(r + \frac{h^2}{\mu} \right) \sin \theta p_s \right] \quad (3)$$

$$\frac{d\Omega}{dt} = \frac{r}{h \sin i} \sin(\omega + \theta) p_\omega \quad (4)$$

$$\frac{di}{dt} = \frac{r}{h} \cos(\omega + \theta) p_\omega \quad (5)$$

$$\begin{aligned} \frac{d\omega}{dt} = & -\frac{1}{eh} \left[\frac{h^2}{\mu} \cos \theta p_r - \left(r + \frac{h^2}{\mu} \right) \sin \theta p_s \right] \\ & - \frac{r \sin(\omega + \theta)}{h \tan i} p_\omega \end{aligned} \quad (6)$$

where $r = \frac{h^2}{\mu(1+e \cos \theta)}$ and p_s , p_r and p_ω are the perturbations. The system of ordinary differential equations can be integrated based on the given equations and the initial orbital parameters of the mission, utilizing a package called ODEINT, which is based on a FORTRAN library.

In order to generate the communication criteria, that is to say, the antenna sighting, trigonometric relationships were employed based on the vectors of Figure 1. They are the vector between the center of the Earth and the satellite, the center of the Earth and the ground station, and, to complete the triangle, between the satellite and the ground station (V_{TS} , V_{TG} and V_{SG} , respectively). With regard to the angles, there is the minimum elevation angle of the ground station antenna for effective communication, defined in the manual, and the angle (γ), which is defined as the communication criteria and is defined by the equation 7.

In the case of the antenna under consideration, situated at the Natal Multi-Mission Station with coordinates -5.8717778° N, -35.206864° W, the minimum elevation is 15° .

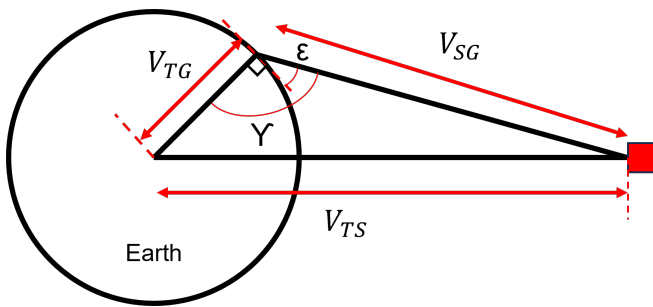


Fig. 1. Relationship between the angles of the satellite, target, and center of the Earth [5].

$$\gamma = \pi - \arccos \frac{V_{TS} \cdot V_{SG}}{|V_{TS}| |V_{SG}|} - \arccos \frac{V_{TG} \cdot V_{TS}}{|V_{TG}| |V_{TS}|} \geq 105^\circ \quad (7)$$

In accordance with the established communication criterion, the remaining communication metrics are delineated, including: contact time, which represents the duration of satellite communication with the ground station; average contact time, which is the mean value of all contact intervals; and the number of passes, which is the frequency of satellite passages through the antenna's field of view.

To evaluate the influence of discrepancies between the planned initial condition and the reference mission, the Latin Hypercube scattering method was employed, resulting in the generation of 1000 samples. The generated samples represent potential variations in the launch, thus enabling a comprehensive analysis of the impact of these uncertainties on the satellite's communication parameters.

In the generated samples, variations in the values of three primary parameters were considered: the semi-major axis, inclination, and longitude of the ascending node for each of the three satellites. The introduced variations were in accordance with the specifications outlined in Table I, with an variation of ± 25 km for the semi-major axis, $\pm 5^\circ$ for the inclination, and $\pm 10^\circ$ for the longitude of the ascending node.

TABLE I
UPPER AND LOWER BOUNDS FROM THE SENSITIVITY ANALYSIS

Satellite	Variables	Lower Bound	Upper Bound
1	SMA ^a	6871 km	6921 km
1	I ^b	93°	103°
1	RAAN ^c	0°	20°
2	SMA ^a	6871 km	6921 km
2	I ^b	93°	103°
2	RAAN ^c	120°	140°
3	SMA ^a	6871 km	6921 km
3	I ^b	93°	103°
3	RAAN ^c	240°	260°

^aSemi-Major Axis.

^bInclination.

^cLongitude of the Ascending Node.

To conduct the sensitivity analysis, two Intel® Xeon® CPU E5-2640 v4 @ 2.40GHz processors were utilized, comprising a total of 20 cores and 125 GB of RAM. This configuration was provided by the Laboratório de Computação Científica (LCC) at the Technological Center of Joinville from the Federal University of Santa Catarina (CTJ-UFSC).

III. RESULT AND DISCUSSIONS

To facilitate the graphical representation of the data, the case with a semi-major axis of 6896 km, an inclination of 98° and the longitude of the ascending node of 10°, 130° and 250° for satellites 1, 2 and 3, respectively, was selected as a reference point. All subsequent cases were then normalized relative to this reference.

In Figure 2, the dispersion of the data, conducted via the Latin Hypercube sampling method, is depicted in this

analysis. It is evident that, despite the presence of some regions that have been less extensively investigated, the dispersion is effective across the entire domain of variables. This efficiency is demonstrated by the representative distribution of the sample points, which are dispersed uniformly throughout the space of the variables.

It is imperative that the distribution of sample points be uniform for a robust analysis, as this ensures that all regions of the domain are properly explored. This characteristic is of particular importance in ensuring that the analysis incorporates a comprehensive and accurate representation of all potential variations within the domain under study. Furthermore, the histograms displayed on the main diagonal of the dispersion matrix indicate that there is no significant concentration of values in any specific region of the range. This suggests that the distribution of points is uniform, thereby reinforcing the effectiveness of the method in comprehensively covering the space of the variables.

The results of the orbital propagation simulations were used to generate a dispersion matrix, which is illustrated in Figure 3. In this matrix, each satellite is represented by a distinct color: black for satellite one, red for satellite two, and green for satellite three.

The data analysis indicates that there is no evident trend in the inclination and longitude of the ascending node parameters. This is reflected in the distribution of results relating to the number of passes with communication, contact time, and average communication, which are scattered throughout the domain, in other words, the average trend is flat, indicating the absence of a discernible trend.

With regard to the semi-major axis, a notable trend emerges with respect to the parameters of communication time and average communication. Minor fluctuations in the semi-major axis, amounting to $\pm 0.4\%$, give rise to variations of up to $\pm 10\%$ in these parameters, thereby underscoring the considerable sensitivity of communication performance with respect to this variable.

Furthermore, the inclination and length of the ascending node exert a minor influence on the communication parameters. The observed variations in these parameters result in a change of approximately $\pm 2.5\%$, which has the effect of preventing the formation of a single, clear line in the data set under analysis. This dispersion indicates that, while the slope and length of the ascending node are not the primary determinants of the results, they nevertheless contribute to the observed variability.

With regard to the number of passes, a similar trend was also discernible, exhibiting a comparatively weaker effect, with variations of approximately $\pm 5\%$. This indicates that, although they are affected, the inclination and longitude of the ascending node have a comparatively minor impact on the number of passages in comparison to the semi-major axis.

In order to evaluate the total contact time of the constellation, a dispersion matrix was generated, relating the semi-major axis, inclination, and longitude of the ascending node of each satellite to the total contact time of the constellation.

The results indicate that the concentration of data occurs predominantly in the central region of the matrix, suggesting that the influence of these parameters on the total contact time of the constellation is not particularly significant.

Figure 4 shows the relationship between the variation of the semi-major axis, inclination and longitude of the ascending node and the total contact time of the satellite constellation for each of the three satellites. The satellites are arranged in a linear sequence, with Satellite 1 situated in the first row, Satellite 2 in the second row, and Satellite 3 in the third row, the arrangement is illustrated on the right. The semi-major axis exhibits a somewhat more discernible trend in comparison to the other parameters. In particular, a change of $\pm 0.4\%$ in the semi-major axis is associated with a change of approximately $\pm 6\%$ in the total contact time. This trend, although more defined, still indicates that the semi-major axis exerts a moderate influence on the total contact time of the constellation, in contrast to the even more subtle influence of the inclination and longitude of the ascending node.

To identify the relationships between communication parameters, the parallel coordinates strategy was used, which provides an effective visualization for exploring multidimensional relationships between different variables and identifying patterns. This approach optimizes data interpretation by focusing on the variables that are most relevant to the study of relationships between communication parameters. Each of the three satellites was analyzed separately to improve the clarity of the visualization.

The parallel coordinate axes, which have identical limits, represent the variations in the semi-major axis (SMA), inclination (Inc), longitude of the ascending node (RAAN), number of passes (NP), and mean communication time (MCT), respectively. Furthermore, a color scheme was employed to illustrate the variation in the total contact time of the constellation, thereby facilitating a more intuitive examination of the relationships between the variables.

The axis representing the communication time of the satellites was excluded from the analysis, as its direct correlation with the average communication time would not contribute any additional insights.

Figure 5 shows the analysis of the first satellite, where it can first be seen that higher values of Semi-Major Axis (SMA) result in a longer total contact time. In addition, there is a clear correlation between SMA and inclination (Inc), with higher SMA values tending to be associated with lower inclination values, indicating an inverse relationship between these two variables.

The data also show a significant dispersion between the axes representing the number of passes and the average contact time. This dispersion suggests that there is no strong correlation between these parameters, indicating a variability in communication results that is not directly related to SMA or tilt.

Satellite two, shown in Figure 6, shows a very similar pattern to satellite one. However, it can be seen that although satellite two tends to have a lower number of passes, the

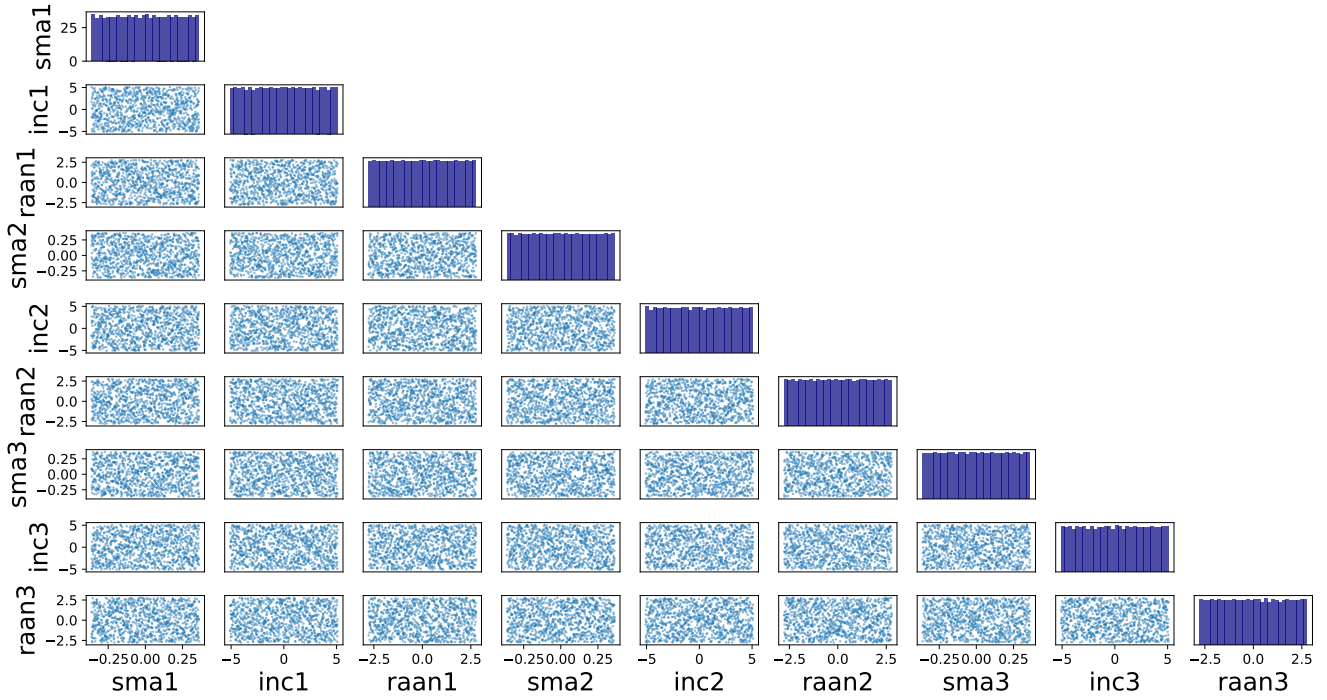


Fig. 2. Initial dispersion scatter matrix.

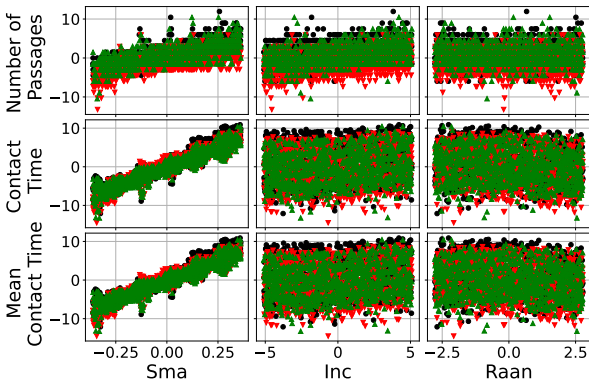


Fig. 3. Communication metrics scatter matrix.

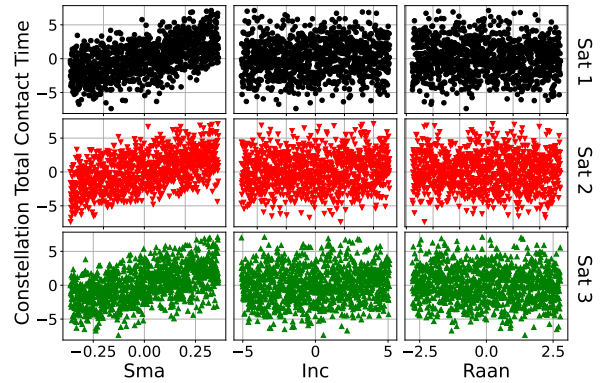


Fig. 4. Constellation total contact time scatter matrix.

average contact time is not affected to the same extent. This suggests that despite the differences in the number of passes, the performance in terms of contact time remains relatively stable, highlighting a robustness in the communication parameters of this particular satellite.

Satellite three, shown in Figure 7, shows a distribution very close to that observed for satellite one. It can be seen that all three satellites show a general consistency in their patterns, indicating similar behavior in terms of communication parameters.

In addition, the distribution of the variation in the total contact time of the constellation shows a remarkable con-

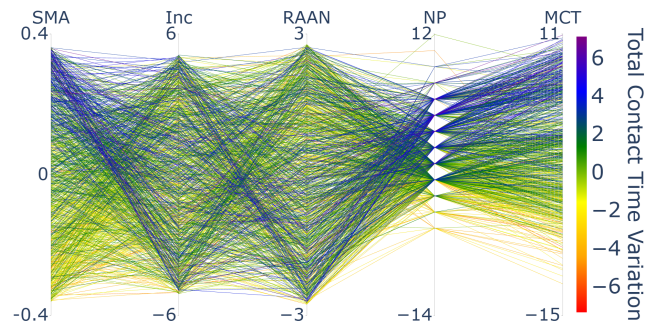


Fig. 5. Satellite 1 parallel coordinates.

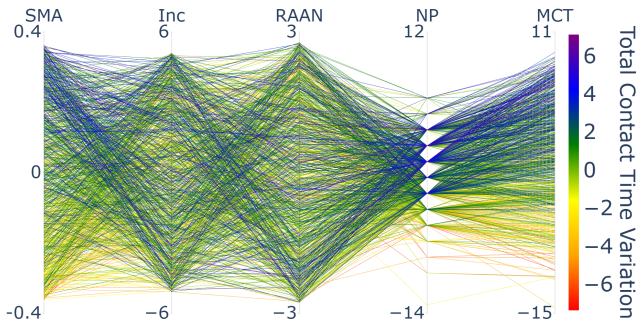


Fig. 6. Satellite 2 parallel coordinates.

sistency, reflecting a stability in the communication characteristics between the satellites. This uniformity suggests that the satellites, despite their individual differences, maintain a relatively homogeneous performance in terms of the total contact time of the constellation.

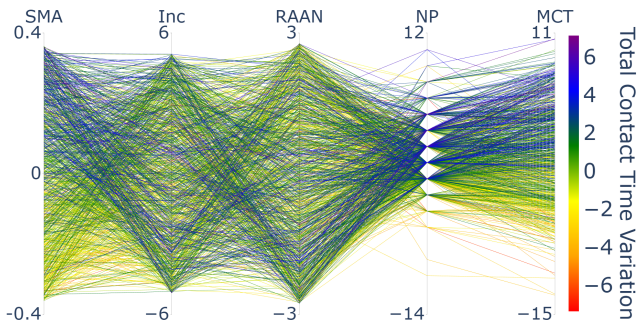


Fig. 7. Satellite 3 parallel coordinates.

The parallel coordinate plots proved to be a valuable tool for gaining insight into the communication parameters of the three satellites in the Catarina constellation. The analysis yielded a correlation between semi-major axis (SMA) and inclination (Inc), whereby higher SMA values were found to be associated with lower inclination values.

Furthermore, the data exhibited considerable dispersion along the axes representing the number of passes and average contact time, indicating significant variability in the communication characteristics between the satellites. Furthermore, an examination of the colors utilized in the graphs indicated that the variation in the total contact time of the constellation is predominantly concentrated in values near zero and four, which are associated with the colors green and blue, respectively.

These findings provide a robust foundation for comprehending the behavior of the satellites with regard to communication and offer invaluable insights for future optimization of the constellation.

IV. CONCLUSIONS

A sensitivity analysis was conducted to ascertain the impact of variations in orbital parameters, particularly the semi-major axis, inclination, and longitude of the ascending node, on the

communication parameters of the satellites. The perturbations were carried out using the Latin Hypercube method, with variations of ± 25 kilometers for the semi-major axis, ± 5 degrees for the inclination, and ± 10 degrees for the longitude of the ascending node. These perturbations correspond to $\pm 0.4\%$, $\pm 5\%$, and $\pm 3\%$, respectively.

The results demonstrated that the number of passages, contact time, and average communication time exhibited absolute variations of up to 20%, 25%, and 25%, respectively. It was observed that the semi-major axis exerts a more pronounced influence on communication parameters than the inclination and length of the ascending node, which did not exhibit discernible trends in communication parameters.

The findings of this study have significant implications for the planning of future space missions. Given the advanced technology and high costs associated with the space field, it is imperative to conduct simulations of various scenarios to guarantee the accomplishment of mission objectives and to substantiate the efficacy of the development process.

ACKNOWLEDGMENT

We would like to thank the Laboratório de Computação Científica (LCC) at Universidade Federal de Santa Catarina (CTJ-UFSC) for providing computational resources.

REFERENCES

- [1] J. Bouwmeester and J. Guo. Survey of worldwide pico- and nanosatellite missions, distributions and subsystem technology. *Acta Astronautica*, 67(7):854–862, October 2010.
- [2] H. Curtis. *Orbital Mechanics: For Engineering Students*. Aerospace Engineering. Elsevier Science, 2015.
- [3] Danylle Cristina Xavier Donati, Rodrigo Cardozo, Talita Possamai, Nicole Borges, Pieter Bernardes, Ludmila Kopko, Christopher Cerqueira, and Augusto Conto. *MISSION DESIGN OF CATARINA CONSTELLATION'S FLEET A: A SYSTEMS ENGINEERING CASE STUDY*. November 2022.
- [4] Marco Falcone, Jörg Hahn, and Thomas Burger. Galileo. In Peter J.G. Teunissen and Oliver Montenbruck, editors, *Springer Handbook of Global Navigation Satellite Systems*, pages 247–272. Springer International Publishing, Cham, 2017.
- [5] Guilherme Peinador Gomes, Rafael Cuenca, Danylle Cristina Xavier Donati, Rodrigo Cardozo, and Talita Possamai. *Optimizing Communication for Catarina Constellation's Nanosatellites*. December 2023.
- [6] Christopher J. Hegarty. The Global Positioning System (GPS). In Peter J.G. Teunissen and Oliver Montenbruck, editors, *Springer Handbook of Global Navigation Satellite Systems*, pages 197–218. Springer International Publishing, Cham, 2017.
- [7] Hank Heidt, Jordi Puig-Suari, Augustus Moore, Shinichi Nakasuka, and Robert Twiggs. CubeSat: A New Generation of Picosatellite for Education and Industry Low-Cost Space Experimentation. 2000.
- [8] Oltjon Kodheli, Eva Lagunas, Nicola Maturo, Shree Krishna Sharma, Bhavani Shankar, Jesus Fabian Mendoza Montoya, Juan Carlos Merlano Duncan, Danilo Spano, Symeon Chatzinotas, Steven Kisseleff, Jorge Querol, Lei Lei, Thang X. Vu, and George Goussetis. Satellite Communications in the New Space Era: A Survey and Future Challenges. *IEEE Communications Surveys & Tutorials*, 23(1):70–109, 2021. Conference Name: IEEE Communications Surveys & Tutorials.
- [9] Herbert J. Kramer and Arthur P. Cracknell. An overview of small satellites in remote sensing*. *International Journal of Remote Sensing*, 29(15):4285–4337, August 2008. Publisher: Taylor & Francis _eprint: <https://doi.org/10.1080/01431160801914952>.
- [10] Erik Kulu. *Nanosatellite Launch Forecasts 2022 - Track Record and Latest Prediction*. August 2022.

- [11] M. D. McKay, R. J. Beckman, and W. J. Conover. A Comparison of Three Methods for Selecting Values of Input Variables in the Analysis of Output from a Computer Code. *Technometrics*, 21(2):239–245, 1979. Publisher: [Taylor & Francis, Ltd., American Statistical Association, American Society for Quality].
- [12] Elizabeth M. Middleton, Stephen G. Ungar, Daniel J. Mandl, Lawrence Ong, Stuart W. Frye, Petya E. Campbell, David R. Landis, Joseph P. Young, and Nathan H. Pollack. The Earth Observing One (EO-1) Satellite Mission: Over a Decade in Space. *IEEE Journal of Selected Topics in Applied Earth Observations and Remote Sensing*, 6(2):243–256, April 2013. Conference Name: IEEE Journal of Selected Topics in Applied Earth Observations and Remote Sensing.
- [13] C.L. Parkinson. Aqua: an Earth-Observing Satellite mission to examine water and other climate variables. *IEEE Transactions on Geoscience and Remote Sensing*, 41(2):173–183, February 2003. Conference Name: IEEE Transactions on Geoscience and Remote Sensing.
- [14] Sergey Revnivkyh, Alexey Bolkunov, Alexander Serdyukov, and Oliver Montenbruck. GLONASS. In Peter J.G. Teunissen and Oliver Montenbruck, editors, *Springer Handbook of Global Navigation Satellite Systems*, pages 219–245. Springer International Publishing, Cham, 2017.
- [15] Michael Stein. Large Sample Properties of Simulations Using Latin Hypercube Sampling. *Technometrics*, 29(2):143–151, 1987. Publisher: [Taylor & Francis, Ltd., American Statistical Association, American Society for Quality].
- [16] Jean-Noël Thépaut, Dick Dee, Richard Engelen, and Bernard Pinty. The Copernicus Programme and its Climate Change Service. In *IGARSS 2018 - 2018 IEEE International Geoscience and Remote Sensing Symposium*, pages 1591–1593, July 2018. ISSN: 2153-7003.
- [17] Stephen Waydo, Daniel Henry, and Mark Campbell. CubeSat design for LEO-based Earth science missions. *IEEE Aerospace Conference Proceedings*, 1, September 2002.

Advancements in GNSS Radio Occultation Techniques: Opportunities and Challenges in CubeSat Platforms

Lucas da Rosa Kieslich, Jérôme Verscheuren, Xisto Lucas Travassos Junior, Carlos Alberto Valderrama Sakuyama, Eduardo Augusto Bezerra

Abstract—The GNSS radio occultation (RO) technique has become a crucial method for precise atmospheric probing, utilizing signals from global navigation satellite systems (GNSS) to derive key atmospheric parameters. Traditionally, RO measurements have been conducted using larger satellites. CubeSats, also known as nanosatellites, offer cost-effective platforms for space missions, including RO instruments. However, the use of CubeSats for RO presents some drawbacks that can jeopardize the mission, due to the restricted volume, such as limited power constraints, antennas with smaller design, limitation for orbit determination and attitude control payloads, reduced orbital lifetime, challenges to get high quality constellation management, data downlink, data quality, calibration and validation. In addition, the CubeSat platform requires reduced weight and power from instruments which in turn restricts the techniques that can be employed. This paper presents a literature review about key technical, operational, data quality issues as long as existing RO methodologies and integration of RO techniques for CubeSat platforms, highlighting their potential benefits and challenges.

Index Terms—GNSS Radio Occultation, CubeSats, Atmospheric Probing, Nanosatellite Platforms, Earth's Atmosphere

I. INTRODUCTION

Satellite observations play a critical role in disaster response and mitigation, especially as the frequency of natural disasters like floods and hurricanes increases [1]. Remote sensing has proven effective in monitoring various natural hazards, including earthquakes, volcanic activity, and wildfires [2]. One key technology for atmospheric monitoring is radio occultation (RO), which leverages the refraction of GNSS signals as they pass through the Earth's atmosphere to collect data on temperature, pressure, humidity, and refractivity—parameters essential for weather forecasting and climate research.

CubeSats, small and cost-effective satellites, have emerged as promising platforms for RO. Despite their

Lucas da Rosa Kieslich, Xisto Lucas Travassos Junior and Eduardo Augusto Bezerra are with the SpaceLab, Federal University of Santa Catarina, SC, Brazil (e-mail: lucas.kieslich@spacelab.ufsc.br, lucas.travassos@ufsc.br, Eduardo.Bezerra@ufsc.br). Jérôme Verscheuren and Carlos Alberto Valderrama Sakuyama are with the University of Mons, Mons, Belgium (e-mail: jerome.verscheuren@umons.ac.be, carlos.valderrama@umons.ac.be).

affordability, CubeSats face limitations, such as reduced power and instrument capacity, which pose challenges for complex tasks like RO.

RO using CubeSats involves receiving GNSS signals and analyzing atmospheric-induced variations, as illustrated in Fig. 1[3]. Although still in its early stages in Brazil, advances in RO technology hold significant potential for enhancing local meteorological research and agricultural planning.

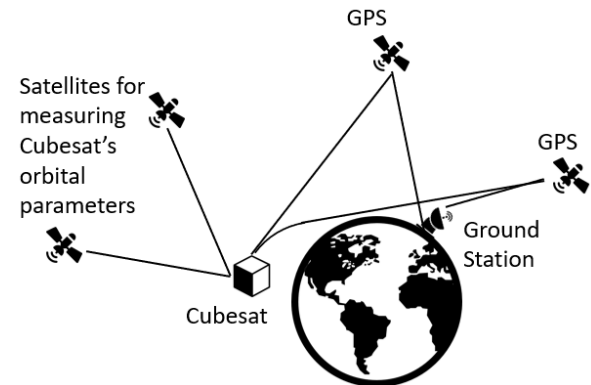


Figure 1: Measurement extracted from a CubeSat and a GNSS based on [3].

A. Objectives

This article explores the integration of RO techniques on CubeSat platforms, providing an analysis of the associated benefits and challenges. We compare established RO methodologies with emerging approaches in CubeSat projects, highlighting technological advancements that have made CubeSat RO missions feasible. Our study emphasizes improvements in signal processing techniques and strategies for overcoming limitations related to power constraints and instrument accuracy.

The primary goal is to establish a solid foundation for the practical development of GNSS signal acquisition and processing techniques in nanosatellites. This will significantly contribute to the ROCUS-1 mission, the first RO mission developed at SpaceLab UFSC, advancing our understanding of Earth's atmosphere and improving our capacity to monitor it.

B. Organization

This article is structured as follows. Section **Context and Problematics** describes the RO technique and its associated challenges. Section **Advanced Techniques for Radio Occultation** examines methods for enhancing RO measurements. Section **Comparative Analysis** provides a comparative review of advanced techniques. Section **Methodology** outlines the methodological framework of the work. Section **Results** synthesizes the study's findings. Finally, Section **Conclusion** summarizes the research and presents perspectives on the future of CubeSat-based RO missions.

II. CONTEXT AND PROBLEMATICS

This section explores the fundamental principles of Radio Occultation (RO), its historical development, and the techniques involved in both tropospheric and ionospheric measurements.

A. The Radio Occultation Principles

Radio Occultation (RO) is a key atmospheric sounding technique that relies on the refraction of radio signals as they pass through the atmosphere. By measuring the bending of the signal, influenced by the atmospheric refractive index, atmospheric parameters such as temperature, pressure, humidity, and composition can be inferred [4].

Before the 1990s, RO was primarily used to study planetary atmospheres, such as that of Jupiter through missions like Pioneer 10 and 11. These early applications demonstrated the technique's ability to penetrate deep into planetary atmospheres, providing high-resolution data on atmospheric structure via signal refraction and attenuation [5].

The advent of Global Positioning System (GPS) technology revolutionized RO applications on Earth. Originally designed for geolocation by the U.S. Air Force, GPS began to be used for atmospheric profiling. GPS satellites, operating at L-band frequencies (1.57542 GHz and 1.2276 GHz), provide stable signal sources. When received by satellites in low Earth orbit (LEO), these signals allow scientists to derive detailed atmospheric profiles. Missions such as CHAMP, GRACE, METOP, and COSMIC have set a high standard for acquiring precise atmospheric data, demonstrating the effectiveness of GPS-based RO in Earth sciences [6], [7].

GNSS RO employs signals from multiple satellite constellations, including GPS, GLONASS, Galileo, and BeiDou, increasing the number of occultations. A single LEO satellite can observe over 500 events daily. Increasing the number of receivers improves global coverage and enhances the high vertical resolution provided by GNSS signals [8], [9].

The emergence of low-cost CubeSats has introduced new possibilities for RO missions. Despite limitations

in power and payload capacity, CubeSats equipped with RO instruments offer a cost-effective means of collecting high-resolution atmospheric data. These nanosatellites can perform RO measurements at a fraction of the cost of traditional satellites, making them an attractive option for expanding atmospheric research [10], [11].

While CubeSats offer exciting opportunities for atmospheric research, the fundamental physical principles of RO remain unchanged. Therefore, we will outline the general aspects inherent to each RO mission, categorized into general techniques, tropospheric measurements, and ionospheric measurements.

1) Overview of General RO Technique:

a) Bending Angle: The primary parameter measured during an RO mission is the bending angle (α), which quantifies how the atmosphere influences the signal (Fig. 2). Due to atmospheric refraction, the signal path deviates from the straight line \vec{r}_{Rx-Tx} , following a curved trajectory (blue line). This curvature occurs as the GNSS signal passes through the atmosphere and reaches the LEO receiver. The bending angle α represents the deviation between the straight-line segments of the trajectory before and after atmospheric refraction. The method for measuring this angle, particularly using the Doppler effect, will be detailed later.

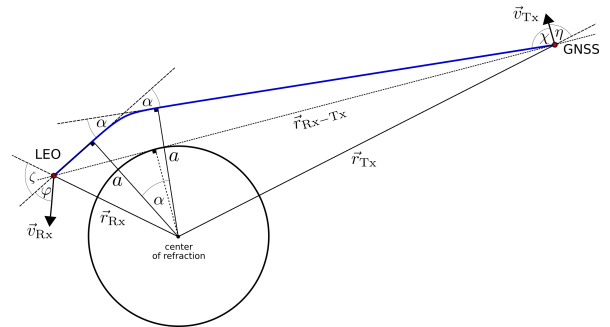


Figure 2: Illustration of the RO geometry showing the α angle of the bent GNSS signal (blue line) received by the LEO satellite (note the straight line \vec{r}_{Rx-Tx}). [12]

b) Extracting Refractive Index from Bending Angle: The bending caused by the atmosphere is a result of the gradient in the refractive index. Using Snell's law, the refractive index can be derived from the bending angle [13]. Figure 3 illustrates this relationship. In a spherically symmetric atmosphere, the product of the refractive index n , the distance to the center of the sphere r , and the angle of incidence θ remains constant (Eq. (1)). This constant, generally referred to as a , is known as the impact parameter.

$$rn \sin \theta = \text{constant} = a \quad (1)$$

The Abel transform inversion formula (Eq. (2)) is used to derive the refractive index $n(a)$ from the bending angle $\alpha(\xi)$ in a spherically symmetric medium.

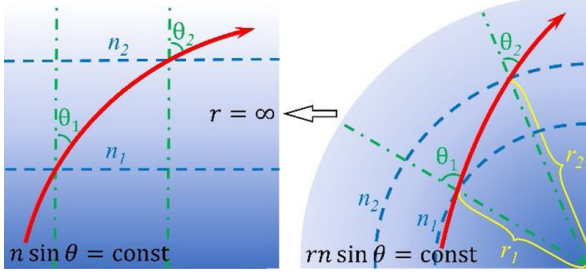


Figure 3: Illustration of Bouguer's rule (right), an extension of Snell's law (left), applied to a spherically symmetric medium [14].

$$n(a) = \exp \left[\frac{1}{\pi} \int_a^\infty \frac{\alpha(\xi)}{\sqrt{\xi^2 - a^2}} d\xi \right] \quad (2)$$

However, deriving $n(a)$ from $\alpha(\xi)$ using the Abel transform inversion assumes spherical symmetry. The Earth's ellipsoidal shape and horizontal atmospheric gradients cause deviations from this idealized symmetry in the refractive index field. Additionally, ray paths during an occultation do not scan the atmosphere radially or tangentially, so measurements of $\alpha(a)$ are influenced by tangential refractivity gradients and occultation geometry, potentially introducing systematic errors. Errors from the Abel transform inversion are generally related to the accuracy of the spherical symmetry approximation. First-order errors due to the Earth's ellipsoidal shape can be minimized by selecting an appropriate center and radius of curvature based on the latitude and orientation of the occultation measurement [6].

c) Doppler Effect on the Signals: The Doppler effect is employed to calculate the bending angle. This calculation is based on analyzing frequency shifts in GPS signals as they pass through different atmospheric layers, allowing for the reconstruction of refractivity profiles when combined with geometric analysis.

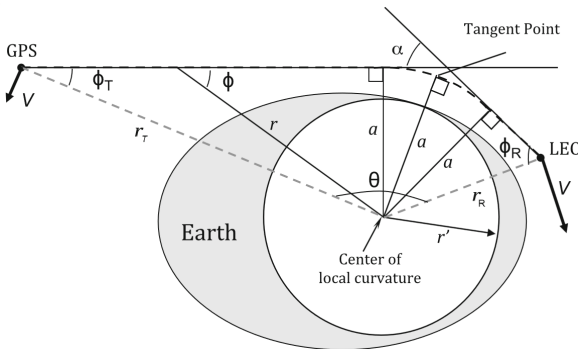


Figure 4: Image derived from [15] showing other geometric aspects compared to Fig. 2 and illustrating the contribution of the Doppler effect to the recovery of α .

The Doppler effect can be implemented using the following equation:

$$f_D = \frac{f_T}{c} (\mathbf{V}_T \cdot \mathbf{k}_T + \mathbf{V}_R \cdot \mathbf{k}_R)$$

However, it is practically used under the vector projection:

$$f_D = -\frac{f_T}{c} (V_T^r \cos \phi_T + V_T^\theta \sin \phi_T + V_R^r \cos \phi_R + V_R^\theta \sin \phi_R) \quad (3)$$

Combining the Doppler effect with Bouguer's rule (Eq. (1)), and considering n close to unity, we get:

$$a = r_T \sin \phi_T = r_R \sin \phi_R \quad (4)$$

The problem geometry allows us to use this relationship between angles:

$$\alpha = \phi_T + \phi_R + \theta - \pi \quad (5)$$

The following variables are used in calculating the Doppler shift and the total bending angle α :

- f_D : The additional Doppler shift, measurable.
- f_T : The known frequency of the GNSS signal.
- c : The speed of light in a vacuum.
- V_T^r and V_R^r : Radial components of the velocity vectors of the transmitting and receiving satellites, respectively (measurable using a GNSS receiver).
- V_T^θ and V_R^θ : Tangential components of the velocity vectors of the transmitting and receiving satellites, respectively (measurable using a GNSS receiver).
- ϕ_T and ϕ_R : Angles between the ray paths and the position vectors of the transmitting and receiving satellites, respectively (initially unknown).
- θ : Angle between position of transmitting and receiving satellite, taken from center of local curvature.

The Doppler effect provides detailed insights into the bending angle, assisting in the measurement of the refractive index profile and thus contributing to atmospheric research and weather prediction [16], [17].

III. ADVANCED TECHNIQUES FOR RADIO OCCULTATION

Beyond the general techniques used in radio occultation (RO), advanced methods are essential for overcoming measurement challenges. RO depends on the accurate interpretation of GNSS signals, which can be distorted by atmospheric phenomena such as ionospheric scintillation, multipath interference, and diffraction. Advanced techniques such as dynamic error estimation, machine learning, and bending angle optimization enhance data precision by addressing these distortions in real-time.

Machine learning algorithms adaptively correct signal distortions, while bending angle optimization and Radio Holographic & Back Propagation methods refine signal processing to reduce errors. Multi-GNSS processing leverages multiple satellite constellations to

improve the reliability of Doppler shift calculations and mitigate ionospheric disturbances. Together, these approaches significantly enhance the quality of RO data.

Improving the accuracy of RO data remains critical for advancing weather forecasting, climate monitoring, and space weather prediction. The following section outlines twelve categories of advanced techniques designed to address and mitigate the majority of challenges encountered in RO engineering.

The following section outlines twelve categories of advanced techniques designed to address and mitigate the majority of challenges encountered in RO engineering.

A. Comparison Criteria and Advanced Techniques

1) *Abel Inversion*: The Abel inversion technique transforms bending angle measurements into refractivity profiles, crucial for accurately extracting atmospheric parameters such as density, temperature, and pressure. Although effective, this method is limited by assumptions of spherical symmetry and is sensitive to noise, particularly in the presence of ionospheric scintillation. *Problems Addressed: Accuracy of Atmospheric Profiles* [18], [19]. This technique falls under the category: **Improvement of Measurement Accuracy**.

2) *Doppler Shift Analysis*: Doppler shift analysis enables precise determination of satellite velocity and trajectory, which is essential for compensating for errors caused by rapid orbital movements. This technique also effectively detects and corrects multipath effects, which arise from radio wave reflections. *Problems Addressed: Doppler Shift, Multipath Interference* [20], [21]. This technique falls under the categories: **Improvement of Measurement Accuracy** and **Multipath Management**.

3) *Advanced Wave Optics Processing*: Advanced wave optics processing models and corrects complex diffraction effects in the atmosphere, thereby improving measurement accuracy under challenging conditions. It is particularly effective in managing multipath interference and signal distortions. *Problems Addressed: Multipath Interference* [22], [23]. This technique falls under the categories: **Improvement of Measurement Accuracy**, **Multipath Management**, and **Processing of Complex Signals and Diffraction**.

4) *Dynamic Error Estimation and Weighting*: Dynamic error estimation and weighting improve the robustness of RO measurements by dynamically estimating and correcting errors in real-time. This technique is especially useful in reducing the impact of ionospheric scintillation and handling real-time variations in atmospheric conditions. *Problems Addressed: Ionospheric Scintillation, Accuracy of Atmospheric Profiles* [24], [25], [26]. This technique falls under the categories: **Correction of Ionospheric Scintillation**

Effects, Dynamic Error Optimization and Correction, and Improvement of Measurement Accuracy.

5) *Variational Inversion*: Variational inversion integrates RO data into numerical models, enhancing the accuracy of weather forecasts. This technique improves the handling of observation errors and allows for the precise incorporation of data into models, which is crucial for large-scale meteorological applications. *Problems Addressed: Accuracy of Atmospheric Profiles, Data Integration in Atmospheric Models* [27], [28]. This technique falls under the categories: **Data Integration in Atmospheric Models** and **Improvement of Measurement Accuracy**.

6) *Bending Angle Optimization*: Bending angle optimization corrects signal distortions by refining the derived bending angles, improving the quality of atmospheric profiles, especially in regions where multipath effects are prominent. *Problems Addressed: Multipath Interference* [29], [23]. This technique falls under the categories: **Multipath Management** and **Improvement of Measurement Accuracy**.

7) *Machine Learning Approaches*: Machine learning techniques detect and correct anomalies in RO data, such as ionospheric scintillation and multipath effects. These approaches improve real-time measurement accuracy by adapting to changing atmospheric conditions. *Problems Addressed: Ionospheric Scintillation, Accuracy of Atmospheric Profiles* [30], [31], [?]. This technique falls under the categories: **Correction of Ionospheric Scintillation Effects, Improvement of Spatial and Temporal Resolution, and Improvement of Measurement Accuracy**.

8) *Radio Holographic & Back Propagation Methods*: Radio holographic and back propagation methods enhance vertical resolution and improve atmospheric profile accuracy by filtering noise and reducing multipath effects. These techniques are especially valuable in complex propagation environments. *Problems Addressed: Multipath Interference, Accuracy of Atmospheric Profiles* [32], [33]. This technique falls under the categories: **Multipath Management, Processing of Complex Signals and Diffraction, and Improvement of Measurement Accuracy**.

9) *Multi-GNSS Processing*: Multi-GNSS processing improves RO coverage and accuracy by utilizing multiple satellite constellations. This technique effectively mitigates the effects of ionospheric scintillation and multipath by combining signals from different GNSS frequencies. *Problems Addressed: Ionospheric Scintillation* [34], [35], [36]. This technique falls under the categories: **Correction of Ionospheric Scintillation Effects, Multipath Management, Improvement of Spatial and Temporal Resolution, and Improvement of Measurement Accuracy**.

10) *Phase Matching*: Phase matching aligns signal phases from different frequencies, improving measurement accuracy by correcting variations caused by multipath interference. This technique is particularly ef-

fective in the lower troposphere. *Problems Addressed: Multipath Interference, Ionospheric Scintillation* [37], [38]. This technique falls under the categories: **Multipath Management** and **Correction of Ionospheric Scintillation Effects**.

11) *Ionospheric Scintillation*: Specific techniques for ionospheric scintillation detection and correction reduce errors caused by rapid signal fluctuations in the ionosphere, thus improving overall data quality. *Problems Addressed: Ionospheric Scintillation* [39], [40], [41]. This technique falls under the category: **Correction of Ionospheric Scintillation Effects**.

12) *Precise Orbit Determination (POD)*: Precise orbit determination is crucial for accurately tracking satellite positions, essential for minimizing errors in RO measurements related to orbital movements and satellite geometry. *Problems Addressed: Accuracy of Atmospheric Profiles* [42], [43]. This technique falls under the categories: **Dynamic Error Optimization and Correction** and **Improvement of Measurement Accuracy**.

In summary, each of these advanced techniques addresses specific challenges in RO data processing. Successful CubeSat-based RO missions require a balance between computational limitations, data quality, and the integration of these techniques to optimize atmospheric observations.

IV. COMPARATIVE TABLE OF ADVANCED TECHNIQUES

Evaluating advanced techniques for CubeSat-based radio occultation (RO) is key to ensuring the success of future missions. This analysis identifies the most effective techniques, highlighting their strengths and limitations for CubeSat missions.

In this study, a comparative analysis of advanced GNSS (Global Navigation Satellite System) radio occultation techniques was conducted, focusing on three specific criteria: **sufficient power supply**, **measurement accuracy**, and **measurement band management**. These criteria were selected based on their importance in previous work [10].

Sufficient power supply evaluates the energy needed to implement a technique on a CubeSat platform. It considers the **algorithmic complexity** and **computational load** as more complex algorithms demand more power, especially on resource-limited platforms.

Measurement accuracy assesses the technique's ability to provide reliable and accurate data. It is evaluated based on the improvements in atmospheric refractivity profiles or bending angles.

Measurement band management refers to the complexity of using and managing GNSS frequency bands to capture occulted radio signals. This criterion considers the **use of multiple frequencies** and **signal processing techniques** where advanced signal processing typically requires complex band management.

Table Table I provides a summary of the techniques and their performance against each criterion. Following this, two comparative analyses will be presented: one comparing techniques based on their differences and another analyzing techniques according to the established criteria.

V. RESULTS

The advancement of CubeSat-based Radio Occultation (RO) techniques represents a promising frontier in atmospheric science and satellite technology. As CubeSats become increasingly utilized for RO missions, addressing the technical challenges of these small, constrained platforms is critical for achieving high-quality atmospheric data. This chapter discusses findings from the literature review, highlights the performance of different techniques, and assesses their applicability to CubeSat-based RO missions. It also presents the results of our comprehensive evaluation of advanced RO techniques, focusing on their performance, advantages, and limitations in the context of CubeSat missions. By analyzing various techniques, we aim to identify the most effective approaches to enhance RO data accuracy and reliability within the constraints of CubeSat platforms.

A. Overview of Key Findings

Our investigation revealed that each advanced RO technique has distinct strengths and limitations when applied to CubeSat missions. The comparative analysis considered several factors, including accuracy, computational requirements, and adaptability to CubeSat constraints such as size and power limitations. The evaluated techniques include Abel Inversion, Advanced Wave Optics Processing, Dynamic Error Estimation and Weighting, Variational Inversion, Bending Angle Optimization, Machine Learning Approaches, Radio Holographic & Back Propagation Methods, Multi-GNSS Processing, Phase Matching, and Ionospheric Correction.

Our evaluation of advanced RO techniques highlights the following key findings.

1) *Abel Inversion*: Abel Inversion remains a foundational technique due to its simplicity and computational efficiency. It allows for the direct retrieval of atmospheric profiles from bending angle data without requiring extensive a priori information. However, its reliance on spherical symmetry and sensitivity to noise limit its accuracy, particularly in the lower troposphere. For CubeSat missions, integrating Abel Inversion with other techniques to enhance error handling and profile accuracy is essential.

2) *Advanced Wave Optics Processing*: Advanced Wave Optics Processing offers significant improvements in handling diffraction effects and enhancing vertical resolution, especially in the lower troposphere. This technique's computational complexity and sensitivity to observation errors are notable challenges.

Advanced Techniques	Embedding Requirements	Computational Complexity	Measurement Accuracy	Minimum Bandwidth	Minimum Space Requirements	References
Abel Inversion	No	Moderate	Moderate	Weak	FPGA only + eventual external memory for managing error estimates.	[18], [19]
Doppler Shift Analysis	Yes (Critical real-time)	High	High	Moderate	FPGA + Dedicated processor for real-time Doppler shift derivation.	[20], [21]
Advanced Wave Optics Processing	No	High	High	Moderate	FPGA + external memory for handling spectral calculations.	[22], [23]
Dynamic Error Estimation and Weighting	Yes (Critical real-time)	High	Moderate	Moderate	Always FPGA + external memory for real-time error management.	[24], [25], [26]
Variational Inversion	No	High	High	Moderate	Always FPGA + external memory for managing complex models.	[27], [28]
Bending Angle Optimization	No	Moderate	Moderate	Moderate	FPGA only + eventual external memory for covariance matrix handling.	[29], [23], [25]
Machine Learning Approaches	Implicit mention of fast processing	High	High	Moderate	Always FPGA + external memory for model and data storage.	[30], [31], [41]
RH & BP Methods	No	High	Moderate	High	Always FPGA + external memory for hologram processing.	[32], [33]
Multi-GNSS Processing	Implicit mention of fast processing	Moderate	Moderate	Moderate	Always FPGA + external memory for real-time multi-signal processing.	[34], [35], [36]
Phase Matching	Yes (Critical real-time)	High	Moderate	High	FPGA only + eventual external memory for managing reflection data.	[37], [38]
Ionospheric Scintillation	Implicit mention of fast processing	Moderate	Moderate	Moderate	FPGA only + eventual external memory for scintillation model storage.	[39], [40], [41]
Precise Orbit Determination (POD)	Yes (Critical real-time)	High	High	High	Always FPGA + external memory for precise orbit data processing.	[42], [43]

Table I: Summary of Criteria for Advanced GNSS Radio Occultation Techniques

For CubeSat missions, balancing computational demands with data quality and potentially combining this technique with simpler methods could enhance performance.

3) *Dynamic Error Estimation and Weighting*: Dynamic Error Estimation and Weighting enhance measurement accuracy through adaptive processing and better error quantification. It optimizes data usage and improves vertical resolution. Despite its potential, this technique's high computational burden and dependency on accurate error models pose challenges. Adapting it to CubeSat constraints requires careful consideration of computational resources and error management.

4) *Variational Inversion*: Variational inversion excels in integrating multiple data sources and handling non-linear problems, leading to more accurate atmospheric profiles. However, its high computational demands and dependence on a priori information can lead to over-constraining. For CubeSat-based RO, improving data quality and leveraging constellation missions are critical.

5) *Bending Angle Optimization*: This technique optimizes bending angles to correct distortions, improving data quality and reducing sensitivity to ionospheric effects. Despite its advantages, bending angle optimization is computationally intensive and relies on statistical methods, which can lead to the loss of small-scale structures. Noise reduction and extending the altitude range are important considerations for CubeSat adaptation.

6) *Machine Learning Approaches*: Machine learning techniques offer significant potential for handling complex data relationships, improving accuracy, and reducing noise post-training. However, these methods require substantial data and are prone to overfitting. Their 'black box' nature and sensitivity to data quality add complexity. Addressing data limitations and onboard processing potential is vital for CubeSat integration.

7) *Radio Holographic & Back Propagation Methods*: This approach provides higher vertical resolution and improved accuracy by resolving multipath effects and analyzing full wave fields. The method's ability to

detect super-refraction is advantageous, but it is computationally intensive and sensitive to noise. Enhancing vertical resolution while managing computational limitations is crucial for CubeSat applications.

8) *Multi-GNSS Processing*: Utilizing multiple GNSS constellations increases data volume and accuracy while reducing system-specific issues. However, the increased complexity and computational requirements pose challenges. Addressing hardware constraints and leveraging constellation synergy are necessary to unlock the full potential of multi-GNSS processing in CubeSat missions.

9) *Phase Matching*: Phase matching improves accuracy and vertical resolution by correcting phase variations and handling multipath effects. While it ensures consistent processing across altitudes, it faces challenges such as computational complexity and dependence on accurate orbit information. Improving lower troposphere retrievals and enhancing vertical resolution are key considerations for CubeSats.

10) *Ionospheric Correction*: This technique enhances accuracy in neutral atmosphere retrievals and extends the altitude range. It offers dual-use potential and mitigates systematic errors but relies on dual-frequency measurements and faces residual errors and computational complexity. Addressing hardware constraints and data quality improvements are critical for effective use in CubeSat-based RO.

B. Performance Analysis of Techniques

The performance analysis reveals that:

- **Accuracy and Reliability**: Techniques such as Variational Inversion, Bending Angle Optimization, and Machine Learning Approaches stand out for their potential to improve accuracy and reliability. Variational Inversion and Bending Angle Optimization excel in handling errors and improving data quality, while Machine Learning Approaches offer adaptability and advanced error correction capabilities.
- **Computational Constraints**: Techniques like Advanced Wave Optics Processing, Radio Holographic & Back Propagation Methods, and Multi-GNSS Processing present significant computational challenges. These methods require substantial processing power and may need optimization or simplification to fit within CubeSat constraints.
- **Adaptation to CubeSat Constraints**: Abel Inversion, Phase Matching, and Ionospheric Correction show potential for adaptation due to their relatively lower computational demands and compatibility with CubeSat missions. However, their effectiveness depends on careful integration with other techniques and robust error handling.

C. Comparative Evaluation

Using criteria detailed in Chapter IV Comparative Analysis and the identified challenges of CubeSat

missions, we classify the techniques as follows:

- **High Potential**: Variational Inversion, Bending Angle Optimization, and Machine Learning Approaches are classified as high potential due to their ability to address accuracy and reliability challenges effectively. These techniques offer substantial improvements in data quality and have potential for adaptation to CubeSat missions with appropriate modifications.
- **Moderate Potential**: Dynamic Error Estimation and Weighting, Phase Matching, and Ionospheric Correction have moderate potential. They offer benefits but also face challenges related to computational constraints and data quality. With careful adaptation and integration, these techniques could enhance CubeSat-based RO performance.
- **Lower Potential**: Advanced Wave Optics Processing, Radio Holographic & Back Propagation Methods, and Multi-GNSS Processing are categorized as having lower potential due to their high computational requirements and complexity. These techniques may be more suitable for larger platforms or require significant optimization for effective CubeSat implementation.

D. Initial Reflections and Future Work

The comparative analysis highlights that integrating advanced techniques, adapting them to CubeSat constraints, and combining their strengths can enhance RO data accuracy and reliability. Future work should focus on:

- **Optimizing Computational Efficiency**: Developing strategies to balance computational demands with the benefits of advanced techniques, ensuring effective use within CubeSat constraints.
- **Enhancing Data Integration**: Combining techniques such as Variational Inversion with Machine Learning Approaches to leverage their strengths and address specific challenges.
- **Exploring New Techniques** Investigating emerging techniques and technologies that could further improve RO data quality and address CubeSat-specific challenges.

These topics reflect the challenges and opportunities identified in the results and offer a pathway for future research in CubeSat-based RO technology.

E. Foundation for the ROCUS-1 Project

The insights and findings from this study lay a solid foundation for the ROCUS-1 project, which represents a significant step forward in integrating advanced GNSS Radio Occultation (RO) techniques with CubeSat platforms. The primary objective of the ROCUS-1 project is to develop and deploy a CubeSat-based RO system that enhances the accuracy and reliability of atmospheric measurements while addressing the unique challenges posed by CubeSat missions.

1) *Structural and System Design*:: Based on the theoretical framework established in this study, the ROCUS-1 project will involve the construction of a comprehensive CubeSat framework, often referred to as the "skeleton" of the satellite. This framework will encompass the design and integration of key components including the payload, communication systems, power supply, and structural elements. The design process will ensure that the CubeSat is optimized for the specific requirements of RO measurements, including size, power, and thermal management.

2) *Development of a System State Machine*:: A crucial aspect of the ROCUS-1 project will be the development of a system state machine, which will manage the CubeSat's operations, including data collection, processing, and transmission. The state machine will coordinate the various subsystems and ensure that the satellite operates efficiently and reliably throughout its mission. This involves designing algorithms for automated error correction, data handling, and system diagnostics.

3) *Integration of Advanced Techniques*:: The project will integrate several advanced GNSS RO techniques reviewed in this study, including Abel Inversion, Advanced Wave Optics Processing, Dynamic Error Estimation and Weighting, and Machine Learning Approaches. The integration of these techniques will be tailored to address the specific challenges of CubeSat missions, such as limited size and power, and will focus on improving the accuracy of atmospheric profiles.

4) *Exploration of Doppler Effect*:: Future work in the ROCUS-1 project will also delve deeper into the Doppler effect, which has been identified as a significant factor in signal processing and data accuracy. This involves developing and implementing advanced algorithms to correct Doppler shift distortions and enhance the precision of RO measurements. Understanding and mitigating the Doppler effect will be crucial for improving the overall performance of the CubeSat-based RO system.

5) *Preliminary Testing and Validation*:: To ensure the effectiveness of the design and integration, the ROCUS-1 project will include rigorous testing and validation phases. This will involve simulations, ground tests, and, where feasible, preliminary flight tests to assess the CubeSat's performance and the accuracy of the RO data. The results from these tests will guide further refinements and optimizations.

In conclusion, the ROCUS-1 project builds on the theoretical base established through this study, providing a pathway to realizing a state-of-the-art CubeSat-based RO system. The project's success will depend on effectively addressing the identified challenges, integrating advanced techniques, and advancing our understanding of critical factors such as the Doppler effect. The outcomes of the ROCUS-1 project will contribute significantly to the field of atmospheric

science, enhancing our ability to obtain accurate and reliable atmospheric data from CubeSat platforms.

VI. METHODOLOGY

The methodology for analyzing GNSS RO techniques for CubeSat platforms involves the following steps:

- **Reviewing Literature:** Conducting a thorough review of approximately 50 articles and 4 books to gain a comprehensive overview of radio occultation. This review aims to consolidate existing knowledge and identify key advancements in the field.
- **Developing an Action Plan:** Formulating a strategic action plan to address the specific challenges and solutions related to CubeSat RO missions. This plan will outline the steps required to overcome identified issues and enhance mission effectiveness.
- **Analyzing Key Challenges and Techniques:** Investigating the primary challenges, techniques, and issues associated with CubeSat missions. This analysis will focus on understanding the constraints and requirements unique to CubeSat platforms.
- **Conducting Comparative and Historical Analysis:** Performing comparative and historical analyses through an extended literature review. This step will involve evaluating the evolution of RO techniques and comparing their effectiveness across different platforms and contexts.
- **Identifying Initial Reflections:** Identifying initial insights and reflections to guide future work. These reflections will help in formulating recommendations and directing future research efforts to address the challenges identified during the analysis.

VII. CONCLUSION

In this study, we explored the integration of advanced GNSS Radio Occultation (RO) techniques with CubeSat platforms to enhance the accuracy and reliability of RO data, while addressing the unique challenges posed by CubeSat missions. We conducted a thorough review of both the fundamental challenges and the state-of-the-art techniques available for improving RO measurements.

We identified several major challenges associated with CubeSat-based RO missions, including limitations in size and power, the need for efficient collision avoidance, and the complexities of data downlink and regulatory compliance. These challenges are compounded by the inherent constraints of CubeSat platforms, which necessitate innovative solutions for successful deployment and operation.

In response to these challenges, we reviewed advanced GNSS RO techniques such as Abel Inversion,

Advanced Wave Optics Processing, Dynamic Error Estimation and Weighting, Variational Inversion, and Machine Learning Approaches. Each technique was evaluated for its ability to address specific issues such as signal distortion, multipath interference, and ionospheric scintillation. Our analysis highlighted the strengths and limitations of each approach, providing a comprehensive overview of their potential applications in CubeSat missions.

The insights gained from this study form the theoretical foundation for the ROCUS-1 project, which aims to implement these advanced techniques in the development of a CubeSat-based RO system. The findings provide a crucial basis for designing and optimizing the CubeSat's structural framework, including its hardware and software components. This includes the construction of the CubeSat's "skeleton" or structural framework and the development of a system state machine to manage the CubeSat's operations effectively.

Looking forward, the ROCUS-1 project will build on these insights to address the practical implementation of advanced RO techniques, with a particular focus on overcoming the challenges identified in this study. Future work will involve constructing and testing the CubeSat's complete framework, integrating the advanced techniques reviewed, and exploring further developments in Doppler effect correction and other related areas.

By laying a solid theoretical groundwork and identifying key areas for future research, this study paves the way for the successful realization of the ROCUS-1 project. The integration of these advanced techniques into CubeSat missions will enhance our ability to obtain accurate and reliable atmospheric profiles, ultimately contributing to improved weather forecasting, climate monitoring, and space weather prediction.

In summary, this research underscores the importance of combining advanced GNSS RO techniques with CubeSat technology to overcome existing limitations and achieve significant advancements in atmospheric observation. The conclusions drawn from this study will guide future research and development efforts, ensuring that the ROCUS-1 project and subsequent missions are well-positioned to address the challenges of CubeSat-based RO and deliver valuable scientific data.

REFERENCES

- [1] N. A. Gadallah and A. A. Siddig, "Space and Ground-Based Earth Observations for Hazards Valuation and Disaster Risk Management in the Era of Climate Change," in *Revolutionizing Earth Observation - New Technologies and Insights* (R. M. Abdalla, ed.), ch. 10, Rijeka: IntechOpen, 2024.
- [2] M. Krichen, M. S. Abdalzaher, M. Elwekeil, and M. M. Fouda, "Managing natural disasters: An analysis of technological advancements, opportunities, and challenges," *Internet of Things and Cyber-Physical Systems*, vol. 4, pp. 99–109, 2024.
- [3] Y.-A. Liou, A. Pavelyev, S. Matyugov, O. Yakovlev, and J. Wickert, *Radio Occultation Method for Remote Sensing of the Atmosphere and Ionosphere*. 02 2010.
- [4] J. Xia, X. Wang, X. Meng, D. Zhao, C. Liu, G. Tan, Z. Liu, and X. Liu, "Applications of GNSS-RO to Numerical Weather Prediction and Tropical Cyclone Forecast," *Atmosphere*, vol. 11, no. 11, p. 1204, 2020.
- [5] V. R. Eshleman, "Jupiter's atmosphere: Problems and potential of radio occultation," *Science*, vol. 189, no. 4206, pp. 876–878, 1975.
- [6] E. R. Kursinski, G. A. Hajj, J. T. Schofield, R. P. Linfield, and K. R. Hardy, "Observing Earth's atmosphere with radio occultation measurements using the Global Positioning System," *Journal of Geophysical Research: Atmospheres*, vol. 102, no. D19, pp. 23429–23465, 1997.
- [7] J. Wickert, G. Beyerle, R. König, S. Heise, L. Grunwaldt, G. Michalak, C. Reigber, and T. Schmidt, "GPS radio occultation with CHAMP and GRACE: A first look at a new and promising satellite configuration for global atmospheric sounding," in *Annales Geophysicae*, vol. 23, pp. 653–658, Copernicus Publications Göttingen, Germany, 2005.
- [8] W. S. Schreiner, S. V. Sokolovskiy, C. Rocken, and D. C. Hunt, "Analysis and validation of GPS/MET radio occultation data in the ionosphere," *Radio Science*, vol. 34, no. 4, pp. 949–966, 1999.
- [9] A. Carlström, M. Bonnedal, T. Lindgren, and J. Christensen, "Improved GNSS radio occultation with the next generation GRAS instrument," in *2012 6th ESA Workshop on Satellite Navigation Technologies (Navitec 2012) & European Workshop on GNSS Signals and Signal Processing*, pp. 1–4, IEEE, 2012.
- [10] L. Qiao, E. Glennon, A. G. Dempster, and S. Chaoui, "Using cubesats as platforms for remote sensing with satellite navigation signals," in *2013 IEEE International Geoscience and Remote Sensing Symposium-IGARSS*, pp. 852–855, IEEE, 2013.
- [11] W. J. Blackwell, "The MicroMAS and MiRaTA CubeSat atmospheric profiling missions," in *2015 IEEE MTT-S International Microwave Symposium*, pp. 1–3, IEEE, 2015.
- [12] J. Innerkofler, G. Kirchengast, M. Schwärz, C. Marquardt, and Y. Andres, "GNSS radio occultation excess-phase processing for climate applications including uncertainty estimation," *Atmospheric Measurement Techniques*, vol. 16, no. 21, pp. 5217–5247, 2023.
- [13] J. M. Kelso, "Ray Tracing in the Ionosphere," *Radio Science*, vol. 3, no. 1, pp. 1–12, 1968.
- [14] G. Feng and J. Huang, "An optical perspective on the theory of relativity—: Space-time invariant," *Optik*, vol. 224, p. 165697, 2020.
- [15] S. Jin, E. Cardellach, and F. Xie, *GNSS remote sensing*, vol. 16, Springer, 2014.
- [16] E. R. Kursinski, G. A. Hajj, S. S. Leroy, and B. Herman, "The GPS radio occultation technique," *Terrestrial Atmospheric and Oceanic Sciences*, vol. 11, no. 1, pp. 53–114, 2000.
- [17] W. Emery and A. Camps, "Chapter 6 - remote sensing using global navigation satellite system signals of opportunity," in *Introduction to Satellite Remote Sensing*, pp. 455–564, Elsevier, 2017.
- [18] M. Hernández-Pajares *et al.*, "Improving the abel inversion by adding ground data to leo radio occultations in ionospheric sounding," *Geophysical Research Letters*, 2000.
- [19] S. S. C. R. W. S. D. H. Y.-H. Kuo, T.-K. Wee and R. A. Anthes, "Inversion and Error Estimation of GPS Radio Occultation Data," *Journal of the Meteorological Society of Japan*, vol. 82, no. 1B, pp. 507–531, 2004.
- [20] G. Kirchengast and S. Schweitzer, "Advanced Retrieval Processing Chain for Derivation of Temperature," *IEEE Transactions on Geoscience and Remote Sensing*, vol. 44, pp. 3015–3031, 2006.
- [21] I. Panagiotis *et al.*, "Preliminary results from COSMIC RO to Doppler shift and satellite velocity variations," *Journal of Geophysical Research: Atmospheres*, vol. 114, p. D18105, 2009.
- [22] M. E. Gorbunov, "Wave optics algorithms for processing radio occultation data in the lower troposphere," *Radio Science*, vol. 39, p. RS3009, 2004.
- [23] I. Culverwell *et al.*, "The radio occultation processing package, ropp," *Atmospheric Measurement Techniques*, vol. 8, pp. 1889–1901, 2015.

- [24] C. M. S. Healy, A. M. Jupp and S. B. Healy, “Dynamic Statistical Optimization of GNSS Radio Occultation Bending Angles,” *Atmospheric Measurement Techniques*, vol. 8, no. 8, pp. 3447–3465, 2015.
- [25] M. S. Lohmann, “Dynamic Error Estimation for Radio Occultation Bending Angles Retrieved by the Full Spectrum Inversion Technique,” *Radio science*, vol. 41, no. 05, pp. 1–12, 2006.
- [26] M. E. Gorbunov and K. B. Lauritsen, “Error estimate of bending angles in gps radio occultations,” *Journal of Geophysical Research: Atmospheres*, vol. 114, p. D07102, 2009.
- [27] G. Wee *et al.*, “A variational regularization of Abel transform for gps radio occultation,” *Journal of Geodesy*, 2018.
- [28] M. E. Gorbunov and S. V. Sokolovskiy, “Principles of variational assimilation of gnss radio occultation data,” *Journal of Atmospheric and Oceanic Technology*, vol. 20, pp. 1314–1324, 2003.
- [29] J. Schwarz *et al.*, “Integrating uncertainty propagation in gnss radio occultation: from excess phase to atmospheric bending angle profile,” *Atmospheric Measurement Techniques*, 2018.
- [30] H. Hassani *et al.*, “Interpolation, satellite-based machine learning, or meteorological models,” *Earth Science Informatics*, 2023.
- [31] L. Mengying, Z. Xuefen, L. Yimei, and Y. Fan, “Analysis of Ionospheric Scintillation Detection Based on Machine Learning,” in *2020 International Conference on Smart Materials, Intelligent Manufacturing and Automation (ICSMD)*, pp. 357–361, 2020.
- [32] M. Gorbunov and K. Lauritsen, “Radio holographic filtering of noisy radio occultations,” in *Atmosphere and Climate: Studies by Occultation Methods*, pp. 127–134, Springer, 2006.
- [33] M. E. Gorbunov, “Radioholographic analysis of radio occultation data in multipath zones,” *Radio Science*, vol. 37, no. 1, pp. 1–9, 2002.
- [34] F. Peng *et al.*, “Satellite formation flight simulation using multi-constellation gnss,” *Advances in Space Research*, vol. 64, pp. 1405–1419, 2019.
- [35] I. Cherniak *et al.*, “Accuracy assessment of the quiet-time ionospheric f2 peak,” *Journal of Geophysical Research: Space Physics*, vol. 126, p. e2020JA028918, 2021.
- [36] Y. Qiu *et al.*, “An innovative fpga-based low-complexity and multi-constellations compatible gnss,” *Remote Sensing*, vol. 13, p. 2001, 2021.
- [37] A. S. Jensen and P. H. Høeg, “Geometrical optics phase matching of radio occultation signals,” *Radio Science*, vol. 39, no. 3, p. RS3009, 2004.
- [38] S. Sievert, G. Beyerle, and T. Schmidt, “Analysis of reflections in gnss radio occultation measurements,” *Atmospheric Measurement Techniques*, vol. 11, no. 9, pp. 4843–4857, 2018.
- [39] S.-H. Chen *et al.*, “Observational error estimation of formosat-3/cosmic gps radio occultation data,” *Journal of Geophysical Research: Atmospheres*, vol. 114, p. D22106, 2009.
- [40] C. S. Carrano and C. L. Rino, “Multiple phase screen modeling of ionospheric scintillation along radio occultation paths,” *Radio Science*, vol. 46, p. RS0D07, 2011.
- [41] V. Ludwig-Barbosa, T. Sievert, A. Carlström, M. I. Pettersson, V. T. Vu, and J. Rasch, “Supervised Detection of Ionospheric Scintillation in Low-Latitude Radio Occultation Measurements,” *Remote Sensing*, vol. 13, no. 9, p. 1690, 2021.
- [42] Z. Kang *et al.*, “Precise orbit determination for grace using gps data,” *Advances in Space Research*, vol. 31, no. 8, pp. 1875–1881, 2003.
- [43] J. Innerkofler *et al.*, “Precise orbit determination for climate applications of gnss radio occultation including uncertainty estimation,” *Journal of Geodesy*, 2020.

The nanoMIRAX-1 Mission – The First Brazilian Astrophysics Space Mission

João Braga, Flavio D'Amico
National Institute for Space Research -
INPE
São José dos Campos, Brazil
joao.braga@inpe.br

Otávio Durão
CRON – Sistemas e Tecnologias Ltda.
São José dos Campos, Brazil
otavio@cronsistec.com.br

Valter Schad
Horusey Tech
São José dos Campos, Brazil
horuseye@horuseye.com.br

Abstract— nanoMIRAX-1 is a 2U cubesat mission for X and gamma rays detection. The scientific payload of the mission (LECX – X-Ray Cosmic Explosions Locator) is an experiment for the detection of hard X-ray and gamma ray radiation in space, possibly from cosmic explosions such as Gamma-Ray Bursts (GRBs). This experiment was initially conceived for a larger bus, but it has never materialized due to its costs. The number of detectors in the payload array was significantly decreased but it will still produce significant results for the mission PI. One exciting possibility is the detection of electromagnetic counterparts of gravitational wave signals detected by the LIGO/Virgo consortium. This was not known when the larger bus was being considered for this mission. Nanomirax-1 will be able to detect, with an accuracy of a few degrees for its origin, explosive cosmic events that manifest themselves mainly through the emission of hard X-rays. This location algorithm was developed in the project according to the X/gamma ray covered area on the array of four sensors in the payload camera. In particular, in the current era of multimessenger astronomy, strongly stimulated by the first detections of gravitational waves from the coalescence of compact objects, it will be extremely auspicious that experiments capable of detecting and localizing the electromagnetic counterparts of these events are "patrolling" the celestial sphere.

The cubesat is a 2U with 1U fully for the payload. The engineering model (EM) was developed and funded under the PIPE (Program for Innovation in the Small Companies) from FAPESP – The State of São Paulo Research Support Foundation. The EM bus was developed by a cluster of small companies and LEX by the INPE and its Instrumental Astrophysics Group. The cubesat was tested for vibration and thermal gradient at INPE's AIT Lab (LIT). With functional testing performed before and after the tests.

The EM uses the same electronics, components and subsystems as the flight model (FM), both for the LECX (it has 3 electronic boards) and the bus. The EM doesn't have the solar panels and the on-board antenna set. The FM is being funded by the Brazilian Space Agency – AEB and INPE. The EM was quite stressed during testing, so the FM needed to be developed with the recurrent ground qualified design, solar panels and on board antenna set. The FM will use space scientific UHF frequency and will be operated by INPE cubesat ground station at its Northeast Regional Center in the city of Natal, RN. All the subsystems, panels and on-board antenna set were delivered and a new version of the OBC data handling software is being implemented. The bus includes a GPS and a module locally designed to stabilize the cubesat and keep determining its attitude for the location of the event in the celestial sphere. Data will also be sent to Earth for post-processing.

Keywords— *multi messenger, astronomy, X-rays, gravitational waves, cubesats.*

I. INTRODUCTION

With the current explosive growth of the nanosat phenomenon based especially on the so-called CubeSat platform new opportunities for fast-development, low-cost small instruments have appeared.

In principle, X- and gamma-ray astrophysical instruments on such small satellites cannot compete with full-sized instruments operating on conventional large and complex satellite buses. Nevertheless, for very specific science goals, it is possible to design instruments compatible with cubesat buses that can meet the desired requirements. In this paper we describe an instrument developed for a cubesat platform that is capable of detecting and locating relatively strong cosmic explosions that manifest themselves electromagnetically mainly in the hard X-ray/low energy gamma-ray range. The experiment, called "Localizador de Explosões Cósmicas de Raios X" (LECX -- Portuguese for Locator of X-ray Cosmic Explosions), will be sensitive enough to detect and localize within a few degrees events like the well-known gamma-ray bursts (GRBs) in the 30-200 keV energy range. With its $53^\circ \times 53^\circ$ FWHM ("Full Width at Half Maximum") field of view (FOV), it is estimated that LECX will detect ~5 GRBs per year.

In the recently-inaugurated multimessenger astrophysics era, it is very important that wide-field space instruments constantly patrol the sky in order to instantly detect electromagnetic counterparts of gravitational wave (GW) and/or neutrino cosmic bursting events. With the increased sensitivities of ground-based observatories of gravitational waves (e.g. LIGO/VIRGO) and neutrinos (e.g. IceCube), it is expected that the rate of such events will gradually increase over the years. X- and gamma-ray space experiments will then have higher probabilities of contributing to multimessenger detections of such phenomena.

II. THE MISSION SCIENCE AND THE PAYLOAD

A. The LECX instrument

NanoMIRAX [1] is a mission designed to detect cosmic explosions in the hard X-ray range and produce localization of the event within a few degrees, depending on the intensity and the zenith and azimuth angles of the event in the satellite coordinates. The experiment, called LECX ("Localizador de

Explosões C3smicas de raios X”), takes the Upper “U” of the satellite and uses 4 X-ray planar detectors made of CdZnTe (CZT) with dimensions 10x10 mm and a thickness of 2 mm, in a 2x2 configuration. The energy range is 30 to 200 keV. The lower limit is imposed by electronics noise and the higher limit is due to detector thickness. The separation between adjacent detector volumes is 3 mm due to the mechanical mounting and the presence of the detectors' ceramic (alumina) substrates. Figure 1 shows the detector plane. CZT room-temperature semiconductor detectors have been extensively used in astronomical X- and gamma-ray space instruments due to their very high photoelectrical efficiency up to hundreds of keV and good energy resolution. They are also easy to handle and can be tiled to cover large surfaces. Pixelated CZT detectors can also be built for imaging instruments.

The array is surrounded by a Pb (1.0mm), Sn (1.7mm) and Cu (0.3mm) graded shield box to minimize background and define the instrument FOV. The distance from the detector plane surface to the top of the shielding box is 20mm. In the upper part of the box there is an aperture of 23mm x 23mm that matches the detector plane area below (considering the gaps between the detectors). The instrument aperture is closed with a 0.4mm-thick carbon fiber plate to prevent the entrance of environment light, which induces noise in the detector electronics.

The detector system is surrounded by a dielectric material (teflon) structure that provides mechanical support and housing for batteries and electronic parts (see Figure 1). Teflon is widely used in space application due to its suitable mechanical properties. The whole system is mounted on a standard 89mm x 89mm cubesat printed-circuit board (the DPCB, for Detector Printed Circuit Board) at the top of the satellite structure (the “top” direction hereafter refers to the instrument axis, i.e. the direction corresponding to the centre of its FOV). The front-end analog electronics for the

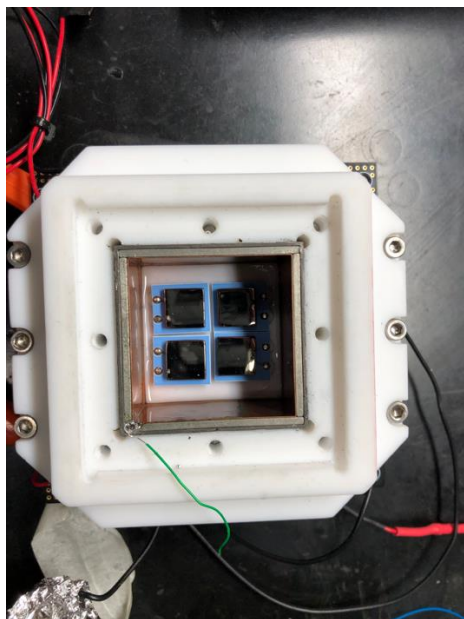


Fig. 1 – The detector plane of LECX with 4 CZT detectors

detectors, which comprises four sets of charge pre-amplifiers and low-noise shaping amplifiers (LNA), is mounted on the opposite (bottom) side of the DPCB. This PCB, as well as the other two, has multiple interconnected copper layers to provide electrical shielding. At the bottom part of the detector substrates lies the bottom part of the shielding box, so that the two electric leads (the one that polarizes the anode with the reverse bias and the one carrying the charge signal pulse from the cathode) perforate the shielding material, in teflon tubes, in order to reach the PCB underneath. The radiation shielding is also connected to the common ground to contribute to the electrical shielding. In Figure 2 we show a computer view of half of the upper board of the detector system. The cylindrical cavities provide housing to the detector batteries.

A second PCB (the TPCB, for Time Printed-Circuit Board), mounted underneath the DPCB, houses the four Height-Time Converter (HTC) electronics, which linearly converts the heights of the pulses coming from the detectors to a digital high level signal. A third PCB, the experiment on-board-computer (EOBC), houses the digital electronics, which is responsible for performing the following tasks: (a) receive signals from the 4 outputs of the TPCB; (b) measure the time duration of the correspondent high level signals and convert them into digital 8-bit words (this is proportional to the deposited energy of each event, divided in 256 channels), (c) flag the individual detector where the event occurred and convert it into a 2-bit word; (d) tag each event with the Universal Time from the satellite on-board computer (OBC), that uses a GPS receiver, with a resolution of 255 microseconds, (e) build the event packages with time, detector ID and energy information (each event will generate a 24-bit word); (f) store data files and send copies to the spacecraft OBC for transmission to ground. The EOBC uses a commercial low power PIC24F32 microcontroller very suitable for this specific application. The power consumption of the LECX electronic system is less than 800 mW.

According to simulations of the radiation level to be measured in orbit the LECX payload will produce ~100 bits/s in nominal operation, which will generate ~540 kbits/orbit and ~8.6 Mbits/day of data. Assuming at least one 10-minute ground station passage every orbit, this will require ~900 bits/s telemetry capacity, well below the envisaged capabilities of the satellite.

The three PCBs of the nanoMIRAX payload, which comprise the LECX experiment, fill the first “U” of the satellite and constitute the payload module. The second “U”, the service module, mounted on the bottom of the payload module, houses the satellite subsystems.

B. The source position determination algorithm

With the four CZT detectors placed inside the passive shielding box, as described in the last section, the FOV of the detector system is a square region of the sky of 53° x 53° FWHM (~7 % of the sky) and 90° x 90° FWZI (“Full Width at Zero Intensity”). In this section we describe a new algorithm we have devised to determine the celestial

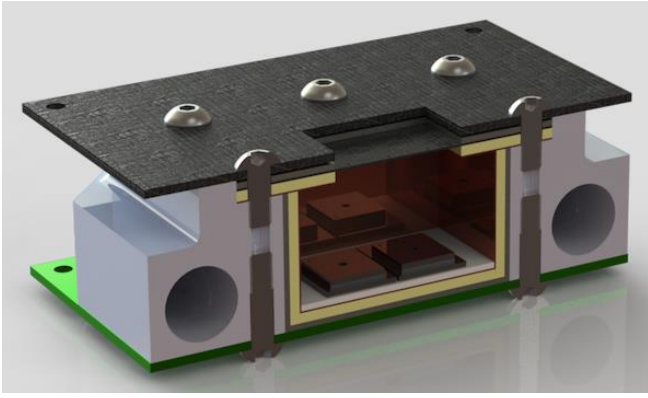


Fig. 2 – A view of the detector system cut in half.

coordinates of strong cosmic explosions based on the intensities measured in each detector during the event.

In standard collimated high-energy detector systems, the fluxes of astrophysical sources are determined by subtracting a background level, measured separately, from the amount of radiation measured when the source is in the collimator FOV. For pixelated detector planes, one can use a coded mask in the aperture to obtain an image of the source field within the FOV (see, e.g. [2]). In the LECX cubesat experiment described here, we have only 4 pixels (the four planar detectors) and a limited sensitivity due to the fact that the total area is only 4 cm². Since we are interested in detecting strong, short-duration point-source cosmic explosions one at a time, a coded mask placed in the experiment's aperture will not be adequate to use due to three reasons: (a) the results to be obtained are not images of source fields, but only measured fluxes of short-duration (~seconds) point sources. The known persistent or transient astrophysical sources will be too weak to detect on those timescales; (b) the advantage of coded-mask systems in measuring source and background simultaneously are not important here, since we will have plenty of time to measure the background anyway, and in the same region of the sky; and (c) there are no "URA-like" mask patterns with 2 x 2 dimensions that could produce images with no intrinsic noise, i.e. there are no 2x2 patterns with a 2D discrete Dirac-delta autocorrelation function. We decided to develop and use instead a different algorithm that takes into account the "shadows" projected on the detector plane by the walls of the shielding box. This has the additional advantage of not partially blocking the FOV with a mask.

During the detection of a radiation burst coming from a single direction (representing a cosmic explosion), the x and y extensions (with respect to the square shielding box and detector orientations) of the wall shadows on the detector plane is a function of the azimuth and zenith angles of the incoming photons. Since the number of source counts in each detector is proportional to the illuminated area, we can determine the source position in the sky by measuring the counts in each detector when the count rates suddenly increase during the occurrence of such an event in the FOV.

To explain the method, let us first define a coordinate system with axes x and y along the detector sides for a given detector plane orientation in which North is to the top (y) and East is

to the right (x); see Figure 3. The relevant units of distance are the detector side s (10mm in this case) and the height of the shielding walls above the detector surface, H (20mm).

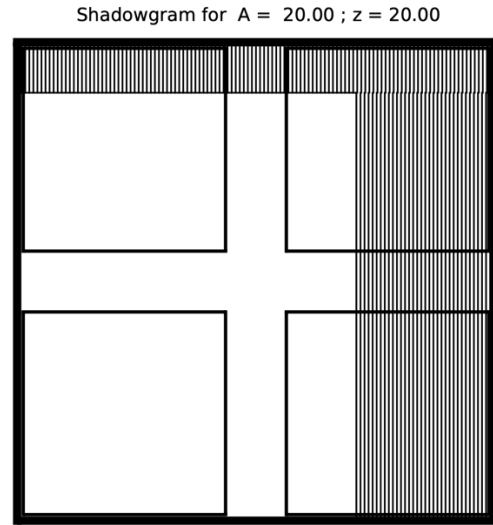


Fig. 3 – The shadows of the shielding walls over the detector plane for an azimuth angle of 20° and a zenith angle of 20°.

The diagram in Figure 3 shows simulations in which the 4 detectors are depicted, along with a surrounding area. The dashed line areas represent the shadow of the shielding walls over the detector plane. In this simulation, the source photons are coming from an azimuth (A) of 20° (1st quadrant) and a "zenith" angle (z) of 20°, both with respect to the instrument coordinate system. The x and y extensions of the shadows (L_x and L_y) will clearly be

$$L_x = H \tan z \cos A ; L_y = H \tan z \sin A$$

Now, starting from the upper left corner, let us call the detector illuminated areas A₁₁, A₁₂, A₂₂ and A₂₁, going clockwise. Then

$$A_{11} = s(s - L_y) ; A_{12} = (s - L_x)(s - L_y) \\ A_{21} = s^2 ; A_{22} = s(s - L_x)$$

Thus, solving these equations for L_x and L_y, we can measure the angles and then calculate the correct positions of cosmic explosion. Since we are going to have knowledge of the satellite attitude and orbit, we can calculate the right ascension and declination of the event.

C. Background and sensitivity

Estimation of the energy spectrum of the background signal and its spatial distribution over the detector plane is crucial for the design of hard X-ray and gamma-ray astronomy telescopes. In the case of an observation of a point source from an orbital space platform (i.e. a satellite), the background consists in the diffuse electromagnetic (EM) radiation coming through the telescope aperture, emission from other sources in the FOV, and the instrumental background, which arises from

interaction of high-energy particles with the detectors and surrounding material. Therefore, in order to foresee the performance of LECX in orbit and its sensitivity to cosmic explosions, we need to have a good estimate of the background radiation the detectors will measure. We have calculated this using the well-known GEANT4 package. Details of our procedure to calculate the background of an instrument from angle-dependent spectra of photons and particles in space can be found in [3]. Considering a near-equatorial low-Earth orbit (LEO) and a mass model of the LECX experiment, we have obtained the main components of the expected background in orbit, outside the South Atlantic Geomagnetic Anomaly (SAGA).

The main contribution come from the diffuse EM flux entering the aperture (up to ~ 140 keV) and the albedo radiation coming from the Earth atmosphere (above ~ 150 keV). During the occurrence of a cosmic explosion event, it is reasonable to consider that the Compton-scattered events and fluorescence on the collimator walls will not add significantly to the background that will be present during the event, since the graded-shield walls were specifically designed to minimize these radiations with the help of GEANT4 simulations.

The sensitivity of LECX can be calculated considering that the number of counts in each detector, for a given integration time and a given energy bin, obey Poisson statistics. In the case of cosmic explosions observations, what will be measured are sudden increases in the total count rate that will last typically from a fraction of a second to tens of seconds during nominal operation. A trigger mechanism will detect these surges and automatically put the experiment in burst mode, which will end when the low count rates resume. During burst mode, the satellite service module will provide more frequent attitude information data. The electronics is designed so that all events will be time-tagged and stored onboard even if the count rate increases by a factor of ~ 100 . All science and spacecraft data will be transmitted to the ground during the ground station passages.

Under nominal operations, the detector system will be measuring background radiation before and after the detected bursting events. We will select the best timescales to get good statistics for the background measurements. Since we may have significant background variations during one orbit, we also have to minimize this integration time to get more accurate values with respect to the background in effect during the occurrence of the event. During the event, we subtract the background counts from the total counts in each selected energy bin to obtain the source spectrum. Using Poisson statistics we can calculate the minimum detectable flux for a given energy bin.

The sensitivity of LECX/nanoMIRAX is shown in Fig. 4. One can see that LECX is capable of detecting a wide range of typical GRB fluxes even with one-second integrations. For longer-duration GRBs, even somewhat weak events could be detected. The spectrum of the Crab nebula is shown in the figure just for comparison purposes, since the Crab it is a strong standard candle in these energies. LECX will not be able to detect the Crab since it would require pointing and very long stabilized observations, capabilities that the nanoMIRAX satellite will not have.

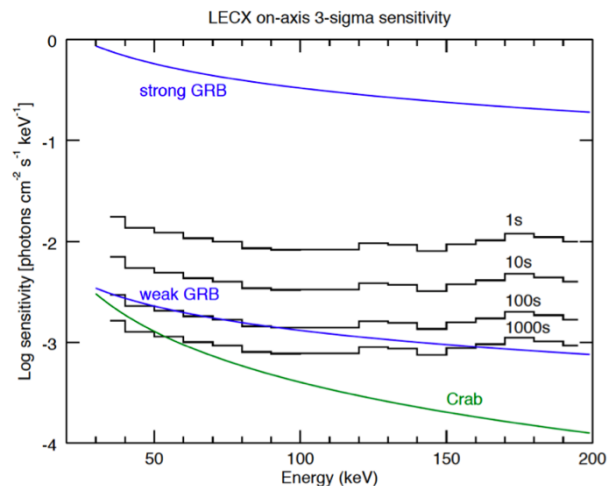


Fig. 4 – The sensitivity of LECX on nanoMIRAX for different integration times.

III THE PLATFORM

The platform for the nanoMIRAX cubesat will have a 2U structure (10cm x 10cm x 20cm) with 1U made available for the payload and 1U made available for the service subsystems [4]. Among these, five are developments made by national companies in the country for the project and three imported from companies that produce them abroad. Two of these can also be developed by national companies, but in order to mitigate further risks to the mission, they are imported from companies that already produce them with significant space heritage.

A. Power Subsystem (MGGE)

Performs the following functions: optimizes the transfer of the energy captured by the solar panels, controls the distribution of energy to the system, manages the generation, storage and consumption of energy by the system, makes all information available for processing by the main on-board system, performs battery protection (voltage and current) by hardware and software, allows the configuration of parameters inherent to battery charging and energy distribution and controls the temperature of batteries by hardware and software.

It uses the MPPT (Maximum Power Point Tracking) operation to maximize the use of the energy that the panels can generate when the system needs to recharge the batteries and does not consume the full capacity of the panels. In this case, all excess consumption is directed to storage. The circuit operates in two MPPT modes: constant voltage and maximum power. Control is made with an Atmel microcontroller, ARM 32bits, M4, from the SAMG55 family, supported by several external function blocks, with high performance and low consumption.

B. Attitude Determination and Control Subsystem (MDCA)

The MDCA uses an Atmel microcontroller, ARM 32bits, M7, from the SAME70 family, supported by several external functional blocks, high performance with moderate consumption, being able to operate up to 300MHz of internal clock (use of the lowest allowable clock for processing for minimum consumption). It can completely turn off the

microcontrol without loss of the onboard time reference. Memory capacity for internal flash code with at least 2 Mbytes and for work (internal RAM) at least 384 kbytes. Forecast for NOR flash with a capacity of 16 Mbytes and for two units of FRAM memories (SPI interface) with a capacity of 512 kBytes each, totaling 1 Mbyte of resource (IC2 and IC3). Interface for SDCard available on the microcontroller using external 8 kbyte E2prom (I2C interface). It communicates with the subsystem's internal attitude sensing devices, through an SPI bus with several selector lines and an I2C Master bus, and with external devices or systems via I2C Slave bus, SPI bus, two asynchronous serial interfaces, one USB interface, and one CAN interface. Firmware load is done via the JTAG interface, accessed by JTAG connector.

It uses as attitude sensors a three axes magnetometer and gyroscopes, both of the MEMS type (for reading in eclipse), and solar sensors, these placed in the cubesat panels. As actuators, three torque coils, one air core and two ferrous core, arranged on the two sides of the subsystem board. The air core coil and the ferrous core coils mounted on opposite faces on the subsystem board, completing the control trihedron. The electronics assembled in the space enclosed by the torque coils on the board. Configuration does not require the solar panels to have magnetic actuators and allows the determination of the attitude throughout the entire orbit.

It has a GPS receiver for on-board orbit determination. GPS antenna placed on the top face of the cubesat. Orbit is obtained autonomously on board, without the need, for this definition, to receive the TLEs (two lines elements) obtained by the earth station via the internet through NORAD. The data read on board, from the platform and the payload, can be associated on board with the point in the orbit at which it was obtained and transmitted to the ground with this identification.

C. Transceiver, on board computer and onboard antenna set

These three subsystems were imported from ISISpace for the reasons decrease risk using subsystems with proven space heritage record. The transceiver is a VHF up link/UHF down link full duplex transceiver. TMTC and beacon are on the same board. The data management module (OBDH) has an MSP430 20MHz ultra low power microcontroller with I2C, UART and SPI interfaces. With antenna release control and 2G bytes flash memory. It performs housekeeping operations and allows the management of payloads. Electronic components with flight heritage and with communication with the other modules. Includes the operating software and library.

The antenna system contains four ribbon spring antennas up to 55 cm long. The system has a thermal knife composed of a wire and two redundant heating elements per tape. RF phasing/BalUn circuits join the antennas in a spool configuration. Depending on the configuration, one or two radios in the cubesat can connect to the antenna system via miniature RF connectors. The top face of the antenna system can accommodate a two-cell solar panel and can be customized to accommodate sensors or other systems that protrude outward. The antenna is compatible with any UHF and/or VHF radio system. It can be mounted on all the frames of the main suppliers of cubesats frames on the market. For custom-made structures, which follow the standard cubesat mechanical envelope, assembly is also possible.

D. Structure

2U aerospace aluminum alloy structure in 7075-T6 alloy with qualified corrosion protection for the environmental conditions of space and vibration at launch. Surface treatment (black sulfuric anodizing 16 to 20 microns); Worm shafts and screws in 304 stainless steel. Kill switch mechanisms to activate the opening of the on-board antennas in stainless steel 316 and aerospace aluminum 7075-T6. External dimensions (width X length X height) of 100 X 100 X 227 millimeters. Weight up to 400 grams.

E. Software

The mission software performs the following functions:

- Manages the on-board data for the nanoMIRAX flight model platform and communication with the platform's subsystems and payloads.
- Acquires and processes telemetry from the satellite and formats and sends telecommands to the satellite
- Integrates on-board software and mission application software.
- Interfaces the on-board computer and platform subsystems.
- Manages on-board software in binary format (installable).

F. Solar panels

Solar Panels for 2U Cubesat, in +-X, Y and Z with temperature sensor and solar with four solar cells assembly (SCA), except in Z where there are 2 SCA in each. Triple-junction solar cells, InGaP/GaAs/Ge, with spatial qualification by ECSS E ST20-08C standard for low orbit, mass between 80-90 mg/cm² and area between 26 and 27 cm². Efficiency greater than 29%, external by-pass protection diode and high radiation resistance.

IV – LAUNCHING AND OPERATION

NanoMIRAX will operate in the frequencies for Space Research and Space Operation as ITU Regulations 2020. Uplink in VHF (149.000 MHz) and downlink in UHF (401.000 MHz). The mission does not require any specific orbit. Due to piggyback opportunities in the marketing most probably it will go in a SSO with 550 km altitude.

The ground station will be located at INPE Northeast Regional Center, in the city of Natal, RN. This ground station has operated the cubesats ITASAT-1 and SPORT, this one a mission in cooperation with NASA and ITA, which operated in the same frequency band as NanoMirax.

V – CONCLUSIONS

The engineering model (EM) of nanoMirax was built under a grant from FAPESP – The São Paulo State Research Support, under the PIPE – Innovation Program for the Small Company. It uses, both for LECX and the platform, the same electronic components and design as the flight model, presently being integrated, except for the on-board antenna

set and the solar panels. Instead, to lower costs and to emulate these two subsystems, it used, respectively, an electric model and a high precision voltage source. The EM was qualified at INPE (The National Institute Space Research) at its Integration and Testing Facility (LIT). Fig. 5 and 6 show it.



Fig. 5 – NanoMirax EM Vibration Test

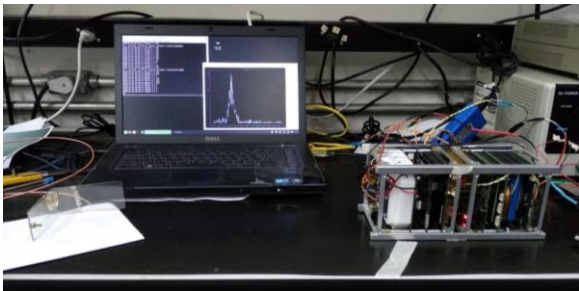


Fig. 6 – Functional tests (X-Ray source over the sheet)

All the subsystems and developments for the nanoMirax are ready. On board and ground station software are undergoing final acceptance tests. Presently integration is being performed. The FM will undergo vibration and thermal

vacuum testing at LIT with parameters less severe than the EM. Launch of nanoMirax is expected for the first semester of 2025.

ACKNOWLEDGMENT

The authors want to thank the Brazilian Space Agency – AEB for funding nanoMirax flight model and FUNCATE - Foundation for Science, Application and Space Technology for their administrative support managing the project.

REFERENCES

- [1] Braga, J.; Durão, O.S.C.; Castro, M.; D'Amico, F.; Stecchini, P.E.; Amirabile, S.; Gonzalez Blanco, F.; Strauss, C.; Silva, W.; Schad, V. R.; Reitano, L. A. "LECX: a cubesat experiment to detect and localize cosmic explosions in hard X rays", *MNRAS*, 493, 4852, 2020.
- [2] Braga, J. "Coded-Aperture Imaging in High-Energy Astrophysics", *PASP*, 132, 1007, 2020. (invited review article)
- [3] Castro, M.; Braga, J.; Penachioni, A.; D'Amico, F.; Sacahui, R. "Background and imaging simulations for the hard X-ray camera of the MIRAX mission", *MNRAS*, 459, 3917, 2016.
- [4] Silveira, J.; Durão, O.; Baptista, J.; Schad, V. "The NASCERR Mission – An University/Private Sector Cooperation with Cubesat", accepted for the LACW24, 2024.



Preliminary design of the communications subsystem for the Chasqui II cubesat mission

Gabriel Flores¹, Elian Rios², Leo Camizan³, and Jose Honorio¹

¹Universidad Nacional de Ingeniería

²Universidad Nacional del Callao

³Universidad Nacional Pedro Ruiz Gallo

Abstract

An important aspect for the successful operation of a CubeSat mission is establishing a robust data transmission and reception connection. Moreover, it is essential to overcome the challenges posed by the space environment and various obstacles encountered along the data signal path. The purpose of this document is to showcase the design, methodology, and simulations of the communication subsystem for the Chasqui II CubeSat mission, which will operate in Low Earth Orbit (LEO).

Then, developing an effective design for this subsystem requires first conducting a study on the communication architecture. This involved understanding signal processing and the interconnection of different components. Additionally, a component tree was developed in this phase. Subsequently, parameters and operational characteristics were comprehended. In this phase, the design of a tape dipole antenna was elaborated using CST Studio simulation software. This entailed modeling and analyzing how the antenna would behave in space alongside the structure. Link budget analysis followed, which involved calculating the amount of signal power available for uplink and downlink based on the communication subsystem's characteristics and the losses incurred by the medium. Finally, the command reception behavior and telemetry transmission were analyzed to design the most suitable operational modes based on the mission's established characteristics, and an energy budget for the components in those modes was created.

The results obtained from this work include a communication architecture design that meets the requirements for the proposed CubeSat mission. Furthermore, the decision was made to operate in the UHF band (437MHz) with Half Duplex communication, FSK modulation, and data packets in AX.25 standard format. Furthermore, a link budget was obtained to ensure signal reliability for uplink and downlink connections, along with operational modes demonstrating the module's behavior throughout the nanosatellite's lifespan. In conclusion, the preliminary design provides information on the necessary components for the communication architecture, various factors, and parameters to consider for a reliable link. It also offers the ability to optimize the communication subsystem's performance according to the requirements of the satellite project.

Persistent-1: The Preliminary Design Overview

Rebecca Quintino Do Ó[✉], Fernanda Paiva[✉], Gabriel Cabral Marcílio[✉], Vitória Beatriz Bianchin[✉],
João Cláudio Elsen Barcellos[✉], Gabriel Marcelino[✉] and Eduardo Augusto Bezerra[✉]

Abstract—Currently, many CubeSats experience high failure rates due to their COTS components, which were never designed to work on-orbit and in a very radiation-intensive and extreme-temperature environment, and are generally without any effective radiation mitigation strategies in their PCB designs. The studies also proved that CubeSat mission failure rates were higher than those of bigger satellites. Neither of these platforms emphasized radiation tolerance or reliability over long periods. This paper describes a new CubeSat platform developed for mitigation of these limitations, mainly concerning the design of a radiation-tolerant Electrical Power System, RE²PS. For the first time, this improved platform will fly on the mission called Persistent-1, following the ECSS standards and making use of fully analogue circuits for enhanced resistance to radiation. A thorough CubeSat architectures review and testing protocols are in process. Electrical and radiation testing is in process. The mid-year due Preliminary Design Review, Persistent-1, will be an important milestone in setting a new standard for CubeSat missions operating in demanding environments.

Keywords—Embedded Systems, Satellite, CubeSats, Subsystems, FloripaSat-2, FloripaSat-1.

I. INTRODUCTION

The Persistent-1 project is the result of a collaborative effort involving researchers, engineers, and students (undergraduate, master's, and doctoral) from SpaceLab and the National Council for Scientific and Technological Development (CNPq). Based at the Technology Center (CTC) of the Federal University of Santa Catarina (UFSC), SpaceLab has been at the leading edge of space systems development in Brazil, with experience in creating multi-mission platforms for CubeSats and conducting various missions, FloripaSat-1 [1], GOLDS-UFSC [2] and Catarina Constellation¹.

SpaceLab's first CubeSat mission was FloripaSat-1, a 1U CubeSat launched in 2019. This cubic-shaped small satellite was composed of the Electrical Power System (EPS) for power management, the Telecommand and Telemetry Control (TTC) for communication with the ground segment, and the On-Board Data Handling (OBDH) for processing and storing data.

Following the success of FloripaSat-1, SpaceLab's members developed the FloripaSat-2 [2] platform, targeting 1U and 2U CubeSats, offering greater capacity for experiments and scientific instruments. This platform is already being utilized

for missions such as GOLDS-UFSC, Aldebaran-1¹, and CI-MATELITE [3], as well as some satellites in the Catarina Constellation, Catarina-A1 and Catarina-A3².

However, as the use of CubeSats for Earth observation (EO) [4] and deep-space applications [5], which require higher reliability, has become more common, SpaceLab's members recognized the need to develop a more reliable platform. In this sense, the first subsystem developed was the EPS, as evidence suggests that it is one of the subsystems most prone to causing mission failures [6]-[7]-[8]-[9]-[10].

Then, the Reliability Enhanced Electrical Power System (RE²PS) was created, aiming to be a reliability-enhanced, radiation-tolerant EPS, composed mainly of fully analog circuits [11]. However, other subsystems that are part of this platform are already under development, such as the ULTRA (which will serve as the satellite's on-board computer) [12] and the telemetry and telecommand (TMTC) subsystem of the FloripaSat-3 platform.

Thus, the Persistent-1 mission was established to test the new platform and ensure its compatibility with the Catarina Constellation. The mission has two main objectives: 1) to contribute to environmental data collection and support the growth of the aforementioned constellation, and 2) to validate the robustness of the new platform. If successful, this platform could be used exclusively for the Catarina Constellation satellites, some of which will be dedicated to radio occultation applications.

On October 11, 2023, the Persistent-1 team successfully completed the Mission Definition Review (MDR), a significant milestone that assessed the feasibility and requirements of the mission. The next phase, the Preliminary Design Review (PDR), is scheduled for mid-2024 and will involve a detailed design assessment of the platform and its subsystems. In preparation for the PDR, the information presented in this document will be essential for a comprehensive assessment and validation of the mission.

To provide context, the subsequent sections of this document offer an overview of the Persistent-1 preliminary design, initially detailing the motivations behind the mission, which led to the goal of validating a new platform. Next, the architecture and operational concept of the mission are detailed, including a description of the division of the satellite into a service sector and a payload sector. Then, the specifics of these sectors will be addressed in the following section. Finally, a feasibility analysis is presented, assessing the mass and power budget of

Rebecca Q. Do Ó, UFSC, Brazil, (rebecca.quintino@spacelab.ufsc.br).
Fernanda P. de Moraes, UFSC, Brazil, (Fernandapaivamorais@gmail.com).
Gabriel C. Marcílio, UFSC, Brazil, (gabrielcabralmarcilio989@gmail.com).
Vitória B. Bianchin, UFSC, Brazil, (vitoria.bianchin@spacelab.ufsc.br).
João C. E. Barcellos, UFSC, Brazil, (joaoclaudiobarcellos@gmail.com).
Gabriel M. Marcelino, UFSC, Brazil, (gabriel.marcelino@spacelab.ufsc.br).
Eduardo A. Bezerra, UFSC, Brazil, (eduardo.bezerra@ufsc.br).

¹<https://www.gov.br/aeb/pt-br/centrais-de-conteudo/publicacoes/instagram-do-periodo-de-defeso-eleitoral-2022/missao-aldebaran-i>

²<https://www.gov.br/aeb/pt-br/acoes-e-programas/desenvolvimento-tecnologico/constelacao-catarina>

the entire satellite. All this information will be used for the Preliminary Design Review (PDR) to thoroughly evaluate and validate the mission.

II. MISSION OBJECTIVE

A. Motivation

Failures in CubeSats are a significant and frequent issue, with one of the primary causes being radiation effects. Satellites in Low Earth Orbit (LEO) are exposed to substantial levels of radiation, receiving an average annual dose of approximately $29.4\text{Gy} = 2.94\text{krad}$ (or 3.36 mGy/h) [13]. This radiation leads to degradation in the electronic components of CubeSats, particularly affecting the power system, which is highly vulnerable to radiation and extreme temperature variations [14]-[15]-[7].

In response to these challenges, studies have been initiated to develop a new satellite power system with radiation-tolerant electronics. The goal of this new EPS is to enhance the durability and resilience of CubeSats in harsh space environments. The importance of this development is further emphasized by the need for a more radiation-tolerant platform for the Catarina constellation, an essential mission for Brazilian environmental data collection and other applications. A more radiation-resistant platform will enable greater longevity and reliability, opening the door to new applications that require extended operational periods in space.

Therefore, the creation of a more radiation-tolerant platform will not only contribute to testing this new EPS but will also benefit the Catarina constellation mission, enhancing its data collection capabilities and supporting a broader range of space applications.

B. Objective

The Persistent-1 mission aims to test a power system module (EPS), designed for small satellites and made mainly of all-analog circuits, in space. Meanwhile, other subsystems and techniques that constitute the mission involve the addition of electronic circuits operating in space with reliability and durability. This mission exists to contribute to the Catarina Constellation by validating a platform currently under development. The platform must meet the typical requirements of Low Earth Orbit (LEO) missions, with a minimum service life of 24 months, and be compatible with Cubesats up to 3U. It also contributes to the training of qualified professionals at the undergraduate level and increases the development of space technology in Brazil.

III. SYSTEM ARCHITETURE

In order to ensure a successful Persistent-1 mission, the various subsystems, both on ground as well as in space, have to work together as one coherent system. This section describes the current status of the bus development, featuring the platform architecture as well as the main subsystem and their interactions.

First, the satellite will be divided into two sectors: service modules and payload modules. This division aims to

ensure the validation of the payload sector without compromising the satellite. The service module sector, which incorporates OBDH, TTC, and EPS, draws on the heritage of the FloripaSat-2 platform used in other missions, such as the Constelação Catarina and GOLDS-UFSC. This heritage underscores the platform's reliability and technological maturity, thereby reducing risk and increasing the probability of mission success.

The service module sector of the Persistent-1 satellite provides the essential infrastructure for the satellite's operation and functionality. On-Board Data Handling (OBDH 2.0) [16] acts as the satellite's central computer, responsible for managing data flow, command execution, and overall system coordination. It interfaces with various subsystems, collecting and processing data, and transmitting it to the ground station or storing it onboard for later retrieval. Telemetry, Tracking, and Command (TTC 2.0) [17] enables communication between the satellite and the ground station, facilitating the exchange of telemetry data and commands. It consists of a beacon for periodic transmission of basic telemetry and a primary communication system for comprehensive data exchange. Electrical Power System (EPS 2.0) [18] is responsible for power generation, storage, and distribution throughout the satellite. It harnesses solar energy through solar panels, manages battery charging, and provides regulated power to the system.

The payload section of the Persistent-1 satellite constitutes the mission's core, accommodating the experiments and technologies subject to validation within the space environment. It comprises five principal modules, each assuming a distinct role in mission execution. Reliability Enhanced Electrical Power System (RE²PS) [19] is responsible for managing the solar energy collected by the solar panels and distributing it to the other modules. Reliability Enhanced On-Board Data Management (REOBDH) is responsible for collecting, processing and storing the data generated by experiments and other modules. Telemetry, Telecommand and Control (TMTC) [20] is the payload sector's telecommunication interface with the Earth. It allows telemetry containing experiment data to be sent and telecommands to be received to control the satellite's operation. Environmental Data Collection (EDC) [21] is a module dedicated to collecting data on the space environment, developed by INPE³, and its main function is to receive and decode signals from data collection platforms (DCPs) that adhere to the Brazilian Data Collection System (SBCD) and the Argos-2 protocol. SpaceLab Camera (SLCAM) [22], developed by SpaceLab's team, is a high-resolution camera designed to capture images of the Earth from space. It enables remote sensing and Earth observation experiments to be carried out, contributing to various areas of research and practical applications. The current state of the satellite configuration is depicted in Figure 1

IV. PRELIMINAR CONCEPT OF OPERATIONS

This section is dedicated to explaining the satellite's operational concept (*CONOPS*), outlining its structure and operational modes for the Persistent-1 mission. The mission

³<https://www.gov.br/inpe/pt-br>

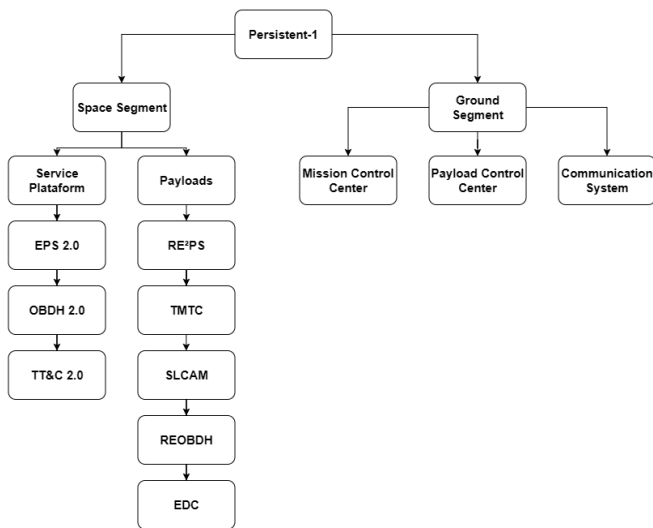


Fig. 1: Persistent-1 Mission architecture

aims to validate a service module, integrated as a payload on the satellite, and to verify the functionality of the EDC and SLCAM added to the satellite. For this purpose, a Low Earth Orbit (LEO) will be utilized at the highest feasible altitude to expose the payloads to the maximum level of radiation possible. These payloads will operate throughout the entire orbit.

The mission architecture, was designed to accommodate the entire mission, considering the communication system between the satellite and Earth, as well as mission control and the data received from the satellite. Thus, the mission will consist of a ground segment composed of SpaceLab's Ground Station, a space segment with the satellite, and a control module also housed in SpaceLab's laboratory.

The Persistent-1 communicates with Ground Station using VHF and UHF antennas. Other modules will either be attached or housed within the laboratory at the Federal University of Santa Catarina.

A. Space Segment

The space segment is the primary component of the mission, consisting of the CubeSat to be placed in orbit.

B. Ground Segment and Mission Control

The mission's Ground Segment will consist of SpaceLab's Ground Station located at the Federal University of Santa Catarina in Florianópolis, Brazil. The station, still under development, features two antennas for satellite data transmission and reception, communicating with the satellite's TTC in orbit, which operates in Very High Frequency (VHF) and Ultra High Frequency (UHF).

C. Mission operation modes

The operation modes will be described in the subsections below:

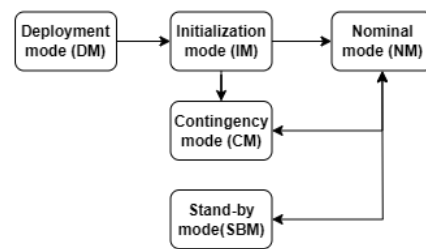


Fig. 2: Persistent-1 mission operation modes.

1) *Deployment mode (DM)*: During satellite launch, it will be in deployment mode, where all functions are deactivated to ensure satellite safety due to non-ideal operating conditions. Once the satellite is stabilized, it will be powered on and transition to the next mode, Initialization Mode (IM).

2) *Initialization mode (IM)*: In initialization mode, system initialization will begin starting with the OBDH subsystem, which initializes the remaining subsystems to achieve full satellite operation. Antennas remain closed throughout this process. After initialization, the satellite aims to transmit periodic beacons to the Ground Station and determine its initial orientation. Upon establishing a transmission link with Earth, the satellite can operate in its nominal mode (NM), contingency mode (CM), or stand-by mode (SBM).

3) *Nominal mode (NM)*: In nominal mode of operation, the satellite operates with all functions active. Both the service modules and payloads are operational, and antennas are ready to transmit and receive information. The satellite communicates with the ground segment to monitor payload parameters and functionality.

4) *Contingency mode (CM)*: This mode is activated if a failure in a critical system is identified in the satellite, whether in one of the service modules or one of the payloads.

5) *Stand-by mode (SBM)*: Stand-by mode is activated when the satellite is in orbits outside the communication footprint with the ground segment, i.e., outside national territory. In this mode, service modules and payloads continue operating, and the OBDH monitors voltage levels, current, battery temperature, and other EPS-generated variables relevant to satellite safety. For redundancy, the EPS periodically transmits this information to the TTC.

V. PAYLOADS

A. Payload Sector

1) *RE²PS*: The module is designed for CubeSat nanosatellites, focusing on increased reliability and robustness. It differs from the EPS2 power system in several key aspects:

The RE²PS uses an integrated circuit (BQ24650 [23]) for managing solar energy harvesting and battery charging, whereas the EPS 2.0 employs a separate battery management system and includes a heating system. For power conversion, RE²PS has two redundant DC-DC converters to distribute power across six buses, compared to EPS 2.0's multiple dedicated converters for various output voltages. Additionally, RE²PS integrates redundancies in critical components to enhance reliability, a feature not present in EPS 2.0. However,

RE²PS lacks a dedicated battery monitoring system and a battery heating system, which EPS 2.0 includes.

The RE²PS is currently undergoing testing and improvement, with its first version already manufactured. The PCB of the payload can be seen in the Figure 3.

Fig. 3: RE²PS



2) *TMTC*: From the FloripaSat-3 platform, the TMTC module enabling essential communication and command functionalities vital for mission operations. This module is integrated with a microcontroller, the TMTC module interfaces seamlessly with other satellite subsystems through standardized protocols such as SPI, UART, I2C, and CAN. A distinguishing feature of the TMTC module from its predecessors is its custom-designed radio architecture developed in-house by the laboratory, rather than acquiring a pre-integrated solution. This approach enhances flexibility and customization options, aligning specifically with mission requirements and optimizing performance for CubeSat operations. Architecturally, the TMTC module is designed to optimize power management and system reliability. It incorporates voltage regulation and monitoring systems to maintain stable power distribution across the satellite subsystems, while temperature sensors ensure operational components remain within safe operating limits. This comprehensive approach enhances the module's resilience and longevity in the challenging environment of space.

3) *OBDHRE*: The module is currently in progress. OBDHRE analyses are underway to determine which On-Boarding Data Handling architecture will be used in the development of this module. The options under consideration include Payload-ULTRA [24]-[12] and the third-version of OBDH [25] from the FloripaSat-3 platform, which are in the development phase. These analyses cover various aspects, including power budget, that will be describe in Section VII, to ensure the selection of the most suitable solution for the project's needs. The design prioritizes reliability and efficiency, incorporating enhanced data validation and error correction mechanisms. A comprehensive set of requirements has been defined to guide the development process, and a modular architecture has been adopted for flexibility and future expansion.

B. SLCAM

The payload was designed to capture images of Earth from space for environmental monitoring and Earth observation. It

uses a 2-megapixel RGB CMOS image sensor, storing images in non-volatile memory and transmitting them to the ground station via the CubeSat's communication module.

The SLCAM is energy-efficient, operating on a 3.3V power supply and consuming between 100 and 450 mW, depending on the mode. The module includes a microcontroller that manages image capture, storage, and transmission, as well as a power management system that ensures a stable and optimized power supply. Communication with the CubeSat's main bus is conducted through standard interfaces like SPI and I2C. The module board can be seen in Figure 4.

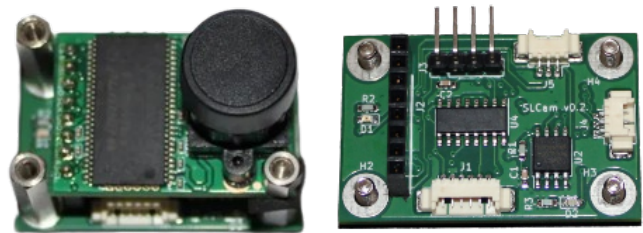


Fig. 4: SLCAM module.

C. Environmental Data Collection

The (EDC) [21] is a CubeSat-compatible payload that decodes signals from Platform Transmitter Terminals (PTTs) belonging to the SBCD and the Argos-2 System. It operates within the $401.635 \text{ MHz} \pm 30 \text{ kHz}$ frequency range and can decode up to 12 PTT signals simultaneously. The EDC attaches a header to decoded messages containing frequency, time, and signal strength details. It communicates with the onboard computer via a full-speed I²C interface and a full-duplex RS-485 interface with fail-safe features. The payload is powered by a 5V supply and includes memory for storing up to 64 decoded messages. Additionally, it generates housekeeping data such as power supply status, board temperature, and signal levels, and can capture a 2048 sample sequence from the received signal upon request. The main features of this payload are listed below, a 3D model of the EDC board can be seen in Figure 5.



Fig. 5: EDC module.

VI. SERVICE SECTOR OVERVIEW

A. EPS 2.0

The board manages energy by harvesting solar power through panels, optimizing it with Maximum Power Point Tracking (MPPT), and distributing it using integrated buck DC-DC converters. The EPS 2.0 stores energy in a battery module and features comprehensive battery management, including voltage, current, and temperature monitoring from the FloripaSat-1 [1] system. Figure 6 illustrates the EPS module.

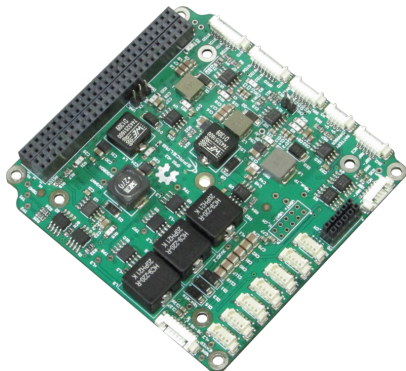


Fig. 6: EPS module.

B. OBDH 2.0

The module, utilizing an MSP430F6659[26] microcontroller, coordinates data flow and commands between satellite modules and Earth. The OBDH 2.0 offers multiple communication interfaces, including I2C, SPI, UART, and JTAG, along with non-volatile memory, sensors, and a PC-104 bus system, as shown in Figure 7.

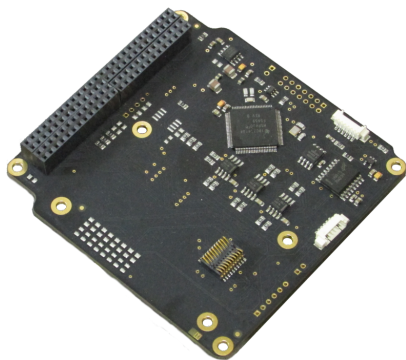


Fig. 7: OBDH module.

C. TTC 2.0

The board supports satellite communication with Earth through a beacon for basic telemetry and a downlink/uplink system for comprehensive data exchange. The TTC 2.0 uses dual microcontrollers and the NGHam protocol with Forward Error Correction (FEC) for reliability. The module's design and functionality are detailed in Figure 8.

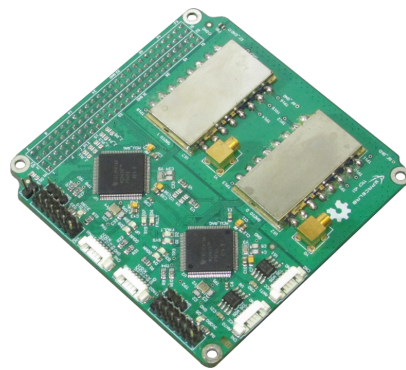


Fig. 8: TTC module.

VII. BUDGETS

A. Mass Budget

The CubeSat standard establishes a weight limit of 2 kg for a 1U CubeSat [27] implying limits of 4 kg and 6 kg for 2U and 3U CubeSats, respectively. However, not all launch providers adhere to these standards, necessitating the consideration of more restrictive scenarios.

Below, a mass budget analysis for the Persistent-1 satellite is presented, considering the mass for all subsystems, including the service, payload, and structural components for both the 2U and 3U configurations, is detailed in Table II.

The analysis reveals that, considering the 3U configuration and the most restrictive mass limits, Persistent-1 falls within the allowed limits, exhibiting a margin of the 36.48%.

TABLE I: Mass budget of Persistent-1 - Service and Payload Sector

Subsystem	Supplier	Model	Margin [%]	Final mass [g] ¹
OBDH 2.0	SpaceLab	OBDH 2.0	5	55.65
TTC 2.0	SpaceLab	TTC 2.0	5	76.65
EPS 2.0	SpaceLab	EPS 2.0	5	94.5
Battery board	SpaceLab	BAT4C	15	270.25
TTC's antenna	ISISpace	AntS	5	93.45
ACS	SpaceLab	Passive ACS	15	59.8
1 st Payload	INPE	EDC	15	86.25
2 nd Payload	SpaceLab	RE ² PS	15	74.75
3 rd Payload	SpaceLab	TMTC 3.0	100	160
4 th Payload	SpaceLab	REOBDH	100	180
5 th Payload	SpaceLab	SLCAM	15	78.2
TMTC's antenna	ISISpace	AntS	5	93.45
Battery board	SpaceLab	BAT4C	15	270.25
Total				1593.2

¹ Values obtained after considering the mass margins.

B. Power Budget

The power budget calculation for a satellite involves three primary steps, as outlined in Section 10.3 of [28]:

- 1) Analyze the satellite's energy generation and consumption, without considering the battery's existence;
- 2) Size the battery;
- 3) Estimate the power degradation and performance of PV modules over the mission's lifetime.

TABLE II: Mass Budget of Persistent-1 - 2U and 3U Combined

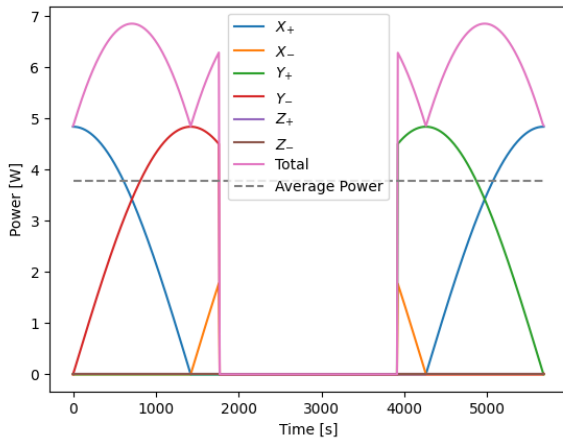
Subsystem	Supplier	Model	Margin [%]	Final Mass [g]
Interface boards	SpaceLab	Interface boards	5	42
PC-104 adapters	SpaceLab	Adapter boards	5	65.1
Solar panels (2U)	Orbital	Solar panels	15	305.9
Solar panels (3U)	Orbital	Solar panels	15	429.26
Shields (2U)	Usiped	Aluminum sheets	15	578.45
Shields (3U)	Usiped	Aluminum sheets	15	809.83
Structure (2U)	Usiped	Structure	15	236.9
Structure (3U)	Usiped	Structure	15	355.35
Cables (2U)	-	-	15	230
Cables (3U)	-	-	15	345
Others (2U)	-	-	15	115
Others (3U)	-	-	15	172.5
Total 2U²				3166.55
Total 3U²				3811.24
Maximum 2U				4000
Maximum 3U				6000
Margin 2U				20.84%
Margin 3U				36.48%

¹ Values obtained after considering the mass margins.

² Values obtained from the sum of the "Total" of the previous tables with the "Final mass" of each subsystem.

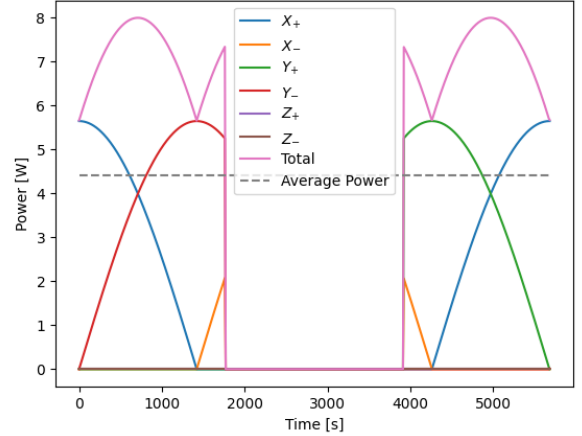
Step 1) involves evaluating the power generation capacity and power consumption of the satellite. This assessment aims to ensure a technical surplus, confirming that the satellite generates more energy than it consumes. In step 2), the focus shifts to determining whether the selected battery has sufficient capacity for the application. If a battery has not been chosen yet, this is the stage where it is appropriately sized. Finally, in step 3), the satellite's behavior as its lifetime approaches the end is analyzed. A comprehensive study, similar to the initial assessment, is conducted to anticipate any required adjustments or adaptations.

1) *Input Power*: Simulations [29]-[30] of power generation by the solar panels, both during maximum sun exposure and during eclipse, are presented in Figures 9a and 9a. The main results are summarized in Table III



(a) 2U maximum eclipse simulation.

2) *Satellite Power Consumption*: The power consumption of the satellite's subsystems is presented in Table IV. Also, the maximum power consumption was calculated considering



(a) 3U maximum eclipse simulation.

Fig. 9: Simulated input power of the solar panels maximum eclipse.

TABLE III: Simulated input power results.

Parameter	Maximum Eclipse	No Eclipse
Peak power [mW]	6852.61	10278.91
Average orbital power [mW]	3771.97	5657.96
Average power during sun exposure [mW]	6062.86	9094.29
Orbit period [s]	5687	5680
Sun exposure period [s]	3547	3540
Eclipse period [s]	2140	2140

the duty cycles and safety margins for each subsystem was estimated for both configurations (2U and 3U), as shown in Table V.

TABLE IV: Typical power consumption of the Persistent-1 subsystems.

Subsystem	Voltage [V]	Consumption [mW]
<i>OBBDH</i> 2.0	3.3	115.5
<i>TTC</i> 2.0 (not transmitting)	3.3	165.66
<i>TTC</i> 2.0 (transmitting)	5	3251
<i>EPS</i> 2.0	7.4	370
<i>BAT4C</i> (idle)	0	0
<i>BAT4C</i> (heater on)	7.4	5002.4
<i>AntS</i> (during deployment)	3.3	1815
<i>AntS</i> (deployed)	3.3	198
<i>EDC</i>	5	1250
<i>RE³PS</i>	7.4	370
<i>TMTC</i> (while not transmitting)	3.3	165.66
<i>TMTC</i> (while transmitting)	5	3251
<i>REOBBDH</i>	TBD	TBD
<i>SLCAM</i> (idle)	5	100
<i>SLCAM</i> (while shooting)	5	700
<i>BAT4C</i> (idle)	0	0
<i>BAT4C</i> (heater on)	7.4	5002.4
<i>AntS</i> (during deployment)	3.3	1815
<i>AntS</i> (deployed)	3.3	198

$$E_{sat} = P_{sat} \cdot (T_E + T_S) \quad (1)$$

$$E_{OAP} = (P_{OAP} \cdot \eta) \cdot (T_E + T_S) \quad (2)$$

TABLE V: Power budget of the Persistent-1.

Subsystem	Duty Cycle [%]	Max. Consumption [mW] ¹
OBDH 2.0	100	121.28
TTC 2.0 (not transmitting)	95	329.18
TTC 2.0 (transmitting)	5	341.25
EPS 2.0	100	388.5
BAT4C (idle)	90	0.00
BAT4C (heater on)	10	525.25
AntS (deployed)	100	210
<hr/>		
EDC	30	393.75
REPS	100	425.5
TMTC (while not transmitting)	95	180.98
TMTC (while transmitting)	5	186.93
REOBDH	TBD	TBD
SLCAM (idle)	90	103.5
SLCAM (while shooting)	10	80.5
BAT4C (idle)	90	0.00
BAT4C (heater on)	10	525.25
AntS (deployed)	100	210
<hr/>		
Total (2U) ²		3683.2
Total (3U) ²		5818.38

¹ Values obtained after considering the margins.

² Values obtained from the multiplication of the "Duty cycle" of the previous tables with the "Typ. power consumption" of each subsystem, considering the margins. Equation 1 was used.

The energy consumed by the satellite in a complete orbit was calculated based on the average orbital power in Equation 2 (Table III), resulting in **3683.2 mWh** for the 2U configuration and **5818.38 mWh** for the 3U configuration. The energy generated by the solar panels, considering an efficiency of 80%, was **4766.93 mWh** for 2U and **7141.6 mWh** for 3U. Therefore, it is observed that the 2U configuration is not feasible due to the energy deficit (**-1051.45 mWh**), while the 3U configuration presents a positive margin of 18.63% (**1330.38 mWh**).

3) *Battery Sizing*: As described in [28], the battery sizing of a satellite can be made by following the steps below:

- 1) Estimate the power required from the satellite (P_{SAT});
- 2) Define the discharge and charge cycles duration, as well as the numbers of charge-discharge cycles;
- 3) Define a maximum DoD ;
- 4) Define the charge rate;
- 5) Compute battery recharge power.

$$DoD = \frac{D_i \cdot D_t}{C} \cdot 100 \quad (3)$$

$$E_{OAP} - P_{SAT} \cdot T_S = E_{sun} \quad (4)$$

Using two BAT4C boards with 36,000 mWh capacity, the current DoD is 12.4% according to the Equation 3, below the 30% limit, indicating the battery is safely oversized. The charge rate is based on a 0.9853-hour cycle and 80% efficiency, yielding 8017.33 mWh. Based on the DoD calculation, the energy consumption during eclipse is 2189.4 mWh for all satellite configurations. As a result, the energy margin of the battery becomes negative for the 2U configuration ($1149.9 - 2189.4 = -1039.5$ mWh), aligning with previous power budget results. However, the battery sizing is well-suited for the 3U configuration, providing a positive energy margin of

($3532.4 - 2189.4 = 1343$ mWh), which supports the planned mission behavior.

Parameter	Value	Unit
Battery capacity	36000	mWh
Energy consumption on sunlight	3621.8	mWh
Energy consumption on eclipse	2189.4	mWh
Sunlight duration	0.9853	h
Eclipse duration	0.5944	h
Depth of Discharge (DoD)	12.44	%
<hr/>		
Total battery energy margin	1343	mWh

TABLE VI: Battery sizing results.

4) *Power Degradation Over Mission Life*: Two major events along the satellite operation should be considered in the power degradation analysis:

- 1) Solar panels degradation
- 2) Battery degradation

The usual number for solar panels' degradation is 5 % per year [28], in other words, the general efficiency of the solar panels decays at a rate of 5 % per year of operation. The Equation 5 can be used to define the PV panels' efficiency (η_{EOL}) after N years. Furthermore, it is possible to create the Table VII to visualize the energy dependence of the satellite over the years.

$$\eta_{EOL} = \eta_{BOL} \cdot (1 - \eta_{degradation})^N \quad (5)$$

TABLE VII: Degradation of the Persistent-1.

Parameter	BOL	1 year	2 years	3 years	4 years
η_{EOL} [%]	30	28.5	25.72	22.05	17.96
P_{OAP} [mW]	5657.96	5375.06	4850.99	4159.12	3387.63
E_{OAP} [mWh]	7141.60	6784.52	6123.03	5249.73	4275.94
E_{sat} [mWh]	5811.22	5811.22	5811.22	5811.22	5811.22
Margin [mWh]	1330.38	973.30	311.81	-561.49	-1535.28

Until the 3rd year, the satellite will generate more power than it consumes. From there, the satellite will start consuming more energy than it can generate, and eventually, it will cease to function. It is worth noting that some considerations have been taken into account, creating a rather pessimistic scenario.

VIII. DISCUSSION: TRENDS AND DIRECTIONS

The Persistent-1 mission has progressed through the Mission Definition Review (*MDR*) phase and is currently in the Preliminary Design Review (*PDR*) phase. During the *MDR* phase, the focus was on outlining the mission, setting clear objectives, and defining general requirements. This phase concluded with a Mission Concept Review. Now in the *PDR* phase, the team is refining both system-level and subsystem-level requirements, identifying potential risks, and further developing the Concept of Operations (*CONOPS*). Additionally, preliminary subsystem designs are being advanced, and the final of this phase will be marked by the presentation of the *PDR*. Following this, a Critical Design Review (*CDR*) will complete the current development stage for Persistent-1.

If successful, the platform developed for Persistent-1 will be used in other satellites within the Catarina Constellation.

Among them, some missions will be intended for radio occultation, which is a technique of study for Earth's atmosphere, using GNSS satellites signals. Using this approach, it would be possible to map temperature, pressure, humidity, and density of the atmosphere with an unprecedented level of detail, together with retrieving important data for weather forecasting and climate studies. While this is demanding RO missions with a lot of measurement accuracy and high reliability-presents a challenge for CubeSats, which traditionally have been at the mercy of their size, power, and cost limits.

Therefore, a initiative within the SpaceLab at the Federal University of Santa Catarina (UFSC) is the development of the Radio Occultation CubeSats (ROCUS) project. Supported by the National Council for Scientific and Technological Development (CNPq), this project aims to launch a technology demonstration satellite, ROCUS-1. The satellite, will use radio occultation to gather atmospheric data focused on the South American region, particularly Brazil. Equipped with an active Attitude Determination and Control System (ADCS), ROCUS-1 will direct GNSS antennas toward Earth's horizon, the critical area for radio occultation measurements. The satellite will also feature several modules designed by SpaceLab would democratize access to RO data, enabling a wider range of scientific and operational applications. The successful validation of the Persistent-1 platform, the platform could be used to validate the technology for future radio occultation missions, contributing significantly to weather prediction in the region and the reliability of the Catarina Constellation.

IX. CONCLUSION

The Persistent-1 mission is a step in testing a new CubeSat platform designed for greater reliability in harsh space environments. The mission's success would not only validate the platform for future use within the Catarina Constellation but also open the door for advancements such as radio occultation CubeSats and even the CubeSat community. The collaboration between students, researchers, and institutions in Brazil is contributing to space technology, with the potential to improve atmospheric and environmental data collection across South America. If the Persistent-1 mission achieves its goals, it could contribute to improving Brazilian environmental data collection. In addition, the Persistent-1 mission seeks not only to validate an EPS module but also to support education and technological development, with the hope of contributing to the growth of the Brazilian space industry.

ACKNOWLEDGEMENTS

The authors want to to acknowledge that this work was supported by CNPq/Brazil (National Council for Scientific and Technological Development - <http://www.cnpq.br>), and by AEB (Brazilian Space Agency - <http://www.aeb.gov.br>).

REFERENCES

- [1] Space Technology Research Laboratory (SpaceLab), *FloripaSat-1 Documentation*, 2019. Available at <<https://github.com/spacelab-ufsc/floripasat-doc>>.
- [2] G. M. Marcelino, A. M. P. de Mattos, J. C. E. Barcellos, B. F. Ribeiro, L. O. Seman, E. M. Filho, and E. A. Bezerra, "Floripasat-2: An open-source platform for cubesats," *IEEE Embedded Systems Letters*, vol. 16, no. 1, pp. 77–80, 2024.
- [3] Y. M. d. Silva, "Desenvolvimento de uma metodologia integrada de projeto para CubeSat: um estudo de caso do projeto CIMATELITE," B.S. thesis, Federal University of Santa Catarina, Joinville, SC, Brazil, 2024.
- [4] S. Wu, W. Chen, C. Cao, C. Zhang, and Z. Mu, "A multiple-CubeSat constellation for integrated earth observation and marine/air traffic monitoring," *Advances in Space Research*, vol. 67, no. 11, pp. 3712–3724, 2021. Satellite Constellations and Formation Flying.
- [5] J. Schoolcraft, A. Klesh, and T. Werne, *MarCO: Interplanetary Mission Development on a CubeSat Scale*. Cham: Springer International Publishing, 2017.
- [6] Y. T. J. C. V. J. M. G. Abderzak Lashab, Mohammad Yaqoob, "Space microgrids: New concepts on electric power systems for satellites," *IEEE Electrification Magazine*, vol. 8, no. 4, pp. 8–19, 2020.
- [7] E. G. Jian Guo, Liora Monas, "Statistical analysis and modelling of small satellite reliability," *Acta Astronautica*, vol. 98, pp. 97–110, 2014.
- [8] M. Tafazoli, "A study of on-orbit spacecraft failures," *Acta Astronautica*, vol. 64, no. 2-3, pp. 195–205, 2009.
- [9] M. Swartwout, "The first one hundred cubesats: A statistical look," *Journal of Small Satellites*, vol. 2, no. 2, pp. 213–233, 2013.
- [10] M. Langer and J. Bouwmeester, "Reliability of cubesats: Statistical data, developers' beliefs and the way forward," in *Proceedings of the USU Conference on Small Satellites*, (S.I.), AIAA, 2016.
- [11] D. Figueiredo, "Reliability enhanced electrical power system for nanosatellites," Master's thesis, Federal University of Santa Catarina (UFSC), Florianópolis, SC, Brazil, 2023.
- [12] M. Boing, "Técnicas de mitigação de efeitos da radiação e sua aplicação no projeto de uma arquitetura de hardware para uso em satélites," 2024.
- [13] C. Granja, S. Polansky, Z. Vykydal, S. Pospisil, A. Owens, Z. Zozacek, K. Mellab, and M. Simcak, "The satram timepix spacecraft payload in open space on board the proba-v satellite for wide range radiation monitoring in leo orbit," *Planetary and Space Science*, vol. 125, pp. 114–129, 2016.
- [14] Abdulaziz Alanazi, Jeremy Straub, "Statistical analysis of cubesat mission failure," in *Small Satellite Conference*, 2018.
- [15] W. Suparta, "Space weather effects on microelectronics devices around the leo spacecraft environments," *Journal of Physics: Conference Series*, vol. 539, no. 1, p. 012012, 2014.
- [16] Space Technology Research Laboratory (SpaceLab), *OBDDH 2.0 Documentation*, 2020. Available at <<https://github.com/spacelab-ufsc/obddh2>>.
- [17] Space Technology Research Laboratory (SpaceLab), *TTC Documentation*, 2021. Available at <<https://github.com/spacelab-ufsc/ttc>>.
- [18] Space Technology Research Laboratory (SpaceLab), *EPS 2.0 Documentation*, 2021. Available at <<https://github.com/spacelab-ufsc/eps2>>.
- [19] SpaceLab, Federal University of Santa Catarina (UFSC), *RE2PS Documentation*, 2024. Available at <https://github.com/spacelab-ufsc/eps-re>.
- [20] SpaceLab, Federal University of Santa Catarina (UFSC), *TMTC 3.0 Documentation*, 2024. Available at <https://github.com/spacelab-ufsc/ttc3-tests/tree/dev>.
- [21] Instituto Nacional de Pesquisas Espaciais (INPE), *Environmental Data Collector User Guide*, October 2019. CNS-MNL-PY-00-002-V01.
- [22] SpaceLab, Federal University of Santa Catarina (UFSC), *SLCAM Documentation*, 2022. Available at <https://github.com/spacelab-ufsc/slcam>.
- [23] Texas Instruments, "Bq24650," 2024. Accessed: 2024-09-14.
- [24] SpaceLab, Federal University of Santa Catarina (UFSC), *ULTRA Documentation*, 2024. Available at <https://github.com/spacelab-ufsc/payload-ultra>.
- [25] Space Technology Research Laboratory (SpaceLab), *OBDDH 3.0 Documentation*, 2024. Available at <<https://github.com/spacelab-ufsc/obddh3-documentation>>.
- [26] T. Instruments, "Msp430f6659." <https://www.ti.com/product/MSP430F6659>, 2024.
- [27] The CubeSat Program, *CubeSat Design Specification*. California Polytechnic State University, San Luis Obispo, CA - EUA, rev 14 ed., July 2020. Available at: <<http://www.cubesat.org/>>.
- [28] J. R. W. Wiley J. Larson, *Space Mission Analysis and Design*. Space Technology Library, Microcosm, 3rd ed., 2005.
- [29] mgm8, "pypsis," 2024. Accessed: 2024-09-14.
- [30] C. A. R. V. d. P. N. R. G. O. V. R. Q. L. Edegar Morsch FilhoL, aio Oriel Seman 2, "Irradiation flux modelling for thermal-electrical simulation of cubesats: Orbit, attitude and radiation integration," *Energies*, vol. 13, no. 24, p. 6691, 2020.

Satellite Operations service - DATASAT: A Study on Noise Mitigation Systems within the ADA Framework

Sérgio Silva Soares
Criar Space Systems
Ribeirão Preto, Brazil

Abstract—A Brazilian ground station network, DATASAT, utilizes Automatic Directional Antennas (ADA) for satellite communication. This research explores noise elimination within the ADA framework, focusing on Surface Acoustic Wave (SAW), helical, and cavity filters. By comparing signal-to-noise ratios with and without filters, the aim is to optimize ADA performance for reliable data transmission. This is crucial in today's environment with an increasingly crowded satellite population. Effective noise reduction improves communication efficiency, benefiting both DATASAT and the broader satellite operations community.

Keywords—Ground station, antenna, satellite telemetry

I. INTRODUCTION

Small satellites, or SmallSats for short, have become a game-changer in the space industry. These tiny spacecraft, typically under 500 kg, are revolutionizing everything from who gets to play in space to the kind of missions we can accomplish. First, let's break down the SmallSat world. They come in various sizes, with picosats starting at a mere 1 kg and microsats topping out at the 500 kg mark. This variety allows for the development of standardized components and launch vehicles, further contributing to the cost-effectiveness of SmallSat missions, as explored by Swanson [1]. This standardization makes it easier for new players to enter the space industry and reduces the barrier to entry.

Several factors have fueled this SmallSat surge. Launch costs have plummeted thanks to new vehicles built specifically for these miniature marvels. This affordability opens the door for universities, startups, and even high schools to join the space club. A study by Andrews [2] highlights how launch costs for SmallSats have decreased by an order of magnitude in the past decade, making space more accessible than ever before.

Technology has also played a starring role. Electronics, sensors, and even propulsion systems are shrinking rapidly, allowing SmallSats to pack a bigger punch. Better batteries mean they can stay operational for longer, too. Miniaturization of these critical components is an ongoing area of research, with promising advancements reported in [3] on miniaturized ion thrusters for SmallSat applications.

Another perk of SmallSats is their lightning-fast development cycles. Compared to their hulking cousins, SmallSats can be designed, built, and launched in a fraction of the time. This agility is perfect for fields like disaster monitoring, where a quick response can make all the

difference. A research paper by [4] explores the benefits of rapid prototyping and iteration cycles enabled by SmallSats for Earth observation missions.

The commercial sector has embraced SmallSats with open arms. Companies are using them to build constellations that beam internet to remote areas, keep an eye on our planet for things like crop health, and even test out new spacefaring tech. The applications of SmallSats in various sectors continue to expand, as detailed in a recent industry report by [5].

The rise of SmallSats is having a ripple effect across the space industry. More players are entering the scene, which sparks innovation and opens doors for new spacefaring entities. These little guys are also ideal for building vast constellations of satellites, working together to provide global coverage for communication or environmental monitoring. Plus, they act as affordable testbeds for new technologies, paving the way for future space missions.

Of course, with great power comes great responsibility. As the SmallSat population explodes, issues like space debris and regulations need to be addressed to ensure this exciting era continues to thrive.

Small satellites are no longer the little guys of the space world. They're transforming the industry, making space more accessible, enabling groundbreaking missions, and pushing the boundaries of technology. As the SmallSat revolution unfolds, we can expect even more amazing applications and advancements in the years to come.

The ever-growing number of satellites orbiting Earth necessitates advancements in ground station technology for efficient operation, tracking, and command (TT&C). DATASAT, a pioneering Brazilian initiative, addresses this challenge with its open-source Automatic Directional Antenna (ADA) network. ADASERVER software controls these ADAs, offering a unique platform for education, research, and innovation in satellite operations.

This paper focuses on a critical aspect of DATASAT – the role of noise elimination systems in optimizing ADA performance. The study by Alves [6] explores the impact of various filter types, including Surface Acoustic Wave (SAW), helical, and cavity filters. However, the quest for optimal noise reduction extends beyond these three options. This review delves into a wider range of filter technologies and their potential applications within the DATASAT framework.

A. SAW Filters: A Strong Contender

SAW filters have emerged as a leading contender for noise suppression in satellite communication due to their unique properties. These filters operate on the principle of converting electrical signals into acoustic waves that propagate on the surface of a piezoelectric substrate [7]. The interaction between these acoustic waves and the electrical signals leads to selective frequency filtering. SAW filters offer several advantages for ADA applications:

- **Compact size:** Their miniature design allows for efficient integration within the limited space constraints of ground stations. This is particularly important for DATASAT's focus on open-source hardware accessibility, where cost-effective and space-saving solutions are paramount. Studies like the one by Huang [8] demonstrate the miniaturization capabilities of SAW filters, making them ideal for modern communication systems with space constraints.
- **Excellent selectivity:** SAW filters exhibit exceptional selectivity, enabling them to precisely pass desired signal frequencies while significantly attenuating unwanted noise at other frequencies. Research by Zhang [9] and Mosteller [10] highlights their effectiveness in enhancing signal-to-noise ratio (SNR) in communication systems by targeting and eliminating specific noise frequencies. This improved SNR translates to clearer and more reliable data transmission between satellites and ground stations.
- **Remarkable temperature stability:** SAW filters maintain consistent performance across a wide range of operating temperatures. This characteristic is crucial for satellite communication equipment, which often experiences significant temperature fluctuations due to environmental factors. A study by Rebeiz [11] explores the design of SAW filters with improved temperature stability, ensuring reliable performance in various operating conditions. This stability is vital for DATASAT, as it guarantees consistent performance regardless of the climatic conditions where the ground stations are deployed.

B. Beyond SAW Filters: Exploring the Filter Landscape

While SAW filters offer a compelling combination of size, selectivity, and temperature stability, they may not always be the ultimate solution. Here's a look at some alternative filter technologies and their potential benefits for ADA systems:

- **Helical filters:** Renowned for their exceptional out-of-band rejection, helical filters excel in suppressing noise outside the desired signal bandwidth. Research by Shao [12] explores the design of miniaturized helical filters for radio frequency (RF) applications, showcasing their potential for integration within ADA systems while maintaining superior noise suppression. However, helical filters can be larger

and more complex to manufacture compared to SAW filters.

- **Cavity filters:** These filters boast exceptional narrowband filtering characteristics, allowing for the precise isolation of the desired signal frequency. A study by Wang [13] investigates the application of cavity filters in satellite communication, demonstrating a significant improvement in SNR through precise noise filtering. This narrowband filtering can be advantageous in scenarios with high levels of closely spaced interfering signals. However, cavity filters can be bulky and expensive compared to SAW filters.
- **Interdigital filters (IDFs):** These planar filters offer a unique combination of compactness and sharp filtering characteristics. Research by Chen [14] explores the design of miniaturized IDFs for microwave applications, demonstrating their potential for size-constrained ADA systems while maintaining good filtering performance. However, IDFs may not offer the same level of out-of-band rejection as helical filters.

C. The Road Ahead: Selecting the Optimal Filter and Beyond

The comparative analysis proposed in [6] will be instrumental in identifying the most suitable filter type for ADA systems by evaluating the impact of each filter on SNR with and without their implementation. This analysis should consider not only SNR improvement but also factors like:

- **Filter size and weight:** For DATASAT's open-source, cost-effective approach, filter size and weight play a crucial role. While some filters, like SAW filters, offer miniaturization, others may introduce size constraints that need to be weighed against their noise suppression capabilities.
- **Power consumption:** The power requirements of different filter technologies should be factored in, especially for remote ground stations with limited power availability.
- **Manufacturing complexity:** DATASAT's focus on open-source hardware necessitates filters that are relatively easy and cost-effective to manufacture.
- **Specific application requirements:** The optimal filter choice may vary depending on the specific application of the ADA system. For instance, in scenarios with exceptionally high signal density and closely spaced interfering signals, cavity filters' narrowband precision might be advantageous, even if it comes at the expense of size or complexity.

By carefully considering these factors and pursuing ongoing research, the DATASAT project can leverage the power of noise elimination systems to optimize ADA performance and ensure reliable, efficient satellite communication in an increasingly crowded orbital environment. The open-source nature of DATASAT further emphasizes the importance of finding a balance between performance and cost-effectiveness, paving the way for wider adoption of this innovative ground station technology.

II. GROUND STATIONS DEVELOPMENT

The immense expansion of the New Space market has forced the development of improvements in the ground sector of space exploration. Thus, companies in this segment are in a rush to produce new technologies capable of meeting the needs of this new market.

While there is something magic, at least amazing, about launchers vehicles and satellites, none of them, or their missions would have a purpose without communication with a ground station. The increasing number of institutions, as Universities or private companies, that build their own satellites boosts all segments of spatial market.

However, how can we communicate to them? How to get their information? Our expertise allows us to know that, a satellite with a polar orbit as ITASAT-1, for example, with a 100 minutes period, approximately, ITA (Technological Institute of Aeronautics), which built and owns this satellite, has no more than 4 passes per day. That means at the most 60 minutes of connection per day.

Being a member of a ground station network would permit ITA to have many more passes, consequently, much more time of communication with ITASAT-1.

Aware of this market, big players known in other areas, as Amazon and Microsoft, have accelerated the development of ground stations and formed ground stations network around the globe, which is known as GSaaS, Ground Station as a Service. These, among other projects, represent the marvels of technology and goal to every satellite developer to work with, however the costs can be prohibitive for some of them.

There are also some free of a charge ground stations network like SatNOGS – Satellite Network Open Ground Stations and Network.

SatNOGS is a platform where members of the community, beginners or experts, exchange information about manufacturing and deploying of low costs ground stations and other related subjects. Users can also publish their knowledge and information about manufacturing and deploying of low costs ground stations. Besides that, they can publish decoded signals captured with their ground stations.

III. DATASAT

DATASAT shall be built by several ground stations standardized equipment that CRIAR SPACE SYSTEMS Company has designed and developed in Brazil since 2018 named ADA (Automatic Directional Antenna).

The goal is to send the ADA to the partners institutes together with a commodate contract, especially to those that are satellite users, thus, they are going to be able to capture its satellite's signals through an ADA antenna located at their place as well as all other ADAs around the globe. All of these benefits fully free of a charge.

ADA, DATASAT and ADASERVER compose a full system of satellites TT&C and can be used by institutions that have courses and disciplines related to engineering, telecommunications, astronomy, astrophysics, among others.

All three components above are part of an open-source software and hardware development system. Every time someone who is related to the partners institutions or simply a user of published data has a suggestion, it will be analyzed by CRIAR SPACE SYSTEMS's board. If it's a pertinent suggestion, it will be provided an update by the Company.

In order to reduce the idle time of each ADA, GRUPO CRIAR, controller of CRIAR SPACE SYSTEMS Company, will use ADA's resources while it's not being used by any course, discipline or capturing any satellite signal.

Nowadays we have three ADAs operating at GRUPO CRIAR and CRIAR SPACE SYSTEMS' headquarters in Brazil and one in Portugal, where the Company also has a subsidiary.

Satélite	Frequência	Data Hora	Estação Terrena	Máxima Elevação	Ações
% 2 SAT	145.875 MHz	2024-07-03 01:13:31 (UTC)	ET-CSS-004	5°	[Icons]
- ITASAT-2	436.400 MHz	2024-07-03 00:49:54 (UTC)	ET-CSS-001	52°	[Icons]
% ITASAT-1	145.860 MHz	2024-07-03 00:22:39 (UTC)	ET-CSS-003	49°	[Icons]
% ITASAT-1	145.860 MHz	2024-07-03 00:21:36 (UTC)	ET-CSS-005	49°	[Icons]
% NDAA-19	137.1 MHz	2024-07-03 00:17:30 (UTC)	ET-CSS-002	56°	[Icons]
% NDAA-19	137.100 MHz	2024-07-03 00:16:12 (UTC)	ET-CSS-001	56°	[Icons]
% CUBEL	405.575 MHz	2024-07-02 23:57:30 (UTC)	ET-CSS-003	42°	[Icons]
- LUMKA-1	437.625 MHz	2024-07-02 23:41:53 (UTC)	ET-CSS-001	24°	[Icons]
% 2 SAT	145.875 MHz	2024-07-02 23:39:30 (UTC)	ET-CSS-004	50°	[Icons]
% 2 SAT	145.875 MHz	2024-07-02 23:39:30 (UTC)	ET-CSS-003	50°	[Icons]
% 2 SAT	145.875 MHz	2024-07-02 23:38:43 (UTC)	ET-CSS-005	50°	[Icons]
% GQMA-4B	400.800 MHz	2024-07-02 20:48:30 (UTC)	ET-CSS-003	14°	[Icons]
% GQMA-4A	400.800 MHz	2024-07-02 20:22:30 (UTC)	ET-CSS-003	54°	[Icons]
- BANDEV	436.030 MHz	2024-07-02 18:23:42 (UTC)	ET-CSS-005	32°	[Icons]
- BANDEV	436.030 MHz	2024-07-02 18:23:42 (UTC)	ET-CSS-001	32°	[Icons]
% PLATONIA-1	405.339 MHz	2024-07-02 17:42:39 (UTC)	ET-CSS-003	11°	[Icons]
- BANDEV	436.030 MHz	2024-07-02 16:47:51 (UTC)	ET-CSS-001	19°	[Icons]

Fig. 1. Examples of captured signals.

Font: <https://criarspacesystems.com.br/site/services/datasat>, accessed on jul 5, 2024

IV. ADA

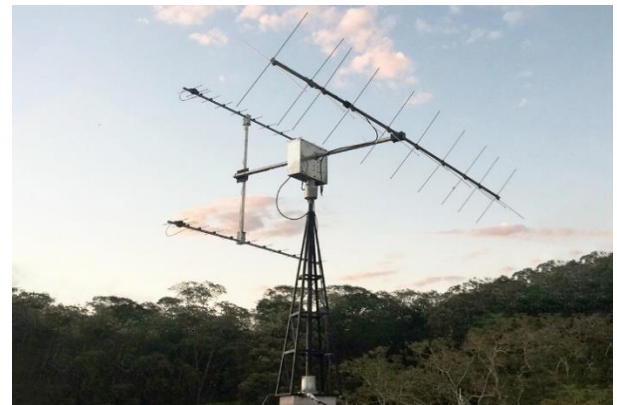


Fig. 2. One of operating ADAs installed in CRIAR SPACE SYSTEMS' s headquarters. Font: <https://criarspacesystems.com.br/site/>, access on jul 5, 2024

Therefore, the ADA project is born as a solution to this market 'pain'. The equipment is capable of commissioning satellites, checking their health, tracking their passages, and capturing signals, among other applications.

Another important factor is that commercial ground stations have a high market value. On the other hand, the equipment described in this article was developed with the intention of satisfying the requirements raised with the lowest possible cost. The entire project was developed based on open-source software and hardware development philosophies, with the exception of some electronic and mechanical components.

V. ADASERVER

The operations between software and hardware take place through the ADA-Server system, which is composed of the integration of three softwares: Ada-server application (with a Plan13 implementation), GQRX and WXTolmg.

In order to perform satellite forecasts, the TLE (two line elements) file of the satellite of interest is searched for in the Celestrak database, Plan13 is activated with the information, and the coordinates and time of the passage are obtained. Soon after, a file of the scheduled satellite is generated.

The system checks the schedule of the next pass, sends the azimuth and elevation coordinates to the microcontroller via serial, and at the same time sends the frequency data to the SDR. The frequencies need to go through a script that does the Doppler effect correction calculation. The SDR records the received signals in a wave file.

DATASAT shall be built by several ground stations standardized equipment that CRIAR SPACE SYSTEMS Company has designed and developed in Brazil since 2018 named ADA (Automatic Directional Antenna).

A. Operational Diagram

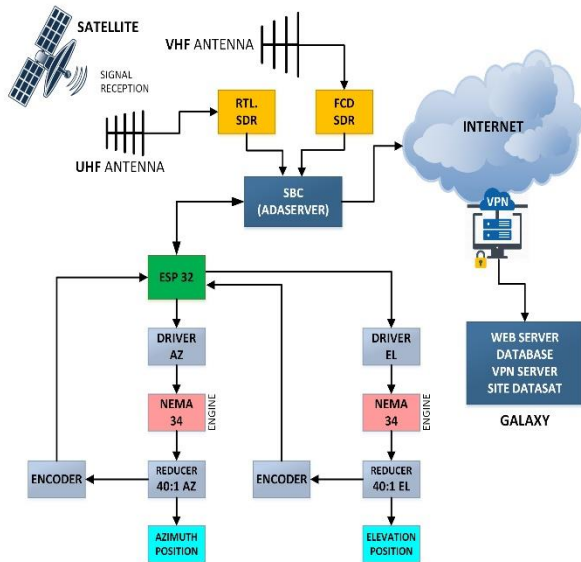


Fig. 3. Operational Diagram of the ADA equipment

B. Example of satellite communication

All information obtained from the communication between an ADA ground station and a satellite is saved on the CRIAR SPACE SYSTEMS server and made available to the public on the startup's website (<https://datasat.space>).

Today there are four ADA stations working, three of them in the company's headquarters in Brazil and the fourth one in its branch in Portugal (see image 8 below). This equipment receives signals and sends them to the site, and much of the data refers to meteorological control.

The NOAA - National Oceanic and Atmospheric Administration - has three satellites in low orbit (NOAA 18 and 19), all of which have a downlink frequency in the VHF range (near 137MHz). After decoding the signal, meteorological images are obtained, which are used to infer weather forecasts. Below is an example image taken from one of the ADA stations, located in the city of Ribeirao Preto - Sao Paulo - Brazil.

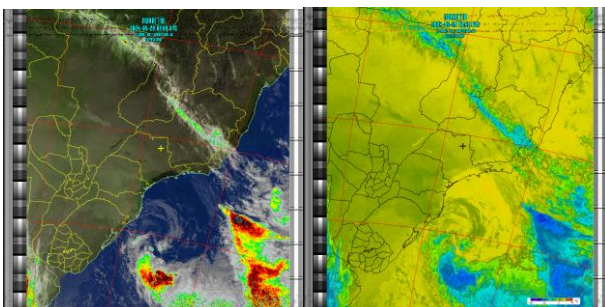


Fig. 4. Examples of images from the NOAA-19 satellite. The one on left is an 'MCIR' (Map Color Infra-Red) image and the one at the right is a thermal image of the ocean.

VI. FILTER RESULTS

The reception quality of the LUSAT satellite signal (Norad Id: 20442) on the 437.1253 MHz frequency was compared using the LFA 11 Element UHF Yagi antenna.

The LUSAT satellite (20442) signal was received by the ground station during a pass with a maximum elevation of 72 degrees on December 20, 2023, with AOS at 16:52 Brasilia time. Two transmission lines were used:

- LFA 11 element Yagi antenna, connected to a 433 MHz BPF SAW filter with an insertion loss of 2.8 dB and connected to an RTL-SDR via an RG-400 coaxial cable;
- LFA 11 element Yagi antenna, connected directly to the RTL-SDR via an RG-400 coaxial cable.

During the pass, the satellite signal reception levels were simultaneously collected through the two transmission lines using the gqrx software version 2.14.5, which utilizes gnuradio version 3.7.13.4.

The difference between the software setups used was related to the rtl's LNA. Without a filter, the signal had to be attenuated due to spurs, and a 24 dB LNA was used. With the filter, the signal was not attenuated, so a maximum 50 dB LNA was applied.

We have the following images with the gqrx screen for the two transmission networks and, in the center, the elevation angle at the moment. The data collections were performed for:

- AOS 5 degrees elevation;
- AOS 20 degrees elevation;
- AOS 50 degrees elevation;
- TCA 72 degrees elevation;
- LOS 50 degrees elevation;
- LOS 20 degrees elevation; and
- LOS 5 degrees elevation.

Note: AOS (Acquisition Of Signal) which sets the beginning of the pass; TCA (Time of Closest Approach) which sets the moment of maximum elevation and LOS (Loss Of Signal) which sets the end of the pass.

For each case the reception levels with and without filter is shown below.

A. AOS – Elevation: 5 degrees

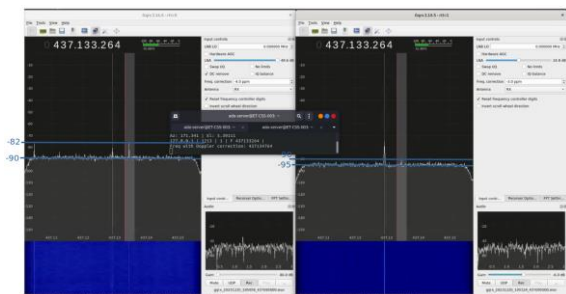


Fig. 5. Reception using gqrx for 5 degrees AOS condition. Right: Gqrx with reception from setup with filter and in Left: Gqrx with reception from setup without filter.

Values obtained for reception system with filter:

- Noise floor: -90 dB;
- LUSAT signal peak: -82 dB;

- Signal-to-noise ratio: +8 dB

Values obtained for reception system without filter:

- Noise floor: -95 dB;
- LUSAT signal peak: -90 dB;
- Signal-to-noise ratio: +5 dB

B. AOS – Elevation: 20 degrees

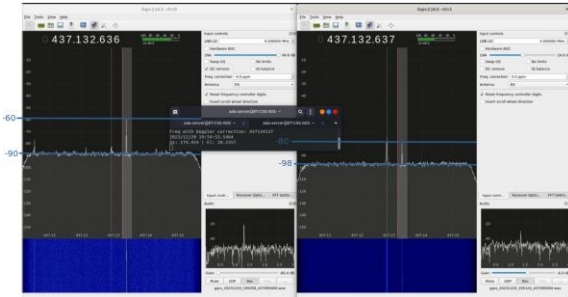


Fig. 6. Reception using gqrx for 20 degrees AOS condition. Right: Gqrx with reception from setup with filter and in Left: Gqrx with reception from setup without filter.

Values obtained for reception system with filter:

- Noise floor: -90 dB;
- LUSAT signal peak: -60 dB;
- Signal-to-noise ratio: +30 dB

Values obtained for reception system without filter:

- Noise floor: -98 dB;
- LUSAT signal peak: -80 dB;
- Signal-to-noise ratio: +18 dB

C. AOS – Elevation: 50 degrees

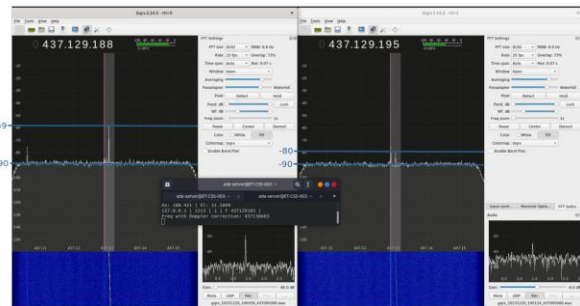


Fig. 7. Reception using gqrx for 50 degrees AOS condition. Right: Gqrx with reception from setup with filter and in Left: Gqrx with reception from setup without filter.

Values obtained for reception system with filter:

- Noise floor: -90 dB;
- LUSAT signal peak: -59 dB;
- Signal-to-noise ratio: +31 dB

Values obtained for reception system without filter:

- Noise floor: -90 dB;
- LUSAT signal peak: -80 dB;
- Signal-to-noise ratio: +10 dB

D. TCA – Elevation: 72 degrees

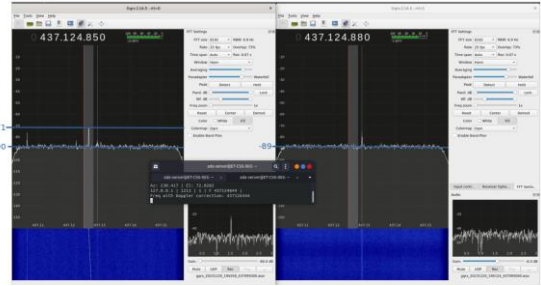


Fig. 8. Reception using gqrx for 72 degrees TCA condition. Right: Gqrx with reception from setup with filter and in Left: Gqrx with reception from setup without filter.

Values obtained for reception system with filter:

- Noise floor: -90 dB;
- LUSAT signal peak: -71 dB;
- Signal-to-noise ratio: +19 dB

Values obtained for reception system without filter:

- Noise floor: -89 dB;
- LUSAT signal peak: N/A;
- Signal-to-noise ratio: N/A

E. LOS – Elevation: 50 degrees

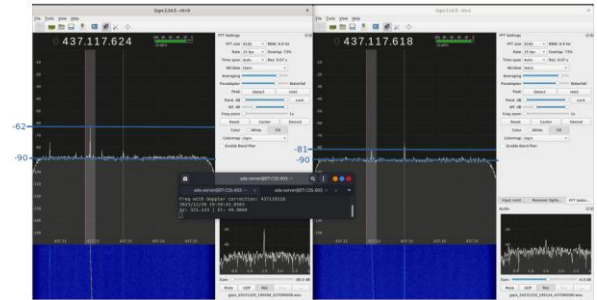


Fig. 9. Reception using gqrx for 50 degrees LOS condition. Right: Gqrx with reception from setup with filter and in Left: Gqrx with reception from setup without filter.

Values obtained for reception system with filter:

- Noise floor: -90 dB;
- LUSAT signal peak: -62 dB;
- Signal-to-noise ratio: +28 dB

Values obtained for reception system without filter:

- Noise floor: -90 dB;
- LUSAT signal peak: -81 dB;
- Signal-to-noise ratio: 9 dB

F. LOS – Elevation: 20 degrees

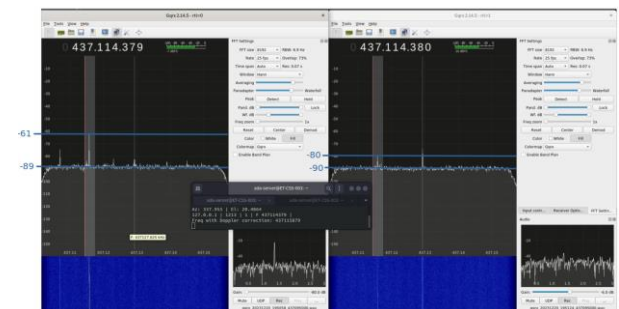


Fig. 10. Reception using gqrx for 20 degrees LOS condition. Right: Gqrx with reception from setup with filter and in Left: Gqrx with reception from setup without filter.

Values obtained for reception system with filter:

- Noise floor: -89 dB;
- LUSAT signal peak: -61 dB;
- Signal-to-noise ratio: +28 dB

Values obtained for reception system without filter:

- Noise floor: -90 dB;
- LUSAT signal peak: -80 dB;
- Signal-to-noise ratio: 10 dB

G. LOS – Elevation: 5 degrees

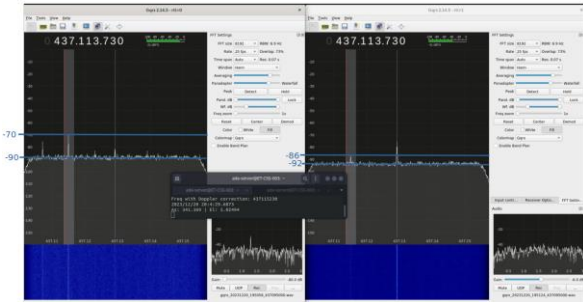


Fig. 11. Reception using gqrx for 5 degrees LOS condition. Right: Gqrx with reception from setup with filter and in Left: Gqrx with reception from setup without filter.

Values obtained for reception system with filter:

- Noise floor: -90 dB;
- LUSAT signal peak: -70 dB;
- Signal-to-noise ratio: +20 dB

Values obtained for reception system without filter:

- Noise floor: -92 dB;
- LUSAT signal peak: -86 dB;
- Signal-to-noise ratio: 18 dB

Based on the results obtained, it is possible summarize them in the Tables 1 and 2.

TABLE I. LEVEL OF SIGNAL RECEIVED FROM A SETUP WITH FILTER

Elevation	Azimuth	Signal (dB)	Noise (dB)	Signal-to-noise (dB)
5° AOS	171°	-82	-90	+8
20° AOS	174°	-60	-90	+30
50° AOS	188°	-59	-90	+31
72° TCA	230°	-71	-90	+19
50° LOS	325°	-62	-90	+28
20° LOS	338°	-61	-89	+28
5° LOS	341°	-70	-90	+20

TABLE II. LEVEL OF SIGNAL RECEIVED FROM A SETUP WITHOUT FILTER

Elevation	Azimuth	Signal (dB)	Noise (dB)	Signal-to-noise (dB)
5° AOS	171°	-90	-95	+5
20° AOS	174°	-80	-98	+18
50° AOS	188°	-80	-90	+10
72° TCA	230°	-89	-89	+0
50° LOS	325°	-81	-90	+9

Elevation	Azimuth	Signal (dB)	Noise (dB)	Signal-to-noise (dB)
5° AOS	171°	-90	-95	+5
20° LOS	338°	-80	-90	+10
5° LOS	341°	-86	-92	+6

It can be observed that the noise floor remains close to -90 dB, except for the transmission line without a filter for an azimuth of 170° at low elevation (less than 20°) where the noise floor was -95 dB for 5° elevation and -98 dB for 20° elevation.

It is noteworthy that the highest dB levels were computed for elevations of 20° and 50°, while at the TCA of 72°, the reception levels were lower, being 19 dB of signal-to-noise ratio for the case with a filter and for the system without a filter, the signal was not detected.

VII. FINAL REMARKS

The noise floor refers to the level of background noise present in a radio receiver system. A lower noise floor indicates a quieter reception environment.

Signal levels, on the other hand, represent the strength of the desired signal being received. Higher signal levels generally translate to better signal quality and stronger reception.

The provided observations highlight the impact of elevation and filter usage on noise floor and signal levels. At lower elevations, the signal is weaker and more susceptible to noise interference, leading to a higher noise floor. The use of a filter helps mitigate noise and improve signal-to-noise ratio, as evident in the higher signal levels observed with the filter at 20° and 50° elevations.

Interestingly, the signal was not detected for the system without a filter at the TCA (Time of Closest Approach), despite being the point of maximum elevation. This suggests that the signal was too weak to be received even with the advantage of the highest elevation angle, emphasizing the importance of noise reduction techniques like filtering.

REFERENCES

- [1] Swanson, P., et al. (2021). Standardization and cost-effectiveness in SmallSat missions. *Acta Astronautica*, 188, 422-430.
- [2] Andrews, R., et al. (2023). A comparative analysis of launch costs for SmallSats in the past decade. *Journal of Spacecraft and Rockets*, 60(7), 1621-1630.
- [3] Gupta, M., et al. (2022). Miniaturized ion thrusters for SmallSat applications. *IEEE Transactions on Plasma Science*, 50(5), 1-8.
- [4] Li, C., et al. (2024). Rapid prototyping and iteration cycles for Earth observation missions using SmallSats. *Remote Sensing*, 16(4), 1024.
- [5] Spaceworks. (2024). The expanding applications of SmallSats: An industry report. Retrieved from <https://www.spaceworks.com/>
- [6] Alves, C. R. et al. (2023). Comparative analysis of noise filtering techniques for automatic directional antennas in satellite communication systems.
- [7] Koul, S. K., Bhat, P. A., & Mirshekhar, S. A. (2019). SAW devices for microwave and millimeter-wave applications. Springer Nature.
- [8] Huang, Y., Xu, X., & Zhu, L. (2014). Design of miniaturized and high-performance surface acoustic wave filter for modern communication systems. *Sensors & Transducers*, 16(7), 1812-1817.
- [9] Zhang, W. et al. (2018). Design of a high-performance 10 GHz surface acoustic wave (SAW) filter for Ku-band satellite communication. 2018 International Conference on Microwave and Millimeter Wave Technology (ICMMT), 1-3.
- [10] Mosteller, M. R. et al. (2020). A high-performance 12 GHz surface acoustic wave (SAW) filter for X-band satellite communications. 2020 IEEE International Symposium on Circuits and Systems (ISCAS), 1-5.

- [11] Rebeiz, G. M. (1990). SAW filters with improved temperature stability. *IEEE Transactions on Ultrasonics, Ferroelectrics, and Frequency Control*, 37(1), 100-105.
- [12] Shao, J. et al. (2020). Design of miniaturized low-loss helical filters for RF applications. *IEEE Access*, 8, 132222-132230.
- [13] Wang, J. et al. (2019). A high-performance cavity filter for satellite communication applications. 2019 IEEE International Conference on Microwave and Millimeter Wave Technology (ICMMT), 1-3.
- [14] Chen, Z., Deng, W., & Yin, W. (2017). Design of miniaturized interdigital filters for microwave applications. *IEEE Transactions on Microwave Theory and Techniques*, 65(12), 5227-5234. *IEEE Xplore*

Proposal and Review of a Ground Sensor Terminal (GST) Design for Environmental Data Collection and LoRa Based CubeSat Missions

1st Rafael F. V. de Mello

Embedded Electronics

Senai CIMATEC

Salvador, Brazil

rafael.mello@aln.senaicimatec.edu.br

2nd Amanda B. A. R. Lima

Embedded Electronics

Senai CIMATEC

Salvador, Brazil

amanda.rigaud@fbest.org.br

3rd Felipe A. M. Lima

Embedded Electronics

Senai CIMATEC

Salvador, Brazil

felipe.macedo@fbest.org.br

4th Edmar S. da Silva

Biomedic Equipaments

Senai CIMATEC

Salvador, Brazil

edmar.silva@fieb.org.br

5th Leonardo F. Daltro

Embededd Electronics

Senai CIMATEC

Salvador, Brazil

leonardo.daltro@fieb.com.br

Abstract—With the surge of CubeSats in the academic and scientific world, establishing a purpose for its mission is very important. Due to its versatility, various technologies can be embedded into these satellites to compose missions, such as cameras, sensors, or just communications modules. This paper focuses on the design of a Ground Sensor Terminal (GST) for the CubeSat store & forward mission CIMATÉLITE-1. Its main objective is to collect environmental data from crop fields and send these to the satellite. By performing a literature review of previous projects and identifying solutions, opportunities, and challenges, an insightful analysis was conducted to guide the conceptual development of the system architecture. The key components, such as sensor integration, power management, and data handling, were thoroughly evaluated to enhance the performance and reliability of the system. The framework obtained by this study will emphasize the necessary trade-offs and considerations required for a successful application in a CubeSat mission, leading to the implementation of said GST in the near future.

Index Terms—CubeSat, GST, Environmental Studies, LoRa.

I. INTRODUCTION

Small satellite projects have become increasingly present in the technology world. Usually used in LEO (Low Earth Orbit), there are already more than 2,300 missions in this niche, predominantly scientific and educational [1].

Usually, these missions use a type of nanosatellite called "CubeSat", a standard for development, establishing characteristics such as size, mass, and an overall design for its structure [4]. The main reason for this model to be developed is to facilitate frequent and affordable access to space [2], without the several limitations that bigger satellite missions have. This makes it possible to carry out missions in several areas, such as meteorology, photography and space research, communication, and geolocation.

However, for CubeSats to be launched, it is first necessary to designate a mission. One example of this is to monitor

regions that do not yet have access to electricity or internet on the planet. Monitoring remote locations is extremely important for mapping natural resources and conducting studies on the geographic characteristics of a given area [3], resulting in feasibility analyses of installing solar or wind power plants in the territory under study, for instance.

To monitor land in remote environments, it is essential to create a Ground Sensor Terminal (GST) to store and transmit the collected data via satellite. These platforms need to be self-sufficient and able to withstand the local climate. The data transmitted by these platforms is captured during missions and then sent to another location for analysis.

This article aims to create a self-sufficient GST for collecting environmental data from a specific location and transmitting it to a CubeSat, which will transmit the data for analysis onward. This platform will form an integral part of the CIMATÉLITE-1 mission, a Store & Forward (S&F) mission focused on studying the climate of Northeastern backlands.

The data collection focal point is to measure variables of interest for the study of crop fields at the Senai CIMATEC Sertão campus and monitor the status of local cultivations. The data can also be utilized as a way to confirm that the region is carbon-free, to create predictive meteorological models, and to observe climate changes over time.

II. LITERATURE REVIEW

Before developing concepts, a literature review of similar stations was carried out to identify technologies, opportunities, and learnings that may be relevant to the project.

A. Application of Small Satellites for Low-Cost Remote Data Using LoRa Transmitters

One of the most notable works in this sort of project was conducted by (Lepcha et al., 2021), which was associated with

the BIRDS-2 Constellation. More specifically this work, the GST for the BHUTAN-1 satellite was developed, which aims to collect environmental data and transmit it to the CubeSat.

The main feature of this station resides in its low cost and robustness. Due to the use of LoRa technology and mostly low-power components, energy consumption is considerably small, and it allows the usage of smaller batteries and solar panels. Even though the system can only last for 9 hours without sunlight, the trade-off for more compact and cheaper designs is notable.

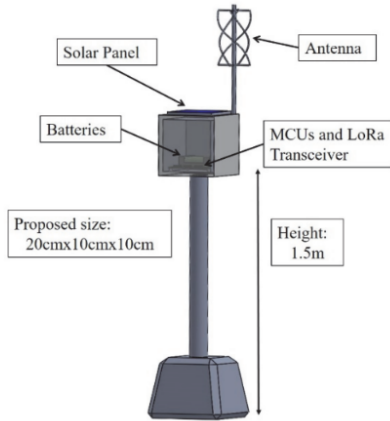


Fig. 1. CAD Model of the papers station. [6]

Choosing simpler components and a more robust composition allows the GST to operate in harsher environments without depending on other infrastructures to be installed. Focusing on Off-the-Shelf products to build the GST significantly reduces manufacturing costs, making the system viable for large-scale deployment in areas without traditional communication infrastructure.

The study demonstrates that utilizing small satellites equipped with LoRa transmitters provides an expandable and cost-effective solution for remote data collection. The report outlines areas for further improvement, including enhancing the energy system and performing long-range communication tests, laying the foundation for future advancements in satellite-based remote sensing systems.

B. Samanaú.PCD

Samanaú.PCD is a GST standard developed in Brazil whose premises are to build a modular, low-cost, and flexible station for environmental data collection [7]. The platform consists of an intuitive system integration, in which data is collected by a self-sustainable structure, sent by Radio-Frequency (RF) by a low-cost transmitter module, handled, and presented in a WEB platform [8].

The design of the GST can be seen in Figure 3. The structure is fairly compact, given the antenna and rain gauge stay separated from the main framework. Despite that, the platform is still adaptable to other sensors and is IOT-compatible.

Following (Souto, 2017), bringing together all development fronts (GST, WEB, and RF) results in the Samanaú.SAT



Fig. 2. Samanaú.PCD node system [7].

project, the combination of all those with the increment of a satellite transmitter, represents an S&F Mission.

C. Data Collection Platform Design using LEO Satellite-based LoRa for Disaster Management in Indonesia

Despite not being exactly environmental data, the study conducted by (Arifim, et al, 2023) aimed to design a GST for disaster management and detection. By using high-sensitive disaster sensors and detectors, and LoRa technology for satellite communication, it was proposed a data collection platform to boost disaster management in Indonesia, a country that is vulnerable to various natural disasters as a result of its geographical location and characteristics.

It proposes a communication architecture that takes advantage of the LoRa capabilities exploring two different scenarios: in urban areas, which already have more options for data uplink, and in rural areas, where satellite communication must be integrated into the GST.

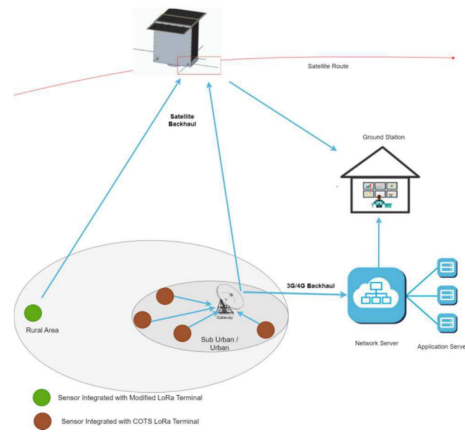


Fig. 3. Communication architecture used for disaster management [10].

In this project, LoRa technology is used in uplink and local communication, highlighted in Figure 4. Urban areas take advantage of gateways, using both satellite and terrestrial backhauls to send data to a ground station. However, in rural regions, an adaptation is needed so that the data can be sent to its destination by LEO satellites since some of these areas

have more restricted access to technology, electricity, and the internet.

And even for LEO communication, LoRa has proven to be an effective way to transmit data. This technology has been compelling for the CubeSat community for a while and papers such as [11] and [12] have shown its efficiency for such applications. Despite only showing simulation results, the paper analyzes the configurable LoRa transmission, searching for the one that has the best link budget at various elevation variations [9]. This characteristic is unique to this protocol and makes it noticeably adaptable to different contexts and missions.

III. METHODOLOGY

This research is an explanatory literature review and case studies of Google, Google Academic, and IEEE Xplore periodical articles. It aims to assist in the choice of embedded devices to apply in Ground Sensor Terminal design for LoRa CubeSat missions and environmental data collection, performing analysis to simplify the equipment's choice.

IV. RESULTS

After studies were conducted reviewing other designs, and given the project requirements that need to be met, the design proposed to de GST follows the diagram presented in Figure 4.

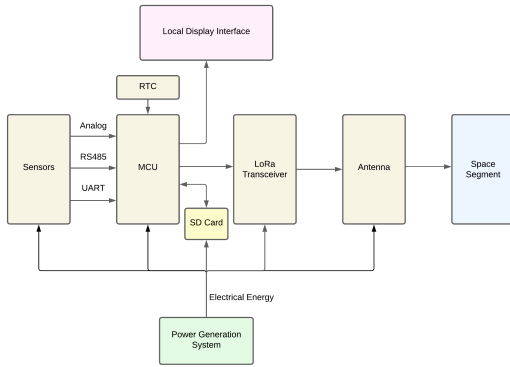


Fig. 4. Diagram of proposed design.

The application will consist of an embedded device to process the data collected and sensors to measure data from the environment described, such as temperature, humidity, wind direction, wind speed, carbon dioxide, and rainfall sensors. The local display interface is a project requirement that will be used to display helpful data to passersby locally, like farmers who want to see the humidity of the soil, and for maintenance operators in the future.

To compare embedded devices, it is important to establish metrics, such as architecture analysis, processor speed, memory capacity, integrated peripherals, programming language, and robustness. However, to compare sensors, the parameters include measurement range, precision, latency, communication interface, and sensitivity.

Unfortunately, just one GST is not enough to cover a big area, and one of the requirements is to cover various crop fields in a region of approximately 600 hectares. The solution is a GST network comprised of one master GST, responsible for satellite communication, and various support GSTs, that will only collect data and send it to the master. This scenario is shown in Figure 5.

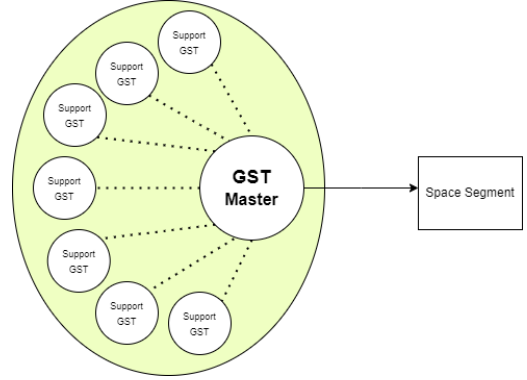


Fig. 5. Diagram representing the proposed GST network.

Given this scenario, the master GST must be able to send all the data packets to the satellite. Since the communication uses LoRa technology, the radio data rate can be calculated as per Equation 1.

$$R_b = SF \cdot \frac{BW}{2^{SF}} \cdot \frac{4}{(4 + CR)} \quad (1)$$

With CIMATÉLITE-1 Mission parameters, a data rate can be obtained. The bandwidth "BW" is 125kHz, the spreading factor "SF" is 10, and the coding rate "CR" is 4. This results in a data rate "R_b" of approximately 610 bits/s. As seen in Figure 6, the maximum packet size for the CIMATÉLITE-1 protocol is 256 bits, in one second the radio can send 2,4 packets to the satellite. It is noteworthy to mention that the protocol is an adaptation of the KITSUNE-1 format present in [13], with the addition of two extra bytes: One for the address of the data start register (STG ADDR), and another with the total number of registers (N of REG).

Byte 0	Byte 1	Byte 2	Byte 3	Byte 4	Byte 5	Byte 6	Byte 7	Byte 8	Byte 9	Byte 10	Byte 11	Byte 12	Byte 13	Byte 14	Byte 15
0x00	0x00	0x00	0x00	0x00	0x00	0x00	0x00	0x00	0x00	0x00	0x00	0x00	0x00	0x01	0x00
GST ID		DATA TYPE	TIME				STG ADDR	N of REG	SENSOR DATA (6 bytes)						CHECK SUM

Byte 0	Byte 1	Byte 2	Byte 3	Byte 4	Byte 5	Byte 6	Byte 7	Byte 8	Byte 9	Byte 10	Byte 11	...	Byte 29	Byte 30	Byte 31
0x00	0x00	0x00	0x00	0x00	0x00	0x00	0x00	0x00	0x00	0x00	0x00	0x00	0x00	0x01	0x00
GST ID		DATA TYPE	TIME				STG ADDR	N of REG	SENSOR DATA (22 bytes)						CHECK SUM

Fig. 6. Communication Protocol for CIMATÉLITE-1 Mission.

On the other hand, the Power Generation System is composed of a solar panel, batteries, and a charge controller. The

specifications of these components were obtained after a Power Budget for the system was made. The key moment where power is needed is during transmission, by powering the radio.

Aiming to lower the power consumption of the GST, two strategies were incorporated: a 10-minute work cycle and a switch activation for the radio. Figure 7 depicts how the loop will be divided. In short, for the most part, the system will be in an "Idle Mode", where the MCU will be in low-power mode and all components besides the LoRa radio will be turned off. During the "Read Mode", sensors will be turned on, making a measurement, and the data packet for the respective read will be created and stored in both the radio buffer for transmission and in an inner SD card.

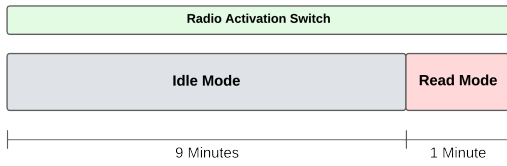


Fig. 7. Cycle of the systems work schedule.

The radio activation switch is a logic created in the MCU that will make the radio emit a transmission pulse every few seconds. Since the successful transmission with the satellite can be detected by the radio module, a stack logic can be used to queue data packets and serve as a buffer.

To optimize the design of the GST system, all components must be selected with precision and in alignment with project-specific requirements. A thorough comparative analysis of various equipment was conducted to identify the optimal solution, prioritizing maximum efficiency, cost-effectiveness, and high performance.

A. Embedded Device

To perform the evaluation, four devices were selected, including the STM32, ESP32, Arduino Uno, and Beagle Bone. When comparing these platforms, it can be seen that the Arduino is a low-cost microcontroller, an 8-bit device with 2KB of RAM, 1KB of EEPROM memory, and 32KB of Flash memory, operating at 16MHz. Additionally, includes peripherals such as USART, SPI, GPIO, and I2C, as well as being an easy-to-apply platform, which is programmed in C++. However, it is not very robust and is best used by beginners in electronics and programming, making it ideal for low-complexity projects [14].

The STM32, from the STM32 Discovery Kit IoT Node range, is a microprocessor with a processing speed of 80 MHz, 1Mb of Flash memory, and 128Kb of RAM. The interfaces include I2C, Bluetooth, WiFi, USARTS, USB, GPIO and SPI. Designed as a 32-bit board, offering flexibility in the development of electronic applications as well as being highly robust, it is usually programmed in C/C++, using the HAL library (Hardware Abstraction Layer) and STMCubeIDE. The device is widely used in professional and industrial projects [15].

The ESP32 is a 32-bit dual-core microprocessor with 160 MHz processing, 448 Kb of ROM memory, 520 Kb of internal RAM, and support for 16 Mb of Flash and external SRAM. It is equipped with GPIO, SPI, I2C, I2S, and UART interfaces, as well as WiFi and Bluetooth. C/C++ is normally used as the programming language, but MicroPython is also supported. The ESP32 is mostly used for IoT applications, with low power consumption, and is a robust device for home automation applications [16].

Finally, the BeagleBone Black Rev C, which uses a 32-bit ARM Cortex-A8 processor with 1 GHz processing power, offers 512 MB of DRAM memory and 4 GB of Flash memory. It provides interfaces such as I2C, SPI, UART, USB, and Ethernet, as well as support for programming in Python and C/C++. It is possible to embed operating systems on the board, such as Linux, making it a highly robust platform for advanced projects [17].

TABLE I
COMPARISON OF MICROCONTROLLERS

Device	Processor	Clock Speed	Flash Memory	RAM	Interfaces	Programming Languages
Arduino Uno	8-bit	16 MHz	32 KB	2 KB	USART, SPI, GPIO, I2C	C++
STM32	32-bit	80 MHz	1 MB	128 KB	I2C, Bluetooth, WiFi, USART, USB, GPIO, SPI	C/C++
ESP32	32-bit dual-core	160 MHz	16 MB (external)	520 KB	GPIO, SPI, I2C, I2S, UART, WiFi, Bluetooth	C/C++, MicroPython
BeagleBone Black	32-bit ARM Cortex-A8	1 GHz	4 GB	512 MB	I2C, SPI, UART, USB, Ethernet	C/C++, Python

The comparative results can be seen in table I. And therefore, it is possible to see that the Beaglebone's processing speed is higher, reaching 1GHz, while the Arduino's is 16MHz, being the lowest, this result is equal to the robustness of the devices presented. Concerning memory, the ESP32 has the largest and the Arduino the smallest, the interfaces of the boards are very similar, with some differences such as WiFi and Bluetooth in the case of the ESP32 and STM32. Lastly, the dominant programming language is C/C++, but Beaglebone contains support for Python and ESP32, MicroPython.

B. Temperature Sensor

To compare temperature sensors, five devices were selected, including the DHT11, DHT22, SEN-11050, and CS215-L. When comparing these sensors, it can be seen that the DHT11 has a temperature range of 0°C to 50°C, a latency of two seconds, and an accuracy of more or less two degrees Celsius. The communication interface is via the one-wire digital communication protocol, the sensor has low sensitivity, as it needs sudden changes in temperature, and is best suited to controlled environments [18].

The DHT22 operates over a range of -40°C to 80°C, with an accuracy of around one degree Celsius and a latency of less than five seconds. It has a communication interface using the one-wire digital communication protocol, the solution is not very sensitive, although it is suitable for basic applications [18].

The SEN-11050 operates as a single-wire interface, with a temperature range of -55°C to 125°C, and an accuracy of approximately 0.5°C. The device has good sensitivity and is also used in industrial monitoring applications [19].

Finally, the CS215-L has a measurement range of -40°C to 70°C , and a latency of 1 millisecond. The device's accuracy in the application range would be around 0.4°C and the communication interface is SDI-12, normally applied in environments where data collection is crucial and precise, due to its high sensitivity [20].

TABLE II
COMPARISON OF TEMPERATURE SENSORS

Sensor	Temperature Range	Accuracy	Latency	Communication Interface	Sensitivity
DHT11	0°C to 50°C	$\pm 2^{\circ}\text{C}$	2 s	One-wire digital	Low
DHT22	-40°C to 80°C	$\pm 1^{\circ}\text{C}$	5 s	One-wire digital	Low
SEN-11050	-55°C to 125°C	$\pm 0.5^{\circ}\text{C}$	N/A	Single-wire	High
CS215-L	-40°C to 70°C	$\pm 0.4^{\circ}\text{C}$	1 ms	SDI-12	High

After evaluating the data above, as seen in Table II, it is possible to identify that the sensor with the highest accuracy, sensitivity, and lowest latency is the CS215-L, all of them have ideal temperature ranges for the application, which would be between 0°C and 40°C , approximately, and the communication interface is the same in most cases, except for the CS215-L, which has a different interface.

C. Humidity Sensor

To collect humidity data as accurately as possible, the T9501, CS215-L, DHT11, and DHT22 sensors were selected as options for the project. The T9501 sensor transmits the information collected via the MODBUS communication protocol. The device has a sensitivity of 0.01% relative humidity (RH) and its main feature is its humidity range of 0 to 95% RH, with an accuracy of $\pm 2.0\%$ RH (20 - 80% RH) and $\pm 3.5\%$ RH (0% to 20%) and (80% to 100%). In addition, the sensor has a latency of less than or equal to 100 seconds, thus providing a rapid response when capturing data [21].

The CS215-L sensor, on the other hand, goes beyond the applications presented in the previous section. The device has a sensitivity of 0.03% relative humidity (RH) and its main feature is its humidity range of -20° to $+60^{\circ}\text{C}$, with an accuracy of $\pm 4.0\%$ RH (0 - 100% RH) and $\pm 2\%$ RH (10% to 90%). The sensor also has a latency of less than or equal to 20 seconds [20].

In terms of collecting humidity data from the DHT11 sensor, the device's main feature is its humidity range of 20 to 80% RH, with an accuracy of $\pm 5.0\%$ RH. In addition, the sensor has a latency of less than or equal to 15 seconds [18].

Finally, the main feature of the DHT22 sensor is its humidity range of 0 to 100% RH, with an accuracy of $\pm 2.0\%$ RH. In addition, the sensor has a latency of around 15 seconds [18].

TABLE III
COMPARISON OF HUMIDITY SENSORS

Sensor	Communication Protocol	Sensitivity (% RH)	Humidity Range (% RH)	Accuracy (% RH)	Latency (s)
T9501	MODBUS	0.01	0 - 95	± 2.0 to ± 3.5	100
CS215-L	N/A	0.03	0 - 100	± 2.0 to ± 4.0	20
DHT11	N/A	N/A	20 - 80	± 5.0	15
DHT22	N/A	N/A	0 - 100	± 2.0	15

By comparing each sensor with the help of Table III, the T9501 sensor was chosen for its exceptional accuracy and

sensitivity over the others, offering 0.01% RH sensitivity and a wide humidity range of 0 to 95% RH. Its accuracy of $\pm 2.0\%$ RH (20–80% RH) surpasses the other options. It is also noteworthy that thanks to its robustness, often being implemented in industrial applications.

D. Wind Speed Sensor

To collect wind speed data as accurately as possible, the SEN0483, S-WSB-M003 and RXW-WCF-900 sensors were selected as options for the project. The SEN0483 measures winds from 0 to 32.4 m/s, with an accuracy of ± 0.3 m/s. It transmits the information collected via the MODBUS communication protocol. The transmitter features quality bearings, low resistance, low starting wind speed, high measurement accuracy, good stability and strong anti-interference capability [22].

With a range of 0 to 76 m/s and an accuracy of $\pm 4\%$, the S-WSB-M003 offers reliable and fast measurements due to its low latency. All sensor parameters are stored inside the smart sensor, which automatically communicates the configuration information to the logger without the need for extensive programming or configuration by the user [23].

The RXW-WCF-900 measures winds from 0 to 76 m/s, with an accuracy of ± 1.1 m/s or $\pm 5\%$. Its low latency and HOBOnet wireless interface facilitate remote installation. Sensitive to light winds, it is efficient for a variety of monitoring purposes. The Wireless Sensor records wind speed, gusts, and wind direction. The data is transmitted directly to the RX3000 weather station or passed on via other wireless sensors to the central station. They come pre-configured and ready to use, and the data is accessed via HOBOLink, Onset's innovative cloud-based software platform [24].

The main differences between these sensors are identified in Table IV.

TABLE IV
COMPARISON OF WIND SPEED SENSORS

Sensor	Wind Speed Range	Accuracy	Communication Interface	Features
SEN0483	0 - 32.4 m/s	± 0.3 m/s	MODBUS	High accuracy, low starting wind speed, good stability
S-WSB-M003	0 - 76 m/s	$\pm 4\%$	Smart sensor (auto-config)	Reliable, fast measurements, low latency
RXW-WCF-900	0 - 76 m/s	± 1.1 m/s or $\pm 5\%$	HOBOnet wireless	Sensitive to light winds, records wind speed, gusts, and direction

The SEN0483 was selected for its superior accuracy of ± 0.3 m/s and robust features. It outperforms the S-WSB-M003 and RXW-WCF-900 in precision and stability, with reliable MODBUS data transmission and excellent anti-interference. Its high accuracy and advanced capabilities make it the optimal choice for precise wind speed measurement.

E. Wind Direction Sensor

In order to collect wind direction data as accurately as possible, the SEN0482, EN-024, and the previously mentioned S-WSB-M003 sensors were selected as options for the project. The SEN0482 sensor transmits the information collected via the MODBUS communication protocol, has a measurement

range of 16 directions, and has a starting speed of 0.3 m/s [25].

The EN-024 Wind Direction Sensor, made of anodized aluminum and stainless steel, is designed for durability. As far as its specifications are concerned, the operating speed range corresponds to 0 to 160 km/h, the starting speed 0.5 m/s, the 360° operating range, and the operating temperature 10°C to +70°C [26].

TABLE V
COMPARISON OF WIND DIRECTION SENSORS

Sensor	Measurement Range	Starting Speed	Operating Temperature	Communication Interface
SEN0482	16 directions	0.3 m/s	N/A	MODBUS
EN-024	360°	0.5 m/s	10°C to +70°C	N/A
S-WSB-M003	0 - 76 m/s (for wind speed)	N/A	N/A	Smart sensor (auto-config)

The SEN0482 was chosen for its precise 16-direction range, low starting speed of 0.3 m/s, and MODBUS communication. Of the options studied, it was the most suitable one for the project.

F. Precipitation Sensor

The evaluated precipitation sensors include the TS221, QMR101, RG13, TB3, TB4, and TB6. The TS221 boasts a 200 mm diameter collection ring and $\pm 1\%$ accuracy at 50 mm/h, with analog communication [27].

The QMR101 provides a 144 mm/h capacity, $\pm 2\%$ accuracy, and 0.2 mm sensitivity, featuring a compact, lightweight design with UV-resistant plastic, ideal for portable setups [28].

The Vaisala RG13 uses a tipping bucket mechanism to detect every 0.2 mm of rain, offering unlimited capacity and a large 225 mm diameter collection area [29].

The TB3 is designed for extreme weather, measuring up to 700 mm/h with $\pm 2\%$ accuracy for 0-250 mm/h and $\pm 3\%$ for 250-500 mm/h [30].

The TB4 is similar to the TB3 but includes an optional RainTrak Undercover system for real-time monitoring and data logging [31].

The SEN0575 delivers precise measurements with a 0.28 mm resolution, operates on 3.3 to 5.5V DC with under 3mA current, features I2C/UART output, and supports temperatures from -40 to 85°C, making it versatile and compact [33].

Lastly, the TB6 builds on the TB3 and TB4 with enhanced component refinement [32].

TABLE VI
COMPARISON OF PRECIPITATION SENSORS

Sensor	Collection Diameter	Accuracy	Capacity	Sensitivity	Features
TS221	200 mm	$\pm 1\%$ at 50 mm/h	N/A	N/A	Analog input communication
QMR101	N/A	$\pm 2\%$	144 mm/h	0.2 mm	Lightweight, UV-resistant plastic
RG13	225 mm diameter	N/A	Unlimited	0.2 mm	Tipping bucket mechanism, large collection area
TB3	N/A	$\pm 2\%$ (0-250 mm/h), $\pm 3\%$ (250-500 mm/h)	700 mm/h	N/A	Suitable for heavy rainfall
TB4	N/A	Similar to TB3	700 mm/h	N/A	Option for RainTrak Undercover system
TB6	Enhanced from TB3/TB4	N/A	700 mm/h	N/A	Improved components

The SEN0575 was chosen for its high resolution of 0.28 mm, versatile I2C/UART output, and robust temperature range. Its combination of precision, adaptability, and compact design makes it a good option for precipitation sensors.

V. CONCLUSION

In conclusion, this study proposes a comprehensive GST design optimized for LoRa-based CubeSat missions aimed at environmental data collection. Through a thorough literature review of similar projects and a systematic evaluation of critical components such as sensors and communication technologies, this work establishes a robust framework for GST deployment. Key technology choices, such as the use of low-power embedded devices like the STM32 and ESP32, were made to ensure efficient processing and data handling, while the integration of LoRa technology guarantees reliable, long-range communication with CubeSats.

The selection of high-precision sensors emphasizes accuracy and reliability in extreme environmental conditions. The proposed system is designed to be energy-efficient, powered by solar energy with low-power modes, and scalable through a network of support GSTs to cover larger areas, such as the 600-hectare scope outlined in the CIMATÉLITE-1 mission.

This design framework not only meets the technical and operational requirements for the CIMATÉLITE-1 mission but also sets the stage for future advancements in GST systems for CubeSat missions, paving the way for enhanced remote sensing and environmental monitoring capabilities in remote areas.

REFERENCES

- [1] KULU, E. Nanosats database. Available at: <https://www.nanosats.eu/>. Accessed on: 25 aug. 2024.
- [2] CubeSat. Available at: <https://www.cubesat.org>. Accessed on: 9 jul. 2024.
- [3] Monitoramento de áreas remotas via satélite: uma nova ferramenta para a gestão de recursos naturais. Available at: <https://geoinova.com.br>. Accessed on: 9 jul. 2024.
- [4] PABST, Antonia Kate Dunford. Development and Testing of LoRa Technology for Satellite Communications. 2022. Dissertação de Mestrado. Pontificia Universidad Catolica de Chile (Chile).
- [5] SALLUM, E. et al. Improving Quality-of-Service in LoRa low-Power Wide-Area Networks through optimized radio resource management. Journal of sensor and actuator networks, v. 9, n. 1, p. 10, 2020.
- [6] LEPCHA, P. et al. Application of small satellites for low-cost remote data collection using LoRa transmitters. TRANSACTIONS OF THE JAPAN SOCIETY FOR AERONAUTICAL AND SPACE SCIENCES AEROSPACE TECHNOLOGY JAPAN, v. 19, n. 2, p. 224-230, 2021.
- [7] Samanaú.PCD. Available at: <https://ccsl.ifrn.edu.br/portfolio-de-projetos/samanau/samanau-pcd/>. Accessed on: 15 jul. 2024.
- [8] SOUTO, Moisés Cirilo de Brito. Gestão de inovação em startup de rede de coleta de dados sem fio, multipropósito e modular: estudo de caso de um spin-off de pesquisa da Plataforma Samanaú. 2017. Dissertação de Mestrado. Brasil.
- [9] ARIFIN, M. A. et al. Data collection platform design using LEO satellite-based LoRa for disaster management in Indonesia. 2023 IEEE International Conference on Aerospace Electronics and Remote Sensing Technology (ICARES). Anais...IEEE, 2023.
- [10] HASBI, W. LAPAN-A2 (IO-86) satellite roles in natural disaster in Indonesia. In: Proc. 70th Int. Astron. Congr.(IAC). 2019.
- [11] PROKOPYEV, V. Y. et al. NORBY CubeSat nanosatellite: design challenges and the first flight data. Journal of physics. Conference series, v. 1867, n. 1, p. 012038, 2021.
- [12] MASKEY, A. et al. One year on-orbit results of improved bus, LoRa demonstration and novel backplane mission of a IU CubeSat constellation. Transactions of the Japan Society for Aeronautical and Space Sciences, v. 65, n. 5, p. 213-220, 2022.
- [13] LEPCHA, Pooja. Design and Development of Low power and Low-cost Sensor Station for Store and Forward Data Collection using CubeSat in Developing Countries. 2022.

- [14] SOUZA, F. Arduino UNO - Conheça o hardware da placa Arduino em detalhes. Available at: <https://embarcados.com.br/arduino-uno/>. Accessed on: 07 sep. 2024.
- [15] LIMA, T. Placa STM32 Discovery Kit IoT Node - Embarcados. Embarcados, , 26 nov. 2018. . Accessed on: 23 aug. 2024
- [16] ELETROGATE. Conhecendo o ESP32 - Introdução (1). Available at: <https://blog.eletrogate.com/conhecendo-o-esp32-introducao-1/>. Accessed on: 24 aug. 2024.
- [17] BeagleBone@ black. Available at: <https://www.beagleboard.org/boards/beaglebone-black>. Accessed on: 23 aug. 2024.
- [18] ELETROGATE. Sensores DHT11 e DHT22: Guia Básico dos Sensores de Umidade e Temperatura. Available at: <https://blog.eletrogate.com/sensores-dht11-dht22/>. Accessed on: 24 aug. 2024.
- [19] SEN-11050 PRODUCT OVERVIEW. DS18B20 high temperature waterproof digital sensors. Available at: https://www.mouser.com/pdfDocs/ProductOverview_DS18B20HighTempWaterproofDigitalSensors-2.pdf. Accessed on: 24 aug. 2024.
- [20] SCIENTIFIC, C. CS215-L - digital air temperature and relative humidity sensor. Available at: <https://www.campbellsci.com/cs215-1>. Accessed on: 01 sep. 2024.
- [21] AMPHENOL. Telaire T9501 Series. Available at: https://br.mouser.com/datasheet/2/18/1/Amphenol_AAS_920_788A_Telaire_T9501_Series_071221_-2483009.pdf. Accessed on: 24 aug. 2024.
- [22] DFRobot. SEN0483 Product Overview: RS485 Wind Speed Transmitter. Available at: https://www.mouser.com/catalog/additional/DFRobot_Productoverview_SEN0483.pdf. Accessed on: 25 aug. 2024.
- [23] SIGMA. Product Manual. Available at: <https://cdn02.duxcloud.com.br/sigma/products/16/files/manual-mLX0wTCT.pdf>. Accessed on: 05 sep. 2024.
- [24] SIGMA. Data Sheet. Available at: <https://cdn02.duxcloud.com.br/sigma/products/298/files/folha-de-dados-OUMYCIPk.pdf>. Accessed on: 05 sep. 2024.
- [25] ENERGETICA. Sensor de Direção do Vento. Available at: https://energetica.ind.br/wp-content/uploads/2016/01/env1_folheto-19.pdf. Accessed on: 25 aug. 2024.
- [26] DFRobot. SEN0482 Product Overview: RS485 Wind Direction Transmitter. Available at: <https://www.mouser.com/pdfDocs/DFRobotRS485WindDirectionTransmitterProductOverview.pdf>. Accessed on: 25 aug. 2024.
- [27] TECMES. Product TS221-Po. Available at: <https://www.tecmes.com/wp-content/uploads/2020/06/ts221-Po.pdf>. Accessed on: 05 sep. 2024.
- [28] VAISALA. Rain Gauge QMR101 and QMR101M. Available at: <https://www.vaisala.com/sites/default/files/documents/QMR101-QMR101M-Datasheet-B211713EN.pdf>. Accessed on: 04 sep. 2024.
- [29] HOBECO. Pluviômetro RG13. Available at: <https://www.hobeco.net/content/pluviometro-rg13>. Accessed on: 04 sep. 2024.
- [30] HOBECO. Pluviômetro TB3. Available at: <https://www.hobeco.net/content/pluviometro-tb3>. Accessed on: 05 sep. 2024.
- [31] HOBECO. Pluviômetro TB4. Available at: <https://www.hobeco.net/content/pluviometro-tb4>. Accessed on: 05 sep. 2024.
- [32] HOBECO. Pluviômetro TB6. Available at: <https://www.hobeco.net/content/pluviometro-tb6-0>. Accessed on: 06 sep. 2024.
- [33] Gravity: Tipping bucket rainfall sensor - DFRobot. Available at: https://wiki.dfrobot.com/SKU_SEN0575_Gravity_Rainfall_Sensor. Accessed on: 06 sep. 2024.

Development of an automated application to collect and filter CubeSat's data

Caique Sales Miranda Gomes[✉],
 Gabriel Mariano Marcelino[✉]
 and João Cláudio Elsen Barcellos[✉]

Abstract—In recent years, the utilization of CubeSats has proliferated across diverse institutions worldwide, marking a transformative shift in space exploration. However, despite their widespread adoption, in low-cost missions there remains a conspicuous lack of comprehensive information and tracking accessibility for the broader community beyond traditional channels like Ham Radio "amateur radio". The NanoSatTrack project serves as a platform using MERN stack (MongoDB, Express, React, and Node.js) with the primary goal of making data generated by nanosatellites accessible to the general public in real time. It achieves this by offering a website equipped with interactive dashboards. These dashboards play a vital role in presenting and visualizing the key telemetry and information derived from the satellite's mission interface. In essence, NanoSatTrack enables anyone to conveniently access and understand the valuable data produced by nanosatellites. It is responsible for creating a dashboard showing the communication between the Earth (a ground station) and a satellite, that are divided in multiple telecommunication links. This project allows for future CubeSat missions to better show their project's achievements and help them ensure an easier approach to its collected data.

Keywords—Tracking, monitoring, platform

I. INTRODUCTION

The satellite industry has been working towards collecting and filtering data for a long time now, some of the biggest challenges with satellite data are volume, velocity, and variety [1]. In the big industry, there are a few programs that work to make up-to-date data accessible to users around the world as free, some examples are Copernicus Open Access Hub, NASA Earthdata, and Google Earth Engine. Although this practice has been fairly common in the satellite industry, little has been shown of how this concept can be implemented for CubeSats, in the cases that has been implemented, those data platforms have helped not only the developer team but also ham radios and students of many majors to have a easier access to satellite data [2].

The constant advance of small satellites has opened up space to a wider range of applications and a broader audience, especially academic institutions, and universities, enabling them to conduct space research with reduced financial investment [3].

Several technical obstacles still need to be resolved when developing these missions. One of the main difficulties is creating data volume [1], for some CubeSat missions, this is mostly done by gathering data from multiple ground stations around the globe. The velocity at which the data is been collected and stored is also a key component to have a real time mission platform. Collecting this high volume of data and keeping the database updated at a fast pace is challenge on its own ,to do in smaller missions with less budget is even harder due to less ground station segment investments. Another significant challenge with the data stored from CubeSat missions is the lack of a platform to make the data obtained easily accessible, with the data already filtered to be in the best way possible

with graphs and grouping of relevant information, although the difficulty, the Alfa Crux mission has created a platform to help their team analyse and keep track of their CubeSat while orbiting the Earth [2]. This is crucial for mission operators, the ham radio community, and the general public who can later on use the data obtained during the satellite's mission.

As it is extremely complicated to gather enough data to build a consolidated database to show enough info from one single orbit cycle, it is also hard to connect all the data sent directly from the satellite to Earth, this makes it difficult to create an updated database without having a connection between ground stations. One solution found by many institutions is to gather data not only from the mission's main ground station but also from ham radio operators around the world who have linked with the CubeSat while its orbit was above their station [4]. This partnership is very beneficial to the mission operators but not very reliable since each ground station only has a short period to connect with the satellite. Additionally, the ham radio collaborators around the world can take some time to send back the data, and this system is not very organized [4].

The FloripaSat-1 and FloripaSat-2 platforms, which were and will be used in nanosatellite missions such as FloripaSat-1, GOLDS-UFSC, Catarina-A1, and Catarina-A3, among others, currently lack a platform to display the data collected during these missions. To address this problem, the NanoSatTracker project was created.

This project aims to filter the data collected from CubeSats and present it in a clear and accessible way, making it easier to monitor the satellite's health status throughout each orbit cycle, as the mission control group obtains data from the missions main ground station, and ham radio partners around the world. Additionally, it seeks to simplify the work of engineers by organizing the information into subsystems, enabling a more efficient analysis of component performance. This approach also helps anticipate and address potential challenges in future missions.

Caique Sales Miranda Gomes, UFSC, Brazil, (kismsg@gmail.com).
 Gabriel Mariano Marcelino, UFSC, Brazil,
 (gabriel.marcelino@spacelab.ufsc.br).
 João C. E. Barcellos, UFSC, Brazil, (joaoclaudiobarcellos@gmail.com).

The network of ham radios that help collecting and sending the CubeSat data is voluntary, so there is no guarantee of data besides the missions main ground station, this challenge is faced by others satellite missions around the world [4]. Although we can't fully solve this problem, NanoSatTracker has a side project which sole purpose is to automate the process of sending the data obtained by the link from a ground station with a CubeSat. By installing code in the ground station's computer, when it receives a CubeSat beacon data, it will redirect the data to a database in the cloud, feeding the NanoSatTracker almost automatically.

Therefore, the main proposal is to develop a data tracking platform for small satellite missions. This platform will allow mission operators to have a better overview of how the system is working in orbit without having to wait for days or even weeks to collect the data needed to run tests and perform basic check-ups on the nanosatellite system. This paper is organized as follows: the methodology applied by other authors will be adapted and elaborated upon in the Methodology section, where the key components will be presented in detail. Further discussions on the project's development are provided in the Discussion section, followed by the Conclusion.

II. METHODOLOGY

The methodology adopted for the NanoSatTracker platform development is structured into 7 stages: 1) a comprehensive literature review, 2) analysis of the FloripaSat-1 mission data, 3) selection of the most valuable data for the developers and community, 4) Client side and server side diagram, 5) Server side development, 6) Client side development, 7) Verification and validation of the platform. The project is in-between stages 6 and 7, the development stages can be seen in Fig.1.

A. Comprehensive literature review

An extensive literature review was first conducted, focusing on existing projects from other institutions to identify best practices, innovative approaches, and the challenges encountered in similar developments. This research is divided into two sections: traditional large satellite missions and CubeSat missions. This division is necessary because these two distinct project models face different challenges and typically require different approaches to problem-solving. Traditional large satellites have a variety of ways to collect, filter, and display their data to users, as can be seen in projects like NASA's Earth Science Data System (ESDS) Program, Earth Observing System (EOS) Program [5], and projects like The Copernicus App Lab project [1], where they have an abundance of data due to many connections with the satellite and a more robust data system. Unlike traditional large satellite missions, CubeSat projects typically operate with smaller teams, making it difficult to allocate developers specifically to the creation of a platform for displaying their data, the FloripaSat-1 is an example of this [6]. By searching for more information we could understand better the 5 main challenges of collecting data for satellite missions (volume, velocity, variety, veracity, and value) [1], and then focus on solving them for our model.

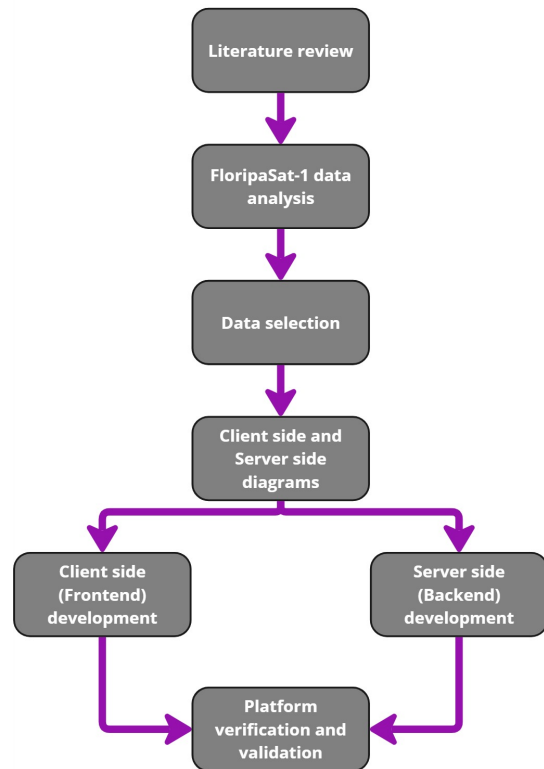


Fig. 1: FloripaSat-1 platform

B. Analysis of the FloripaSat-1 data

In this section, we will go through the basic subsystems of the FloripaSat-1 platform that are important for the CubeSat mission, so we can have a better understanding of where the mission's data comes from. The OBDH (On-Board Data Handling Module), the EPS (Electrical power system module), and TT&C (Telemetry, Tracking & Command). For its simplicity, data available, and user-friendly display of information, this work will be centered around the FloripaSat-1 platform (1U CubeSat) designed and built by the Space Systems Laboratory (Spacelab) at the Federal University of Santa Catarina. The FloripaSat-1 platform is shown in in Fig.2.

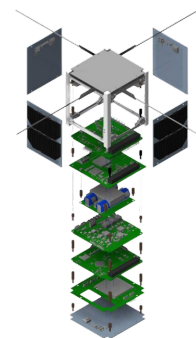


Fig. 2: FloripaSat-1 platform

The On-Board Data Handling Module (OBDH) main goal is to manage all the CubeSat information. The OBDH2 is respon-

sible for synchronizing actions and the data flow between other modules (ie. EPS, Payloads) and the Earth segment. Some of the most important satellite data comes from the OBDH, such as the date, hour, temperature sensors, and much more that tell about how the system is handling the orbit cycle. The OBDH data is one of the most important data collected since it describes the health status of the CubeSat [7]. The Electrical and Power System (EPS) collects data from different sensors around the EPS PCB and also the battery PCB. This module not only is one of the most complexes in the satellite but also is one with a large number of sensors regarding temperature and energy, it counts with electrical current and voltage measurements in the module and also in all solar panels, temperature sensors in the module and some more in the batteries PCB that is attached to the main PCB. Although all data is important, the most significant data for the battery's health and duty cycle are the OVERALL temperatures, the voltage and current in the solar panels, and in the EPS [7]. The Telemetry, Tracking & Telecommand (TT&C) is responsible for making the communication between the earth (a ground station) and a satellite and is divided into two sub-modules: Beacon and downlink/uplink., which is responsible for capturing data from Earth (ground stations) and transmitting it to the TT&C. Since the most common communications are the three mentioned above, as the NanoSatTracker is in its Beta version, the most simplified data set was chosen to be displayed in the platform, the Beacon, as it can be seen in Table I.

Column	Content	Column	Content
0	Year (UTC)	21	RESERVED
1	Month (UTC)	22	RESERVED
2	Day (UTC)	23	RESERVED
3	Hour (UTC)	24	RESERVED
4	Minute (UTC)	25	RESERVED
5	Second (UTC)	26	RESERVED
6	Battery cell 1 voltage	27	RESERVED
7	Battery cell 2 voltage	28	RESERVED
8	Battery monitor temp.[°C]	29	RESERVED
9	Battery current in A	30	RESERVED
10	Battery charge in Ah	31	RESERVED
11	Solar Panel -Y current in [A]	32	RESERVED
12	Solar Panel +X current in [A]	33	RESERVED
13	Solar Panel -X current in [A]	34	RESERVED
14	Solar Panel +Z current in [A]	35	RESERVED
15	Solar Panel -Z current in [A]	36	EPS temp.[°C]
16	Solar Panel +Y current in [A]	37	SatNOGS observation
17	Solar Panel -Y +X voltage	38	Callsign
18	Solar Panel -X +Z voltage	39	Grid locator
19	Solar Panel -Z +Y voltage		
20	Energy Level		

TABLE I: Beacon Data table.

C. Selection of the most valuable data for the developers and community

Based on previous Beacon information we received from the FloripaSat-1 mission regarding the main subsystems we gathered a total of the 20 content information shown in Table I, and another 19 different content information from the OBDH and mission payload. The organization of the database (CSV files) is described in Fig.3, as it can be seen most of the

information regards the EPS subsystem, although there is still space RESERVED to upcoming modules to send other data.

Column	Content
0	Year (UTC)
1	Month (UTC)
2	Day (UTC)
3	Hour (UTC)
4	Minute (UTC)
5	Second (UTC)
6	Battery cell 1 voltage
7	Battery cell 2 voltage
8	Battery monitor temperature in Celsius
9	Battery current in A
10	Battery charge in Ah
11	Solar panel -Y current in A
12	Solar panel +X current in A
13	Solar panel -X current in A
14	Solar panel +Z current in A
15	Solar panel -Z current in A
16	Solar panel +Y current in A
17	Solar panel -Y +X voltage
18	Solar panel -X +Z voltage
19	Solar panel -Z +Y voltage
20	Energy level
21	RESERVED
22	RESERVED
23	RESERVED
24	RESERVED
25	RESERVED
26	RESERVED
27	RESERVED
28	RESERVED
29	RESERVED
30	RESERVED
31	RESERVED
32	RESERVED
33	RESERVED
34	RESERVED
35	RESERVED
36	EPS microcontroller temperature in Celsius
37	SatNOGS observation
38	Callsign
39	Grid locator

Fig. 3: Beacon data CSV file

1) *Database Design:* To decide which database model would be best for this project, we focused on the Beacon data package. There were a couple of options to choose for the NanosatTracker database, the first decision we made was to go with a NoSQL database for a couple of reasons.

- Flexibility NoSQL databases allow for schema-less data storage, making it easier to remove fields without the need for a major schema migration, since the structure of the database is changing along with the evolution of the CubeSat project and its needs to collect different information that might change over time.
- Scalability The NoSQL databases are easy to work with large volumes of data, making it a good choice to

store hundreds of thousands of Beacon data packages throughout the months of the CubeSat mission.

- Simplicity SQL databases are great for working with complex data structure schemas, but for the Nanosat-Tracker we use only one simple schema that is fetched when needed, so it makes sense to go with a simpler and more practical NoSQL database in this case.

D. Client side and server side diagram

To design the client-side and server-side diagrams for the NanoSatTracker application, we structured the platform around the data itself. The server-side architecture was specifically developed based on the data structure provided by the Beacon file, ensuring an intuitive and data-driven design for both sides of the application. Given the high volume of data and the lack of need for a structured SQL database, the most intuitive approach was to use the MERN stack to develop both the client-side and server-side of the application. The client side diagram can be seen in Fig.6, and the server side diagram can be seen in Fig.5.

1) *MERN Stack*: Since the database solution was chosen to be a NoSQL, it was natural to decide to use a Stack that works well with this database, the chosen stack was the MERN (MongoDB, Express.js, React, Node.js).

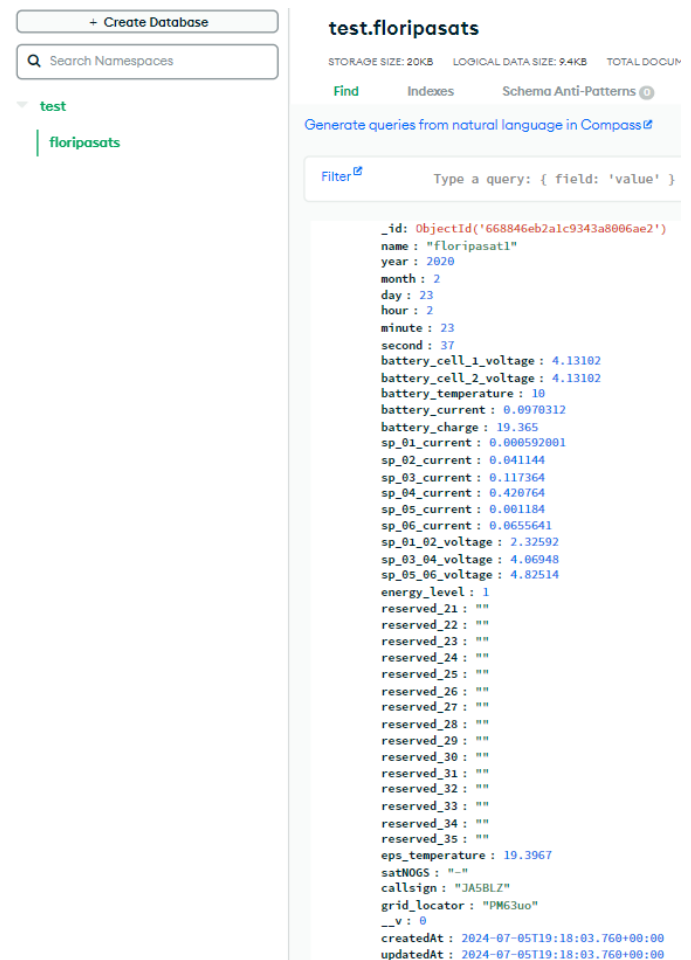
- MongoDB MongoDB is a NoSQL database that stores data in JSON-like documents. The database will store all the CubeSat's Beacon data related to the mission, such as date and time information, temperature sensors, logs, metrics, and other RESERVED content. Its flexibility and simplicity allow for easy changes to the data structure as the project evolves.
- Express.JS Express is a fast and minimalist web framework for Node.js that supports web and mobile applications, APIs, and middleware. The Express framework will be used to create the backend logic and structure for the project. It will handle the server-side logic, process requests from the user side (frontend), interact with the MongoDB database, and send the appropriate responses to the fetched data.
- React React is the library for web and native user interfaces. React will be used to build the user side (frontend) of the NanosatTracker project. It will enable to create a dynamic and interactive user interface where not only the operators of the project will have access to the data collected but also any person who has the web page link will be able to manage data, view dashboards, and interact with various components. Reacts User Interface will facilitate to create a responsive screen size for many devices, like cell phones and tablets.
- Node.JS Node.js is an open-source server environment that runs on various platforms and uses JavaScript on the server. Node.js will serve as the platform to run the server-side part of the NanosatTracker project. It will execute the JavaScript code written in Express.js, manage server operations, and handle asynchronous events. This will ensure that the server can handle multiple user requests efficiently, making the application simple and scalable.

III. IMPLEMENTATION

Through all the studies previously carried out, the MERN stack was chosen. To execute the projects plan we started first building the database, then the server side of the application (backend), and lastly the client side (frontend). Throughout the project evolution some changes were made, not only in the database format but also in the way the backend worked fetching data from the MongoDB and the frontend displayed the data, always trying to make the logic simpler and more user-friendly to the future users of the platform.

A. Database

The database structure was chosen based on simplicity and flexibility, so the beta model result included all the content the beacon was sending to the ground station and 4 more information, the ID of the element, the name of the CubeSat mission, and two date/time information about the creation and update of the element. The beta model data structure can be seen in Fig.4.



The screenshot shows the MongoDB Compass interface. On the left, there's a sidebar with a search bar and a tree view showing the 'test' namespace containing the 'floripasats' collection. The main area displays a document from the 'test.floripasats' collection. The document is a JSON object with the following fields:

```

{
  "_id": ObjectId('668846eb2a1c9343a8006ae2'),
  "name": "Floripasat1",
  "year": 2020,
  "month": 2,
  "day": 23,
  "hour": 2,
  "minute": 23,
  "second": 37,
  "battery_cell_1_voltage": 4.13102,
  "battery_cell_2_voltage": 4.13102,
  "battery_temperature": 10,
  "battery_current": 0.0970312,
  "battery_charge": 19.365,
  "sp_01_current": 0.000592001,
  "sp_02_current": 0.041144,
  "sp_03_current": 0.117364,
  "sp_04_current": 0.420764,
  "sp_05_current": 0.001184,
  "sp_06_current": 0.0655641,
  "sp_01_02_voltage": 2.32592,
  "sp_03_04_voltage": 4.06948,
  "sp_05_06_voltage": 4.82514,
  "energy_level": 1,
  "reserved_21": "",
  "reserved_22": "",
  "reserved_23": "",
  "reserved_24": "",
  "reserved_25": "",
  "reserved_26": "",
  "reserved_27": "",
  "reserved_28": "",
  "reserved_29": "",
  "reserved_30": "",
  "reserved_31": "",
  "reserved_32": "",
  "reserved_33": "",
  "reserved_34": "",
  "reserved_35": "",
  "eps_temperature": 19.3967,
  "satN06S": "",
  "callsign": "JA5BLZ",
  "grid_locator": "PM63uo",
  "_v": 0,
  "createdAt": "2024-07-05T19:18:03.760+00:00",
  "updatedAt": "2024-07-05T19:18:03.760+00:00"
}

```

Fig. 4: MongoDB data structure.

B. Server side (backend)

The server side of the web application was structured using Express and Node.JS. The structure is divided into 4 main

sub-areas, Controllers, Models, Routes, and Data(only used in Beta testing model). The server division can be seen in Fig.5.

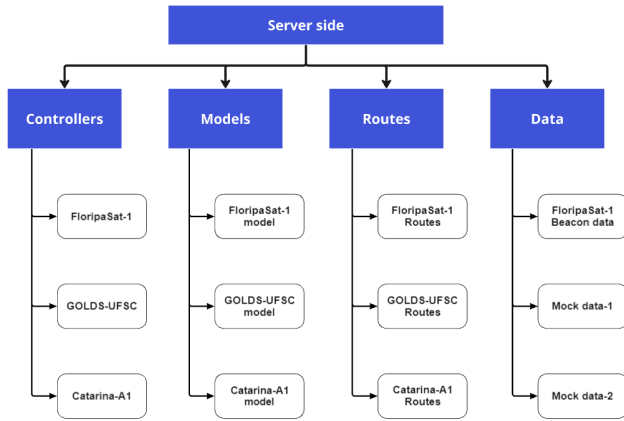


Fig. 5: Server side structure.

1) *Controllers*: The controller’s code will define the logic that handles incoming HTTP requests. Controllers usually act as an intermediary between the data models (data layer) and the views (UI/Client layer). They get the incoming requests and then process them, perform the necessary operations such as querying the database or processing data, and then send the corresponding responses back to the client.

2) *Models*: The model’s code is used to define the structure of the data that will be stored in the MongoDB database. The model is created using Mongoose, which is an Object Data Modeling (ODM) library for MongoDB and Node.js. The schema was defined using the already existing beacon data from the FloripaSat-1 and then analyzed the best solution to model the application data in a way that facilitates query data fetch from the web application.

3) *Routes*: The Route’s code on the server creates the endpoints that the server will respond to. It specifies the URLs that the server will handle and also maps these URLs to the corresponding controller functions, which contain the logic to process each HTTP request from the client side.

4) *Data*: The Data’s code is basically mock data used in the Beta testing model for the first interactions while the ground stations do not yet feed the database with the CubeSat beacon data.

C. Client side (frontend)

The client side of the web application was structured using the React framework for developing of the user interface(UI). The client side of the application is responsible for not only displaying the (UI), but also handling the user’s interaction, inputs, and events. The frontend structure is divided as seen in Fig.6.

IV. RESULT

The result of this project was a Beta model of the Nanosat-Tracker web application, it consists of a web platform that is divided into 6 pages dedicated to different aspects of the satellite, it was decided to use the FloripaSat-1 CubeSat as

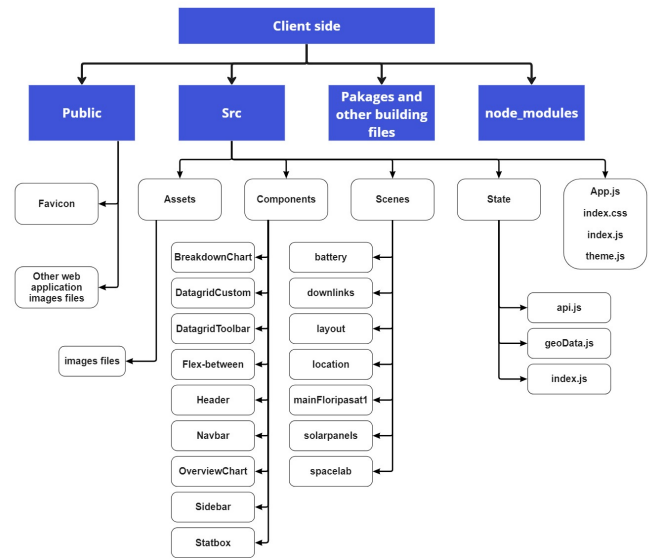


Fig. 6: Client side structure.

an example for the Beta model as for it’s easy access to the nanosatellite data and information throughout the mission, all the data and information is presented in GitHub(<https://github.com/floripasat>). The reason we divided the satellite beacon data into 6 different pages was that they would be better arranged and it would be better for analysis during and after the mission to see the data separated in this way rather than mixed together, thus ensuring that the data that is presented together has high relevance to each other, and can be compared. The 6 pages created are Spacelab, FloripaSat-1, Downlink, Battery, Solarpanel, and Location. Each of the 6 pages has a main focus as we will see later.

A. Overview of the NanosatTracker platform

NanoSatTrack serves as a platform with the primary goal of making data generated by nanosatellites accessible to the general public. It achieves this by offering a website equipped with interactive dashboards. These dashboards play a vital role in presenting and visualizing the key telemetry and information derived from the satellite’s mission interface. In essence, NanoSatTrack enables anyone to conveniently access and understand the valuable data produced by nanosatellites. It is responsible for creating a dashboard showing the communication between the earth (a ground station) and a satellite, that are divided in two sub-modules: Beacon and downlink/uplink.

B. Spacelab page

The Spacelab page is the main page of the web application, it is also the simplest out of the 6 pages. Its only goal is to give the user an overview of the Spacelab laboratory projects and what will be shown on the next pages. An image of the Beta version of the Spacelab page can be seen in Fig.7.

C. FloripaSat-1 Main page

The FloripaSat-1 Main page is a page dedicated to the FloripaSat-1 mission, it will give a brief explanation of the

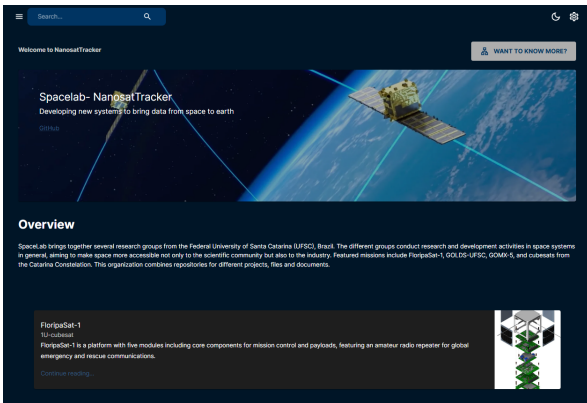


Fig. 7: Spacelab page.

Fig. 9: Downlink page.

payloads and subsystems inside the CubeSat. An image of the Beta version of the FloripaSat-1 Main page can be seen in Fig.8.

graphs are displayed on the screen they will have the same size and collected data pattern so the user can analyze the graphs simultaneously. An image of the Beta version of the Battery page can be seen in Fig.10.

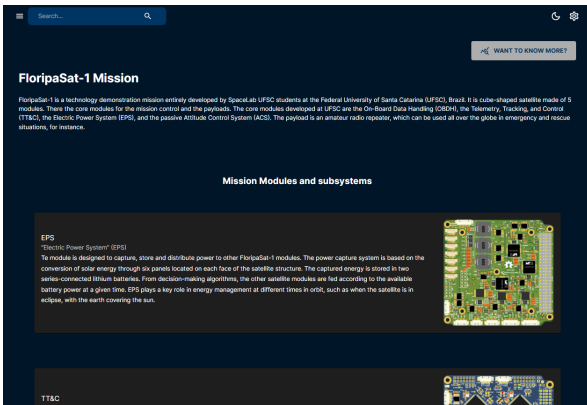


Fig. 8: FloripaSat-1 Main page.

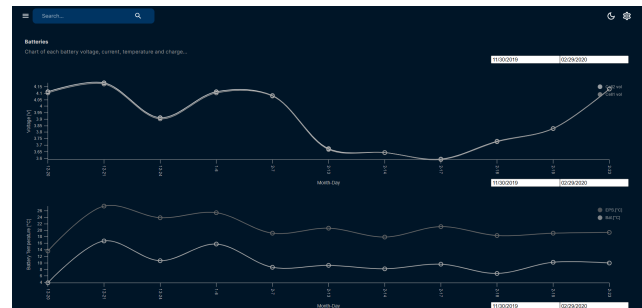


Fig. 10: Battery page.

D. Downlink page

The Downlink page has the goal of displaying all the collected data from the FloripaSat1 beacon in a simple and organized table, arranged per date of received data. It enables the team behind the CubeSat mission to see the data collected in a simpler and more organized way. An image of the Beta version of the Downlink page can be seen in Fig.9.

F. Solar Panels page

The Solar Panels page is the page dedicated to the data collected from the solar panels. Here, the data fetched from the project database is displayed in two different graphs, one of the graphs focuses on the current of all 6 solar panels, making it possible to see the different solar emissions each panel receives at a given time. The other graph is dedicated to each solar panel section's voltage, the 6 solar panels system is divided into 3 sets of 2 solar panels, making three different voltage values for each set. An image of the Beta version of the Solar Panels page can be seen in Fig.11.

E. Battery page

The Battery page is where we can find the data related to the Energy Power System. The three most important data we collected from the EPS were the temperature around different elements in this system, the voltage, and the current. Since the FloripaSat-1 Cubesat had only two battery cells, we decided to fetch the voltage data from each cell and plot a graph to compare those two. Fetching the temperatures of the system we also created another graph to display the temperatures of the EPS's PCB and the batteries' PCB. Lastly, we created a graph for the battery current and another for the battery charge levels. We decided to structure the page in a way that when the

G. Locations page

The Locations page fetches the data responsible for the ground station location information of each downlink connection made with the CubeSat around the world. After gathering the data we process it to plot a map that allows us to see all the countries that made contact with the Cubesat while in orbit. We only obtained this much data thanks to several Ram radio operators and partner institutions around the world. An image of the Beta version of the Locations page can be seen in Fig.12.

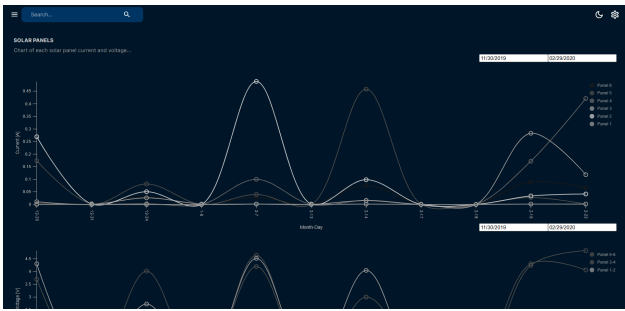


Fig. 11: Solar Panels page.



Fig. 12: Locations page.

V. DISCUSSION: TRENDS AND DIRECTIONS

After completing the Beta version of the project, we presented it for analysis to technical members of the FloripaSat-1 and FloripaSat-2 engineering and development teams. We received many positive feedbacks regarding the display of information that was previously unavailable to the group. The data presented in NanoSatTracker was considered crucial for analyzing not only past missions but also for predicting future situations regarding how the CubeSat might operate in orbit, thereby aiding the evolution of future projects. The possibility of simultaneously updating the page was also considered and will be the next step to make the web application even more useful to CubeSat teams. To achieve a platform with a fast data update rate we will need a strong collaboration of different ham radio operators, and laboratories around the world to help collect the CubeSat data and feed our database to have a more reliable and efficient data system to rely on. The ground station code segment of the NanoSatTracker is the solution to this current problem, so that's where our energy will be directed for the next phase of this project.

VI. CONCLUSION

In conclusion, the NanoSatTracker has achieved success in solving the critical gap in the accessibility and visibility of CubeSat telemetry data. Using the MERN stack, the project provides a user-friendly platform that democratizes access to real-time satellite data, enabling not only the satellite mission team but also the broader community to engage with and understand CubeSat missions more effectively. The positive feedback received from the Spacelab team (FloripaSat-1, and FloripaSat-2) underscores the value of this platform, particularly in enhancing the analysis of past missions and aiding

in the prediction of future operational scenarios. Now, the focus will shift to enhancing the platform's real-time data update capabilities, which will require close collaboration with ham radio operators and laboratories worldwide. By refining the ground station code and bolstering our data collection infrastructure, NanoSatTracker will become an even more indispensable tool for CubeSat teams, driving the evolution of future space missions.

ACKNOWLEDGEMENTS

The author wants to thank not only the Spacelab laboratory team but also Professor Eduardo Bezerra for all the encouragement given throughout the project. A huge thanks to Laura Beatris, your support and mentoring were essential for the creation of NanoSatTracker.

The authors want to acknowledge that this work was supported by CNPq/Brazil (National Council for Scientific and Technological Development - <http://www.cnpq.br>), and by AEB (Brazilian Space Agency - <http://www.aeb.gov.br>).

REFERENCES

- [1] K. Bereta, H. Caumont, U. Daniels, E. Goor, M. Koubarakis, D.-A. Pantazi, G. Stamoulis, S. Ubels, V. Venus, and F. Wahyudi, "The copernicus app lab project: Easy access to copernicus data," 2019.
- [2] R. A. Borges, A. C. dos Santos, W. R. Silva, L. Aguayo, G. A. Borges, M. M. Karam, R. B. de Sousa, B. F.-A. García, V. M. d. S. Botelho, J. M. Fernández-Carrillo, J. M. Lago Agra, F. A. Agelet, J. V. Q. S. Borges, A. C. A. de Oliveira, B. T. de Mello, Y. d. C. F. Avelino, V. F. Modesto, and E. C. Brenag, "The alfacruz cubesat mission description and early results," *Applied Sciences (Basel, Switzerland)*, vol. 12, no. 19, p. 9764, 2022.
- [3] N. Saeed, A. Elzanaty, H. Almorad, H. Dahrouj, T. Y. Al-Naffouri, and M.-S. Alouini, "Cubesat communications: Recent advances and future challenges," *IEEE Communications Surveys Tutorials*, vol. 22, no. 3, pp. 1839–1862, 2020.
- [4] J. P. Mason, T. N. Woods, P. C. Chamberlin, A. Jones, R. Kohnert, B. Schwab, R. Sewell, A. Caspi, C. S. Moore, S. Palo, S. C. Solomon, and H. Warren, "Minxss-2 cubesat mission overview: Improvements from the successful minxss-1 mission," *Advances in Space Research: The Official Journal of the Committee on Space Research (COSPAR)*, vol. 66, no. 1, pp. 3–9, 2020.
- [5] H. Ramapriyan, "The role and evolution of nasa's earth science data systems," no. GSFC-E-DAA-TN24713, 2015.
- [6] G. M. Marcelino, S. Vega-Martinez, L. O. Seman, L. Kessler Slongo, and E. A. Bezerra, "A critical embedded system challenge: The floripasat-1 mission," *IEEE Latin America Transactions*, vol. 18, no. 02, pp. 249–256, 2020.
- [7] G. M. Marcelino, A. M. P. de Mattos, J. C. E. Barcellos, B. F. Ribeiro, L. O. Seman, E. M. Filho, and E. A. Bezerra, "Floripasat-2: An open-source platform for cubesats," *IEEE Embedded Systems Letters*, vol. 16, no. 1, pp. 77–80, 2024.

A Base Model Architecture System for CubeSat Development

Thiago Duque Saber de Lima
Electrical Circuits Departament
Universidade Federal de Juiz de Fora
Juiz de Fora, Brazil
thiago.saber@estudante.ufjf.br

Juliana Silva Marquione
Universidade Federal de Juiz de Fora
Juiz de Fora, Brazil
marquione.juliana@estudante.ufjf.br

Lucas Delgado Coelho
Electrical Circuits Departament
Universidade Federal de Juiz de Fora
Juiz de Fora, Brazil
lucas.coelho@estudante.ufjf.br

Yuri Gilberto Baptista
Universidade Federal de Juiz de Fora
Juiz de Fora, Brazil
gilberto.yuri@estudante.ufjf.br

Rafael Bonioli Kneip
Universidade Federal de Juiz de Fora
Juiz de Fora, Brazil
rafael.kneip@estudante.ufjf.br

João Vítor Lira da Cunha Araujo
Universidade Federal de Juiz de Fora
Juiz de Fora, Brazil
araujojv04@yahoo.com

Estêvão Coelho Teixeira
Electrical Circuits Departament
Universidade Federal de Juiz de Fora
Juiz de Fora, Brazil
estevao.teixeira@ufjf.br

Washington Orlando Irrazabal Bohorquez
Mechanical Engeneering Departament
Universidade Federal de Juiz de Fora
Juiz de Fora, Brazil
wirraz@engenharia.ufjf.br

Abstract—The article discusses the evolution of CubeSats from educational tools to versatile platforms for real missions. It emphasizes the importance of developing a robust general embedded system model to facilitate adaptable satellite designs for various applications. Thus, this work aims to present a system architecture structure to achieve this goal through the implementation of seven main systems - the Energy Power System, On-Board Data Handling, Attitude and Orbit Control System, Telemetry, Tracking, and Command, Thermal Control System, Structural Design, and Payload System -, as a partial result of the development of the Tupã CubeSat, a 2U academic satellite designed to collect lightning data using computational vision. Furthermore, this work intends to contribute to the discussion about CubeSats as educational tools, providing resources to students implementing high-level projects ready for real-world application.

Index Terms—CubeSat, multi-mission platform, embedded systems, satellite hardware

I. INTRODUCTION

Although real world mission using CubeSats have been popularized [1] [2], the cubic satellites still play a significant role as educational tools, the goal they were initially introduced to achieve [3]. The limited size of CubeSats encourages the optimization and evolution of the equipment used, which promotes advances in various areas of the electronics, materials and energy efficiency industries [5].

Academic competitions, where students are encourage to work on solutions for certain aerospace problems, contributing to their professional formation, can act as an introduction to specific technology and first contact to the a development of solutions up to real-world problems.

For academic satellites, development is often focused directly on the overall project and not on system development, which is restricted to a single functionality. Even though a multi-mission platform have been recently presented for CubeSats that can receive a wide variety of payloads [4], this working methodology is more discussed in industry [6].

Aiming to meet all the survival requirements of a space system in a single platform, regardless of the type of orbit, pointing, power generation, thermal control, data management and telecommunication services, but also meet the competition criteria and mission requirements of CubeDesign, a student competition organized by the National Institute for Space Research (INPE) [7], Supernova, academic rocket and satellite team of Federal University of Juiz de Fora, developed Tupã, a student 2C CubeSat for lightning assessment

Considering that a CubeSat could have both educational and real-world application, and that in an academic competition team scenario a periodic renewals of members could affect project development overtime, it is useful to establish an adaptable satellite design for different missions. In this sense, the multi-mission platform was idealized.

Then, article aims to propose a methodology, based on a novel multi-mission platform, for the development of CubeSat satellites in academia, developing a robust general embedded system model. The paper is divided as follows: Section II shows how the project was organized and designed to be developed in a modular way to meet the project requirements. Section III reports the results of Tupã. Section IV presents the experience acquired with the project and the proposed improvements that have been identified for the next version.

II. ARCHITECTURE SYSTEM BASE MODEL

Due to this objective, some systems are requirable to achieve this goal, as: On-Board Data Handling (OBDH), Telemetry, Tracking, and Command (TTC), Energy Power System (EPS), Thermal Control System (TCS), Attitude and Orbit Control System (AOCS) and Structural Design (SD). Some requirements are necessary to be extremely refined due the type of the CubeSat's orbit, as an example, there is the Attitude and Orbit Control System (AOCS) system that is capable of control the attitude of the satellite.

The Fig. 1 illustrates the proposal for a satellite using a multi-mission platform, in which the combination of the subsystems Energy Power System (EPS), On-Board Data Handling (OBDH), AOCS, Telemetry, Tracking, and Command (TTC), Thermal Control System (TCS) and Structural Design (SD) represent the multi-mission platform and the Payload represents the system responsible for the satellite's functionality and purpose.

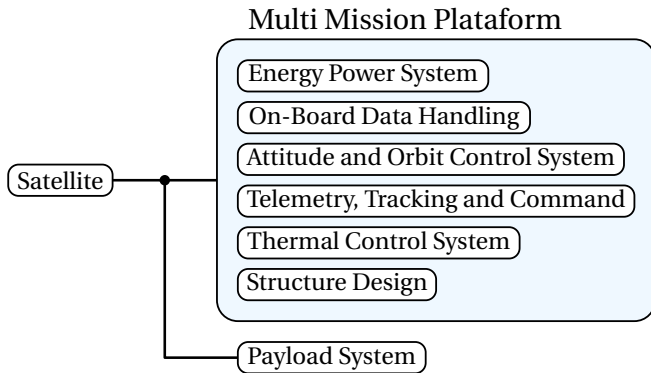


Fig. 1. Architecture of Satellite with Multi-Mission Platform.

In this scenario, the multi-mission platform there are to be presented is related to development of all the systems of Tupã, in the next subsections all of the subsystems and project requirements will be separately discussed. The payload subsection is amply discussed as a result of this work, as it is the core of the platform introduced.

A. Energy Power System

The Electrical Power System is responsible for the generation, storage, regulation and distribution of electrical power to all of the Cubesat subsystems. The EPS block diagram describes the functionalities of the EPS, exposed at Fig.2. The functions are delimited by the requirements established in Concept Operations System (CONOPS), such as the satellites dimensions, orbit and adequacy for launch vehicles. With this information it is possible to define the Mission and Design Requirements, which define the operational requirements for the system.

Energy generation is limited by the size of the satellite, as it imposes a limit on the number of photovoltaic cells the project can use. The pointing of the satellite is also an important point to consider in generation calculations, as is the orbit to define

the times of sunlight, when the satellite receives sunlight, and eclipse, when the satellite does not receive sunlight.

Storage is crucial for times when the satellite is in eclipse, as it is responsible for powering the subsystems during this period. It is usually done using batteries, which can be Li-ion, for example. The battery cells can be grouped in series or parallel, depending on the voltage and current required to power the system.

Power Regulation consists of supplying the correct voltage level to the equipments. To do this, DC-DC converters are used and buses are established to supply the voltage levels set by each subsystem. A direct-energy-transfer (DET) is used if the power provided by the solar panels does not need to be controlled. A peak-power-traker (PPT) can be used to control the power supplied by the solar panels. The system adopted in this project uses PPT. Finally, distribution takes the energy to the subsystem equipment [8].

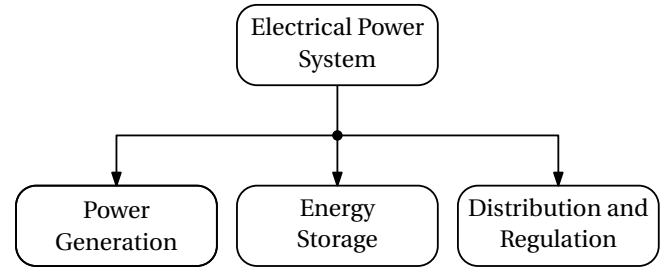


Fig. 2. Power Subsystem Architecture.

EPS requirements are defined in the base model:

- Bus supply voltage of 3.3V , 5V and 12V.
- Maximum DoD of 20%.
- Battery life of at least 5 hours, operating in communication mode.
- Removed before flight required.
- Solar panels required

"Depth-of-Discharge (DoD) is simply the percent of total battery capacity removed during a discharge period" [8]. Keeping the DoD low is essential to preserve the health of the batteries and the life of the satellite [9].

The first version of the project uses a body mounted array, cells that are affixed to the body of the satellite and not deployed panel. The panels have an effective area of $0.3 m^2$ and generate an average of 6.5W. The battery pack consists of three cells connected in series and provides an average voltage of 12V and 2450 mAh.

Distribution is achieved using PC104 connectors to supply power to the subsystems. Two regulated buses are used, with 3.3V and 5V, and an unregulated 12V bus. The system is grounded to the satellite structure at a single point [10]. The 3 shows the general diagram of the EPS, with the flow of energy and equipment at each stage.

B. On-Board Data Handling

The OBDH is the subsystem responsible for handling all the data generated and received by the satellite, and its tasks are to

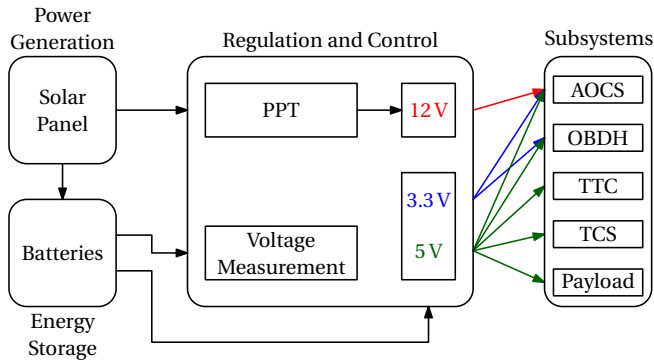


Fig. 3. EPS General Diagram.

process, encode, verify, store and make the data available for transmission to the ground station or for internal communicate with other subsystems in spacecraft. In general, the OBDH can be characterized as the brain of the multi-mission platform [8].

In this project, the OBDH was designed to be not only the brain, but also the bridge between all the systems. Through the OBDH, information from all systems is centralized and available as needed.

The Fig. 4 illustrates the connections and communications of the OBDH. The OBDH communicates with the AOCS subsystem via a Universal Asynchronous Receiver/Transmitter (UART) interface, where the pointing setpoints and the trigger to generate the antenna deploy signal, and the attitude information and data from all the sensors are received.

For the Tupā project, the OBDH receives the data from the payload and sends a trigger to start the operation via UART protocol. In addition, this subsystem communicates with the TTC via UART or SPI communication, depending on the frequency at which you want to send the data to a ground station.

C. Attitude and Orbit Control System

On larger satellites, the AOCS is the system responsible for pointing and controlling the satellite's trajectory. This requires various sensors, such as a star tracker - a sensor to determine the satellite's orientation - a sun sensor - a sensor to detect the direction of the sun - an Inertial Measurement Unit (IMU) to measure the satellite's pointing and angular velocity, among others. In addition, actuators are also needed, such as reaction wheels or control moment gyros to rotate the satellite and point it at the desired point, at many others. [11].

For the design of the multi-mission platform, due to size and power limitations in CubeSats, some components present in conventional satellites were suppressed - a common occurrence in smallsats. As such, the AOCS was designed to contain a temperature sensor (BMP-280 barometer), which will be used to take temperature measurements inside the satellite, communicating with the AOCS via a UART interface. An IMU is connected to the AOCS via an SPI interface, and its data and measurements will be used to point the satellite.

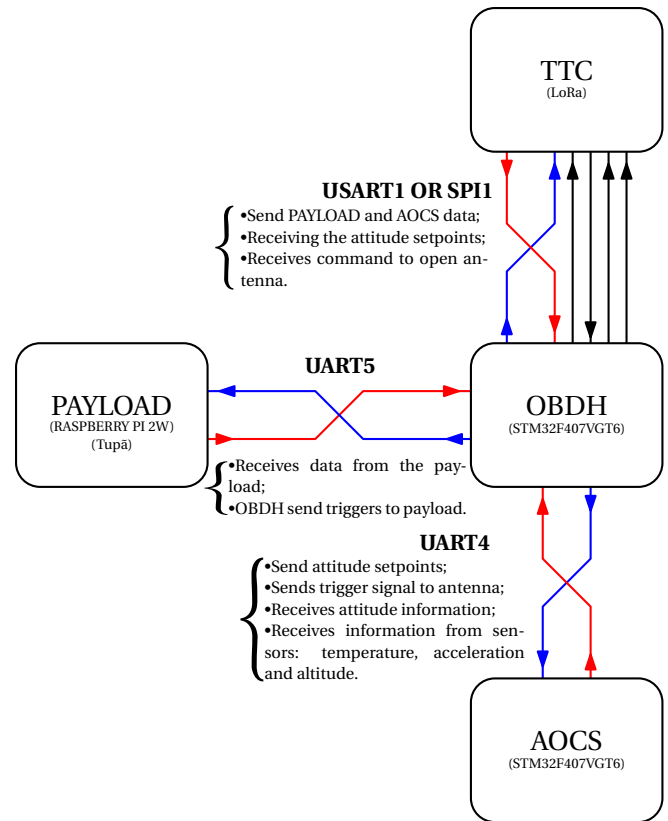


Fig. 4. On-Board Data Handling's communications and connections diagram.

A servo motor will be used to deploy the antenna, which will be interfaced with the AOCS via a Pulse Width Modulation (PWM) output. In addition, analog outputs and PWM signals will be needed to act on the power electronics responsible for driving the reaction wheels. The AOCS board is designed to be able to control up to three reaction wheels.

Furthermore, as this is an academic project with a focus on learning, the platform has an Global Positioning System (GPS), to help locate the satellite in the event of a suborbital rocket launch.

In terms of communication, the AOCS is designed to communicate with the OBDH subsystem via the UART communication protocol. In this communication channel, the AOCS sends all the attitude and location data, and receives the respective setpoints and trigger to deploy the antenna.

In Fig. 5, the connections between the AOCS and the aforementioned sensors and the other subsystem are shown, as well as the communication protocols and components used.

D. Telemetry, Tracking, and Command

The TTC subsystem is responsible for the communication interface between the satellite and the base station. Its main operations are command reception and detection, telemetry modulation and transmission, as well as subsystem operation and control. In order to project the TTC subsystem, three parts of the satellite design must be considered [8]:

- **requirements:** capacity (channels and bandwidth), coverage area, signal strength, connectivity (direct links, crosslinks etc), availability (link times per period) and mission lifetime.
- **constraints:** limits of the subsystem such as power, size and mass available budget, both dependent on mission design and the launch vehicle.
- **regulations:** international law and regulations regulate specially frequencies, power flux density on surface etc. The main regulatory agency is the International Telecommunications Union (ITU).

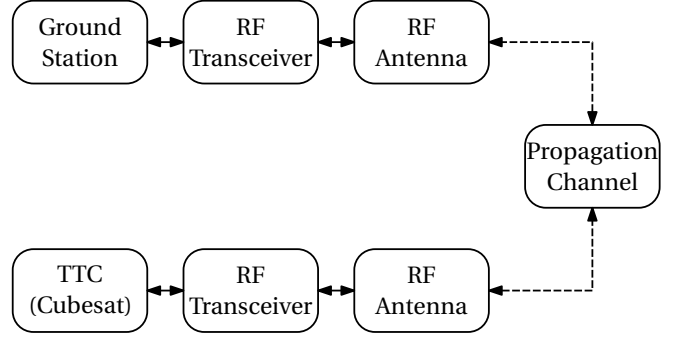


Fig. 6. Simplified diagram of the communication interface.

In terms of the ground-satellite communication, all operations go through the TTC subsystem communication interface, which can be summarized in Ground Station, Ground Transceiver, Propagation Channel, Cubesat Transceiver and Cubesat TTC subsystem.

As shown in the Fig. 6, the Ground Station should perform the needed operations over tracking, telemetry, command, control and data processing [12]. The Ground Station is connected to the transceiver, which is determined by requirements including power, frequency, bandwidth and data rate. Typically, a low noise amplifier is used between Transceiver and Antenna to amplify and also filter the signal. Amplifiers should have high efficiency as well as the antennas, which must also have high gains. Initially, the propagation channel can be modeled by the attenuation in free space. It is given

by the following equation

$$A_{FS}(dB) = 92.44 + 20 \log_{10}(f_{GHz}) + 20 \log_{10}(d_{km}), \quad (1)$$

where f_{GHz} is the frequency in gigahertz and d_{km} the distance in kilometers. The relationship (1) is plotted in Fig. 7 for the frequency of 915 MHz and a distance of up to 2000 km.

However, total losses should include losses in the atmosphere, cables, equipment, thermal noise, polarization and pointing. As for the TTC subsystem in Cubesat, it consists of a properly designed antenna, a radio frequency transceiver, capable of receiving and sending telemetry and telecommands, connected to the OBDH subsystem as shown in Fig. 4. For the Tupā project, the TTC receives data from the OBDH

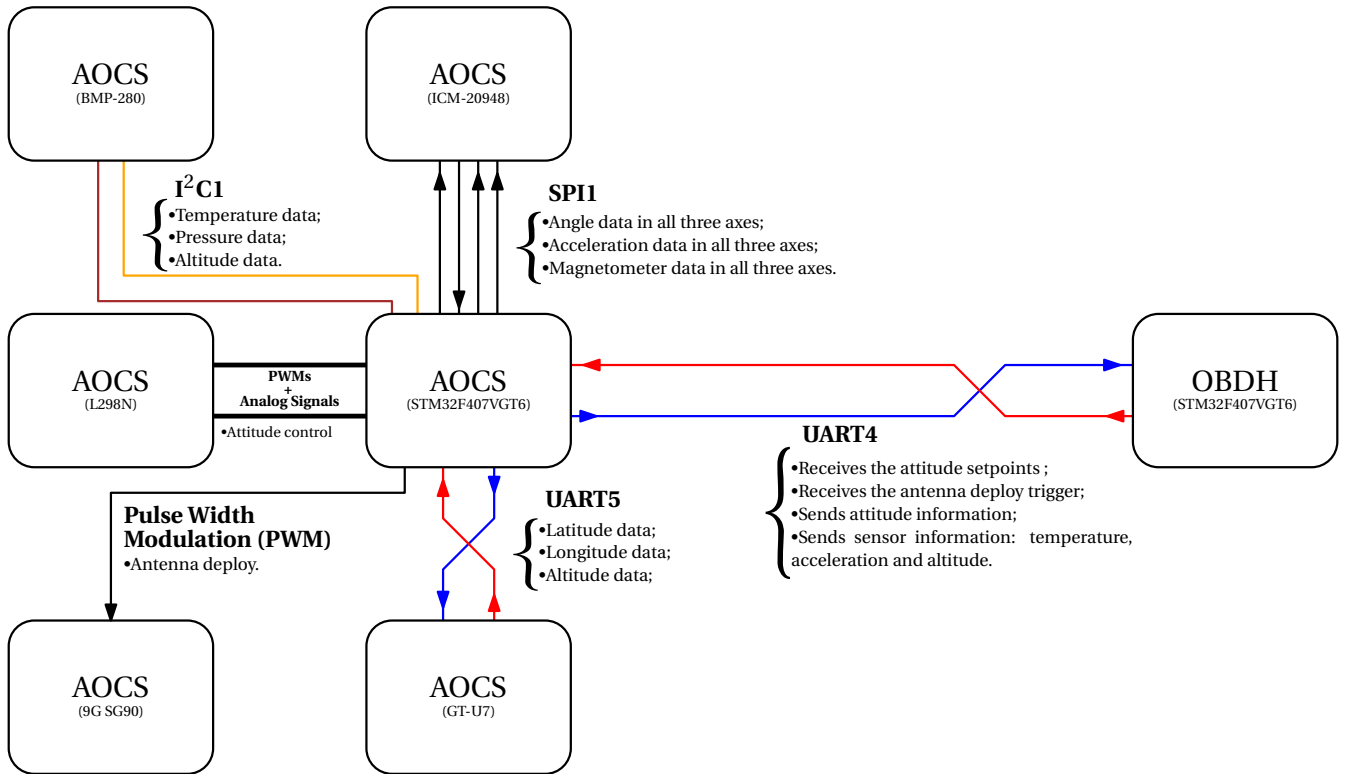


Fig. 5. Attitude and Orbit Control System's communications and connections diagram.

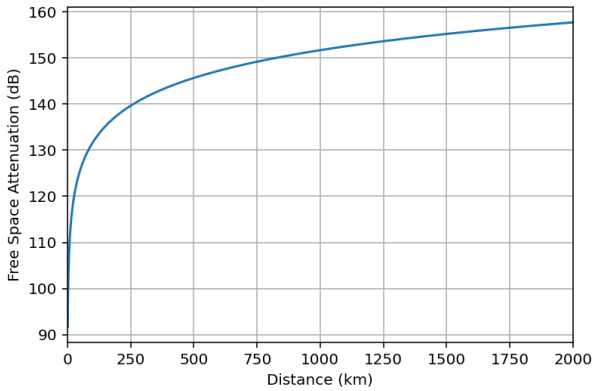


Fig. 7. Attenuation in free space with distance

Microcontroller Unit (MCU). The data packet, on the main transceiver, is transmitted by UART to the LoRa transceiver, chosen at 915 MHz, since attenuation will be lower the lower the transmission frequency. This was the lowest unlicensed frequency that meets the bandwidth and data rate requirements is desired. The power received on one side of the link can be calculated from the (2) below, derived from the Friis formula [13]

$$P_R = P_T + G_T - A_{Total} + G_R, \quad (2)$$

where P_R is the received power, P_T the transmitted power, G_T the transmission gain, G_R the reception gain and A_{Total} is the total attenuation which includes attenuation in free space given by (1), plus other attenuations mentioned above.

E. Thermal Control System

The thermal control subsystem in CubeSats ensures components remain within safe operational temperatures throughout the mission, protecting against extreme space temperature variations. Key heat sources include direct solar radiation, infrared radiation from Earth, and heat generated by onboard electronics.

Effective thermal control requires understanding the space environment, selecting appropriate materials and integrating the system efficiently into the satellite's structure. Proper satellite orientation can also reduce direct solar exposure to sensitive components. Thermal control can be passive or active, depending on the project requirements and specifics [14].

The integration of resistors in Tupā power supply must respect the voltage and current parameters to avoid overloads. In addition, to maximize the efficiency of thermal dissipation and ensure that the system operates within safe thermal limits, a mini-cooler is added. It actively removes heat from the resistors and the metal surface, improving heat transfer and contributing to the overall thermal control of the CubeSat.

This approach not only helps manage heat generated by electronic components but in the future can also be combined

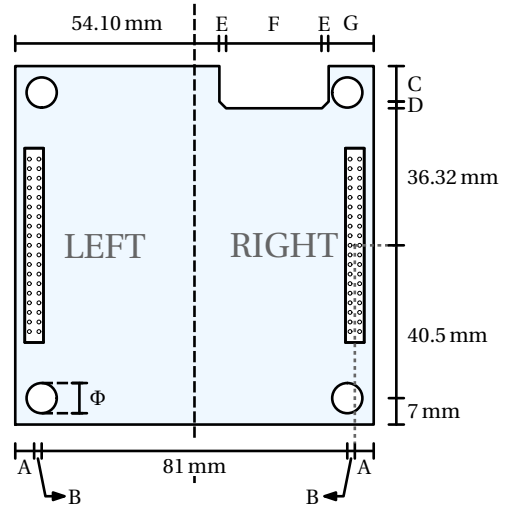


Fig. 8. Circuit board with dimensions.

TABLE I
STRUCTURE BOARD DIMENSIONS.

Label	Dimension	Label	Dimension	Label	Dimension
A	5.00 mm	D	1.78 mm	G	11.94 mm
B	2.00 mm	E	1.78 mm	Φ	5.00 mm
C	9.40 mm	F	25.40 mm		

with passive systems, like heat sinks, to create a hybrid solution. This balances thermal efficiency, energy consumption, and cost considerations.

CubeSats face unique challenges due to their size, requiring careful planning and optimization of heat distribution. In long-duration missions, material degradation and space radiation can impact thermal control, underscoring the importance of durable and reliable solutions for future projects.

F. Structural Design

As one may imply, CubeSats have a cubic format. More the one cube can be used in a CubeSat project, and, in fact, those cubes can be rearranged in order to fit better the application planned. Fixed combinations have been imposed, which leads to fixed volumes and size limits for CubeSat projects [15].

Unlike the volume, depending on the mission conducted, some structure adaptation may have to take place. As for Tupā, one of the mission requirements was the deployment of an antenna, which had to be taken into account for the design. Moreover, the choice for components of the other subsystems also consider the internal arrangement of the components, such as the boards, which dimensions are shown in Fig. 8. The sizes referenced in the figure are shown in the Table I.

G. Payload System

The Payload subsystem is defined as the equipment inserted into the spacecraft that acts directly on the mission objective. In short, the payload is the main reason why the mission was developed, and directs the entire development of the project

in terms of size, costs and risks [8]. CubeSats can be applied to accomplished a series of different missions.

The payload acts as a simple mission executor, without the need to supply information or act in such a way as to maintain the spacecraft's survival. Furthermore, this platform also makes it easier and quicker to modify existing satellites as well as makes it maintenance and changes. The Independence of the payload system is shown on the architecture system diagram, shown in Figure 4.

Payload can be developed separately from the other systems or even completely changed, as long as the systems compatibility includes the communication protocol, discussed at Subsection II-B, but the others relations between the systems. As for the structure, for example, as previously stated CubeSats have fixed dimensions, so the payload system have to able to properly assemble in this volume, as well as be supplied with enough energy to successfully achieve the mission.

III. RESULTS

Tupã is a satellite developed by members of the Supernova competition team, from the Universidade Federal de Juiz de Fora, for the Cube Design competition, hosted by Instituto Nacional de Pesquisas Espaciais (INPE). The development of this satellite achieved interesting results that will have a strong impact on the team's future projects.

For hardware development, a methodology achieve the use of reusable schematic sheets, so that each page corresponds to a micro-functionality, such as a sensor, a signal conditioning circuit, a dc-dc converter and other similar things. These schematic sheets have inputs and outputs and follow a hierarchy of systems, to be used later on. After that, each subsystem represents a part of a printed circuit board or even a entire printed circuit board.

As for firmware development, the whole multi-mission platform was programmed in C language, the standard for developing embedded systems, it does not have native support for classes. Thus, the concept of object orientation was implemented using structs and functions to simulate behavior similar to a class. In this way, structs and functions were made separated for a micro-functionality in such a way that it can be reused in various codes and projects. An example of that is a PID controller, where we have a struct to store the parameters of controller and function to perform the mathematical calculation.

The Fig. 9 shows the hardware result obtained. From top to bottom, the first board is the payload board, which will be presented in the next subsection. The second board contains the EPS regulation and distribution part. The third contains the entire OBDH and TTC system, and the fourth contains all the AOCS components.



Fig. 9. Printed Circuit Boards to subsystems.

This methodology makes it easier to update and create new projects, as it modularizes the entire development. In addition, this modularization facilitates testing, since it makes it possible to manufacture electronic circuits for bench testing of each module, so that each part of the circuit can be tested separately.

Another benefit of using this methodology is the ease of maintaining knowledge, since modularization separates the entire project into smaller portions, making it easily understandable to personnel who were not present at the initial scope of the project, a fact that is very relevant to the competition team scenario, which suffers from the constant renewal of members.

A. Tupã - initial results

The main mission of Tupã is lightning detection through imaging, processing two distinct scenarios, and transmitting telemetry as instructed via telecommand. The first integration test of Tupã is being shown in Figure 10.



Fig. 10. Tupã first integration test.

The payload architecture described applies a Raspberry Pi Zero 2W Single-Board Computer (SBC) and a 5MP camera for lightning detection via computer vision, using a Python developed code using OpenCV. The Figure 11 shows a sequence of images that are outputs of each process carried-out by the code, responsible to provide information regarding the are affected by a lightning, such as its centroid.

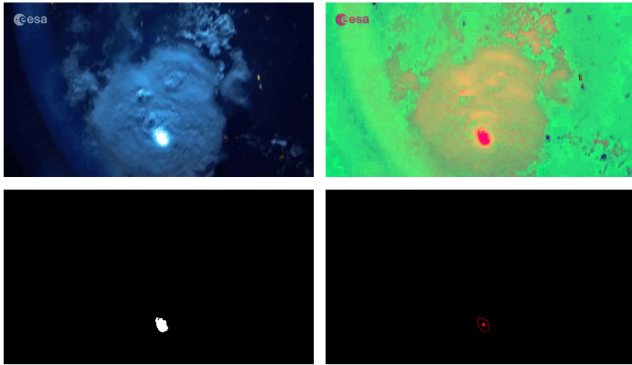


Fig. 11. Output images.

The embedded Wi-Fi and Bluetooth connectivity of the Raspberry Pi Zero 2W, although not used in this project, offers opportunities for future missions requiring satellite-to-satellite communication or more efficient data transfer to ground stations. Additionally, the use of the OpenCV library for image processing makes the solution highly scalable, enabling the implementation of more complex algorithms, such as those based on machine learning. The camera can be used for environmental monitoring, Earth imaging, or astronomical studies. The Raspberry Pi Zero 2W, in turn, can be configured to process different types of collected data, such as vegetation analysis, atmospheric pollution monitoring, or climatic phenomena. The combination of accessible, lightweight, and low-power consumption components is highly versatile and adaptable to different mission contexts.

IV. CONCLUSION

The modularity and adaptability of the multi-mission platform presented in this work, a robust hardware design foundation for future CubeSat missions that require visual data capture and processing originated from the development of Tupã, saves time and resources in developing new solutions, while also enhance the efficiency of future missions.

The integration and communication between the subsystems has already been tested and validated. The next step is to carry out environmental tests, studying electromagnetic compatibility, structural stability and simulating the space environment (Thermovacuum Test). With these advances, the team is validating a system for operation in low orbit.

Furthermore, this work intends to contribute to the discussion about CubeSats as educational tools, providing resources to students implementing high-level projects ready for real-world application. In an academic competition team scenario,

where there are periodic renewals of members, the platform can be used a way to facilitate knowledge maintenance management. The authors hope that this work can be helpful in this context, committing to improve where the CubeSats first started.

REFERENCES

- [1] Sano, K., Nakagawa, T., Matsuura, S., Takimoto, K., Takahashi, A., Fuse, T., Cordova, R., Schulz, V., Lepcha, P., Örgen, N. & Others Astronomical 6U CubeSat mission VERTECS: Scientific objective and project status. *Space Telescopes And Instrumentation 2024: Optical, Infrared, And Millimeter Wave*. **13092** pp. 214-224 (2024)
- [2] Colosimo, J., Fox, D., Falcone, A., Palmer, D., Hancock, F., Betts, M., Bevidas, W., Buffington, J., Burrows, D., Catlin, Z. & Others Expected Gamma-Ray Burst Detection Rates and Redshift Distributions for the BlackCAT CubeSat Mission. *The Astrophysical Journal*. **969**, 138 (2024)
- [3] M. Rycroft and N. Crosby. *Smaller Satellites: Bigger Business?: Concepts, Applications and Markets for Micro/Nanosatellites in a New Information World*. Springer Science & Business Media, 2013.
- [4] Degrave, J. M. L. "PLATAFORMA MULTI-MISSÃO PARA NANOSATÉLITES CUBESAT", 2021.
- [5] NASA, *State-of-the-Art of Small Spacecraft Technology*, Available at: <https://www.nasa.gov/wp-content/uploads/2024/03/soa-2023.pdf?emrc=8ad1a1>, Accessed on: September 1, 2024.
- [6] Instituto Nacional de Pesquisas Espaciais (INPE), *Plataforma Multi-Missão (PMM)*, Available at: https://www.lit.inpe.br/pt-br/pmm_plataforma_multi_missao, Accessed on: September 1, 2024.
- [7] Instituto Nacional de Pesquisas Espaciais (INPE), *CubeDesign*, Available at: <https://www.inpe.br/cubedesign/>, Accessed on: September 1, 2024.
- [8] W. J. Larson and J. R. Wertz, *Space Mission Analysis and Design*. USA: USDOE, 1992, p.
- [9] Renata N. Mota Macambira, *Otimização do consumo de energia em uma rede de satélites de baixa órbita em cenários de alta vazão.*, Dissertação, Universidade Federal do Amazonas/Programa de Pós Graduação em Engenharia Elétrica, 2021.
- [10] Mukund R. Patel, *Spacecraft Power Systems*, CRC Press, 2004.
- [11] Y. Kumar, "Satellite Attitude and Orbit Control System or AOCs in a Nutshell," *Space Navigators*, 28 May 2023. [Online]. Available: www.spacenavigators.com/post/satellite-attitude-and-orbit-control-system-or-aocs-in-a-nutshell. [Accessed: 11-Sep-2024].
- [12] P. Fortescue and G. Swinerd and J. Stark, *Spacecraft Systems Engineering*, UK: Wiley, 2011, p. 477 author=,
- [13] Christian M. Ho, Charles Wang, Kelly Gritton, and Krisjani S. Angkasa, *Microwave Propagation Attenuation due to Earth's Atmosphere and Weather at SHF Band*, 2004. Available at: <https://api.semanticscholar.org/CorpusID:128319322>.
- [14] Meseguer, J., Pérez-Grande, I. & Sanz-Andrés, A. *Spacecraft thermal control*. (Elsevier,2012)
- [15] The CubeSat Program, "CubeSat Design Specification", 2021.

Investigating the Impact of CubeSat Size on Power Generation

Gabriel Kawanaka Rubio¹,
Leonardo de Moraes Alvarenga²,
Maria Eduarda Emiliano Rezende²,
João Cláudio Elsen Barcellos²,
Laio Oriel Seman²,
Edemar Morsch Filho²

Abstract—The power generation in CubeSats is intricately linked to their size, primarily relying on photovoltaic cells mounted on external surfaces to obtain electrical energy. This configuration, while simple and devoid of deployable solar panels, limits the amount of power a CubeSat can sustainably generate, necessitating engineers to ensure it aligns with mission objectives throughout orbital operations. The required power level of a CubeSat directly impacts the size and costs of the space segment, compelling development teams to establish a realistic electrical power system (EPS) strategy early in project phases, encompassing photovoltaic panel specifications and battery capacity. To address this challenge, this research undertakes modeling and simulating power generation for standard CubeSat sizes: 1U, 2U, 3U, 6U, and 12U. Transient available power during orbits is modeled as a function of incoming solar radiation and photovoltaic panel temperature, important factors influencing efficiency. While higher solar radiation enhances power generation, elevated panel temperatures diminish solar cell efficiency. As expected, the results show that larger CubeSat sizes exhibit greater energy output. Yet, power generation is not strictly proportional to CubeSat size due to interdependencies with attitude and orbit variables. The study reveals that a marginal increase in power can result from larger CubeSats with unfavorable attitude configurations, underscoring the importance of realistic power generation scenarios that incorporate mission attitude control systems. These practical implications can guide engineers and development teams in designing and planning CubeSat missions, ensuring optimal power generation and mission success.

Keywords—power generation, photovoltaic cell, electrical power system, simulation

I. INTRODUCTION

Power generation in CubeSat missions is a critical concern, as it dictates the amount of electrical energy available to operate the subsystems. Most CubeSats use photovoltaic panels on their external surfaces to convert solar radiation into usable energy. However, the amount of available solar radiation depends on several parameters. As the CubeSat follows its orbit, part of it may occur under the Earth's shadow, preventing power generation through the photovoltaic effect. During these periods, rechargeable batteries are commonly used to operate the main systems.

Depending on the available solar radiation, voltage and temperature, the photovoltaic panels may have different levels of power generation, as seen in Fig. 1.

However, even when the CubeSat is not in the Earth's shadow, its attitude directly impacts power generation because it governs its orientation, and unfavorable attitude scenarios can jeopardize power generation. Additionally, for identical orbit and attitude scenarios, CubeSats of different sizes will experience different levels of power generation.

Therefore, it is crucial to estimate a CubeSat's power generation capacity before sending it to orbit to ensure proper operation. In this work, we present a numerical model of

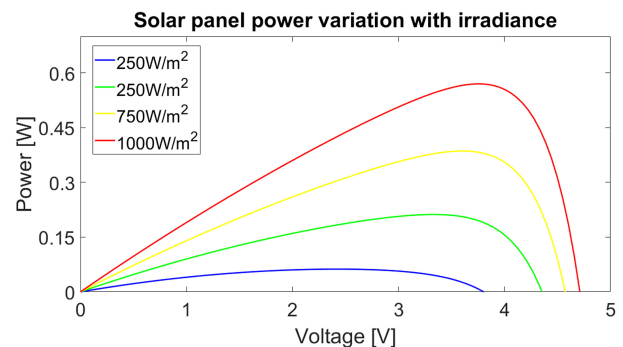


Fig. 1: Power for different radiation fluxes and temperatures, as a function of voltage [1].

photovoltaic cells to estimate power generation in orbit for typical CubeSat mission scenarios, considering 1U, 2U, 3U, 6U, and 12U sizes.

II. BIBLIOGRAPHY REVIEW

The photovoltaic panel, also commonly called a solar panel, is the most widely used device for supplying electrical energy to artificial satellites orbiting the Earth. This technology is capable of absorbing the energy emitted by the Sun in the form of radiation and converting it into electrical energy through the photovoltaic phenomenon [2]. Some results indicate an average power generation of 1.9 W for a CubeSat 1U, and 4.5 W for 3U [3].

Gabriel Kawanaka Rubio, UNESP, Brazil (gabriel.k.rubio@unesp.br).
Leonardo M. Alvarenga, UNESP, Brazil, (leonardo.alvarenga@unesp.br).
Maria E. Emiliano Rezende, UFSC, Brazil (dudarezende14@gmail.com).
João C. E. Barcellos, UFSC, Brazil, (joaoclaudiobarcellos@gmail.com).
Laio Oriel Seman, UFSC, Brazil, (laooseman@gmail.com).
Edemar Morsch Filho, UFSC, Brazil, (edemar.filho@unesp.br).

In addition to the materials used in the construction of a solar panel, the generation of energy through the photovoltaic effect also depends on the magnitude of the irradiance and temperature of the cells. Basically, a low level of irradiance results in low energy generation, while a high temperature also reduces the capacity to produce energy. Therefore, extracting maximum efficiency from photovoltaic modules is a complex task, which depends on an adequate combination of several parameters.

In this sense, if the satellite is in a region without sunlight, that is, in an eclipse position where the Earth is between the Sun and the satellite, blocking solar radiation, the batteries are the only sources of energy to power the satellite's subsystems, and must provide energy until they are recharged again. Therefore, the orbit in which a satellite is located also affects its ability to generate energy [4].

Another issue that also makes it difficult to obtain electrical energy through the photovoltaic effect is the satellite's attitude, which refers to its pointing and rotation. Even if the satellite is not under the Earth's eclipse, certain external surfaces may not be exposed to the Sun, or may even be shaded by other parts of the satellite itself. In these cases, the ability to generate energy through the photovoltaic effect is limited by the panels projected in the direction of the Sun, and is impaired when the sun's rays do not reach the surface at a normal angle.

An adequate estimate of the energy generation in orbit and the temperatures to which the CubeSat is exposed are essential for the dimensioning of the CubeSat. One approach in this sense is known as "Hardware-In-the-Loop" (HIL), such as the "Sun simulator" seen in [5], [6], where the authors connected LED lamps to the LabView software to emulate the orbital conditions and evaluated the operation of the solar panels and batteries, both focusing on the CubeSat FloripaSat-I. Another example of HIL was implemented in the development of the CubeSat MOVE-II to simulate the electrical behavior of the photovoltaic panel in the space environment [7], as well as in the CubeSat e-st@r-I [8].

Although all these examples fall into the category of an experimental approach, the controlled variables of the tests are previously obtained through analytical models and simulations, and this work also contributes to this direction.

III. METHODOLOGY

To estimate the power generation of a CubeSat in orbit, it is essential to have a model for solar radiation, which depends on the orbit and attitude of the CubeSat. This parameter serves as an input for the photovoltaic cells. The following sections describe each of these models in detail.

A. Solar radiation

One hypothesis adopted for this work was to consider that the solar rays that reach the CubeSat surfaces are parallel due to the great distance between the Sun and the Earth. Therefore, the radiation flux coming from the Sun is governed by Eq. 1:

$$Q_{Sol} = Q_s A_{sat} F_{sun} \zeta \quad (1)$$

where Q_s is the solar radiation flux of 1365 W/m² [9], A_{sat} is the area in each side of the CubeSat [m²], F_{sun} is the projection of each side towards the Sun [-] and ζ [-] is the term used to indicate whether the satellite is inside or outside the shadowed region (eclipse) of the Earth. The estimation of ζ [-] is based on orbital mechanics, while F_{sun} is a function of the attitude model [4].

To compute the Earth's shadow, the first step is to determine the sun's vector (\mathbf{r}_{sun}) [4]. After that, Eq. (2) is applied to check if the CubeSat is in the Earth's shadow.

$$\chi_c = \cos^{-1} \left(\frac{R_E}{|\mathbf{r}|} \right) \quad (2a)$$

$$\chi_{sun} = \cos^{-1} \left(\frac{R_E}{|\mathbf{r}_{sun}|} \right) \quad (2b)$$

$$\chi = \cos^{-1} \left(\frac{\mathbf{r} \cdot \mathbf{r}_{sun}}{|\mathbf{r}| |\mathbf{r}_{sun}|} \right) \quad (2c)$$

$$\zeta = \begin{cases} 0, & \chi_c + \chi_{sun} \leq \chi \\ 1, & \text{otherwise} \end{cases} \quad (2d)$$

In these equations, R_E is the Earth's radius. More details can be found in [4].

B. Orbit

An orbit model is necessary to find the position of the CubeSat in orbit. The classical problem to describe an orbit is solved through the implementation of a perifocal frame of reference [10], given in Eq. for the position of CubeSat.

$$\mathbf{r}_{\bar{x}} = \frac{h^2}{\mu} \frac{1}{1 + e \cos(\theta)} \begin{bmatrix} \cos(\theta) \\ \sin(\theta) \\ 0 \end{bmatrix} \quad (3)$$

The transformation to the geocentric equatorial frame is made by the classical Euler sequence shown in Eq. (4).

$$\mathbf{r} = \{[R_3(\omega)][R_1(i)][R_3(\Omega)]\}_{X_{\bar{x}}}^T \mathbf{r}_{\bar{x}} \quad (4)$$

The parameters Ω , ω and i are angles known as the Euler angles, and they are the right ascension of the ascending node, the argument of perigee, and orbit inclination, respectively.

C. Attitude

An attitude model is necessary to simulate the rotation of the satellite around its axis. To define the attitude, the reader must specify the rotation matrices, which are functions of an angle and axis of rotation, and combine them for various scenarios [4]. In this study, the CubeSat maintains a constant attitude relative to the Earth's center, rotating only in synchronization with its angular velocity around the Earth. More details can be found in [4].

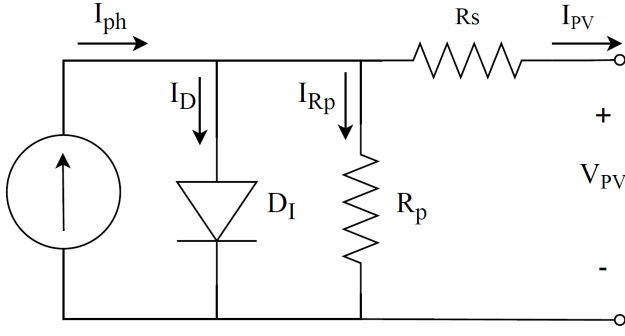


Fig. 2: Equivalent photovoltaic cell's circuit [11].

D. Photovoltaic cell

To estimate the power generated by the photovoltaic panels throughout the orbit, Fig. 2 illustrates the electrical model for a panel. This model shows a PN junction diode in parallel with a current source I_{ph} and a bypass resistor R_p , and in series with a resistor R_s , due to the metal contacts with the semiconductor [11].

Performing the sum of the currents I_{ph} (generated by the photovoltaic effect), I_{DI} (diode inverse saturation current), I_{R_p} (resistor current) and I_{PV} (solar cell current), the following Eq. 5 is obtained:

$$I_{PV} = I_{ph} - I_{DI} - I_{R_p} \quad (5)$$

This equation provides the current generated in a solar cell for each instant. Eq. 6 provides the current generated by the photovoltaic effect, being calculated as a function of the short circuit current, I_{SC} , for a given solar radiation Q''_{Sun} and solar cell temperature T .

$$I_{ph} = I_{SC} \frac{Q''_{Sol}}{Q''_0} [1 + \Delta I_{SC}(T - T_0)] \quad (6)$$

where Q''_0 and T_0 are the solar radiation and the reference temperature for which I_{SC} was obtained and ΔI_{SC} [A/K] is the coefficient of variation I_{SC} with the temperature.

Equation 7 gives the diode current:

$$I_{DI} = I_S \exp \left[\frac{-q(V_{PV} + I_{PV}R_s)}{\eta k T} - 1 \right] \quad (7)$$

where I_S is the saturation current, q is the electron charge, V_{PV} is the photovoltaic panel voltage, η is the ideality factor of the diode and k the Boltzmann constant. The equation to calculate the saturation current of the diodes is used, according to Eq. 8:

$$I_S = \left(\frac{I_{SC}(T_0)}{\exp \frac{qV_{OC}(T_0)}{\eta k T_0} - 1} \right) \left(\frac{T}{T_0} \right)^{\frac{3}{\eta}} \exp \frac{qV_q}{\eta k \left(\frac{1}{T} - \frac{1}{T_0} \right)} \quad (8)$$

where V_q is the crystalline silicon voltage and V_{OC} is the open circuit voltage.

Substituting these terms into Eq. 5, the following expression for the current I_{PV} of the photovoltaic panel is obtained:

$$I_{PV} = I_{SC} \frac{Q''_{Sol}}{Q''_0} [1 + \Delta I_{SC}(T - T_0)] - I_S \exp \left[\frac{-q(V_{PV} + I_{PV}R_s)}{\eta k T} - 1 \right] - \frac{V_{PV} + I_{PV}R_s}{R_p} \quad (9)$$

This equation is solved by the Newton-Raphson iterative method for each instant of time, with the main input data being the solar radiation flux Q''_{Sol} and cell temperature T , and photovoltaic panel voltage (V_{PV}). Multiplying the photovoltaic panel current I_{PV} by the voltage it is coupled gives the power P generated at each instant. A fixed point voltage (2.3 V) is used in this work for current and power estimations.

The other parameters of the energy generation model by the photovoltaic panel are constant and are listed in Tab. I.

TABLE I: Parameters of the photovoltaic panel model [11].

Parameter	Value
η	3,25
k	$1,3806 \times 10^{-23} \text{ m}^2\text{kg/s}^2\text{K}$
V_q	1,12 eV
q	$1,602 \times 10^{-19} \text{ C}$
I_{SC}	0,41 A
V_{OC}	2,564 V
R_s	0,2242 Ω
ΔI_{SC}	0,07
R_p	$1 \times 10^8 \Omega$
R_s	0,2242 Ω
Q_0	1000 W/m ²
T_0	298 K

E. Case studies

The scenarios to be tested include the sizes 1U, 2U, 3U, 6U, and 12U. These sizes are introduced into the formulation through the A_{sat} (ignoring the projection towards the Sun) parameter seen in Eq. 1, which defines the area (m²) of each side of the CubeSat according to the sequence [+X -X +Y -Y +Z -Z]. In this work, the following scenarios of sizes will be assessed:

- 1U: $A_{sat}=[0.1 \ 0.1 \ 0.1 \ 0.1 \ 0.1 \ 0.1]$;
- 2U: $A_{sat}=[0.2 \ 0.2 \ 0.2 \ 0.2 \ 0.1 \ 0.1]$;
- 3U: $A_{sat}=[0.3 \ 0.3 \ 0.3 \ 0.3 \ 0.1 \ 0.1]$;
- 6Ua: $A_{sat}=[0.3 \ 0.3 \ 0.6 \ 0.6 \ 0.2 \ 0.2]$;
- 6Ub: $A_{sat}=[0.6 \ 0.6 \ 0.3 \ 0.3 \ 0.2 \ 0.2]$;
- 12U: $A_{sat}=[0.6 \ 0.6 \ 0.6 \ 0.6 \ 0.4 \ 0.4]$;

The only difference between configuration 6Ua and 6Ub is the orientation of the CubeSat, which will be used to demonstrate the impact of attitude on the results.

For all of these scenarios, the same orbit and attitude will be applied. The orbit is circular, has 500 km of altitude, an inclination of 97.8°C, and its β angle (angle between the orbit and the Sun [9]) is 0°, resulting in an orbit with maximum eclipse for that altitude.

IV. RESULTS

The values for current obtained on each side of the CubeSat, as well as the total current, for each instant of the orbit, are shown in the following figures. In all of the scenarios, there

is a gap in the middle caused by the passage of the CubeSat under the Earth's shadow.

The solar radiation available over the CubeSat's surfaces are displayed in Fig. 3. This scenario is valid for all the study cases.

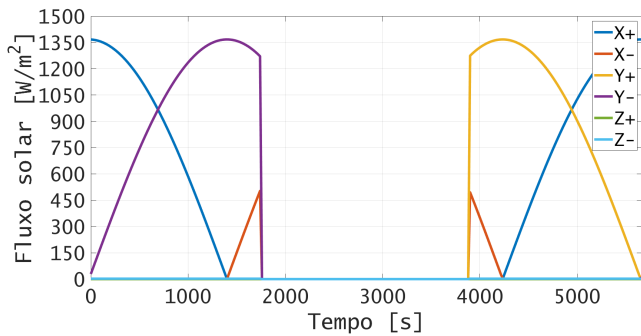


Fig. 3: Solar radiation.

Figure 4 shows the scenario where the minimum current is generated, as expected, due to the small size of the CubeSat 1U. Opposite to it, the size 12U (Fig. 9) presents the highest current generation. All intermediate CubeSats (Figs. 5 to 8) have currents within these limits, with linear variations on each side, according to their sizes. The results show that changing the size from 1U to 12U does not increase the current peak by a factor of 12, because the geometry does not allow the current generation on all the photovoltaic panels simultaneously.

The attitude used in these simulations results in a scenario where the sides +Z and -Z do not generate any current because they are precisely oriented in a condition where the solar rays do not reach these surfaces (the solar rays are perpendicular to the surface's normal plane). Therefore, in this specific condition, the photovoltaic panels on +Z and -Z would not be useful for the mission.

The comparison between the configuration 6Ua and 6Ub (Figs. 7 and 8) shows that the orientation of the CubeSat must be accounted for when determining the power budget of the CubeSat. The only difference for these cases is the orientation, which promotes the exposition of the greatest surface for more time towards the sun in configuration 6Ua than 6Ub.

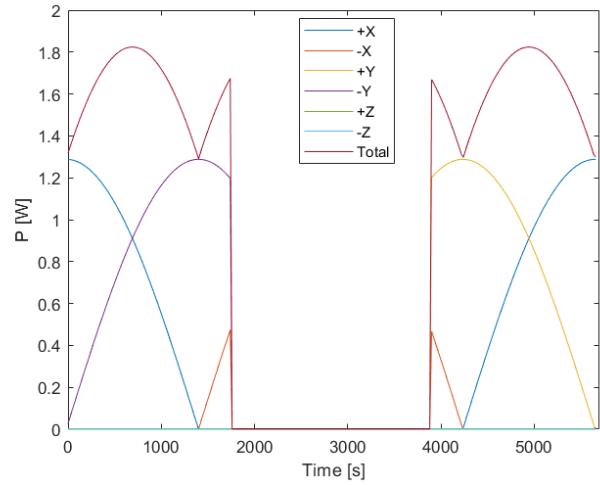


Fig. 4: CubeSat 1U.

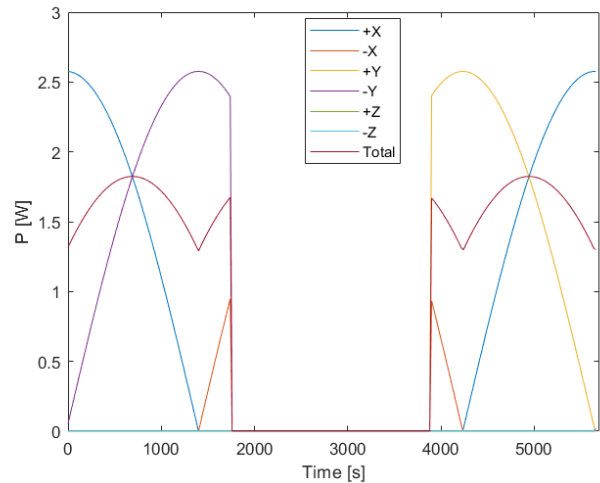


Fig. 5: CubeSat 2U.

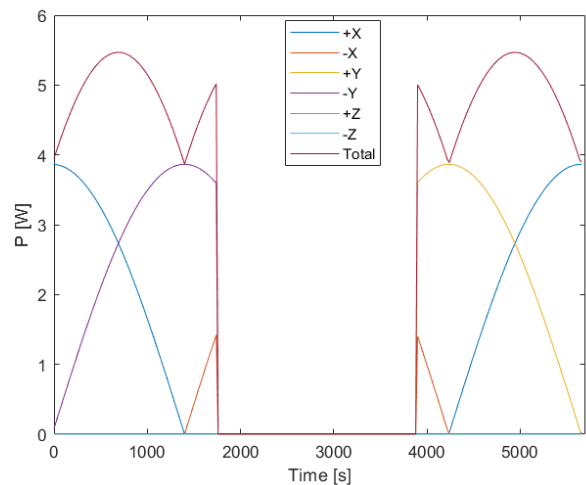


Fig. 6: CubeSat 3U.

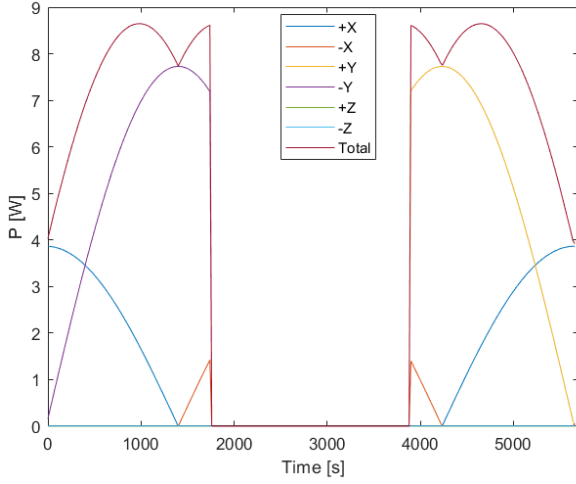


Fig. 7: CubeSat 6Ua.

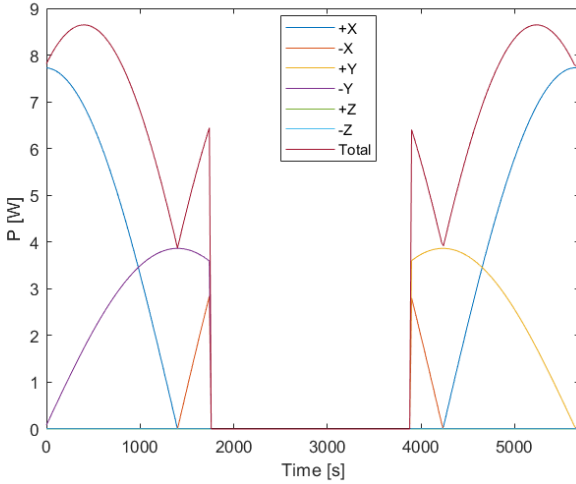


Fig. 8: CubeSat 6Ub.

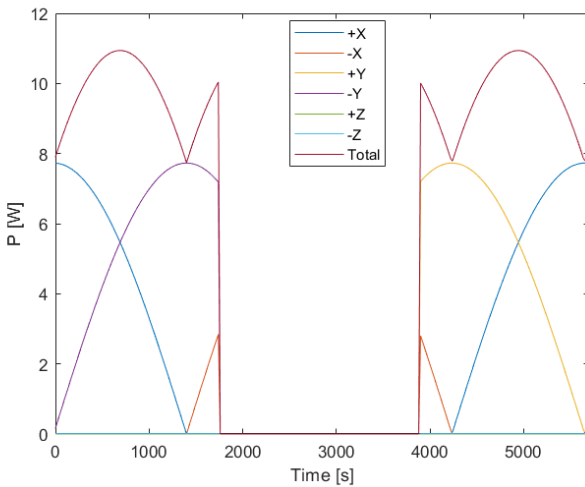


Fig. 9: CubeSat 12U.

The total power generation of previous cases was estimated, considering the transient current discussed previously and a constant solar panel voltage of 2 V. The result of this analysis is summarized in Tab. II, where the total power is calculated, as well as the magnitude of each size proportional to the standard size 1U.

As expected, the smallest size will generate less power, while the greatest size 12U will have more power. For cases 2U and 3U, the size increment resulted in a power increase at the same rate. However, it is interesting to notice a non-linear power increase for sizes beyond 6U. The models 6U (version a and b) do not produce six more power than 1U, and neither does size 12U produces 12 more than 1U. This is a consequence of a CubeSat geometry with solar panels mounted over all its surfaces, where photovoltaic panels located on opposite sides can not produce simultaneously. Using case 12U as an example, for the scenario tested, a similar total power could be achieved with a smaller Cubesat by employing deployable solar panels integrated with an attitude control dedicated to pointing them toward the sun. The impact of the attitude in power generation is more evident between cases 6Ua and 6Ub, where both have the same size but configuration 6Ua is able to produce 8.4% more as a consequence of its attitude.

TABLE II: Total power for each study case.

	1U	2U	3U	6Ua	6Ub	12U
Power [W]	1.61	3.22	4.84	7.55	6.96	9.68
Increase (U#/U1)	1.00	2.00	3.00	4.68	4.31	6.00

V. CONCLUSION

This study focused on how the CubeSat size impacts its power generation. As expected, larger CubeSats typically generate more power due to increased surface area, but factors like attitude and orbit must be considered to provide a wider overview of this relationship. Simulations show that power output varies with CubeSat orientation, highlighting the need for effective attitude control, and increasing CubeSat size alone does not proportionally increase the power generation due to the CubeSat's geometry.

ACKNOWLEDGEMENTS

The authors are grateful for the financial support from Fundação de Amparo à Pesquisa do Estado de São Paulo (grant number 2023/08742-8) and from the Pró-Reitoria de Pesquisa - Coordenação de Iniciação Científica e Tecnológica da Unesp (grant number PROPe 9/2023 - 10261).

REFERENCES

- [1] L. Kessler Slongo, S. Vega Martínez, B. Vale Barbosa Eiterer, and E. Augusto Bezerra, "Nanosatellite electrical power system architectures: Models, simulations, and tests," *International Journal of Circuit Theory and Applications*, vol. 48, no. 12, pp. 2153–2189, 2020.
- [2] H. Dehbonei, S. R. Lee, and H. Nehrir, "Direct energy transfer for high efficiency photovoltaic energy systems part i: Concepts and hypothesis," *IEEE Transactions on Aerospace and Electronic Systems*, vol. 45, no. 1, pp. 31–45, 2009.

- [3] C. Clark, "Huge power demand...itsy-bitsy satellite: Solving the cubesat power paradox." 24th Annual AIAA/USU Conference on Small Satellites.
- [4] E. M. Filho, L. O. Seman, C. A. Rigo, V. d. P. Nicolau, R. G. Ovejero, and V. R. Q. Leithardt, "Irradiation flux modelling for thermal-electrical simulation of cubesats: Orbit, attitude and radiation integration," *Energies*, vol. 13, no. 24, 2020.
- [5] G. M. Marcelino, S. Vega-Martinez, L. O. Seman, L. Kessler Slongo, and E. A. Bezerra, "A critical embedded system challenge: The floripasat-1 mission," *IEEE Latin America Transactions*, vol. 18, no. 02, pp. 249–256, 2020.
- [6] L. Slongo, S. Martínez, B. Eiterer, T. Pereira, E. Bezerra, and K. Paiva, "Energy-driven scheduling algorithm for nanosatellite energy harvesting maximization," *Acta Astronautica*, vol. 147, pp. 141–151, 2018.
- [7] J. Kiesbye, D. Messmann, M. Preisinger, G. Reina, D. Nagy, F. Schummer, M. Mostad, T. Kale, and M. Langer, "Hardware-in-the-loop and software-in-the-loop testing of the move-ii cubesat," *Aerospace*, vol. 6, no. 12, 2019.
- [8] S. Corpino and F. Stesina, "Verification of a cubesat via hardware-in-the-loop simulation," *IEEE Transactions on Aerospace and Electronic Systems*, vol. 50, no. 4, pp. 2807–2818, 2014.
- [9] D. G. Gilmore, *Spacecraft Thermal Control Handbook, 2nd Edition*. 1801 Alexander Bell Drive, Reston, Virginia 20191-4344: American Institute of Aeronautics & Astronautics (AIAA), 2002.
- [10] H. D. Curtis, *Orbital Mechanics for Engineering Students*. Boston: Butterworth-Heinemann, third ed., 2014.
- [11] S. V. Martinez, E. M. Filho, L. O. Seman, E. A. Bezerra, V. de Paulo Nicolau, R. G. Ovejero, and V. R. Q. Leithardt, "An integrated thermal-electrical model for simulations of battery behavior in cubesats.," *Applied Sciences*, p. 11, 2021.

EPS Control for a CubeSat

Vinícius A. Souza

Aerospace Engineering
Universidade Federal de Minas Gerais
Belo Horizonte, Brazil
e-mail: viny272@gmail.com

Maria C. Pereira

Department of Mechanics Engineering
Universidade Federal de Minas Gerais
Belo Horizonte, Brazil
e-mail: cecilia@demec.ufmg.br

Patrícia N. Pena

Department of Electronics Engineering
Universidade Federal de Minas Gerais
Belo Horizonte, Brazil
e-mail: ppena@ufmg.br

Abstract—This research work focuses on modeling and simulating energy cycling tests to characterize the Li-S battery of the academic CubeSat “PdQSat” payload and establishing an interface between the battery and the satellite’s EPS for emergency energy supply. Utilizing Supervisory Control Theory (SCT) of Discrete Event Systems (DES), the study aims to guarantee a well coordinated transition between the satellite’s operational modes during the mission. The integration of models developed in previous works, along with the synthesis of SCT plants and supervisors, form the core of the methodology. The simulation of these components allows for the analysis of their closed-loop behavior in various situations, such as in extreme conditions. The study also delves into fundamental theories such as Supervisory Control Theory, Orbital Mechanics, Battery Management Systems, and Reliability to provide a comprehensive understanding of the subject matter. Through collaborative efforts with advisors, colleagues, and contributors, this work contributes to the advancement of control systems in aerospace engineering.

Index Terms—CubeSat, Discrete Event Systems, Supervisory Control Theory, Electrical Power Subsystem, Simulation, Energy Cycling, Payload

I. INTRODUCTION

CubeSat, a small satellite standard established in 1999 [1], has evolved from a tool for academic study to a competitive technology in the space market, mainly due to its advantages in development time, cost and reliability [2]. PdQSat is a CubeSat under development at the Universidade Federal de Minas Gerais (UFMG), with the mission of technological demonstration and validation, in a space environment, of a commercial battery with Lithium-Sulfur (Li-S) cells, and a supercapacitor also developed at UFMG. All aspects of the satellite’s mission, such as its architecture, requirements, risk analysis, and other concepts, are defined based on academic work by a group of university’s undergraduate students.

This work aims to continue developing control tools to increase the mission’s reliability, through the supervision of PdQSat’s Electrical Power Subsystem (EPS), based on the results obtained in previous undergraduate students works [3]. The control focus, in this case, is on the characterization of the Li-S battery, which is going to have its operation variables (such as current, voltage, etc) measured during a number of charge and discharge cycles throughout the mission, and which will be able to donate the charge that is no longer going to be used in the cycling tests to the satellite’s bus battery (the EPS battery responsible for charging all the satellite’s systems).

This interaction between the batteries can be better seen on Fig. 1.

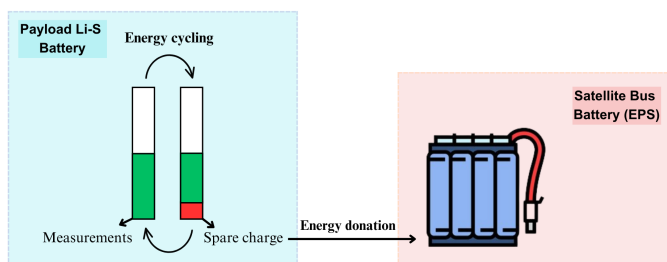


Fig. 1. Batteries interaction.

Therefore, the objective of this work is to model and simulate energy cycling tests to characterize the PdQSat payload’s Li-S battery, as well as an interface between the battery and the satellite’s EPS for emergency energy supply, through Supervisory Control Theory (SCT) of Discrete Event Systems (DES), ensuring the success of transitions between operational modes during the mission.

II. THEORETICAL FRAMEWORK

This section covers the fundamental theories of Supervisory Control Theory (SCT), Orbital Mechanics, Battery Management Systems (BMS), and Reliability, necessary to understand this work.

A. Supervisory Control Theory

A system can be defined as an environment, physical or theoretical, in which different elements interact with each other. If these elements, in turn, have well-defined states that change through the occurrence of discrete events (independent of time), then we have a Discrete Event System [4]. For example, if a television starts off, and is turned on by a button, the Television environment is a system in which there are the states “television off” and “television on”, which change through the discrete events “turn on button pressed” and “turn off button pressed”.

Supervisory Control Theory (SCT) relies on languages and automata. A finite and non-empty set of events is denoted by Σ , where a sequence of events forms a string (with ϵ

representing the string of length zero) [5]. A collection of strings is referred to as a language.

An automaton is defined by the quintuple $G = (Q, \Sigma, \delta, q_0, F)$, where Q represents the set of states, Σ is the set of events, δ is the transition function, q_0 is the initial state, and F is the set of final states [5]. For the preparation of this work, the diagrams for the *automata* are generated using UltraDES Python [6].

An automaton models a system's behavior through two languages: generated (all possible event sequences) and marked (sequences completing specific tasks).

Parallel composition is an operation that synchronizes two *automata* by simultaneously executing events that occur in both *automata*. Events that are local to each automaton are allowed if they are permitted in the original automaton.

SCT is a formal method for designing non-blocking supervisors that constrain the system's behavior to adhere to specified restrictions (such as safety, fairness, security, etc.). SCT is implemented by disabling controllable events (events that can be chosen to happen by a supervisor) ($\Sigma_c \subseteq \Sigma$). The existence of a supervisor that restricts the plant to a desired language K depends on whether K is controllable, which means that only controllable events can be disabled [7]. The supervisor enforces the minimally restrictive behavior.

To avoid creating large supervisors, an extension of SCT known as Local Modular Supervisory Control is used. The synthesis process is similar, but each supervisor has a partial view of the plant. To ensure the same behavior as classical SCT, a verification of non-conflict must be performed.

B. Orbital Mechanics

Considering that the electrical power is generated through solar panels, that depends on the orbit, in order to simulate the work and performance of PdQSat one has to understand its motion while in orbit.

In this context, Kepler's Laws describes the satellite's orbit trajectory around the Earth, its area sweeping properties and orbital period (T) duration. From all these laws, one can derive Kepler's Equation [8]:

$$M_e = u - e \sin u, \quad (1)$$

in which M_e stands for mean anomaly, the angle corresponding to the time elapsed since the satellite passed through the perigee, if the satellite were in a circular orbit with constant velocity, and u is the eccentric anomaly, related to true anomaly (angle between periapsis direction and position vector of the satellite) and eccentricity (e) of the orbit.

Since (1) cannot be analytically solved, a numeric procedure must be used to obtain the satellite's orbital position at all times.

C. Battery Management Systems

The basic task of a Battery Management System is to ensure the optimal use of energy within a battery and minimize the risk of failure by monitoring and controlling its charging and discharging processes [9]. This can be ensured through

some control actions already addressed in the context of other PdQSat works [10].

Furthermore, in relation to the control of charge and discharge, the irregular behavior of a battery's energy levels near its upper and lower limits stands out, where the charge and discharge speed is much faster than at intermediate levels of the battery's state of charge [11]. This behavior can be seen in Fig. 2.

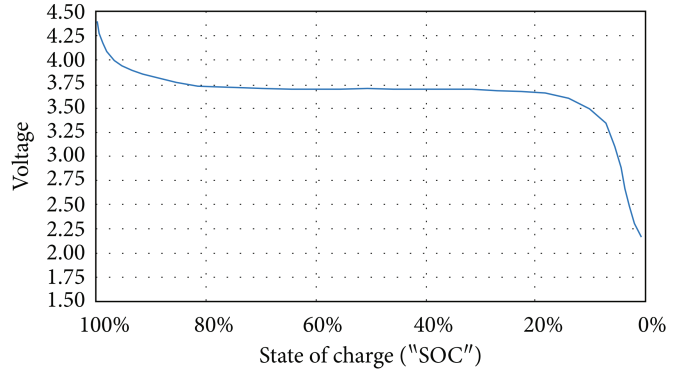


Fig. 2. Typical Li-ion discharge voltage curve [11].

D. Reliability

Reliability is the "probability that a product will function correctly, during a specific time interval, under its designated operating conditions, without failing" [12]. For small satellites, the highest failure contribution rate for systems comes from the EPS [13], with overall reliability levels decreasing with the increase in mission duration.

One way to ensure higher levels of reliability in any system is through the use of redundancies [12]. This redundancy is achieved by using additional components, above the minimum number necessary for satisfactory operation, or by ensuring alternative means of performing the same action in a system, as is done in this work by the addition of an alternate power supply in case of need.

III. PROBLEM MODELLING

This work relies on the models provided in previous work [3]. There, the first modeling and simulation of the PdQSat's EPS control is performed, using Supervisory Control Theory. As that work is the main basis for this one, the details of the modeling of the problem addressed and the respective simulations' results are discussed in this section. During the development of the work, the authors [3] design three supervisors, which are then simulated in orbits of interest, using the MATLAB software [14], in order to analyze the behavior of the supervisors from the reception of sunlight on the PdQSat's photovoltaic panels during the mission.

The first supervisor (S_1) has the function of identifying if any of the lateral faces of the PdQSat is receiving sunlight. If these faces are not facing the sun, the supervisor has to allow the maneuver such that the satellite reaches an illuminated state.

The second supervisor developed (S_2) has the function of switching the PdQSat's power supply between the photovoltaic panels and the satellite bus' battery, depending on whether sunlight is being received by the panel sensors or not.

Finally, the third supervisor developed, which is the focus of this work, has the function of switching the operating mode of the PdQSat according to the battery level of the satellite bus.

The first plant of this supervisor, which performs the controllable switching between operating modes, is shown in Fig. 3. Its states define the satellite's operating modes: Normal operating mode (NO) and Emergency operating mode (EM), with the controllable events that switch to normal (ζ_1) or to emergency mode (ζ_2).

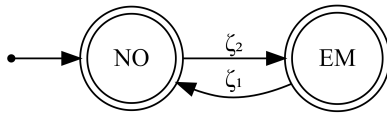


Fig. 3. Plant of the transition between operating modes, G_{OP} [3].

Since the operating modes are determined according to the satellite bus' battery level, the second plant of the supervisor monitors this battery level, using a safety limit of 25% charge, which is the minimum charge level that lithium-based batteries can generally support without considerable damage to their integrity [7]. The automaton of the plant can be seen in Fig. 4.

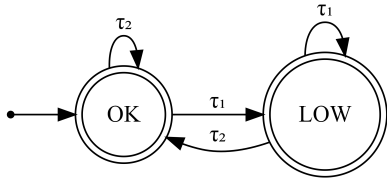


Fig. 4. Plant of the battery level monitoring system, G_{GSOC} [3].

Its states are defined according to the battery level relative to the previously determined safety limit: if the satellite bus' battery level is above the limit (OK), or below the limit (LOW), with their uncontrollable events identifying if the battery level is at, or below the safety limit (τ_1), or if it's above the limit (τ_2).

The last supervisor is then generated from the plants and specifications in a monolithic form, as it does not share any events with the plants of the other supervisors. Its automaton is shown in Fig. 5.

To conduct the simulation, the author [3] uses orbital mechanics equations, as discussed in section II-B, to define the satellite's position relative to the chosen test orbit. A time step is defined in which, at each iteration, within the time of an orbital period, the satellite's position in the orbit is calculated.

Since the simulation defines the moment when the satellite starts receiving sunlight, depending on its position relative to Earth, the supervisors S_1 and S_2 already have all the necessary

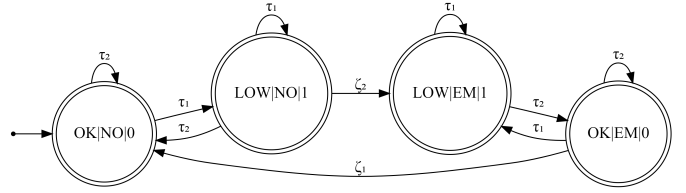


Fig. 5. Supervisor of the transitioning system between operating modes, S_3 [3].

information to identify the satellite's states at each iteration until the simulation time reaches the orbital period.

Finally, for calculating the satellite bus' battery energy levels, technical references are used to define the energy consumption values of the satellite systems and the energy gains from the solar panels. Based on this information, the satellite bus' battery charge levels are also calculated at each iteration to provide the necessary information for the S_3 supervisor's actions.

In the case of the initial state of the satellite bus' battery, it is defined as having a 30% level to incite the supervisors' actions more quickly by reaching the 25% charge safety limit faster.

Regarding the emergency mode, it is also defined that the action taken by this mode is the deactivation of some PdQSat systems, reducing the satellite bus' battery energy consumption by half while in this mode.

Although the results in [3] represent the success of the supervisors' actions implemented, the lack of an alternative for power supply during emergency mode load levels is part of the motivation for conducting this work. By implementing this new alternative to the models developed previously, a more reliable control system is generated that does not rely solely on reducing the energy consumed by the PdQSat systems, since this solution is not recommended for satellite activity, even if it is effective.

IV. METHODOLOGY

Beginning with the modeling, the necessary requirements for energy cycling in the battery and for supplying power to the satellite bus are detailed, and the different systems involved in these processes are defined. Principles of BMS and reliability are used to ensure robust models with a low chance of failure during the mission.

Next, the constraints or specifications applicable to these models are defined to simulate real mission conditions or even impose desired behaviors on the system, since supervisory control can generate various possible behaviors that must be delimited to assist in the satellite's decisions.

The respective plants and specifications are then composed through the processes of SCT detailed in section II-A, for the generation of the supervisors. All plants and supervisors are obtained using the UltraDES Python [6], which allows visualization and manipulation of the *automata*.

The models are then combined with the ones developed previously [3], with focus on the third supervisor (S_3), so

that the new behavior of the system for transitioning between operating modes is capable of implementing the new method of battery charge reception from the payload.

For the simulation, using the MATLAB software [14], tests are simulated to verify the supervisors' actions in real situations. These situations follow the same principles as those performed so far [3], with the satellite's position in the orbit of interest, and the reception of sunlight on its panels being the uncontrollable physical events that generate the main *stimuli* for the supervisors' actions.

The logic used in the complete simulation code is shown in Fig. 6.

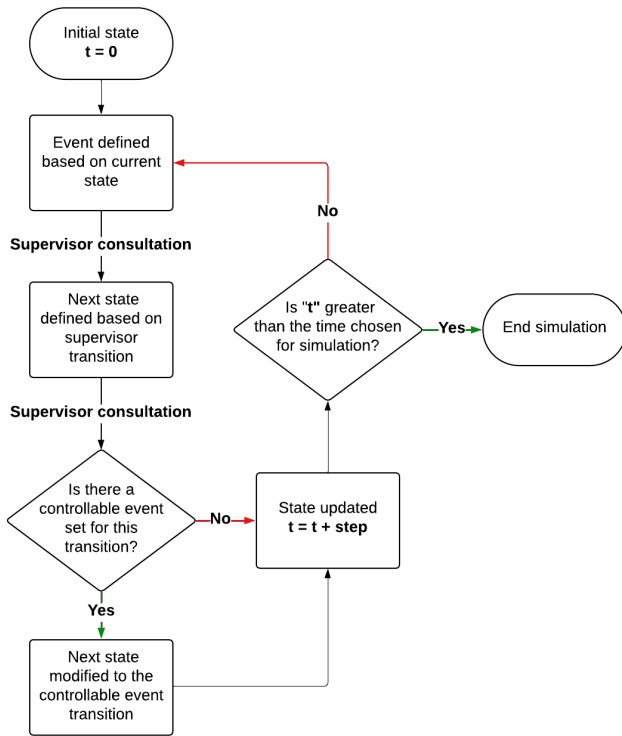


Fig. 6. Action flow of the simulation code.

V. RESULTS AND DISCUSSION

This section presents the defined models with more detailed descriptions of their functionalities and the results of the plants and supervisors simulation for various situations.

A. Li-S Battery Modeling

The Li-S battery model assumes 8 cells, arranged in two sets of 4, prioritizing high energy density and low weight. The system involves two batteries: the Main Battery (MB), which undergoes the charge cycles, and the Secondary Battery (SB), responsible for storing excess charge. The MB is monitored by a Battery Management System (BMS) and is used for testing, while the SB provides reserve energy to the satellite bus when needed. This can be seen in Fig. 7.

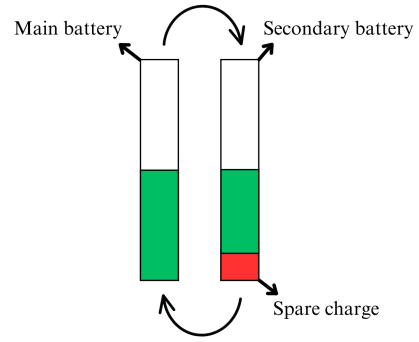


Fig. 7. Model of the Li-S batteries.

As an example, it is arbitrated that the satellite will perform 4 stages of charge cycling during the mission, each one with a specific quantity of charge and discharge cycles, and possibly an extra stage with more cycles after the mission if there is still enough charge for the tests.

In the first stage, the MB will cycle from 0% to 100% charge a defined number of times. During this cycle: the MB discharges, and its behavior is monitored by the BMS; the charge drained from the MB is stored in the SB; once discharged, the SB returns the charge to the MB, allowing observation of the MB's behavior during the charging process; the cycle repeats itself until the end of the stage.

In the second stage, the same events happen, but with a cycle from 0% to 90% charge on the MB, and the storage of 10% charge on the SB. The next stages follow this same principle, increasing the amount of energy that can be spared in the SB.

In Fig. 8, a schematic of the test functioning and a plant of the Li-S battery stages are presented, where each state represents the amount of spare charge available in the secondary battery, and the controllable events " δ_{10} " represent an additional 10% charge transfer to the reserve, indicating a new test stage. Furthermore, the last state represents the post-mission stage, in which the supervisor returns to previous stages to redo them, but that are not specified in this work. The controllable event "PM", which leads to them, has the same name as the state and only represents the transition to these new non-modeled cycles.

Along with the cycle model presented in Fig. 8, the reserve charge of the secondary battery is also modeled. Since the function of the reserve is to be used by the satellite bus' battery, it is necessary to define whether this reserve has any remaining charge or if it is empty, either because the main battery is operating in the first charge stage or if the spare charge has been fully consumed by the satellite bus at some point.

In Fig. 9, the automaton modeling the spare charge is presented. Its new states and events are: "reserve empty (EMP)", "reserve with spare charge (LEFT)", and the uncontrollable events in which the reserve empties (ϕ_1), or receives some

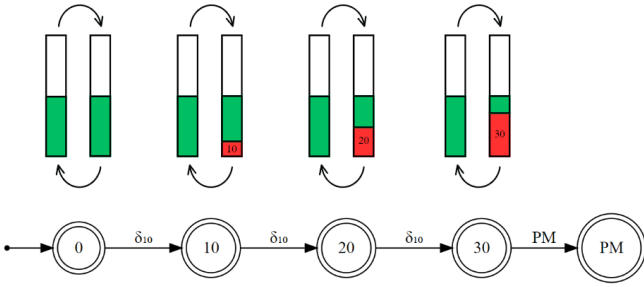


Fig. 8. Plant of the Li-S battery charge cycling stages.

charge (ϕ_2).

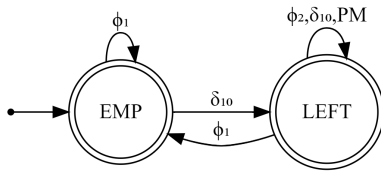


Fig. 9. Plant of the reserve.

To combine both behaviors into a single model, a parallel composition of the cycling and reserve plants presented above is performed.

The behavior determined by this new general plant indicates that, except for the initial state, which uses 100% of the battery charge, all states have transitions to a state of remaining charge (δ_{10}), even if this charge is depleted immediately (ϕ_1). At the end of the main stages, if the entire reserve charge is used, it is not possible to perform post-mission cycles since they would use the remaining charge to redo previous stages. Otherwise, the model moves to the post-mission states.

B. Satellite Operating Modes Modeling

In the previous work [3], a supervisor responsible for changing the PdQSat operating modes between “normal operation mode” and “emergency operation mode” is developed. With the new possibility of receiving charge from the Li-S batteries, there is a need to create a new operating mode.

Two plants for the operating modes are generated: one with controllable switching events between the modes (shown in Fig. 10) and one with uncontrollable events of charge level variation on the satellite bus (shown in Fig. 11).

The three states for the operating modes of Fig. 10 are determined according to the situations in which the satellite functions normally (normal mode - NO), receives charge from the Li-S battery and don't reduce energy consumption (receiving mode - REC), or shuts down part of its systems to reduce energy consumption, but also receives charge from the Li-S battery reserve, if it has charge to donate (emergency mode - EM).

As an initial hypothesis, each operating mode should be executed according to specific charge levels of the satellite

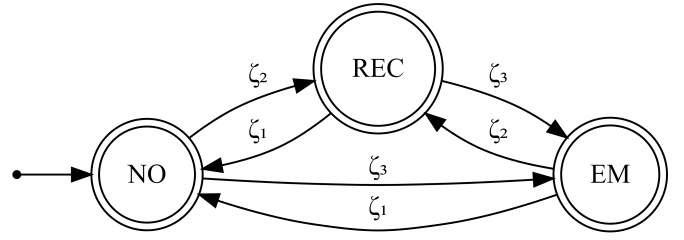


Fig. 10. New plant G_{OP} of the operating mode switching.

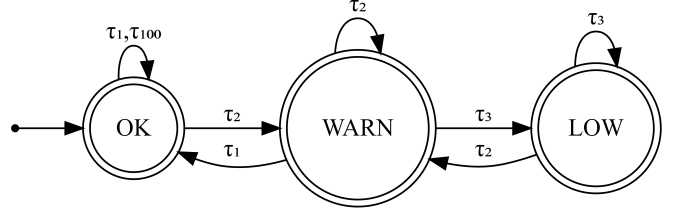


Fig. 11. New plant G_{GSOC} of the satellite bus charge level variation.

bus. Thus, the states defined for the plant of the Fig. 11 are: charge levels ranging from 100% to 25% (OK), 25% to 15% (WARN) and 15% to 0% (LOW).

Their events, in turn, are:

- ζ_1 - Controllable event that switches to normal operation mode;
- ζ_2 - Controllable event that switches to receiving mode;
- ζ_3 - Controllable event that switches to emergency mode;
- τ_1 - Uncontrollable event indicating that the satellite bus charge level is above 25%;
- τ_2 - Uncontrollable event indicating that the satellite bus charge level is between 25% and 15%;
- τ_3 - Uncontrollable event indicating that the satellite bus charge level is below 15%;
- τ_{100} - Uncontrollable event indicating that the satellite bus charge level is above 40% during receiving mode. This event has a specific purpose, as it will be explained later in this section.

Note that in the operating mode model, it is possible to switch directly between normal and emergency modes, which happens so that, in case the Li-S batteries cannot donate charge to the satellite bus, the satellite can switch directly to the emergency mode, even if the G_{GSOC} model state is in the WARN state.

Since the transition logic between operation modes depends on factors such as the satellite bus battery charge level, the presence of charge in the Li-S battery reserve, and charging from solar panels, the following requirements are defined:

- 1) Normal operation mode should occur when the satellite bus battery level is in the OK state.
- 2) Exception to requirement 1: if the satellite is both in eclipse and in receiving mode, it should only transition to normal mode when:
 - the solar panels receive sunlight;

- event τ_{100} is reached;
- or the Li-S battery reserve is depleted.

Without this, the satellite could loop between normal and receiving modes during eclipse.

- 3) Receiving mode should occur when the satellite battery is in the WARN state and the Li-S battery has available charge.
- 4) If the satellite exits eclipse in WARN state, the Li-S battery stops supplying power, but the satellite remains in receiving mode until the OK level is reached.
- 5) Emergency mode should occur when the satellite battery is in the LOW state.
- 6) Emergency mode should also occur if the battery is in the WARN state and the Li-S battery reserve is depleted.
- 7) If the satellite is in emergency mode (WARN state) and the Li-S battery regains charge, it should transition to receiving mode.
- 8) In emergency mode, if the battery is being charged by the solar panels, systems deactivated for power saving should be reactivated, even though the satellite remains in emergency mode.

Since the information about whether the Li-S battery reserve is empty or not is provided by the plant in Fig. 9, it is only necessary to define the constraints that will be applied to the operation modes model to achieve the desired behavior.

Finally, by combining the new plants G_{OP} , G_{GSOC} , and specifications, the new monolithic supervisor S_3 is generated with the desired behaviors for the transitions between operation modes.

C. Simulation Definitions

According to the original model [3], all events are triggered by the presence of sunlight on the PdQSat's solar panel sensors. Since the simulation presented in this work follows the same principle, the models that consider the physical aspects of sunlight perception are reused, so that the only changes in the simulations are related to the new implementations of the payload cycles and the charge reception mode of the Li-S battery.

At each time instant t of the simulation, Kepler's Equation is solved as described in section II-B, obtaining the satellite's true anomaly θ . With this, (2) is used to calculate the Y coordinate of the satellite's position, and to evaluate if it lies between the limits of the Earth's shadow projection ($R_e > Y > -R_e$), with the Sun position considered always at the left side of the Earth.

$$Y = r \sin \theta \quad (2)$$

In the case of the orbit used in the simulations, one with the same major semi-axis and eccentricity of the International Space Station (ISS) is chosen, same used in the previous work, with $e = 0.001$, $a \approx 6785 \text{ km}$ and an altitude of $z = 400 \text{ km}$ [15]. Also, for simulation simplicity, it was chosen an inclination of $i = 0^\circ$.

For calculating the variation in the charge level of the PdQSat satellite bus' battery, [3] uses (3), which relates the time step used in the simulation Δt , the temporal capacity of charging or discharging a commercial battery C , and the charging or discharging power applied to the battery P .

$$\Delta SoC(\%) = \left[\frac{\Delta t[s]}{\frac{C[mWh]}{P[mW]}} \times \frac{1}{3600} \right] \times 100. \quad (3)$$

In the case of PdQSat, a Commercial off the Shelf (COTS) battery specifically developed for CubeSats [16] with a capacity C of 22500 mWh , is chosen for simulation. Also, a time step Δt of 60 s is defined.

For the satellite bus' battery, powers for 4 different cases are defined:

- **Solar panel charging** - Maximum power recommended by the manufacturer [16];
- **Nominal energy consumption** - Average power budget of a 3U CubeSat [17];
- **Emergency mode energy consumption** - Half of the nominal energy consumption;
- **Charging in receiving mode** - Maximum power recommended by the manufacturer.

In the case of the payload battery, due to its extremely high energy density, it is defined that the charge donation, for the receiving operation mode, will be one-fifth of the charge received by the satellite bus.

Therefore, the power values and respective charge level variations in each case, calculated by Equation (3), are presented in Table I.

TABLE I
CALCULATED VALUES FOR THE CHARGE LEVEL VARIATIONS OF EACH BATTERY.

Battery	Action	Power [W] ($\Delta SoC(\%)$)
Sat bus	Solar panel charging	16 (1.2)
Sat bus	Nominal energy consumption	-13.5 (-1)
Sat bus	Emergency energy consumption	-6.75 (-0.5)
Sat bus	Charging in receiving mode	16 (1.2)
Payload	Donation in receiving mode	-3.2 (-0.24)

Although the rate of charge and discharge of the batteries vary when near the limits of charge, and shown in Fig. 2, in the simulations it is considered that those rates are constants during all times [11].

At last, for the simulation of the Li-S battery testing stages, it is defined that each stage will last the same period of time during the simulation, except for the post-mission portion, which will be tested for a shorter period of time.

Since the PdQSat mission is expected to last at least 3 months, it is not practical to simulate the testing stages as how they are about to happen in real life. For this reason, it is simulated that the tests are conducted during only one orbital period or three periods, if one period is not enough to observe the behavior of the control laws. For illustration, the

logic followed for simulations lasting three periods is shown in Fig. 12.

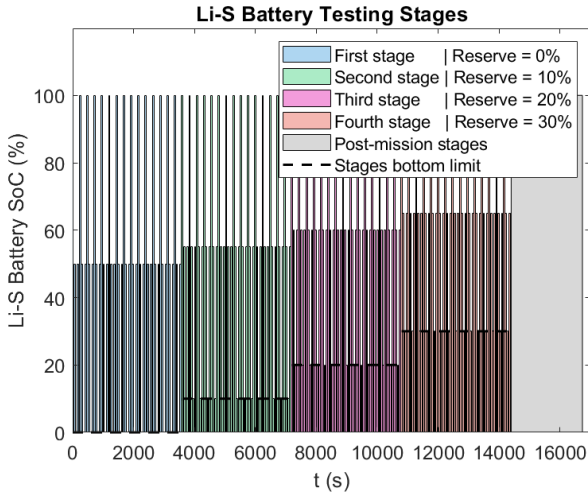


Fig. 12. Logic of the Li-S battery testing stages for a time of three orbital periods.

It should be noted that the Fig 12 do not represent the real behavior of the stages; it only didactically present the logic of how they are simulated and the period of time which each test phase lasts.

D. Simulation Results

For the simulation cases, four situations are analyzed: one general case for one orbital period to check if the simulation is working, and other three extreme cases to simulate the failure of the satellite components or systems

To carry out the simulations, the supervisors S_1 and S_2 from previous work [3] are reused, as they are responsible for part of the orbital dynamics responses of the problem and generate state transitions in the satellite that are necessary for the application of the new supervisors that are being simulated.

Figure 13 shows the behavior of the new supervisor of the mode transition system for a general simulation of the problem.

From the start of the flight, the satellite bus' battery begins to have energy consumed since the satellite is in an eclipse. Upon reaching the 25% level, it transitions to emergency mode, as the Li-S battery is still in its first test cycling stage and has no reserve for donation. However, it can be noted that, after some time, the satellite enters receiving mode, staying there until the battery returns to the OK level and switches back to normal operation mode.

To better visualize the functioning of the modes, Fig. 14 shows the same results as Fig. 13, but with the state of charge levels visualized over the simulation time.

It is noted that, shortly after the first 2000 seconds of the simulation, there is a drop in the charge level, which soon starts rising again. This aligns with the behavior presented in literature [3], where the sunlight is no longer detected by the panels, and the satellite maneuvers to be illuminated again.

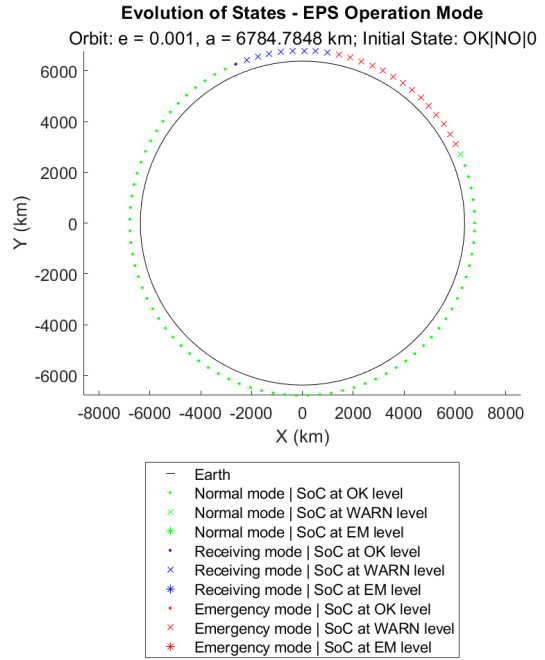


Fig. 13. Behavior of the operating modes' switching system.

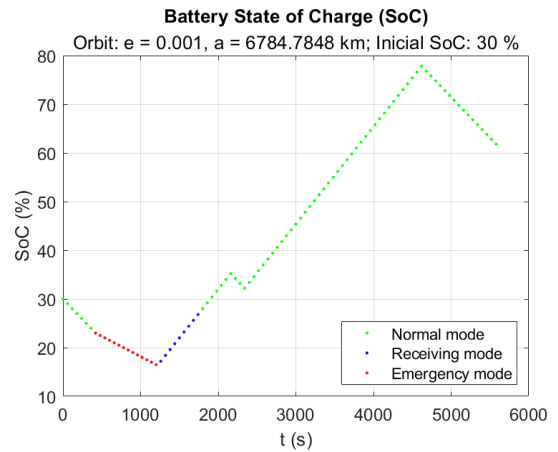


Fig. 14. Satellite bus battery's State of Charge variation during one orbital period.

To show the supervisors work in one of the other cases that explore more extreme situations, the third case is presented. To represent the situation of the emergency mode failure, it is defined that the battery reserve already has some charge, i.e., it has already completed the first test cycling stage, as it can be seen in Fig. 15.

It is important to note that this simulation does not deactivate the *automata* operation but the satellite's physical ability to reduce energy consumption. The emergency mode continues to switch. However, as the emergency mode definition includes the charge donation from the reserve, if it is not empty, this switching does not prevent charge reception for the satellite

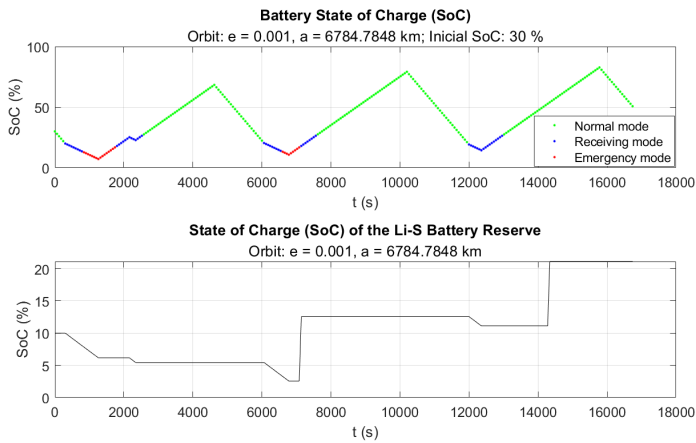


Fig. 15. Satellite bus and battery reserve SoC variations during three orbital periods of simulation 3.

bus.

Thus, if there is a failure in the emergency mode, but some charge remains in the reserve, it is shown that the reserve can support the energy consumption for a considerable time during the mission.

Although not presented in this paper, the other simulations also met good responses from the supervisors actions, proving their success with the proposed objectives of this work [18].

VI. CONCLUSION

This paper aimed primarily at modeling and simulating energy cycling tests for characterizing the Li-S battery of the PdQSat payload, as well as creating an interface between the battery and the satellite's power supply subsystem for emergency power supply during the mission.

During its execution, two main models were developed: a general plant model of the Li-S battery' behavior, focusing on monitoring the test cycles and the presence of reserve charge in their containers, and a monolithic supervisor for the transition between the satellite's operation modes.

During the simulations of the supervisors actions, the observed behaviors were found to be in agreement with the initially established requirements, demonstrating the success of the union between Supervisory Control Theory and satellite design. Regarding the results obtained, it was noted that the combination of emergency and receiving modes created a tool capable of maintaining the satellite's operation, with optimal performance at times when it was already possible to use the reserve charge of the payload battery.

Despite the success in creating and simulating the models, the lack of specific information about the battery that will be used in the PdQSat mission brought some levels of uncertainty to the results obtained in the simulations, as the input variables of the Li-S battery powers may have been overestimated. Thus, it is strongly recommended that the tests be redone in future works, as more information about the modeled components

becomes available, aiming to generate results that can ensure greater reliability in the use of the tools created here.

REFERENCES

- [1] CalPoly. (2022) Cubesat design specification, rev 14.1. [Online]. Available: <https://www.cubesat.org/cubesatinfo>
- [2] J. Straub, T. Villela, C. A. Costa, A. M. Brandão, F. T. Bueno, and R. Leonardi, "Towards the thousandth cubesat: A statistical overview," *International Journal of Aerospace Engineering*, vol. 2019, 2019. [Online]. Available: <https://doi.org/10.1155/2019/5063145>
- [3] E. J. T. Santos, M. C. Pereira, and P. N. P., "Pdqsat electric power subsystem control using a discrete event system model," in *IAA-LA CubeSat Workshop & IAA-LA Symposium on Small Satellites*, Brasília, Brazil, Nov. 2022, pp. 484 – 493.
- [4] C. G. Cassandras and S. Lafortune, *Introduction to Discrete Event Systems*, 2nd ed. Springer, 2008.
- [5] J. E. Hopcroft, R. Motwani, and J. D. Ullman, *Introduction to Automata Theory, Languages, and Computation*, 3rd ed. S.I.: Addison-Wesley, 2007.
- [6] L. V. Alves and P. N. Pena, "Ultrasdes project - a multiplatform discrete event systems tool," *IFAC-PapersOnLine*, vol. 56, no. 2, pp. 6081–6086, 2023, 22nd IFAC World Congress. [Online]. Available: <https://www.sciencedirect.com/science/article/pii/S2405896323010765>
- [7] P. J. Ramadge and W. M. Wonham, "The control of discrete event systems," *Proceedings of the IEEE*, vol. 77, no. 1, pp. 81–98, 1989.
- [8] H. Curtis, *Orbital Mechanics for Engineering Students*, 4th ed., ser. Elsevier Aerospace Engineering Series. Elsevier, 2020.
- [9] H. J. Bergveld, W. S. Kruijt, and P. H. L. Notten, *Battery Management Systems*, 1st ed., ser. Philips Research Book Series. Springer Dordrecht, November 2005.
- [10] M. F. F. de Almeida, "Definition process of the pdqsat's physical architecture [processo de definição da arquitetura física do pdqsat]," 2023.
- [11] F. Cheruyot and D. Seger, "A master-slave salp swarm algorithm optimizer for hybrid energy storage system control strategy in electric vehicles," *Journal of Energy*, vol. 2022, pp. 1–20, 09 2022.
- [12] E. Elsayed, *Reliability Engineering*, ser. Wiley Series in Systems Engineering and Management. Wiley, 2012. [Online]. Available: <https://books.google.com.br/books?id=NdjF5G6tFLQC>
- [13] R. P. Perumal, H. Voos, F. D. Vedova, and H. Moser, "Small satellite reliability: A decade in review," 2021.
- [14] The MathWorks Inc., "Matlab version: 23.2.0 (r2023b)," Natick, Massachusetts, United States, 2023. [Online]. Available: <https://www.mathworks.com>
- [15] European Space Agency (ESA), "ISS: International Space Station," <https://www.esa.int/>, 2020.
- [16] ISISPACE, "ieps type a, type b and type c datasheet," <https://www.isispace.nl>, 2020, accessed: 2022-04-21.
- [17] S. S. Arnold, R. Nuzzaci, and A. Gordon-Ross, "Energy budgeting for cubesats with an integrated fpga," in *2012 IEEE Aerospace Conference*. IEEE, 2012.
- [18] V. A. Souza, "Pdqsat payload energy cycling control using a discrete event system model," 2024.

An Endured On-Board Computer for Small Satellites, using Low Cost COTS Combined with Radiation-Hardened Devices and Fault-Tolerance Strategies

Miguel Boing

Dept. de Engenharia Elétrica e Eletrônica

SpaceLab - UFSC

Florianópolis, Brasil

miguel.boing@spacelab.ufsc.br

Kleber Gouveia

Electronics BU

TMC

Eindhoven, The Netherlands

kleber.gouveia@tmc.nl

João Cláudio Elsen Barcellos

Dept. de Engenharia Elétrica e Eletrônica

SpaceLab - UFSC

Florianópolis, Brasil

joao.claudio.barcellos@spacelab.ufsc.br

Eduardo Bezerra

Dept. de Engenharia Elétrica e Eletrônica

SpaceLab - UFSC

Florianópolis, Brasil

eduardo.bezerra@spacelab.ufsc.br

Abstract—Space radiation is harmful to electronic devices, leading to transient and permanent faults in the on-board systems of a satellite. In traditional satellites, radiation-hardened (rad-hard) devices are employed to mitigate the radiation effects on the electronics. However, in Cubesat based missions, a solution based entirely on rad-hard components is not always feasible due to its high costs, and the limited availability of this type of devices. Therefore, in low-budget small satellite missions, alternative development approaches are needed to mitigate the radiation effects on their systems. One such approach is the combination of rad-hard devices and commercial-off-the-shelf (COTS) components in order to create a cost-effective, fault-tolerant system for use in the satellite's subsystems and payloads. This paper describes the design of a processing module for Cubesats, employing a rad-hard SoC FPGA device combined with COTS components. Additionally, it outlines strategies for the mitigation of radiation effects, resulting in a new fault-tolerant computing platform for CubeSat missions. The work shares decisions, considerations, and studies made during the ongoing project. Furthermore, the research and development activities are conducted in the context of a cooperation between Spacelab at the Federal University of Santa Catarina (UFSC), Brazil and the European Space Agency (ESA), The Netherlands. The anticipated outcome is the expansion of possibilities for CubeSat missions allowing, for instance, deep-space missions. Initially, the proposed processing system is expected to be used as the on-board computer of an endured version of the FloripaSat platform.

Index Terms—Fault-Tolerant, SoC FPGA, CubeSat, rad-hard, COTS

I. INTRODUCTION

CubeSats typically use only Commercial-off-The-Shelf (COTS) components, that is, instead of using specific and customized components for each mission, components commonly used in the industry and available in large quantities

are employed. This characteristic increases development speed and reduces costs, but it brings new challenges to satellite reliability since COTS are not typically designed for applications in space environments where they are exposed to radiation and vacuum, and their behavior may not be predictable or reliable.

Several strategies have been developed and employed in CubeSats to overcome radioactive effects and increase the survivability of their electronic components. Components that use radiation techniques or strategies are known as "radiation-hardened" or "rad-hard." Currently, there are several techniques to mitigate the effects of radiation, ranging from manufacturing processes to printed circuit board design. These techniques are not centralized and are usually grouped by research lines in certain areas, such as microelectronics and systems engineering.

Currently, we have commercially available radiation-resistant components, such as power converters and even Field-Programmable Gate Array (FPGA)s. However, besides the fact that these components can cost up to twenty times more [1], this market is focused in the United States, which, due to military potential, restricts external sales through International Traffic in Arms Regulations (ITAR) and Export Administration Regulations (EAR) regulations [2].

The Space Systems Research Laboratory at Universidade Federal de Santa Catarina (UFSC), SpaceLab, in partnership with European Space Agency (ESA), has developed payloads (CubeSat modules that carry the experiment or final application of the CubeSat, i.e., the mission's objective) for CubeSats using FPGAs and System-on-Chip (SoC) FPGAs rad-hard from the French startup NanoXplore. Two payloads have been developed for use in missions, Payload-X and Payload-XL, which will be launched in the Global Open coLlecting Data

System (GOLDS)-UFSC and Cassini missions.

This work aims to describe the architecture of a fault-tolerant computational platform developed to be used in CubeSat missions using the NanoXplore NG-ULTRA SoC FPGA along with COTS and radiation mitigation techniques.

II. RADIATION ON ELECTRONIC DEVICES

Electronic components are sensitive to radiation effects, especially semiconductors. In a space environment, there are highly energetic particles (heavy ions, protons, and electrons). When these particles collide with electronic components, they generate various effects, ranging from performance loss and abrupt shutdowns to catastrophic failures. When an energetic particle collides with a semiconductor, part of the particle's energy is transferred to the electronic component. This transferred energy is called Linear Energy Transfer (LET), which is expressed as the energy deposited per unit length along the path of the ionizing particle.

The radiation effects resulting from this energy transferred by the energetic particle to the semiconductor device can be divided into transient effects and long-term effects.

Transient effects can occur in electronic components through Single Event Effects (SEE)s or due to high radiation doses. Their susceptibility increases as the device size decreases and as circuit signal speeds increase [3]. The effects of SEE are so impactful in small-scale technologies that they are becoming an issue in terrestrial applications with sub-65nm CMOS technology [4].

Exposure to a radioactive environment causes progressive degradation of the component in a stable and predictable manner. These effects tend to produce long-term changes in the operational characteristics of devices. Long-term radiation will cause the threshold voltage curve to shift and generate leakage currents. The first effect is more relevant for larger transistors, and the latter for smaller devices [5].

III. COMPONENT SELECTION CRITERIA

In Fig. 1, a suggested classification criterion for Technology Readiness Levels (TRL), based on [6] is presented, developed for the context of CubeSat submodules. According to this criterion, it is mandatory that the component has at least TRL-3. Tests in a space or similar environment may include flight heritage, radiation effects testing, or tests in a thermal vacuum chamber.

In [7], recommended derating factors for various component families are provided. These factors represent the percentage difference between, for example, the absolute maximum voltage specified in the datasheet and the application voltage. Table I presents a compilation of the most relevant factors for CubeSat module design.

IV. DESIGN

Since this is a module following CubeSat standards (i.e., an area of 10cm x 10cm and power constraints) [8], in some cases, solutions were prioritized that were not necessarily the

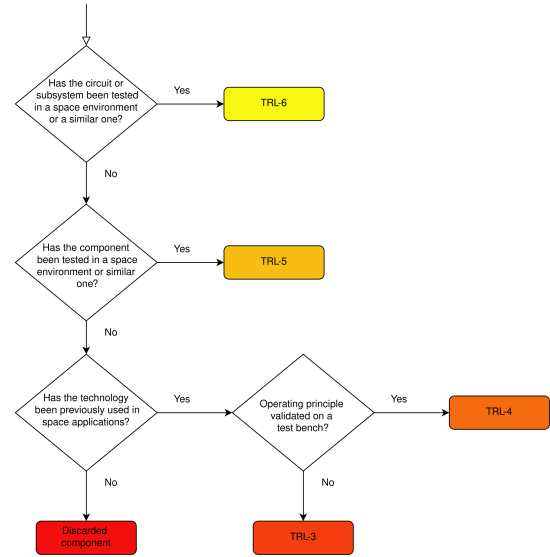


Fig. 1. TRL classification criteria

TABLE I
DERATING TECHNIQUES GROUPED BY COMPONENT CATEGORIES.

Component group	Derating (load ratio or limit)	Factor
Capacitors (Ceramic Chip)	Voltage	60%
Resistors (Chip)	Voltage	80%
Resistors (Chip)	Power (rms)	50%
Non-volatile memories	Supply voltage	$\pm 5\%$
Switching regulators	Output current	80%
Switching regulators	Maximum input voltage	90%
MOSFET	Power dissipation	65%
MOSFET	Voltage (VDS)	80%
MOSFET	Drain current	75%

most robust but provided a good balance between reliability, space, and power consumption.

To parallelize the development of firmware applications while the hardware is being developed, the goal was to maintain compatibility with the Development Kit (DevKit) version 1.1 [9], especially in the parts of the SoC responsible for storing and loading the bitstream. By reusing parts of the DevKit hardware, we ensure the functionality of the circuit, raising the reliability level to TRL-4 and enabling compatibility with the development and debugging tools provided by NanoXplore.

Since this computational platform is not developed for a specific mission, it is not possible to define an orbit and, consequently, a LET spectrum to select components based on their cross-section. Therefore, the performance of the central component of the module, the NG-ULTRA SoC FPGA, will be used as a reference, and components with similar performance in terms of radiation tolerance will be chosen. In terms of SEE, the NG-ULTRA is immune to up to $65 \frac{MeV \cdot cm^2}{mg}$, and in terms of Total Ionizing Dose (TID), it withstands up to 50krads [10].

For the selection of COTS, derating factors were used, as well as the TRL criteria (Section III).

A. Processing System

The architecture of the SoC is available in [11]. A specific Boundary-Scan (BSCAN) bank is provided for configuration. In it, it is possible to define, through exclusive pins: operation mode, bitstream loading configurations, reset pins, status reading, among others.

To facilitate the configuration of the FPGA SoC, Inter Integrated Circuit (I^2C) converters capable of interfacing with the configuration pins of the BSCAN were used. Additionally, there is a Joint Test Action Group (JTAG) interface for configuring the internal registers and isolated pins for configuring the FPGA mode. These resources are made available on a dedicated connector to be compatible with NanoXplore tools.

The BSCAN also features a Universal Asynchronous Receiver / Transmitter (UART) interface for debugging. This interface is connected to one of the channels of a Silicon Labs CP2105-F01-GM converter for RS-485 and is externalized.

To store the bitstream intended for loading, four Infineon S25FL512 NOR memories were selected. The memories can be configured for sequential reading or, using only three, in Triple Module Redundancy (TMR) mode. Additionally, it is possible to load the bitstream directly via SpaceWire, which is externalized.

For the four R-52 processors in the Processing System (PS), six IS43DR16640C Double Data Rate (DDR)2 memories from ISSI are available. These are connected to the SoC's DDR controller. This controller provides protection to the DDR2 memory devices using Reed-Solomon coding and can tolerate up to one faulty device.

With the exception of the memories, these circuits are used only for configuration and debugging and are therefore not designed to be used in a space environment. Thus, a connector capable of disconnecting them from the power bus has been added. The RS-485 converter is powered directly by the external connector and therefore poses no risk to the power bus. The memories were chosen with compatibility with the DevKit in mind. In the case of the bitstream memories, NanoXplore recommends specific part numbers to ensure compatibility with their programming tools, and the DDR2 memories were selected to allow the reuse of validated circuits from the DevKit, which allows us to consider a TRL-4 level for both types of memory.

B. Processing Logic

The NG-ULTRA features 4 direct banks (24 I/O per bank), 10 complex banks (34 I/O per bank), 8 High Speed Serial Link (HSSL) banks, and 7 Phase Locked Loop (PLL) clock generators.

The 4 direct banks and 2 complex banks were used. The HSSL banks and clock generators were not utilized as they were deemed unnecessary within the scope of CubeSats. The following subsections detail the components connected to the Programmable Logic (PL).

1) *Memories*: For data storage, memories were selected to provide different degrees of the trade-off between reliability, capacity, and speed to enhance application possibilities in various mission types.

A NAND *flash* memory of the eMbedded Multimedia Card (eMMC) type was chosen for the storage of Linux-based operating systems and mass data storage, providing high capacity and speed. The Kingston EMMC128-IY29-5B111 memory, with 128GB, features an eMMC 5.1 HS400 interface allowing up to 400MB/s. This memory does not have radiation testing, flight heritage, or validation in other projects, thus it does not offer high reliability; however, this type of memory technology has been employed in CubeSat modules, as in [12], and we can assign it a TRL-3 level.

For critical data, a Magneto-resistive Random Access Memory (MRAM) EM064LXQADG13IS1T from Everspin, with 64Mb, operating at 133MHz and featuring Serial Peripheral Interface (SPI) interface up to Octal SPI, is provided. This specific memory has not yet been tested against radiation effects or in other CubeSat applications, but as described in [13], its immunity against radiation effects is high, ensuring a TRL-3 level.

Finally, to provide an alternative that offers medium capacity and latency but high reliability, three MT29F4G08ABADAWP NAND *flash* memories were selected to operate in TMR. This memory has been characterized in [14], [15], and [16]. With accumulated TID, this memory begins to show errors in memory blocks at approximately 38krad, but it remains functional even after 100krad. No Single Event Latchup (SEL) was observed with LET up to $67.7 \frac{MeV \cdot cm^2}{mg}$; Single Event Upset (SEU) may occur starting from $1.1 \frac{MeV \cdot cm^2}{mg}$, which are mitigated by TMR. We can classify it as TRL-5.

C. Sensing System

For this application, several sensors were chosen for system management, telemetry collection, and satellite management.

To monitor the power systems, two INA226AQDGSRQ1 power sensors from Texas Instruments were selected to monitor the 3V3 and 5V buses. This sensor does not have flight heritage and has not been tested against radiation effects; however, it is widely used in SpaceLab projects, and its operation has been proven in vacuum and vibration chambers through tests conducted on the CubeSat GOLDS-UFSC, which utilizes the Telemetry and TeleCommand (TTC) 2.0 submodule that, in turn, employs this sensor [17]. Thus, we sought to leverage the circuit used in TTC 2.0, ensuring a TRL-6 level for the circuit.

For temperature monitoring, the TMP112AQDRLRQ1 sensor was chosen, which has flight heritage from the CubeSat GRIDS-2 [18], guaranteeing a TRL-5 level. Additionally, two sensors were selected to ensure redundancy in case one of the modules fails.

The temperature and power sensors share the same I^2C serial bus. This type of bus is often problematic and susceptible

to failures; therefore, *buffers* were used to isolate the bus from the individual branches in case of failures, as shown in Fig. 2.

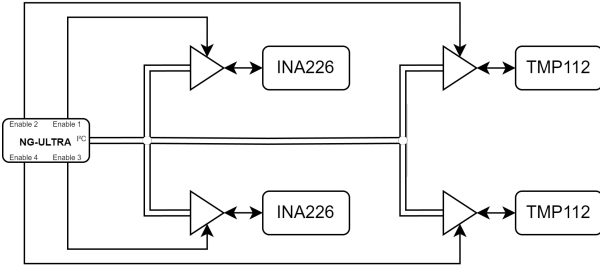


Fig. 2. Node isolation system using *I2C* buffers.

To enhance the module’s ability to act as an onboard computer, a magnetometer MMC5983MA from Memsic and a gyroscope IAM-20380 from TDK InvenSense were included for attitude control. They are configurable, allowing the choice between using *I2C* or SPI buses. To increase reliability, a dedicated SPI bus was implemented solely for these two sensors. The magnetometer is being employed for the CubeSat of the CLIMB mission, which will monitor radiation from the Van Allen belts, and space environment simulation tests have already been conducted. Therefore, we can assign a TRL-5 level. So far, no missions have directly used the gyroscope; however, there are proposals for Attitude Determination and Control System (ADCS) systems, as in [19], leading us to assign a TRL-3 level.

Finally, an Analog-to-Digital Converter (ADC) was implemented to allow reading of simple analog pins. The chosen converter was the ADC128S102 from Texas Instruments. It features a 12-bit resolution SPI interface and up to 8 channels. The project is illustrated in Fig. 3. To avoid the need to design an isolated power supply for the analog supply, an RC filter was used to eliminate ripple in the analog power. Five channels were made available with a bandwidth of up to $BW_{signal} = 48kHz$ and a F_{sclk} of up to $16MHz$; its use must meet Nyquist’s criterion expressed in Inequality 1, where N corresponds to the number of channels being sampled.

$$F_{sclk} > 32 \cdot BW_{signal} \cdot N \quad (1)$$

The ADC was characterized concerning TID and SEE, as described in [20]. Single Event Transient (SET) was observed starting from $18.5 \frac{MeV \cdot cm^2}{mg}$, Single Event Functional Interrupt (SEFI) and changes in the *step current* were observed starting from $32.1 \frac{MeV \cdot cm^2}{mg}$, and SEL was noted from $60 \frac{MeV \cdot cm^2}{mg}$. The component was tested up to $30krad$ and showed promising results with only changes in power currents. It can be classified as TRL-5.

1) *Interfaces*: As there is no defined and exclusive mission for this module, its communication system was designed to offer great flexibility and alternatives for communication buses. Below are the interfaces connected to the banks of

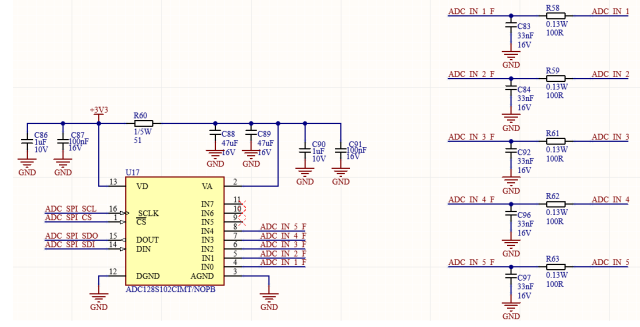


Fig. 3. ADC design for reading external analog pins.

the FPGA available for communication with other satellite modules.

- 3 SpaceWire channels connected to the optimized banks of the FPGA.
- 1 Controller Area Network (CAN) channel.
- 1 bus of Low-voltage differential signaling (LVDS) pins available for implementation.
- 1 bus of generic pins available for implementation.
- 1 bus externalizing the 5 channels of the ADC.
- 1 UART channel for debugging connected to the second channel of the RS-485 converter.

For the implementation of the CAN bus, a SN65HVD232 transceiver from Texas Instruments was used. This transceiver is extremely popular and was chosen because it has been extensively tested in SpaceLab projects; however, no studies were found that mention it has flight heritage, thus it has a reliability level of TRL-4.

SpaceWire was implemented without routers, using the pins of the optimized complex banks for SpaceWire, which feature dedicated controllers, thereby simplifying and increasing the efficiency of the application.

D. Power System

The consumption estimate followed the procedure described in [21]. The power of the external Integrated Circuit (IC)s is presented therein, estimating an average consumption without any type of burst readings from the memories or sensors, and the maximum power estimate considers the most power-consuming operational mode for the IC (disregarding latch-up states). The total estimated power is $1.366W$ and $5.408W$, respectively. All these components were selected with a supply voltage of $3V3$, except for the DDR2 memories, which use $1V8$.

To estimate the consumption of the FPGA SoC, the NX-PowerEstimator tool was used. Since the project does not yet have a defined mission, there are no planned applications to be executed on the FPGA SoC. Thus, to estimate a consumption, a resource-intensive application was considered, using about 75% to 80% of the resources.

The expected current consumption for the FPGA SoC is shown in Table II, specified for each power rail. The total power was $4.62W$.

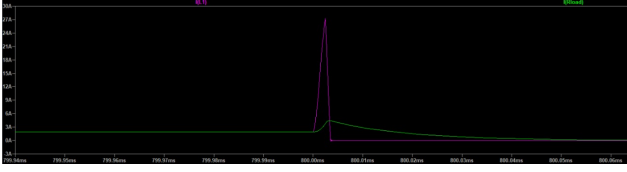


Fig. 4. Simulation of the operation of the LTC4361-2 surge stopper against current surges.

TABLE II
CURRENT CONSUMPTION IN DIFFERENT POWER RAILS

Voltage (V)	Ultra Consumption (mA)	ICs Consumption (mA)	Total Consumption (mA)
3.3	31	745	776
1.8	277	690	967
1.0	4014	-	4014

1) *Power Cascade*: With the consumption estimate, we can develop the power cascade. Due to limited space for the CubeSat module, this design will prioritize area.

The 3V3 voltage will serve only as power for the simple banks of the FPGA and for the external ICs. Due to physical limitations, we can save area on the Printed Circuit Board (PCB) by directly receiving this voltage from the Electrical Power System (EPS) bus; however, a maximum tolerance of no more than 5% is stipulated to comply with derating rates.

The voltages of 1V8, 1V, and 0V9 will be converted directly on the module as they are more sensitive and power the logic of the FPGA, the SoC, and the DDR2 memories, in addition to not being buses commonly available in the EPS. To minimize the high current, an additional input voltage of 5V was chosen for the conversions.

E. Latch-up Protection

Although the NG-ULTRA supports up to 2000V on its pins, the external ICs are COTS and must therefore be protected in the event of SEL occurrences. To achieve this, we can add surge stoppers in series with the converters; specifically, the LTC4361-2 from Analog Devices is an excellent option and is widely used in CubeSat missions ([22], [23], [24], [25], among others). Its circuit is simple and similar in different implementations, ensuring TRL-6. Its operation occurs through monitoring the bus via the terminals of a shunt resistor. The device then controls the switching of an N-channel MOSFET, which can open the power circuit, preventing damage. After 130ms, the bus is reconnected. In Fig. 4, the LTC4361 can be seen activating and disconnecting the bus in response to a current spike of 28A, thus protecting the bus. Surge stoppers will be added to the 3V3 and 1V8 supplies of the COTS ICs. In Fig. 5, the implementation of the protection circuit on the 1V8 power bus can be visualized.

F. Power Converters

To implement the power cascade, it is necessary to convert 5V to 1V, 1V8, and generate the reference voltages for the

memories and the SoC.

The converter chosen for the 1V8 conversion was the ST1S10 from STMicroelectronics, which has the advantage of integrating its MOSFETs within the chip, saving space. This buck converter supports up to 2A of current and is synchronous, which increases conversion efficiency. However, the second MOSFET tends to reduce the converter's lifespan due to cumulative effects of TID. Despite this, in [26], this converter was characterized and supports up to 125krads without damage. In [27], the ST1S10 was characterized under SEE, showing resistance to SEL and SEFI for LETs greater than $67.7 \frac{MeV \cdot cm^2}{mg}$; however, SETs may occur from $1 \frac{MeV \cdot cm^2}{mg}$. Another positive aspect of choosing this converter is its flight heritage from the KySat-2 mission [22], which guarantees it a reliability level of TRL-5. The converter's design was made using the tool provided by the manufacturer for designing DC-DC sources. A maximum input voltage variation of 10% was considered. In Fig. 5, we can see the designed circuit; in Fig. 6, the efficiency of the converter is presented. At a maximum predicted consumption of 1.92A, the converter achieves an efficiency of 83.7% and a ripple of 0.14%.

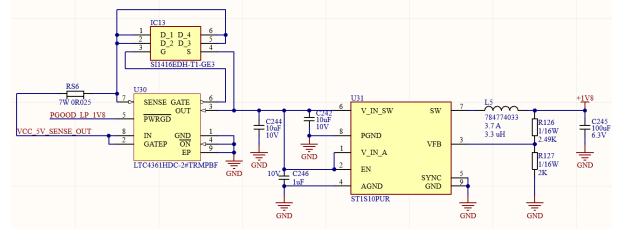


Fig. 5. 1V8 voltage conversion circuit with latch-up protection.

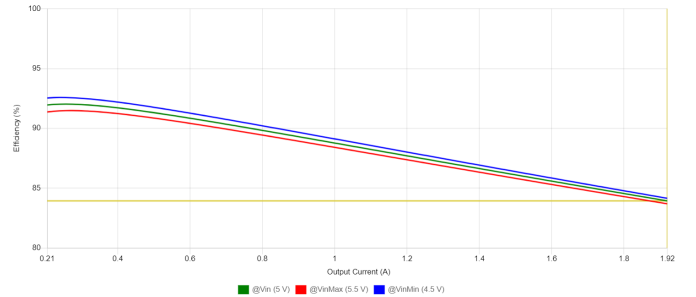


Fig. 6. Efficiency of the 1V8 power supply.

The 1V voltage is intended to power the cores of the SoC and the FPGA, and it is recommended by the manufacturer to dedicate two isolated buses. Thus, the LTM4619 buck converter from Analog Devices was chosen, which provides two outputs of up to 4A each and features such as power good and soft start. It was characterized against radiation in [28] and survived up to approximately 200krad. In this same work, it was tested against SEEs of $200 \frac{MeV \cdot cm^2}{mg}$, but it did

not survive and was not tested near the NG-ULTRA resistance values ($\leq 65 \frac{MeV \cdot cm^2}{mg}$). Thus, this result is not relevant for this application, and a new test with a LET value closer to this should be proposed. The design of this converter was made using the component's datasheet as a reference, and its design was validated using the SPICE model provided by the manufacturer. Both channels were designed to have a soft start of $1.4ms$ and a ripple of approximately 0.2%. The efficiency is shown in Fig. 7; at maximum predicted consumption, the efficiency is approximately 81.9%. This converter has flight heritage from the 12U CubeSat of the Aoxiang-Sat1 mission [29] and for the COVE payload to power the rad-hard Xilinx Virtex-5QV FPGA [30], ensuring TRL-5.

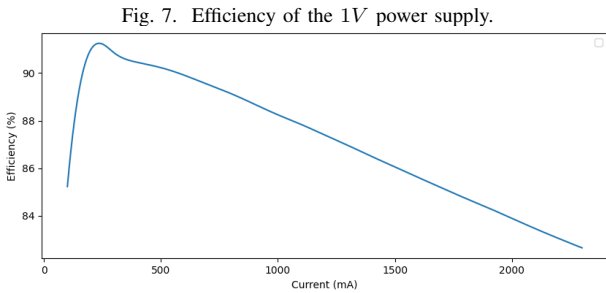


Fig. 7. Efficiency of the 1V power supply.

Finally, Low-Dropout Regulator (LDO)s are needed to obtain the reference voltages for the memories and the DDR bank of the SoC. Specifically, the TPS51200 was chosen, which is designed for this functionality. In [31], SEE tests were conducted, establishing a threshold LET between $11 \frac{MeV \cdot cm^2}{mg}$ and $18 \frac{MeV \cdot cm^2}{mg}$ for the occurrence of SEL. To circumvent the problem, the supply for these LDOs will also be protected by the LTC4361-2 surge stoppers. The TPS51200 is used in the NG-Ultra DevKit and in Payload-XL [32], allowing us to classify it as TRL-5.

Finally, the resulting power cascade is illustrated in Fig. 8.

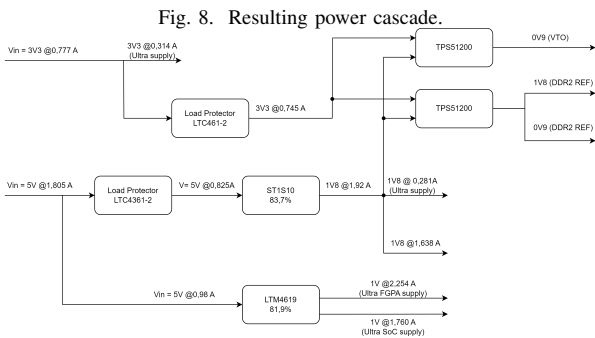


Fig. 8. Resulting power cascade.

V. CONCLUSION

In this work, it was possible to develop the architecture of a platform with fault tolerance characteristics by integrating a SoC FPGA with COTS components.

The next step in the development of the module consists of designing the physical layout of the PCB for the computational platform and testing the Power Delivery Network (PDN). For this, the works of [32] and [21] will be used as a basis, describing radiation mitigation techniques focused on layout using the ECSS standards developed by the ESA. Due to the planned compatibility with the DevKit, it is expected that firmware work can be carried out with some parallelism through it.

There are currently no confirmed missions for the developed module. However, it is anticipated that it will be integrated into the Persistent-1 and ROCUS-1 missions of SpaceLab.

REFERENCES

- [1] J. D. O. Benfica, and F. Vargas, "Plataforma para testes e qualifica (thesis, benfica, 2015)," Ph.D. dissertation, Universidade Federal de Santa Catarina, Nov. 2015.
- [2] K. L. B. Cook, "The itar and you - what you need to know about the international traffic in arms regulations," in *2010 IEEE Aerospace Conference*, 2010, pp. 1–12. DOI: 10.1109/AERO.2010.5446878.
- [3] R. Gaillard, "Single event effects: Mechanisms and classification," in *Soft Errors in Modern Electronic Systems*, M. Nicolaidis, Ed. Boston, MA: Springer US, 2011, pp. 27–54, ISBN: 978-1-4419-6993-4. DOI: 10.1007/978-1-4419-6993-4_2. [Online]. Available: https://doi.org/10.1007/978-1-4419-6993-4_2.
- [4] M. L. Alles, R. D. Schrimpf, R. A. Reed, *et al.*, "Radiation hardness of fdsoi and finfet technologies," in *IEEE 2011 International SOI Conference*, 2011, pp. 1–2. DOI: 10.1109/SOI.2011.6081714.
- [5] R. D. Schrimpf, "Radiation effects in microelectronics," in *Radiation Effects on Embedded Systems*, R. VELAZCO, P. FOUILLAT, and R. REIS, Eds. Dordrecht: Springer Netherlands, 2007, pp. 11–29, ISBN: 978-1-4020-5646-8. DOI: 10.1007/978-1-4020-5646-8_2. [Online]. Available: https://doi.org/10.1007/978-1-4020-5646-8_2.
- [6] *Technology readiness levels*, <https://www.nasa.gov/directorates/somd/space-communications-navigation-program/technology-readiness-levels/>, Acessado em Junho 22, 2024, NASA, 2024.
- [7] *Space product assurance*, Standard ECSS-Q-ST-30-11C Rev.1, The Netherlands: ECSS, 2011.
- [8] *Cubesat design specification*, Available at <https://www.cubesat.org/cubesatinfo/>, 2022.
- [9] NanoXplore, *Devkit ng-ultra*, <https://nanoxplore-wiki.atlassian.net/wiki/spaces/NAN/pages/94044161/Devkit+NG-ULTRA>, Accessed: Oct. 16, 2024, 2024.
- [10] NanoXplore, "Ng-ultra heavy ion radiation test report," NanoXplore, Tech. Rep. AD1, Nov. 2023. [Online]. Available: <https://nanoxplore-wiki.atlassian.net/wiki/spaces/NAN/pages/9961482/NG-ULTRA>.

- [11] NanoXplore, *Ng-ultra family/nx2h540atsc datasheet*, <https://nanoxplore-wiki.atlassian.net/wiki/spaces/NAN/pages/9961482/NG-ULTRA>, Acessado: 2024-06-22, 2024.
- [12] GOMspace, *NanoMind HP MK3*, Accessed: 2024-07-04, 2024. [Online]. Available: [https://gomspace.com/shop/subsystems/command-and-data-handling/nanomind-hp-mk3-\(1\).aspx](https://gomspace.com/shop/subsystems/command-and-data-handling/nanomind-hp-mk3-(1).aspx).
- [13] Z. Zhang, Z. Lei, Z. Yang, *et al.*, “Single event effects in cots ferroelectric ram technologies,” in *2015 IEEE Radiation Effects Data Workshop (REDW)*, 2015, pp. 1–5. DOI: 10.1109/REDW.2015.7336734.
- [14] L. Salvy, A. Varotsou, A. Samaras, *et al.*, “Total ionizing dose influence on the single event effect sensitivity of active eee components,” in *2016 16th European Conference on Radiation and Its Effects on Components and Systems (RADECS)*, 2016, pp. 1–8. DOI: 10.1109/RADECS.2016.8093123.
- [15] B. Vandevelde, “Heavy ions report - report single event effects mt29f4g08abadawp (dc1350) 4gb, x8 nand flash memory from micron,” European Space Agency, Tech. Rep., Sep. 2015.
- [16] L. Salvy, “Total ionizing dose test report - mt29f4g08abadawp (dc1350) 4gb, x8 nand flash memory from micron,” European Space Agency, Tech. Rep. ESA-TID-2024-01, Jul. 2015.
- [17] SpaceLab, *Ttc2*, <https://github.com/spacelab-ufsc/ttc2>, Accessed: 2024-05-27, 2024.
- [18] X. Zheng, H. Gao, J. Wen, *et al.*, “In-orbit radiation damage characterization of sipms in the grid-02 cubesat detector,” *Nuclear Instruments and Methods in Physics Research Section A: Accelerators, Spectrometers, Detectors and Associated Equipment*, vol. 1044, p. 167 510, 2022, ISSN: 0168-9002. DOI: <https://doi.org/10.1016/j.nima.2022.167510>. [Online]. Available: <https://www.sciencedirect.com/science/article/pii/S0168900222008026>.
- [19] A. E. Elsantawy, M. ElFallal, I. Abuaitta, *et al.*, “Design and implementation of attitude determination and control subsystem for cube satellites,” in *The International Undergraduate Research Conference*, The Military Technical College, vol. 6, 2022, pp. 1–7.
- [20] D. Hu, “Cots components radiation test activity and results at mssl,” in *2016 IEEE Radiation Effects Data Workshop (REDW)*, 2016, pp. 1–7. DOI: 10.1109/NSREC.2016.7891708.
- [21] C. A. Rigo, “Projeto de placas de circuito impresso com fpgas para uso em ambiente espacial,” M.S. thesis, Universidade Federal de Santa Catarina, 2019.
- [22] T. M. Lim, A. M. Cramer, J. E. Lumppp, and S. A. Rawashdeh, “A modular electrical power system architecture for small spacecraft,” *IEEE Transactions on Aerospace and Electronic Systems*, vol. 54, no. 4, pp. 1832–1849, 2018. DOI: 10.1109/TAES.2018.2803598.
- [23] S. M. Oktaviani, I. H. Saugi, A. T. Santaso, *et al.*, “Development of a commercial-off-the-shelf imaging payload with onboard image classification and processing,” in *IGARSS 2022-2022 IEEE International Geoscience and Remote Sensing Symposium*, IEEE, 2022, pp. 7260–7263.
- [24] I. Fajardo, A. A. Lidtke, S. A. Bendoukha, *et al.*, “Design, implementation, and operation of a small satellite mission to explore the space weather effects in leo,” *Aerospace*, vol. 6, no. 10, 2019, ISSN: 2226-4310. DOI: 10.3390/aerospace6100108. [Online]. Available: <https://www.mdpi.com/2226-4310/6/10/108>.
- [25] F. Kuroiwa, S. A. Bendoukha, K.-i. Okuyama, H. Morita, and M. Nishio, “A redundancy and operation of power control system for a deep-space small probe,” *Journal of Automation and Control Engineering Vol*, vol. 4, no. 5, 2016.
- [26] S. Dhawana, O. Baker, H. Chen, *et al.*, “Commercial-off-the-shelf dc-dc converters for high energy physics detectors for the slhc upgrade,” in *2009 16th IEEE-NPSS Real Time Conference*, 2009, pp. 129–136. DOI: 10.1109/RTC.2009.5322122.
- [27] R. Pilia, F. Malou, D. Dangla, *et al.*, “Compendium of recent see, and tid test results conducted by cnes from 2011-2016,” in *2017 17th European Conference on Radiation and Its Effects on Components and Systems (RADECS)*, 2017, pp. 1–8. DOI: 10.1109/RADECS.2017.8696134.
- [28] J. Ameel, D. Amidei, S. Baccaro, *et al.*, “Radiation-hard power electronics for the atlas new small wheel,” *Journal of Instrumentation*, vol. 10, no. 01, p. C01009, Jan. 2015. DOI: 10.1088/1748-0221/10/01/C01009. [Online]. Available: <https://dx.doi.org/10.1088/1748-0221/10/01/C01009>.
- [29] L. Peng, Z. Jun, and Y. Xiaozhou, “Design and on-orbit verification of eps for the world’s first 12u polarized light detection cubesat,” *International Journal of Aeronautical and Space Sciences*, vol. 19, pp. 718–729, 2018.
- [30] D. Bekker, P. Pingree, T. Werne, T. Wilson, and B. Franklin, “The cove payload—a reconfigurable fpga-based processor for cubesats,” in *Small Satellite Conference*, 2011.
- [31] F. Irom, G. R. Allen, and S. Vartanian, “Single-event latchup measurements on cots electronic devices for use in iss payloads,” in *2017 IEEE Radiation Effects Data Workshop (REDW)*, 2017, pp. 1–6. DOI: 10.1109/NSREC.2017.8115428.
- [32] K. R. G. Júnior, “Fluxo de apoio à concepção de hardware para o segmento espacial visando melhoria de confiabilidade de missões cubesat,” M.S. thesis, Universidade Federal de Santa Catarina, 2021.



Maximizing Power Potential: Designing an Algorithmically Optimized Solar Cell Array Design for the Peruvian 3U CubeSat CHASQUI II

John Casana¹, Josue Giraldo², and Luis Varas¹

¹Universidad Nacional de Ingeniería

²Universidad Nacional Mayor de San Marcos

Abstract

In the development of various CubeSat missions, efficient and secure power energy management represents a significant challenge. This is due to the multiple conditions that CubeSat must face throughout the orbit, becoming a recurrent problem, even defining whether the mission is successful or not. The purpose of this work is to develop an efficient Electrical Power Subsystem (EPS) for the ongoing mission of the Peruvian 3U CubeSat, CHASQUI II, which will orbit in LEO to study electromagnetic pulse disturbances at low L-layer values induced by Superbolts. This is aimed at enabling participation in the APSCO Cubesat Competition (ACC). To achieve this, the team conducted a thorough investigation of different past 3U CubeSats missions, highlighting the relevant aspects of each one, as well as lessons learned and information obtained from the first Peruvian nanosatellite, CHASQUI-I. A simulation model was developed to represent all conditions in which the CubeSat will face in orbit. Furthermore, the Maximum Power Point Tracking (MPPT) algorithm was implemented to generate maximum power from the solar cells under various temperature and irradiation conditions. This information allowed for the compilation of different power budgets from past CubeSats missions, in order to generate an estimated power budget for the correct functioning of the other subsystems that comprise CHASQUI II. Likewise, operational modes

were analyzed for different scenarios that CubeSat will encounter during this mission in orbit, defined by changes in solar cells and battery parameters, as well as to prevent total mission failure only for internal EPS problems. Additionally, a product tree was elaborated, summarizing all components and the defined architecture used in the power control subsystem, in order to obtain important parameters of the CubeSat and mission, such as total mass, dimensions of each element and the estimated total price. Following this research, a reliable and functional power control subsystem is obtained for different 3U CubeSat missions. This study makes it possible to understand the general procedure for developing an EPS that provides the highest amount of energy from all solar panels, using specialized algorithms for ongoing or future nanosatellites missions, and considering essential points before developing a final model of the subsystem. In conclusion, this work will provide enough information about general procedure to develop an EPS for 3U CubeSats, and also gives tools to numerous university organizations involved in aerospace and satellite research for including specialized algorithms like MPPT to their power control subsystem, which is adaptable to any solar cell model and brings benefits in the generation of electrical energy.

The influence of different scenarios on the temperature response of CubeSat's battery

Felipe Teodoro Mendes¹,
Maria Eduarda Emiliano Rezende²,
Caique Sales Miranda Gomes³,
Laio Oriel Seman⁴,
Elaine Maria Cardoso⁵,
Edemar Morsch Filho⁶

Abstract—Before a CubeSat starts to operate in orbit, several tests are performed to ensure its subsystems work according to design specifications. In this sense, numerical simulations are a fundamental tool for testing representative operating scenarios, which are often difficult to reproduce in the laboratory, especially because of the microgravity environment, vacuum, temperature, and radiation levels found in space. In a satellite project, including CubeSats, some questions to be answered before the satellite is even manufactured include its temperature in orbit, especially the battery, which is one of the most temperature-sensitive components and usually requires thermal control to prevent failures. Operating the battery in temperature ranges outside those recommended by the manufacturer can increase its degradation or even cause permanent failure, which puts the entire mission at risk. The temperature scenario in which a CubeSat is exposed depends directly on its orbit and attitude, which also impacts the temperature field of the battery. However, internal heat generation occurs naturally during battery operation and must be considered in thermal modeling. This phenomenon depends, among other factors, on the current drawn and the time it is being used. This work seeks to thermally model in CFD (Computational Fluid Dynamics) the thermal behavior of a battery integrated into a CubeSat to obtain the battery's temperature scenarios. To achieve this, the thermo-electrical modeling of the battery and the thermal modeling of the CubeSat are created and solved in the Ansys CFX software. Different orbits and currents are considered in the analyses to present possible temperature scenarios for the battery, which can assist in the planning and development of the Electrical Power System (EPS) and Thermal Control subsystem of a CubeSat mission. The results indicate scenarios in which attention should be paid to the thermal management of the battery to avoid temperatures that are too low, and this could be used to design the thermal control subsystem.

Keywords—numerical simulation, heat transfer, battery, thermal management

I. INTRODUCTION

The first CubeSat launch, which is a category seen within nanosatellites, took place on June 30, 2003, placing Danish, Japanese, Canadian, and North American nanosatellites into orbit. The first use of a CubeSat for a scientific mission came through NASA's Ames Research Center. In 2006, the *Biological CubeSat* group launched GeneSat-1 to conduct biological experiments in space and the success of the mission resulted in great acceptance of the idea of nanosatellites and CubeSats by the scientific community [1].

According to [2], in its study on the failure rate in small satellites, by the year 2016, 41.3% of all satellites in this category faced total or partial failures, with 6.1 % of these failures caused by failures in the launch vehicle, 11% correspond to partial failures of the nanosatellite and the remaining 24.2% represent total failures of the space mission.

In this sense, it is worth noting that the increased complexity in the requirements of modern space missions has also resulted in new challenges for the operation, maintenance, and longevity of missions using satellites. Thus, the use of nanosatellites makes the problem even more challenging, for example, due to their limited mass, volume, and external area

available for the allocation of photovoltaic panels for energy generation, dissipation of heat, and for integration of different subsystems that would be usual for large satellites [3], [4].

Therefore, to carry out tests and analyzes before launch are extremely important to reduce any risks that could make the space mission unfeasible. In other words, it is essential for the success of missions to carry out several CFD (Computational Fluid Dynamics) simulations aimed at sizing subsystems and verifying their operation, as well as helping to obtain adequate behavior while in orbit.

Given the above, the main objective of this work is to numerically simulate the heat transfer in a CubeSat, focusing on the temperature achieved at solar panels and batteries for different orbit scenarios.

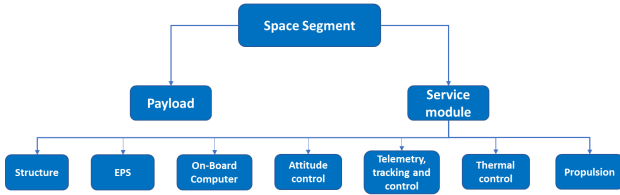
II. BIBLIOGRAPHY REVIEW

Regardless of the size of the satellite, in general, they are all made up of a set of subsystems, as indicated in Fig. 1. Each of these subsystems has a function within the mission, but only the Electrical Power System (EPS) and Thermal Control will be highlighted here.

The objective of the EPS is to generate, store, regulate and distribute the electrical energy that the satellite needs to complete the mission requirements. It is divided into primary and secondary energy sources, represented by solar panels and batteries, respectively. Solar panels correspond to the arrangement of dozens of individual solar cells, capable of generating from a few watts to tens of kilowatts. Batteries are

Felipe Teodoro Mendes, UNESP, Brazil (felipe.teodoro@unesp.br).
Maria E. Emiliano Rezende, UFSC, Brazil (dudarezende14@gmail.com).
Caique Sales Miranda Gomes, UFSC, Brazil (kiqsmg@gmail.com).
Laio Oriel Seman, UFSC, Brazil (laoioseman@gmail.com).
Elaine Maria Cardoso, UNESP, Brazil (elaine.cardoso@unesp.br).
Edemar Morsch Filho, UFSC, Brazil (edemar.filho@unesp.br).

Fig. 1: CubeSat's subsystems



used for the secondary energy generation system, providing it in periods when the primary system is not available, such as during eclipse phases. In this way, the batteries provide energy during the absence of solar incidence on the satellite and are recharged during the period in which there is incidence [5].

The objective of thermal control is to guarantee the operation of electronic and mechanical equipment within the operating temperature limits, efficiently and reliably. In general, electronic equipment in space needs to be kept in a temperature range between -15°C and $+50^{\circ}\text{C}$, while batteries must be kept between 0°C and $+20^{\circ}\text{C}$ [6].

To develop the thermal control of a satellite, a fundamental step is to estimate the heat transfer it will have in orbit. To this end, in the initial development stage of CubeSats projects, the analytical formulation approach provides general results, with great agility and low cost. However, as the project moves into more advanced phases, approaches with more precise formulation become necessary. For this reason, numerical simulations are widely used to understand the behavior of nanosatellites, being capable of generating results with high accuracy and levels of detail [7]. Among the numerical methods available and most used for these problems, there is the Finite Difference Method (FDM), the Finite Element Method (FEM), and the Finite Volume Method (FVM).

The work of [8] shows that passive thermal control is more than sufficient to keep electronic components for aerospace use within their recommended operating values, as seen in Tab. I. To reach this conclusion, the authors implemented thermal simulations in MATLAB using FEM, where the temperature conditions for multiple orbits and their extremes were evaluated.

TABLE I: Operational temperature of subsystems [9].

Components	T_{min} [$^{\circ}\text{C}$]	T_{max} [$^{\circ}\text{C}$]
Electronics (PCB)	-40	+85
Battery (charge)	0	+45
Battery (discharge)	-40	+60
Structure	-40	+85
Solar panels	-100	+100

In the work of [9], the authors computationally analyzed nanosatellites operating at altitudes between 500 km and 2000 km, considering a passive thermal control system, also obtaining satisfactory results for all electronic components, with the exception of the battery. The authors employed a nodal model based on energy conservation. The work also showed that the temperatures of photovoltaic panels are extremely sensitive to the type of material used in the surface coating of the panels.

However, as also observed in [8], the authors emphasize that for extreme negative temperature conditions, the use of heaters for the batteries is recommended to guarantee operability in all conditions during orbit, especially during the eclipse phase.

The studies carried out by [10] and [11] also simulate CubeSats in orbit, and these authors employ equivalent resistances to model thermal behavior. For the first work, the author compared the results obtained by using equivalent resistances with an analysis carried out in the *ESATAN-TMS* software, obtaining the same temperature distribution for both analyses. For the second study, a software tool was developed based on the equivalent resistance technique, focusing on modeling the thermal behavior of small satellites, being used to evaluate the performance of the Canadian Space Agency's CASTOR satellite, obtaining a difference less than 5% in the satellite's surface temperatures.

Thermal analyses were also performed to estimate the performance of the nanosatellite, developed by students at the University of Texas. In this project, participants carried out experimental thermal cycle tests and thermal analyses, with the thermal cycle being carried out in Chamber-N at the Johnson Space Center, for extreme cold and heat scenarios, while thermal analyses were carried out using the Method of Finite Elements [12]. Among the results, there were temperature peaks that were similar between the model and the data from the experimental tests, with the use of a thermal blanket being used to help maintain the satellite's thermal balance in extreme cold conditions, but which was not able to avoid battery overheating in extreme heat condition.

Through a thermal model developed in Matlab, [13] aimed to evaluate and verify compliance with the requirements established for the mission of the Falconsat-2 program in 2001. Through the tool developed in Simulink, it was possible to choose an approach for thermal control, based on compiling a history of external flow inputs to the satellite in an orbit, later using them to analyze the thermal behavior of the satellite in orbit, using the FDM. At the end of the work, a passive thermal control edge was chosen using aluminum and Kapton tape on the faces of the external structures, as this proved to be capable of keeping the components operating within the temperature specifications desired for the project.

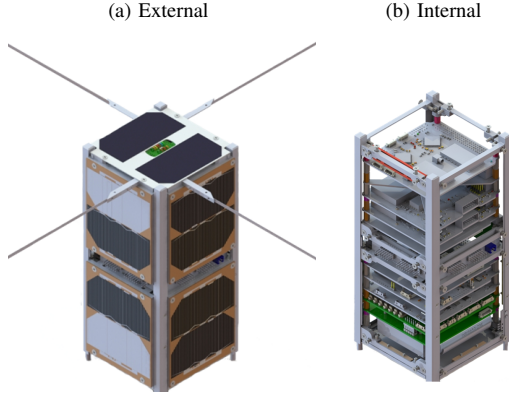
The work of [7] focused on the transient thermal simulation of a 1U CubeSat, where the heat transfer by conduction and radiation (external and internal) were solved using the FVM. To solve the internal radiation in the CubeSat, the Gebhart method and an obstruction model were implemented, and three conditions for the internal emissivity were tested. The results showed a significant impact of the internal heat transfer by radiation on the temperature field of the entire satellite, and comparisons with a simpler nodal model showed good agreement, although the latter did not consider three-dimensional effects.

III. METHODOLOGY

The problem to be solved is based on the geometry of the CubeSat 2U called GOLDS-UFSC, which is presented in Fig. 2. This CubeSat is under development at SpaceLab (<https://>

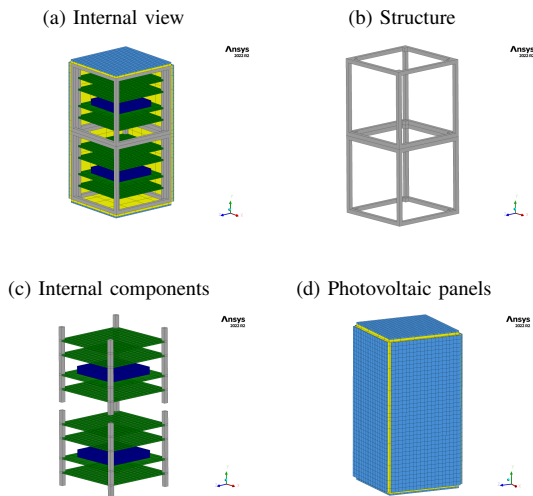
[//spacelab.ufsc.br/en/home/](http://spacelab.ufsc.br/en/home/)) and is scheduled to be launched in 2025.

Fig. 2: CubeSat GOLDS-UFSC [14].



From this model, the geometry to be used in the simulations of this work was created, as seen in Fig. 3, which is composed of 2 main aluminum structures (gray), each measuring $100 \text{ mm} \times 100 \text{ mm} \times 100 \text{ mm}$. Internally, it has four corners for fixing Printed Circuit Boards (PCBs) to the structure using screws, these being representative of the different electrical and electronic subsystems of the nanosatellite. The nanosatellite has four PCBs (green) for each floor U, with $80 \text{ mm} \times 80 \text{ mm} \times 2 \text{ mm}$ each. In the center of a PCB of each CubeSat unit there is a battery, represented by the dark blue component. Furthermore, in order to minimize problems arising from radiation encountered in orbit on the electronic components, there are shields made of aluminum (yellow) for each of the satellite's faces, each measuring $100 \text{ mm} \times 100 \text{ mm} \times 3 \text{ mm}$. Finally, the photovoltaic panels (light blue) are attached to the outer face of each of the shields, and aim to transform the incident solar radiation into electrical energy to power the nanosatellites various subsystems.

Fig. 3: Main CubeSat's parts



A. Mesh and simulation parameters

A mesh independence test was performed to verify the convergence of the simulation. Three meshes were created, with a total of 72,366, 214,153, and 522,089 cells. To verify the influence of the mesh on the results, the temperature on the +X and +Y panels were monitored in a prescribed flow condition over the faces. The results obtained through this analysis are in Tab. II. As a result of the mesh independence test, it was decided to carry out the case studies of this research with Mesh 2, as it presents the best relationship between computational cost and accuracy among the evaluated meshes.

TABLE II: Mesh independence test

Mesh	N° of cells	Temp. +X [°C]	Temp. +Y [°C]
1	72.366	7.23	6.53
2	214.153	8.12	6.72
3	522.089	8.20	6.77

As a time step, 10 s was used, and around 15 complete orbits were simulated until a response with a cyclic pattern was reached. To present the results, only the last orbit is considered. As a convergence criterion, a residual (RMS) of 10×10^{-7} was used for the energy equation.

B. Heat transfer

In order to simulate heat transfer in the CubeSat in orbit, an energy balance will be used, considering the assumptions of transient regime, constant material properties, and perfect vacuum, according to Eq. 1:

$$\rho c_p \frac{\partial T}{\partial t} = k \nabla^2 T + \dot{q} \quad (1)$$

where ρ is the density [kg/m^3], c_p is the specific heat at constant pressure [J/kg.K], T is the temperature [K], t is the time [s], k is the thermal conductivity [W/m.K] and \dot{q} is the source term.

In this work, the heat transfer that occurs in the CubeSat involves only conduction and radiation transfer modes. However, the internal heat exchange by radiation will be ignored as this phenomenon requires calculations of obstructions and reflections, which requires a more sophisticated formulation. In order to simplify the analyses, this work assumes that all external surfaces of the CubeSat are opaque, gray (radiation independent of wavelength), and diffuse (radiation independent of direction).

C. Boundary conditions

The boundary conditions involved in the CubeSat's heat exchange are based on four forms: absorption of solar flux, albedo, and infrared, in addition to its own emission. Each of these terms is modeled according to the work of [15].

The material properties used in the thermal simulation are listed in Tab. III.

The values used for the absorptivity and emissivity of the surfaces will be discussed later, together with the definition of the case studies.

TABLE III: Material properties [15].

Component	Material	k [W/mK]	c_P [J/kgK]	ρ [kg/m ³]
Structure	Aluminium	140	948	2810
PCB	RF4	1.03	1103	2325
Battery	Lithium	21	933	2122
Shielding	Aluminium	140	948	2810
Solar panel	RF4	1.03	1103	2325

D. Heat generation at the battery

Aiming to understand the thermo-electric behavior of batteries typically used in CubeSat projects, the proposed model by [16] was implemented. It is worth noting that in the analyses, the electrical behavior of the battery does not interfere with the electrical model of the photovoltaic panel, nor vice versa.

The battery's heat generation rate, \dot{q}_b [W/m³], is given by:

$$\dot{q}_b = \frac{I}{V_b} \left[IR + T \frac{\partial U_O}{\partial T} \right] \quad (2)$$

where V_b is the battery volume [m³], I is the charge and discharge current [A], R is its resistance [Ω], T is the battery temperature and $\partial U_O / \partial T$ is the thermal entropy coefficient.

According to [17], the thermal entropy coefficient, in the unit of millivolts, can be obtained by:

$$\frac{\partial U_O}{\partial T} = -0.355 + 2.154 \times SoC - 2.869 \times SoC^2 + 1.028 \times SoC^3 \quad (3)$$

where SoC (State of Charge) indicates how much charge capacity remains in the battery, with the maximum value being 1 (full battery) and the minimum being 0 (empty battery).

The general equation for the SoC is given by:

$$SoC = SoC_{in} - \frac{It}{Q_c} \quad (4)$$

where SoC_{in} is the initial charge value [-], Q_c is the nominal battery capacity [Ah] and t is the time [s].

To complete the model, according to [18], the electrical resistance of a battery is not constant, varying according to its temperature and state of charge (SoC), and can be calculated in $m\Omega$.

In this work it is assumed that the battery capacity (Q_c) is 2 Ah and the initial state of charge (SoC_{in}) is 1, that is, the battery is always initially fully charged.

Although the other electronic components of a satellite also end up generating heat during its operation, these will be disregarded in this work.

E. Study cases

In terms of orbit, two configurations will be evaluated: with and without eclipse. In order to evaluate representative CubeSat scenarios, the orbit is 506 km high, circular, and has an inclination of 90°.

For each orbit, two attitude conditions will be evaluated, that is, CubeSat pointing and rotation, which here will be called Nadir and Maximum Projection. For the Nadir scenario, the CubeSat constantly points one of its faces towards the center of the Earth, while the Maximum Projection case consists of a configuration where the CubeSat constantly maintains three of its faces towards the Sun.

IV. RESULTS

Figure 4 shows the temperature at the center of each panel and the CubeSat battery throughout a complete orbit, for varying attitude and orbit conditions. Although the CubeSat is 2U, with ten photovoltaic panels and two batteries, the results indicated that the temperatures on the same side are very close and, therefore, it was decided to show only one panel on each side. For batteries, the temperatures are also very close and therefore only one will be shown. In all cases of Fig. 4 there is an absorptivity (α) and emissivity (ϵ) of 0.3 for both, in addition to a null current (I) passing through the battery.

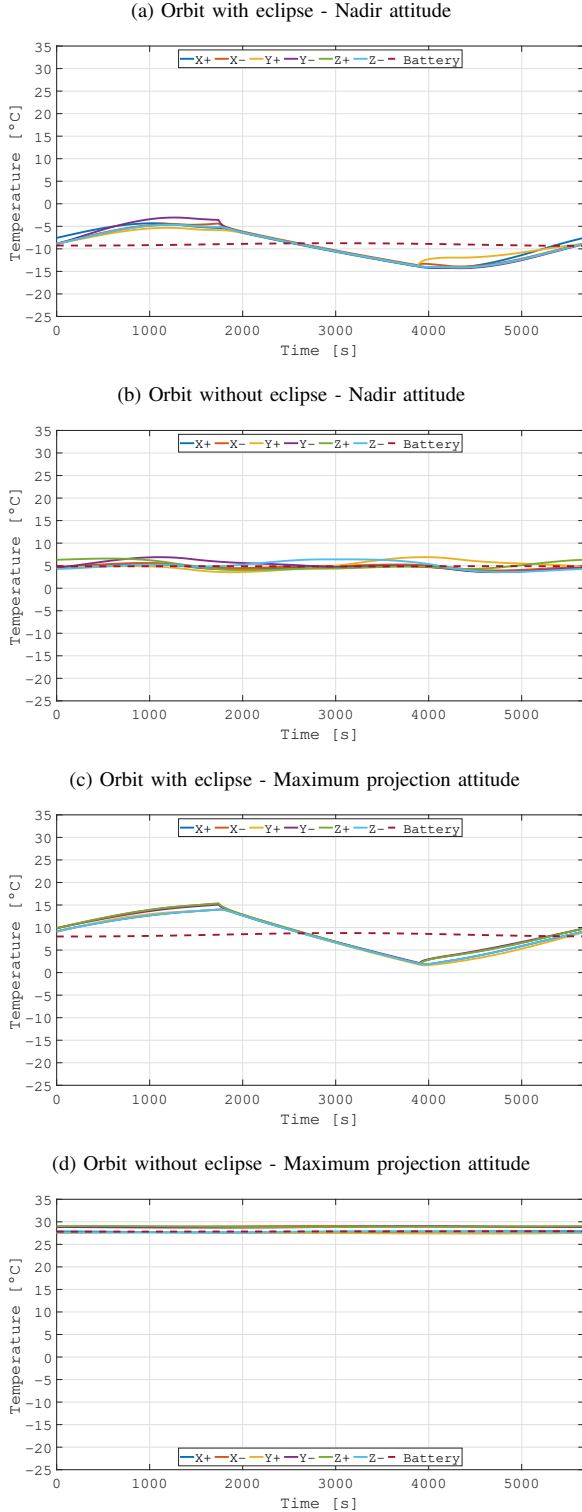
Analyzing the behavior of the Fig. 4 curves, it is noted that the lowest operating temperatures occur for the Nadir scenario with eclipse, while the highest operating temperatures are for the Maximum Projection attitude without eclipse. This behavior results from the magnitudes for the total thermal radiation fluxes over the CubeSat. Although the thermal radiation peak is greater for the Nadir attitude, the Maximum Projection case has more surfaces facing the sun simultaneously. For all observed cases, the battery temperature is practically constant throughout the orbit, being approximately an intermediate value between the absolute temperature extremes of the photovoltaic panels. This behavior can be explained by the thermal inertia of the batteries combined with the fact that the thermal loads on them are less intense, precisely because they are located inside the CubeSat. It is worth noting that the thermal radiation fluxes only affect the external faces of the CubeSat, that is, only on the photovoltaic panels, while internally the modeling of the problem assumes a zero exchange for radiation. In this way, the temperatures of the batteries result only from the exchange of heat through conduction, which reaches them through the internal structure of the CubeSat, and from its internal generation of heat when a current passes.

Cases without an eclipse present higher temperature levels when compared to cases with an eclipse, this being an expected result because, throughout the time that the CubeSat is under the earth's shadow, it stops receiving thermal radiation of the solar-type and albedo, which are the most significant, respectively. In fact, the lowest temperatures are associated with the last moment in which the satellite is under the Earth's shadow. Furthermore, it is observed that the cases evaluated in Fig. 4 indicate that the greatest temperature variations throughout an orbit occur for the Nadir attitude, this result being explained due to the greatest variations in the total radiation flux for this case.

Table IV highlights the maximum and minimum temperatures of solar panels obtained for each of the attitude and orbit conditions analyzed so far, where it is possible to verify that the highest temperatures are obtained for the Maximum Projection scenario without the occurrence of an eclipse. The maximum temperature is approximately 29°C, while the minimum is -15°C for the case with eclipse at Nadir attitude.

In order to compare the impact of the absorptivity and emissivity of photovoltaic panels on their temperature, simulations were also carried out for two different conditions of these parameters. The scenario chosen to be analyzed was the Nadir with eclipse because the satellite presents a more

Fig. 4: Solar panel and battery temperature for $\alpha = 0, 3$, $\epsilon = 0, 3$ and $I = 0$ A



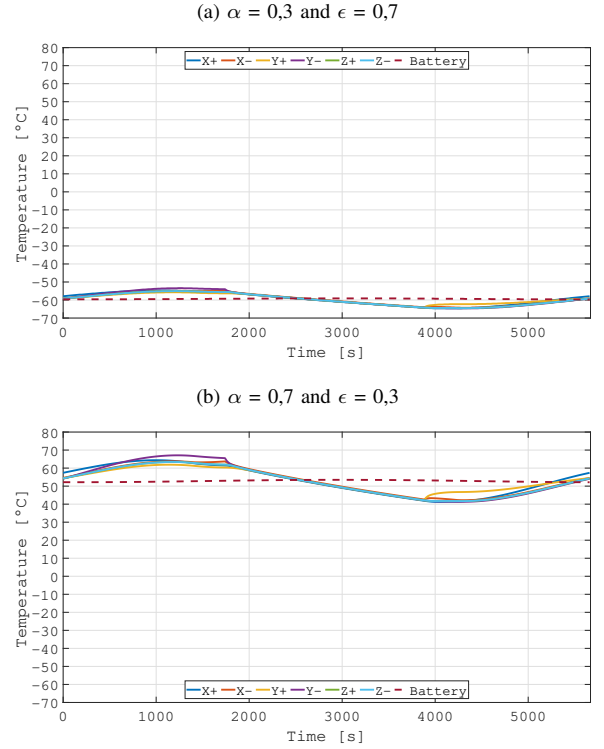
dynamic behavior for incident radiation flows. The results of this analysis consider that there is no current passing through the battery ($I=0$ A) and they are in Fig. 5.

It is possible to note, as expected, that absorptivity and emis-

TABLE IV: Extreme temperatures

Case	T_{max} [°C]	T_{min} [°C]
Nadir with eclipse	-3,05	-14,30
Nadir without eclipse	6,88	3,56
Maximum projection with eclipse	15,30	1,62
Maximum projection without eclipse	28,85	27,90

Fig. 5: Solar panel and battery temperature, orbit with eclipse and Nadir attitude



sivity have a direct relationship with the temperature reached by the satellite's photovoltaic panels. The most extreme cases are found in conditions where the values between constants differ. The results indicate that a low ratio for α/ϵ , that is, the lower the absorptivity and the higher the emissivity, result in a lower temperature reached by the panels, as observed in Fig. 5a. On the other hand, the higher the absorptivity of the panel and the lower the emissivity, that is, a high ratio of α/ϵ , the hotter the panel will be, as shown in Fig. 5b.

According to Tab. V, the hottest solar panel temperatures are obtained for the condition of highest absorptivity and lowest emissivity, that is, when the satellite has a high capacity to absorb heat, but is unable to emit it. On the other hand, for the scenario where emissivity is higher than absorptivity, the satellite ends up being more likely to lose heat with the environment, thus justifying the low temperatures observed.

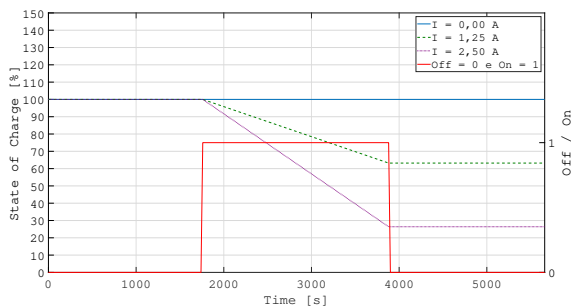
TABLE V: Extreme temperatures for different absorptivities and emissivities

Case	T_{max} [°C]	T_{min} [°C]
$\alpha/\epsilon = 0, 3/0, 7$	-53,40	-64,60
$\alpha/\epsilon = 0, 7/0, 3$	67,09	41,27

To discuss the thermal results relating to the use of the battery, it is first necessary to illustrate its operation. In this work it was considered that the battery would only be used when the CubeSat was under the Earth's eclipse, therefore scenarios without an eclipse are not addressed here, and no assessment related to its charging was carried out. To illustrate the analysis, only the Nadir attitude scenario with eclipse will be discussed for different currents passing through the battery. The occurrence of these currents in CubeSats was not evaluated and was only used to demonstrate the scope of the simulations in this work.

Figure 6 shows the battery's operating relationship and the behavior of the SoC (Eq. 4). Until the eclipse starts, the SoC for the 3 currents remains at its maximum value of 100% and the battery remains disconnected. After the start of the eclipse at time 1740 s, the battery is turned on, and this behavior is represented by the ascending step function of the red line. The SoC is represented by blue for 0 A, green for 1.25 A, and purple for 2.50 A. It is possible to visualize a descending straight line of the SoC during the eclipse phases, demonstrating the reduction in the charge stored in the battery, reaching minimum values of 63% and 28% for $I = 1.25$ A and $I = 2.50$ A, respectively. After the end of the eclipse at 3900 s, the battery is turned off, illustrated by the red line returning to value 0, while the SoC gradually returns to the 100% state by accumulating the excess energy generated by the photovoltaic panels, although this situation was not addressed in this work.

Fig. 6: Battery operation and SoC through the orbit



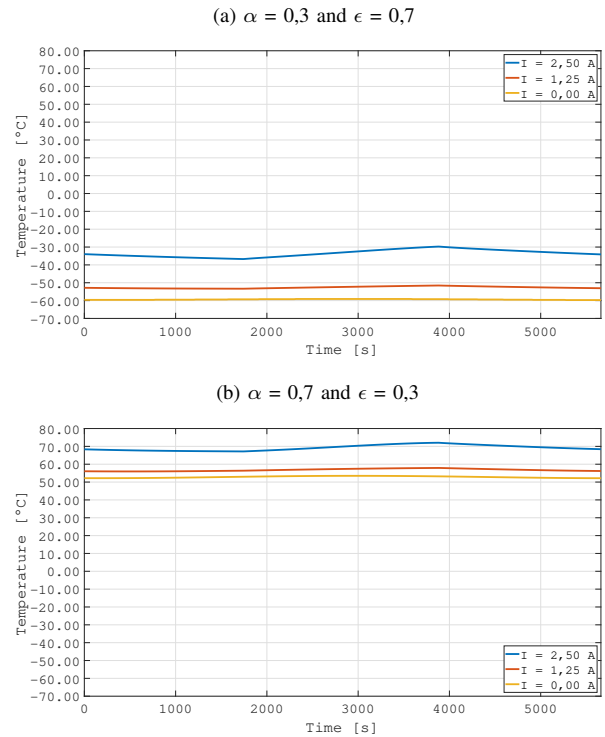
Analyzing Fig. 7, an expected behavior can be confirmed, which consists of higher temperature values when using higher currents. This behavior can be seen in both absorptivity and emissivity parameter scenarios, with the temperature for the highest current in Fig. 7a being on average 40% higher than the case without any current, resulting in an increase in approximately 30°C. For Fig. 7b, which corresponds to the hottest scenario, the battery temperature for a constant current of 2.50 A is 27% higher than that of 1.25 A and 35% for the case without no current.

These results indicate that the thermal analysis of a CubeSat battery must take into account the current passing through it, and it is necessary to know the magnitude over time.

V. CONCLUSION

Based on all the results obtained through computer simulations for the various attitudes and orbits, it was possible to see

Fig. 7: Battery temperature for different currents



that these are responsible for generating a significant impact on the satellite's thermal scenarios. Therefore, the correct dimensioning of the components is extremely important for the satellite to be able to fulfill its mission. In addition, it was possible to verify that the battery represents the greatest potential risk of the electronic components since when exposed to extreme cold and heat conditions, it exceeds the thermal specifications determined by the manufacturers. The results indicated that surface parameters such as absorptivity and emissivity directly impact the CubeSat's temperature, and promote very different levels, depending on their combination.

Finally, simulations involving the battery also reinforce the need for the thermal and electrical areas to be integrated and resolved in a single model to estimate their behavior.

ACKNOWLEDGEMENTS

The authors are grateful for the financial support from Conselho Nacional de Desenvolvimento Científico e Tecnológico (grants number 117582/2024-7).

REFERENCES

- [1] Space Foundation, "Cubesats," 2022. https://www.spacefoundation.org/space_technology_hal/cubesats/.
- [2] S. A. Jacklin, "Small-satellite mission failure rates," *NASA Ames Research Center*, p. 46, 2019.
- [3] F. D. P. M. JUNIOR, "Avaliação do uso de tubos de calor para o controle térmico em nanossatélites," 2017. Dissertação de mestrado.
- [4] J. T. Sebastian and V. Y. Baby, "Numerical investigation of thermal energy storage panel using nanoparticle enhanced phase-change material for micro satellites," *International Research Journal of Engineering and Technology (IRJET)*, vol. 5, no. 4, pp. 2330–2335, 2018.

- [5] C. Cappelletti, S. Battistini, and B. Malphrus, *CubeSat Handbook: From Mission Design to Operations*. London Wall, London - United Kingdom: Academic Press, 2020.
- [6] P. Fortescue, G. Swinerd, and J. Stark, *Spacecraft Systems Engineering, 4th Edition*. Hoboken, New Jersey - United States of America: John Wiley & Sons Inc., 2011.
- [7] E. Morsch Filho, L. O. Seman, and V. de Paulo Nicolau, "Simulation of a cubesat with internal heat transfer using finite volume method," *Applied Thermal Engineering*, vol. 193, p. 117039, 2021.
- [8] S. Corpino, M. Caldera, F. Nichele, M. Masoero, and N. Viola, "Thermal design and analysis of a nanosatellite in low earth orbit," *Acta Astronautica*, vol. 115, pp. 247–261, 2015.
- [9] M. Bulut and N. Sozbir, "Analytical investigation of a nanosatellite panel surface temperatures for different altitudes and panel combinations," *Applied Thermal Engineering*, vol. 75, pp. 1076–1083, 2015.
- [10] P. Reiss, P. Hager, C. Bewick, and M. MacDonald, "New methodologies for the thermal modeling of cubesats," 06 2012.
- [11] J. A. Richmond, *Adaptive thermal modeling architecture for small satellite applications*. PhD thesis, Massachusetts Institute of Technology, 2010.
- [12] M. Diaz-Aguado, J. Greenbaum, W. Fowler, and G. Lightsey, "Small satellite thermal design, test, and analysis," *Proceedings of SPIE - The International Society for Optical Engineering*, 05 2006.
- [13] R. Lyon, J. Sellers, and C. Underwood, "Small satellite thermal modeling and design at usafa: Falconsat-2 applications," 02 2002.
- [14] U. SpaceLab, "GOLDS-UFSC," 2024. <https://spacelab.ufsc.br/en/golds-ufsc/>.
- [15] E. M. Filho, *A coupled irradiance: thermal 3D numerical framework for simulation of CubeSats*. PhD thesis, Universidade Federal de Santa Catarina, Florianópolis, Santa Catarina - Brasil, 2021.
- [16] D. Bernardi, E. Pawlikowski, and J. Newman, "A general energy balance for battery systems," *Journal of The Electrochemical Society*, vol. 132, p. 5, jan 1985.
- [17] Y. Lai, W. Wu, K. Chen, S. Wang, and C. Xin, "A compact and lightweight liquid-cooled thermal management solution for cylindrical lithium-ion power battery pack," *International Journal of Heat and Mass Transfer*, vol. 144, p. 118581, 2019.
- [18] S. Xin, C. Wang, and H. Xi, "Thermal management scheme and optimization of cylindrical lithium-ion battery pack based on air cooling and liquid cooling," *Applied Thermal Engineering* 224 (2023), p. 12, 2023.

Analysis of the collimation of an electron beam in a Magnetic Mirror for Possible Plasma Thruster Applications

1st Luis Ángel Fernández Ramos
Space Science and Technology Postgraduate Program
Instituto Nacional de Astrofísica, Óptica y Electrónica
 Tonantzintla, Puebla, México
 lfernandez@inaoep.mx

2nd José Eduardo Mendoza Torres
Dept. of Astrophysics
Instituto Nacional de Astrofísica, Óptica y Electrónica
 Tonantzintla, Puebla, México
 mend@inaoep.mx

Abstract— In this paper, we study the dynamics of an electron beam inside a magnetic bottle when a constant electric field parallel to the bottle axis is applied, we use Particle-in-Cell (PIC) simulations with a 1D-3V model in \hat{z} direction. It is considered that the electron beam has a temperature of 1 eV and follows a Maxwellian distribution function. We study two different cases. In the first case, the electron beam is injected inside an annular device which consists of two stages. In the first stage, called the acceleration stage, the electrons are accelerated by a constant electric field parallel to the bottle axis for a distance equal to half the total length of the annular channel of the device. Then, the accelerated electrons enter a magnetic bottle in order to control the beam divergence and reduce its mobility perpendicular to the magnetic field. This stage is called the collimation stage. In this stage, we consider the force exerted by the magnetic field gradient on the electrons. For the second case, we study the response of the electrons when the electric field and the magnetic bottle span the entire length of the annular channel. In both cases, the electric and magnetic fields point in \hat{z} direction. For simplicity, we do not consider the electric fields that could be generated by charge separation or density gradients. Finally, we also study the behavior of those electrons that fulfilled the reflection condition and are trapped between both fields.

Keywords—Electric Thruster, Magnetic Bottle, Particle in Cell, Plasma.

I. INTRODUCTION

Electric thrusters are used for small satellites, as Cubesat, and also for deep space missions. In the case of small satellites, this type of thruster is used for orbit correction, since the atmosphere interaction with the satellites produces changes in their orbit. One of the types of thrusters suitable for this purpose is the Hall effect thruster, which is very efficient. Although its thrust is small, it is also used for missions requiring long distances. In Hall thrusters, keeping the electrons in a given area is important to ionize the atoms that serve as fuel. The magnetic system of the thruster generates a magnetic field, similar to a magnetic bottle, which allows the confinement of the electrons. However, some instabilities cause a number of the electron population to leave this confinement, which decreases both the thruster's thrust and its lifetime.

Let us consider a magnetic field that points mainly in \hat{z} direction and its magnitude varies in the same direction. Let us consider, also, that the field is axisymmetric with $B_\theta = 0$ and without azimuthal variations $\partial/\partial\theta = 0$. The magnetic field must have a radial component B_r that allows the convergence of the field lines. This magnetic field topology is commonly known as a magnetic bottle.

The force that a charged particle experiences in this field is due to the Lorentz force that, in cylindrical coordinates, is represented as

$$F_z = e(v_\theta B_r - v_r B_\theta) \quad (1)$$

$$F_r = e(v_z B_\theta - v_\theta B_z) \quad (2)$$

$$F_\theta = e(v_r B_z - v_z B_r) \quad (3)$$

Since the components F_r and F_θ only produce the cyclotron motion, we are interested in analyzing the electron motion due to the axial component of the magnetic force F_z . Due to the symmetry, the component $B_\theta = 0$, and only the radial component of the magnetic field B_r needs to be found through divergence of the magnetic field, which in cylindrical coordinates is represented as

$$\vec{\nabla} \cdot \vec{B} = \frac{1}{r} \frac{\partial(rB_r)}{\partial r} + \frac{1}{r} \frac{\partial B_\theta}{\partial \theta} + \frac{\partial B_z}{\partial z} = 0 \quad (1)$$

It can be shown that if $\partial B_z/\partial z$ does not vary much with r , the radial component of the magnetic field can be expressed as

$$B_r = -\frac{1}{2} r \frac{\partial B_z}{\partial z} \quad (2)$$

Once the magnetic field components are known, we can use the momentum equation to analyze the movement of the electrons

$$\frac{d\vec{v}_e}{dt} = \frac{e}{m_e} (\vec{E} + \vec{v}_e \times \vec{B}) - \frac{\vec{\nabla} P_e}{m_e n_e} - \nu_{en} (\vec{v}_e - \vec{v}_n) \quad (3)$$

where \vec{v}_e is the velocity vector of the electrons, \vec{E} is the electric field, P_e is the pressure term, \vec{B} is the magnetic field vector, e and m_e are the charge and mass of the electron, n_e is the electron number density, ν_{en} is the collision frequency between electrons and neutral atoms and \vec{v}_n is the neutral bulk velocity.

We consider a collisionless, cold plasma, therefore, the momentum equation in (6) takes the form

$$m_e \frac{d\vec{v}_e}{dt} = e(\vec{E} + \vec{v}_e \times \vec{B}) \quad (4)$$

Equation (7) can be expanded into a set of differential equations of the form.

$$\frac{dv_z}{dt} = \frac{e}{m_e} (E_z + (v_\theta B_r - v_r B_\theta)) \quad (8)$$

$$\frac{dv_r}{dt} = \frac{e}{m_e} (E_r + (v_z B_\theta - v_\theta B_z)) \quad (9)$$

$$\frac{dv_\theta}{dt} = \frac{e}{m_e} (E_\theta + (v_r B_z - v_z B_r)) \quad (10)$$

Since we are interested in the motion of the electrons parallel to the axis of the magnetic bottle, we only need to solve the axial component of motion (8). Due to the assumption of the axisymmetric field concerning the azimuthal coordinate, then, only the radial coordinate of the magnetic field needs to be substituted, such that

$$\frac{dv_z}{dt} = \frac{e}{m_e} E_z - \frac{1}{2} \frac{e}{m_e} v_\theta r \left(\frac{\partial B}{\partial z} \right) \quad (5)$$

where the dependence on B_θ was removed due to the axisymmetric geometry. If we consider that $v_\theta \approx \text{constant}$ during the gyromotion, $v_\theta = v_\perp$. Furthermore, since r represents the Larmor radius, then the axial component of the momentum equation can be represented as

$$\frac{dv_z}{dt} = \frac{e}{m_e} E_z - \frac{1}{m_e} \mu \left(\frac{\partial B}{\partial z} \right) \quad (6)$$

In (12) we have used the mathematical definition of the Larmor radius $r_L = v_\perp / \omega_{ce}$, where $\omega_{ce} = eB/m_e$ is the cyclotron frequency, and we have also substituted the equation for the magnetic moment $\mu = m_e v_\perp^2 / 2B$. The expression found for the momentum equation in (12) allows us to know the motion of the electrons parallel to the axis of the bottle, furthermore, the force produced by the field gradient is opposite to the motion of the particle, similar to the force acting on a diamagnetic particle.

The magnetic field described above is used as one of the main schemes for plasma confinement. Confinement is possible due to the invariance of the magnetic moment, however, not all electrons entering the bottle are confined. The confinement depends on the ratio of the maximum value B_m to the minimum value B_0 of the magnetic field called the mirror ratio $R = B_m/B_0$, and the angle formed by the velocity vector with respect to the magnetic field called the pitch angle. A more detailed explanation of plasma confinement and magnetic moment invariance can be found in [1] and [2]. A consequence of the magnetic bottle structure is the decrease in the area initially covered by the electron beam as it moves to regions of higher intensity. The relationship between the initial area covered by the beam and the final area can be obtained using the definition of magnetic moment and its relationship to the magnetic field. The magnetic moment generated by an electric current is given by

$$\mu = IA \quad (7)$$

where I is the current generated due to the trajectory of the charged particle around the magnetic field line and A is the area formed by the cyclotron motion. This area is characterized by the Larmor radius. If we use (13) and the magnetic moment definition (12), we obtain

$$IA = \frac{1}{2} \frac{m_e v_\perp^2}{B} \quad (8)$$

It can be shown that the following equation is fulfilled.

$$\frac{B_0}{B_m} = \frac{A_m}{A_0} \quad (9)$$

where B_0 and B_m are the minimum and maximum values of the magnetic field, while A_0 and A_m represent the area covered by the electron beam in the regions of minimum and maximum magnetic field. For a more detailed explanation see [3].

II. PROBLEM DESCRIPTION

We simulated two different cases in order to analyze the dynamics of an electron beam in a magnetic bottle. In both cases, the electron beam enters an annular channel device through which a constant electric field is applied, parallel to the axis of the bottle, both in the \hat{z} direction. According to the assumptions of the theory described in the previous section, the only forces acting on the electrons will be the electric force and the force generated by the axial gradient of the magnetic field.

In the first case, two different stages are considered during the trajectory of the electrons. In the first stage, called the acceleration stage, the electron beam is accelerated for half the length of the channel due to a constant electric field in the axial direction. Then, the electrons enter inside a magnetic bottle, in the axial direction, to reduce the divergence of the beam. This stage is called the collimation stage. In this case, the electric and magnetic field gradient forces are considered separately.

In the second case, the electric and magnetic fields are applied along the entire channel, and the beam dynamics are analyzed when both forces act at the same time, following the mathematical model described in the previous section.

To study both cases, we used 1D-3V Particle in Cell simulations, in the axial direction. In the first part of the code, we designed the simulation domain. The domain length L , which represents the channel length, was $L = 0.115$ m with a spatial resolution Δx , and temporal resolution Δt , which follow the criteria established in [4], i.e., $\Delta x < \lambda_D$ where λ_D is the Debye Length and $\Delta t < 0.2/\omega_{pe}$ where ω_{pe} is the electron plasma frequency. We used a one-dimensional exponential model to generate the bottle, however, because the one-dimensional model cannot capture the convergence of magnetic field lines, the gradient force must be explicitly added to simulate the confinement. The model used for the magnetic field was [5]

$$B = \exp(-2(z-1)^2) + \exp(-2(z+1)^2) \quad (16)$$

with $z = z_0/L \in [-1,1]$ where z_0 is the electron position and L the domain length. The mathematical model for the magnetic field gradient was obtained by deriving the above equation

$$\frac{dB}{dz} = -[4(z-1)(\exp(-2(z-1)^2))] - [4(z+1)(\exp(-2(z+1)^2))] \quad (17)$$

From (16) it is easy to see that the magnetic field has its maximum for $z = 1$ and the minimum for $z = 0$, which gives a mirror ratio $R \approx 3.70$. This mirror ratio reduces the initial area covered by the electrons, in the same proportion.

The next step was to create the electron beam, assuming that the electrons follow a Maxwellian distribution and are uniformly distributed throughout the simulation domain. The

number of macroparticles per cell of the domain must follow the criterion $N_{cell} > 50$ [4]. The criterion of the number of macroparticles per cell is not as severe as the temporal and spatial restrictions, especially when high plasma densities are involved because the charge separation and motions on the order of the plasma frequency or even the cyclotron frequency must be solved. To get a better idea of the stringency of the restrictions, suppose a plasma of density $n \approx 1 \times 10^{18} m^{-3}$ with an electron temperature of $T \approx 20$ eV (approximate conditions of a Hall thruster), the spatial resolution, for these conditions, requires that $\Delta x < 20 \mu m$, while the temporal resolution, to solve the cyclotron motion, requires that $\Delta t < 2 \times 10^{-12}$ sec, for this reason, one must be careful when selecting the characteristics of the plasma to be studied.

III. PIC SIMULATIONS

We use a fully kinetic simulation which resolves the motion of electrons around magnetic field lines. Although we are interested in the motion of particles in the direction of the magnetic field, we need to solve the perpendicular component of the velocity at each integration step to maintain the invariance of the magnetic moment. We use the Boris method to integrate the velocity in the presence of the magnetic field, such that

$$\frac{\vec{v}^{k+0.5} - \vec{v}^{k-0.5}}{\Delta t} = \frac{q}{m} \left(\vec{E}^k + \frac{\vec{v}^{k+0.5} + \vec{v}^{k-0.5}}{2} \times \vec{B}^k \right) \quad (18)$$

where k represents the current time, q and m the charge and mass of the particle, respectively, and Δt is the time resolution. Boris's method effectively solves the magnetization of electrons and conserves energy by eliminating the electric field by defining a new pair of variables

$$\vec{v}^{k-0.5} = \vec{v}^- - \frac{q}{m} \vec{E}^k \frac{\Delta t}{2}; \quad \vec{v}^{k+0.5} = \vec{v}^+ + \frac{q}{m} \vec{E}^k \frac{\Delta t}{2} \quad (19)$$

with these substitutions a pure rotation is obtained

$$\frac{\vec{v}^+ - \vec{v}^-}{\Delta t} = \frac{q}{2m} (\vec{v}^+ + \vec{v}^- \times \vec{B}^k) \quad (20)$$

where the angle of rotation is

$$\tan\left(\frac{\theta}{2}\right) = -\frac{q \Delta t}{m} B \quad (21)$$

and the rotation vector can be written as

$$\vec{t} = -\hat{b} \tan\left(\frac{\theta}{2}\right) \quad (22)$$

We can use (22) to obtain the first rotation of the velocity vector

$$\vec{v}' = \vec{v}^- + \vec{v}^+ \times \vec{t} \quad (23)$$

Equation (23) rotates the velocity vector $\Delta t/2$. For the next rotation, we scale the magnitude to maintain the magnitude of the velocity

$$\vec{v}^+ = \vec{v}' + \vec{v}' \times \vec{s} \quad (24)$$

where the vector \vec{s} is

$$\vec{s} = \frac{2\vec{t}}{1 + t^2} \quad (25)$$

Since we are simulating a one-dimensional model, the gradient force must be added explicitly to the Boris method, in order to capture the reflection of the electrons, such that the variables \vec{v}^+ and \vec{v}^- are obtained using the following expressions

$$\vec{v}^- = \vec{v}^{k-0.5} + \frac{\Delta t}{2m} \left(q\vec{E}^k - \mu^k \frac{\partial B^k}{\partial z} \right) \quad (25)$$

and

$$\vec{v}^{k+0.5} = \vec{v}^+ + \frac{\Delta t}{2m} \left(q\vec{E}^k - \mu^k \frac{\partial B^k}{\partial z} \right) \quad (26)$$

Once the new velocities are known, the new positions are obtained

$$\vec{x}^{k+1} = \vec{x}^k + \vec{v}^{k+0.5} \Delta t \quad (27)$$

In this case we only update the axial position. The method described above can be summarized with the next sequence of steps:

1. Compute the magnetic field B in the particle position in the time k using (16).
2. Compute the magnetic moment μ of the particle i in the time k .
3. Compute the magnetic gradient $\partial B/\partial z$ in the particle position in the time k using (17).
4. Compute \vec{v}^- using $\vec{v}^{k-0.5}$ using (25).
5. Compute the first half rotation \vec{v}' using (23).
6. Compute the second half rotation \vec{v}^+ using (24).
7. Compute $\vec{v}^{k+0.5}$ using (26).
8. Update the particle position using Leap-Frog (27).

IV. RESULTS

The simulations were done at the LABORATORIO NACIONAL DE SUPERCÓMPUTO DEL SURESTE DE MÉXICO (LNS) of the Benemérita Universidad Autónoma de Puebla (BUAP). For both cases, an electron beam with a numerical density $n = 1 \times 10^{12} m^{-3}$ and a temperature $T = 1$ eV was simulated. A maximum magnetic field of $B_{max} = 300$ Gauss and an electric potential $\phi = 300$ V were used. For these characteristics, the stability criteria, i.e., the conditions for not having values generated by computational errors in the simulation process, require that $\Delta x < 7 \times 10^{-3}$ m and $\Delta t < 2 \times 10^{-10}$ sec. The values used for spatial and temporal resolution were $\Delta x = 2 \times 10^{-3}$ m and $\Delta t = 1 \times 10^{-10}$ sec. The spatial resolution leaves a total of 58 nodes and 57 cells, so 2875 macroparticles were simulated. In both cases, the electron beam was uniformly distributed along the domain.

For the first case, we simulated a total time of $t = 15 \mu s$ corresponding to 75000-time steps (vertical axis of the left panels of figure 1). We analyzed the behavior of the electron beam through the numerical density and the evolution of the velocity distribution function. We developed four simulations associated with Figures 1 – 4, the reason why the velocity distribution of the electrons is slightly different in each figure, is a consequence of the generation of random numbers,

however, the initial conditions for each simulation were the same. The simulations show the formation of two populations of electrons along the domain (Figure 2), with approximately the same number of particles. The fast population represents those electrons accelerated by the electric field, and the slow population is associated with those electrons placed inside the bottle without being accelerated before.

Another important phenomenon is the accumulation of electrons that forms right in the middle of the channel from iteration 7500, once both populations are fully visualized. This accumulation travels along the domain, and near iteration 40000, the population of fast electrons decreases due to the exit of electrons from the channel and the force due to the gradient, which slows down their movement. In fact, in the left panel of Figure 3 between the values 0.6 and 0.8 of the horizontal axis, between iteration 20000 – 50000, almost vertical lines can be seen associated with those electrons that experienced accelerations in a small-time interval, that is, they were very close to the entrance to the magnetic bottle, such that when entering this region, the force due to the magnetic field gradient could produce their deceleration, confining them inside the bottle. Furthermore, the histogram in Figure 3

shows a dramatic reduction in the population of fast electrons, suggesting that electrons with higher velocities escape from confinement. These points are supported by the fact that, out of 2875 simulated electrons, 1321 escaped, a value that represents less than 50%, i.e. those electrons close to the magnetic bottle were confined.

For the second case, we performed two simulations. In the first simulation, we used the same values as the first case for the magnetic field and the electric potential. The simulation shows that the gradient force is not strong enough to confine the electrons and before 8000 iterations, the electron beam had completely escaped. For the second simulation, we increased the value of the magnetic field, the gradient, and the mirror ratio and found that the electron beam remains confined and bounces between the ends of the bottle. In the right panel of Figure 4, it can be seen that around iteration 3000, those electrons whose pitch angle was smaller than the critical angle escaped, while all the others were reflected. Areas of lower density can also be seen near the exit of the bottle; this indicates that the reflection of the electrons does not occur precisely in the area of the highest magnetic field intensity.

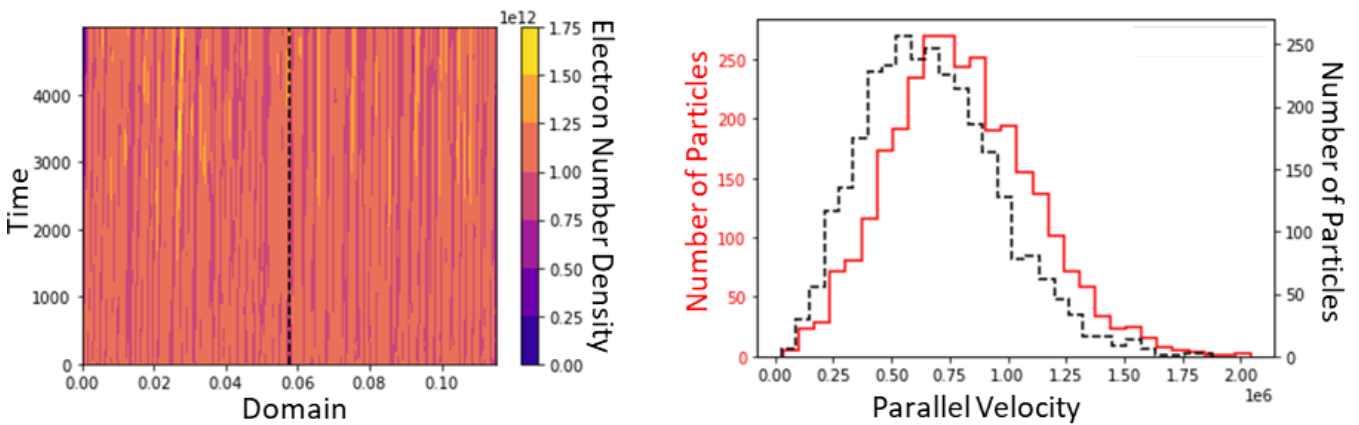


Figure 1. **Left.** Representation of the electron density for different times as a function of the position in the spatial domain. On the y-axis, the time expressed in terms of iterations is represented. On the x-axis, the spatial domain is represented by a position within the channel. The colors represent the density according to the bar on the right side. This particular case corresponds to the time $t=5000$ iterations. The dashed line corresponds to the location where the fields separate. **Right.** Velocity distributions for the initial time of the simulation (black line) and, for the final time (red line). The scales corresponding to each distribution are shown with the corresponding colors. On the x-axis, the velocity of the electrons is represented in a direction parallel to the axis of the magnetic bottle. It can be seen that the velocity values cover a range from 0 to 2×10^6 m/s.

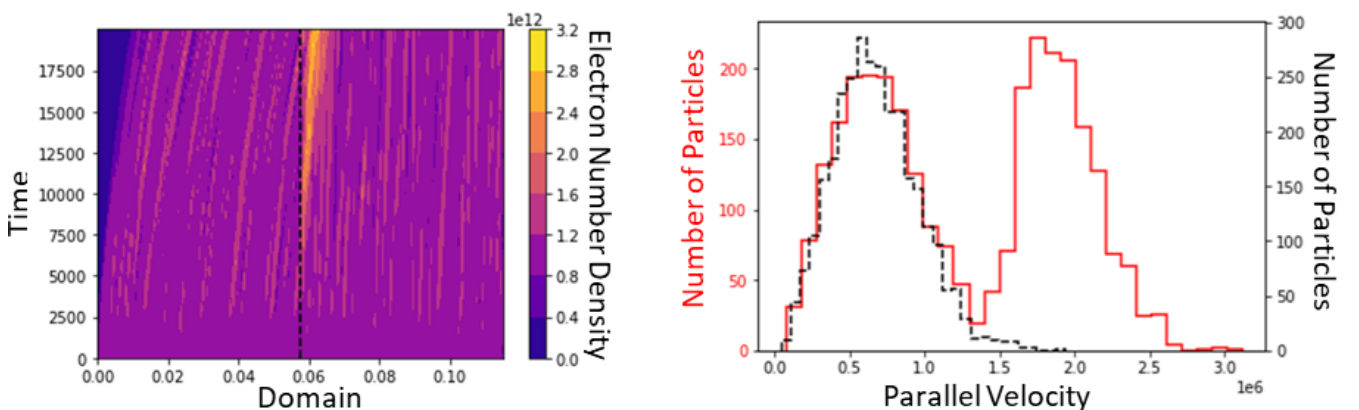


Figure 2. **Left.** Like Figure 1, the left panel shows the number density of electrons. This particular case corresponds to the time $t=20000$ iterations. The dashed line corresponds to the location where the fields separate. **Right.** For this specific case, a third velocity distribution (red line) can be observed. This distribution is associated with a population of fast electrons, which was accelerated by the electric field.

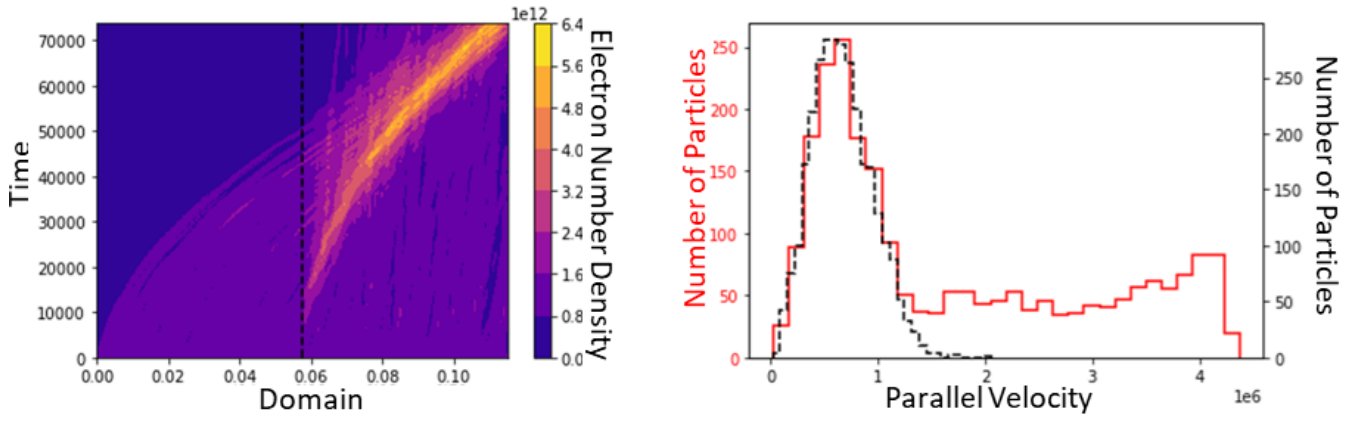


Figure 3. **Left.** Like Figure 1, the left panel shows the number density of electrons. This particular case corresponds to the time $t=75000$ iterations. The dashed line corresponds to the location where the fields separate. **Right.** A decrease in the fast electron population is observed. This decrease is associated with the fact that some fast electrons have escaped from confinement.

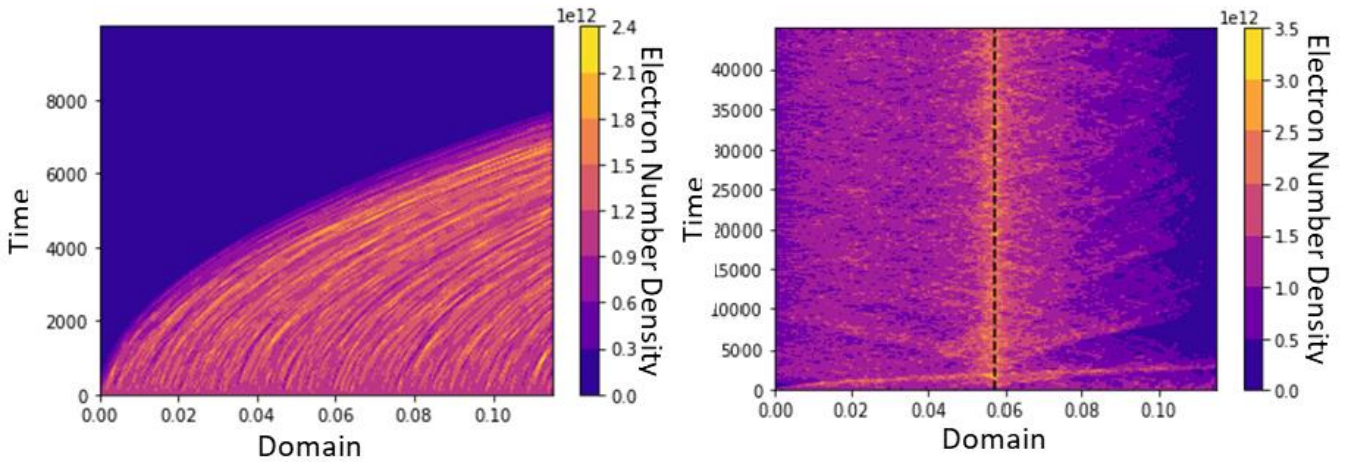


Figure 4. **Left.** Representation of the electron density for different times as a function of the position in the spatial domain. On the y-axis, the time expressed in terms of iterations is represented. On the x-axis, the spatial domain is represented by a position within the channel. The colors represent the density according to the bar on the right side. This particular case corresponds to the time $t=10000$ iterations. **Right.** Representation of the electron density for different times as a function of the position in the spatial domain. On the y-axis, the time expressed in terms of iterations is represented. On the x-axis, the spatial domain is represented by a position within the channel. The colors represent the density according to the bar on the right side. This particular case corresponds to the time $t=45000$ iterations. The dashed line corresponds to the location where an accumulation of electrons is observed

Finally, we calculate the thrust that can be produced with this number of macroparticles. In practice, it is simpler to calculate thrust using the particle beam current due to the mass flow rate

$$T = \dot{m}v_{ex} = MQv_{ex} = \frac{I_b M v_{ex}}{e} \quad (28)$$

where T is the thrust, \dot{m} is the mass flow rate, v_{ex} is the exhaust velocity, M is atomic mass, Q is the flow rate and I_b is the beam current.

In Figure 5 we plot different values of the thrust generated by the electron beam as a function of the pitch angle dispersion, represented as the standard deviation of the angle distribution function, and the inverse mirror ratio. A decrease in thrust can be observed as the mirror ratio increases, this is due to electron confinement. Likewise, if we increase the pitch angle dispersion, the number of confined electrons also increases. A more detailed analysis of this thrust generation process can be found in [3].

V. DISCUSSION

In the previous analysis, we neglected thermal motions and collisions because the velocity of the particles is modified. In addition, those magnetized particles modify their pitch angle also, which causes them to disperse and escape from confinement easily. For the study, it would seem that adding collisions between particles could be beneficial because it would decrease the number of trapped particles, producing more thrust. However, we must remember that the diffusion of the plasma, perpendicular to the magnetic field, is directly proportional to the collision frequency, which could represent a problem of plasma loss due to diffusion. For this reason, the research should be extended to two dimensions and the use of other mathematical models to simulate the magnetic bottle, or failing that, other collimation methods, in order to quantify the loss of thrust as a consequence of electron trapping or diffusion processes, as well as the effects of the model on the accumulation of particles in some regions, to find physically more precise results. This last point is important because this accumulation can generate instabilities in the plasma and thrust reduction.

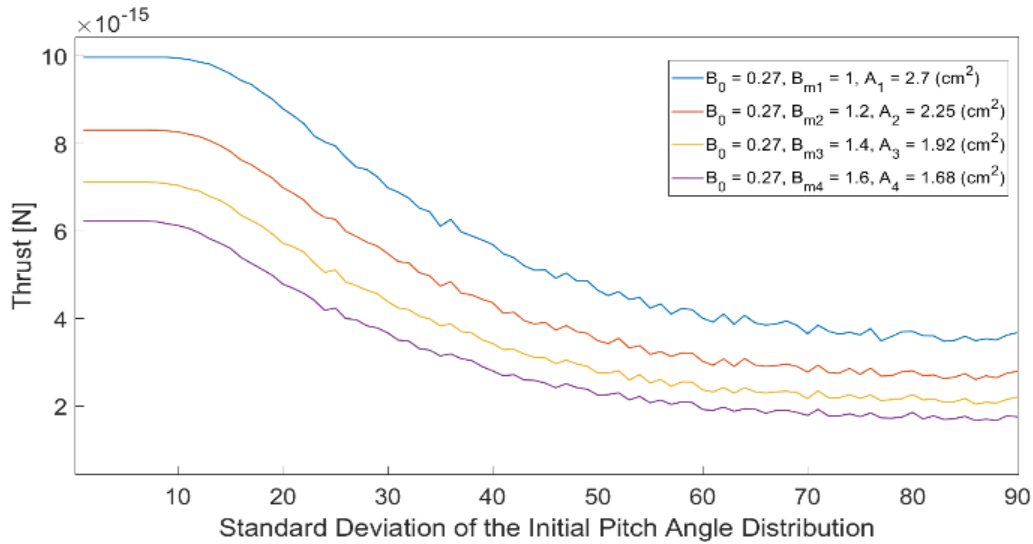


Figure 5. Values corresponding to Case 2. Thrust generated by the electron beam after being accelerated, for different values of the mirror ratio. In the x-axis, the dispersion of the pitch angle is represented by a standard deviation of the initial distribution for 2875 electrons. The parameter A corresponds to the area the electrons cover after being collimated.

VI. CONCLUSIONS

Applying the electric and magnetic fields separately generates the formation of a third population of electrons that escape from the bottle. This new population produces the thrust. To prevent a certain part of the electrons from being confined and losing thrust, the electrons must be accelerated from the left boundary of the domain (which represents the entrance to the thruster channel), otherwise, a large part of the simulated particles (approximately 50%) will be trapped in the bottle.

The shift of the maximum value of the number density in Figures 1-3 allows us to get an idea of the number of particles trapped in the bottle. The application of the magnetic bottle allows us to obtain a reduction of the area initially covered by the electrons, according to (15).

From the left panel of Figure 4, we can conclude that all the electrons escape from the bottle to produce thrust but, if the magnetic field intensity is increased (right panel of Figure 4), the electron dynamics become more complex because the beam bounces off the domain boundaries, forming regions of high and low electron density. Furthermore, on the right side of the dashed line, in the time interval 5000 - 10000, a slope is formed and increases its steepness in the interval of 5000 iterations. Around iteration 25000, the slope appears to remain constant. This behavior is not perceived on the left side of the dashed line.

A rather interesting pattern is the evolution of the maximum density, tracing a vertical line in yellow

corresponding to the highest values in Figure 4. This region, of high density values, is formed in regions close to the middle of the domain. This phenomenon needs to be studied further to understand the causes and conclude whether it is related to the mathematical model.

ACKNOWLEDGMENTS

Luis Ángel Fernández Ramos wants to thank Consejo Nacional de Humanidades, Ciencia y Tecnología (CONAHCYT) for the postgraduate grant. The authors thank Benemérita Universidad Autónoma de Puebla for allowing the use of Laboratorio Nacional de Supercómputo del Sureste de México (LNS) for the time allocated to do a series of simulations that served to obtain some of the results presented in this work.

REFERENCES

- [1] Chen, F. F., "Introduction to Plasma Physics and Controlled Fusion" Springer, pp. 29 – 33, 2016.
- [2] L. Ángel Fernández, J. E., "Charged particle reflection in a magnetic mirror". *Rev. Mex. Fis. E*, pp. 1 – 5, 2024.
- [3] Fernández-R., L. A.-T., "Thrust Generation Through a Collimated Electron Beam in a Magnetic Mirror and its Possible Applications in Plasma Thrusters". In *International Journal of Engineering and Advanced Technology*, pp. 1 – 7, 2024.
- [4] Boeuf, J. P., Tutorial: Physics and modeling of Hall thrusters. *J. Appl. Phys.*, 2017.
- [5] Brieda, L., "Plasma Simulations by Example", CRC Press, pp. 270 – 271, 2019.

Initial development of a Gas-Fed Pulsed Plasma Thruster for Nano and Pico Satellites

1st Helbert de O. C. Junior 2nd João David Moreira 3rd João Victor R. Bitencourt 4th Marcus Vinicius Batistuta
Gama Campus [FGA] *Phys. Inst. [IF] PPL* *Phys. Inst. [IF] PPL* *Gama Campus [FGA]*
Univ. of Brasília [UnB] *Univ. of Brasília [UnB]* *Univ. of Brasília [UnB]* *Univ. of Brasília [UnB]*
Brasília, Brazil Brasília, Brazil Brasília, Brazil Brasília, Brazil
hoc.junior@gmail.com joaodm12@hotmail.com prof.joaobitencourt@gmail.com mvbatist@gmail.com

5th José Leonardo Ferreira 6th Rodrigo A. Miranda 7th Paolo Gessini 8th Júlio César de Melo Almeida
Phys. Inst. [IF] PPL *Gama Campus [FGA]* *Gama Campus [FGA/UnB]* *Phys. Inst. [IF] PPL*
Univ. of Brasília [UnB] *Univ. of Brasília [UnB]* *Brazilian Space Agency [AEB]* *University of Brasília [UnB]*
Brasília, Brazil Brasília, Brazil Brasília, Brazil Brasília, Brazil
jleonardoferreira@uol.com.br rmiracer@gmail.com paolo.gessini@aerospace.unb.br julio.eletromec.if@gmail.com

Abstract—The application of electric propulsion systems in CubeSats can increase lifetime and diversity of possible missions, with improved capabilities in orbital maneuvers. In this work, a control and power electronics circuit for a pulsed plasma thruster was developed, constructed and tested, considering restrictions in size, weight, and power availability of a CubeSat. This proof of concept made use of 3D printing technology for rapid prototyping, and its initial testing was done in an atmospheric environment, in order to acknowledge circuit and geometry capabilities.

Index Terms—CubeSats, PocketQube, Pulsed Plasma Thruster, Power Electronics

I. INTRODUCTION

The space industry is constantly searching for better ways to extend its lifetime and reduce manufacturing and launching costs for commercial satellites. The development of smart materials and alloys, alongside the miniaturization of electronic circuits, allowed the creation of small satellites, known as CubeSats, and more recently, PocketQubes [1].

CubeSats are nanosatellites, going up to a few kilograms, with a form factor of 10 cm cubes (1U). With this modular design, several units can be put together to form a larger CubeSat, increasing the capabilities of this small satellite. For example, there are proposals for a 3U CubeSat [2] and a 6U CubeSat [3].

Since its overall mass goes up to a few kilograms, the launch of a Cubesat has a reduced cost, making it possible to catch a ride in other launches (piggyback), be deployed from the International Space Station (ISS), or share the costs of launching several satellites at once.

The reduced cost allows universities and private companies to experiment with space-bearing technologies, train and qualify personnel to work in the space industry, and realize scientific missions. Indeed several studies were made forecasting the increase in small satellite launches.

With new technologies migrating to CubeSats and increased market demand for space-based platforms, the next step in the

Cubesats long march could be the integration of small electric propulsion systems. These propulsion systems have shown their worth by extending the satellite's lifetime, allowing orbital maneuvers and different science missions as seen in the SpaceX StarLink constellation or the Hayabusa and Rosetta missions.

A. Electric Propulsion Systems

Propulsion systems are how satellites achieve different maneuvers in space. They rely on Newton's third law to move forward by pushing backward the propellant mass. In chemical rockets, this is achieved by burning up the rocket fuel and expelling the resulting hot gasses. In an electrical thruster, the propellant mass accelerates by electricity, pushing it backward and the space vessel forward.

According to reference [4], from the rocket equation, we can get two physical quantities: Thrust and Specific Impulse (ISP). The first one, thrust, describes how much force a propulsion system can apply to the vehicle. Specific Impulse is a thrust efficiency measurement, defined by the rate between thrust and propellant consumption rate. The higher a thruster's ISP is, the faster its ejected mass is. In other words, greater ISP allows higher final velocities. Electric thrusters achieve low thrust but very high ISP's, being more efficient than chemical rockets and allowing higher velocities.

The drawback of electric thrusters is their low thrust, meaning that take more time to accelerate. Electric propulsion involves several types of thrusters, with different geometry, forms of ionization, and means of accelerating charged particles. But all of them have in common the use of electricity to modify and (or) accelerate the propellant. We can divide these systems into three major categories: electrothermal, electrostatic, and electromagnetic, with several more subcategories.

Electrothermal thrusters utilize a heating element to heat the propellant, generating pressure in the heating chamber due to thermal expansion. This pressure is released similarly to chem-

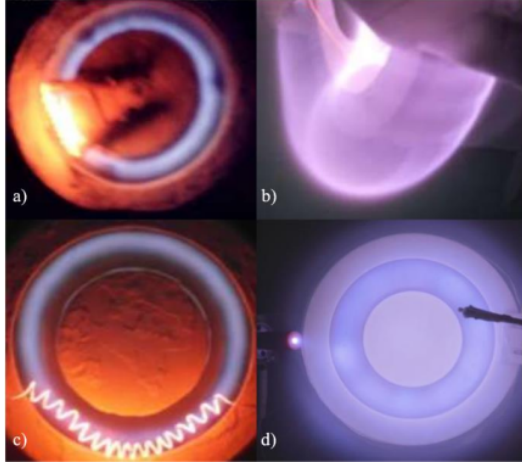


Fig. 1. The family of PHALL Thrusters developed at PPL. a) PHALL-I, with a 27 cm diameter and 260 Gauss magnetic field. b) PHALL-IIa, with 15 cm diameter and 1100 Gauss magnetic field. c) PHALL-IIb with 15 cm and 100 Gauss magnetic field at the center of the channel. d) PHALL-IIc with the introduction of Macor ceramics, hollow cathode, and SmCo magnets.

ical rockets, obtaining thrust from the exhaustion of hot gases. One example of this thruster is the ResistorJet. Electrostatic thrusters depend on electric fields and their interaction with the charged propellant particles to accelerate them and obtain their thrust. For example, we have the Gridded Ion Thruster. Electromagnetic thrusters have a combination of electrical and magnetic fields interacting together with the charged propellant particles to achieve thrust. An example is the Hall thruster.

1) *Hall Thrusters*: This electric thruster is very common in the aerospace industry due to its high thrust and high ISP compared to other electric thrusters. For example, we have the SMART-1 mission [5]. This thruster utilizes a hollow cathode as a source of electrons. It's responsible to ionize the propellant gas and neutralize the propulsion plume. The electrons shooting generated by the hollow cathode travel inwards the thruster chamber, attracted by the anode ring. In this chamber, there is a magnetic field that traps the electrons in a circular pattern. The collisions between the circulating electrons and the neutral gas atoms ionize the propellant and the difference in electrical potential between the Hall current and the anode propels the positive ions.

Here at UnB, in the Plasma Physics Laboratory, a Hall thruster with permanent magnets was developed, achieving over 45 mN of thrust. We can see one iteration of this development in Fig. 1.

2) *Ampibolar Thrusters*: These electric thrusters accelerated positive ions and negative charges as well, resulting in a neutral plume. One advantage of this kind of thruster is the lack of necessity to have a hollow cathode neutralizing the exhaust plume. According to reference [6] the propellant is injected in a chamber that has an antenna around it. The oscillating electromagnetic field emanating from the antenna ionizes the neutral gas and heats the plasma. The interaction between the plasma, the static magnetic field, and

the oscillating electric field accelerates the charged particles creating thrust. This phenomenon is being studied at the Plasma Physics Laboratory at UnB.

3) *Pulsed Plasma Thrusters*: This electric thruster known as PPT can work with solid, liquid, or gaseous propellants. In the solid state first, we have the ablation process, then ionization and acceleration. The latter two are very similar in all three states. An initial high-voltage arc discharge is responsible for ablating the material (if solid propellant is utilized) and creating a path of low impedance between the electrodes. Then, a low voltage high current discharge contributes to the ionization of the propellant and the heating of the plasma gas. The interaction between the potential across the electrodes and the induced magnetic fields accelerates the charged particles generating thrust. This cycle repeats several times in succession, giving a pulsed operation regime.

4) *Electric Thruster in the Market*: In the following table I we can see some parameters of electric thrusters currently under development. This data was taken of [16] (p. 52).

TABLE I
ELECTRODYNAMIC PROSULSORS (PROPULSORES ELETRODINÂMICOS)
(PULSED)

Thruster Model	Thrust	Isp	Power	Size
CAT xenon (PhaseFour)	2.77 mN	498 s	50 W	$1.2 - 2 \text{ U}$
CAT water (PhaseFour)	0.44 mN	7852 s	50 W	$1.2 - 2 \text{ U}$
uPPT (Busek)	0.5 mN	700 s	2 W	0.5 U
uBLT (U.I. USA)	54 uN	–	4 W	250 g
PPTCUP (Mars Space)	$25 - 35 \text{ uN}$	600 s	2 W	280 g
uCat (GWU)	$1 - 20 \text{ uN}$	3000 s	10 W	200 g

II. GFPPT'S CAD MODEL

Following an iterative design methodology, where each cycle brings improvements and corrections to the development process, we elected a parallel plate geometry for our initial step. The chosen dimensions aim for a 1U volume (10 cm^3), capable of housing the thruster, electronics, and propellant storage. Another factor taken into consideration was the availability of rare earth magnets and gas connections in PPL's stores, allowing for the rapid manufacturing of this first prototype. Table II encompasses all dimensions for the discharge chamber and permanent magnet's housing.

TABLE II
DIMENSIONS OF THE GFPPT-I

Dimension	Value [mm]
Chamber Length	25
Chamber Width	23
Flap Length	13
Parallel Electrode Separation	18
Parallel Electrode Width	20
Parallel Electrode Thickness	0.3
Arc Discharge Electrode Separation	between 10 and 15

Aiming for rapid prototype development, we utilized 3D printing technology for quick thruster adjustments and testing.

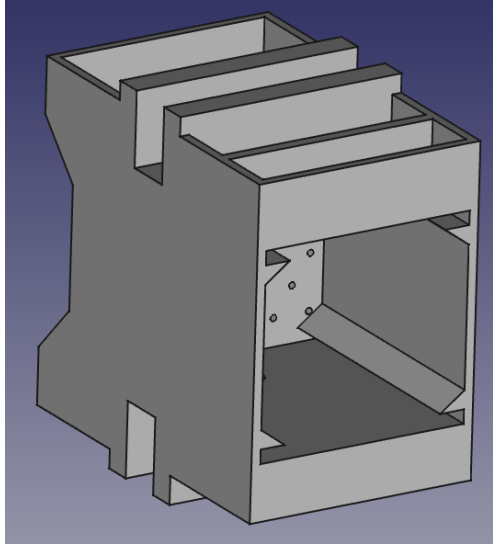


Fig. 2. CAD model of the GFPT-I, with supports for its different components. This model was then 3D printed in semi-flexible resin.

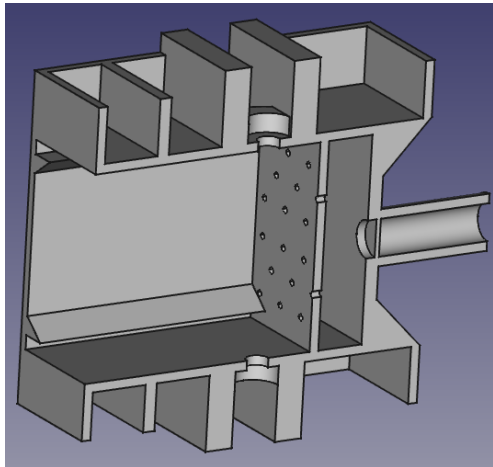


Fig. 3. A sectional view of the GFPT-I, showing in detail the perforated bulkhead, magnets quarters, and discharge chamber dimensions.

Also using already available materials, an M2 stainless steel screw was used to secure the electrodes, and high-voltage connections, and to act as initial, high-voltage, discharge electrodes. All magnets used were Samarium-Cobalt (SmCo) rare earth magnets, in cube format with 6 mm edges. Parallel electrodes were made from stainless steel.

Figs 2 and 3 show the 3D model of this iteration and its sectional view. In these figures, it is possible to see the magnet spaces, electrode supports, and a perforated bulkhead for better distribution of propellant gas. This is a preliminary iteration of this bulkhead, with CFD simulations being prepared for optimal gas distribution inside the discharge chamber. Then Fig. 11 brings its 3D printed counterpart, already with electrodes and magnets.

III. ELECTRONIC CIRCUIT

Pulsed Plasma Thrusters require two sets of electrical discharges, first a high-voltage and low-current discharge in order to ionize our gaseous propellant, creating a low resistance path for the second, relatively low-voltage and high-current discharge. Some geometries rely on two sets of electrodes or a dual-purpose single set of electrodes, like our prototype that utilizes high-voltage diodes to have separate circuits feeding the same set of parallel electrodes.

For this goal, we've defined some initial conditions to guide our circuit development, as seen in table III.

TABLE III
CIRCUIT PARAMETERS

Parameter	Value
Maximum Power Consumption	25 W
Voltage Rail	12 V
Control Circuit Voltage Rail	3.5 V and 5 V
Boost DC-DC Converter Output	between 120 V and 200 V
High-Voltage Output Pulses	between 2 kV and 13 kV
Parallel Electrode Width	20
Parallel Electrode Thickness	0.3
Arc Discharge Electrode Separation	between 10 and 15

A. Circuit

In this work, we will focus on the DC-DC Boost Converter and Flyback Pulse Driver. The boost converter is responsible for elevating our 12V power rail up to 200V (at maximum) and storing that energy in a capacitor. This is needed to give our discharge the energy density required, between 0.5 and 2 Joules per pulse. On the other hand, the flyback pulse driver generates high-voltage and low-current pulses, ionizes the propellant gas, and creates a low resistance path for the high-energy discharge.

Starting from the basic boost topology, comprising of an inductor, capacitor, diode, and switch, and with some initial conditions and design parameters, calculations were made to determine our component values. Then, these results were adjusted to commercial and ready available values. Fig. 12 brings this adjusted topology, utilizing inductors refurbished from old notebooks switched power supplies. A 555 timer generates a PWM signal for controlling both MOSFETs. A two-stage configuration was used in this initial prototype, and simple push-pull transistor amplifiers were used for driving the MOSFETs.

Then Fig. 13 has the first iteration of the flyback pulse driver, utilizing an external control signal, being from an Arduino or a 555 timer circuit, the same push-pull transistorized amplifier, and an old CRT monitor fly-back. Same as in the boost circuit, a few parasitic impedances were taken in consideration, and are in these circuit simulations. Also, we had to adjust the calculated values to commercial, and available, ones.

IV. PRELIMINARY RESULTS

We utilized free software for these computer-aided simulations, such as FREECAD, FEMM, and LTSPICE XVII. In

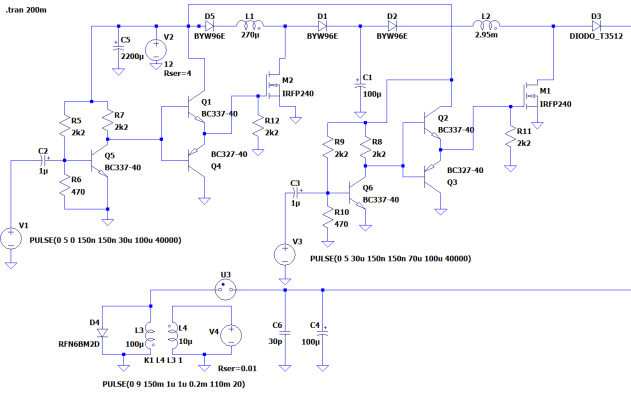


Fig. 4. DC-DC Boost converter schematic on LTSpice XVII. This topology was utilized in simulations, with some parasitic losses considered.

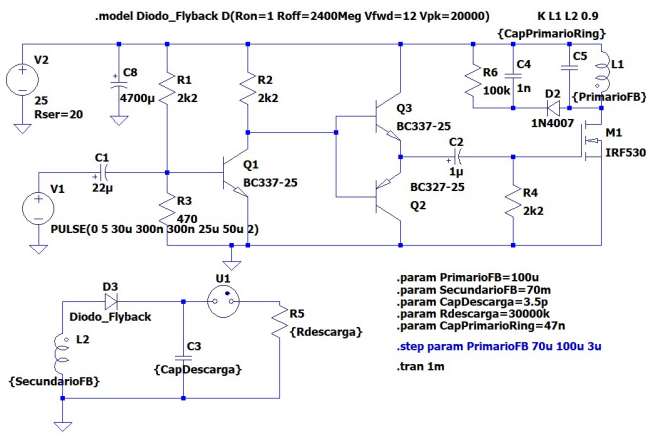


Fig. 5. Flyback Pulse Driver Circuit. This schematic is responsible for generating high-voltage pulses from TTL (transistor-transistor logic) signals.

the Frecad software, we designed this iteration model, and CFD simulations are in development. FEMM was utilized to visualize magnetic field lines, as well as to determine the best orientation for the magnetic north of SmCo magnets. Lastly, LTSpice XVII was responsible for electronic circuit simulations.

Then a prototype thruster was printed utilizing UV light-activated resin. Non-magnetic stainless steel was used as the parallel electrodes, and brass screws were used as high-voltage electrodes, as seen in Fig. 11.

A. Simulation Results

1) *Magnetic Field Simulation:* The Magnetic Field confines the plasma inside the thruster's chamber, and in this interaction, the plasma density and the temperature will increase. This also confines the ionized gas collum to a nozzle shape, similar to a chemical thruster's nozzle, where this gradient in magnetic field lines can be referred to as a Magnetic Nozzle. This allows the expansion of ionized gas following the specific geometry, aiming to increase the perforce of the PPT.

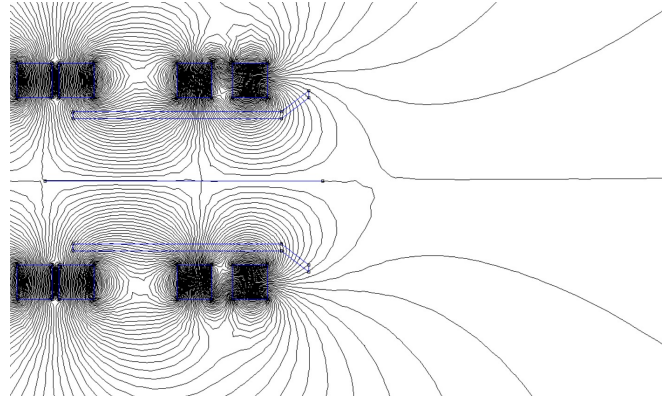


Fig. 6. FEMM simulation, showing the magnetic field lines. This permanent magnet arrangement was chosen to recreate both field nozzle geometry and strength alongside the center line.

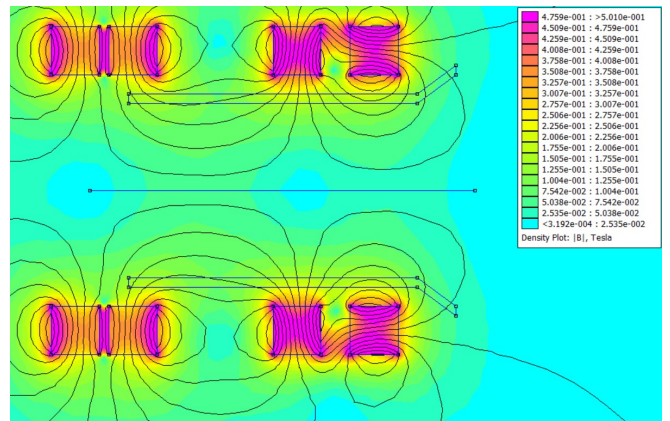


Fig. 7. FEMM simulation, showing magnetic density, in Tesla. As shown in this figure, there is a magnetic nozzle on the output of the thruster, and a field strength of around 500 Gauss around the high-voltage discharge region, reducing around 200 Gauss near the exit, producing a gradient in magnetic field.

This specific field geometric is based on the HPD experiment here in PPL and behaves similarly to other commercial thrusters, such as the Busek (MiXi), T4Innovation (Regulus), Empulsion (IFM NanoThruster) e PhaseFour (CAT-CubeSat Ambipolar Thruster) [16]. These thrusters have in common the use of neodymium or samarium-cobalt permanent magnets, in a ring shape with different diameters and thicknesses, for the creation of the required magnetic field gradient.

2) *LTSpice Simulations:* In the LTSpice XVII environment, we can run different circuit analyses. For this work, and to prove our circuits can reach the desired output, we had run Transient analysis only. With these results, we could see possible heat spots, peaks in current draw, transients, and power consumption, leading to component choices and redesigns.

First, as seen in Fig. 5, the flyback driver circuit was tested. By utilizing a Neon bulb model, in comparison with the Mayr Arc Discharge model [17], [18], we could recreate the dynamic of this arc discharge. The output of this simulation can be

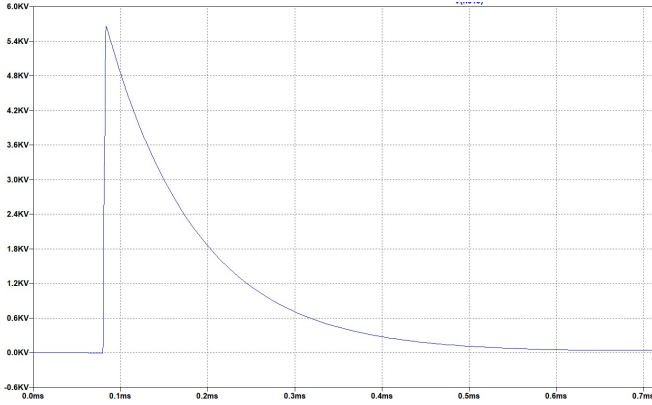


Fig. 8. LTSpice simulation, showing the high-voltage output of the flyback transformer. It is possible to see a sudden rise in voltage, characteristic of the driving pulse, followed by the discharge of this system, going from around 6 kV down to 0 V.

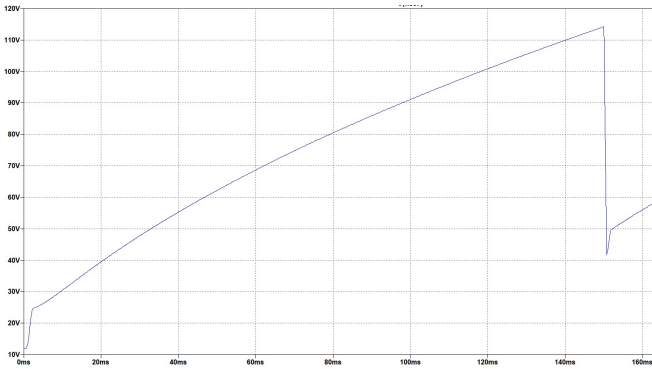


Fig. 9. LTSpice simulation of the DC-DC boost circuit output. In this graph we can see the charging of output capacitor, during 150ms, then its discharge trough a neon bulb, after which its charging cycle continues. A left over voltage is also considered in this simulation, since due to plasma arc discharge dynamics, in this model, a residual charge always stays in the output capacitor.

seen in Fig. 8. When there is a pulse signal on the flyback’s primary coil, a high-voltage pulse is observed on its secondary coil. This, in turn, triggers the neon bulb, allowing current to flow from one electrode to another. Since there are energy storage components in this circuit, we have that characteristic capacitor discharge curve, from 5.5 kV down to 0 V. This cycle repeats every 150 ms, for a frequency of around 6 Hz.

Then we have the boost charge curve, followed by its discharge when a high voltage pulse triggers the neon bulb, as can be seen in Fig. 4. During the period of 150 ms charges are accumulated in its output capacitor, reaching a potential energy of over 100V. This is necessary to achieve an energy density between 0.5 J and 2 J. Fig. 9 brings one of these cycles, showing a charge period, discharge pulse flowed by another charge period. Since the plasma generated is a dynamic entity, is natural that its time-varying impedance wouldn’t sustain low resistance pathways indefinitely, leaving some energy behind on the capacitor. For this, charge and discharge periods can be adjusted to maintain constant discharge energies.



Fig. 10. 3D Printed GFPPT-I. Following the CAD design and specifications, three permanent magnets were inserted in the front most dedicated space. Stainless steel was utilized on the parallel electrodes, with a 45° flap, and steel screws were utilized to attach the high-voltage feed cables, as well to act as a high-voltage electrode.

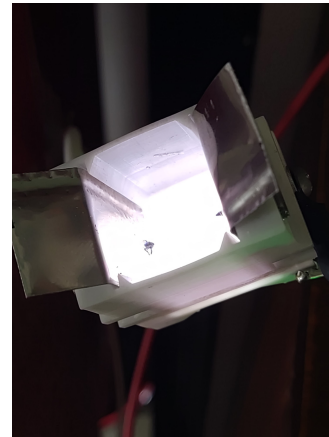


Fig. 11. GFPPT proof of concept. The main body was 3D printed utilizing semi-flexible resin, SmCo magnets were temporarily inserted in its locations, stainless steel electrodes were handcrafted and brass screws acted as high-voltage electrodes. For this initial circuit test, the thruster was at atmospheric pressure, and argon gas was inserted in the discharge chamber, giving this distinct whiteish glow (without the presence of argon gas, this atmospheric discharge has a purple-pink glow, characteristic of air ionization.)

B. Electronic Circuit Prototype

Following the simulation results, a prototype circuit was built utilizing a universal perforated board. Initial testing of both circuits has shown great results, with repetitive high-voltage pulses ranging from a few Hertz up to tens of kilo Hertz, and on the other hand, the boost circuit was able to achieve over 130 V within a 3 Hz test cycle.

Fig. 12 brings the boost circuit prototype. The PWM signal comes from an external source, responsible for driving both MOSFETs. Since our push-pull amplifier inverts the control signal, the Duty-Cycle has to also be inverted. For this, our control signal has a 10 kHz frequency, with a duty cycle of 30%. This in turn has a 70% duty-cycle exciting both

MOSFETs gates. A 50% duty cycle was also utilized in both simulation and testing.

Then, Fig. 13 has the prototype circuit of the flyback-driver, mounted also on a universal perforated board. This circuit was utilized in different high-voltage experiments in LFP/IF. For this application, the frequency of the pulses was reduced to 3 Hz, with a pulse width of 300 μs. Arcs could be obtained within 30 mm of electrode separation, in the presence of argon gas.

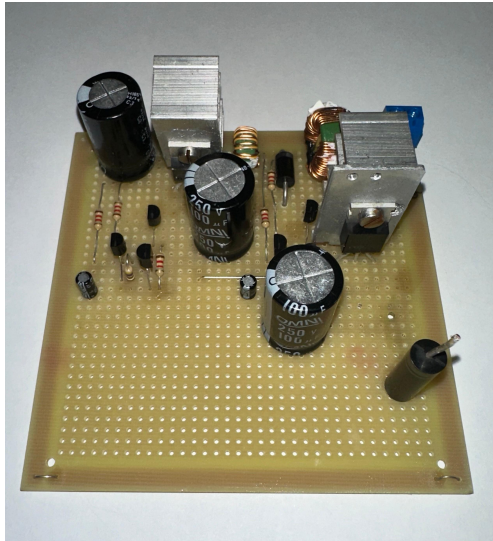


Fig. 12. GFPPT boost circuit prototype. At present time, the control signal comes from an external source, and the upright diode is the output. The empty space on the perforated board is reserved for later application of the dedicated timer circuit.

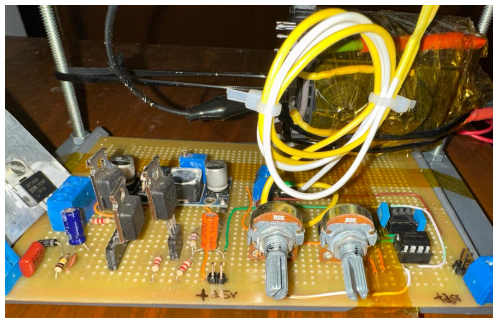


Fig. 13. GFPPT flyback pulsed prototype. This circuit is responsible for creating the high voltage pulse responsible of ionizing the gas inside the chamber

V. FUTURE STEPS

The current state of the GFPPT has achieved important milestones in its development. Although the results shown here are from its first iteration, it reassured the team in pursuing this line of Electric thrusters and development rhythm.

However, there are still some steps to achieve the final product and fully understand this kind of Electric Thruster. Here are some of the next steps in further development:

- Test the GFPPT in the vacuum chamber with different bulkhead geometries;
- Simulate the neutral gas dynamics after it passes the bulkhead. Does a turbulent flow improve ionization efficiency, or will a laminar flow be better at achieving higher thrust?
- Analyze the magnetic field inside the GFPPT's Chamber with different permanent magnet arrangements and orientations, with changes being backed from FEMM simulations in association with experimental results;
- Use a Langmuir probe to measure plasma characteristics;
- Miniaturize the GFPPT and its essential circuitry to use on CubeSats, and later with PocketQubes;
- Use a 'load cell' to measure directly the thrust of the GFPPT in its varied configurations;
- Compare the thrust and specific impulse of a GFPPT with, and without permanent magnets, in order to validate the improved performance,

The future of the GFPPT holds a lot of possibilities and innovative solutions.

VI. CONCLUSIONS

In this work, a control and power electronics circuit for a pulsed plasma thruster was developed, constructed, and tested, considering restrictions in size, weight, and power availability of a CubeSat. A DC-DC Boost voltage converter circuit was designed to drive the electrical propulsion system and simulated with the LTSPICE XVII software, using Mayr's discharge model [17], [18], with the discharge energy being estimated to be around 0.5 J per pulse. An electric power and control circuit prototype was built, with off-the-shelf components. In an atmospheric condition, the circuit was evaluated to validate its performance, through a dielectric breakdown of air and a mixture of air and pure argon gas. Both circuits operated within 30 W of electrical power. Improvements in the efficiency of this circuit can be made, in order to better accommodate the needed power within a CubeSat solar power budget. According to simulations the magnet's orientation can produce a magnetic nozzle, with a strong magnetic mirror closure at the beginning of the discharge chamber, and around 200 Gauss of field intensity alongside its center line. Lastly, resin 3D printing technology was used to rapidly prototype this thruster.

ACKNOWLEDGMENT

The authors appreciate the effort of the Plasma Physics Laboratory (PPL/IF), the Advanced Space Propulsion Laboratory (ASP Lab/LaSE), and the University of Brasilia (UnB), along with its faculty, for providing us with the means to develop this pulsed thruster.

REFERENCES

- [1] M. S. Uludag, et al, "Design of a Micro-Propulsion Subsystem for a PocketQube", Delft University of Technology, 2019.
- [2] Conversano, Ryan W., and Richard E. Wirz. "Mission capability assessment of cubesats using a miniature ion thruster." *Journal of Spacecraft and Rockets* 50.5: 1035-1046, 2013.
- [3] Tsay, Michael, et al. "LunarCube: A deep space 6U CubeSat with mission enabling ion propulsion technology.", 2015.

- [4] Goebel, Dan M., Ira Katz, and Ioannis G. Mikellides. *Fundamentals of electric propulsion*. John Wiley & Sons, 2023.
- [5] Milligan, D., et al. "SMART-1 electric propulsion operational experience." *Proceedings of the 29th International Electric Propulsion Conference*. 2005.
- [6] Wright, W. P., and P. Ferrer. "Electric micropropulsion systems." *Progress in Aerospace Sciences* 74: 48-61, 2015.
- [7] J. L. Ferreira, et al, "A Permanent Magnetic Hall Thruster for Satellite Orbit Maneuvering with Low Power", *Proc. of the 37th COSPAR Scientific Assembly*, Montreal, Canada, p. 160, 2008.
- [8] J. L. Ferreira, et al, "Permanent Magnet Hall Thruster Development for Future Brazilian Space Missions", *Computer Applied Mathematics Springer (SBMAC)*, 2015.
- [9] E. E. N. Macau, et al, "The Aster Mission: Exploring for The First Time a Triple System Asteroid", *Proc. of the 62th International Astronautical Congress (IAC)*, 2010.
- [10] F. Marchis, P. Descamps, D. Hestroffer and J. Berthier, *Nature*, pp. 436-565, 2005.
- [11] V. V. Zhurin, H. R. Kaufmann and R. S. Robinson, "Physics of Closed Drift Thruster (review article)", *Plasma Sources Science and Technology*, vol. 8, p. R1, 1999.
- [12] M. D. Goeble and I. Katz, "Fundamentals of Electric Propulsion: Ion and Hall Thrusters", *JPL Space Science and Technology Series*, 2008.
- [13] O. C. Winter, et al, "Controlling The Eccentricity of Polar Lunar Orbits with Low Thrust Propulsion", *Mathematical Problems in Engineering/Space Dynamics*, Ed. Hindauy Publishing Corporation, 2009.
- [14] A. A. Sukhanov and A. F. B. Prado, "Constant Tangential Low-Thrust Trajectories Near an Oblate Planet", *Journal of Guidance, Control and Dynamics*, vol. 24, no. 4, pp. 723-731, 2001.
- [15] A. A. Sukhanov, "Aster Project: First Brazilian Mission to Deep Space (invited talk)", *Proc. of the XVIII Colóquio Brasileiro de Dinâmica Orbital I-2*, p. 25, 2016.
- [16] H. O. Coelho Júnior, "Desenvolvimento de um Propulsor Elétrico Pulsado Para Cubesat", *Universidade de Brasília*, 2020.
- [17] U. Habedank, "Application of a new arc model for the evaluation of short-circuit breaking tests," *IEEE Transactions on Power Delivery*, vol. 8, no. 4, pp. 1921-1925, 1993, doi: 10.1109/61.248303.
- [18] A. Parizad, H. R. Baghaee, A. Tavakoli, and S. Jamali, "Optimization of arc models parameter using genetic algorithm", in *2009 International Conference on Electric Power and Energy Conversion Systems (EPECS)*, 2009, pp. 1-7.

Development of a Radiofrequency Cathode for Hall Thrusters

1st Jhonatha W. S. Paula 2nd Hudson M. Costa 3rd José L. Ferreira 4th Rodrigo A. Miranda
Dept. of Aerospace Engineering Faculty of Technology Institute of Physics Dept. of Aerospace Engineering
and Institute of Physics and Institute of Physics University of Brasília (UnB) and Institute of Physics
University of Brasília (UnB) University of Brasília (UnB) Brasília, Brazil University of Brasília (UnB)
Brasília, Brazil Brasília, Brazil jleonardoferreira@uol.com.br Brasília, Brazil
jhonathawillianrock@gmail.com hudson_m.costa@outlook.com rmiracer@gmail.com

Abstract—The development of radiofrequency (RF) cathodes for Hall thrusters marks a pivotal advancement in the realm of electric propulsion for space exploration. This paper describes the technological evolution and practical applications of RF cathodes as electron sources, elucidating their impact on enhancing the efficiency and reliability of Hall thrusters. The RF cathode’s ability to generate and sustain plasma through radiofrequency principles offers notable advantages over conventional cathodes, including extended operational lifespan, reduced maintenance requirements, and greater adaptability to diverse propulsion demands. Through a comprehensive analysis of the RF cathode’s design, performance metrics, and integration within Hall thruster systems, this study underscores the potential of RF cathodes to revolutionize space propulsion, supporting a new era of satellite technology and interplanetary missions.

Index Terms—Hall thrusters, lifespan, plasma, radiofrequency cathode, RF

I. INTRODUCTION

The radiofrequency (RF) cathode represents a significant advancement in electric propulsion technology, specifically within Hall thrusters. By serving as a reliable electron source, the RF cathode enhances the performance and efficiency of space propulsion systems. This innovative technology leverages the principles of radiofrequency to generate and sustain plasma, offering numerous benefits over traditional cathodes, including improved lifespan, reduced maintenance, and better adaptability to various propulsion needs. This article explores the technological development and practical applications of RF cathodes in modern space exploration and satellite technology.

II. PHYSICS OF THE RADIOFREQUENCY CATHODE

A. Working Principle

A radiofrequency cathode operates by using a radiofrequency (RF) power source to ionize a gas, typically noble gases, in this case is argon (Ar), creating a plasma. This plasma is then used to emit electrons, which are necessary for neutralizing the ion beam in a Hall thruster or other ion propulsion systems. The RF power induces oscillating electric fields in an RF antenna, which in turn ionize the

gas without requiring direct contact with electrodes, thereby reducing erosion and extending the lifespan of the cathode. This method provides a stable and efficient electron source for space propulsion applications.

B. Design of the RF Cathode

The RF cathode, also known as a plasma cathode, was designed to serve as a neutralizer for a Hall thruster, replacing the more expensive and shorter-lived hollow cathode typically imported from abroad. This innovative device represents a new technology developed in Brazil by the Physics of Plasmas Laboratory (LFP) at the University of Brasília (UnB) specifically for the Hall thruster being developed at LFP-UnB. The permanent magnet Hall thruster, developed under the PHall project, will be equipped with the plasma cathode for future experimentation and implementation in a 3U CubeSat in collaboration with the Brazilian Space Agency (AEB) and the National Council for Scientific and Technological Development (CNPq).

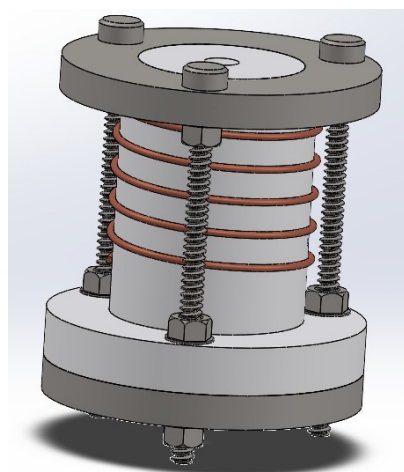


Fig. 1. The final geometry of the radiofrequency Cathode, computer-assisted design.

JLF acknowledges support from CNPq (grant 405907/2022-2). RAM acknowledges support from CNPq, Brazil (grants 407341/2022-6, 407493/2022-0), FAPDF, Brazil (grant 383/2023) and COPEI/UnB (grant 7178).

III. NUMERICAL SIMULATIONS OF THE TEMPERATURE DISTRIBUTION

A. Isometric View of the RF Cathode

Due to the high temperatures generated by the plasma inside the RF cathode chamber, a simulation was necessary to select appropriate materials for the device. The cathode was modeled using Ansys finite element software, with the power of the device set at 60 Watts. The simulation results, depicted in Fig 2 show the temperature distribution across the technology.

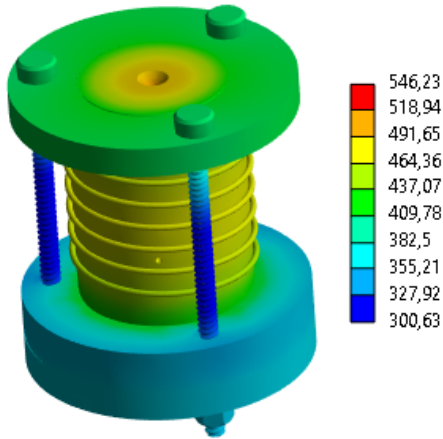


Fig. 2. The color-coded simulated temperature distribution of the RF Cathode A, in units of Celsius ($^{\circ}\text{C}$).

B. Longitudinal Section of the RF Cathode

A longitudinal section of the simulated cathode reveals a maximum temperature of 546.23°C within the plasma chamber, indicating the intense thermal environment the cathode must withstand during operation (see Fig. 3). Conversely, the minimum temperature of 300.63°C was observed on the exterior at the M3 screws of the device, highlighting the effectiveness of the cooling mechanisms and thermal management strategies in place. These temperature gradients are critical for ensuring the structural integrity and performance of the cathode under operational conditions.

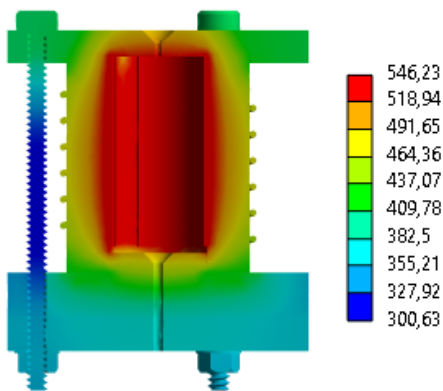


Fig. 3. Internal view of the simulated temperature distribution of the RF Cathode B.

The simulation determined the optimal material for use in the device. Macor, the selected ceramic, can withstand a maximum temperature of 800°C under applied loads and up to 1000°C without any load. This high-temperature resilience makes Macor an excellent choice for the application.

IV. EXPERIMENTAL RF CATHODE

After simulating the device and selecting the appropriate materials, the cathode was machined to precise specifications. The primary materials chosen were stainless steel 316 L and Macor (a machinable ceramic), due to their excellent properties for this application. Stainless steel 316 L was selected for its high corrosion resistance and strength, while Macor was chosen for its electrical insulation and thermal stability.

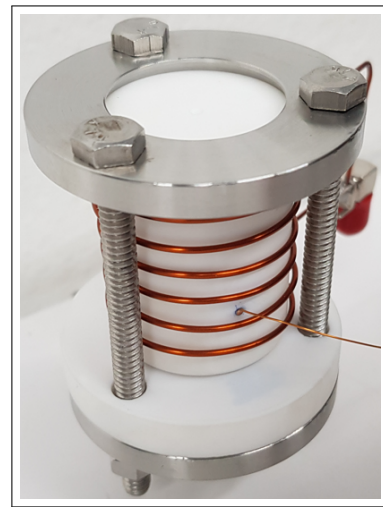


Fig. 4. The assembled experimental device.

Figure 4 illustrates the assembly of the device within the experimental system, highlighting key components and their configuration. This setup is designed to optimize the performance and reliability of the RF cathode during testing and experimentation.

V. PLASMA CATHODE TESTS INSIDE THE VACUUM CHAMBER

A. RF Antenna

To ensure the reliability of the system, the RF antenna was tested inside a vacuum chamber. Using an RF generator operating at 13.56 MHz, with varying power levels, the antenna was rigorously evaluated to qualify it for integration into the device. This testing process was crucial to verify the antenna's performance and durability under vacuum conditions, which mimic the operational environment. The following image demonstrates the setup and results of this testing, highlighting key performance metrics and confirming the antenna's suitability for the device.

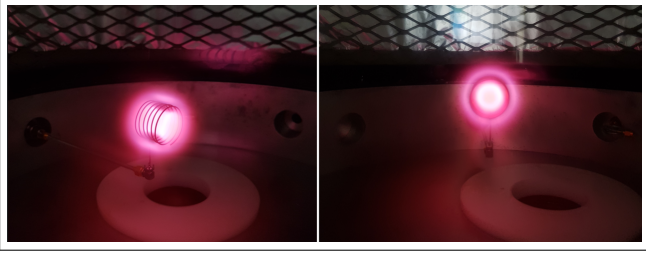


Fig. 5. Operation of the RF antenna inside the vacuum chamber, viewed at an angle (left-side image) and a frontal view (right-side image).

The number of turns of the RF antenna was specifically configured for the tested device to match the system's impedance requirements. This careful adjustment ensured optimal performance and efficiency of the antenna within the experimental setup.

B. Experimental RF Cathode Tests

The cathode was assembled into its system and tested inside the vacuum chamber, with the pressure set to approximately 10^{-5} Torr. A constant power of 60 Watts was generated by the RF generator during the testing process. The following image was captured under these specific configurations, illustrating the setup and conditions used to evaluate the performance of the cathode.

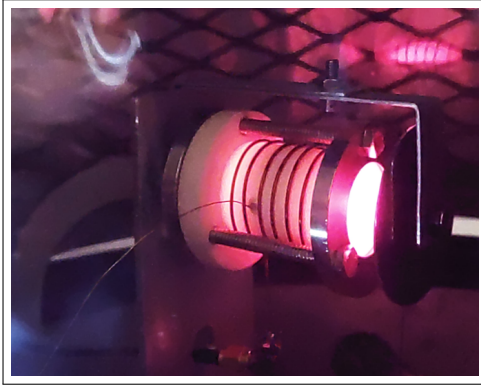


Fig. 6. Plasma Cathode under operation in the vacuum chamber.

Argon was used as the noble gas for the experiments due to its favorable ionization properties and cheaper costs. A small voltage was applied to the electrode positioned in front of the cathode to attract electrons into the plasma chamber. This setup is critical for sustaining the plasma and ensuring the efficient operation of the device.

C. Tests with Different Mass Flows

To achieve an extracted electron current from the cathode, the system was configured as previously described. Experiments were conducted with argon mass flow rates set at 5 sccm and 6 sccm. Under these conditions, the cathode's performance was carefully monitored, yielding valuable data on electron extraction efficiency and current stability. The images obtained in these tests are shown per mass flow rate.

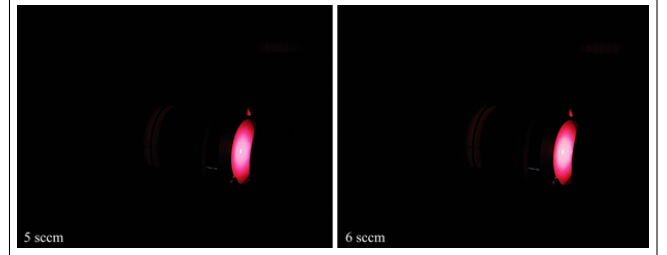


Fig. 7. The Electron Current for a mass flow rate of 5 sccm (left-side figure) and 6 sccm (right-hand figure).

The results obtained under these specific mass flow rates are presented in the following table. This data highlights the significant influence of gas flow on the cathode's operation, illustrating how variations in mass flow rate impact key performance parameters such as stability, efficiency, and temperature distribution. By thoroughly analyzing these results, we can gain a deeper understanding of the optimal operating conditions for the cathode. This insight will enable us to fine-tune the mass flow rate to achieve enhanced performance, ensuring the cathode operates at peak efficiency while maintaining stability and optimal temperature profiles.

TABLE I
ELECTRON CURRENT OF THE RF CATHODE

Extracted Electron Current as a Function of the Mass Flow		
Number of Tests	Mass Flow [sccm]	Current [mA]
Test I	5.00	0.083
Test II	6.00	0.085

The best performance was obtained in Test II, which was conducted using the previously mentioned parameters and a mass flow rate of 6 sccm. Although the extracted current was low, this is attributed to the low voltage applied to extract the electrons from within the chamber. Despite the reduced current, the efficiency and stability of the cathode were markedly superior in this configuration. This suggests that the mass flow rate and extraction voltage are critical factors in optimizing the cathode's performance. Further testing with varied voltages could provide additional insights into achieving higher current extraction without compromising the system's stability.

VI. EQUATIONS OF PERFORMANCE

To ensure the efficiency of the RF cathode compared to other similar devices, we utilize a set of performance equations. The first of these equations pertains to the Electron Extraction Cost (EEC), which can be expressed as follows:

$$C = V + \frac{P}{I} \quad [W/A] \quad (1)$$

The next critical performance metric is the Gas Utilization Factor (GUF), which evaluates the efficiency of gas consumption. This dimensionless factor provides key insights into how effectively the gas is being utilized within the system. The GUF is crucial for optimizing operational parameters

and ensuring minimal waste of propellant resources. The following expression delineates the equation used to calculate this essential parameter:

$$U = \frac{I}{k \cdot \dot{m}} \quad (2)$$

The following table presents the results obtained after comprehensive calculations and analysis. These results provide valuable insights into the performance metrics and characteristics of the system under study, highlighting key parameters and their implications for the overall efficiency and effectiveness.

TABLE II
DATA OF PERFORMANCE OF THE RF CATHODE

Electron Cost & Gas Utilization Factor		
Number of Tests	EEC [W/A]	GUF [Dimensionless]
Test I	722,923.57	0.19
Test II	705,914.35	0.16

The Electron Emission Coefficient (EEC) was observed to be high, while the Gas Utilization Factor (GUF) remained low. This outcome can be attributed to the low voltage applied to the electrode. The low voltage resulted in reduced energy imparted to the electrons, which in turn influenced the ionization efficiency and gas utilization dynamics. Consequently, the high EEC indicates efficient electron emission, whereas the low GUF suggests suboptimal utilization of the supplied gas under the given conditions. These findings highlight the critical influence of electrode voltage on the overall performance and efficiency of the plasma cathode system.

VII. CONCLUSIONS

In this paper we presented the development of a RF cathode for a Hall thruster including numerical simulations of the temperature distribution and experimental results obtained from a prototype in a vacuum chamber. The simulated temperature distribution is qualitatively in agreement with the experiments. Our preliminary results indicate that increasing the mass flow rate and applying more voltage on the electrode leads to variations in the current improving the device performance. These results can contribute for the development of low-cost Hall thrusters for satellites and nanosatellites (CubeSats) at the Plasma Physics Laboratory at the University of Brasília.

ACKNOWLEDGMENT

We would like to thank everyone who contributed to this work, including our colleagues, mentors, and funding agencies. Special appreciation goes to those who provided invaluable support, guidance, and resources throughout the research process. Their contributions have been instrumental to the success of this project.

REFERENCES

- [1] S. Jahanbakhsh and M. Celik, "Theoretical Investigation and Modeling of Current Extraction from a Radio-Frequency Cathode," 2014, DOI: 10.2514/6.2014-3402.
- [2] M. Celik and H. Kurt, "Ferromagnetic enhanced inductively coupled plasma cathode for thruster ion neutralization," 2018, DOI: 10.1063/1.5053403.
- [3] P. Smirnov, M. Smirnova, J. Schein, and S. Khartov, "Research and development of radio-frequency cathode neutralizer," 2019, available at: <https://electricrocket.org/2019/840.pdf>.
- [4] T. Hatakeyama, M. Irie, H. Watanabe, A. Okutsu, J. Aoyagi, and H. Takegahara, "Preliminary Study on Radio Frequency Neutralizer for Ion Engine," 2007, available at: https://www.researchgate.net/publication/238102258_Preliminary_Study_on_Radio_Frequency_Neutralizer_for_Ion_Engine.
- [5] D. M. Goebel and I. Katz, Fundamentals of electric propulsion: ion and Hall thrusters. USA: John Wiley & Sons, 2008.
- [6] F. F. Chen, Introduction to Plasma Physics and Controlled Fusion, 3rd ed. USA: Springer, 2015.
- [7] R. G. Jahn, Physics of Electric Propulsion, 1st ed. USA: McGraw-Hill, 1968.
- [8] F. M. White, Fluid Mechanics, 9th ed. USA: McGraw-Hill, 2021.
- [9] Y. A. Cengel, Heat Transfer: A Practical Approach, 2nd ed. USA: McGraw-Hill, 2002.

Comparative study of propellant injection modes in a low power helicon thruster

1st Sarah Gomes da Silva Paes da Costa 2nd Rodrigo Andrés Miranda Cerda 3rd Julio Cesar de Melo Almeida
Campus Gama, UnB *Campus Gama, UnB* *Institute of Physics, UnB*
Plasma Physics Laboratory *Plasma Physics Laboratory* *Plasma Physics Laboratory*
Brasilia, Brazil Brasilia, Brazil Brasilia, Brazil
s.gspcosta@gmail.com rmiracer@gmail.com julio.eletromec.if@gmail.com

4th Thamiris Thomazini Libard
Campus Gama, UnB
Plasma Physics Laboratory
Brasilia, Brazil
thamirislibardthomazini@gmail.com

5th José Leonardo Ferreira
Institute of Physics, UnB
Plasma Physics Laboratory
Brasilia, Brazil
jleonardoferreira@uol.com.br

Abstract—This paper investigates the performance of a low-power ambipolar thruster through the analysis of the molecular flux density resulting from two distinct propellant injection modes, namely, normal and vortex. Numerical simulation reveal that the vortex mode significantly enhances gas density within the thruster's discharge chamber, achieving a 43% increase compared to the normal mode. This improvement is attributed to the radial injection flow and increased gas residence time. The findings highlight the importance of injection configurations in optimizing thruster performance, contributing to advancements in propulsion technology for CubeSats and other miniaturized satellites.

Index Terms—cubesats, ambipolar thruster, molecular flux density, electric propulsion

I. INTRODUCTION

In recent years, the use of miniaturized satellites, particularly CubeSats, has grown considerably. This technology holds the potential to revolutionize the space industry by enabling individual countries, regional governments, and small companies to establish their own space missions [1].

The economic advantages of small satellites drive their growing adoption, with the development of propulsion systems being crucial for enhancing CubeSat capabilities. Complex missions demand precise orbit control and maintenance, necessitating specialized propulsion systems. Additionally, concerns over space debris have led to stringent regulations that emphasize the necessity for efficient propulsion systems [1], [2].

Electric propulsion refers to propulsion devices that employ electricity to accelerate a propellant, and it was first elucidated by Robert Goddard in 1906 and later described by Tsiolkovskiy in 1911 [3]. After that, its application was developed

by Hermann Oberth in 1929 and by Sheperd and Cleaver in 1949. Since the 60's the United States and Soviet Union have made important contributions and investments in space applications for electric propulsion. Since 2004 the Plasma Physics Laboratory of University of Brasilia (LFP-UnB) is developing electric propulsion devices, including a Hall-type thruster with permanent magnets, reducing the power required for operation [4].

Integrating propulsion into CubeSats presents significant challenges due to the intricate design of space thrusters and the stringent requirements for mass, volume, power, and cost. For example, Hall thrusters can achieve higher thrust levels compared to ion thrusters, and are simpler to construct, however, their scalability to smaller dimensions compatible for micro and nano-satellites present several challenges. For example, since the surface-to volume ratio in the annular channel increases, the collisions between particles and walls increase as well, leading to heating and higher erosion rates. Moreover, the reduced thruster dimensions makes the magnetic circuit difficult to maintain. The scaling down of HTs to various power levels has been the subject of several studies [5], [6].

The cylindrical Hall thruster is an alternative concept first developed at the Princeton Plasma Physics Laboratory [7]. It consists of a cylindrical region and a short annular channel with variable depth, and presents an increased volume-to-surface ratio in comparison to compact HTs, potentially reducing wall erosion. A low-power cylindrical Hall thruster exhibited enhanced performance when subjected to a propellant inlet vortex within the discharge chamber [8]. This mode of diffuse gas injection into the propellant is achieved through the angle of the propellant supply holes, allowing for a radial injection flow that increases the residence time of the gas in

the chamber, subsequently raising its density.

The aim of this work is to analyze this phenomenon through numerical simulation of the molecular flux density of neutral gas in a low-power ambipolar thruster. Two propellant injection modes are considered: the normal mode, in which the propellant is injected longitudinally in the chamber, and the vortex mode, in which the injection occurs with the angulation of the input channels to form a vortex.

This article presents a detailed model of the proposed ambipolar thruster and the methodology adopted for the numerical simulation. This paper is organized as follows. The device is described in detail in section II. The numerical methods and numerical model are presented in section III. The results are discussed in Section IV, and the conclusions are presented in Section V.

II. LOW POWER AMBIPOLAR THRUSTER

Electric propulsion devices such as the ion thruster and the Hall thruster have achieved a high technological maturity to be employed in satellites and spacecrafts, however, their operational lifetime is limited due to several factors such as erosion of channel walls and electrodes, and loss of plasma to the internal walls. The helicon plasma thruster (HPT) is an electric propulsion device that operates without electrodes, providing durability and reliability. It uses electromagnetic radiofrequency (RF) systems to generate and accelerate the plasma, generating thrust [9]. A low-power version of the HPT, also known as the ambipolar thruster, was developed as a consequence of the miniaturization trend currently observed in the aerospace industry [9], [10].

The main components of the device are displayed in Fig. 1, and its operation can be described as follows. Neutral gas is injected into the discharge chamber via distributor holes, which are responsible for the homogeneous distribution of the gas inside the chamber. A radiofrequency antenna surrounds the discharge chamber, and is responsible for ionization. The resulting plasma is radially confined by magnetic fields, provided by two rings of permanent magnets. The use of permanent magnets can help reduce the power requirements of the device. The magnetic field is directed toward the axial direction at the center of the rings. The strength of the magnetic field due to the ring that is close to the physical nozzle is weaker, resulting in a magnetic nozzle configuration that directs the plasma outside the discharge chamber. Since the mass of the electrons is smaller than the mass of the ions, the electrons are ejected first, creating an electric field that accelerates ions.

III. METHODOLOGY

We employ the molecular flow model of the COMSOL Multiphysics software [11] to perform numerical simulations of the neutral gas density inside the discharge chamber. We compute two different configurations for the distributor holes, namely, the “normal mode” in which the holes are aligned with the normal of the gas injection plate, and the “vortex” mode, in which the holes describe an angle with respect to the

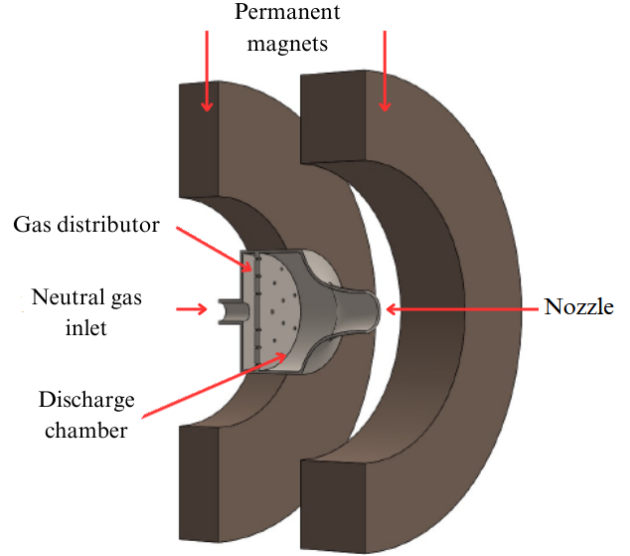


Fig. 1. Schematic diagram of the low-power helicon thruster, showing its main components, namely, the permanent magnets, the discharge chamber, physical nozzle, the neutral gas inlet, and the gas distributor plate with the injection holes. The helicon antenna, described in the text, is not shown here.

normal of the injection plate, resulting in a circulation vortex inside the chamber.

The first configuration, designated the “normal mode,” involves the direct injection of propellant perpendicular to the axial axis. In the second configuration, designated the “vortex mode”, the propellant supply channels are angled in relation to the walls of the injector plate, generating an entry vortex. In this section we describe the molecular flow model employed in this paper, and the normal and vortex modes.

COMSOL Multiphysics

The COMSOL Multiphysics software is a finite element simulation software widely utilized across various physical and engineering domains, particularly in scenarios involving coupled and multiphysics phenomena. The molecular flow module stands out for its capability to simulate free molecular flows within intricate geometries.

This module computes crucial parameters such as molecular flow, pressure, and density not only at the surface of the model but also at any specified point within the flow domain. The core methodology employed is the angular coefficient method of interactions, a specialized variant of the radiation method tailored specifically for vacuum applications. This approach involves aggregating the incoming molecular flux to a surface element with the outflow from all other visible areas.

For internal density calculations within the domain, the Molecular Flow module leverages Numerical Density Reconstruction. This technique derives the numerical density n at a surface which is given by

$$n = J \sqrt{\frac{\pi m}{2k_B T}} \quad (1)$$

where J is the outgoing flux, m is the molecular mass, k_B is Boltzmann's constant, and T is the temperature. In this simulation, the initial conditions were set as follows: a mass flow rate of 12sccm of argon (with a molecular weight of 0.4 kg/mol), a surface temperature of 293.15 K , and a pressure of 0.00133 Pa (approximately 10^{-5} Torr).

We have verified the applicability of the molecular flow model by computing the Knudsen number K_n , which characterizes the degree of gas rarefaction, and is defined as the ratio of the equivalent molecular free path to a representative physical length scale

$$K_n = \frac{l}{a},$$

where l is the equivalent molecular free path, and a is the representative physical length scale. The equivalent molecular free path is given by

$$l = \frac{\mu v_m}{P},$$

where v_m is the most probable molecular velocity, which can be obtained as follows

$$v_m = \sqrt{\frac{2K_B T}{m}},$$

P represents the gas pressure, and μ is the gaseous viscosity. The Knudsen number K_n within the simulation domain obtained is larger than 1, therefore, intermolecular collisions can be neglected, and the molecular flow model is valid.

Normal Mode

The configuration in question is illustrated in Figure 2. In this configuration, the propellant enters the system through a main channel, where it meets a pre-mixing chamber and finally passes through the injector plate to the discharge chamber.

The injector plate will serve as the focus of our analysis. It is 1 mm thick and comprises 25 cylindrical-shaped input holes with a radius of 0.25 mm . However, for the numerical simulation, the study is based on the internal gas flow. Therefore, it was necessary to model the gas path inside the propellant, as illustrated in Figure 3. In this model, the cylindrical inlet channels gave way to two-dimensional circular surfaces.

Vortex Mode

In vortex mode, the neutral gas follows the same path described in normal mode, but its injection into the chamber occurs radially, resulting in the formation of a vortex throughout the thruster. This effect provides an increase in the residence time of the gas as well as its density, which in turn favors its propulsive characteristics [8].

This phenomenon is a consequence of the angle applied to the holes in the plate, which describe an angle of 30 with the wall and its associated with the direction of rotation of the holes, as illustrated in Figure 3 (b). This figure represents the flow inside the discharge chamber for purposes of simulation. Consequently, the injection channels are reduced to ellipses

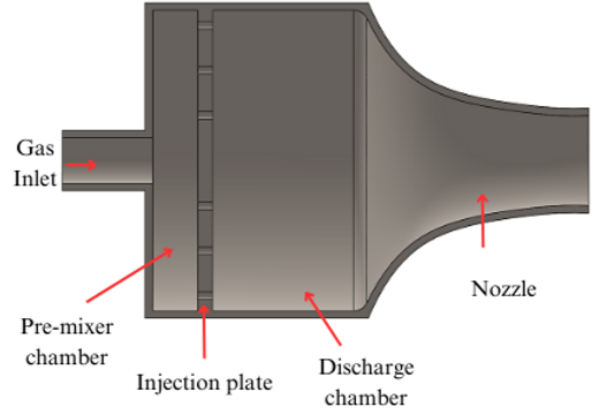


Fig. 2. Site view of the low-power helicon thruster showing its main components, namely, the gas inlet, the pre-mixer chamber, the injection plate with holes, the discharge chamber, and the nozzle. The version shown here corresponds to the “normal mode” prototype.

with a larger radius of 0.5 mm and a smaller radius of 0.25 mm .

IV. RESULTS

Figure 4(a) shows a cross-section of the resulting neutral gas density for the “normal” mode, whereas Fig. 4(b) shows the neutral density for the “vortex” mode. The cross section is defined as a surface at an axial distance of 1 mm from the injection plate. The injection holes are represented by continuous thin lines, superposed to each figure as a reference. This figure shows that the neutral density increases around the injection holes as expected, and is highest in a region surrounding the central area of the discharge chamber. Note that the color scales in Figs. 4(a) and 4(b) are different. For the normal mode, the maximum value of the neutral density is $1.51 \times 10^{21}\text{ m}^{-3}$, whereas the vortex mode has a maximum value of $2 \times 10^{21}\text{ m}^{-3}$. This indicates that the vortex mode results in an increase of the neutral gas density, close to the injection plate.

Figure 5 shows the neutral gas density as a function of the axial distance from the injection plate, obtained at the center of the discharge chamber. The normal mode is shown in blue, while the vortex mode is shown in red. Both curves display similar shapes, with a maximum value near the injection plate, and decreasing values as the distance increases. The density decreases at a faster rate at a distance around 15 mm , which is close to the physical nozzle near the exit region. From this figure it is clear that the neutral gas density of the vortex mode is higher than the normal mode for all values of the axial distance, demonstrating that the vortex mode leads to an increase of the gas density inside the discharge chamber. Close to the injection plate, the vortex mode results in a 43% increase with respect to the normal mode.

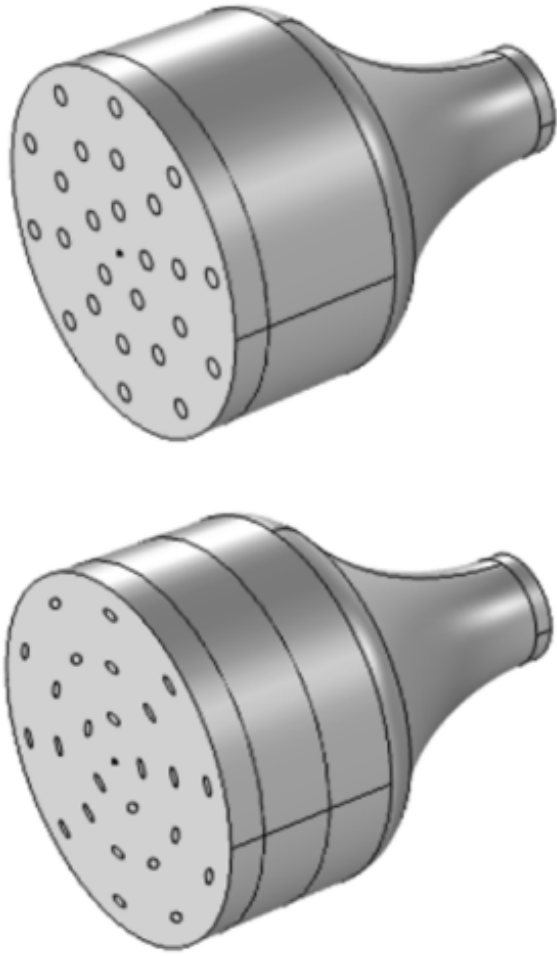


Fig. 3. Perspective view of the simulation domain, showing the gas distributor plate in the normal mode (top panel), and the vortex mode (bottom panel).

V. CONCLUSION

In this study, we examined the behavior of neutral gas injection in a low-power ambipolar thruster under two distinct propellant injection modes, namely, the normal mode and the vortex mode. The numerical simulations performed using the COMSOL Multiphysics software have yielded results that highlight the impact of injection configurations on the gas density distribution and molecular flux density within the thruster.

The findings indicate that the vortex mode significantly enhances the gas density within the discharge chamber, achieving a 43% increase compared to the normal mode. This enhancement can be attributed to the increased residence time of the gas due to the radial injection flow by the angled propellant supply holes. This study highlights the significance of neutral gas injection configuration in optimizing the performance of

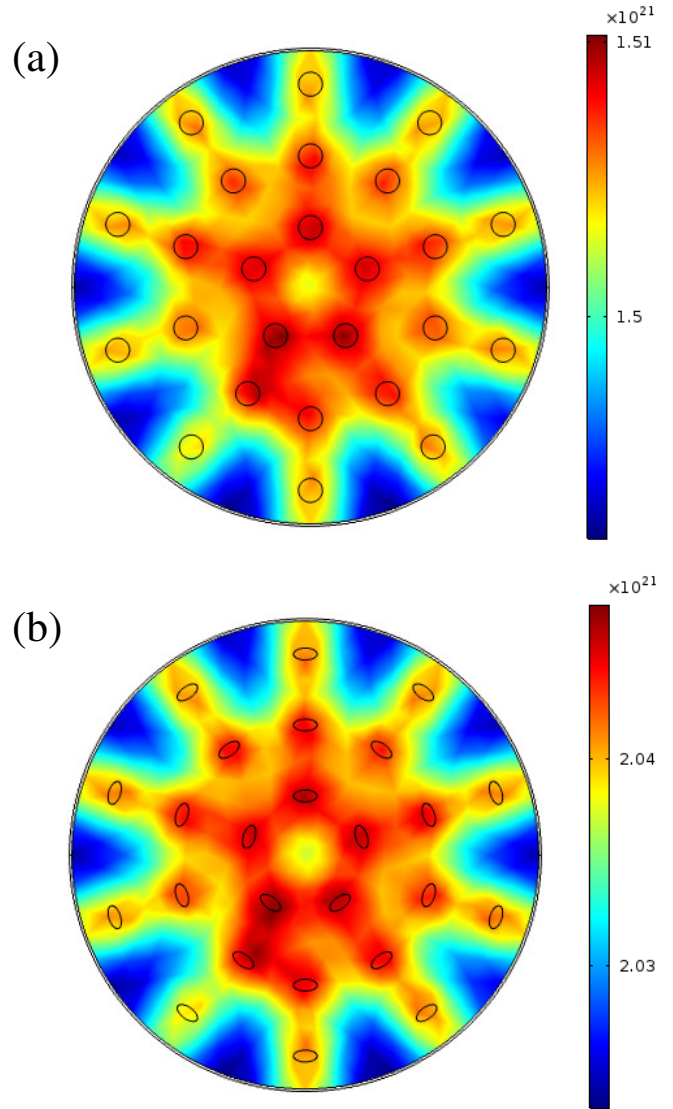


Fig. 4. Density distribution of neutral gas in a cross-section plane for (a) the normal mode, and (b) the vortex mode. Thin lines indicate the contour of the distributor holes. Color scales are indicated for each panel.

ambipolar thrusters and potentially other analogous propulsion systems.

The results obtained provide a solid foundation for future experimental validations and further exploration of neutral gas injection techniques to improve the efficiency and performance of low-power thrusters for CubeSats and other miniaturized satellites. The findings of this study contribute to the advancement of propulsion technology, paving the way for more efficient and sustainable space missions.

The neutral gas density profiles obtained in this paper can be employed in numerical simulations of plasma particles in electric propulsion devices. The particle-in-cell (PIC) approach is a common technique to perform numerical simulations of astrophysical, space and laboratory plasmas [12], [13]. In this approach plasma particles are represented as com-

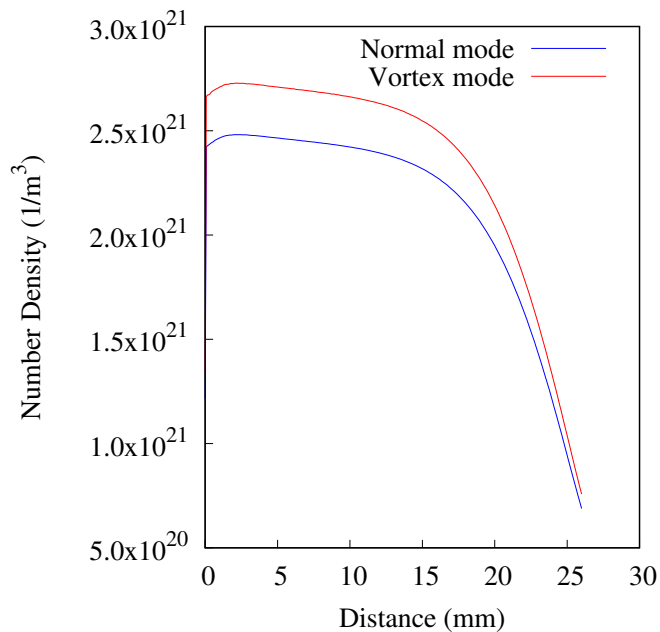


Fig. 5. The neutral gas density distribution as a function of the distance (in mm) from the injection plate, computed at the center of the discharge chamber, for the normal mode (blue line) and vortex mode (red line).

puter particles with positions, velocities, and electromagnetic fields self-consistently solved from the equations of motion and Maxwell's equations. The Plasma Physics Laboratory at the University of Brasilia have implemented PIC models of propulsion devices, for example, Miranda et al. [14] applied the PIC approach to a model of a cylindrical Hall thruster, and described a number of techniques that can help reduce the execution time of the numerical simulations. The specific impulse and thrust computed from their simulations are in agreement with laboratory experiments. Braga and Miranda [15] compared the performance of two types of Hall thrusters, namely, the SPT-100 and the PHall-IIc, the latter being developed by the Plasma Physics Laboratory at the University of Brasilia. This comparison was carried out by performing PIC simulations. Their results indicate that the thrust and the specific impulse of the PHall-IIc attain lower values than the SPT-100, which is expected since the PHall-IIc operates at a lower power in comparison with the SPT-100. Miranda et al. [16] described a numerical model of a helicon plasma thruster device currently under development at the University of Brasilia. The two-dimensional model is obtained by representing the device using a cylindrical geometry, and neglecting variations in the azimuthal direction. The computational code solves the electrostatic equations and the equations of motion of charged particles self-consistently using the PIC approach. Their model predicts the emergence of a structure similar to a current-free double-layer in the plasma, which has been detected in similar experiments. Most of the works cited above employ simplified models for the spatial distribution of the neutral gas, which is an important input that can influence

the density of the plasma from the numerical results. The neutral gas distribution obtained using the molecular flow model presented in this paper will allow for more realistic numerical simulations of the plasma particles and accurate results, and will be used in future works.

ACKNOWLEDGMENTS

RAM acknowledges support from CNPq, Brazil (grants 407341/2022-6, 407493/2022-0), FAPDF, Brazil (grant 383/2023) and COPEI/UnB (grant 7178). SGSPC acknowledges support from CNPq (grant 407341/2022-6). JCMA acknowledges support from CNPq (grant 407493/2022-0). TTL acknowledges financial support from FAP DF (fellowship 9986B). JLF acknowledges support from CNPq (grant 405907/2022-2). All numerical simulations were performed using computational resources at the Laboratory for Simulation of Plasma and Electric Propulsion (LaSPPE) at the Institute of Physics, UnB. RAM thanks the Asociación de Universidades Grupo Montevideo, V. Pinto, M. Stepanova and the University of Santiago, Chile (USACH) for kind hospitality during the finalization of this paper.

REFERENCES

- [1] H. Heidt, J. Puig-Suari, A. Moore, S. Nakasuka, and R. Twiggs, "Cubesat: A new generation of picosatellite for education and industry low-cost space experimentation," 2000.
- [2] M. Manente, F. Trezzolani, M. Magarotto, E. Fantino, A. Selmo, N. Bellomo, E. Toson, and D. Pavarin, "Regulus: A propulsion platform to boost small satellite missions," *Acta Astronautica*, vol. 157, pp. 241–249, 2019.
- [3] D. M. Goebel, I. Katz, and I. G. Mikellides, *Fundamentals of electric propulsion*. John Wiley & Sons, 2023.
- [4] J. L. Ferreira, A. A. Martins, R. Miranda, A. B. Schelin, L. de Souza Alves, E. G. Costa, H. O. Coelho, A. C. Serra, and F. Nathan, "Permanent magnet hall thruster development for future brazilian space missions," *Computational and Applied Mathematics*, vol. 35, pp. 711–726, 2016.
- [5] B. E. Beal, A. D. Gallimore, and W. A. Hargus, "Plasma properties downstream of a low-power hall thruster," *Physics of plasmas*, vol. 12, no. 12, 2005.
- [6] Y. Ding, D. Yu, D. Jia, G. Yan, and H. Li, "Scaling design and experimental study on hall thrusters with curved magnetic field," *Contributions to Plasma Physics*, vol. 51, no. 1, pp. 68–82, 2011.
- [7] Y. Raitses and N. Fisch, "Parametric investigations of a nonconventional hall thruster," *Physics of Plasmas*, vol. 8, no. 5, pp. 2579–2586, 2001.
- [8] Y. Ding, B. Jia, Y. Xu, L. Wei, H. Su, P. Li, H. Sun, W. Peng, Y. Cao, and D. Yu, "Effect of vortex inlet mode on low-power cylindrical hall thruster," *Physics of Plasmas*, vol. 24, no. 8, 2017.
- [9] M. Magarotto, M. Manente, F. Trezzolani, and D. Pavarin, "Numerical model of a helicon plasma thruster," *IEEE Transactions on Plasma Science*, vol. 48, no. 4, pp. 835–844, 2020.
- [10] J. Sheehan, B. W. Longmier, I. Reese, and T. Collard, "New low-power plasma thruster for nanosatellites," in *50th AIAA/ASME/SAE/ASEE Joint Propulsion Conference*, 2014, p. 3914.
- [11] COMSOL, *Introduction to the Molecular Flow Module*, COMSOL, available at <https://doc.comsol.com/5.4/doc/com.comsol.help.molec/IntroductionToMolecularFlowModule.pdf>.
- [12] C. K. Birdsall and A. B. Langdon, *Plasma physics via computer simulation*. London: CRC press, 2004.
- [13] D. L. Bruhwiler, R. E. Giacone, J. R. Cary, J. P. Verboncoeur, P. Mardahl, E. Esarey, W. Leemans, and B. Shadwick, "Particle-in-cell simulations of plasma accelerators and electron-neutral collisions," *Physical Review Special Topics-Accelerators and Beams*, vol. 4, no. 10, p. 101302, 2001.

- [14] R. A. Miranda, A. A. Martins, and J. L. Ferreira, "Particle-in-cell numerical simulations of a cylindrical hall thruster with permanent magnets," in *Journal of Physics: Conference Series*, vol. 911, no. 1. IOP Publishing, 2017, p. 012021.
- [15] L. L. Braga and R. A. Miranda, "Particle-in-cell numerical simulation of the phall-ic hall thruster," in *Journal of Physics: Conference Series*, vol. 1365, no. 1. IOP Publishing, 2019, p. 012013.
- [16] R. A. Miranda, D. B. Da Trindade, J. M. d. J. Luz, S. da Costa, and J. L. Ferreira, "Particle-in-cell model of the helicon plasma thruster experiment at the university of brasilia," in *Journal of Physics: Conference Series*, vol. 1365, no. 1. IOP Publishing, 2019, p. 012009.

..

Design and preliminary characterization of a helicon plasma device for aerospace propulsion.

*

1st William W. T. Sinésio
Institute of Physics, UnB
Plasma Physics Laboratory
Brasília, Brasil
williamwennerp@gmail.com

2nd José Leonardo Ferreira
Institute of Physics, UnB
Plasma Physics Laboratory
Brasília, Brasil
jleonardoferreira@uol.com.br

3rd Rodrigo Andrés Miranda
Campus Gama, UnB
Plasma Physics Laboratory
Brasília, Brasil
rmiracer@gmail.com

4th Julio Cesar de Melo Almeida
Institute of Physics, UnB
Plasma Physics Laboratory
Brasília, Brasil
julio.eletromec.if@gmail.com

5th Helbert de Oliveira Coelho Júnior
Campus Gama, UnB
Plasma Physics Laboratory
Brasília, Brasil
hoc.junior@gmail.com

5th João David Moreira
Institute of Physics, UnB
Plasma Physics Laboratory
Brasília, Brasil
joaodavidm12@gmail.com

Abstract—The versatility of helicon plasma devices (HPDs) has led to their prominence in contemporary applications, including electric propulsion on space missions. The production of plasma through helicon discharges, which are created when gases pass through a chamber at low pressure and absorb Helicon and Trivelpiece-Gould (TG) waves, results in a plasma of high electronic density and low energy. This plasma can be utilized in a variety of applications. In order to conduct research and apply these sources, a helicon-type device was designed and constructed at the Plasma Physics Laboratory (LFP) at the University of Brasília (UnB). This article describes preliminary measurements and the device construction project.

Index Terms—Plasma physics, Plasma source, Helicon Source, Device, Preliminary Results, HPD, LFP, UnB.

I. INTRODUCTION

Micro and nano-satellites have attracted much attention of scientific and commercial entities due to their relative low cost. The operating lifetime of a mission can be increased by using thrusters for orbit-correction, orbit transfer, and station-keeping control. Electric propulsion can provide high values of specific impulse with low quantities of propellant. Among them, electrodeless thrusters are an interesting option because of their simple construction and increased lifetime compared to electric propulsion devices with electrodes. Low-power helicon thrusters, or ambipolar thrusters, are an example of electrodeless thrusters specifically designed for nano-satellites. In this thruster a background magnetic field is necessary for plasma confinement, generation of helicon waves and overall operation, and can be provided by permanent magnets, reducing the power requirement of this device. Due to the reduced size of this device, experimental studies depending on plasma diagnostics can be a challenge. For example, the

plasma inside the ionization chamber can be inaccessible for a Langmuir probe. For this reason, in this paper we focus on a helicon plasma device with an increased size. This device allows to collect data using probes, which would not be possible in the case of the original device with reduced dimensions. The scaled device can give important insights on the plasma processes occurring in the smaller device.

The Helicon plasma devices (HPD) are the subject of considerable interest in the present era. Its broad applicability is due to its distinctive characteristics, including high electronic density (on the order of 10^{13} m^{-3}) and low temperatures (a few eV), which allow its use in a variety of fields [1], [2]. Recently, the application of this technology in the space area has manifested in the form of the helicon plasma thruster (HPT), a thruster that employs this type of source to generate propulsion [2]. The plasma is generated by the absorption of helicon waves, which are whistler waves with normal modes of vibration that propagate through the plasma in an axial and radial manner [1], [3]. In consideration of the aforementioned advantages, the plasma physics laboratory at the University of Brasília, which is dedicated to research in the field of electrical propulsion, designed and constructed a device of this nature for the purposes of research and applications.

Helicon waves are electromagnetic waves with frequencies between electro and ion-cyclotronic frequencies that arise in coupled plasmas. Ionization in the system is caused by two main waves: a Helicon wave and a Trivelpiece-Gould wave (TG) [5]. With the presence of a TG wave in the vicinity of the RF source, greater absorption by the plasma surface is observed. Concurrently, the helicon wave traverses the plasma core, resulting in the heating of its innermost regions [6], [8], [9]. The coupling between the plasma and the antenna is a consequence of the normal modes of vibration, which are

dependent on the antenna and the magnetic field direction. Moreover, its dispersion relationship is analogous to that of a whistler wave [1], [4]. In essence, the coexistence of these two waves serves as the underlying mechanism that facilitates the generation of high-density, low-energy plasmas.

An HPD designed for electrical propulsion comprises a radio frequency (RF) source and a magnetic field that guides the plasma through a magnetic nozzle [3]. The magnetic nozzle serves as a driver in the ejection of ions and electrons, which creates propulsion through the conservation of momentum. Due to the difference in mass between the specimens, the electrons are thrown at a lower speed than the ions forming polarized areas in the plasma. This polarization creates a high drop in plasma potential (V_p), forming a structure known as a double layer, detected on plasmas by Irving Langmuir [7] and observed in helicon plasma by C. Charles and R. Boswell in 2003 [12].

In light of recent research in propulsion and the various HPDs currently built around the world, there is a clear need to develop a system for researching this type of sources. The Plasma Physics Laboratory at the University of Brasília, which is engaged in research into aerospace propulsion, has designed and constructed its first example of an HPD. The system in question comprises two glass chambers. The first, which encompasses the system with coils and an RF source. The second chamber is used for dispersion of the magnetic nozzle, where most of the measurements are carried out. The magnetic coil system is designed in such a way that different field geometries can be tested. In this manner, the initial measurements were conducted to characterize this device, including electron density, the axial profile of the plasma potential, the profile of the magnetic field, and other relevant quantities.

This article presents the preliminary measurements of electron density, magnetic field, and the axial potential profile of the developed system. Additionally, it outlines the methodology used to construct the device in the Plasma Physics Laboratory at the University of Brasília. The structure of this paper is the following. Section II presents the design and construction of the experimental device, and the set of plasma diagnostics. The results are shown in section III, including measurements and simulations of the magnetic field, and the measurements of plasma diagnostics. Finally, our conclusions are presented in Section IV.

II. METHODOLOGY

This article's methodology has the following steps: design and construction of the experimental apparatus, preliminary characterization of magnetic fields, electronic profile, and plasma potential of the thruster.

A. Design and Construction of the Experimental Apparatus

The experimental device is constructed with a glass tube (boron silicate) of 1000mm in length and 100mm in diameter. This tube is surrounded by two mobile coils with 730 turns of

cooper wire each and it is connected to a dispersion chamber with 750mm in length and 300mm in diameter.

A helicon antenna was designed with normal modes of $m = 1$ or $m = -1$, depending on the axial magnetic field. It provide control of the parallel wave number $K_{||}$ [1]. It was designed to operate between frequencies of 13.56 MHz and 25 MHz up to 1000 W of rf power. In this paper, our tests and diagnostics were made with about 25 W.

We use the COMSOL software to perform magnetic fields simulations, visualization and positioning of the magnetic configuration, shows the schematic diagram of the experimental assembly Fig. 1.

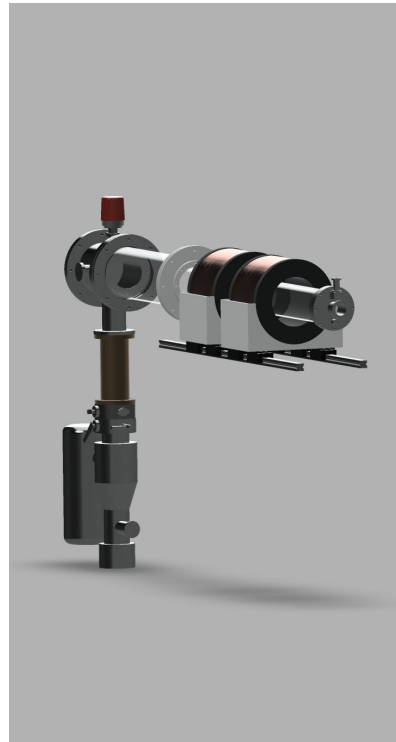


Fig. 1. CAD of the experimental assembly.

Figure 2 shows a photograph of the device under operation. Note that linear rails were added to support both magnetic coils, allowing us to test different spacing and field geometries. The working gas is Argon, which is inserted inside the vacuum chamber through a needle valve located at the edge of the first glass tube (the opposite end of the dispersion chamber). A simplified schematic of the system can be seen in Fig. 3.

B. Measurement system

The measurement system consists of Hall probe (Walker Scientific MG-3D), Langmuir probe, and pressure gauges. The axial Hall probe measure the axial component of the magnetic field, and can be moved along the center of the glass tube.

The Langmuir probe is cylindrical, made from tungsten wire of 0.35mm in diameter, encapsulated by alumina tubes, having the ability to move coaxially along the dispersion chamber.

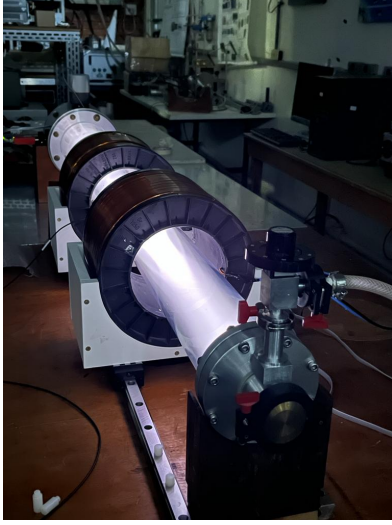


Fig. 2. Plasma source assembled and its first operation.

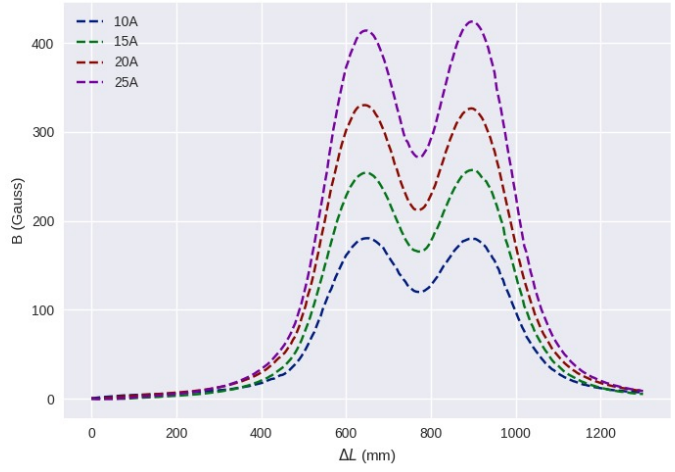


Fig. 4. Intensity of the axial magnetic field at the center of the tube, for different currents.

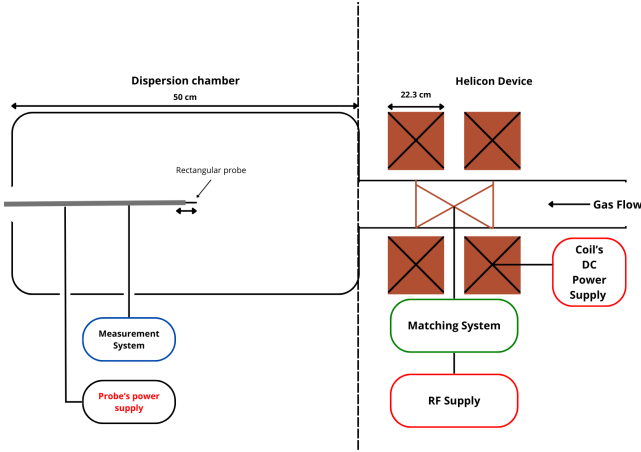


Fig. 3. Schematic of the experimental system for plasma measurements.

Its purpose was to measure the plasma potentials. A reference shunt resistor of 1 k Ω , a ramp power supply (ranging from -150V to 150V), and a parallel, true rms, multimeter complete the measuring setup. All reference potentials were connected to the metallic wall of the metallic flange of the dispersion chamber.

III. RESULTS

A. Magnetic Field

The axial magnetic field for different currents is shown in the Fig. 4

The coils induce magnetic fields of approximately 300G. We select this configuration to perform numerical simulations and observe if the field lines make a magnetic nozzle in the dispersion chamber.

We can see from Fig. 5 that the magnetic nozzle is present around the connection between the two chambers, in the direction of the gradient of the magnetic field. Furthermore,

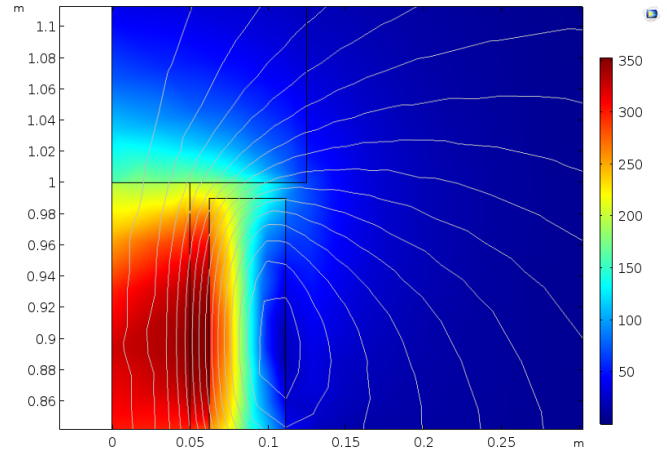


Fig. 5. Simulation of axial magnetic field for a current of 15A. Continuous lines indicate magnetic field lines.

we can see that most of the field lines pass through the center of the tube, confining the plasma away from the tube wall. Experimentally, we can confirm this behavior shown in the Fig.6. Therefore, we could ignore the border effects and proceed with the measurements without considering the diameter of the dispersion chamber.

B. Axial Potential measurements

Plasma potential measurements were conducted along the tube using a Langmuir probe. The measurements were performed from the center of the antenna to approximately 200 mm away, in intervals of 20 mm. Each point represents a measurement of an voltage-current (I-V) curve and their subsequent analysis to obtain electron density, plasma potential, and saturation current. Figure 7 depicts the I-V characteristic curve of the Langmuir probe for a distance of 500 mm.

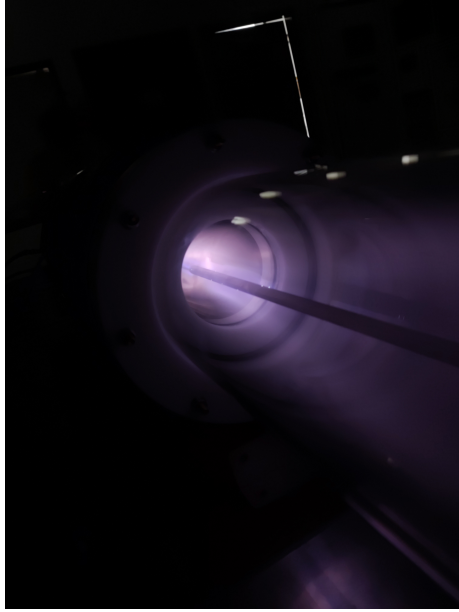


Fig. 6. Magnetic Nozzle at first device qualitative test. Notice that sputtering occurs on the body of the probe indicating that some ions are gaining energy.

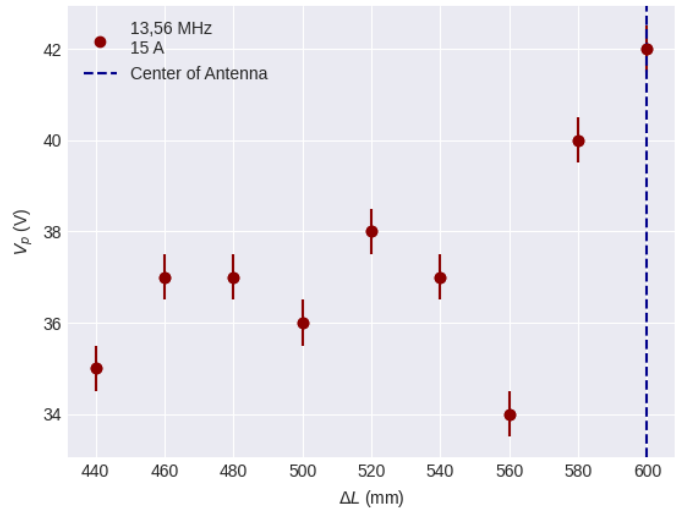


Fig. 8. Plasma potential profile along the axial axis of the tube. The vertical dashed line indicates the center of the antenna

still possible to observe that the plasma begins to decay rapidly at approximately 150 mm away from the antenna, indicating that it will continue to fall. This behavior is indicative of the potential presence of a double layer in the vicinity of this region.

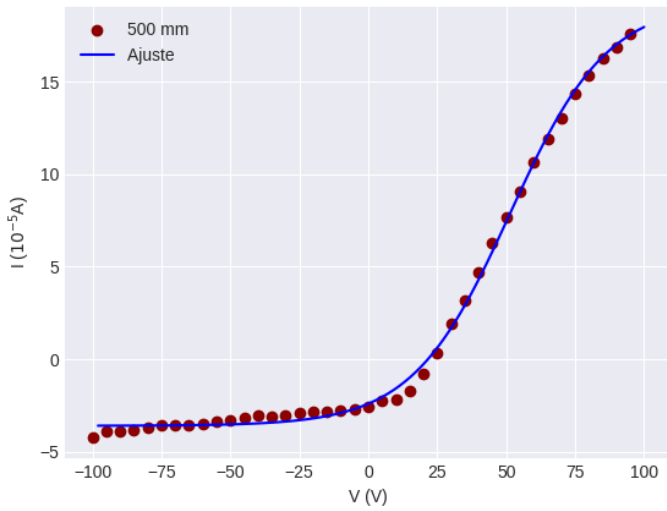


Fig. 7. Characteristic I-V curve for the measurement at 500mm.

The plasma potential points were obtained by plotting a logarithm graph and crossing the line that follows the growth of the curve with the line that follows electronic saturation current. Secondly, the characteristics obtained through the I-V curves, as observed in Figs. 8, 9 and 10, were plotted.

The plasma potential obtained near the antenna in Fig. 8 demonstrates its variation along the axial axis of the tube. As illustrated in the figure, the potential begins at high intensity and with noise due the proximity of the antenna, which is expected due to RF interference in the probe. However, it is

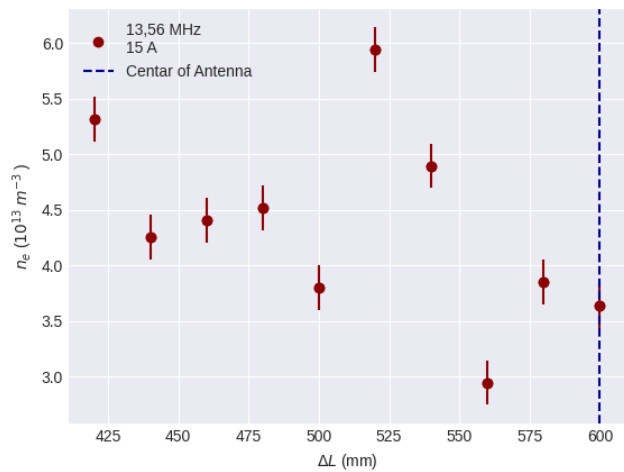


Fig. 9. Electron density along the axial axis of the plasma. The vertical dashed line indicates the center of the antenna

Fig. 9 illustrates a high electron density, in the order of 10^{13} m^{-3} . This high value demonstrates the effectiveness of a helicon RF source in producing high-density plasmas even at low power.

Moreover, as illustrated in Fig. 10, the estimation indicates a considerable ion density in the area where the plasma

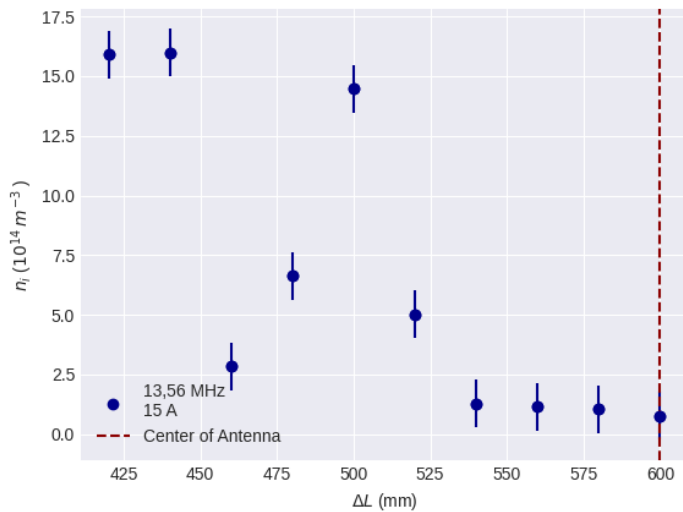


Fig. 10. Ionic density estimated using the floating potential (V_f). The vertical dashed line indicates the center of the antenna

potential is declining and the electron density is approximately one order of magnitude lower. This discrepancy in densities, coupled with the reduction in plasma potential, may suggest the existence of a double layer in that region, which will be subject to further investigation in the future.

The formation of double layers is a consequence of the ejection of electrons at high speeds and ions at lower speeds. The difference in speed between the two specimens results in the creation of polarized regions with high density relative to each other, which in turn leads to a potential difference indicated by a sudden drop in plasma potential [11]. Consequently, a more comprehensive characterization of the device is necessary to confirm the presence of a double layer in our system. Furthermore, as the system is designed for propulsion, it is essential to investigate whether this double layer affects thrust.

The measurements conducted revealed that the helicon RF source is capable of producing a high electron density plasma and that there are indications an existence of double layer in the vicinity of 200 mm from the antenna on the magnetic cusp. Additionally, there is a notable amount of sputtering, suggesting that ions are being ejected from the center of the thruster towards the end of the chamber, gaining kinetic energy in the process.

IV. CONCLUSION

Upon consideration of the presented results and the held discussions, it was observed that the helicon source met the expectations of the team. The plasma obtained reached a high electron density, on the order of 10^{13} m^{-3} , and a high ionic density was estimated, on the order of 10^{14} m^{-3} , indicating a possible concentration of ions in that region. It was observed that the plasma potential decreased as the probe was distanced

from the source. Additionally, a sudden drop in the dispersion chamber was observed at approximately 200 mm from the source, in the same region where the high density was present. The observed conjunction of these features may be indicative of the presence of a double layer. To substantiate this hypothesis, it is necessary to conduct further measurements that extend over a greater distance from the antenna. Consequently, the primary experiment yielded several encouraging outcomes for the system, prompting further inquiry into the underlying causes of the elevated ionic density and the precipitous decline in potential within that region.

V. ACKNOWLEDGEMENT

JLF acknowledges support from CNPq (grant 405907/2022-2). RAM acknowledges support from CNPq, Brazil (grants 407341/2022-6, 407493/2022-0), FAPDF, Brazil (grant 383/2023) and COPEI/UnB (grant 7178). The authors would like to express their gratitude to the UnB Plasma Physics Laboratory Group, as well as the agencies that facilitated the realization of this project: CNPQ, AEB, and UnB.

REFERENCES

- [1] Shinohara, Shunjiro. 2018. "Helicon High-Density Plasma Sources: Physics and Applications." *Advances in Physics: X* 3 (1). doi:10.1080/23746149.2017.1420424.
- [2] F. F. Chen, "A Compact Permanent-Magnet Helicon Thruster," in *IEEE Transactions on Plasma Science*, vol. 43, no. 1, pp. 195-197, Jan. 2015, doi: 10.1109/TPS.2014.2361476.
- [3] Stenzel, Reiner & Urrutia Vélaz, Juliana. (2015). Helicon waves in uniform plasmas. II. High m numbers. *Physics of Plasmas*. 22. 092112. 10.1063/1.4930106.
- [4] S. Isayama, S. Shinohara, and T. Hada, "Review of Helicon High-Density Plasma: Production Mechanism and Plasma/Wave Characteristics," *Plasma and Fusion Research*, vol. 13, pp. 1101014, May 2018. Online ISSN: 1880-6821. Available: <https://doi.org/10.1585/pfr.13.1101014>.
- [5] A. W. Trivelpiece, R. W. Gould; *Space Charge Waves in Cylindrical Plasma Columns*. *J. Appl. Phys.* 1 November 1959; 30 (11): 1784-1793. <https://doi.org/10.1063/1.1735056>.
- [6] K.P. Shamrai and S. Shinohara, *Phys. Plasmas* 8, 4659 (2001)
- [7] I. Langmuir, "The interaction of electron and positive ion space charges in cathode sheaths," *Physical Review*, vol. 33, no.
- [8] D. Arnush, *Phys. Plasmas* 7, 3042 (2000).
- [9] Y. Mouzouris, J. E. Scharer; *Wave propagation and absorption simulations for helicon sources*. *Phys. Plasmas* 1 December 1998; 5 (12): 4253-4261. <https://doi.org/10.1063/1.873161>
- [10] Charles, Christine, and Rod Boswell. "Current-free double-layer formation in a high-density helicon discharge." *Applied Physics Letters* 82.9 (2003): 1356-1358.
- [11] LANGMUIR, IRVING. "The Interaction of Electron and Positive Ion Space Charges in Cathode Sheaths." *Physical Review*, vol. 33, no. 6, Jun. 1929, pp. 954-989. <https://doi.org/10.1103/physrev.33.954>.
- [12] Block, Lars P. "A double layer review." *Astrophysics and Space Science* 55 (1978): 59-83.

Evaluation of the effects of disturbances capable of altering the orbit of the BiomeSat satellite

Liana Dias Gonçalves
Divisão de Mecânica Espacial e
Controle - DIMEC
Instituto Nacional de Pesquisas
Espaciais - INPE
São José dos Campos, Brasil
liana.goncalves@inpe.br

Evandro Marconi Rocco
Divisão de Mecânica Espacial e
Controle - DIMEC
Instituto Nacional de Pesquisas
Espaciais - INPE
São José dos Campos, Brasil
evandro.rocco@inpe.br

José Batista da Silva Neto
Divisão de Mecânica Espacial e
Controle - DIMEC
Instituto Nacional de Pesquisas
Espaciais - INPE
São José dos Campos, Brasil
jose.batista@inpe.br

Ronan Arraes Jardins Chagas
Divisão de Sistemas Espaciais - DISEP
Instituto Nacional de Pesquisas
Espaciais - INPE
São José dos Campos, Brasil
ronan.araes@inpe.br

Antonio Carlos de Oliveira Pereira
Junior
Divisão de Pequenos Satélites - DIPST
Instituto Nacional de Pesquisas
Espaciais - INPE
São José dos Campos, Brasil
acarlos.pereira@inpe.br

Abstract – If the effect of orbital perturbations were not considered, the orbit of an artificial satellite would remain fixed in a fixed plane, in a conical shape (ellipse, parabola or hyperbola), defined by the initial conditions at the instant in which the satellite is injected into orbit. However, in practice, the size and shape of the orbit do not remain constant, since the action of disturbing forces changes the satellite's velocity and, consequently, the orbital movement. Therefore, this work will present a study of the effects of the main disturbances capable of altering the orbit of the BiomeSat Mission satellite, which is being developed by the National Institute for Space Research (INPE). The BiomeSat Mission aims to perform remote sensing to provide data for planning, monitoring and controlling the health conditions of Brazilian forests, in addition to assisting in the assessment of degraded and deforested areas. The AOCS subsystem is responsible for carrying out operational control of the propulsion, which is used for orbit correction maneuvers for the BiomeSat mission. It is also the responsibility of the AOCS subsystem to maintain the satellite's attitude and orientation in relation to space, allowing the satellite to comply, in all operating modes, with pointing and stability requirements, as well as orbit acquisition and maintenance requirements. The analysis to be presented is extremely important for a mission project, as it is capable of sizing the fuel consumption necessary to mitigate the effects of disturbances in the artificial satellite's orbit and maintain the orbit so that mission requirements can be achieved.

Keywords – *BiomeSat Mission, CubeSat, AOCS, Perturbation*

I. INTRODUCTION

The preservation of forests and biomes is extremely important, as they play a fundamental role in maintaining the balance of the planet. Forests are home to a great diversity of plants, animals and microorganisms, in addition to playing a crucial role in regulating the climate, purifying the air and maintaining essential natural resources available for the maintenance of life.

The National Institute for Space Research currently operates satellites with the main objective of monitoring

Brazilian forests and biomes. In order to complement the missions of the CBERS and Amazonia satellites, contributing to the provision of data for planning, monitoring and control of the health conditions of Brazilian forests, in addition to assisting in the assessment of degraded and deforested areas, INPE is currently developing the BiomeSat mission, which will feature a 6U CubeSat satellite weighing less than 12 kg. The satellite's orbit is still being defined, but it is already known that it will be sun-synchronous, with an altitude ranging from 550 km to 650 km.

The AOCS (attitude and orbit control system) subsystem is responsible for keeping the satellite as close as possible to its reference trajectory. In the absence of perturbations, the satellite would develop a perfect Keplerian orbit and no orbital maintenance maneuvers would be necessary. However, in practice, these perturbative forces exist and must be measured so that we know in advance how the satellite will behave in its orbit.

In the case of a satellite with the characteristics of BiomeSat, the main perturbations capable of significantly altering the orbit are the Earth's gravitational potential, the gravitational attraction of the Sun and Moon as third bodies, solar radiation pressure and atmospheric drag. Therefore, this work evaluates the behavior of such perturbative forces, as well as the deviations caused in the orbital elements.

A detailed analysis of the orbital perturbations acting on a satellite around the Moon can be found in [1] and in the vicinity of Mars and its natural satellites, Phobos and Deimos, in [2], as well as a discussion of the importance of not neglecting the effect of perturbations on the dynamics of the orbital motion of an artificial satellite.

II. METHODOLOGY

The methodology adopted to carry out the studies and analyses will be briefly presented below.

A. Spacecraft Trajectory Simulator (STRS)

The Spacecraft Trajectory Simulator (STRS) was used to develop this work [3]. It is an orbital trajectory simulator that uses continuous propulsion and closed-loop trajectory control, and is capable of simulating impulsive and low-thrust maneuvers. It operates calculating the state of the spacecraft at each step of the simulation, considering orbital disturbances in the calculation of the current state of the vehicle, in addition to allowing the constructive aspects of the spacecraft, such as the nonlinearities of the actuators and sensors, to be modeled.

The block diagram in Figure 1 represents the closed-loop orbital trajectory control system used by the STRS.

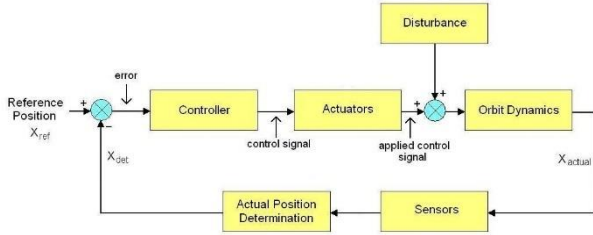


Fig. 1. Closed-loop trajectory control.

B. Orbital motion dynamics

The dynamics of the orbital motion is given by the solution of the Kepler equation at each step of the simulation, defined as one of the input parameters in the simulator, given an initial state and a time interval. The keplerian elements of the orbit are obtained through the equations of orbital dynamics that define the orbital elements as a function of the state variables. Using the Kepler equation, the propagated keplerian elements are obtained for the considered time interval and from the new Keplerian elements the state variables are obtained through the equations of orbital dynamics that define the state variables as a function of the orbital elements [4].

C. Orbital perturbations

The theory and equations used to consider the main perturbations capable of altering the orbit of an artificial satellite around the Earth in the simulations will be briefly presented below.

Earth's Gravitational Potential

The Earth's gravitational potential is defined using the EGM2008 model, which is based on spherical harmonic modeling using (1) [5].

$$U(r, \lambda, \phi) = \frac{\mu}{r} + \frac{\mu}{r} \sum_{n=2}^{\infty} \sum_{m=0}^n \left(\frac{a_e}{r}\right)^n (\bar{C}_{nm} \cos m\lambda + \bar{S}_{nm} \sin m\lambda) \bar{P}_{nm}(\sin \phi) \quad (1)$$

where G is the universal gravitational constant, M is the mass of the planet, a_e is the equatorial radius, \bar{P}_{lm} are the

normalized associated Legendre polynomials of degree l and order m , r is the radial coordinate fixed on the body, ϕ is the latitude and λ is the longitude, and \bar{C}_{lm} and \bar{S}_{lm} are the normalized coefficients of the expansion of the spherical harmonics.

The model output provides the x , y and z components for the disturbing acceleration at each instant of time. With the model EGM2008 [6] it is possible to consider spherical harmonics up to degree and order 120. Thus, a difference is made between the disturbing acceleration provided by the EGM2008 model and the acceleration of gravity of a central field, in order to obtain the components of the disturbing velocity increment on the satellite. In this way, from the equations of celestial mechanics it is possible to calculate the keplerian elements that characterize the satellite's orbit.

Gravitational attraction of the Moon and Sun as third bodies

According to [7] and [8] the general three-body problem provides a simple way to calculate the disturbing accelerations due to the gravitational attraction of the bodies, obtained from Newton's law of gravitation, given by the set of (2).

$$\begin{aligned} \ddot{\vec{r}}_1 &= -Gm_2 \frac{\vec{r}_1 - \vec{r}_2}{|\vec{r}_1 - \vec{r}_2|^3} + Gm_3 \frac{\vec{r}_3 - \vec{r}_1}{|\vec{r}_3 - \vec{r}_1|^3} \\ \ddot{\vec{r}}_2 &= -Gm_3 \frac{\vec{r}_2 - \vec{r}_3}{|\vec{r}_2 - \vec{r}_3|^3} + Gm_1 \frac{\vec{r}_1 - \vec{r}_2}{|\vec{r}_1 - \vec{r}_2|^3} \\ \ddot{\vec{r}}_3 &= -Gm_1 \frac{\vec{r}_3 - \vec{r}_1}{|\vec{r}_3 - \vec{r}_1|^3} + Gm_2 \frac{\vec{r}_2 - \vec{r}_3}{|\vec{r}_2 - \vec{r}_3|^3} \end{aligned} \quad (2)$$

where \vec{r}_1 , \vec{r}_2 and \vec{r}_3 are the position vectors of the bodies, m_1 , m_2 and m_3 are the masses of the bodies and G is the gravitational constant.

Solar radiation pressure

The disturbance due to solar radiation pressure occurs due to the incidence of photons on the satellite, from the radiation emitted by the Sun. The photons, when incident on the satellite, can be absorbed or reflected in a specular or diffuse manner. For each of these situations, the disturbing force is given by (3), (4) and (5) [9]:

$$d\vec{F}_a = \frac{I}{c} [c_a (-\cos \theta \hat{n} + \sin \theta \hat{s})] \cos \theta dA \quad (3)$$

$$\vec{F}_{re} = \frac{I}{c} [-(1 + c_{re}) \cos \theta \hat{n} + (1 - c_{re}) \sin \theta \hat{s}] \cos \theta dA \quad (4)$$

$$d\vec{F}_{rd} = \frac{I}{c} \left[-(\cos \theta + \frac{2}{3} c_{rd}) \hat{n} + \sin \theta \hat{s} \right] \cos \theta dA \quad (5)$$

where I is the radiant energy per unit area, θ is the angle of incidence of radiation, c is the speed of light, c_a , c_{re} and c_{rd} are the absorption, specular reflection and diffuse reflection coefficients, \hat{n} is the vector normal to the surface and \hat{s} is the vector.

Atmospheric drag

The perturbative force due to atmospheric drag occurs as a result of friction between the satellite and the planet's atmosphere, causing the satellite to lose orbital energy and, consequently, its orbit to gradually decay. For satellites with an altitude of less than 1000 km, this force cannot be neglected.

Para o presente trabalho, a perturbação devido ao arrasto atmosférico foi considerada a partir do modelo MSIS(R) [10].

III. RESULTS AND DISCUSSIONS

The results of studies carried out to dimension the variation of orbital elements in possible orbits of the BiomeSat mission satellite, due to the perturbation of the gravitational potential, gravitational attraction of the Sun and Moon, solar radiation pressure and atmospheric drag, are presented below.

A. Selected orbit

Since the orbit of the BiomeSat mission satellite has not yet been fully defined, some possibilities that satisfy the mission objectives were obtained and one of them, whose initial orbital elements are presented in Table 1, was selected for the simulations. It is worth remembering that the satellite must have a sun-synchronous orbit, with an altitude between 550 km and 650 km.

TABLE I. ÓRBITA SELECCIONADA PARA ESTUDO

Semieixo maior	6995.25 km
Excentricidade	0.001253
Inclinação	97.821
Ascensão reta do nodo ascendente	90
Argumento do perigeu	180
Anomalia média	0

For this study, the simulation was performed for one Earth day, on February 12, 2025.

B. Orbital perturbations

Figure 2 shows the total velocity increment acting on the satellite, for each simulation step, due to the Earth's gravitational potential, the Sun's gravitational attraction, the Moon's gravitational attraction, atmospheric drag and solar radiation pressure. Figures 3 to 7 show the contribution of each disturbance individually, with Figure 8 referring to the disturbance due to the Earth's gravitational potential, Figure 9 due to the Sun's gravitational attraction, Figure 10 due to the Moon's gravitational attraction, Figure 11 due to solar radiation pressure and Figure 13 due to atmospheric drag. Each figure shows the perturbation on each of the x , y and z axes, as well as the resultant, considering the Earth-Centered Inertial Reference Frame (ECI).

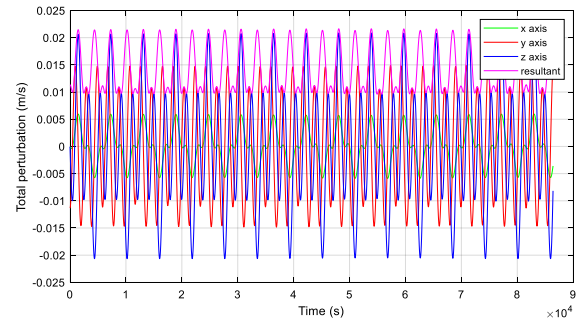


Fig. 2. Total perturbation.

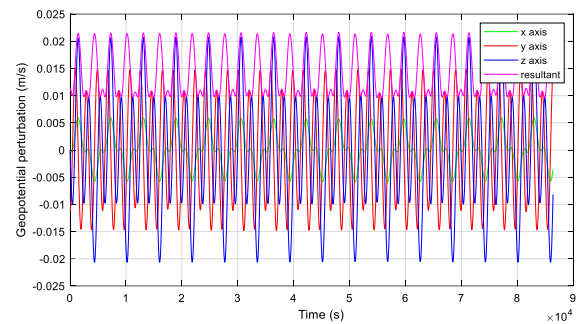


Fig. 3. Geopotential perturbation.

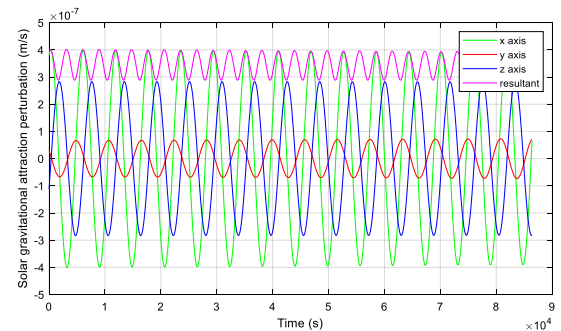


Fig. 4. Solar gravitational attraction perturbation.

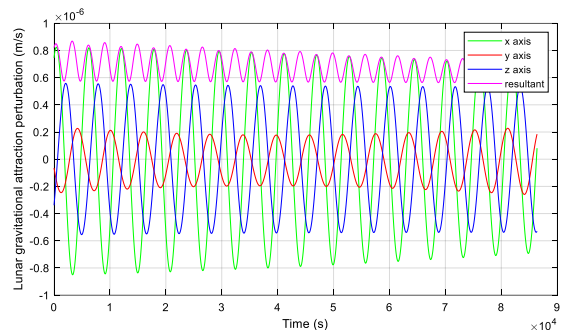


Fig. 5. Lunar gravitational attraction perturbation.

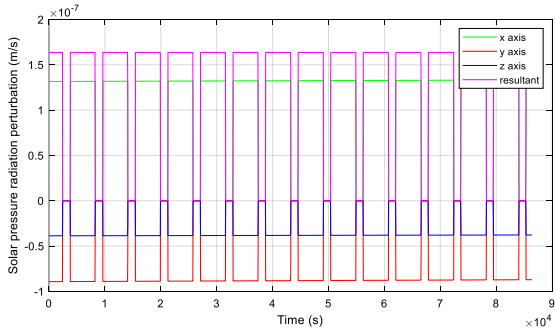


Fig. 6. Solar pressure radiation perturbation.

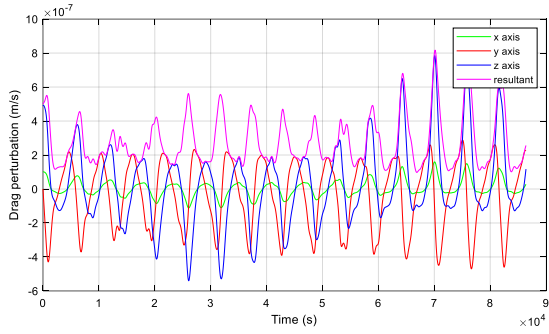


Fig. 7. Drag perturbation.

From Figures 3 to 7 we can see that the perturbation that exerts the most significant contribution is the perturbation due to the Earth's gravitational potential, shown in Figure 3. Since we are working with a sun-synchronous orbit, the perturbation due to the gravitational potential acts by rotating the orbital plane. Therefore, in this case, the perturbation due to the Earth's gravitational potential works in favor of the mission objectives, and corrections to the right ascension of the ascending node are not necessary. However, the gravitational potential also causes effects on the other orbital elements, in addition to the other perturbations acting on the satellite, which, even if of lower magnitude, as seen in Figures 3 to 7, are capable of degrading the orbit, and may require the control system to operate to perform periodic correction maneuvers.

From Figure 3 we can see that the maximum velocity increment over the satellite, due to the Earth's gravitational potential, is around 0.02 m/s at each simulation step. Figures 4 and 5 show that the maximum velocity increment over the satellite, due to the gravitational attraction of the Sun and the Moon, are of the order of $4 \times 10^{-7} \text{ m/s}$ and $0.8 \times 10^{-6} \text{ m/s}$, respectively. For the case of solar radiation pressure, Figure 6, the maximum velocity increment is around $1.6 \times 10^{-7} \text{ m/s}$. In Figure 6 we can observe moments in which the perturbation is zero. This happens when the satellite enters the Earth's shadow region, not being hit by sunlight. The perturbation due to atmospheric drag, shown in Figure 7, is a function of the satellite's altitude. Therefore, we can observe moments of greater and lesser intensity of this perturbation, depending on whether the satellite is at perigee or apogee. When the satellite approaches perigee, the magnitude of the disturbance is of the order of $8 \times 10^{-7} \text{ m/s}$, at each step of the simulation.

C. Variation in orbital elements

Figures 8 to 13 show the effect on the orbital elements for the case of the orbit selected for study, caused by the perturbations acting simultaneously on the satellite, for the simulation time of one Earth day. In this study, the perturbations were applied to the satellite's movement and no type of orbital correction was performed.

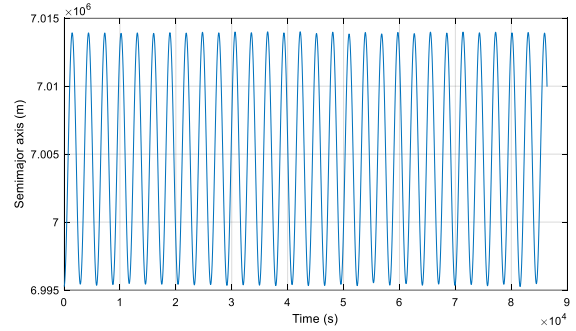


Fig. 8. Semimajor axis.

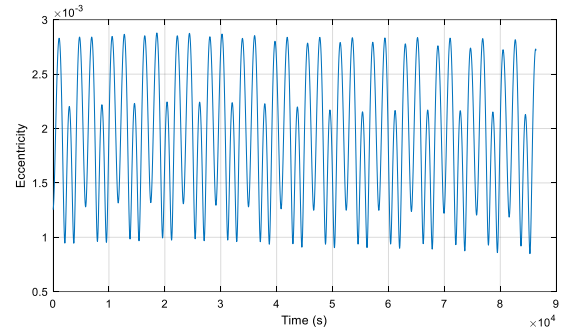


Fig. 9. Eccentricity.

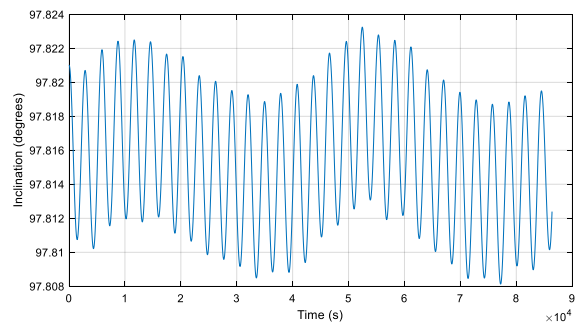


Fig. 10. Inclination.

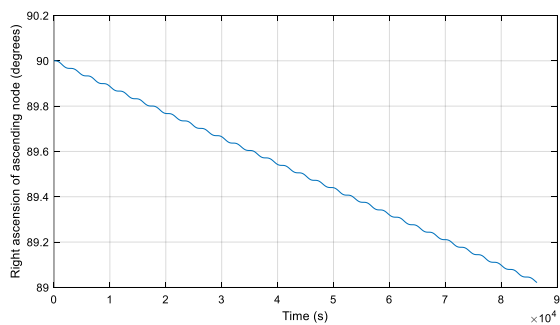


Fig. 11. Right ascension of ascending node.

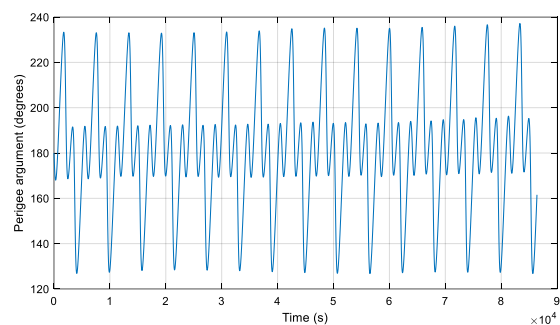


Fig. 12. Perigee argument.

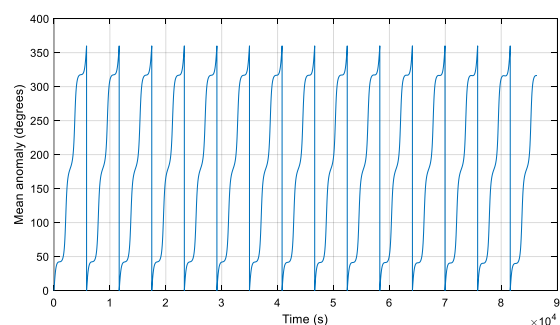


Fig. 13. Mean anomaly.

Figure 8 shows the behavior of the semi-major axis, which varies due to the variation in the eccentricity of the orbit (Figure 9). In Figure 10, we can see a small, but noticeable, variation in the orbital inclination. In Figure 11, we can see the important characteristic of the sun-synchronous orbit, since the variation in the right ascension of the ascending node was 0.98 degrees for the simulation time of one day. The argument of perigee, shown in Figure 12, oscillates, but its mean remains constant. Finally, the mean anomaly for a situation without disturbance would present a behavior similar to the sawtooth, with a variation from 0 to 360°. However, with the presence of perturbations, the results present small oscillations, as can be seen in Figure 13.

Figure 14 shows the variation of the satellite's altitude at perigee, for a simulation time of one day. Since the satellite's orbit is not circular, the satellite's altitude varies cyclically. Figure 15 shows the variation of the satellite's altitude at

perigee, but for a simulation time of 15 days. In this case, we can see the satellite's altitude decreasing, which clearly shows us that correction maneuvers will be necessary to ensure that the satellite remains in the desired orbit and the mission lifetime is achieved.

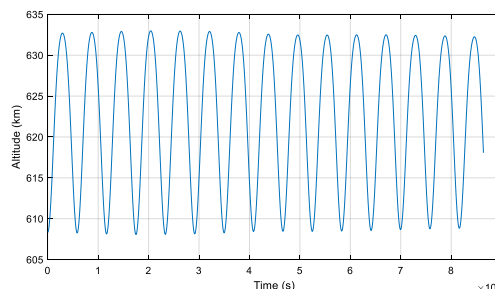


Fig. 14. Altitude satellite during one day.

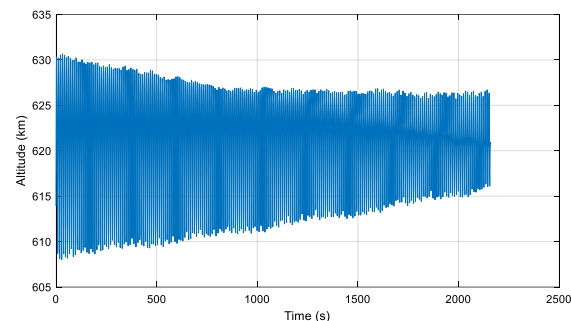


Fig. 15. Altitude satellite during 15 days.

Finally, Figures 16 to 18 show the sum of the velocity increments that acted on the satellite during the entire simulation time. In other words, the total value of the velocity increment suffered by the satellite during one day is presented. Figure 16 shows the sum of all the velocity increments suffered by the satellite, due to all the disturbances acting simultaneously. As already observed in Figures 2 to 7, the perturbation due to the Earth's gravitational potential is the most significant. Therefore, the sum of the velocity increment due only to the Earth's gravitational potential is presented in Figure 17. The sum of the other perturbations analyzed is presented in Figure 18. In this way, we can evaluate the total velocity increment suffered by the satellite and, from Figures 17 and 18, the contribution of each perturbation individually, during one day.

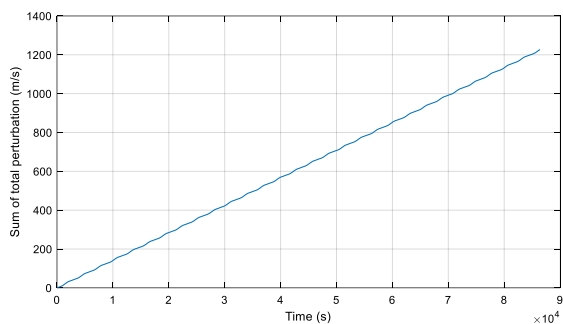


Fig. 16. Sum of total perturbations

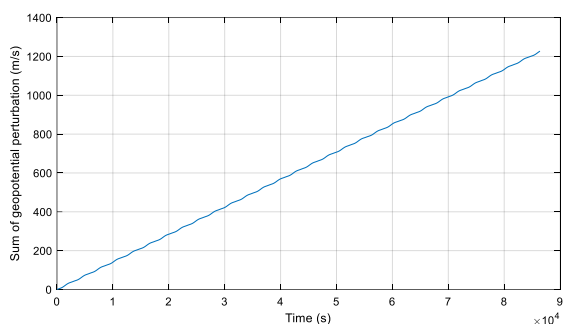


Fig. 17. Sum of geopotential perturbation

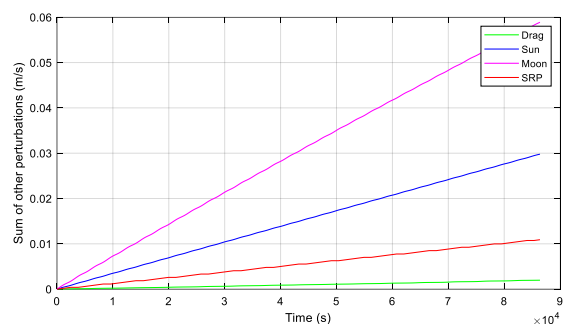


Fig. 18. Sum of other perturbations

CONCLUSIONS

In this study, the main perturbations capable of altering the orbit of an artificial satellite around the Earth's surface were evaluated: Earth's gravitational potential, gravitational attraction of the Sun and Moon, solar radiation pressure and atmospheric drag. These forces directly impact the satellite's

orbit, causing variations in all the orbital elements that define it.

The most significant perturbation is the perturbation due to the Earth's gravitational potential. However, the others, even small ones, should not be neglected, as they can significantly affect the orbit in the long term.

Finally, it is concluded that it is important to evaluate the perturbations acting on the satellite so that it is possible to adequately dimension the capacity of the propulsion system, keeping the satellite in the desired orbit, in order to guarantee the success of the mission.

ACKNOWLEDGMENT

The authors would like to thank National Institute for Space Research (INPE) and CNPq (Process number 407075/2022-4) for supporting the project.

REFERENCES

- [1] L. D. Gonçalves, "Manobras orbitais de satélites artificiais lunares com aplicação de propulsão contínua". 2013. 301 p. IBI: <8JMKD3MGP7W/3DL2KKS>. (sid.inpe.br/mtc-m19/2013/02.28.17.28-TDI). Dissertação (Mestrado em Mecânica Espacial e Controle) - Instituto Nacional de Pesquisas Espaciais (INPE), São José dos Campos, 2013. Disponível em: <http://urlib.net/ibi/8JMKD3MGP7W/3DL2KKS>.
- [2] L. D. Gonçalves, "Trajetórias perturbadas por forças de origem gravitacional e não gravitacional aplicadas a um satélite artificial na vizinhança de Marte, Fobos e Deimos". 2018. 197 p. IBI: <8JMKD3MGP3W34R/3QTLK85>. (sid.inpe.br/mtc-m21c/2018/04.17.17.02-TDI). Tese (Doutorado em Mecânica Espacial e Controle) - Instituto Nacional de Pesquisas Espaciais (INPE), São José dos Campos, 2018. Disponível em: <http://urlib.net/ibi/8JMKD3MGP3W34R/3QTLK85>.
- [3] E. M. Rocco, "Earth albedo evaluation and analysis of the trajectory deviation for some drag-free missions." In: 8th Brazilian Conference on Dynamics, Control and Applications - DINCON'09, 2009, Bauru. Proceedings of the 8th Brazilian Conference on Dynamics, Control and Applications - DINCON'09, 2009. v. 1. p. 1-18.
- [4] V. A. Chobotov, Orbital mechanics. Washington, DC: American Institute of Aeronautics and Astronautics, 1991. 365p.
- [5] W. M. Kaula, Theory of satellite geodesy. New York: Dover, 1966.
- [6] N. K. Pavlis, S. A. Holmes, S. C. Kenyon, J. K. Factor (2012). "The development and evaluation of the Earth Gravitational Model 2008 (EGM2008)". Journal of Geophysical Research: Solid Earth, 117(B4), B04406. <https://doi.org/10.1029/2011JB008916>.
- [7] A. F. B. A. Prado, H. K. Kuga, H.K. Fundamentos de tecnologia espacial. São José dos Campos: Instituto Nacional de Pesquisas Espaciais, 2001. ISBN: 85-17-00004-8.
- [8] V. Szebehely, Theory of orbits. New York: Academic Press, 1967.
- [9] M. Harris, R. Lyle, Spacecraft radiation torques. Washington: NASA, 1969.
- [10] D. P. Drob, J. T. Emmert, J. W. Meriwether, J. J. Makela, E. Doornbos, M. Conde, et al., "An update to the NRLMSISE-00 empirical model of the atmosphere: NRLMSISE-00". Earth and Space Science, 2(6), 2015, 301-319. <https://doi.org/10.1002/2015EA000146>.



LATIN AMERICAN CUBESAT WORKSHOP SALVADOR, BR

DOI: 10.1234/example-doi-06

3U CubeSat Detumbling and Attitude Control with Magnetorquers

Iva Franco Pereira¹, Ana Carolina Lima Oliveira¹, Marcelo Alves Santos¹, and Maria Cecilia Pereira¹

¹UFMG

Abstract

PdQSat is an academic satellite aimed at characterizing a Lithium-Sulfur (Li-S) Battery and a microsupercapacitor under space environmental conditions. The high energy density of the Li-S Battery will enable it to contribute to lightweight satellite design. Adhering to the requirements of CDS v14, the Li-S Battery is strategically placed within the central region of the satellite body, resulting in a non-uniform moment of inertia. For positioning in Low Earth Orbit (LEO), the B-dot law has proven to be a useful approach in the detumbling process due to its simplicity, ease of implementation, and minimal computational demands. Consequently, the B-dot law has been widely applied as a CubeSat control system for detumbling after launch. Therefore, this study aims to address the detumbling of the CubeSat considering its characteristic moment of inertia. Subsequently, we design a control law for attitude control to validate its effectiveness in the task. This validation using the B-dot law was performed using simulation results of a CubeSat detumbling, presenting the attitude behavior of the satellite with the necessary current levels and providing conditions for analysis. Lastly, from the delineation across most orbits proposed by the development team for PdQSat, the preferred insight orbits of the designated family were presented. Thus, for this mission, where no special requirements are given regarding the orientation of the payload, attitude directives flow from the communications subsystem. Since communication operations do not require accurate pointing of the spacecraft, there is a strong indication that the same actuator can be used for both phases of attitude control, as stated by the TT&C team.

Therefore, it might be feasible to use a single actuator that allows for the possibility of turning the antenna to the ground when necessary, in conformity with what was stated by the TT&C team. Herein, a comprehensive set of results pertaining to both detumbling and attitude control is provided, along with the control effort profile. This establishes the finding that a single actuator can be used during both phases of the mission by modifying only the control law. These contributions will lay the groundwork for future missions, continuously developing the area of attitude control strategies for CubeSats.

Hardware-in-the-Loop (HiL) and Software-in-the-Loop (SiL) System for CubeSat ADCS Testing

F. C. Juliano, S. H. Franz, X. L. Travassos, E. A. Bezerra

*Dept. of Electrical Engineering
Federal University of Santa Catarina
Florianópolis, Brazil*

felipe.juliano@spacelab.ufsc.br, samuel Franz.h@gmail.com, lucas.travassos@ufsc.br, eduardo.bezerra@ufsc.br

Abstract—This paper proposes a low-cost testbed for a CubeSat attitude control system using Helmholtz coils to mimic the geomagnetic field in Low Earth Orbit. The testbed consists of square coils arranged along three axes, allowing for precise magnetic field control along the X , Y , and Z axes. The system is managed by a Hardware-in-the-Loop (HiL) setup, which enhances the Attitude Determination and Control System (ADCS) capabilities through closed-loop operation. This configuration ensures that the magnetic field can be accurately simulated, providing a realistic environment for testing and improving ADCS performance. Implementing such a testbed is not only cost-effective but also offers a high level of precision, making it a necessary tool for developing and testing CubeSat attitude control systems.

Index Terms—Attitude control, ADCS, CubeSat, Helmholtz coil, Test platform, Small satellites

I. INTRODUCTION

This discussion explores the use of Hardware in the Loop (HiL) simulators looking at Helmholtz coil systems in the context of aerospace testing and verification processes which create a controlled setting to mimic real-world situations effectively. The document discusses a budget method for building such a setup by emphasizing the use of accessible elements such as the *OPA548* operational amplifier, for managing the coils. An important area where these systems are used is the development and testing of CubeSats. These small satellites are commonly launched as part of research initiatives at universities offering students and researchers the chance to participate in hands-on space missions. CubeSats typically consist of components such, as the Onboard Data Handling (OBDH) computer, the Electrical Power System (EPS) the Telemetry, Tracking, and Command (TT&C) system, and the Attitude Determination and Control System (ADCS). Each of these components serves a purpose, in ensuring the CubeSat mission operates smoothly and achieves its objectives successfully.

Creating a platform such, as a CubeSat comes with its share of obstacles to overcome. The experiences with CubeSat missions have shown that a large number of them have encountered issues either during launch or while in orbit. For example between 2002 and 2017 about half of the CubeSat

missions failed to launch according to research. This highlights the need, for testing and validation processes to guarantee the success and reliability of these missions. In this scenario, the suggested approach, for calibrating magnetorquers via *HiL* simulators is meant to tackle these issues by allowing testing of CubeSat parts focused on attitude control specifically. Simulating the space setting and the interplay, between the CubeSat magnetorquers and Earth's magnetic field enables researchers to optimize the *adcs* subsystem's performance and boost the reliability of the CubeSat mission.

The particular *HiL* simulation described in the document is created to cater to CubeSat units up to 1 unit, in size specifications of 100mm x 100mm x 113mm and weighing, up to 2kg typically used for a 1 unit CubeSat. This experimental setup is capable of accommodating sized CubeSat units with meticulous accuracy.

A. Requirements

Designing a CubeSat experiment platform requires strict adherence to standardized dimensions. The platform must conform to accommodate CubeSat specifications in a physical space of 100x100x113.5mm.

While the Earth's magnetic field in Low Earth Orbit (LEO) reaches a maximum of $0,6G$ and the local field is approximately $0,54G$, the system's capacity will be amplified to $2,4G$ [9]. This oversizing allows for calibration adjustments and future upgrades, ensuring a minimum current of $2,5A$ per axis to effectively counteract the geomagnetic field [9].

To achieve high precision in magnetic field measurements, a 16-bit resolution is essential. Moreover, field uniformity within the physical space is paramount and should ideally be minimized to at least 1% around a 1U volume, following established standards in [11].

II. THEORETICAL FRAMEWORK

A. Mathematical modeling of the Helmholtz coil

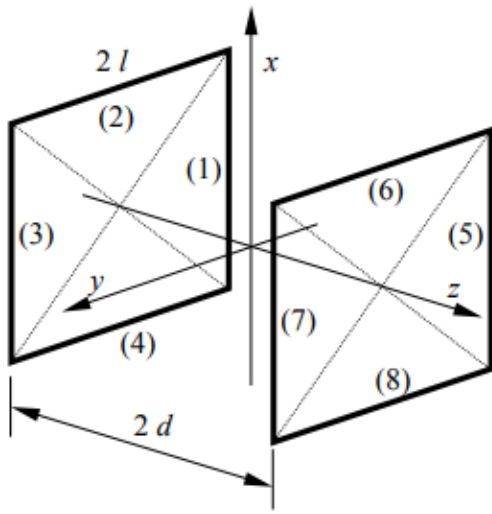
The first step involves calculating the magnetic field strength at the center of the coils for a specific axis. This resulting

magnetic field at a specific point due to a current-carrying wire can be calculated using Biot-Savart's law [11].

$$dB = \frac{\mu_0 I, dl}{4\pi r^2} \sin \theta \quad (1)$$

The equations depend on the distance, indicated as r , between the wire and the magnetic field point, dl represents an infinitesimal element along the wire, and \sin indicates the direction of the field vector. Finally, I represent the current. In this context, Biot-Savart's law is used to calculate the magnetic field at a specific point generated by a single wire. To model a complete coil, consisting of four wires, a mathematical analysis is applied.

Fig. 1: Helmholtz coil coordinate systems



SourceFonte: Adapted from [11]

We must integrate the equation and express it in an alternative form.

$$dB = \frac{\mu_0 I}{4\pi} \int_{li}^l \frac{R}{\sqrt{(R^2 + x^2)^3}} dx \quad (2)$$

Finally, by solving the integral, we derive the equation for the value of the magnetic field B at all geometry.

$$B = 2 \frac{\mu_0 I}{\pi} \frac{l^2}{[(x^2 + d) + 2l^2][(x^2 + d) + 2l^2]^{\frac{1}{2}}} + \frac{l^2}{[(x^2 + d) + 2l^2][(x^2 + d) + 2l^2]^{\frac{1}{2}}} \quad (3)$$

In this research, the Helmholtz Coil generates the magnetic field needed to simulate the space environment. The coil's center must contain a volume corresponding to the nanosatellite's dimensions, ensuring the highest possible field uniformity within this space. The image below illustrates the uniform magnetic field area between the coils, where the satellite should be positioned to experience optimal field conditions.

B. Uniformity of magnetic field

For instance, the Helmholtz coil provides high uniformity of magnetic field, and the un-ambiguity of calibration is achieved by exposing the magnetometer only to the uniformity provided by Helmholtz coil. This made it possible to calibrate as well as to set it accurately and this proved it would work to the expectations of the applications it was designed for.

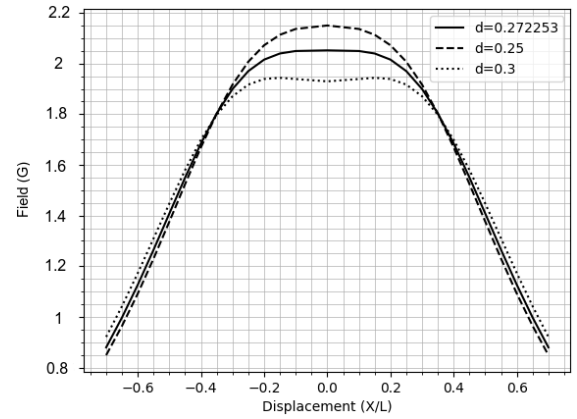
In this context, to achieve the highest possible uniformity, it is necessary to obtain the second derivative of the magnetic field at the center of the coil on equation (2.7). The first derivative is essentially zero, as the field is static. However, to achieve the lowest degree of variation along the axis, it is necessary that the second derivative is also zero, to get the value of zero on the second derive the distance between the two coils needs to be $d = 0,544506$. [9].

After getting the distance between the coils it's needed to calculate the effective value in relation to the d distance of the coils, the coil uniformity can be calculated by [11]:

$$\frac{B_0}{B_z} \quad (4)$$

Where B_z is the field with the variation during the axis of the two coils named x .

Fig. 2: Uniformity of field calculated in Helmholtz Coil



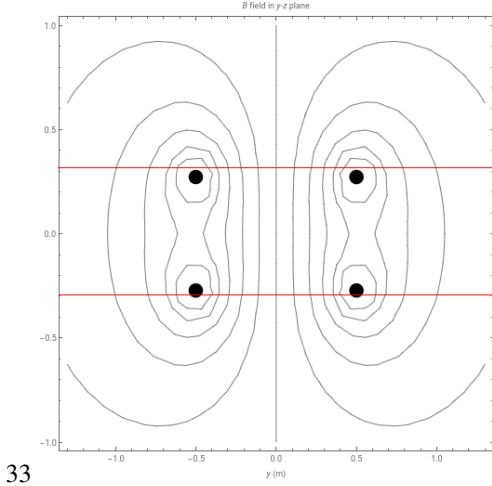
SourceFonte: From author

Considering a 1U CubeSat for the testing area, the uniformity is around 0.02%.

C. Simulation of coil

The coil design was validated through CDF simulations using Wolfram [17]. The magnetic field uniformity factor, as shown in Fig. 3, is oriented in two dimensions and sufficient to accommodate a minimum nanosatellite, the area of 113.5 mm for a 1U nanosatellite is highlighted by red lines. This image represents a Helmholtz coil along one axis with a top-down view, and the displayed lines correspond to magnetic field lines. As we can observe, the field lines remain free of imperfections along the Y-axis until they reach 0.3 m, which is sufficient for testing a 1U CubeSat with the highest possible uniformity.

Fig. 3: Simulation and estimation of magnetic field lines.



Source: The author

D. Electrical parameters for coils

Given that the desired magnetic field strength is to be achieved at the coil's center, where there is no variation of I along the axis, we can then determine that:

$$B_0 = 2.0359 \times \frac{\mu_0 N I}{\pi L} \quad (5)$$

Solving the equation to $2,4G$, N needs assum 60 turns and I assum $2,5A$ for satisfying the requirements, to calculate the wire diameter, the following equation is employed, where v takes the value of $2,3 \cdot 10^6 A/m^2$ [5].

$$d = \sqrt{\frac{i}{v}} \quad (6)$$

For the approximate wire resistance, it is found it using the following equation [5], where k is the resistivity of copper and the value is $2.195 \times 10^{-8} \Omega m$, df is the wire diameter and L is the total length of a coil.

$$R = \frac{k}{df^2} l \quad (7)$$

The inductance of the coils (L_s) can be approximated through mutual inductance, as long as they are connected in series [5].

$$L_s = 2n^2 L (\Phi_{11} + \Phi_{12}) \quad (8)$$

Where L is the total length of the coil, which is 1m in this case, Φ_{11} and Φ_{12} represents the normalized and mutual magnetic fluxes, n is the number of turns.

III. COIL CALIBRATION

The first step for calibration is to collect the values from the coils to analyze the error present in the system. The methodology for collecting this data is to set a coil control system with the same voltage value. With the same voltage

TABLE I: Calculated values for the coil design

Expected maximum values of the one axes coil (two winding)			
Parameter	unit	value	
Length (L)	(m)	0,5	
Total winding length (two coils)(l)	(m)	240	
Current (i)	(A)	2,5	
Wire type	(AWG)	17 AWG	
Wire diameter	(mm)	1,043	
Approximate resistance	(Ω)	4,84	
L_s	(mH)	6.462	

data, we can analyze the field difference between the axes. According to the measured data, this difference was $33.9 (mG)$ between the (X) and (Z) axes.

TABLE II: Measure coil values before calibration

Parameters measured in each coil				
axes	voltage (V)	Resistance (Ω)	current (A)	field value (mG)
X	7.10	4.31	1.647	804.7
Y	7.10	4.37	1.623	793
Z	7.10	4.5	1.577	770.8

The calibration method used will be the third-order method presented by X, the model is performed by the equation [5].

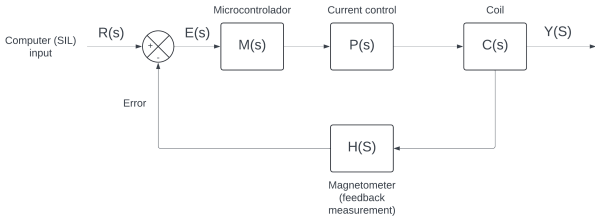
$$\hat{B} = K_4 B^4 + K_1 B + K_2 B^2 + K_3 B^3 \quad (9)$$

The result of this equation is the magnetic field observed in the sensor, \hat{B} . The vector B is a 3×1 vector containing the field values from the microcontroller, while B_1 and B_2 are 3×1 vectors containing the second-order terms related to the theoretical field. K_1 , K_2 , K_3 , and K_4 are coefficients that need to be determined.

IV. HIL (HARDWARE-IN-THE-LOOP)

The microcontroller, programmed to interpret the received data, orchestrates the behavior of a DAC81408EVM module. This module, in turn, precisely regulates the input current supplied to the driver of the Helmholtz coils. The coils, arranged in a specific configuration, generate a magnetic field within the test environment, mimicking the Earth's magnetic field experienced by a spacecraft in orbit. The current range of $-2.5A$ to $+2.5A$ provides flexibility in simulating various orbital altitudes and corresponding magnetic field strengths enough to test, but the system is capable of generating $-5A$ to $+5A$. The readings of the HMC5883L magnetometer are then fed back into the control loop, enabling the system to make real-time adjustments to the coil currents, thus maintaining a precise replication of the desired magnetic field. To ensure the accuracy and fidelity of the simulated magnetic field, the system incorporates a high-precision AlphaLab MGM magnetometer.

Fig. 4: Closed loop system block diagram



Source: The author

A. Control system and clock

The system operates in closed-loop, and the transfer function of the plant is shown below:

$$G_{\text{total}}(s) = C(s) \cdot H(s) \quad (10)$$

By substituting the values and analyzing the system's step response.

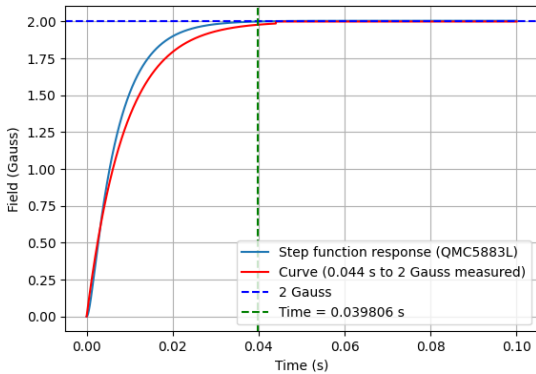
$$C(s) = \frac{1}{1 + sT_{\text{bobina}}} \quad (11)$$

$$H(s) = \frac{G}{\tau s + 1} \quad (12)$$

Where scale is the range of field that the sensor was set to, and sT_{bobina} in the function should be approximately equal to $\tau \approx \frac{L}{R}$ [5].

It's possible to note that we reach a peak value of 2 G in 0.04 seconds of operation, as shown in Fig. 5. This indicates that this is the time required for the coil to generate the value and provide feedback to the sensor. For magnetic field error control, the system's sampling frequency is 250 Hz, and the frequency of new magnetic field values is Hz.

Fig. 5: Time of response for 2 Gauss



Source: The author

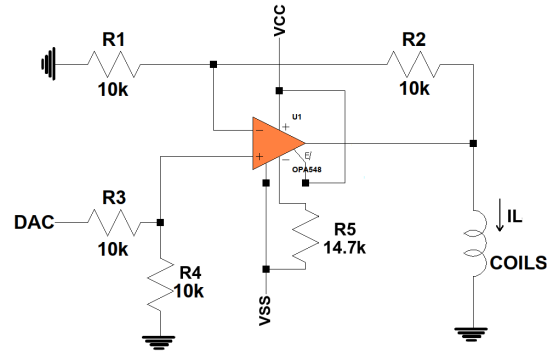
B. Drive of Coils

In the realm of coil current control, stringent requirements must be met. Noise levels should be minimized, ideally matching or even surpassing the low noise performance of the connected Digital-to-Analog Converter (DAC). To achieve this, the OPA548, operational amplifier will be employed in its non-inverting configuration, chosen for its ability to effortlessly manage currents up to 3A., with peak currents of 5A. Given this configuration, the current flowing through the coils will be regulated by a VCC voltage source and be directly influenced by the load resistance. This approach capitalizes on the amplifier's substantial current capacity and robust design to guarantee dependable operation. The relationship between load current and input voltage V_{in} , assuming uniform resistor values, can be observed as follows:

$$i_o = \frac{V_i}{KR_L} \quad (13)$$

Where $K = \frac{R1}{R2}$, the current source circuit shown in Fig.

Fig. 6: Drive to control the coils.



Source: The author

C. Simulation of drive circuit

The VCC source designed with the OPA548 operational amplifier was meticulously simulated in LTSpice. The resulting circuit design successfully delivered the anticipated output current range of 2,5A to 2,5A considering the load resistance, aligning with the project's specifications.

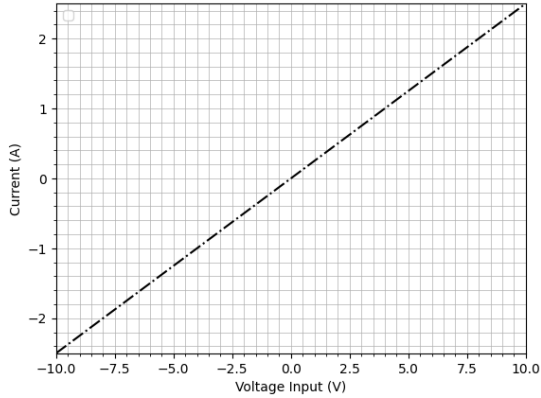
D. Performance analyses of coil current control

As previously mentioned, minimizing noise in the current driver is crucial. The selected Digital-to-Analog Converter DAC exhibits a precision of 1 Least Significant Bit LSB Integral Non-Linearity INL. This means the smallest bit fluctuates, contributing to overall system noise.

By applying this to the coil driver's transfer equation, we determine that the DAC-induced noise will be 0.3mV. Consequently, any additional noise introduced by the driver itself must remain below this threshold.

To assess the impact of noise on the driver, a test was conducted where an aleatory value was introduced as an input

Fig. 7: Current observed in coils.

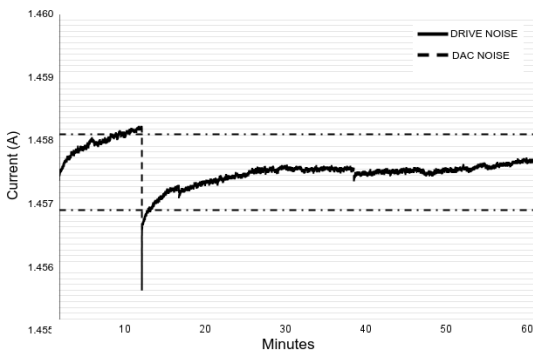


Source: The author

for drive control. The results of this test were then compared with the DAC's performance.

To mitigate noise and enhance voltage references, an LM350 regulator was implemented for the positive voltage supply (VCC), and an LT1033 regulator was employed for the negative voltage supply VSS of the OPA548 operational amplifier. These measures collectively contribute to reducing the overall noise floor of the system. All measurements were collected using the DMM6500, multimeter. The low noise of the drive contributes to future updates, upgrading a system to 24-bit in the future can bring significant benefits in terms of accuracy, resolution, and data processing capacity. In measurement systems, such as those using analog-to-digital converters (ADCs), moving from 16- or 12-bit resolution to 24-bit allows much greater detail to be captured in analog signals, making measurements more accurate and sensitive to small variations.

Fig. 8: Noise measurement of drive



Source: The author

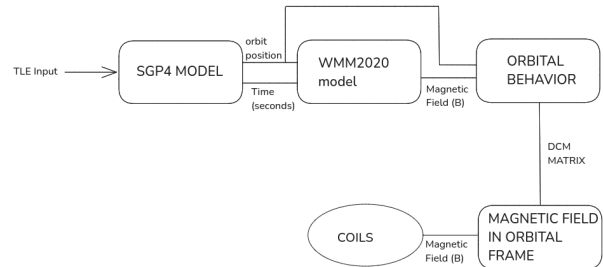
V. SOFTWARE IN THE LOOP AND SIMULATIONS

The simulation leverages the power of the Simplified General Perturbations 4 (SGP4) model, a well-established analytical tool in orbital mechanics. SGP4 takes Two-Line

Element Sets (TLEs) as input, which encapsulate a satellite's orbital parameters at a specific epoch. By propagating these TLEs forward in time, SGP4 calculates the satellite's position and velocity with remarkable accuracy, considering primary gravitational forces and significant perturbations like Earth's oblateness and atmospheric drag. This allows for the precise visualization of the satellite's trajectory in three dimensions, revealing its position components' evolution over time.

In parallel, the simulation employs the World Magnetic Model 2020 (WMM2020) [11], a state-of-the-art model for representing Earth's magnetic field. As SGP4 predicts the satellite's position, WMM2020 calculates the corresponding magnetic field vectors at each point. This information is crucial for comprehending how the satellite interacts with the ever-changing magnetic environment in space. To accurately model the interaction between a satellite and Earth's magnetic field, the output of the World Magnetic Model (WMM2020), which is provided in the North-East-Down (NED) coordinate system, must be transformed into the satellite's orbit frame. This is achieved by first obtaining the satellite's attitude information, which defines its orientation relative to the NED frame. Using this attitude data, a transformation matrix is constructed, allowing for the conversion of the magnetic field vector from the NED frame to the orbit frame. This conversion is essential for various applications, such as designing attitude control laws, analyzing magnetometer data, and studying space weather effects, as it provides a precise understanding of how the magnetic field interacts with the spacecraft in its own reference frame.

Fig. 9: Software in the loop diagram

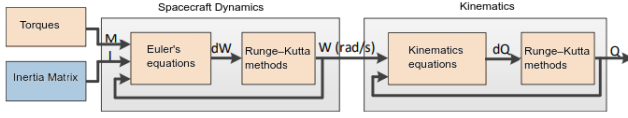


Source: The author

VI. SPACECRAFT DYNAMICS AND KINEMATICS

Spacecraft motion is predicted and controlled by a variety of mathematical models and numerical techniques. Satellites' future location and velocity are determined via orbital propagation algorithms, like the (sgp4), using information about their current state and perturbative forces. Because rotational dynamics is non-linear, methods such as Euler's method or more sophisticated numerical integrators can be used to integrate the equations of motion for attitude dynamics. The software tools utilized by mission planners and operators to assist in the planning and execution of space missions incorporate these concepts [12].

Fig. 10: Spacecraft dynamic calculation



Source: Adapted from [5]

Euler's equations for rotational motion explain how torques result in angular acceleration while accounting for the body's moment of inertia, a measurement of the mass distribution concerning the rotational axis. The linear and angular accelerations of a rigid body under the effect of external loads, such as gravity, friction, and contact forces, can be found using the kinetics equations. In summary, Euler's equation states that the external moment of force on a rigid body equals the sum of two terms [5]. Expanding the equations for each axis:

$$M_x = I_{xx}\dot{\omega}_x + \omega_y\omega_z(I_{zz} - I_{yy}) \quad (14)$$

$$M_y = I_{yy}\dot{\omega}_y + \omega_z\omega_x(I_{xx} - I_{zz}) \quad (15)$$

$$M_z = I_{zz}\dot{\omega}_z + \omega_x\omega_y(I_{yy} - I_{xx}) \quad (16)$$

Euler's equations of motion for a rigid body rotating about a fixed point, in a body-fixed frame, are:

$$\dot{\omega}_x = \frac{1}{I_{xx}} [M_x - \omega_y\omega_z(I_{zz} - I_{yy})] \quad (17)$$

$$\dot{\omega}_y = \frac{1}{I_{yy}} [M_y - \omega_z\omega_x(I_{xx} - I_{zz})] \quad (18)$$

$$\dot{\omega}_z = \frac{1}{I_{zz}} [M_z - \omega_x\omega_y(I_{yy} - I_{xx})] \quad (19)$$

The derivative of the kinematics of a quaternion is used to represent rotations in three-dimensional space. Quaternions are a more efficient way to describe rotations, avoiding some of the complexities associated with other representations like Euler angles [25]. The derivative of the kinematics of a quaternion is given by:

$$\mathbf{q}' = \frac{1}{2}\mathbf{\Omega}'\mathbf{q}, \quad (20)$$

Given that \mathbf{q} is the quaternion representing the attitude of the body and $\mathbf{\Omega}'$ is the skew-symmetric matrix formed by the angular velocity in the body's axes, as defined by Eq. (4.48):

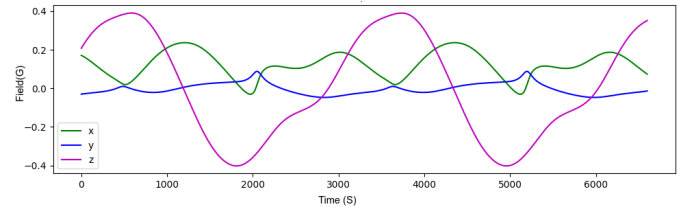
$$\mathbf{\Omega}'(\boldsymbol{\omega}) = \begin{bmatrix} 0 & \omega_z & -\omega_y & \omega_x \\ -\omega_z & 0 & \omega_x & \omega_y \\ \omega_y & -\omega_x & 0 & \omega_z \\ -\omega_x & -\omega_y & -\omega_z & 0 \end{bmatrix} \quad (21)$$

A. Simulation results

The simulation leverages the power of the sgp4 model, a well-established analytical tool in orbital mechanics. sgp4 takes TLE as input, which encapsulates a satellite's orbital parameters at a specific epoch. By propagating these TLEs

forward in time, SGP4 calculates the satellite's position and velocity with remarkable accuracy, considering primary gravitational forces and significant perturbations like Earth's oblateness and atmospheric drag. This allows for the precise visualization of the satellite's trajectory in three dimensions, revealing its position components' evolution over time [8]. In parallel, the simulation employs the wmm2020, a state-of-the-art model for representing Earth's magnetic field. As sgp4 predicts the satellite's position, wmm2020 calculates the corresponding magnetic field vectors at each point. The simulated satellite below was COSMOS 2361, with the date 2024-09-11 and a time of 16:05:30 UTC.

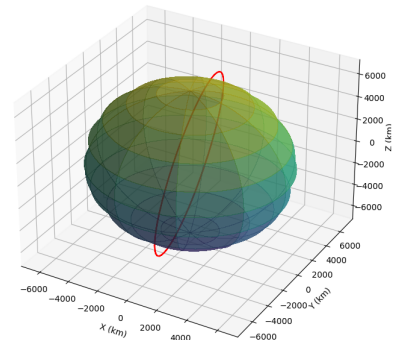
Fig. 11: Magnetic field in LEO orbit over time



Source: The author

To provide a clearer visualization of the satellite's orbit, the graph in Fig. 15 presents the trajectory in a three-dimensional format. This enhanced representation offers a more comprehensive view of the orbital path, allowing for a better understanding of the satellite's movement and position throughout its orbit. With the magnetic field data calculated, the next step is to compute the CubeSat's positional graph. The calculation block, shown in Fig. 13, uses previously mentioned data such as angular velocity, initial position, and the inertia matrix to determine the satellite's position. To approximate the graph to the duration of a full orbit, this work implements the Runge-Kutta algorithm.

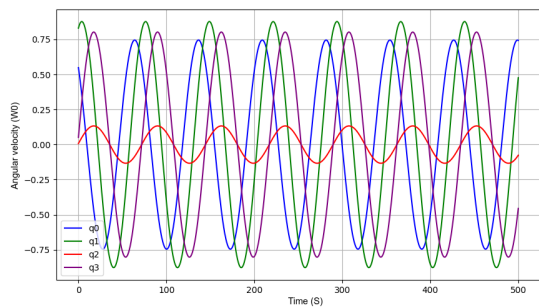
Fig. 12: CubeSat position in a 3D orbit



Source: The author

The final step in the process involves rotating the magnetic field, as depicted in Fig. 11, using the quaternion data from Fig. 13. This rotation is crucial to accurately represent the

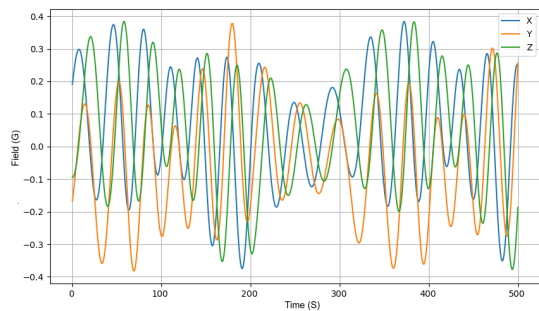
Fig. 13: Position of rotation



Source: The author

magnetic field as it is experienced by the satellite in its orbital path. By applying this transformation, we obtain the magnetic field orientation that corresponds to the satellite's actual observation in space. This final adjustment ensures that the simulated magnetic field aligns with the real-world conditions encountered by the satellite.

Fig. 14: Rotated magnetic field



Source: The author

VII. CONCLUSIONS

A. Methodology for uniformity testing

In this method, shown by [27], a wooden ruler marked in centimeters is aligned along the axis. The MGM Alphaslab magnetometer is then positioned at the indicated points on the ruler, with readings taken at every necessary point, considering the extremities of a 1U CubeSat. Taking the axis origin as the center of the cage, the measurement span covers the range from -57 mm to 57 mm.

B. Precision discussion

This paper proposes a three-axis Helmholtz coil system for 1U CubeSats, achieving 0.4% field uniformity for reliable low Earth orbit magnetic field testing [8]. Achieved uniformity offers good accuracy of less than (1% error) in LEO orbit field reproduction. Model accuracy varies based on mission requirements and ADCS sensors. Missions with precise pointing may require an error of less than 0.05%. The adaptable power source, scalable to 6U or larger satellites, provides up to 5A,

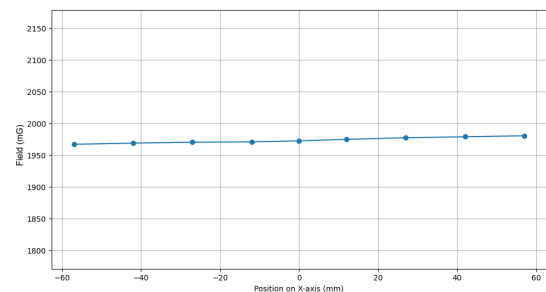
helping enhance ADCS reliability for TRL9. The uniformity of the system was measured in the center of the coil for a 1U CubeSat volume.

TABLE III: Measure coil values before calibration

Parameters measured in each coil			
Distance	-57 (mm)	center B_0 (mm)	57mm (mm)
Magnetic field value	1967.23	1972.63	1980.72

The graph below shows the uniformity measured along the X-axis of the constructed coil. The measurement was taken precisely from the center of the coil to the space sufficient for testing a CubeSat 1U. The effective value measured for the uniformity was around 0.4%.

Fig. 15: Field values measure by Alphaslab milligauss meter



Source: The author

Even though the obtained uniformity is greater than estimated, the values obtained are within the acceptable range, even for commercial coils. The discrepancy in values can be attributed to the measurement methodology, as it was physically impossible to remove all magnetic objects around the coil. Additionally, it is also due to the manual winding methodology used for the wires, which was performed to minimize assembly costs.

REFERENCES

- [1] S. M. Adame, J. C. O. Galvan, E. C. Littlewood, R. E. Perez, and E. B. Brisset, "Coil systems to generate uniform magnetic field volumes," in *Proc. Excerpt COMSOL Conf.*, Oct. 2010, pp. 1–7.
- [2] A. Alanazi and J. Straub, "Statistical Analysis of CubeSat Mission Failure," 2018.
- [3] P. Alken, A. Chulliat, M. Nair, S. Maus, and C. Woods, "The US/UK World Magnetic Model for 2020-2025: Technical Report," National Centers for Environmental Information (NCEI), NOAA, Silver Spring, MD, USA, Tech. Rep. NESDIS/NGDC-1, 2020.
- [4] C. Ananda and N. Bartel, "CaNOP 3U CubeSat Attitude Determination and Control Testing System: Helmholtz Cage Design," *Proceedings of the Wisconsin Space Conference*, vol. 1, 2018, doi: 10.17307/wsc.v1i1.222.
- [5] D. Batista, F. Granziera Jr, M. Tosin, and L. Melo, "Three-Axial Helmholtz Coil Design and Validation for Aerospace Applications," *IEEE Transactions on Aerospace and Electronic Systems*, vol. PP, no. 1, 2017, doi: 10.1109/TAES.2017.2760560.
- [6] J. Bouwmeester and A. Miele, *Spacecraft Systems Engineering*, Springer, 2010.
- [7] J. Campbell and N. G. Leung, "Introduction to the Helmholtz Coil in Aerospace Engineering," *Aerospace Engineering Journal*, vol. 12, no. 2, pp. 200-215, 2003.

- [8] R. Cardoso da Silva, I. Ishioka, C. Cappelletti, S. Battistini, and R. Borges, "Helmholtz Cage Design and Validation for Nanosatellites HWIL Testing," *IEEE Transactions on Aerospace and Electronic Systems*, vol. PP, no. 1, 2019, doi: 10.1109/TAES.2019.2898309.
- [9] V. Carrara, "A 3-axis Helmholtz coils design for geomagnetic field simulation," in *Proc. 6th Nat. Congr. Mech. Eng.*, Aug. 2010, pp. 1–11.
- [10] J. Chaisakulsurin et al., "Hardware-in-the-Loop Simulation Testbed for Three-Axis Earth's Magnetic Field Generation Based on 2.4-Meter Square Helmholtz Coils," 2023 IEEE/ION Position, Location and Navigation Symposium (PLANS), Monterey, CA, USA, 2023, pp. 829-834, doi: 10.1109/PLANS53410.2023.10139939.
- [11] A. Chulliat, P. Alken, M. Nair, A. Woods, S. Maus, and S. Macmillan, "The US/UK World Magnetic Model for 2020–2025," *NOAA Technical Report NESDIS*, 160, 2020.
- [12] V. A. Chobotov, *Orbital Mechanics*, AIAA Education Series, 2002.
- [13] CALPOLY, "CubeSat Design Specification Rev.14.1," Cal Poly SLO, 2022.
- [14] C. Davis, "Hardware-in-the-Loop Simulation for Control System Validation," in *Journal of Control and Automation*, vol. 22, no. 1, 2021, pp. 45-56.
- [15] A. Derbyshire, "Unknown Aspects of Helmholtz Coils," in *Proceedings of the International Conference on Magnetic Field Studies*, 2007, pp. 456-467.
- [16] J. Diebel, "Representing Attitude: Euler Angles, Unit Quaternions, and Rotation Vectors," *Technical Report*, Stanford University, 2006.
- [17] Euripides, Peter. "Square Helmholtz Coils CDF." Wolfram Demonstrations Project, Peter Euripides, 27 Dec. 2007, demonstrations.wolfram.com/SquareHelmholtzCoils/.
- [18] C. C. Finlay et al., "International Geomagnetic Reference Field: The eleventh generation," *Geophysical Journal International*, vol. 183, no. 3, pp. 1216-1230, 2010.
- [19] G. Franklin, J. Powell, and A. Emami-Naeini, *Feedback Control of Dynamic Systems*, 7th ed., Pearson, 2015.
- [20] A. Gallina, D. Knapik, K. Kolek, M. Rosół, A. Tutaj, and P. Zagórski, "Design of an ADCS test stand for nanosatellites," 2022 26th International Conference on Methods and Models in Automation and Robotics (MMAR), Miedzyzdroje, Poland, 2022, pp. 459-463, doi: 10.1109/MMAR55195.2022.9874310.
- [21] P. G. Haddox, "The development of a hardware-in-the-loop attitude determination and control simulator for Illiniset-2," in *52nd Aerospace Sciences Meeting*, 2014, p. 0007.
- [22] R. Hurtado-Velasco and J. Gonzalez-Llorente, "Simulation of the Magnetic Field Generated by Square Shape Helmholtz Coils," *Applied Mathematical Modelling*, vol. 40, 2016. doi: 10.1016/j.apm.2016.06.027.
- [23] B. Jean and H. Weiss, "Hardware-in-the-Loop Simulation: The Key to Accurate and Efficient Control System Design," in *Proceedings of the 5th International Conference on Simulation and Modeling*, 2001.
- [24] I. S. Kinoshita, S. Battistini, C. Cappelletti, and R. A. Borges, "Design and development of an active magnetic actuator for attitude control system of nanosatellites," in *4th IAA Conference on Small Satellites*, International Academy of Astronautics, 2017.
- [25] J. B. Kuipers, *Quaternions and Rotation Sequences: A Primer with Applications to Orbits, Aerospace, and Virtual Reality*, Princeton University Press, 1999.
- [26] J. Lee and K. Lee, "Mission Scenario Rehearsal for CubeSats Using Hardware-in-the-Loop Simulation," *Space Mission Analysis and Design Journal*, vol. 20, no. 3, pp. 245-257, 2016.
- [27] J. V. Lopes de Loiola, L. Cmara van der Ploeg, R. Cardoso da Silva, F. Cardoso Guimares, R. A. Borges, G. A. Borges, S. Battistini, and C. Cappelletti, "3 axis simulator of the earth magnetic field," in *Aerospace Conference*, 2018 IEEE. IEEE, 2018.
- [28] T. Jones and K. Wang, "Collaborative Engineering Using Hardware-in-the-Loop Simulations," in *IEEE Transactions on Automation Science and Engineering*, vol. 16, no. 2, 2019, pp. 345-357.
- [29] R. Lenz and J. A. Schenck, "Precision Calibration of Magnetometers Using Helmholtz Coils," *IEEE Transactions on Instrumentation and Measurement*, vol. 33, no. 3, pp. 256-261, 1984.



LATIN AMERICAN CUBESAT WORKSHOP SALVADOR, BR

DOI: 10.1234/example-doi-07

Development and Performance Analysis of an Attitude and Orbit Simulator for CubeSat

Ana Carolina Lima de Oliveira¹ and Thadeu Augusto Medina de
Carvalho²

¹UFMG

²ITA

Abstract

The Attitude and Orbital Control System (AOCS) is essential to the mission's success, once payloads, antennas, and thrusters must maintain a precise orientation throughout nearly every phase of the spacecraft mission. With every mission, there are specific requirements defined by its payload and other subsystems that must be followed. Therefore, simulations are essential for verifying possible solutions, assessing calibration parameters, and guaranteeing the system's efficiency in diverse scenarios that the spacecraft may face during its mission. When considering the subsystem design, it is crucial to take into account a variety of potential scenarios, such as various spacecraft operation modes and disturbances. The objective of this project is to detail the development of an attitude and orbit simulator. This simulator will cover both the detumbling phase and the LVLH Attitude Acquisition phase for the CubeSat ITASAT2. Additionally, it will account for the various orbital altitudes that the spacecraft may encounter throughout its mission, ranging from 370 km to 400 km considering a two-body orbital model. In the detumbling phase, the B-dot control law was implemented, which is a commonly used method to stabilize satellites in the early stages of their flight in low Earth orbit. This technique takes advantage of the interaction between the Earth's magnetic field and an artificial magnetic field created by magnetic coils on the satellite. To the Attitude Acquisition phase, reaction wheels were used to achieve the desired pointing. Consequently, it was necessary to account for the

saturation limits of the wheels. To address this, the momentum dumping technique was applied, using magnetic coils for the correction. The article discusses the proposed simulator and shows a comparative performance analysis with Ansys Systems Tool Kit® (STK) software.

Analysis of fuel consumption for orbital correction maneuvers to mitigate injection errors after launch

Evandro Marconi Rocco
Divisão de Mecânica Espacial e
Controle - DIMEC
Instituto Nacional de Pesquisas
Espaciais - INPE
São José dos Campos, Brasil
evandro.rocco@inpe.br

Liana Dias Gonçalves
Divisão de Mecânica Espacial e
Controle - DIMEC
Instituto Nacional de Pesquisas
Espaciais - INPE
São José dos Campos, Brasil
liana.goncalves@inpe.br

José Batista da Silva Neto
Divisão de Mecânica Espacial e
Controle - DIMEC
Instituto Nacional de Pesquisas
Espaciais - INPE
São José dos Campos, Brasil
jose.batista@inpe.br

Ronan Arraes Jardins Chagas
Divisão de Sistemas Espaciais - DISEP
Instituto Nacional de Pesquisas
Espaciais - INPE
São José dos Campos, Brasil
ronan.araes@inpe.br

Antonio Carlos de Oliveira Pereira
Junior
Divisão de Pequenos Satélites - DIPST
Instituto Nacional de Pesquisas
Espaciais - INPE
São José dos Campos, Brasil
acarlos.pereira@inpe.br

Abstract – The BiomeSat mission satellite, which is being developed by the National Institute for Space Research (INPE), consists of a remote sensing nanosatellite, CubeSat type, in the 12 kg class, with a dimension of 6U. The objective of the mission is to collect radiometric data from Brazilian territory in the visible and near-infrared bands of the electromagnetic spectrum. In addition, the satellite must be capable of receiving transmissions from environmental data collection platforms and information about vessels that use the AIS system. To ensure mission success, preliminary studies must be carried out carefully. Among them, we can highlight the studies presented in this paper, which define the possibilities of transfer and correction maneuvers necessary to transfer the satellite from the orbit into which it was injected by the launcher to the nominal orbit, as well as an analysis of the fuel budget necessary to perform such maneuvers in Launch and Early Orbit Phase (LEOP) operations.

Keywords – BiomeSat mission, AOCS, Orbital maneuver, Fuel budget.

I. INTRODUCTION

The National Institute for Space Research (INPE) is currently working on the BiomeSat mission. This time, the studies and work are focused on a remote sensing nanosatellite, a CubeSat type, in the 12 kg class, with a dimension of 6U, with the objective of collecting radiometric data of the Brazilian territory in the visible and near-infrared bands of the electromagnetic spectrum. In addition, the satellite must be capable of receiving transmissions from environmental data collection platforms and information about vessels that use the AIS system.

The development of the satellite considers the designs of the various subsystems that compose it, including the Attitude and Orbit Control System (AOCS) subsystem, responsible for controlling the satellite's orbit and attitude. A

distinctive feature of the BiomeSat mission satellite is that it has a thruster, measuring 0.8 U and a total impulse of 450 Ns.

The problems to be faced and analyzed by the AOCS subsystem are numerous and varied. We can highlight the study presented by [1], who proposed an algorithm to estimate and correct the three most common errors in sensor measurements: bias, misalignment, and non-orthogonality. Another interesting study involving problems to be analyzed and faced by the AOCS subsystem can be found in [2], in which they analyzed the impact of a thruster's PWM parameters in the non-latching flexible booms dynamics, motivated by the ITASAT-2 mission. Focusing on the problem of a CubeSat flight formation, [3], also motivated by the ITASAT-2 mission, evaluated simulation and movement control techniques to verify and evaluate the behavior of the following vehicles using different phase angles in detachment and rendezvous maneuvers in relation to the movement of the chief CubeSat. Independent of the central body, orbital maneuvers to be performed by the AOCS subsystem may be necessary. In [4] we see a discussion about changing the orbital plane using swing-by maneuvers for an artificial satellite around the Moon.

Thus, with the aim of contributing to the preliminary studies to be carried out for the BiomeSat mission, and with the studies and analyses involving the application of small satellites, the present work proposes to analyze the possibilities of maneuvers that transfer the satellite from the orbit in which it was injected by the launcher, to the nominal orbit. Since fuel is an important and limiting factor in space missions, an analysis of the fuel budget needed to perform the correction and transfer maneuvers is also necessary.

As with any space mission, preliminary studies must be carried out. Among them, we can highlight the analysis of the possibilities of maneuvers that transfer the satellite from the orbit in which it was injected by the launcher, to the nominal orbit. Since fuel is an important and limiting factor in space missions, an analysis of the fuel budget needed to perform the correction and transfer maneuvers is also necessary.

It has already been defined that the orbit of the BiomeSat mission satellite will be sun-synchronous and frozen. There are several possibilities of orbits with combinations of semi-major axis, eccentricity and inclination that meet this requirement. However, in this work, to estimate the fuel

consumption of the Launch and Early Orbit Phase (LEOP) operations, a nominal circular orbit with an altitude of 600 km will be considered. Since the launcher of the BiomeSat mission has not yet been defined, possibilities of injection orbits are adopted and, from them, correction limits are established for the orbital elements, depending on the capacity of the fuel tank, and the orbital requirements already defined for the mission.

II. METHODS

The methods used to calculate correction and transfer maneuvers, as well as the fuel consumption to perform each of them, will be presented below.

A. Correction and transfer maneuvers

One of the most common and efficient maneuvers in orbital mechanics is the Hohmann maneuver, presented in Figure 1. This maneuver can be used to correct the semi-major axis, in which, from an insertion orbit, the transfer to the final orbit is made using two impulses.

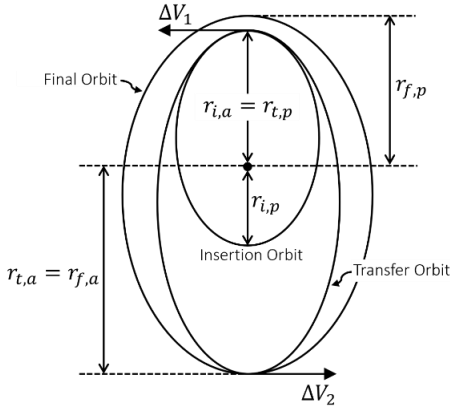


Fig. 1. Configuration of the Hohmann maneuver for the LEOP semi-major axis correction stage.

The first impulse, ΔV_1 , creates the so-called transfer orbit and the second impulse, ΔV_2 , regularizes the transfer orbit to the final orbit. In the presented case, the perigee of the final orbit ($r_{n,p}$) is aligned with the apogee of the insertion orbit ($r_{i,a}$), therefore, the apogee of the final orbit ($r_{n,a}$) is aligned with the perigee of the insertion orbit ($r_{i,p}$). The transfer orbit to be created by the ΔV_1 given in $r_{i,a}$, will have its perigee ($r_{t,p}$) equal to $r_{i,a}$, and its apogee ($r_{t,a}$) equal to $r_{n,a}$. Finally, ΔV_2 will be given in $r_{t,a}$ to complete the maneuver, reaching the final orbit. The impulse ΔV_1 , given by the difference between the velocities at $r_{t,p}$ ($V_{t,p}$) and $r_{i,a}$ ($V_{i,a}$) defined by the vis-viva equation, is given by (1) [5]:

$$\Delta V_1 = V_{t,p} - V_{i,a} = \sqrt{\mu} \left(\sqrt{\frac{2}{r_{t,p}} - \frac{1}{\left(\frac{r_{t,a} + r_{t,p}}{2}\right)}} - \sqrt{\frac{2}{r_{i,a}} - \frac{1}{\left(\frac{r_{i,a} + r_{i,a}}{2}\right)}} \right) \quad (1)$$

where, μ , the Earth's gravitational parameter, is equal to $3.9860064 \times 10^{14} \text{ m}^3/\text{s}^2$.

The impulse ΔV_2 , given by the difference between the velocities at $r_{t,a}$ ($V_{t,a}$) and $r_{f,a}$ ($V_{f,a}$) defined by the vis-viva equation, is given by (2):

$$\Delta V_2 = V_{f,a} - V_{t,a} = \sqrt{\mu} \left(\sqrt{\frac{2}{r_{f,a}} - \frac{1}{\left(\frac{r_{f,a} + r_{f,p}}{2}\right)}} - \sqrt{\frac{2}{r_{t,a}} - \frac{1}{\left(\frac{r_{t,a} + r_{t,a}}{2}\right)}} \right) \quad (2)$$

The total velocity increment of the semi-major axis correction phase, ΔV_h , is given by (3):

$$\Delta V_h = \Delta V_1 + \Delta V_2 \quad (3)$$

The inclination correction maneuver (Δi) will be performed by using an impulse (ΔV_3) to be given in the direction perpendicular to the plane of the nominal orbit at the moment the satellite passes through the intersection with the final orbit, resulting from the Hohmann maneuver phase described above. In order to simplify the problem, and considering the low eccentricity of the final orbit, we will consider the orbit as circular. Thus, the impulse (ΔV_3) is given by (4):

$$\Delta V_3 = 2v \sin\left(\frac{\Delta i}{2}\right) \quad (4)$$

The total velocity increment, ΔV_t , for the LEOP phase is given by:

$$\Delta V_t = \Delta V_1 + \Delta V_2 + \Delta V_3 \quad (5)$$

In a space mission, the satellite passes through different orbits, since in most cases it is not injected by the launcher exactly into the nominal orbit. In addition, adjustments may be necessary, and, whether small or large, every change requires energy.

B. Fuel Budget

As mentioned in Section A, the total velocity variation, ΔV_T , of a mission is the sum of all velocity changes that are transmitted to the satellite throughout the mission. Thus, with the total velocity variation, or the total velocity increment, ΔV_T , the propellant cost to be spent throughout the orbital maneuvers can be obtained, since there is a direct correlation between the velocity increment and the fuel consumption.

For a preliminary study, we can estimate the propellant mass, m_p , required to apply all velocity increments using the rocket equation, given by [6]:

$$m = m_0 e^{(\Delta V_T / I_{sp} g)} \quad (6)$$

where m_0 is the dry mass of the satellite, ΔV_T the total velocity increment applied to the satellite, $I_{sp} = \frac{V_0}{g}$ the specific impulse, with V_0 being the thruster exhaust velocity, and g the acceleration of Earth's gravity at the surface.

III. RESULTS AND DISCUSSIONS

The results and discussions regarding the possibilities of maneuvers to correct and transfer the satellite from the orbit into which it was injected by the launcher to the nominal orbit will be presented below.

Figures 2, 3 and 4 present a generic study of the variation in the velocity increment required to perform the maneuvers, in which the altitude varies between 500 km and 700 km, considering a semi-major axis error of -20 km, an inclination error of 0.2 degrees and an eccentricity error of 0.005. Figure 1 presents the results obtained for the velocity increments related to the first and second impulses of the Hohmann transfer added together ($\Delta V_1 + \Delta V_2$), situation in which coplanar maneuvers are performed to adjust the semi-major axis and eccentricity of the orbit. Figure 2 presents the results obtained for the non-coplanar maneuver to adjust the orbital inclination (ΔV_3) and Figure 3 presents the results for the velocity increments of all maneuvers, coplanar and non-coplanar, added together (ΔV_T).

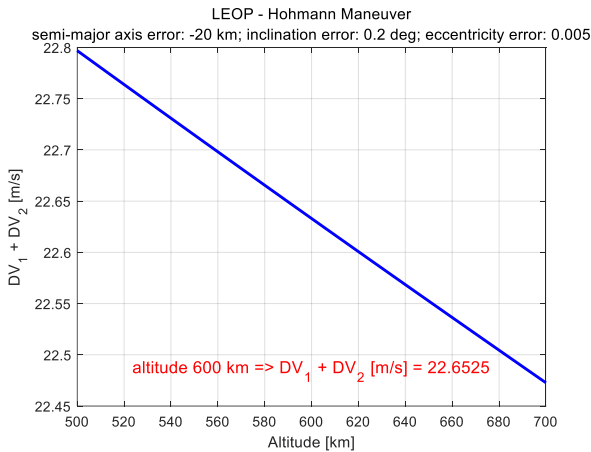


Fig. 2. Velocity increment of the first two maneuvers ($\Delta V_1 + \Delta V_2$).

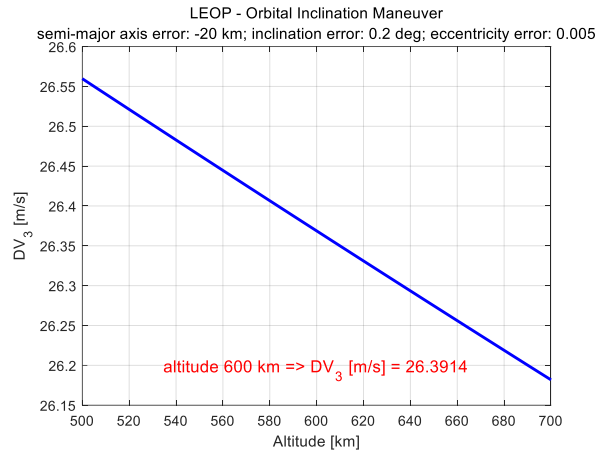


Fig. 3. Velocity increment of the third maneuver (ΔV_3).

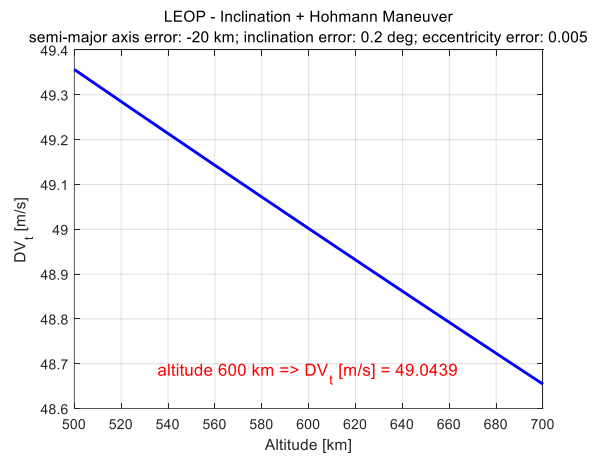


Fig. 4. Total velocity increment (ΔV_T).

From this study, the satellite altitude is restricted to around 600 km, with an error of 20 km below and 20 km above, for an analysis of fuel budget as a function of the error of the semi-major axis, the error of the injection eccentricity and the injection inclination, from the application of the Hohmann maneuver and the inclination adjustment maneuver, respectively. The results are presented in Figures 4 to 8.

Figure 5 shows the fuel budget for performing the Hohmann maneuver considering the injection error in the semi-major axis and in the eccentricity. From a numerical analysis, it was concluded that, for this case, the maximum velocity increment is 22.6655 m/s, resulting in a maximum fuel budget of 0.1122 kg. The fuel consumption for the inclination adjustment maneuver is shown in Figure 6, requiring a maximum velocity increment of 26.3687 m/s to perform the maneuver, with a maximum fuel budget of 0.1292 kg. The velocity increment and fuel budget required to perform the Hohmann and orbital inclination adjustment maneuvers, are shown in Figure 7, with a maximum velocity increment of 49.0343 m/s and a fuel mass of 0.2414 kg.

The results presented in Figure 7 represent a fuel budget greater than the fuel tank capacity of the propellant found on the market for satellites in the BiomeSat type category. Therefore, it became interesting to restrict the requirement for

injection error in orbit by the launcher. This scenario is presented in Figure 8, with an eccentricity error of 0.004 and an inclination error of 0.1 degrees. The results show a more suitable situation, with a fuel budget of 0.1585 kg. However, since this consumption would be spent only in LEOP, the remaining fuel may be small or not sufficient for routine orbital maintenance maneuvers. Even in a more favorable scenario, it is still interesting that less fuel is spent in LEOP, so that the satellite has a longer useful life and has enough fuel for any necessary deviation, or even for de-orbit.

Therefore, Figure 9 presents another case, with an eccentricity error of 0.0025 and an inclination of 0.1 degrees, with a maximum velocity increment of 26.4116 m/s and fuel budget of 0.1307 kg. It is worth remembering that the greatest fuel expenditure is for changing the orbital inclination and, in the case of Figure 8 and Figure 9, the error in the inclination was maintained. A restriction on the requirement for the maximum orbital inclination error that the launcher can inject the satellite into orbit could bring even more significant savings in the fuel consumption.

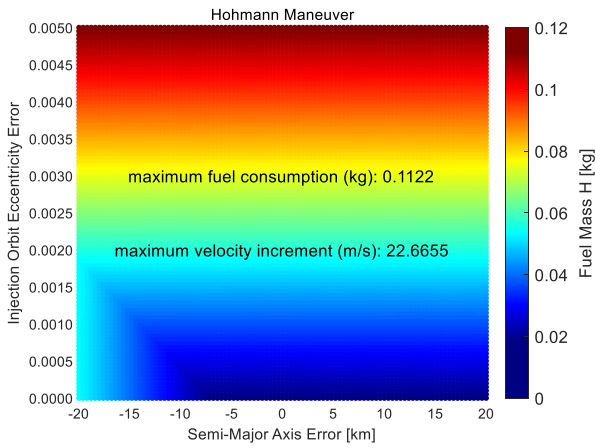


Fig. 5. Fuel budget for Hohmann maneuver.

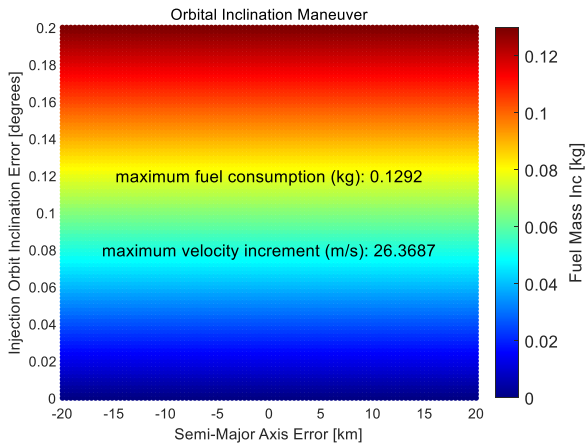


Fig. 6. Fuel budget for inclination maneuver.

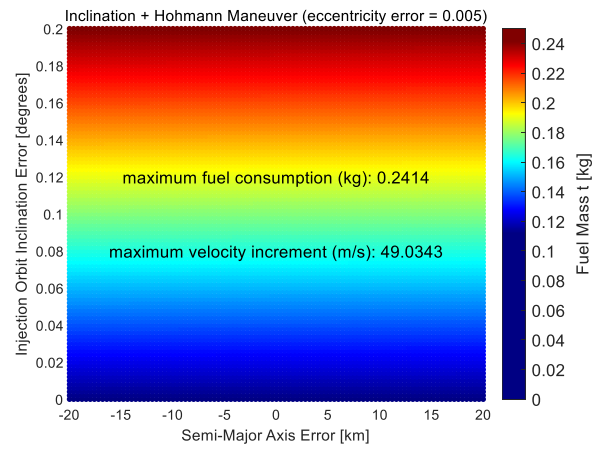


Fig. 7. Fuel budget for Hohmann and inclination maneuver ($e = 0.005$).

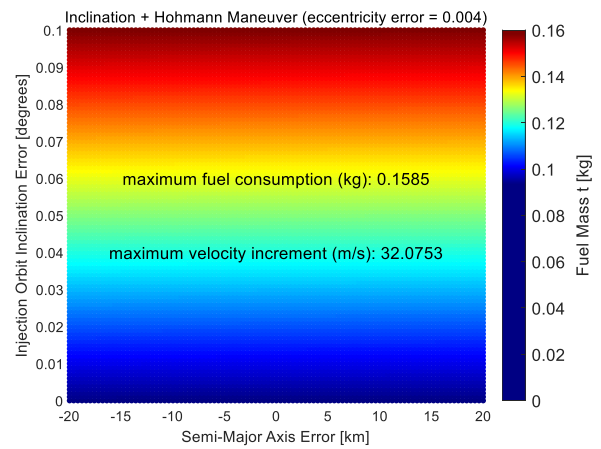


Fig. 8. Fuel budget for Hohmann and inclination maneuver ($e = 0.004$).

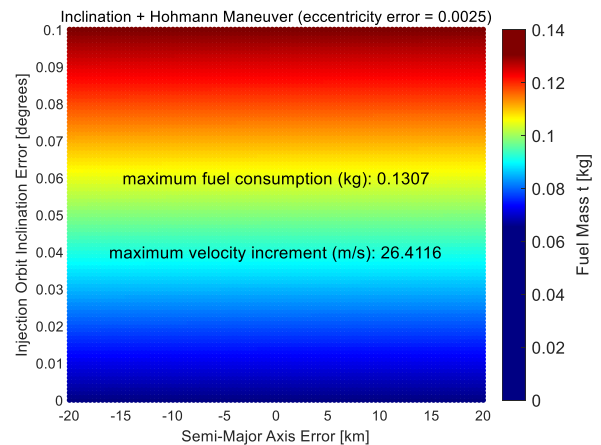


Fig. 9. Fuel budget for Hohmann and inclination maneuver ($e = 0.0025$).

CONCLUSIONS

The design of a space mission requires preliminary studies and analyses that define the scenario in which the project is

inserted, presenting important needs and limitations that must be taken into consideration to guarantee the success of the mission.

With the aim of contributing to such studies and analyses, the present work presents possibilities of correction and transfer maneuvers, with the aim of correcting the semi-major axis and the eccentricity of the satellite, and orbital inclination adjustment maneuvers.

The first results found showed the possibility of maneuvers whose fuel budget could exceed the tank capacity of satellites in the BiomeSat type category. Therefore, the results were refined and new results were obtained, restricting the possibilities in which the fuel budget in LEOP remains within the tank capacity, and still prioritizing a leftover in the fuel for margin of error, guaranteeing a longer useful life, any deviation that may be necessary during the mission, or even for carrying out the de-orbit.

The results presented are in agreement with the theory, showing that inclination change maneuvers are those that require the highest fuel consumption, bringing a need for attention to the type of maneuver. Minimizing the need for this type of maneuver can bring significant savings in fuel budget, increasing the chances of mission success.

Finally, it is worth highlighting that a good choice of launcher is essential for the success of the mission, since this criterion directly impacts the need to carry out transfer and correction maneuvers.

ACKNOWLEDGMENT

The authors would like to thank National Institute for Space Research (INPE) and CNPq (Process number 407075/2022-4) for supporting the project.

REFERENCES

- [1] R. A. J. Chagas, W. J. S. Marques, T. A. M. Carvalho, P. A. S. Oliveira, G. M. C. Hotta, "A self-calibration algorithm for satellite sensors based on vector observations". *Aerospace Science and Technology*, v. 114, p. 106759, jul. 2021.
- [2] L. Q. Mantovani, W. G. Santos, F. L. C. Ribeiro, J. C. Santos, "Influence of thrust modulation on a satellite with flexible non-latching booms. *Journal of the Brazilian Society of Mechanical Sciences and Engineering*, Oct. 2022.
- [3] T. C. Franco, W. G. Santos, "ITASAT-2: Formation flying maneuver and control considering J_2 disturbances and differential drag". *Simpósio de Aplicações Operacionais em Áreas de Defesa – SIGE*. Set. 2020.
- [4] J. B. S. Neto, A. F. B. A. Prado, J. K. S. Formiga, "Out-of-plane orbital maneuvers using swing-bys with the Moon". *Journal of Physics. Conference Series (Print)*, v. 641, p. 012014, 2015.
- [5] S. S. Fernandes, M. C. F. P. S. Zanardi, *Fundamentos de astronáutica e suas aplicações*. São Bernardo do Campo, SP: EdUFABC, 2018. v. 2. 459 p. ISBN 978-85-68576-77-9.
- [6] WERTZ, J. R. (ed.). *Space mission analysis and design*. 3. ed. Dordrecht, The Netherlands: Kluwer Academic, 1999. 969 p., 306936 cm. ISBN 1-881883-10-8.R.

Management Theory and Documentation Standards Integrated with Graph-Based Project Organization: A Case Study for PdQSat CubeSat Project

Mateus Vilela Oliveira

Departamento de Engenharia Elétrica
Universidade Federal de Minas Gerais
Belo Horizonte, Brasil
mateus.vilela025@gmail.com

Alice Torres de Aguiar

Departamento de Engenharia Mecânica
Universidade Federal de Minas Gerais
Belo Horizonte, Brasil
alicerresdeaguiar@gmail.com

Maria Cecilia Pereira

Departamento de Engenharia Mecânica
Universidade Federal de Minas Gerais
Belo Horizonte, Brasil
cecilia@demec.ufmg.br

Abstract—This study explores the application of management theory and graph-based information traceability in the PdQSat project, currently in progress at Federal University of Minas Gerais (UFMG). Project management standards, such as PM-BOK® and ECSS, and NASA’s System Engineering guidelines provide a strong foundation for development, yet each project demands a tailored approach. The goal of this research is to streamline PdQSat’s documentation by focusing on essential templates, improving administrative processes and enhancing efficiency. The authors employ a graph-based method to visualize dependencies between requirements, stakeholders, subsystems and other project artifacts, facilitating better communication and agility. By integrating management theory and graph-based tools, this approach aims to improve project outcomes and inspire similar aerospace engineering projects, highlighting the value of management in technical development. Additionally, the study seeks to support the formation of skilled workforce in the aerospace industry through academic projects.

Index Terms—project management, requirements, documentation, traceability

I. INTRODUCTION

As technology continues to evolve, the inherent complexity of engineering projects inevitably increases, presenting a myriad of challenges and opportunities for innovation. In response, a variety of methods and tools to deal with such complexity increase have been created and are widely used. Large-scale projects, such as satellites, exemplify the need for robust management strategies more than ever before, as they are composed of a variety of study fields and technical requirements, needing to be also reliable, efficient and capable of delivering the project’s needs.

Even so, projects in the same domain tend to differ a lot, which brings the need to develop and apply more tailored approaches that can contribute to their advancement. Regarding these tools, management theory and information traceability show up to be extremely helpful during the earlier stages of

We would like to express our deepest gratitude to the Brazilian Space Agency (AEB) for their invaluable support and sponsorship of this project. Their commitment to advancing the aerospace field in Brazil enables research and development opportunities like this one. This project would not have been possible without their generous contributions and continuous encouragement.

projects, and also facilitate the later stages by retaining useful information in a organized and traceable way. That being said, this work focuses on the application of the mentioned tools in a real academic engineering project: The development and construction of the PdQSat CubeSat.

The proposal behind the target project of this study [1] is to enhance the Brazilian aerospace sector and scientific production through the project, planning and construction of a CubeSat named “PdQSat”. The project involves several areas of the School of Engineering at UFMG, such as Aerospace, Mechanical, Electrical, Control and Systems Engineering, and is coordinated by LISA (*Laboratório Integrado de Sistemas Aeroespaciais*). The proposed mission for the satellite involves testing a lithium-sulfur (Li-S) battery and a supercapacitor developed at UFMG during flight in order to enable its use in future missions.

The landscape of management theory has undergone significant evolution, with extensive documentation available not only within the realm of project management standards but also tailored to specific applications. Key references such as PMBOK® have emerged as guiding principles for a multitude of projects, spanning technical and non-technical domains alike. Meanwhile, standards such as ECSS stand out for their specialized focus on space-related endeavors.

Despite the richness of these standards, it is evident that the unique characteristics of different projects, even within the same domain, necessitate tailored approaches to documentation and management tools. Against this backdrop, this study endeavors to navigate the array of options for an academic CubeSat, with a clear objective: to distill only the essential documentation required for advancing the project. Through careful selection and integration of management documentation into a refined subset of templates, the study seeks to streamline the project’s administrative processes, thereby enhancing operational efficiency.

Central to the investigation is the concept of traceability – the capacity to track and trace crucial project information such as requirements, stakeholders and subsystems. Employing a graph-based approach, the aim is to unravel the web of

dependencies inherent within the project's framework. By visually representing these relationships, the intention of this research is to facilitate easy access to critical information, fostering a more agile and responsive project environment. It is anticipated that this approach will yield tangible improvements in project efficiency and communication, two fundamental pillars for successful project outcomes.

Therefore, the approach combines management theory, standard documents and new project organization methods. By using the knowledge from these different areas, the goal is to improve the management of aerospace engineering projects, which could benefit similar researches worldwide. Exploring the intersection of management theory and graph-based information traceability within the context of the PdQSat project aims to provide valuable insights for future endeavors in aerospace engineering and beyond.

In order to further develop the concepts introduced in this section, section II will deal with the methods and important definitions for the understanding of the current work, while section III addresses the results obtained with the application of the Systems Engineering tools in the PdQSat project, followed by the conclusions regarding the work in section IV.

II. METHODS

Since its start, the PdQSat project has been developed with the usage of systems engineering tools to assist in the organization, planning and execution steps. Currently, systems engineering makes itself more needed and crucial than ever on the execution of large-scale projects, and is applied in a variety of fields, ever so contributing to the success of such projects.

As defined by the International Council on Systems Engineering (INCOSE) [2], a system consists of an arrangement of parts that together exhibit behaviour that the individual constituents do not. This definition aptly applies to satellite projects of any scale or purpose, making systems engineering tools ideal for guiding development from the project's earliest stages.

The first tool applied to the project was the adaptation of management guides to the context of the project, aiming to create general templates and define its scope. Following these definitions, it is proposed the usage of graphs to view and organize relevant information relative to any stage and of easy usage and adaptability. As a starting point, a revision of the PdQSat project is contained in subsection II-A, while subsection II-B will deal with the details regarding the conception and development of documentation used throughout the project, and subsection II-C will approach the usage of graphs as a facilitating mechanism for traceability.

A. The PdQSat Project

As mentioned in section I, the current work is inserted in the context of the nanosatellite named PdQSat-1, currently being developed at Federal University of Minas Gerais (UFMG) and sponsored by the Brazilian Space Agency (AEB). The project started in 2020 [1] having four main objectives, as follows:

- 1) Testing a lithium-sulfur (Li-S) battery in space environment;
- 2) Testing a super microcapacitor, developed and manufactured at UFMG, in space environment;
- 3) Qualify Brazilian workforce in high-tech engineering at the university;
- 4) Strengthen the state of Minas Gerais in the national aerospace sector.

In order to achieve such goals, a platform should be designed and manufactured in order to meet the payload requirements. As for the workforce qualification, students and professors of the university have been involved in every step of the project, following a problem based learning (PBL) approach.

Regarding the solution itself, the satellite contains eight subsystems that include platform and payload subsystems. The latter, for instance, consists of the electronic components to be tested and an additional circuit for each one, in order to run the tests. These subsystems are:

- 1) ADCS - Attitude Determination and Control System;
- 2) EPS - Electrical Power System;
- 3) S&M - Structure and Mechanisms;
- 4) OBDH - On-Board Data Handling;
- 5) TCS - Thermal Control System;
- 6) TT&C - Telemetry, Tracking and Command;
- 7) Payloads:
 - a) Lithium-Sulfur (Li-S) Battery + Battery Characterization Circuits;
 - b) Supercapacitor + Supercapacitor Characterization Circuit.

Due to the participation of students and professors from various academic areas, the PdQSat project stands out as a highly multidisciplinary endeavor, engaging multiple generations of students over time. For instance, as of the writing of this work, 12 undergraduate theses related to the project have been completed, with additional ones currently in progress.

In order to enable the integration of new students and teachers, and ensure the continued progression of the project, effective management tools are essential. Motivated by these factors, this work aims to present methodologies and research in this areas of project management and information traceability, as detailed in the subsequent sections.

B. Management Theory

Project management in high-complexity sectors, such as aerospace, is crucial to ensure the success of missions that involve multiple technical disciplines, tight deadlines, strict quality standards and the need to efficiently allocate resources. In the context of the PdQSat project, it became essential to develop management practices to ensure that all of these challenges were addressed in a structured and efficient manner. To do so, a careful adaptation of the following management theories was carried out.

The PMBOK® (Guide to the Project Management Body of Knowledge) [3], developed by the Project Management

Institute (PMI), is a consolidated reference that brings together a set of ideal practices for project management. PMBOK® methodology organizes this management in five groups: *Initiating, Planning, Executing, Monitoring & Controlling* and *Closing*. These groups embrace the whole project life cycle, ensuring that each individual phase is approached in a systematic and predictable way. Beyond that, PMBOK® defines ten knowledge areas such as *Integration, Scope, Time, Costs, Quality, Resources, Communications, Risk, Procurement* and *Stakeholders*, which can be customized according to the needs of different projects.

On the other hand, the management challenges faced specifically in space systems projects, from design to launch, have led the European Cooperation for Space Standardization (ECSS), an initiative supported by the European Space Agency (ESA) and other space organizations, to offer a set of detailed standards for planning, monitoring and control of space projects. These standards are divided in four main segments: *Management, Engineering, Product Assurance* and *Sustainability*. Within the management scope, the ECSS-M-ST-10C standard [4] details the best practices for planning and execution of space projects, focusing on critical aspects such as requirements definition, risk management and quality assurance.

In addition, the space systems project processes established by NASA [5] were also analyzed, since they occur repeatedly in the project life cycle until the desired objectives are achieved. Based on the definition of stakeholder expectations, taking into account objectives, constraints and success criteria for the mission, the high-level requirements survey serves as a reference for establishing a logical and functional decomposition for the project. This is followed by an iterative cycle of project design and trade studies to define the breakdown of the product structure, associated requirements and concept of operation. Finally, a series of questions are addressed to evaluate whether this proposal is fit to continue as a project solution and, if not, it is sent for reformulation.

Regarding the PdQSat, the PMBOK® methodological structure was essential to organize the activities and establish a management reference for the team, ensuring that the main aspects of the project were conducted properly and aligning stakeholders' expectations with planned deliverables. Besides, the study of ECSS's Project Planning and Implementation standard and NASA's System Engineering Handbook was important to evolve the PdQSat project from a perspective of risk mitigation and quality assurance for the final product, so that processes can be executed with higher precision and safety, as demanded by the aerospace sector.

Thus, by integrating the best practices from these methodologies, a customized management model was created for the PdQSat project. This model, structured through documentation templates, balances the need for rigorous control with the flexibility required to accommodate the particularities of an academic environment throughout the project's development.

C. Use of Graphs in Information Traceability

Regarding the field of systems engineering, traceability is defined by INCOSE [6, Pages 201 – 202] as a relationship established between two or more entities, thus enabling the tracking of changes of such entities throughout the project. By tracking the evolution of these entities, it becomes possible to evaluate changes in the project and mitigate negative effects that may arise of such changes, like impacts on financial budget or project timeline. The concept of traceability itself can be decomposed into *Bidirectional Traceability, Horizontal Traceability* and *Vertical Traceability*, as defined below [6]:

- *Bidirectional Traceability*: This type of traceability enables navigation in both directions across the relationships between entities, allowing for a comprehensive view of how requirements and related elements are interconnected;
- *Horizontal Traceability*: This type of traceability is present in relationships between entities of the same type in the project, thus enabling the connection of artifacts that may be in different life cycles;
- *Vertical Traceability*: Lastly, vertical traceability involves the connection between entities of different types, which makes possible to track the evolution of artifacts in the project from high level to low level concepts.

Traceability is a major topic regarding managing projects, especially large ones, since the scale of the connecting elements can become overwhelming and if not properly handled can cause the failing of the project or at least avoid it's full completion. Concerning a satellite project, traceability surely becomes fundamental for the success of the proposed task when considering the final product as an arrangement of complex individual subsystems that also communicate and depend on one another to achieve the desired behaviour. In this way, the most basic information to be traced on the project are the satellite subsystems, which are eight in total (including two payloads), as defined in subsection II-A.

Another data of interest is the stakeholders, which are the interested and/or affected parts involved in the project, being divided in two categories in this case: organizational entities and development groups [7]. Each stakeholder has its own set of interests, or needs, regarding the project and its execution. These needs, in the case of organizational entities, are sets of documents and norms to be followed, such as presented by Johnstone [8]. After mapping the needs of the stakeholders, the next step is to generate the appropriate requirements, thus capturing the information in a more technical and non-ambiguous way.

Previous works on the project, such as the ones by Manfrini [9] and Fraga [10], have already mapped several needs and requirements related to each subsystem and to the participating stakeholders, and the current proposal is to organize and connect such topics through the use of a graph, aiming to guarantee easy access to critical information as well as link important topics.

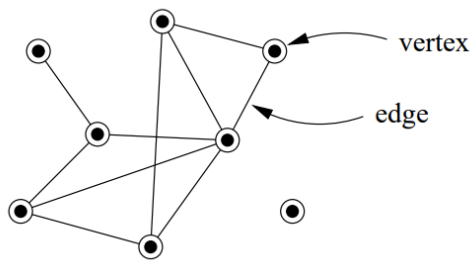


Fig. 1: Example of graph structure highlighting the difference between vertex and edge [11]

According to Newman [11], a graph, also known as a network, is a set of items (i.e., vertices) interconnected by edges, as illustrated in Figure 1, that can vary in type and have weights if necessary, as well as the vertices. Networks have been a subject of study for a long time but gained substantial force in recent years due to its application in several areas, not only limited to mathematics, but present also in fields like biology and social sciences.

More focused on software projects, Schwarz, Ebert, and Winter [12] identify a set of activities related to traceability and the importance of each one to the correctly achieving of so. Although similar, the focus of the work is more specific to tracing changes on information, and not just information itself, revealing the wide range of applications for graph theory in this field.

Due to its usefulness, graph-based traceability has also been applied as a tool on project management. Ruiz-Martin and Poza [13], on the one hand, combine the usage of PMBOK® concepts with graph theory aiming to trace an sequence of documents to be executed in a project management plan, pointing metrics to evaluate the nodes (documents) of the achieved graph and analyze the ideal pipeline.

Additionally, Ríos-Zapata, Pailhes, and Mejía-Gutiérrez [14] highlight the importance of projects early stages as well as for the design. For such, the authors define the steps involving the information, from conception to technical definition, passing through a high to low level of abstraction through the use of graphs. One particular interesting aspect of this application is the quantification of requirements on the lower level and it's integration in project related equations, which definitely facilitates the evaluation of parameter and variable changes all throughout the project, like temperature, frequency or even financial budget.

To create the graph and manage the desired information, the Obsidian software has been used due to its versatility and ease of use. Obsidian is a note-taking platform that works based on markdown files that can be interconnected and viewed in a graph display on the software. This application is primarily used for daily note-taking and other productivity tasks, but fits perfectly for the task of managing project information, due to it's feature of linking (citing) other notes.

In order to refer to another note, one just needs to write

it's name inside two brackets (i.e., `[[Note Name]]`) thus making possible to access the cited note through the file and also creating a visual connection between them on the graph. Beyond that, it is possible to associate tags with each note in the software by simply creating a name for the desired tag and writing it after a hash (#) symbol.

III. RESULTS AND DISCUSSION

The purpose of this section is to highlight and discuss the results achieved by further developing the methods proposed in section II. These methods are the application of management theory to develop custom documentation associated with the project, as well as a graph-based approach to interconnect and track relevant artifacts and information from the PdQSat project.

Results regarding the study of management theory are contained in subsection III-A and the results derived from the application of graphs in the project are discussed in subsection III-B.

A. Documentation Templates

The creation of management documentation templates for the PdQSat was motivated by the need to ensure that each phase of the project is managed efficiently and with technical rigor, providing a solid framework adapted to the project's particularities. Considering the project's early stage, the necessity to establish a set of standard documents and guide management activities was identified, thus ensuring that the project progressed in a structured and organized manner, as documented by Aguiar [15].

Given the academic nature of PdQSat, which aims to train qualified professionals, the project extends over several months, with a natural rotation of collaborators. This dynamic requires standardized and robust management to ensure continuity and consistent use of the initial planning as a reference aligned to the satellite mission's final objectives, while maintaining the ability to adapt to changes that may arise throughout its development.

The creation of these templates involved a detailed analysis of demands specific to the PdQSat, based on the recommended metrics from PMBOK®, the guidelines from NASA and the norms from ECSS. From this analysis, ten main documents were created, each one tailored to a specific and critical role in the project management:

- 1) **Project Charter** (*Termo de Abertura do Projeto - TAP*): PdQ-M-01 - Formalizes the start of the project by detailing it's main objectives, scope, deliveries and the main stakeholders. It is essential to guarantee a strategic alignment of all the stakeholders within the project.
- 2) **Work Breakdown Structure** (*Estrutura Analítica do Projeto - WBS*): PdQ-M-02 - Decomposes the project in manageable work packages, facilitating planning, execution and monitoring of the activities. It guarantees that all of the necessary tasks are identified and structured in a logical and efficient way.

- 3) **Team Breakdown Structure** (*Estrutura Analítica da Equipe - TBS*): PdQ-M-03 - Defines the organization of the team work groups, specifying clearly the responsibilities of each member related to the work packages defined in the WBS. It is crucial to ensure that the functions and responsibilities are distributed coherently.
- 4) **Execution Schedule** (*Cronograma de Execução*): PdQ-M-04 - Organizes the project activities in a detailed timeline, allowing for precise tracking of progress and identification of possible delays. It is vital to ensure that the project remains within the established schedule.
- 5) **Cost Schedule** (*Cronograma de Custos*): PdQ-M-05 - Estimates and plans the costs associated with each activity from the project, ensuring that the budget is strictly followed and financial resources are optimally used.
- 6) **Mission Definition Review** (*Revisão de Definição de Missão - MDR*): PdQ-M-06 - Evaluates and validates the mission definition, including early technical requirements. It is fundamental to ensure that all critical aspects from the mission are approached in an appropriate way from the start.
- 7) **Preliminary Design Review** (*Revisão Preliminar de Projeto - PDR*): PdQ-M-07 - Performs an analysis of the preliminary design, verifying its compliance with technical requirements, budget and schedule. It is essential to ensure that the project is ready to move to the detailed development phases.
- 8) **Critical Design Review** (*Revisão Crítica de Projeto - CDR*): PdQ-M-08 - Conducts an in-depth analysis of the final project design, ensuring it is ready for the production and testing phase. It is critical to identifying and mitigating any remaining risks before satellite construction.
- 9) **Flight Readiness Review** (*Revisão de Prontidão de Voo - FRR*): PdQ-M-09 - Assesses the satellite's readiness for launch, including verification of all technical, operational and safety aspects. The FRR is essential to ensure the satellite is fully prepared for the mission.
- 10) **Project Closure Document** (*Documento de Encerramento do Projeto - DEP*): PdQ-M-10 - Formalizes the project's closure, documenting the achievement of objectives and the project's performance in relation to the planned schedule and budget. It is crucial for post-project analysis and capturing lessons learned, specially in an academic environment.

B. Obsidian Graph

The flow of information between the different types of notes created is shown in Figure 2. Basically, a Stakeholder has a Need that generates an Requirement associated with a Subsystem managed by a Team Member. The reference is made backwards, with the notes referring to other notes that generated or are responsible for them.

It is important to note, however, that there are cases where intermediate connections can be made, for example the De-

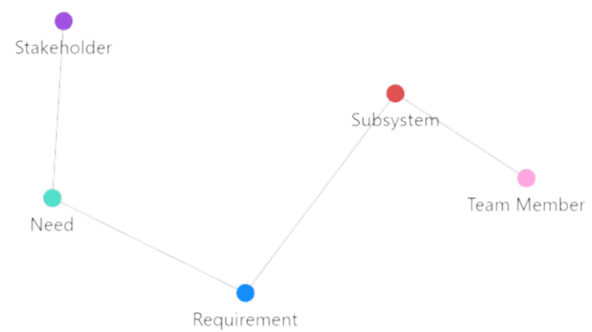


Fig. 2: Example of connections between types of nodes

partments where Team Members work, that are Stakeholders as well, and, in this case, a connection between Member and Stakeholder is made. Also, regarding the PdQSat project and the determination of needs made by Queiroz [7], it is quite common that the needs themselves refer to the subsystems as well as the requirements.

By evaluating the flow of information generated by this logic, it appears that the graph resembles more with an Information Network, once the nodes refer to each other in a directed and informative way, like requirements being originated from a need or a need belonging to a stakeholder. Also, once the information represented follows some kind of order, the graph is mostly acyclic, meaning that there are almost none closed loops occurring.

Beyond linking the notes on the software, Obsidian allows customization by changing the color of the graph's nodes, making it easier to find and visualize information. The color change is made through the use of the tags created in the software, such as #Requirement or #Stakeholder, which can be divided into sub-tags, like #Requirement/Functional to disguise notes from the same group. With that in mind, nine major tags were created, some of them containing sub-groups of tags:

- #Requirement: Project requirements, derived from established needs.
- #Requirement/Functional: Requirements that describe functions of the system.
- #Requirement/Non_Functional: Requirements related to restrictions, security, performance, reliability, and others.
- #Level: Relative to the level of each requirement within the project.
 - #Level/Mission: The highest level of the project, relative to requirements regarding the project as a whole.
 - #Level/System: Applied to requirements that involve the CubeSat or the Ground Segment systems.
 - #Level/Subsystem: Relative to each subsystem in the project.
 - #Level/Component: Requirements in the low-

est form in the project, normally making reference to properties or parts of a subsystem.

#Criticality: Represents the importance of an requirement.

- #Criticality/Low
- #Criticality/Medium
- #Criticality/High

#Status: Indicates the completeness of requirements.

- #Status/OK
- #Status/NOK

● **#Need:** Project needs, normally associated with a Stakeholder.

- #Need/System: Needs from a system as a whole.
- #Need/Battery: Needs from the battery.
- #Need/Supercapacitor: Needs from the supercapacitor.
- #Need/Platform: Needs from the platform.

● **#Subsystem:** The major systems that compose the satellite.

- #Subsystem/Platform
- #Subsystem/Payload

● **#Members:** The people involved in the project.

- #Members/Management
- #Members/Systems_Engineering
- #Members/Space_Segment

● **#Stakeholder:** Parties that are interested and/or affected by the project.

● **#Document:** The documents created following the developed templates.

Based on previous work made on the project, the templates for some categories of artifacts, such as needs and requirements, were already available and were adapted to be used in Obsidian, as shown below on File 1 and File 2, respectively. Beyond these, an additional template was created for the team members, shown on File 3. As for documents, stakeholders and subsystems, the templates contain only the field for the tag, with the rest of the file being initially empty.

In File 1, the need's type is identified by the {type} field in the tag, with its name or ID, being automatically filled with the name of the file. The Origin field references the associated stakeholder that originated the need, written in the Need section, and the Characteristic field highlights an associated subsystem or another characteristic, such as Test or Mission.

File 1: Need Template

```
Type: #Need/{type}
---
- **ID**:: {{title}}

- **Origin**::

- **Characteristic**::
```

```
- **Need**::
---
```

Regarding File 2, the fields {type}, {level} and {criticality} establish the three different tags for each requirement, identified by its ID and written explicitly in the Description field. As for the Origin, it references the parent need or requirement, with Allocation being analogous to the Characteristic filed for the needs, thus referencing the context of the requirement, such as a subsystem. Finally, there was also created the Verification field to write down what is necessary to verify the completeness of each requirement. Note that the Status tag in the template is started as NOK, but can be changed whenever the requirement is satisfied.

File 2: Requirement Template

```
Type: #Requirement/{type}
Level: #Level/{level}
Status: #Status/NOK

---
- **ID**:: {{title}}

- **Description**::

- **Origin**::

- **Allocation**::

- **Criticality**:: #Criticality/{criticality}

- **Verification**::
---
```

The final file template created in Obsidian is shown in File 3, in which the working team is delimited by the {team} tag for each member identified by Name. Field is used to identify the role of expertise of each member, as well as Location identifies a working location, such as a laboratory from the university. Finally, there is also contact information, such as E-mail and Phone.

File 3: Member Template

```
Allocation: #Members/{team}

---
- **Name**:: {{title}}

- **Field**::

- **Location**::

- **E-mail**::

- **Phone**::
---
```

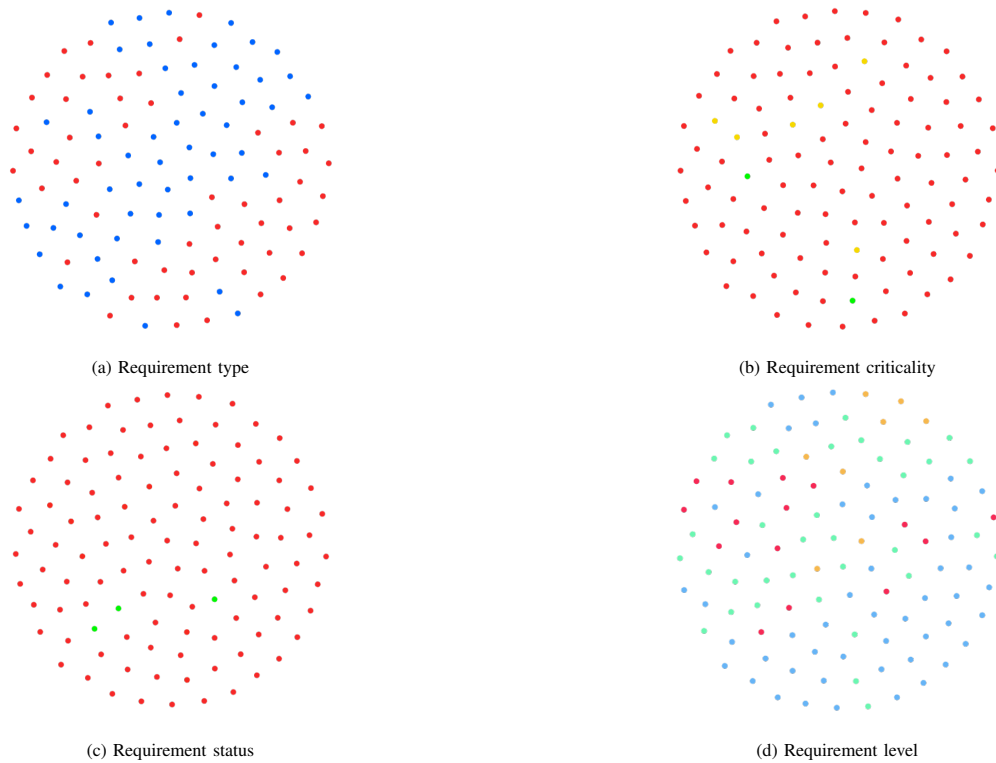


Fig. 3: Current documented requirements distinguished by groups

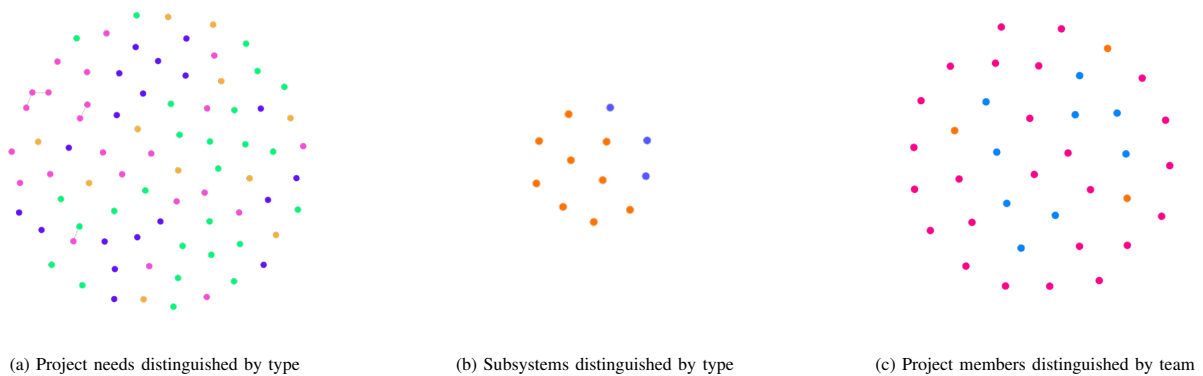


Fig. 4: Needs, subsystems and team members grouped by type

On Figure 3, the requirements are shown divided by its respective four group highlights: Requirement Type on Figure 3a, Criticality on Figure 3b, Status on Figure 3c and Level on Figure 3d. Also, the needs, subsystems and crew members are displayed coloured by type on Figure 4a, Figure 4b and Figure 4c, respectively. Note that, for now, there are only three payload subsystems on Figure 4b, them being the battery, the supercapacitor and the circuit responsible for the characterization of the supercapacitor. Also, work packages like orbit, propulsion and ground segment were considered subsystems on the graph view.

Figure 5 shows the complete graph for the current state of the project. From the figure, it is possible to notice that some of

the notes have a substantially higher number of connections, thus highlighting that they consist of key elements for the project, such as the two payload subsystems, on the top of the graph, or the TBS document created for the project, which interconnects all of the team members and subsystems.

By taking advantage of the tags system inside the Obsidian software, several analyses can be performed, like viewing the subsystems and it's respective Functional or Non-Functional Requirements, as in Figure 6 or even with the requirements divided by level, as shown in Figure 7. From these two analyses, it is possible to note that Functional Requirements and Requirements in the Subsystem level are responsible for most of the interconnections between the different subsystems.

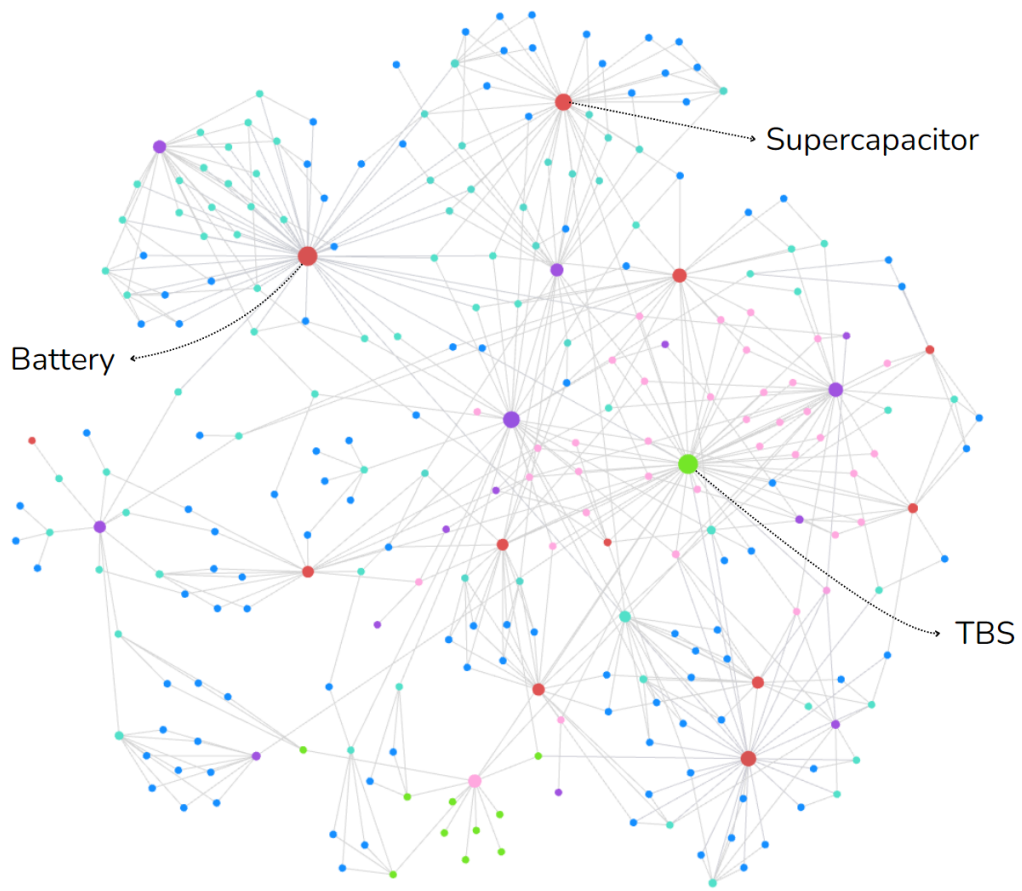
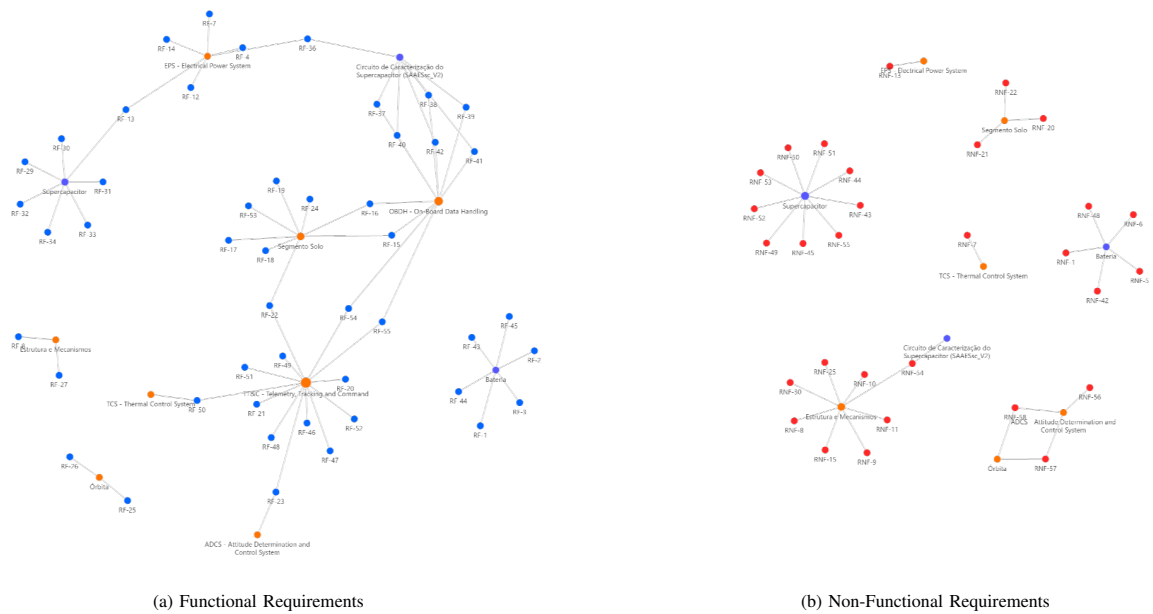


Fig. 5: Complete graph for the current state of the project, with highlights on the payloads and TBS nodes



(a) Functional Requirements

(b) Non-Functional Requirements

Fig. 6: Subsystems view of requirements divided by type

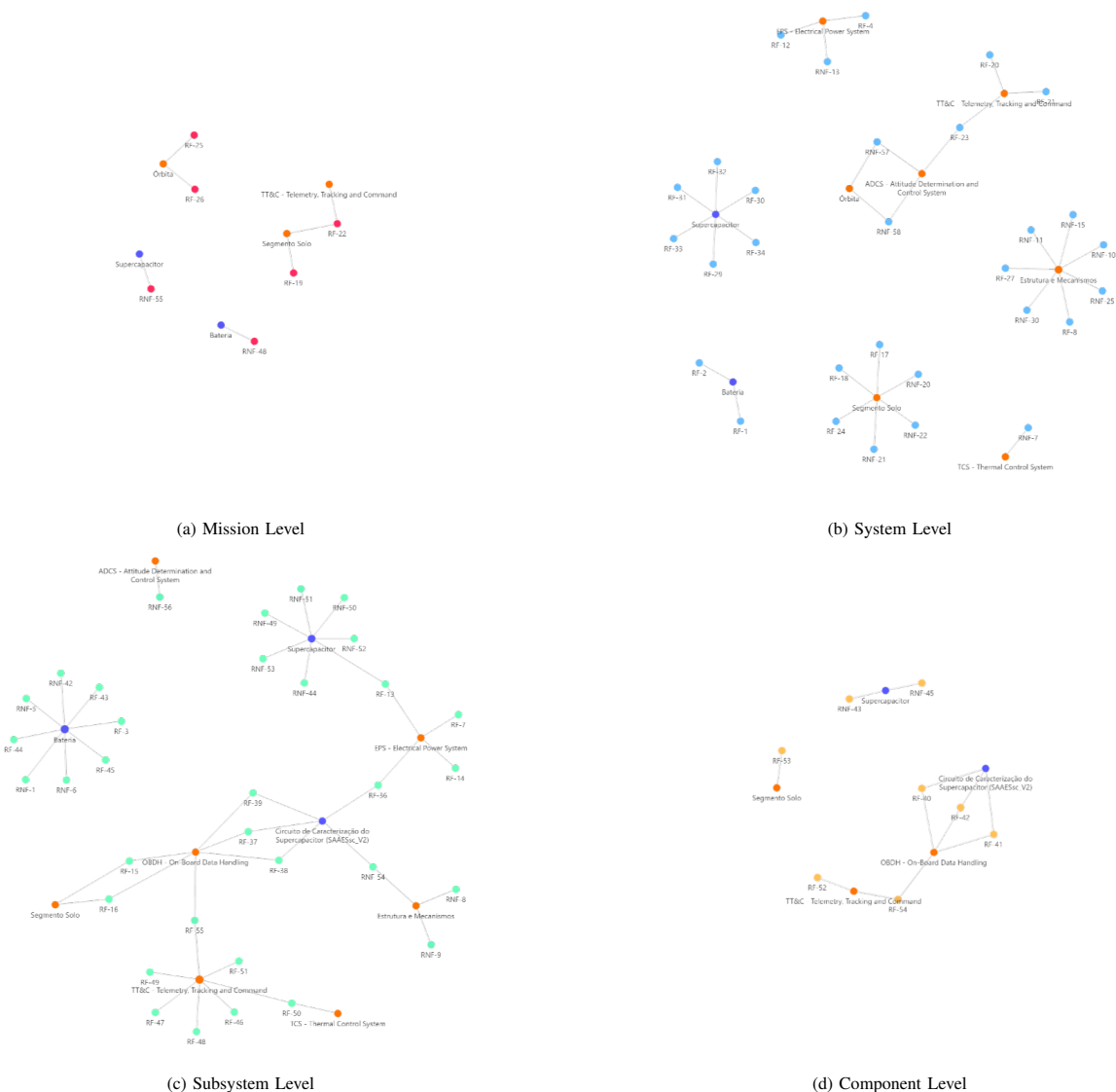


Fig. 7: Subsystems view of requirements divided by level

IV. CONCLUSION

Throughout the review of well known practices and guides, such as PMBOK®, NASA or ECSS, and with the study of similar applications of graphs within traceability in real projects, this work presented unique and tailored approaches concerning the use of such tools in the context of a real project: the development and construction of a real academic CubeSat, the PdQSat.

Motivated by the need to create a customized management structure suitable to the academic and technical nature of the project, and with the guidance of well established standards for management documentation, a set of ten documents was created, with each one approaching a key aspect or design phase for the project, such as schedules, team divisions, reviews and others. These documents contributed to establish

a management model that is suitable for the project, thus allowing it to be carefully developed and to last through multiple generations of students.

Beyond the documentation created, the current work also delved into the study of graphs and their application regarding information traceability within real projects. By analysing the particularities of the PdQSat project and review works made by other students, a division of the most important classes of artifacts became clear, thus allowing to organize key information from the project. Uniting these studies with the selection of a familiar and flexible tool, the Obsidian software, it was possible to validate the proposed structure in the context of the project and establish new paths to trace in order to expand the implementation and aggregate ever so more value to the ongoing work being developed at the university.

V. ACKNOWLEDGMENTS

We would like to express our deepest gratitude to everyone who contributed and still contributes to the development of the PdQSat project. First, we thank the Brazilian Space Agency (AEB) for their invaluable support and sponsorship, which made this research and development project possible.

We are also immensely grateful to the Federal University of Minas Gerais (UFMG), whose infrastructure, expertise and high-end professionals provided the foundation for the PdQSat's development. A special thanks to all the students who contributed through their projects and theses, exploring areas such as mission analysis, subsystem design, requirements engineering and more. Your dedication and hard work have been crucial to both the advancement of this research and the PdQSat project, and your contributions continue to shape the future of this academic mission.

REFERENCES

- [1] M. C. Pereira, K. R. Marques, M. L. R. Fraga, and P. H. Picanço, "PdQSat I - Projeto e Construção de um CubeSat Acadêmico Para Fins de Demonstração Tecnológica [PdQSat I - Design and Construction of an Academic CubeSat for Technology Demonstration Purposes]," Federal University of Minas Gerais (UFMG), Belo Horizonte, MG, Tech. Rep., 2020.
- [2] International Council on Systems Engineering (INCOSE), *Definition of System: General Case*, Retrieved from <https://www.incose.org/about-systems-engineering/system-and-se-definitions/general-system-definition>. Accessed: May 28, 2024, 2024.
- [3] P. M. Institute, *Guide to the Project Management Body of Knowledge (PMBOK® Guide)*, 6th ed., PMBOK® Guide, Project Management Institute (PMI), Pennsylvania, EUA, 2017, ISBN: 9781628253900.
- [4] *ECSS-M-ST-10C Rev.1: Space Project Management - Project Planning and Implementation*, ECSS Secretariat, ESA-ESTEC, P.O. Box 299, 2200 AG Noordwijk, European Cooperation for Space Standardization, Noordwijk, The Netherlands: ESA Requirements and Standards Division, Mar. 2009.
- [5] *NASA Systems Engineering Handbook: NASA/SP-2007-6105*, Rev. 1, NASA, 2007, ISBN: 1791362699, 9781791362690.
- [6] INCOSE, *INCOSE Systems Engineering Handbook: A Guide for System Life Cycle Processes and Activities*, 5th ed., D. D. Walden, Ed. Hoboken, NJ, USA: John Wiley & Sons, 2023, INCOSE-TP-2003-002-05, ISBN: 9781119814920.
- [7] B. Queiroz, "Aplicação de Metodologias de Engenharia de Sistemas para o Ciclo de Vida do PdQSat I - CubeSat Acadêmico [Application of Systems Engineering Methodologies for the Life Cycle of PdQSat I - Academic CubeSat]," B.S. Thesis in Systems Engineering, Federal University of Minas Gerais (UFMG), 2022.
- [8] A. Johnstone, *CubeSat Design Specification*, Revision 14.1, Available at: <https://www.cubesat.org/cubesatinfo>, California Polytechnic State University, San Luis Obispo, CA, Feb. 2022.
- [9] L. L. Manfrini, "Análise de Missão do Satélite PdQSat [PdQSat Satellite Mission Analysis]," B.S. Thesis in Aerospace Engineering, Federal University of Minas Gerais (UFMG), 2022.
- [10] M. L. R. Fraga, "Definição de Requisitos e Propostas de Verificação para PdQSat - CubeSat Acadêmico [Definition of Requirements and Verification Proposals for PdQSat - Academic CubeSat]," B.S. Thesis in Aerospace Engineering, Federal University of Minas Gerais (UFMG), 2022.
- [11] M. E. Newman, "The structure and function of complex networks," *SIAM review*, vol. 45, no. 2, pp. 167–256, 2003.
- [12] H. Schwarz, J. Ebert, and A. Winter, "Graph-based traceability: A comprehensive approach," *Software & Systems Modeling*, vol. 9, pp. 473–492, 2010.
- [13] C. Ruiz-Martin and D. J. Poza, "Project configuration by means of network theory," *International Journal of Project Management*, vol. 33, no. 8, pp. 1755–1767, 2015.
- [14] D. Ríos-Zapata, J. Pailhes, and R. Mejía-Gutiérrez, "Multi-layer graph theory utilisation for improving traceability and knowledge management in early design stages," *Procedia CIRP*, vol. 60, pp. 308–313, 2017.
- [15] A. T. d. Aguiar, "Modelos de Documentação Gerencial para o Projeto do Satélite Acadêmico PdQSat [Management Documentation Models for the Academic Satellite PdQSat Project]," B.S. Thesis in Aerospace Engineering, Federal University of Minas Gerais (UFMG), 2022.

Systems Engineering of a Brazilian Amazon Imaging CubeSat Constellation: FritzSAT Mission

Damylle C. X. Donati
Technological Center of Joinville
Federal University of Santa Catarina
Joinville, Brazil
damylle.donati@gmail.com

Henrique M. Lehmkuhl
Technological Center of Joinville
Federal University of Santa Catarina
Joinville, Brazil
henrique.lehmkuhl@gmail.com

Ludmila Kopko
Technological Center of Joinville
Federal University of Santa Catarina
Joinville, Brazil
ludmila.kopko@gmail.com

Thiago C. Carreiro
Technological Center of Joinville
Federal University of Santa Catarina
Joinville, Brazil
thiagocelstinocarr@gmail.com

Talita Sauter Possamai
Technological Center of Joinville
Federal University of Santa Catarina
Joinville, Brazil
talita.possamai@ufsc.br

Abstract—The FritzSAT mission aims to develop a constellation of nanosatellites dedicated to imaging the Brazilian Amazon, addressing the strategic importance of the region and the growing demand for precise environmental data. Despite the presence of existing monitoring systems, significant gaps persist in coverage, revisit frequency, and, notably, the autonomy of private companies in acquiring environmental data. This lack of autonomy hampers these companies' ability to effectively meet their operational and strategic needs, resulting in a dependency on external data sources and limiting innovation in the sector. This study details the initial phase of systems engineering for the FritzSAT mission, and was structured into four key stages: analyzing the environmental monitoring scenario in the Amazon, identifying and analyzing stakeholders, defining mission goals and objectives, and estimating potential system configurations. The scenario analysis involved a comprehensive evaluation of the primary entities responsible for monitoring the Amazon, their data requirements, and relevant data suppliers. A subsequent feasibility analysis of the proposed configurations led to the identification of a constellation of nanosatellites with segmented missions and the definition of operational concepts and system interfaces. This structured framework serves as a guide for the ongoing development of the project, providing a solid foundation for the subsequent phases of the FritzSAT mission, which aims to enhance the autonomy and effectiveness of environmental monitoring efforts in the Brazilian Amazon.

Index Terms—CubeSat, Systems Engineering, Imaging, Stakeholders, Nanosatellite

I. INTRODUCTION

The deployment of satellites has been a crucial factor in the advancement of environmental monitoring, particularly in regions with high ecological significance, such as the Amazon. Notable satellite systems such as the Landsat series [7] [5] [2] [4], Sentinel-2, and MODIS [11] [12] [13] have played a pivotal role in providing high-resolution imagery and crucial data for hydrological studies, deforestation monitoring, and forest fire detection. To illustrate, the long-term time series data provided by Landsat has been invaluable in monitoring deforestation trends, while the multispectral imaging capa-

bilities of Sentinel-2 [13] have facilitated the assessment of vegetation health. Similarly, the Moderate Resolution Imaging Spectroradiometer (MODIS) on NASA's Terra and Aqua satellites has enabled the detection of active fires, providing near-real-time information that is crucial for disaster response. Notwithstanding the invaluable contributions of these large satellite systems, they frequently encounter challenges pertaining to revisit times, spatial resolution, and the capacity to capture localized, rapidly changing events.

The advent of nanosatellite constellations, driven by the new space movement, offers a transformative approach to overcoming these limitations. The deployment of numerous, cost-effective satellites allows for more frequent and targeted monitoring of specific regions [10] [9] [8] [6] [3]. Private sector initiatives are at the vanguard of this innovation, propelling the frontiers of what is feasible in environmental surveillance. The FritzSAT project, inspired by this new space paradigm, proposes a constellation of nanosatellites dedicated to addressing critical environmental monitoring needs in the Amazon.

The FritzSat Project is defined as a hypothetical space mission to monitor the Brazilian Amazon territory. The project is motivated by the training of human resources at the Laboratory of Applications and Research in Space (LARS) of the Federal University of Santa Catarina, Joinville campus (UFSC-CTJ) in relation to the mission design process and space systems engineering. It envisages the eventual contracting of the laboratory to build a design solution for environmental data acquisition for post-processing resale. The objective of this work is to delineate the phases of systems engineering that have been undertaken in order to define the mission, objectives, requirements, and principal systems that comprise the project.

The project was devised in response to the need for an effective monitoring system for the Brazilian Amazon territory. It was initiated with a comprehensive survey of the

current monitoring landscape, encompassing the prevailing methodologies, data requirements, equipment requirements, and data suppliers. In light of this understanding, two principal conclusions informed the design of the mission: the gap to be filled and the mission constraints directly associated with the scenario.

II. SCENARIO ANALYSIS

A. Deforestation monitoring

Monitoring deforestation in Brazil is essential for preserving its diverse biomes—Amazon, Cerrado, Atlantic Forest, Caatinga, Pantanal, and Pampas—amid pressures from agriculture, livestock farming, and logging. Satellite technologies, such as PRODES, DETER, and TerraClass [1], are critical tools for tracking land use, deforestation, and vegetation regeneration. By utilizing high-resolution images from satellites like Landsat, CBERS, and Sentinel, these systems assess environmental impacts and identify illegal activities. Despite this, challenges such as cloud cover and resolution limits can hinder image clarity. To improve accuracy, additional tools like high-resolution satellites, drones, and LIDAR systems are employed, and continuous temporal analysis helps uncover seasonal patterns.

B. Fire monitoring

Monitoring forest fires in Brazil is crucial for safeguarding vulnerable biomes like the Amazon, Cerrado, and Pantanal, which are prone to both natural and human-induced fires, such as those caused by agricultural burning. This monitoring relies on advanced technologies, including satellites, thermal sensors, unmanned aerial vehicles (UAVs), and real-time alert systems. The National Institute for Space Research (INPE) is central to this effort, employing systems like QUEIMADAS and INPE Fire [1] to deliver detailed information on hotspot locations and fire intensity.

The data collected covers hotspot locations, flame intensity, affected area, and meteorological conditions—such as temperature, humidity, and wind speed—that influence fire spread. Satellite images from the Terra and Aqua satellites, equipped with the MODIS sensor, are crucial for tracking large-scale fires, with updates ranging from a few hours to a few days for near real-time monitoring. High-resolution systems like GOES offer continuous surveillance of risk areas. Challenges include cloud cover obstructing fire detection and the need for rapid response, especially during droughts. To enhance accuracy, drones with thermal cameras and LIDAR systems can map burnt areas and assess damage. Integrating meteorological data and fire propagation models is essential for predicting fire behavior and guiding firefighting efforts. Continuous analysis and coordination are key to effective monitoring and response.

C. Hydrological monitoring

Hydrological monitoring in Brazil is crucial for maintaining ecosystem health and ensuring the availability of water resources for consumption, irrigation, and energy production. Given the country's numerous river basins, including

the Amazon, São Francisco, and Paraná, precise tracking of rivers, lakes, and reservoirs is essential for predicting floods and droughts and maintaining water quality. This monitoring employs a range of technologies, such as hydrometric stations, water level sensors, satellite imagery, and mathematical models, with the National Water and Sanitation Agency (ANA) and the National Institute for Space Research (INPE) playing key roles.

The monitored data includes river levels, flow rates, rainfall, evaporation, water quality, and soil moisture. Hydrometric stations provide real-time or periodic measurements, while water level sensors, rain gauges, and quality probes contribute essential data. Satellites like Sentinel-1 and Landsat offer radar and optical imagery that help analyze flooded areas, track changes in water surfaces, and detect hydrological anomalies. This data is integrated into geographic information systems (GIS) and hydrological models to forecast extreme events such as floods and droughts. Nonetheless, challenges include difficulties in accessing remote areas, maintaining equipment, and the limitations of data resolution for capturing short-duration or small-scale events. The increasing use of drones, remote sensors, and Internet of Things (IoT) technologies is helping to address these issues.

D. Scenario's constraints and possible payloads

The implementation of environmental monitoring in Brazil is constrained by a number of technical limitations, which can be quantified in terms of cloud cover, spatial resolution, and satellite revisit time. Cloud cover in the Amazon, for instance, can reach up to 80% during the rainy season [1], which significantly constrains the acquisition of clear images, particularly in regions where continuous monitoring is crucial. To address this issue, satellites equipped with radar sensors, such as Sentinel-1, which can penetrate cloud cover, are employed. However, these satellites offer a spatial resolution that can range between 5 and 20 meters [13]. While this resolution is sufficient for the detection of large-scale deforestation or fires, it may prove inadequate for the identification of smaller events or subtle changes in the landscape.

Moreover, the spatial resolution of the most commonly utilized optical satellites, such as Landsat and CBERS, ranges from 10 to 30 meters, enabling the detection of extensive affected regions but potentially lacking the capacity to capture finer details. Furthermore, the revisit time of the satellites, defined as the interval between consecutive passes over the same area, represents another significant limitation. Concerning Landsat, the revisit time is 16 days, whereas Sentinel-2 [13] has a revisit time of approximately 5 days. This interval may prove inadequate for the rapid detection of changes or the prompt response to rapidly evolving events such as forest fires or flash floods. To circumvent this limitation, the integration of data from multiple satellites and the deployment of complementary technologies, such as drones with high temporal and spatial resolution, are becoming increasingly crucial to ensure effective and responsive monitoring.

To efficiently monitor deforestation, forest fires and hydrological conditions, a mission must be equipped with the following types of sensors and instruments:

- 1) High-resolution optical camera: Capture detailed images of the Earth's surface for monitoring deforestation, flooded areas, and identifying changes in the landscape. Resolution: 10 to 30 meters, or better;
- 2) Synthetic Aperture Radar (SAR) sensor: Capturing images through clouds and in low light conditions, essential for monitoring in tropical areas and at night. Resolution: 5 to 20 meters;
- 3) Thermal sensor: Detects hotspots, allowing identification of forest fires and areas with anomalous temperatures. Resolution: 100 meters or less, with high thermal sensitivity;
- 4) Multispectral radiometer: Collects data in multiple bands of the electromagnetic spectrum to analyze vegetation, water quality and detect environmental changes. Spectrum: Visible, near infrared (NIR) and mid infrared (MIR);
- 5) Spatial rain gauge: Precipitation measurement, crucial for monitoring the hydrological cycle and predicting floods. Technology: Precipitation radar and microwave radiometry;
- 6) Radar altimeter: Precise measurement of the elevation of the water surface in rivers and lakes, for hydrological monitoring. Vertical resolution: Centimeter;
- 7) Imaging spectroradiometer: Detailed analysis of water quality and detection of pollutants or nutrients in water bodies. Spectrum: Includes ultraviolet (UV) and mid-infrared (MIR) bands;
- 8) GNSS (Global Navigation Satellite System) receiver: Provides precise location data, necessary for georeferencing observations and correcting altimetric data;
- 9) Real-time data communication system: Immediate transmission of data to ground stations, crucial for monitoring and rapid response to forest fires and floods;
- 10) On-board processing unit: Preliminary processing of collected data, including image compression and real-time anomaly detection, to optimize the use of bandwidth and speed up the transmission of relevant data;
- 11) Power Supply subsystem: CubeSats with demanding payloads typically require 10-20% of their total volume and weight for power systems (solar panels, batteries, regulators).

To facilitate a comprehensive understanding of satellite equipment requirements, two tables are presented. Tab. I provides a comparative analysis of various camera models utilized in satellite applications. This table details the resolution, volume, and mass of different camera types, ranging from high-resolution models such as the WorldView-3 to compact miniaturized CubeSat cameras. The comparison elucidates the trade-offs between high-resolution imaging capabilities and the constraints of size and weight, which are critical for selecting suitable cameras for satellite missions.

In addition, Tab. II summarizes the mass, volume, and CubeSat Units (U) required for each type of satellite equipment, including optical cameras, radar sensors, thermal sensors, and other essential components. This table provides a total for the combined payload, offering insights into the overall space and weight requirements necessary for accommodating all instruments on a satellite.

Given the constraints outlined in the tables, it becomes evident that a single spaceborne system encompassing all required functions is not feasible due to its substantial size and the corresponding financial investment. The integration of diverse instruments—such as high-resolution optical cameras, radar sensors, thermal sensors, and other critical components—within a single satellite exceeds the typical size and weight limits of current satellite platforms. Consequently, at this stage of the project, a strategic decision must be made between two primary options: reducing the number of functions to fit within a single satellite or disaggregating the system into multiple smaller satellites.

Alternatively, the project could consider leveraging existing legacy systems that already cover some of the required functions, thereby reducing the need for a fully integrated new system. Another approach could involve integrating satellite platforms with other remote sensing technologies such as Data Collection Platforms (DCPs) or Unmanned Aerial Vehicles (UAVs), which could provide complementary data and enhance the overall system capabilities. Additionally, combining multiple smaller satellites in a constellation, each focused on specific functions, could offer a modular and scalable solution. Each of these alternatives presents distinct advantages and challenges related to cost, integration complexity, and mission objectives, requiring careful evaluation to align with the project's overall goals.

In order to gain insight into the present situation and the underlying dynamics, it is crucial to identify the key stakeholders who exert influence and are affected by these circumstances. A stakeholder analysis provides a comprehensive examination of the interactions and interests of the parties involved, elucidating their respective functions, motivations, and roles in the development and implementation of the discussed strategies. This understanding is fundamental to ensuring that the proposed actions are aligned with the expectations and needs of the different groups, thereby guaranteeing the effectiveness of the initiatives and minimizing potential conflicts.

III. STAKEHOLDERS' ANALYSIS

A stakeholder is defined as an actor who participates in a project and holds a vested interest in its outcome. In other words, they have expectations and needs related to the results obtained from the implementation of the project in question. Stakeholders may include direct and third-party suppliers, contracting clients or end users, as well as consultants and service providers whose work has an impact on the development of the project.

In the context of the FritzSat mission, it is postulated that UFSC, via LARS, will be contracted to develop an imaging

TABLE I
COMPARISON OF CAMERA MODELS FOR SATELLITE APPLICATIONS

Camera Model	Resolution	Volume (m ³)	Mass (kg)	Suitability
WorldView-3	31 cm (panchromatic), 1.24 m (multispectral)	0.5	150	High resolution but large
Landsat-8 OLI	30 m (multispectral), 15 m (panchromatic)	0.3	50	Good resolution, relatively compact
Miniaturized CubeSat Camera	Up to 3 m	0.05	10-20	Compact and suitable for CubeSats

TABLE II
COMPARISON OF SATELLITE EQUIPMENTS

Equipment	Mass (kg)	Volume (m ³)	Number of U
High-resolution optical camera	50	0.2	200
Synthetic Aperture Radar (SAR) sensor	150	0.4	400
Thermal sensor	30	0.1	100
Multispectral radiometer	40	0.15	150
Spaceborne rain gauge	100	0.3	300
Radar altimeter	50	0.15	150
Imaging spectroradiometer	60	0.2	200
GNSS receiver	10	0.05	50
Real-time data communication system	20	0.1	100
Onboard processing unit	25	0.08	80
Power supply subsystem	75	0.15	150
Total	673	1.73	1780

data acquisition mission with the objective of monitoring the Brazilian Amazon territory. The project is predicated on the interest of a private company in reselling environmental data to prospective users/customers of the company, subsequent to the processing and treatment of the data packages obtained by the systems. The Brazilian government has been incorporated into the project as a regulator and a source of financial support, given that the majority of funding is anticipated to originate from calls for proposals issued by the Brazilian government's Ministry of Science, Technology and Information (MCTI). Figure 1 illustrates the connections and the principal interests and products provided by these key stakeholders in the form of a rich picture.

While the primary interest of secondary customers is in the final mission data, the contracting company also places importance on the training of human resources to enable the independent operation of the space system following the conclusion of the project. The University of Santa Catarina (UFSC) is identified as a supplier, contributing to the advancement of space research, technology, and innovation through the training of students and educators, as well as the promotion of local industrial growth. The Brazilian government serves as a facilitator and regulator, ensuring compliance with established guidelines and standards. The National Institute for Space Research (INPE) comprises two divisions: one responsible for qualification testing and the other for operating a possible Ground Station for communication and control of space missions. Private companies act as customers, interested in developing their own acquisition systems and utilizing imaging data for commercial purposes. Their involvement stimulates economic growth and innovation in the space sector.

The primary financial supporters of the mission are the Ministry of Science, Technology, and Innovation (MCTI) and other government entities, which provide crucial backing for

the advancement of national technology. Additionally, the objective is to utilize media projection as a means of showcasing the country's technological achievements. Government funding is of critical importance in enabling long-term research and large-scale projects, thus ensuring the sustainability of space initiatives.

The ultimate beneficiaries of the mission are the secondary customers and users who utilize the data and images obtained. Such data is employed in a variety of applications, including border monitoring, vegetation analysis, terrain assessment, and meteorology. The availability of both processed and unprocessed data allows for a wide range of potential applications, including academic research, commercial endeavors, and government initiatives. It is of the utmost importance that the needs of these beneficiaries are met in order to ensure the success of the mission and the practical significance of the technologies developed.

IV. GOALS AND OBJECTIVES

Table III details the objectives and goals of a mission focused on imaging, highlighting various aspects of environmental monitoring and technological development in Brazil. The goals and objectives are divided into four main categories, each with a specific focus ranging from data acquisition to national technology development.

The first goal focuses on obtaining critical data to monitor the Brazilian Amazon. The associated objectives include acquiring data necessary for identifying deforestation, fires, monitoring livestock, vegetation, and water resources in the Amazon region.

The second goal is aimed at developing legacy documentation, with a specific objective: to develop a methodology for adapting systems engineering standards for space projects to nanosatellite projects. This objective is crucial to ensure that established knowledge and practices in the space sector

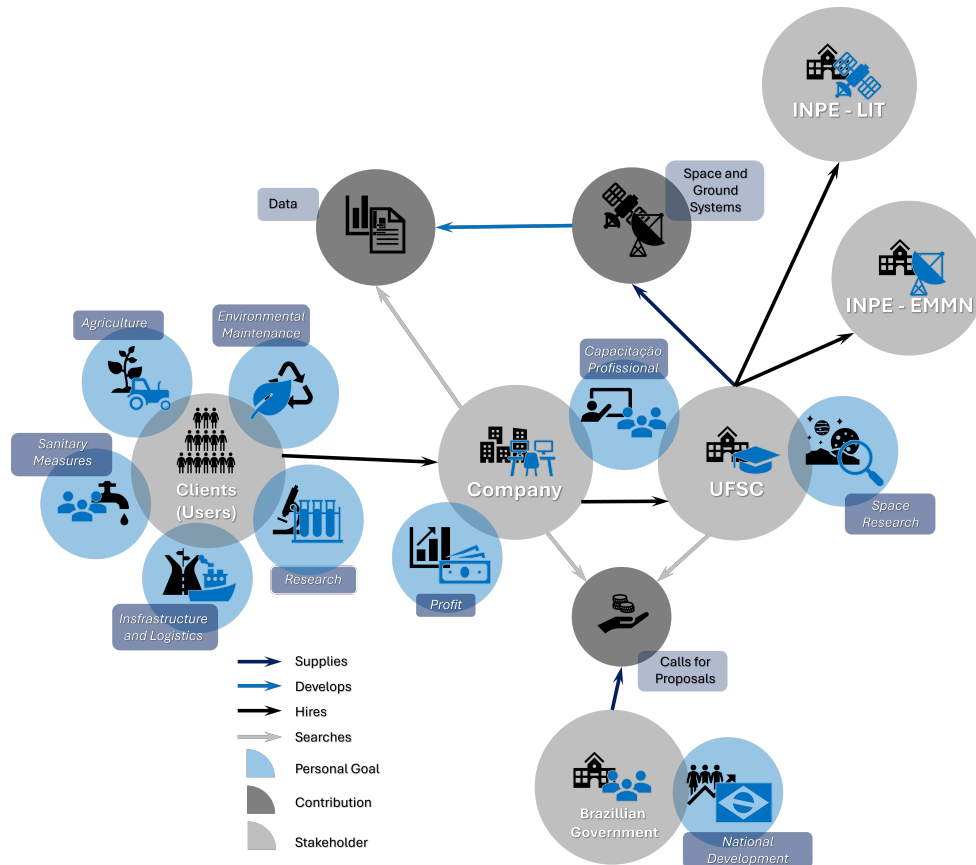


Fig. 1. The primary stakeholders involved in the project and the nature of their connections.

can be applied and adjusted to the needs and specifics of nanosatellites. Such adaptation is essential to ensure the effectiveness and sustainability of future missions utilizing this miniature technology, ensuring compliance with quality and safety standards.

The third goal addresses the development of nanosatellite imaging technology in Brazil. Objectives include providing data access to the client, training company staff, and developing national technology in accordance with the PNAE. This set of objectives emphasizes the importance of not only creating the technology but also ensuring that end-users can utilize it effectively and that national technical capacity is enhanced through training. Alignment with the PNAE indicates a commitment to national strategic guidelines and goals for the space sector.

The fourth goal is similar to the first but focuses on the Santa Catarina territory. Objectives include acquiring data to identify deforestation, fires, monitoring livestock, vegetation, and water resources in the Santa Catarina region. The geographical specificity of this goal highlights the importance of monitoring different biomes and regions of Brazil, recognizing that each area has its own environmental needs and challenges. Expanding the mission to other territories enhances the client’s portfolio but adds complexity to mission development, and for

this reason, it is considered a **secondary goal**.

A. Feasibility Analysis of the Space Mission

In evaluating the feasibility of the proposed space mission with a focus on cost-efficiency and data autonomy, it is essential to explore various approaches, including the use of existing systems, a mix of existing and newly developed systems, large satellites, and constellations of nanosatellites. Each approach presents unique advantages and challenges that impact both cost and the ability to manage and utilize data independently.

- 1) **Utilization of Existing Systems:** One approach is to rely entirely on existing systems, such as legacy satellites and ground-based infrastructure, to achieve the mission objectives. This approach can significantly reduce development and operational costs, as it leverages proven technologies and infrastructure. Since the mission’s primary goal is to acquire and utilize data, utilizing these pre-existing systems can be efficient if they meet the required specifications for data acquisition and processing. However, this approach may be limited by the availability and suitability of these systems, potentially necessitating compromises in mission capabilities or data quality.

TABLE III
MISSION GOALS (G) AND OBJECTIVES (O)

Goal	Objective
G.1: Acquire imaging data of the Brazilian Amazon	O.1.1: Acquisition of data required for deforestation identification in the Amazon region O.1.2: Acquisition of data required for fire detection in the Amazon region O.1.3: Acquisition of data required for livestock monitoring in the Amazon region O.1.4: Acquisition of data required for vegetation monitoring in the Amazon region O.1.5: Acquisition of data required for hydrological monitoring in the Amazon region
G.2: Develop legacy documentation	O.2.1: Develop methodology for adapting systems engineering standards for space projects to nanosatellite projects
G.3: Develop national nanosatellite imaging technology	O.3.1: Provide data access to the client O.3.2: Staff training O.3.3: Development of national technology according to the PNAE
G.4: Acquire imaging data of the Santa Catarina territory	O.4.1: Acquisition of data required for deforestation identification in the Santa Catarina region O.4.2: Acquisition of data required for fire detection in the Santa Catarina region O.4.3: Acquisition of data required for livestock monitoring in the Santa Catarina region O.4.4: Acquisition of data required for vegetation monitoring in the Santa Catarina region O.4.5: Acquisition of data required for hydrological monitoring in the Santa Catarina region

- 2) **Combination of Existing and Newly Developed Systems:** Another viable approach involves a hybrid solution, integrating both existing systems and newly developed technologies. This strategy allows for leveraging the cost advantages and reliability of existing systems while incorporating new technologies to address specific mission requirements that current systems may not fulfill. For instance, existing satellites could handle broad data collection tasks, while newly developed nanosatellites or advanced payloads could address specialized needs such as high-resolution imaging or specific data types. This mix can provide a balance between cost savings and enhanced mission capabilities but requires careful coordination to ensure compatibility and integration between different systems.
- 3) **Large Satellites:** Deploying large, high-capability satellites is an alternative that offers extensive data acquisition and processing capabilities. Large satellites typically provide higher resolution sensors and greater onboard processing power, which can enhance data quality and reduce the need for extensive ground-based processing. However, the high cost of development, launch, and maintenance associated with large satellites can be a significant drawback. The financial burden of such an approach may be prohibitive, especially if budget constraints are a major concern.
- 4) **Constellation of Nanosatellites:** Using a constellation of nanosatellites presents a cost-effective and flexible solution. Nanosatellites are smaller, lighter, and less expensive to build and launch compared to large satellites. Deploying multiple nanosatellites in a constellation allows for a distributed approach to data acquisition,

providing broader coverage and more frequent revisits to target areas. This approach can enhance data collection efficiency and resilience, as the failure of a single satellite does not critically impact the mission. However, managing a constellation involves complexity in terms of coordination, data integration, and ensuring consistent communication between satellites. Additionally, the initial setup cost for a constellation may still be substantial, though it generally remains lower than that of a large satellite mission.

The evaluation of these approaches involves two primary metrics: cost-efficiency and data autonomy. Cost-efficiency refers to the overall financial investment required for development, launch, and operation. In contrast, data autonomy assesses the ability of the system to independently acquire, process, and utilize data without excessive reliance on external support.

- **Cost-Efficiency:** Utilizing existing systems provides the lowest cost but may limit mission capabilities. A hybrid approach balances cost and functionality but requires integration efforts. Large satellites, while offering high capabilities, entail high costs. Nanosatellite constellations offer a scalable and cost-effective solution but introduce management complexities.
- **Data Autonomy:** Large satellites and well-integrated existing systems can provide high data autonomy with advanced onboard processing capabilities. Nanosatellite constellations, with their distributed approach, enhance data acquisition frequency and coverage, supporting effective data autonomy if managed well. Hybrid solutions can also offer enhanced autonomy by combining the strengths of existing and new technologies.

In conclusion, the feasibility of the mission, focusing on low cost and data autonomy, is best supported by a constellation of nanosatellites or a hybrid approach that incorporates existing systems with new technologies. These strategies offer a balance of cost-efficiency and operational capability, aligning well with the mission's goals of acquiring and utilizing data independently.

V. MISSIONS DEFINITION

The findings from the preceding study have concluded that a constellation of nanosatellites offers the most effective configuration for achieving the mission objectives. This approach enables specialized focus and enhanced data collection capabilities for distinct environmental monitoring tasks. Consequently, three distinct missions have been defined within the FritzSAT project: FritzSat Ycatu for hydrological monitoring, FritzSat Tatá for forest fire monitoring, and FritzSat Yby for deforestation monitoring. Each nanosatellite within this constellation is equipped with a primary payload tailored to its specific mission. FritzSat Ycatu is outfitted with a Synthetic Aperture Radar (SAR) to capture detailed hydrological data. FritzSat Tatá features a thermal infrared sensor to detect and monitor forest fire hotspots, while FritzSat Yby is equipped with a multispectral camera to assess changes in vegetation and forest cover. This strategic payload allocation ensures that each mission effectively addresses its targeted environmental issue.

Building upon the mission definitions, the subsequent sections will elaborate on the essential system interfaces and operational concepts (ConOps) that underpin the successful execution of the FritzSAT missions. The interface section will detail the interactions between each nanosatellite and its respective monitoring scenario, as well as the communication protocols with ground systems. Additionally, the ConOps section will outline the operational strategies and procedures for each mission, ensuring that the payloads operate effectively and the mission objectives are achieved. These sections provide a comprehensive framework for understanding how the nanosatellites will function and interact throughout their lifecycle.

A. Interfaces

The interfaces of the systems that comprise the space mission must be defined to understand their relationships and identify the requirements for effective communication. From the perspective of the components:

• FritzSat Ycatu - Hydrological Monitoring Mission

– Space System \rightleftharpoons Monitoring Scenario:

- * **Primary Payload:** Synthetic Aperture Radar (SAR)
- * **Data Types:** Radar images capturing soil moisture, water levels, and flood areas.
- * **Transmission Mechanisms:** SAR data is processed onboard to extract key hydrological indicators, reducing the data volume before transmission.

- * **Transmission Requirements:** Data is transmitted via X-band for high-rate downlink to ensure timely delivery to ground stations. UHF/VHF links are used for telemetry and command operations.

– Space System \rightleftharpoons Ground System:

- * **Data Types:** Processed radar images and telemetry data.
- * **Transmission Mechanisms:** Data is transmitted using X-band for radar images and UHF/VHF for telemetry and control. Ground stations receive the data and integrate it into hydrological models.
- * **Transmission Requirements:** Reliable and continuous communication to ensure real-time monitoring and immediate analysis of hydrological events.

• FritzSat Yby - Deforestation Monitoring Mission

– Space System \rightleftharpoons Monitoring Scenario:

- * **Primary Payload:** Multispectral Camera
- * **Data Types:** Multispectral images capturing vegetation indices and forest cover changes.
- * **Transmission Mechanisms:** Onboard processing to detect changes in vegetation indices and reduce data volume.
- * **Transmission Requirements:** Data is transmitted via S-band or X-band, with a focus on maintaining high image quality and frequent updates.

– Space System \rightleftharpoons Ground System:

- * **Data Types:** Multispectral images and telemetry data.
- * **Transmission Mechanisms:** Data is transmitted using S-band or X-band for multispectral images and UHF/VHF for telemetry and control. Ground stations analyze the data to assess deforestation rates.
- * **Transmission Requirements:** High-frequency data transmission to ensure continuous monitoring and rapid detection of deforestation activities.

• FritzSat Tatá - Forest Fire Monitoring Mission

– Space System \rightleftharpoons Monitoring Scenario:

- * **Primary Payload:** Thermal Sensor (Infrared)
- * **Data Types:** Thermal images capturing fire hotspots and temperature anomalies.
- * **Transmission Mechanisms:** Onboard processing prioritizes data associated with detected fire events for immediate transmission.
- * **Transmission Requirements:** Low-latency transmission via X-band to ensure rapid response capabilities. UHF/VHF links are used for telemetry and control.

– Space System \rightleftharpoons Ground System:

- * **Data Types:** High-resolution thermal images and telemetry data.
- * **Transmission Mechanisms:** Data is transmitted using X-band for thermal images and UHF/VHF

for telemetry and control. Ground stations use this data to generate real-time alerts for firefighting teams.

- * **Transmission Requirements:** Ultra-low latency and high reliability to support immediate detection and response to forest fire events.

B. Concepts of Operation

Concepts of Operation (ConOps) are structured narratives that describe how a system, such as a nanosatellite mission, will be employed to meet its objectives. ConOps provide a detailed understanding of the mission from the perspective of end-users and stakeholders, outlining how the system will function throughout its lifecycle. The application and understanding of ConOps are crucial because they ensure that all parties involved have a shared vision of the system's goals, operational scenarios, and constraints. This shared understanding is essential for aligning the technical design with the mission's intended purpose, facilitating effective communication, and supporting decision-making processes across the project lifecycle.

• FritzSat Ycatu - Hydrological Monitoring Mission

- **Objective:** To monitor hydrological variables such as soil moisture, water levels, and flood areas using Synthetic Aperture Radar (SAR).
- **Operation Concept:**
 - * **Data Collection:** The SAR payload operates in a specific mode (broadband or narrowband) depending on the monitoring objective, capturing radar images of the Earth's surface.
 - * **Data Processing:** Onboard processing is conducted to reduce raw data volume, focusing on extracting key hydrological indicators before transmitting to the ground.
 - * **Data Transmission:** Processed data is transmitted via X-band to ground stations, with UHF/VHF links used for telemetry and control.
 - * **Data Analysis:** Ground stations receive the data, which is further analyzed and integrated into hydrological models, providing real-time insights into water levels, soil moisture, and potential flood zones.

• FritzSat Yby - Deforestation Monitoring Mission

- **Objective:** To monitor changes in forest cover and detect deforestation activities using a Multispectral Camera.
- **Operation Concept:**
 - * **Data Collection:** The multispectral camera captures images in various bands (visible, NIR, SWIR) at regular intervals, allowing for continuous monitoring of forested areas.
 - * **Data Processing:** Onboard processing reduces the data load by focusing on detecting changes in vegetation indices, which are critical for identifying deforestation.

- * **Data Transmission:** Multispectral images, along with metadata, are transmitted to ground stations using S-band or X-band communication links.
- * **Data Analysis:** Ground stations analyze the data to assess changes in forest cover, providing actionable intelligence for environmental protection agencies and policymakers.

• FritzSat Tatá - Forest Fire Monitoring Mission

- **Objective:** To detect and monitor wildfires using a Thermal Sensor (Infrared).
- **Operation Concept:**
 - * **Data Collection:** The thermal sensor continuously scans for infrared radiation indicative of fire hotspots, with a focus on rapid detection of temperature anomalies.
 - * **Data Processing:** Onboard processing includes automatic identification of potential fire events, prioritizing data for immediate transmission.
 - * **Data Transmission:** High-resolution thermal data is transmitted via X-band, with a priority on low latency to enable real-time response. UHF/VHF links are used for telemetry and control.
 - * **Data Analysis:** Ground stations receive and process the data, generating alerts for firefighting teams and providing real-time maps of active fire zones.

• Joint Operation Concept (Constellation-Wide)

- **Objective:** To maximize the overall effectiveness of the constellation in monitoring the Brazilian Amazon across multiple domains (hydrological, deforestation, and fire monitoring) without inter-satellite communication.
- **Operation Concept:**
 - * **Data Collection:** Each satellite operates independently, collecting data specific to its mission (SAR, multispectral, or thermal).
 - * **Data Scheduling:** Ground stations manage data collection schedules for each satellite, ensuring coverage optimization across different monitoring needs.
 - * **Data Transmission:** Each satellite transmits its data to the ground independently, with scheduling to avoid conflicts and ensure that all data is captured and processed in a timely manner.
 - * **Data Integration:** Ground stations integrate data from all satellites, providing a comprehensive view of environmental conditions across the Amazon, which is then shared with relevant stakeholders.

• General Operation Concept (Lifecycle of the Constellation)

- **Conception:** Initial assessment of environmental monitoring needs, leading to the decision to deploy a nanosatellite constellation focusing on hydrological monitoring, deforestation, and fire detection.

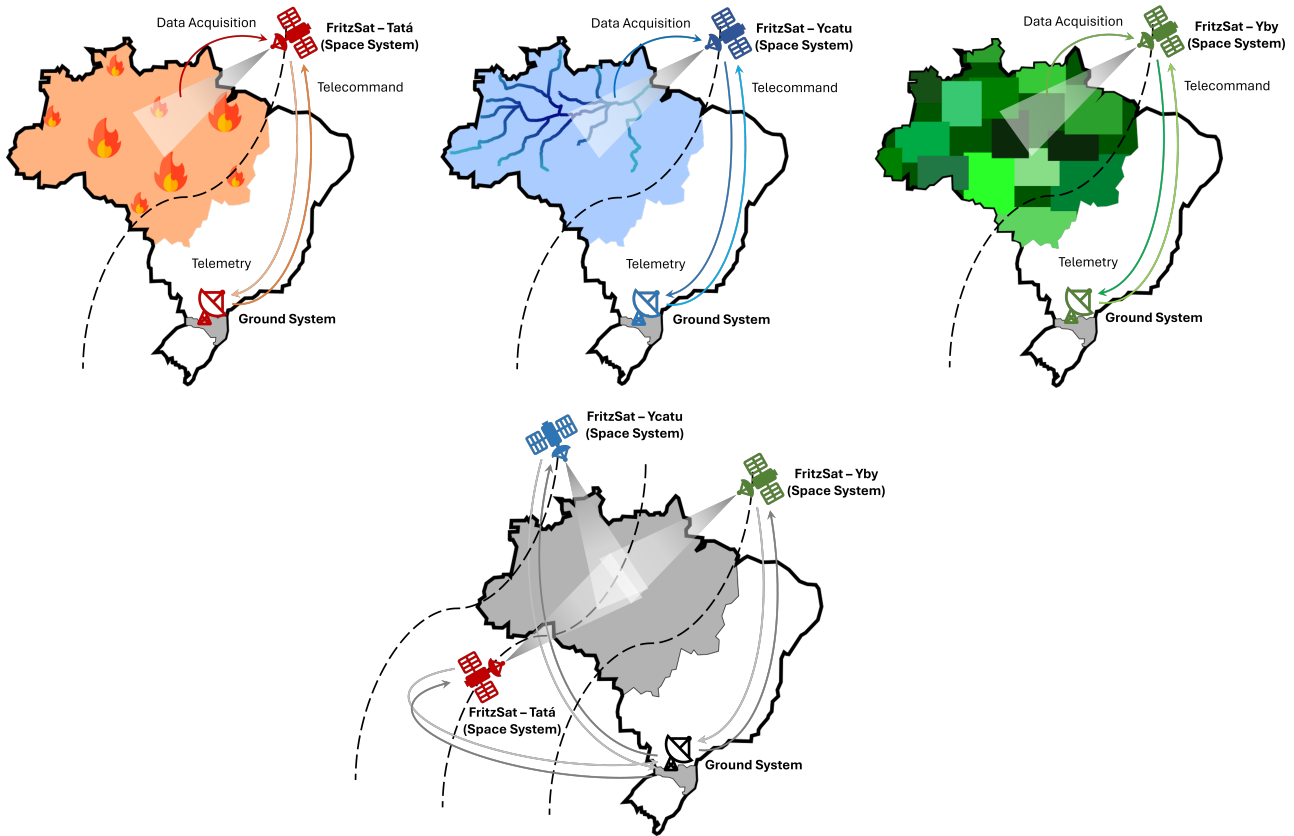


Fig. 2. Concepts of operation for the three main missions (above) and the general concept of operation (below).

- **Design:** Detailed design of the satellites, including payload selection (SAR, multispectral camera, thermal sensor) and system interfaces. Mission concepts and data requirements are established during this phase.
- **Manufacturing:** Construction and testing of the nanosatellites, ensuring that each meets the specifications necessary for its intended mission. This phase includes payload integration and system validation.
- **Launch:** Deployment of the constellation into orbit, ensuring that each satellite reaches its designated position. Launch procedures include final system checks and initial calibration.
- **Commissioning:** Post-launch testing and calibration of each satellite, including payload operation and data transmission validation. Ground stations begin receiving and analyzing initial data.
- **Operation:** The constellation enters full operation, with each satellite carrying out its mission as planned. Ground stations manage the schedule and integrate data from all satellites to provide continuous monitoring.
- **Decommissioning and Disposal:** At the end of the mission's life, satellites are decommissioned. Procedures are followed to ensure safe disposal,

minimizing space debris and ensuring compliance with international guidelines.

Figure 2 provides a graphical approach to better understand the operation concepts described above.

VI. CONCLUSION

The FritzSAT nanosatellite missions, which include FritzSat Ycatu for hydrological monitoring, FritzSat Yby for deforestation monitoring, and FritzSat Tatá for forest fire monitoring, represent a significant advancement in autonomous environmental observation. This study provides a comprehensive account of the mission development process, from the initial analysis of the Amazon's monitoring requirements to the integration of specialized payloads and the formulation of comprehensive operational concepts. The missions are designed to address gaps in current monitoring capabilities, thereby enhancing the autonomy of data acquisition, particularly for private entities.

The study emphasized the necessity of establishing unambiguous system interfaces between the space systems and both the monitoring scenario and ground systems. The selected payloads—a synthetic aperture radar (SAR), a multispectral camera, and a thermal sensor—were chosen based on their capacity to fulfill specific mission objectives. A comprehensive operational concept was devised, encompassing data types,

transmission mechanisms, and requirements, to guarantee effective communication and data utilization throughout the mission lifecycle.

In conclusion, the FritzSAT missions offer a robust framework for enhancing environmental monitoring in the Amazon. The comprehensive approach to system design, stakeholder analysis, and mission planning ensures that these nanosatellites will make a significant contribution to addressing critical environmental issues. The insights derived from this study will inform the various stages of the missions, thereby facilitating the sustainable management and expeditious response to environmental changes.

REFERENCES

- [1] National Institute of Space Research (INPE). Monitoramento da cobertura florestal da Amazônia por satélites: sistemas PRODES, DETER, DEGRAD e queimadas 2007-2008. São José dos Campos: INPE, 2008.
- [2] J. Chen, Y. Wang, J. Wang, Y. Zhang, Y. Xu, O. Yang, R. Zhang, J. Wang, Z. Wang, F. Lu, and Z. Hu, "The Performance of Landsat-8 and Landsat-9 Data for Water Body Extraction Based on Various Water Indices: A Comparative Analysis," *Remote Sens.*, vol. 16, pp. 1984, 2024. Available: <https://api.semanticscholar.org/CorpusID:270196288>
- [3] K. Kwapien, P. Lasota, M. Kedzierski, and P. Walczykowski, "Design and Performance Analysis of a Constellation of Nanosatellites to Monitor Water Quality in the Southern Catchment of the Baltic Sea," *Sensors (Basel, Switzerland)*, vol. 23, 2023. Available: <https://api.semanticscholar.org/CorpusID:259530655>
- [4] D. T. Gök, D. Scherler, H. Wulf, and D. T. Gök, "Land surface temperature trends derived from Landsat imagery in the Swiss Alps," [Conference], Available: <https://api.semanticscholar.org/CorpusID:269808234>
- [5] A. Byrne, D. Lomeo, W. Owoko, C. M. Aura, K. Nyakeya, C. O. Odoli, J. Mugo, C. Barongo, J. Kiplagat, N. M. Mwirigi, S. Avery, M. A. Chadwick, K. Norris, and E. J. Tebbs, "LAQUA: a Landsat water QUALity retrieval tool for east African lakes," *Remote Sens.*, 2024. Available: <https://api.semanticscholar.org/CorpusID:271809574>
- [6] I. S. Molina, L. M. Rodríguez, D. G. Díez, M. S. Anfres, J. M. Diaz, and J. J. A. Delgado, "Mission analysis of nanosatellite constellations with OpenSatKit," 4th Symposium on Space Educational Activities, 2022. Available: <https://api.semanticscholar.org/CorpusID:251117621>
- [7] A. Bocharov, A. G. Kostianoy, and S. A. Lebedev, "Assessment of the accuracy of determining the Caspian Sea surface temperature by Landsat-5, -7 satellites based on the measurements of drifters," *Ecologica Montenegrina*, 2024. Available: <https://api.semanticscholar.org/CorpusID:271563609>
- [8] R. Rose, C. S. Ruf, and H. Seki, "Ocean altimetry and wind applications of a GNSS nanosatellite constellation," *Asia-Pacific Environmental Remote Sensing*, 2012. Available: <https://api.semanticscholar.org/CorpusID:38919388>
- [9] A. A. Spiridonov, V. Baranova, V. A. Saetchnikov, and D. Ushakov, "The regional nanosatellite constellation modelling formation by a piggyback launch from different spaceports," *Journal of the Belarusian State University. Physics*, 2022. Available: <https://api.semanticscholar.org/CorpusID:250198254>
- [10] A. Schwarzenberg-Czerny, W. Weiss, A. Moffat, R. E. Zee, S. Rucinski, S. Mochnecki, J. Matthews, M. Breger, R. Kuschnig, O. Koudelka, P. Orleanski, A. Pamyatnykh, A. Pigulski, and C. Grant, "The BRITe Nanosatellite Constellation Mission," 38th COSPAR Scientific Assembly, 2010.
- [11] H. Talebi, S. Samadianfard, and H. Çıtakoğlu, "Estimating reference evapotranspiration in an arid region using a MODIS sensor and machine learning algorithms," *Advanced Engineering Days*, 2024.
- [12] F. Jalal and A. S. Mahdi, "Detection the Dust Storms Using MODIS Reflection Mode," *Iraqi Journal of Science*, 2024.
- [13] Z. Faraji, A. Kaviani, and L. Khosravi, "Downscaling the MODIS land surface temperature using a trapezoidal concept applied to the MODIS and sentinel 2 images," *Environmental Monitoring and Assessment*, 2024.

FEA-Based Vibration Analysis of Cubesat Battery Structures

1st David Pablo Alves Primo
Projetos Mecânicos
Senai Cimatec
Salvador, Brazil
david.primo@fbter.org.br

2nd Yan da Silva Moura
Simulações e Cálculos
Senai Cimatec
Salvador, Brazil
yan.moura@fbter.org.br

3rd Rodrigo Silveira de Santiago
Simulações e Cálculos
Senai Cimatec
Salvador, Brazil
0009-0000-4642-494X

4th Artur Iagê Correia dos Santos Ferreira
Projetos Mecânicos
Senai Cimatec
Salvador, Brazil
artur.ferreira@fieb.org.br

5th Lucas Lincoln Fonseca Soares
Simulações e Cálculos
Senai Cimatec
Salvador, Brazil
lucas.fs@fieb.org.br

6th Valter Estevão Beal
Projetos Mecânicos
Senai Cimatec
Salvador, Brazil
0000-0003-4651-0383

7th Juan Carlos Romero Albino
Simulação e Cálculos
Senai Cimatec
Salvador, Brazil
0000-0003-4880-4182

8th Leonardo Ferreira Daltro
Eletrônica Embarcada
Senai Cimatec
Salvador, Brazil
leonardo.daltro@fieb.org.br

9th Edmar Soares da Silva
Eletrônica Embarcada
Senai Cimatec
Salvador, Brazil
edmar.silva@fieb.org.br

Abstract—This paper presents a finite element analysis (FEA) of the structural behavior of the battery pack of a 1U CubeSat nanosatellite developed at Senai Cimatec, with a focus on battery fixation. The static analysis reveals that the structure remains within stress limits during assembly and launch. Modal analysis identifies critical natural frequencies and vibration modes, highlighting the need for structural reinforcement to mitigate resonance effects. Random vibration analysis demonstrates that the battery pack components can withstand the expected random vibrational loads during launch. It is recommended to implement additional docking mechanisms or support structures to enhance the structural robustness of the CubeSat.

Index Terms—Cubesat, 1U, Battery Module, FEA, Modal Analysis, Random Vibration

I. INTRODUCTION

CubeSats emerge as a revolution in space exploration, offering an accessible and flexible platform for a variety of scientific, commercial, and educational missions. They enable the development of low-cost missions with a mission lifespan of over a year. Among the various challenges faced in CubeSat projects, the proper fixation of batteries is of utmost importance, as they play a crucial role in supplying power for satellite operations. Additionally, precise and robust battery fixation is essential to ensure the operational integrity of the CubeSat during launch and operations in orbit. Therefore, it is important to develop a robust fixation component that meets the satellite's operational and launch requirements. [1].

The design of a nanosatellite (CubeSat) is standardized by special agencies from different countries such as NASA or ESA. To verify the high-intensity vibro-acoustic effects

induced on the payload during the satellite's launch and operation, the NASA-STD 7001B [2] standard can be used, along with experimental tests using shakers [3]. Alternatively, the use of numerical simulation tools through the finite element method allows for the reduction of project costs and optimization of components to meet standard requirements. [3] [4] [5] [6].

In this work, it is proposed to assess the structural behavior of the power supply and battery assembly of a 1U CubeSat using the finite element method in Ansys Mechanical. It will be analyze the bolt assembly and random vibration to verify the risk of battery detachment or component failure.

II. GEOMETRY AND ASSEMBLY

For the development of this work, the 1U CubeSat is used as a case study. This satellite is being developed at Senai CIMATEC as a technological demonstrator for satellite development. The project inherits flight heritage from FloripaSat, developed by the SpaceLab laboratory at the Federal University of Santa Catarina (UFSC).

The Fig. 1 presents the geometry of the 1U CubeSat evaluated in this work, particularly focusing on the battery assembly, which is the subject of this study, located in the lower region of the structure.

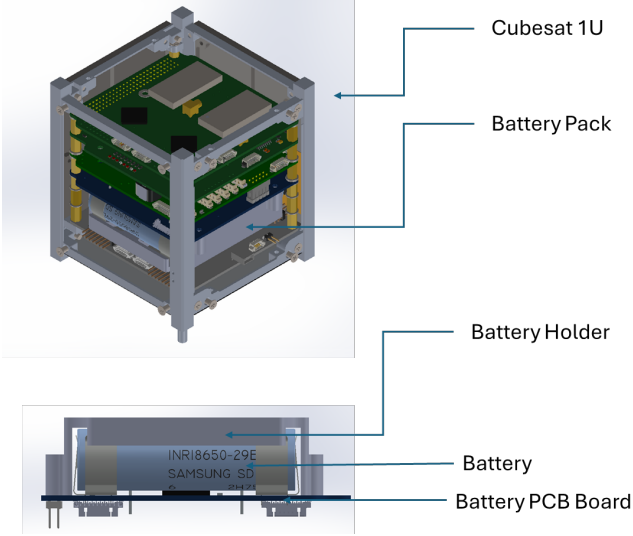


Fig. 1. Cubesat 1U and Battery Pack.

III. NUMERICAL ANALYSIS

The CAD model of the CubeSat was developed in SolidWorks. To analyze the effect of random vibration on the battery support component, a modal simulation analysis was performed using the Ansys Mechanical APDL software.

The numerical model was developed and analyzed using the commercial program ANSYS Mechanical APDL to develop the finite element method (FEM) model, detailing where the modal and random vibration analysis was conducted on the battery support component.

Initially, a linear static analysis was conducted to predict the stress state in the structure caused by the assembly of components. These results were used as a pre-stress condition for the modal analysis model, which estimated the modes of vibration and natural frequencies to which the structure is subjected. Subsequently, the results of the modal analysis were incorporated into a random vibration model that allowed for estimating the structure's response to a normal distribution of excitation probability, aiming to represent possible damages or failures during the satellite launch stage.

2 illustrates the steps used for simulation.

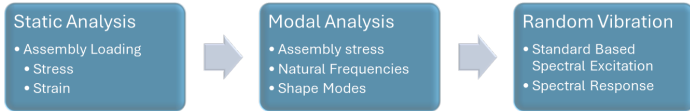


Fig. 2. Model Structure

A. Concepts in Modal Analysis

The modal analysis model calculates the equation of motion assuming harmonic motion, as shown in (1):

$$[M]\ddot{\mathbf{u}} + [K]\mathbf{u} = 0 \quad (1)$$

Where $[M]$ is the mass matrix, \mathbf{u} is the nodal displacement vector, $\ddot{\mathbf{u}}$ is the nodal acceleration vector, and $[K]$ is the

stiffness matrix. The problem is solved through eigenvalues (Natural Frequencies - ω_i) and eigenvectors (Mode Shapes - ϕ_i), as shown in equation (2):

$$([K] - \omega_i^2[M])\phi_i \quad (2)$$

The mass participation factor (γ_i) indicates the amount of mass participating in the vibration in each direction and can be obtained through equation (3):

$$\gamma_i = \phi_i^T[M]\phi_i \quad (3)$$

The effective mass ($M_{eff,i}$) indicates the amount of mass associated with each mode of vibration and can be obtained through equation (4):

$$M_{eff,i} = \gamma_i^2 \quad (4)$$

B. Model Simplification and Assumptions

In this work, the following simplifications were considered:

- Linear elastic behavior;
- Small deformations;
- Frictionless contact between the bolt and the PCB, and between the PCB and the battery holder.
- The remaining components have "bounded" contact since a fixing resin is used during the assembly of electronic components.

The materials adopted for the components were defined as:

- Electronic Board: PCB;
- Bolts: Stainless Steel 304;
- Mounting Bracket: Brass;
- Battery Holder: PEEK
- Batteries: Lítio;

The Table I presents the mechanical properties of the materials used in the model.

TABLE I
MATERIALS PROPERTIES.

Material	PCB	304SS	Brass	PEEK	Lítio
E [GPa]	24.0	210.0	137.0	3.8	4.9
S_{ut} [MPa]	321	690	275	106.5	1.4
S_y [MPa]	321	448	76	99.5	2.4
ρ [$kg \cdot m^{-3}$]	1850	7850	8712	1310	535
Poisson [-]	0.18	0.3	0.345	0.4	0.36

For the static analysis, only three boundary conditions were considered:

- Tightening load on the bolts: 350 N;
- Acceleration on the bodies of the components: 8G;
- Fixed Support (restriction of all degrees of freedom) on the faces of the mounting holes of the standoffs.

To model the assembly and launch stages of the satellite, pre-load was applied to the screws at a time instant prior to the application of acceleration in the model. The stress fields, displacements, and contact conditions between the bodies were used as pre-loading for the modal analysis. Fig. 3 presents the boundary conditions used in the static analysis.

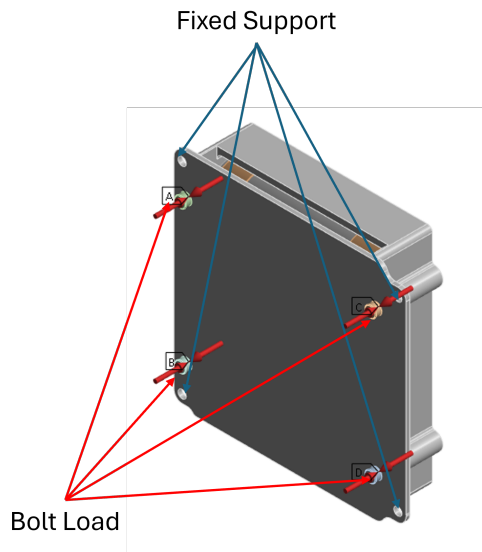


Fig. 3. Boundary Condition.

For the random vibration model, the loading was obtained from the NASA-STD 7001B standard [1] along with the natural frequencies and mode shapes obtained from the modal analysis, as shown in Table II:

TABLE II
RANDOM VIBRATION LOADING.

Frequencies [Hz]	Power Spectral Density [g^2/Hz]
20	0,01
20 - 80	+3 dB/oct
80 - 500	0,04
500 - 2000	-3 dB/oct
2000	0,01
Overall Level	6.8 grms

C. Mesh

The mesh refinement was developed using the method of nodal difference not significant, resulting in a mesh with 972281 nodes and 428623 elements. For this, the mesh parameters presented in Table III were used. Fig. 4 presents the mesh used in this study.

TABLE III
MESH PARAMETERS.

Parameter	Element Size	Selection	Other Parameters
Body Sizing	1,25 mm	Battery Support	-
Body Sizing	0,5 mm	Bolts	-
Body Sizing	1,0 mm	Electronic Board	-
Body Sizing	3,0 mm	Batteries	-
Body Sizing	1,0 mm	Mounting Brackets	-
Face Sizing	0,2 mm	Fixing Holes of the Electronic Board	Influence on Volume: 1,5 mm
Face Sizing	0,2 mm	Fixing Holes of the Battery Holder	Influence on Volume: 1,5 mm



Fig. 4. Mesh.

IV. RESULTS AND DISCUSSIONS

A. Static Analysis

Figure 5 shows the Von Mises stress field during assembly and the safety factor for the structure during launch. It can be noted that the highest stresses were in the contact region between the screws and the battery holder. However, it is observed that outside this region, the stress did not exceed the material yield limit (PEEK: 99.5 MPa), allowing the screw to be fixed without the need for metallic inserts, resulting in a safety factor of 1.7.

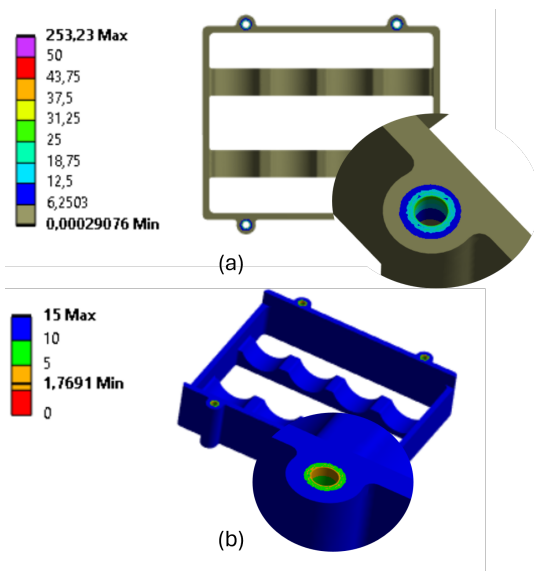


Fig. 5. Results of Static Analysis: (a) Von Mises stress field during assembly [MPa] and (b) Safety factor during launch stage.

B. Modal Analysis

Table IV presents the first 10 natural frequencies of the modal analysis model. It can be observed that only the first 5

frequencies are within the frequency limits(2000 Hz) described in the NASA-STD 7001B standard [1], as shown in Table II, which are the modes of vibration of the structure that were analyzed.

TABLE IV
MESH PARAMETERS.

Mode	Frequency [Hz]
1,00	990,39
2,00	1378,60
3,00	1760,90
4,00	1934,40
5,00	1991,10
6,00	2572,00
7,00	2778,30
8,00	2892,60
9,00	3202,40
10,00	3324,40

The tables IV, V, and VI show the participation factor, the effective mass, and the critical modes of the structure, respectively. The critical modes of the structure are obtained by multiplying the participation factor by the effective mass. Based on the results presented for the participation factors and effective mass, it can be observed that the first mode of vibration, with a natural frequency of 990.39 Hz, shows the highest coefficients for the degrees of freedom of rotation in X (Xr) and Y (Yr). Thus, only these two points have non-zero values when evaluating the critical modes through Tab. VII. This indicates that the set of components of the satellite battery plate can be excited in the X and Y directions when the structure is loaded with a frequency close to 990.39 Hz, exciting this natural frequency. In this case, it is necessary to interlock the structure in the X direction, perpendicular to the oscillatory motion, increasing stiffness and damping, thereby reducing the effect of this mode of vibration. Fig. 6 shows the mode of vibration for the critical natural frequency of 990.39 Hz.

TABLE V
PARTICIPATION FACTOR.

Modo	X	Y	Z	Xr	Yr	Zr
1,00	0,00	0,00	-0,01	-1,08	0,99	0,11
2,00	0,00	0,00	0,00	-0,27	-0,01	-0,34
3,00	0,00	0,00	0,00	0,20	-0,01	0,01
4,00	0,00	0,00	0,00	0,04	-0,18	-0,43
5,00	0,00	0,00	0,00	-0,45	0,23	-0,28

TABLE VI
EFFECTIVE MASS.

Mode	X	Y	Z	Xr	Yr	Zr
1,00	0,00	0,00	0,00	1,17	0,98	0,01
2,00	0,00	0,00	0,00	0,07	0,00	0,12
3,00	0,00	0,00	0,00	0,04	0,00	0,00
4,00	0,00	0,00	0,00	0,00	0,03	0,18
5,00	0,00	0,00	0,00	0,21	0,05	0,08

TABLE VII
CRITICAL MODES.

Mode	X	Y	Z	Xr	Yr	Zr
1,00	0,00	0,00	0,00	-0,73	0,79	0,00
2,00	0,00	0,00	0,00	0,00	0,00	0,00
3,00	0,00	0,00	0,00	0,00	0,00	0,00
4,00	0,00	0,00	0,00	0,00	0,00	0,00
5,00	0,00	0,00	0,00	-0,01	0,00	0,00

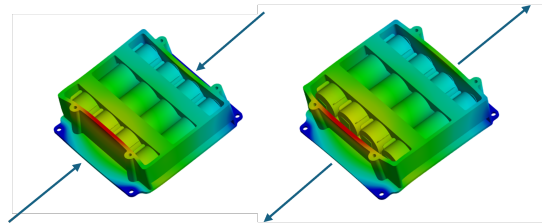


Fig. 6. Mode of vibration for the natural frequency of 990.39 Hz

C. Random Vibration Analysis

The analysis of random vibration is critical for the design and testing of aerospace structures. In this case, the response of the second battery within the battery pack is evaluated based on the loading presented in Table II, which is applied in the Z direction, equivalent to the launch direction. Figure 7 shows the results obtained for the random vibration analysis.

As expected from the modal analysis, the structure exhibited a peak at approximately 10^3 Hz, close to the first natural frequency, reaching higher values in the Z direction, equivalent to the direction of loading. In the X direction, it showed the second highest peak at this frequency due to lower stiffness and the lack of interlocking of the structure, a behavior that had already been verified by the modal analysis. Despite this, the PSD values found in the model are within the limits established in the NASA-STD 7001B standard [2].

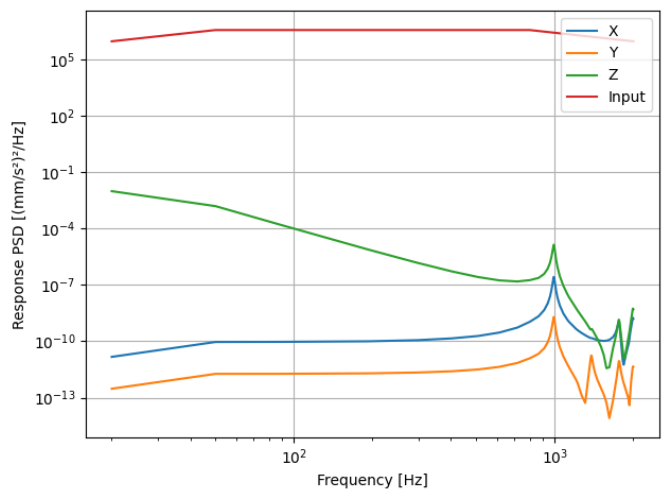


Fig. 7. Power Spectral Density [(mm/s²)²/Hz].

Figure 8 shows the Von Mises stress field for the random vibration analysis of the evaluated structure. It can be observed that none of the components of the battery pack exhibited equivalent stresses exceeding 10 MPa, except for the electronic board, which reaches a stress peak in the region of the mounting holes and the application of vibration loading of 163.89 MPa. This value is below the yield strength of the material (PCB: 321 MPa) and does not pose a risk to the structure of the board. It is worth noting that since the loading was applied directly to the mounting holes of the board, without considering the attenuation and damping of the loading due to the effect of the satellite structure under real launch conditions, this effect will be reduced.

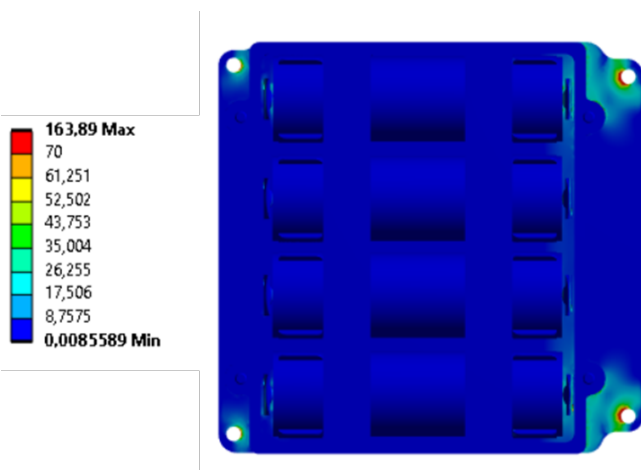


Fig. 8. Von Mises Stress Field during Random Vibration Analysis [MPa].

V. CONCLUSIONS

In this work, numerical analyses using Finite Element Methods were conducted for the assembly and launch stages of the battery pack of a nanosatellite (Cubesat 1U). Through static structural, modal, and random vibration analyses, it was verified whether the structure is prepared to withstand the forces, comparing the results with the NASA-STD 7001B standard [2].

The static analysis revealed that the battery support structure within the CubeSat remains within the allowable stress limits during assembly and launch. Although the stresses at the battery support mounting hole are low, it is suggested to use threaded metal inserts to ensure the structural integrity of the component.

The results obtained from the modal analysis showed the natural frequencies and vibration modes of the battery support structure. The critical mode, associated with a frequency of approximately 990 Hz, highlights potential areas of concern for the structural response during launch. This mode primarily affects the X and Y directions in their rotational degrees of freedom, indicating the need for additional structural reinforcement in these directions to mitigate potential resonance effects.

The random vibration analysis demonstrated that the components of the battery pack can withstand the expected vi-

brational loads during launch. Despite localized stress concentrations observed at the PCB mounting holes, these remain within safe limits and are unlikely to compromise the structural integrity of the system as a whole.

To enhance the structural robustness of the CubeSat, it is recommended to implement interlocking mechanisms or additional support structures to mitigate the effects of critical vibration modes. Additionally, refining the PCB mounting strategy, such as incorporating reinforcements around the mounting holes, could alleviate stress concentrations and improve overall reliability.

REFERENCES

- [1] A. Poghosyan, A. Golkar, CubeSat evolution: Analyzing CubeSat capabilities for conducting science missions , *Progress in Aerospace Sciences*, 2017. <https://doi.org/10.1016/j.paerosci.2016.11.002>.
- [2] National Aeronautics and Space Administration. NASA-STD-7001B: Payload Vibroacoustic Test Criteria.2017.
- [3] A. Ampatzoglou, V. Kostopoulos, Design, Analysis, Optimization, Manufacturing, and Testing of a 2U Cubesat , *International Journal of Aerospace Engineering*, 2018. <https://doi.org/10.1155/2018/9724263>.
- [4] A. Elshaal, W. Faris Aizat Wan , M. Okasha, E. Sulaeman, A. Halim Jallad, Evaluation of Finite Element Analysis Techniques for CubeSat Structure: a comparative study on alainsat-1, *Ieee International Geoscience And Remote Sensing Symposium*, 2023. <http://dx.doi.org/10.1109/igarss52108.2023.10281761>.
- [5] A. Dhariwal, N. Singh , A. Kumar Kushwaha, Structural Analysis Of 1U CubeSat Designed For Low Earth Orbit Missions , *2023 International Conference On Iot, Communication And Automation Technology (Icicat)*, 2023. <http://dx.doi.org/10.1109/icicat57735.2023.10263601>.
- [6] G.I. Barsoum, H. H. Ibrahim , M. A. Fawzy, Static and Random Vibration Analyses of a University CubeSat Project , *Journal of Physics: Conference Series*, 2019. <http://dx.doi.org/10.1088/1742-6596/1264/1/012019>.

Design of a Low-Cost Solar simulator for Cubesats

Maria Eduarda Emiliano Rezende[✉],
 Caique Sales Miranda Gomes[✉],
 Edemar Morsch Filho[✉],
 João Cláudio Elsen Barcellos[✉],
 Anderson Wedderhoff Spengler[✉]
 and Eduardo Augusto Bezerra[✉]

Abstract—CubeSats have become a popular satellite-standard choice for space missions due to their versatility and affordability. Despite their widespread use, extensive testing is still necessary to minimize in-orbit failures. In this paper, the design of a solar simulator, primarily for evaluating the energy management of CubeSats, is presented. The simulator consists of a box with LEDs on its internal walls, where a CubeSat is placed inside. By controlling the LEDs, it is possible to emulate the in-orbit conditions in which the CubeSat operates, allowing its power generation capacity to be assessed. Though the tests are conducted under non-space conditions, the controlled environment makes it possible to identify problems in CubeSat’s power management, as well as to analyse the operation of its Electric Power System (EPS). The solar simulator can evaluate transient energy generation as well as battery performance by simulating varied orbits. It can also expose the CubeSat to critical scenarios to test its behavior under these conditions. Then, this paper outlines the design of the solar simulator and its components, such as the selection of LEDs and heatsinks. It also presents a preliminary methodology for controlling LEDs aiming to replicate in-orbit conditions. The solar simulator is currently under development, but it is expected to aid in the design and testing of CubeSats. This includes evaluating individual components like photovoltaic panels and batteries, as well as subsystems such as the EPS, ultimately benefiting the overall design of the space segment.

Keywords—Power generation, Testing, Photovoltaic cell

I. INTRODUCTION

CubeSats, which are a category of small satellites commonly referred to as nanosatellites, are distinguished by their compact and modular design. Each CubeSat is based on a standard structure measuring $10 \times 10 \times 10 \text{ cm}$, known as a “U.” This standardized unit allows for flexibility in satellite design, as multiple units can be combined to create larger CubeSats, making them a versatile option for a wide range of space missions and applications, as can be seen in [Figure 1](#).

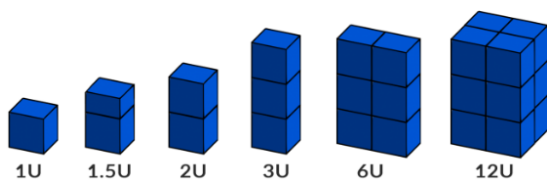


Fig. 1: CubeSat standard sizes [1]

The development of small satellites, in contrast to the larger and more complex ones, has significantly increased space accessibility to a broader audience. One of the main areas impacted is academia and universities, which, even with less investment, now have the opportunity to conduct research in space.

Maria E. Emiliano Rezende, UFSC, Brazil (dudarezende14@gmail.com).
 Caique Sales Miranda Gomes, UFSC, Brazil, (kiqsmg@gmail.com).
 Edemar Morsch Filho, UFSC, Brazil, (edemar.filho@unesp.br).
 João C. E. Barcellos, UFSC, Brazil, (joaoclaudiobarcellos@gmail.com).
 Anderson W. Spengler, UFSC, Brazil, (anderson.spengler@ufsc.br).
 Eduardo Augusto Bezerra, UFSC, Brazil, (eduardo.bezerra@ufsc.br).

Many technical difficulties still need to be resolved in developing these missions (e.g., communication, attitude control, and energy management). Therefore, previous studies of the structures are carried out to predict these errors, but one of the main difficulties is still estimating the energy generation in a satellite in orbit.

As it is extremely complicated to capture data directly from the battery after the satellite is launched, this makes it difficult to simulate this information without prior testing.

Many institutions have developed sun simulators to analyze power generation from solar panels. One example is the indoor simulator, designed with LEDs to mimic solar irradiation, as described in [2].

This paper focuses on a similar application, placing the CubeSat inside a sun simulator platform to primarily test the functionalities of the Electrical Power System (EPS), simulating a scenario that closely resembles the conditions found in orbit.

The idea for creating the box was inspired by [3], where other institutions simulated sunlight in a controlled environment to test photovoltaic cells. This concept was then adapted for use in the space sector.

Therefore, The primary goal is to develop a test bench that accommodates a full 2U CubeSat with all its subsystems operational. This setup will allow for testing the functionality of the EPS by powering solar panels with an artificial solar source and evaluating the distribution of the energy throughout the nanosatellite system.

To achieve this goal, it will be necessary to ensure that all subsystems of the CubeSat are integrated and operational during testing. This includes not only the functionality of the power supply system but also the communication between subsystems, thermal management, and the structural stability

of the satellite while it operates on the test bench. The test bench must be designed to simulate realistic operating conditions, using artificial solar light sources that emulate the space environment, thereby allowing for an accurate assessment of the CubeSat's performance in future missions.

This work will be organized as follows: the methodology applied by other authors will be adapted and detailed in the Methodology section [Section II](#), where details of each main part will be presented. Further discussions on the project development will be explained in the section Discussion: Trends and Directions [Section V](#), followed by a Conclusion section [Section VI](#).

II. METHODOLOGY

This section will outline the key aspects considered in the development of the project, including the structure of the satellite that will be tested in the solar simulator. The methodology was based on a thorough review of previous work and was adapted to this case, incorporating a complete nanosatellite within the structure along with its critical systems.

A. Main system of GOLDS-UFSC

In this subsection, the subsystems of the GOLDS-UFSC, platform FloripaSat-2 [\[4\]](#), that are important for the Sun simulator design will be presented, highlighting the structure, the EPS, and Telemetry, Tracking & Command (TT&C). This way, the entire project will be based on the Cubesat developed at the Federal University of Santa Catarina by the Space Systems Laboratory (Spacelab).

1) *Structure*: The structure developed for the GOLDS-UFSC project measures $10x10x20cm$ (CubeSat 2U), and it aims to organize and stabilize all of the other subsystems safely during all the mission phases (from fabrication to end of life). Furthermore, it was designed to be efficient when integrating PCB and cables. As can be seen in [Figure 2](#), the sides are hollow for the possibility of internal handling after assembly. Then, when the assembly is complete, over each side solar panels are mounted, as observed in [Figure 3](#).

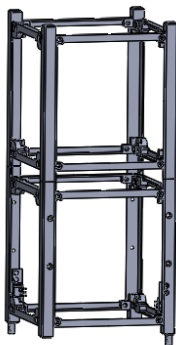


Fig. 2: Structure of GOLDS-UFSC CubeSat

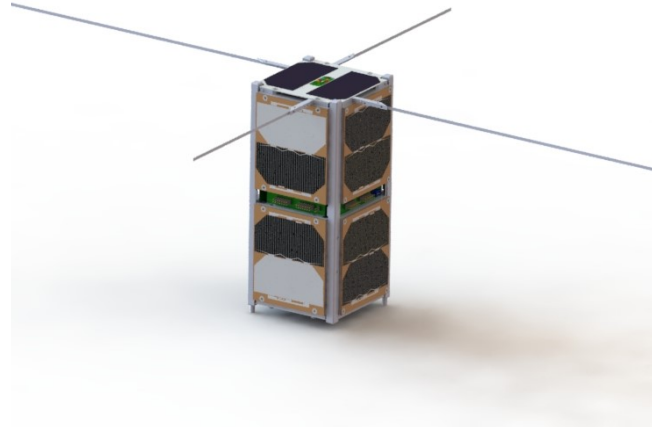


Fig. 3: Isometric view of GOLDS-UFSC CubeSat

2) *EPS*: It is a critical subsystem of a CubeSat's service module, interfacing between the solar panels, batteries, and the satellite's loads (including other subsystems of the service module). Essentially, the EPS manages energy collection, storage, and conditioning for the entire system.

As detailed in [\[5\]](#), this subsystem is typically divided into three units: the Energy Harvesting Unit (EHU), the Energy Storage Unit (ESU), and the Power Distribution Unit (PDU). The EPS2 of GOLDS-UFSC follows this same structure.

The EHU of the EPS2 includes three boost converters, one for each pair of parallel solar panels. To optimize the power transfer from the panels to the loads and batteries, it employs a Maximum Power Point Tracking (MPPT) algorithm, specifically the perturb and observe method. The control signals for this process are generated by the MCU (MSP430).

Regarding the ESU, the EPS2 uses an integrated circuit to monitor the batteries, which also provides protection mechanisms and manages the charging and discharging processes.

Finally, the PDU in the EPS2 contains multiple Buck converters to supply 3.3V, 5V, and 6V buses to the satellite's loads.

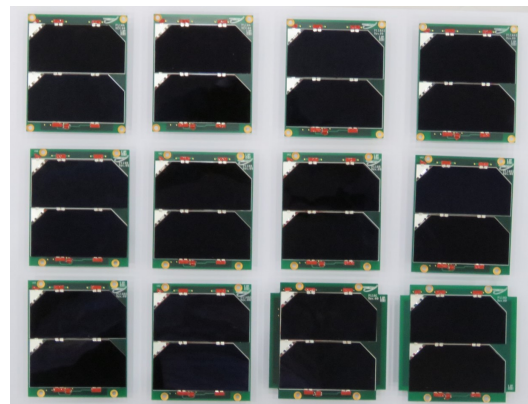


Fig. 4: Photovoltaic panels

3) *TT&C*: It is responsible for establishing communication and decoding data between Earth and the nanosatellite. The

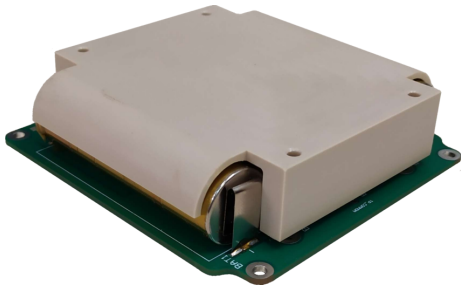


Fig. 5: Battery board

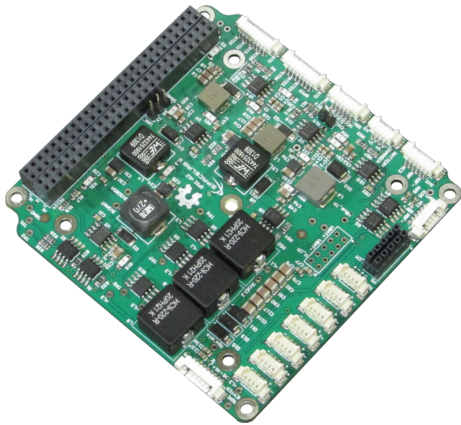


Fig. 6: EPS2

main component of this subsystem valid to mention here is the antenna, which is responsible for capturing data from Earth (ground stations) and transmitting it to the *TT&C*. The antenna model (Figure 7) is from the ISIS model has 1314 mm opened in orbit.



Fig. 7: Antenna

B. Dimensions of the Sun Simulator

The construction of a Sun simulator follows certain standards to obtain the necessary irradiance, imitating the sunlight that the satellite would encounter in orbit. In this subsection will be in-depth subsystem and its parts compound by: the box, leds, coolers and the support for the satellite.

1) *The Box*: : It is the combination of the six plates of the material will be discussed in the next subsection [subsection II-D](#). Two plates are $340 \times 340 \times 20 \text{ mm}$ and four of them are $440 \times 330 \times 20 \text{ mm}$ as can be seen in the image [Figure 8](#)

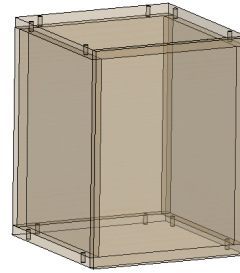


Fig. 8: Box utilized control volume

2) *The LEDs*: : the system is compound with 10 LEDs placed two on the bigger plates and one at the smallest ones. The LEDs are $40 \times 40 \times 6 \text{ mm}$ as is shown in [Figure 9](#). The number of LEDs was determined based on the radiation requirement per square meter, aiming to make the simulator as close as possible to the solar reality. The corresponding calculations will be presented later in [Section II](#)

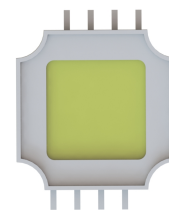


Fig. 9: LED structure

3) *Coolers*: following the same number of LEDs with 10 sets, each one is placed behind a LED composing the system: LEDs, coolers, and heatsinks, as presented in [Figure 10](#).

4) *Support for the Satellite*: is a structure designed to uphold the Cubesat to not enter in contact with the bottom LED directly. The tablet is made of Poly-lactic Acid (PLA) and its dimension is $108 \times 108 \times 100 \text{ mm}$, as at the [Figure 12](#)

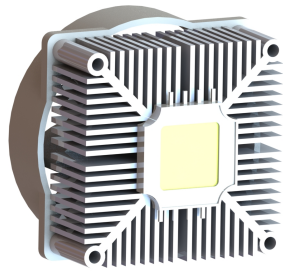


Fig. 10: The structure of LED, heatsink and cooler

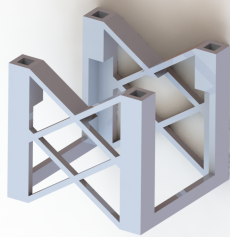


Fig. 11: Support for the satellite

C. Structure

For the design of the isolated system, a box was designed that had the necessary dimension to fit the entire 2U satellite, and due to thermal requirements.

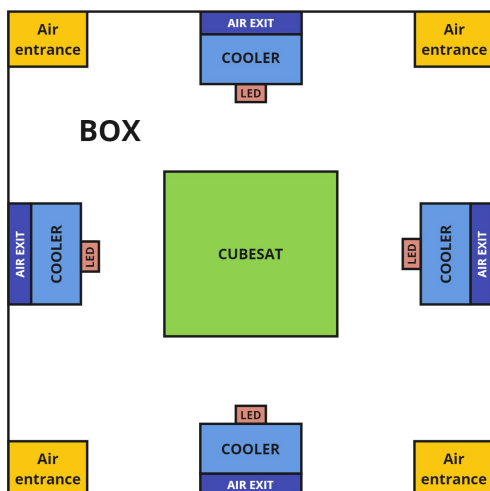


Fig. 12: Simplified schema of final box configuration

D. Material's selection

For the selection of the material for the enclosure, materials with good heat transfer properties and availability in the Brazilian market were considered. The options included:

Medium Density Fiberboard (MDF) and PLA. Throughout the proposed design, careful attention was given to the necessary air outlets to prevent the system from overheating due to the high temperatures of the LED.

1) *MDF*: good thermal dispersion, previously used in solar simulator projects, such as [3], and low heat absorption.

2) *PLA*: is a biodegradable thermoplastic derived from renewable resources like corn starch or sugarcane. It is less heat-resistant compared to other plastics and can become brittle over time. And it was also used in a similar project [6].

Following can be seen at table [Table I](#), the comparison of PLA and MDF principal thermal characteristics.

TABLE I: Parameters of each evaluated box material.

Parameters	PLA	MDF
Melting temperature [°C]	170	225
Thermal conduction [W/mK]	0,10-0,15	0,13-0,25
Cost (\$/kg)	60	40

III. DESIGN

The design of the Sun simulator plays a critical role in the development of systems that test the thermal behavior of the satellite in orbit. This process involves the careful selection of materials and the study of the optimal configuration of LEDs to accurately represent solar irradiance, as well as the system's thermal management. The precise implementation of these elements is essential to ensure that the simulator faithfully reproduces environmental conditions, thus creating a controlled volume that closely approximates the satellite's orbital environment without requiring the use of a vacuum chamber.

For the project development, the use of 10 white light LEDs was stipulated, providing 6500K, 100W of power, and 36V of load, in order to simulate the irradiance of 1000 watts per square meter, thereby approximating the simulation as closely as possible to real solar radiation.

These LEDs will be controlled by a specific power source to simulate the solar radiation in the satellite's orbit. Thus, the satellite remains stable, but the radiation in each LED varies to mimic all the phases the satellite will go through, from total solar eclipse to constant radiation.

According to [7], the thermal behavior of a satellite is influenced by its altitude and orbit, highlighting that the duration a satellite spends in Earth's shadow varies with its altitude. CubeSats can achieve orbits of up to 2000 km, classified as Low Earth Orbit (LEO) as noted at [8]. The temperature profile used in this study was simulated for the FloripaSat-1 nanosatellite, which is designed to travel in circular orbits at an altitude of 400 km and an inclination of 51.5°. The satellite completes a full orbit around Earth in approximately 5125 seconds, with 3053 seconds in sunlight and 2072 seconds in Earth's shadow. For the GOLDS-UFSC, a 2U CubeSat, the same orbital parameters as FloripaSat-1 were used to simulate its orbit with the LEDs in the Sun simulator.



Fig. 13: CubeSat Orbit obtained by STK [7]

To implement these changes, the following parameters of the LEDs will be monitored: voltage and current at each point.

In addition to selecting the material, other measures must be applied to the project to prevent overheating. Therefore, 10 commercial¹ heat sinks were stipulated to dissipate the excess internal heat within the enclosure. Consequently, the structure has the form presented in Figure 14



Fig. 14: Chosen commercial heat sink

Thus, with the carefully selected number of LEDs and the estimated control strategy in place, the design can now be finalized, ensuring that all parameters meet the expected performance standards. Moreover, addressing the potential thermal challenges, such as overheating, contingency plans have been outlined, which include the strategic use of coolers and heat sinks to maintain optimal operating temperatures. With these precautions and design considerations taken into account, the project is well-positioned for the next phase, which is the practical implementation and testing of the system in real-world conditions.

IV. IMPLEMENTATION

Building on the studies and design choices outlined before, the implementation phase of the project followed a structured approach to ensure accurate simulation and control of the

¹<https://www.coolermaster.com/pt-br/products/i30/>

heat transferred to the CubeSat. We began the implementation phase by configuring the hardware, focusing on the construction of the box and the setup of the LEDs, we then focused on the power source system to replicate the solar irradiance conditions. Following this, the software for controlling the LEDs' radiation phases was developed. In parallel, we conducted the thermal simulations and feedback systems. Throughout the project, many adjustments were made both in the hardware selection/configuration and the software algorithms to optimize the system's performance, aiming for an accurate representation of our orbit's conditions, following [7].

Based on all the studies conducted previously, the number of LEDs was determined according to the total volume of the box, as shown in Equation 3. Following the parameters established in the methodology to achieve 1000 watts per square meter at the CubeSat surface, resulted in a total of 10 LEDs being required in the box. This number ensures that the lighting system meets the power density criteria while maximizing efficiency and uniformity of light distribution across the box surface. Thus, 10 LEDs were chosen as the optimal configuration to meet the specified energy and lighting requirements.

$$V_{total} = L \cdot W \cdot H \quad (1)$$

$$V_{total} = 440 \cdot 340 \cdot 340 \quad [mm^3] \quad (2)$$

$$V_{total} = 50,776,000 \quad [mm^3] \quad (3)$$

As a result, the heat sinks follow the same number of LEDs to prevent the box from overheating. The material chosen, based on the data summarized in Table I, was MDF due to its lower cost, higher range heat transfer efficiency, and melting temperature.

Thus, the final result of the project prototyping was a design featuring 10 LEDs, 10 heat sinks, a support structure for the 2U satellite, and a central box with dimensions of $440 \times 340 \times 340 mm$, as can be seen in Figure 15. This configuration was carefully selected to ensure the optimal performance of the system, balancing thermal management, structural integrity, and space efficiency. The design reflects the culmination of detailed planning and precise engineering to meet the project's requirements while maintaining practicality and functionality throughout the process.

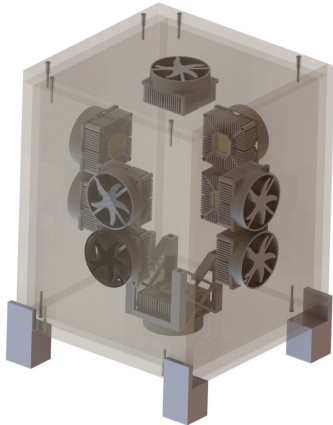


Fig. 15: Isometric view of a complete Low-Cost Sun Simulator

V. DISCUSSION: TRENDS AND DIRECTIONS

With the advancement of this project, it is evident that there is a need to develop a Sun simulator to model the energy distribution throughout the CubeSat system. The energy system is one of the most critical components of a satellite, as previously demonstrated.

It is crucial to conduct an in-depth study of the thermal dynamics within the CubeSat box, using finite element simulations to predict the behavior of heat generated by the 10 LEDs and the heat sinks. This study will help to understand how heat is distributed and dissipated within the CubeSat, which is essential for ensuring the efficiency and longevity of the electronic components.

Once the prototyping phase is completed, it is important to be aware of potential future issues that may arise during the assembly and execution of the box's functions. These issues should be thoroughly analyzed and discussed to ensure that all concerns are addressed effectively.

In conclusion, it is essential to recognize that as we advance in the prototyping and implementation of the CubeSat, ongoing monitoring of emerging trends and adaptation to new technologies will be crucial for the project's success. The development of solar simulators and detailed thermal studies are just the beginning. The ability to identify and address potential future issues during assembly and operation, along with integrating technological innovations, will allow for the optimization of the CubeSat's performance and reliability. Commitment to critical analysis and adaptation to new trends will ensure that the CubeSat's energy system remains robust, efficient, and capable of meeting mission demands.

VI. CONCLUSION

The design and development of the Sun simulator proposed in this study represent a significant advancement in the testing and validation of CubeSats, particularly regarding their EPS. By simulating in-orbit conditions using LEDs and an optimized control system, the simulator provides a controlled

environment to assess the performance of photovoltaic panels, batteries, and overall energy distribution in nanosatellites. The implementation of the simulator is not only cost-effective but also essential for mitigating risks associated with energy management in space missions. The findings from this work contribute to the ongoing evolution of CubeSat technology, enabling more reliable testing protocols and enhancing the resilience of these small satellites in future space endeavors. Future work will focus on refining the thermal management aspects and addressing potential challenges identified during the prototyping phase.

ACKNOWLEDGEMENTS

The authors want to acknowledge that this work was supported by CNPq/Brazil (National Council for Scientific and Technological Development - <http://www.cnpq.br>), and by AEB (Brazilian Space Agency - <http://www.aeb.gov.br>).

REFERENCES

- [1] GisGeography, "The cubesat: Small satellites for big ideas," 2024.
- [2] H. Garg, A. Shukla, I. Madhuri, R. Agnihotri, and S. Chakraverty, "Development of a simple low-cost solar simulator for indoor collector testing," *Applied Energy*, vol. 21, no. 1, pp. 43–54, 1985.
- [3] E. Viesser *et al.*, "Análise experimental de dispositivos térmicos para ampliação energética em nanossatélites," 2023.
- [4] G. M. Marcelino, A. M. P. de Mattos, J. C. E. Barcellos, B. F. Ribeiro, L. O. Seman, E. M. Filho, and E. A. Bezerra, "Floripasat-2: An open-source platform for cubesats," *IEEE Embedded Systems Letters*, vol. 16, no. 1, pp. 77–80, 2024.
- [5] A. Edpuganti, V. Khadkikar, M. S. E. Moursi, H. Zeineldin, N. Al-Sayari, and K. Al Hosani, "A comprehensive review on cubesat electrical power system architectures," *IEEE Transactions on Power Electronics*, vol. 37, no. 3, pp. 3161–3177, 2022.
- [6] E. López-Fraguas, J. M. Sánchez-Pena, and R. Vergaz, "A low-cost led-based solar simulator," *IEEE transactions on instrumentation and measurement*, vol. 68, no. 12, pp. 4913–4923, 2019.
- [7] E. Morsch Filho, E. Bohrer, T. Possamai, K. Paiva, and X. Travassos Junior, "Numerical investigation of the influence of the orbit inclination on thermal control of a nanosatellite in leo," in *II Latin American IAA CubeSat Workshop*, 2016.
- [8] K. Woellert, P. Ehrenfreund, A. J. Ricco, and H. Hertzfeld, "Cubesats: Cost-effective science and technology platforms for emerging and developing nations," *Advances in space Research*, vol. 47, no. 4, pp. 663–684, 2011.

Stratospheric Balloons as a Multi Mission Platform Testbed for Scientific and Technological Applications

Antonio Cassiano Julio Filho
Small Satellite Division
National Institute for Space Research
São José dos Campos, Brazil
cassiano.filho@inpe.br

Antonio Carlos O. Pereira Jr.
Small Satellite Division
National Institute for Space Research
São José dos Campos, Brazil
acarlos.pereira@inpe.br

Walter Abrahao dos Santos
Small Satellite Division
National Institute for Space Research
São José dos Campos, Brazil
walter.abrahao@inpe.br

Marcus Vinicius Cisotto
National Institute for Space Research
São José dos Campos, Brazil
marcus.cisotto@inpe.br

Auro Tikami
National Institute for Space Research
São José dos Campos, Brazil
auro.tikami@inpe.br

Pollyanna Prado Clemente
National Institute for Space Research
São José dos Campos, Brazil
pollyanna.clemente@inpe.br

Keener Mikael Amaral
National Institute for Space Research
São José dos Campos, Brazil
keener.amaral@inpe.br

Camilo Maia Pires
National Institute for Space Research
São José dos Campos, Brazil
camilo.pires@inpe.br

Pedro Borin Salvestro
National Institute for Space Research
São José dos Campos, Brazil
pedro.salvestro@inpe.br

Abstract—The National Institute for Space Research (INPE) is responsible by technological development of remote sensing satellites, such as Amazonia and CBERS families, and small satellites for educational, scientific and technological applications, for example the BiomeSat mission. INPE's Small Satellite Division carries out activities for the small, educational, scientific and technological satellite missions has a multidisciplinary laboratory equipped for the development, integration and testing of miniaturized satellites, as well as their reception systems, ground command and control. In this context, one activity is the development of a Georeferenced Multi Mission Platform for collecting environmental data of scientific and technological experiments on board of stratospheric balloons. The main goals are an educational and technological dissemination purposes and meeting the main requirements of small satellites. The data obtained by the platform in the stratosphere can be used in investigations and studies of atmospheric phenomena and other specific experiments. The stratosphere, due to its environment presenting extreme factors of temperature, pressure and radiation, is also a viable and low-cost alternative as a stage for the development and testing of prototypes of space systems that can be sent into space. The system is composed of a Multi Mission Platform to be launched on small stratospheric balloons and one or more low-cost transportable and mobile ground stations for tracking, receiving telemetry and sending telecommands. This paper presents the INPE's Multi Mission Platform development, which is composed by a hardware subsystem (antenna, transceptor, processor, GPS, temperature sensors, pressure sensor, power supply and thermal control), based on the CubeSat structure, and the onboard software subsystem for controlling the platform. The paper either provides the ground segment, which is composed by telemetry, tracking and command ground stations hardware subsystem and a software control subsystems. In addition, the system architecture of the multi-mission platform is formally presented. This system architecture is based on Model-Based System Engineering (MBSE). MBSE is a modern method for modeling system architectures, used by the aeronautical, automotive and space sectors, as well as in academic research. In the space area, the main adoption initiatives are by the National Aeronautics and Space Administration (NASA) and

the European Space Agency (ESA). The paper also describes the Multi Mission platform integration, control and operation planning; integration and testing of ground stations; the planning and execution of laboratory tests; radio frequency link validation tests in the open field; planning and testing in INPE's Integration and Testing Laboratory (LIT), under the leadership of multidisciplinary teams. Finally, the launch, tracking and recovery campaigns for the platform are presented. The design's status, lessons learned, and the contributions to overcome challenges associated to development a georeferenced Multi Mission platform, and ensure the system accomplishment are presented

Keywords— CubeSat, Ground Segment, High Altitude Balloon MBSE, Model-Based System Engineering, Multi Mission Platform, Small Satellite, Stratospheric Balloon.

I. INTRODUCTION

The National Institute for Space Research (INPE) is responsible by technological development of remote sensing satellites, such as Amazonia and CBERS families, and small satellites for educational, scientific and technological applications. In this context, one activity is the development of a Georeferenced Multi Mission Platform for collecting environmental data of scientific and technological experiments on board of stratospheric balloons.

The main goals are an educational and technological dissemination purposes and meeting the main requirements of small satellites. The data obtained by the platform in the stratosphere can be used in investigations and studies of atmospheric phenomena and other specific experiments.

An experiment to be carried on a stratospheric balloon is the Environmental Data Collector (EDC), developed by INPE-RN. It is a payload compatible with the CubeSat standard, and its function is to receive and decode signals from the Data Collection Platforms (DCP) belonging to the Brazilian Data Collection System (SBCDA) and the Argos-2 system. The EDC will be used in other missions such as the Catarina Constellation and BiomeSat Mission.

The BiomeSat Mission aims to provide the Brazilian remote sensing community with data for planning, monitoring, and controlling the health conditions of Brazilian forests and assist in the assessment of degraded and deforested areas, being a complementary mission to the CBERS series satellites.

This document is organized as follows: section II presents the fundamental concepts; section III outlines the Multi Mission Platform and Ground Segment; section IV describes the MMP and Ground Station Tests; section V presents Launch Campaign Results, and section VI the Conclusions.

II. FUNDAMENTAL CONCEPTS

This section presents a summary of the main concepts applied in this work.

A. Model-Based Systems Engineering

MBSE is defined as the formal application of modeling to support the requirements of systems, design, analysis, verification and validation of activities initiated in the conceptual design phase and continuing throughout the development of the later stages of the life cycle [1, 2].

According to [3], MBSE defines formal semantics for technical information and allows constructing patterns defining element relationships and facilitating auditing and completeness checking.

During the systems engineering process, a substantial amount of information is collected, generated, and/or maintained regarding the characteristics of the system of interest, composite elements, and interacting entities/environments. MBSE utilizes models as a means of aggregating and managing these disparate pieces of information about a system in a centralized repository that can serve as a single source of truth and technical baseline regarding a system of interest [4].

MBSE often involves combining several activities from the Systems Engineering processes concurrently and iteratively, namely system behavior description, requirements analysis, system architecture, and test.

The main initiatives for the adoption of MBSE in the area of space systems are: NASA's Systems Engineering Group [5] began evaluating the adoption of model-based systems engineering approach in 2011 and ESA has selected the Euclid mission [6] as a use case to demonstrate the benefits of MBSE in the context of ground segment engineering.

MBSE is supported by several methodologies [7]. This work was based on ARChitecture Analysis and Design Integrated Approach (ARCADIA) and Capella tool [8]. Arcadia method promotes [9] collaborative work among all key players, from the engineering phase of the system and subsystems, until their Integration, Verification and Validation. It is supported by various kinds of diagrams inspired by UML and SysML.

B. ARCADIA Architecture Levels

The ARCADIA approach presents five main levels with different diagrams and concepts: Operational Analysis, System Analysis, Logical Architecture, Physical, and End Product Breakdown Structure [8, 10, 11], presented in Fig. 1.

Operational analysis studies “what the users of the system need to accomplish”, at this level, the analysis of issues related to operational users is carried out, identifying the actors who must interact with the system, their activities, and interactions with each other.

System analysis studies “what the system has to accomplish for the users”. This means that the system is considered a black box, where the interface functional between the system and the actors are allocated to the system.

The logical architecture level studies “How the system will function to meet expectations”. At this level, the internal functional analysis of the system is performed, the sub functions that must be executed are defined, and the logical components that execute these sub functions are identified.

The physical architecture studies “How the system will be developed and built”, the goal of this level is the same as that of the logical architecture, except that it defines the final architecture of the system as it must be created.

Lastly, the End Product Breakdown Structure (EPBS) defines what is expected from the component suppliers.

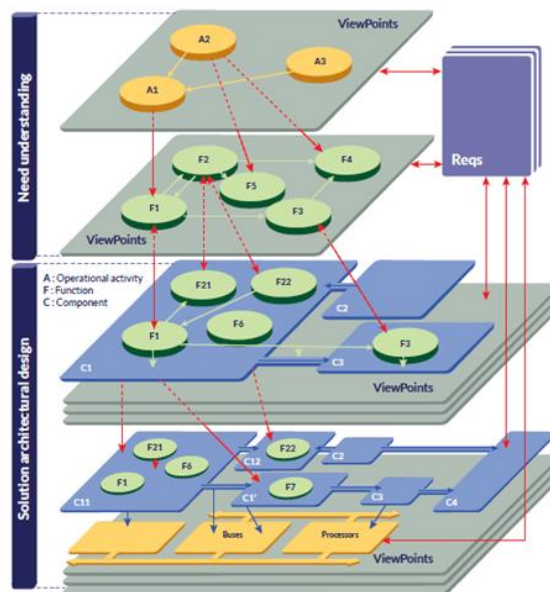


Fig. 1. ARCADIA Architecture Levels.

III. MULTI MISSION PLATFORM AND GROUND SEGMENT

The system is comprised of a Multi-Mission Platform (MMP), a ground segment divided in a Ground Station (GS) and a Mobile Ground Station (MGS). This system architecture was modeled using Model-Based Systems Engineering (MBSE), the ARCADIA method, and the Capella software tool.

The MMP is launched on small stratospheric balloons and must communicate with one or more low-cost mobile and transportable ground stations for tracking, receiving telemetry, and sending telecommands.

INPE's MMP is based on CubeSat's architecture, dimensions 10 x 10 cm, PC104 connector, weight below 1200g, low cost, and power components. It consists of subsystems of structure, thermal control, on-board handling (OBDH) with integrated GPS, telemetry and telecommand

(TM/TC), power, and the onboard software subsystem for controlling the platform.

TM/TC can vary its parameters such as transmit and receive frequencies, power, data rate and modulation type. It generally works on UHF (440-433 MHz) and sub-GigaHertz (900-930 MHz) frequencies, allowing a link of up to 900 km.

The GS [12, 13] comprises the antenna, transceptor, processor, GPS, power supply, Yagi antenna, Pan Tilt Controller, and Inertial Measurement Unit subsystems.

The MGS comprises the antenna, transceptor, processor, GPS, power supply, monopole antenna subsystems.

Fig. 2 illustrates a representative model of the operational entities for MMP, GS, and MGS. This model was developed based on the ARCADIA methodology and the Capella Software tool.

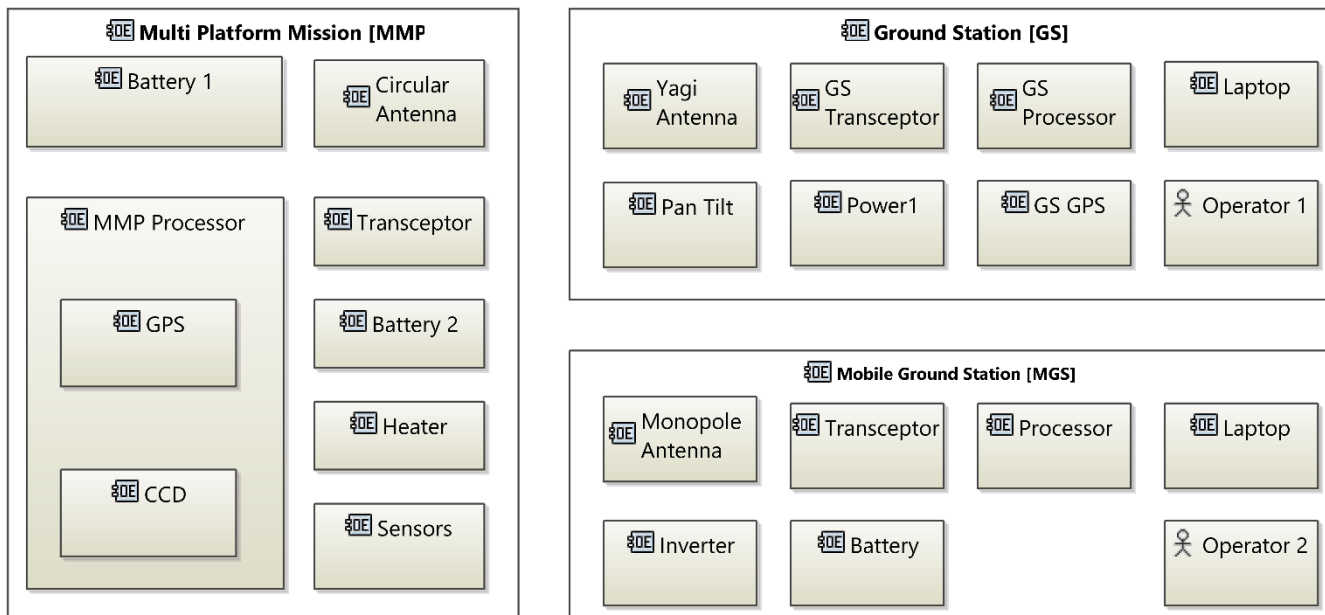


Fig. 2. Representative Model - Operational Entities for Multi-Mission Platform and the Ground Stations.

A. MMP's subsystems

The MMP, Fig. 3, is comprised of the following subsystems:

- MMP processor is responsible for managing the activities of subsystems and on-board data processing.
- Transceptor is UHF Communications subsystem. It is responsible for transmitting collected telemetry to the ground station and receiving telecommands from the GS. The main features are: NiceRF RF4463F30 module, GFSK modulation at 1200 bps, 30 dBm output power, 433 MHz frequency, minus 125 dBm receiver sensitivity, transmission and reception share the same antenna.
- Circular Antenna is responsible for transmitting and receiving radio signals in the UHF band (433 MHz).
- Battery1 supplies power to MMP subsystems.
- Battery2 supplies power to Heater subsystem.
- Camera (CCD) provides images that are processed and stored by the MMP processor.
- Structure is based on the 1U CubeSat platform and capable of withstanding temperature and pressure variations in the stratosphere.

- Sensors are responsible for collecting the external and temperatures of the MMP elements.

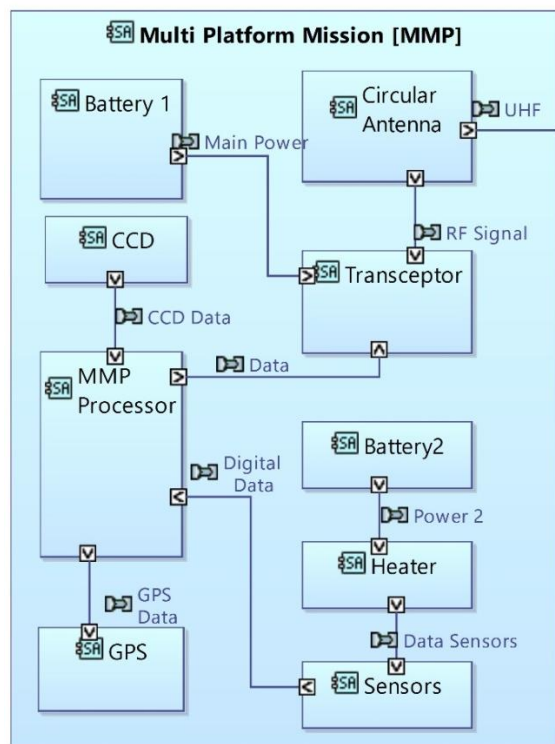


Fig. 3. Representative Model of System Entities for MMP.

B. GS's subsystems

GS consists of subsystems similar to the MMP, as described in section named "Description MMP's subsystems". In addition to these subsystems, the following were added: a Yagi Antenna, a Pan Tilt Controller Module, which are described below.

Fig. 4 is a representative model of System Entities for GS, using the Capella Software Tool.

- Yagi Antenna is a directional antenna used for receiving and transmitting radio frequency signals.
- Pan tilt and IMU is a subsystem that allows the orientation of the Yagi Antenna to be adjusted, moving it in two directions (horizontal and vertical).
- Laptop acts as a control and monitoring interface for the system. It allows the operator to interact with the system, view real-time data.
- Operator 1 is responsible for entering commands, monitoring system performance, and making operational decisions.

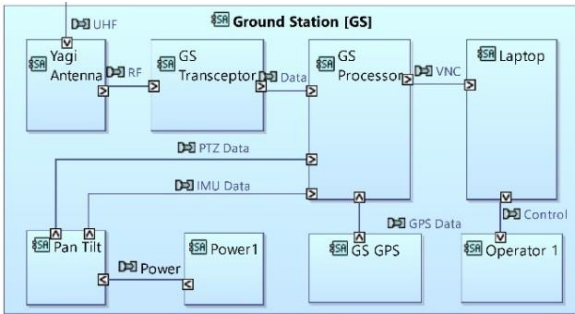


Fig. 4. Representative Model of System Entities for GS.

C. Balloon System

Fig. 5 illustrates the Balloon System which comprise by a MMP, a GS and a MGS. Each subsystem has related components (small blue box), the associated functions (green box), and data flow. The Balloon System is controlled by a three software subsystems.

MMP software was developed to manage data collection and communication with the ground during stratospheric balloon missions. Designed to operate in real time, it efficiently integrates various subsystems, such as temperature, pressure, and GPS sensors, in addition to controlling image capture and the transmission of telemetry via radio frequency (RF).

Communication with the ground segment is continuous, and the software ensures that received telecommands are processed correctly. Developed in Python, the code follows a modular architecture with threads dedicated to critical functionalities, enhancing performance and reliability.

GS software, also written in Python, is responsible for receiving, processing, storing, and displaying telemetry data sent by the MMP. It ensures continuous communication with the platform, enabling real-time monitoring and the sending of telecommands during missions.

MGS software, similar to the GS, differs by incorporating a specific antenna system and an optimized graphical interface for user operation in mobile environments. Additionally, the MGS is designed to be transported and operated in different locations or while in motion, maintaining robust data reception.

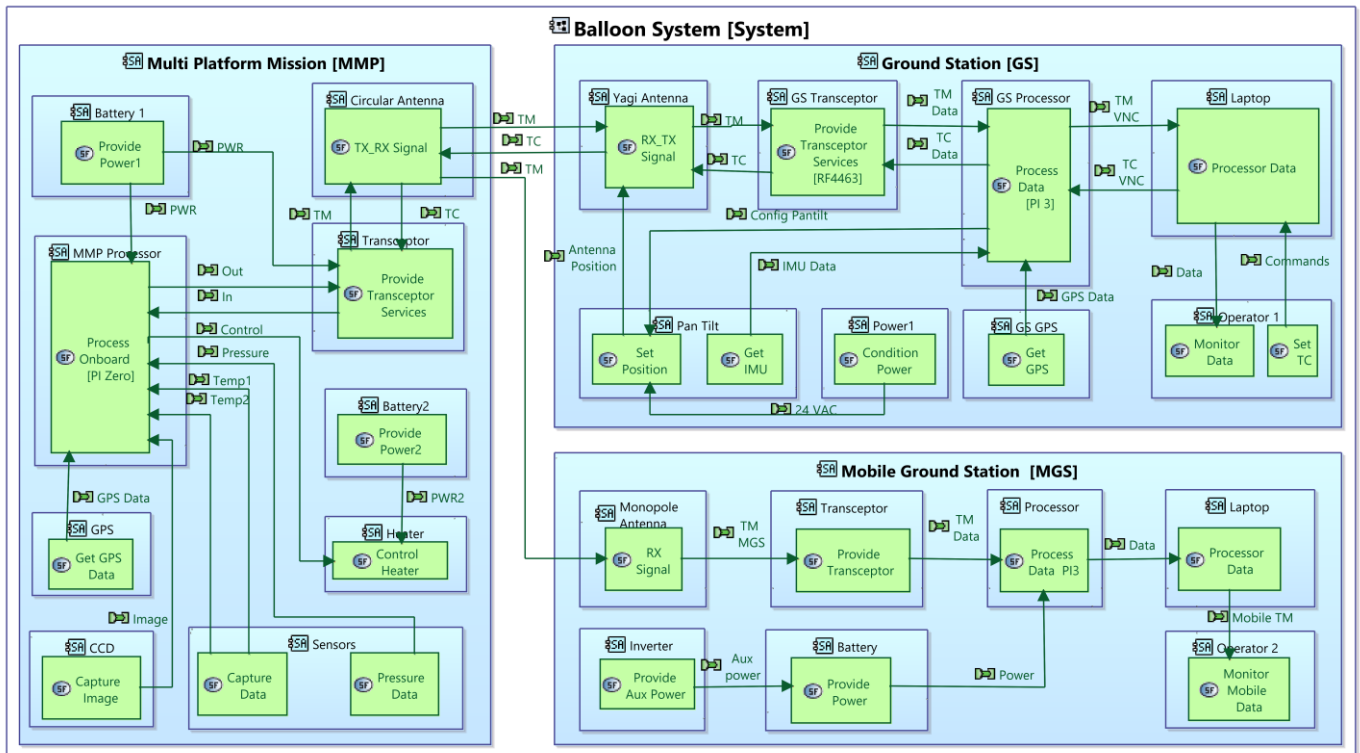


Fig. 5. Representative Balloon System Model.

IV. MMP AND GROUND STATION TESTS

INPE's Small Satellite Division carries out activities for the small, educational, scientific and technological satellite missions has a multidisciplinary laboratory equipped for the development, integration and testing of miniaturized satellites, as well as their reception systems, ground command and control.

A. MMP and GS Tests

The MMP was submitted to functional tests, transmission and reception tests in the anechoic chamber with the GS, tests of ambient temperature variation and in the vacuum chamber.

The GS is responsible for sends Telecommands to MMP and receives Telemetry from MMP in UHF band at frequency of 433 MHz.

Fig. 6 shows the MMP, based on the CubeSat structure, prepared to carry out the temperature test.

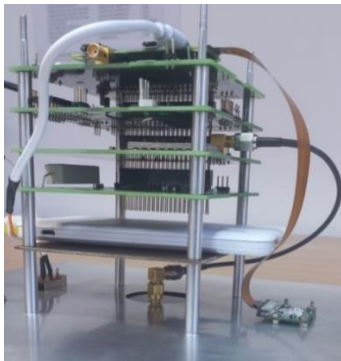


Fig. 6. MMP prepared to temperature tests.

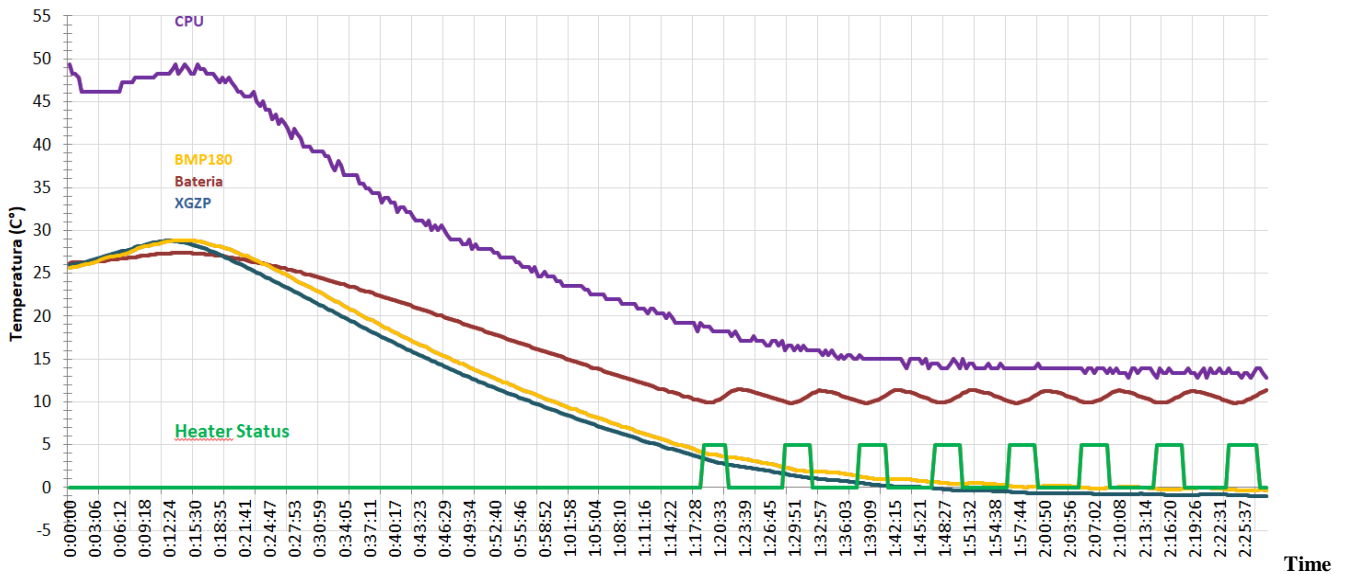


Fig. 8. Temperature test result.

B. Radio Frequency Link Test

Two types of tests were performed. The first, called short link, involves placing the MMP system at a distance of 115 m, with direct line of sight, from the GS. The second, called long link, involves placing the MMP system at a distance of 10 km, with direct line of sight from the GS in open field.

Fig. 7 illustrates the environments for carrying out the tests for MMP inside the anechoic chamber at INPE's Integration and Testing Laboratory (LIT), under the leadership of multidisciplinary teams.

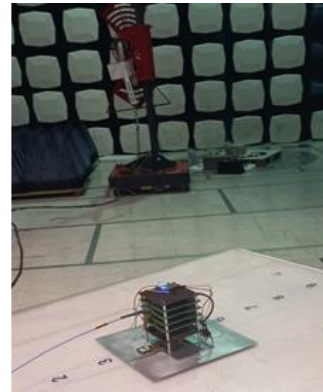


Fig. 7. MMP inside the anechoic chamber.

Fig. 8 shows the results of the tests related to the external temperature setup to minus 80 ° Celsius for two hours and twenty-five minutes and the respective internal temperatures for CPU, BMP180 sensor, battery, and XGZP sensor.

For this test, the internal temperature should vary from 10°C to 11°C, as shown in the red line. It is also possible to observe the activation of the heater (green line) to maintain the internal temperature in the desired range.

The objective of the test was to obtain the Received Signal Strength Indication (RSSI), considering the transmission power of 30 dB, the calculated free space loss, the loss caused by the cables and connections. TABLE I shows the values obtained by GS.

The results indicate that the RF link can reach up to 900 km, considering the receiver sensitivity of -120 dBm.

TABLE I. RSSI LEVELS.

Distance (m)	RSSI (dBm)	
	Calculated	GS
115	- 35.93	- 34.01
10,000	- 74.70	- 77.20

V. LAUNCH CAMPAIGN RESULTS

The third launch campaign was carried out in March 2024 from INPE's headquarters located in São José dos Campos, São Paulo State, Brazil.

The objectives of this campaign include the launch of HAB with the MMP weighing 800 g, the tracking and reception of TM in real time by the GS installed at INPE. The tracking is also performed by a MGS installed on a vehicle to facilitate the recovery of the MMP.

TABLE II presents the criteria defined for this launch campaign. All mandatory criteria were met and a desirable criterion, MMP recovery, was also met.

TABLE II. SUCCESS CRITERIA.

Item	Success Criteria	Status
1	Launch the stratospheric balloon	Ok
2	Track the MMP by GS	Ok
3	Receive TM by GS	Ok
4	Send TC by GS	Ok
5	Track MMP by MGS	Ok
6	Receive TM by MGS	Ok
7	Perform MMP's thermal control	Ok
8	Recover the MMP	Ok
9	Analyze mission data	Ok

TABLE III. displays a data summary related to HAB's slant range, and altitude. The maximum slant range was 87.708 m and the maximum altitude was 33.475 m.

TABLE III. ALTITUDE AND SLANT RANGE FOR HAB.

Item	Time (UTC)	Altitude (m)	Slant Range (m)
1	12:46:46	2,603	2,404
2	14:37:04	19,930	87,708
3	16:26:20	33,475	43,806

Fig. 9 presents a summary of the results obtained from the third launch campaign. It primarily displays information on the altitude of the stratospheric balloon, the ambient temperature and the temperatures indicated by the internal sensors of the MMP. The horizontal axis represents elapsed time, the vertical axis, on the left side of the graph, shows the altitude in kilometers and the vertical axis, on the right side, indicates the temperature in degrees Celsius.

The red line illustrates that the maximum altitude reached was 33.5 km, with an ascent time of 3 hours and 55 minutes and an average speed of 9.56 km/h. The descent time was 51 minutes, resulting in total flight duration of 4 hours and 46 minutes. The overall campaign time, including the waiting period for launch and the recovery period, was 7h, validating the energy system used in the MMP.

Regarding the ambient temperature (blue line), the MMP was subjected to a temperature range from minus 60°C to 25°C. During this period, the internal temperature of the MMP (yellow line) in the battery region varied between the configured limits (minimum of 15°C and maximum of 16°C) for the automatic activation of the internal heating subsystem.

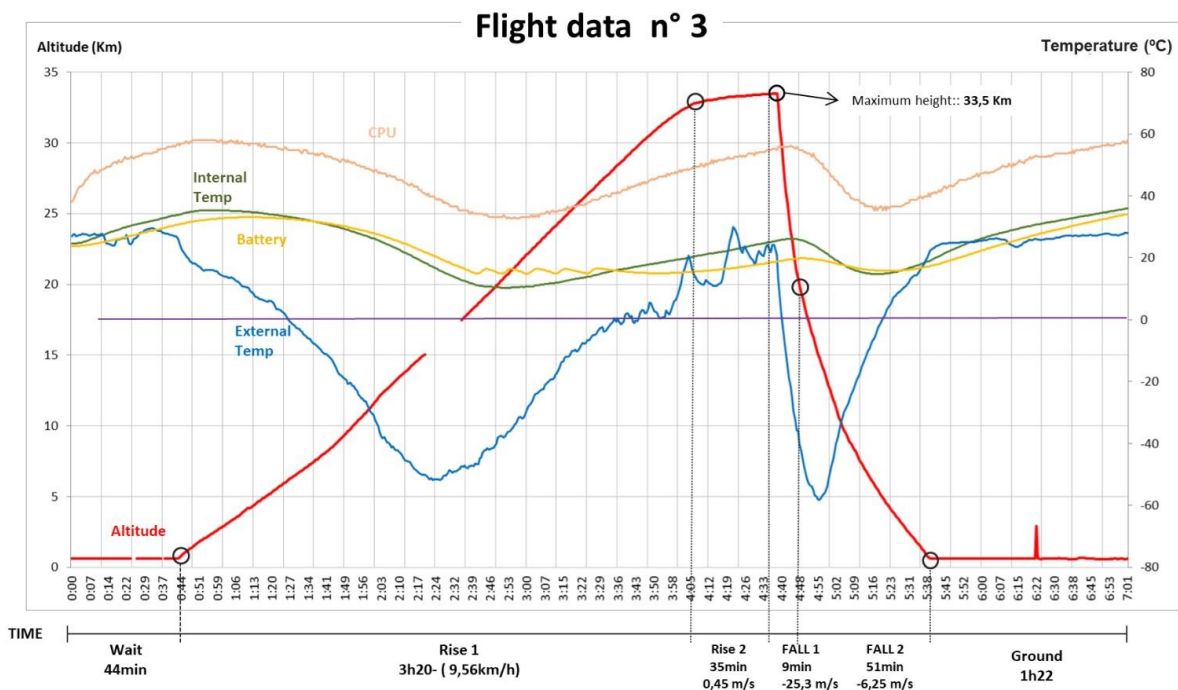


Fig. 9. Flight Data for number 3 launch

VI. CONCLUSIONS

The Multi-Mission Platform, based on the CubeSat architecture and the ground segment are available to meet the growing demand for the deployment of scientific and technological experiments from stratospheric balloons, as indicated by the results obtained during the development phase, operational and validation tests, and flight campaigns.

The development of the MMP relied on the Model-Based Systems Engineering (MBSE) approach, which allows the development of candidate architectures for the implementation of systems. MBSE uses the essence of systems engineering processes and is a powerful alternative to improve the development of system architectures, anticipate design solutions, and collaborate in the management and implementation of systems.

An integration and testing between the EDC and the MMP is underway. The next step is to launch a HAB with an EDC installed as a payload from the MMP. This campaign is scheduled for November 2024 from INPE in São José dos Campos, São Paulo.

Next phase of activities includes the launch of an MMP carrying an Environmental Data Collector (EDC) as a payload. This campaign is scheduled for November 2024 from INPE in São José dos Campos, São Paulo.

Additionally, a subsequent EDC launch campaign is planned for December 2024, to be conducted from the Natal Multimission Station (EMMN), in Natal, Rio Grande do Norte, Brazil.

ACKNOWLEDGMENT

We thank the Brazilian Space Agency (AEB, acronym in Portuguese), the Brazilian National Institute for Space Research (INPE, acronym in Portuguese) for their support, and the National Council of Scientific and Technological Development (CNPq, acronym in Portuguese) for the financial support afforded to Ms. Pollyanna Prado Clemente, Mr. Keener Mikael Amaral, and Mr. Camilo Maia Pires.

Special thanks to coworkers from the Small Satellite Division: Gabriela M. S. Queiroga, Ana Beatriz O. e Silva, Luiz Antonio dos Reis Bueno, Eduardo Piacsek B. Franco, Luiz Carlos de Almeida, Benedito A. das Neves, Lincoln Teixeira, Lázaro A. P. Camargo, Henry C. Souza, and Daniel Monaghan.

REFERENCES

- [1] International Council on Systems Engineering (INCOSE) (2020) "Systems Engineering Vision 2020, version 2.03". Seattle, WA: International Council on Systems Engineering, Seattle, WA, INCOSE-TP-2004-004-02.
- [2] Smith, R.R., Schimmels, K. A., Lock, P.D., Valerio, C.P. (2014). "A Model-Based Approach to Developing Your Mission Operation System". In: Proceedings International Conference on Space Operations, Pasadena, CA. Proceeding URL: <http://arc.aiaa.org/doi/pdf/10.2514/6.2014-1793>.
- [3] Friedenthal, S.; Moore, A.; Steiner, R. (2009). "Practical guide to SysML: the systems Modeling Language". Amsterdam, The Netherlands: Morgan Kaufmann. ISBN 978-0-12-378607-4.
- [4] SEBoK Editorial Board. 2024. The Guide to the Systems Engineering Body of Knowledge (SEBoK), v. 2.10, N. Hutchison (Editor in Chief). Hoboken, NJ: The Trustees of the Stevens Institute of Technology. Accessed [2024, Aug.]. www.sebokwiki.org. BKCASE is managed and maintained by the Stevens Institute of Technology Systems Engineering Research Center, the International Council on Systems Engineering, and the Institute of Electrical and Electronics Engineers Systems Council.
- [5] Holladay, J. B., Knizhnik, J., Weiland, K. J., Stein, A., Sanders, T., Schwindt, P., "MBSE Infusion and Modernization Initiative (MIAMI): "Hot" Benefits for Real NASA Applications". In IEEE Aerospace Conference Proceedings, 2019.
- [6] Fischer, D., Keck, F., Wallum, M., Spada, M., Stoitsev, T. (2018) "Leveraging MBSE for ESA ground segment engineering: Starting with the euclid mission" In: International Conference on Space Operations, 15th, Marseille, France.
- [7] Jeff A. E., "Survey of Model-Based Systems Engineering (MBSE) Methodologies" Jet Propulsion Laboratory California Institute of Technology, Pasadena, California, U.S.A
- [8] Roques, P. (2017) "Systems Architecture Modeling with the Arcadia Method: A Practical Guide to Capella", ISBN-13: 978-1785481680, Elsevier Ltd, Kidlington, Oxford, United Kingdom.
- [9] <https://www.eclipse.org/capella/arcadia.html>. Accessed April 2024.
- [10] National Aeronautics and Space Administration (NASA). (2013) "NASA Procedural Requirements - NPR 7123.1B. Systems Engineering Processes and Requirements". Washington, DC.
- [11] Julio Filho, A. C., Ambrosio, A. M., Ferreira, M. G. V., "Model-Based System Engineering (MBSE) applied to Ground Segment Development of Space Missions: New Challenges". In: International Astronautical Congress, 72th Online Proceedings...2021
- [12] European Cooperation for Space Standardization (ECSS) (2008) "ECSS-E-ST-70C. Space engineering - ground systems and operations". <<http://www.ecss.nl/>>.
- [13] CCSDS TM Space Data Link Protocol. Recommended Standard. CCSDS 132.0-B-1. Blue Book. Issue 1. Washington, D.C., September 2008.

Cyber Attack Tree Analysis on Natal Multi-Mission Station for Satellite TT&C: Systematic Literature Review

Ana Livia Vicente Torres*, Ana Clara Melo de Araújo*, Moisés Cirilo Brito Souto*

*IFRN - Instituto Federal de Educação, Ciência e Tecnologia do Rio Grande do Norte
Campus Natal Central of Natal, CCSL - Centro de Competências em Soluções Livres of Natal
Email: livia.v@escolar.ifrn.edu.br, melo.araujo@escolar.ifrn.edu.br, moises.souto@ifrn.edu.br

Abstract—The Natal Multi-Mission Station (EMMN) acts as an intermediary to ensure secure communication between remote operators and orbiting satellites. Access to the station is achieved through a Virtual Private Network (VPN), allowing operators to perform Telemetry, Tracking, and Command (TT&C). The Message Queuing Telemetry Transport (MQTT) protocol is essential for sharing and synchronizing data, optimizing the coordination of operations within the EMMN communication system. Given the crucial role of the EMMN in tracking CubeSats and NanoSats, this study analyzes cybersecurity, with an emphasis on the use of VPNs and the MQTT protocol. The methodology involves a systematic review of vulnerabilities in ground infrastructures for space systems. Based on this, an attack tree will be created to identify threats, utilizing the MITRE ATT&CK framework to detail tactics, techniques, and procedures (TTPs). The goal is to strengthen remote communication and optimize the data management system of the EMMN. Among the identified vulnerabilities are susceptibility to jamming techniques and Distributed Denial of Service (DDoS) attacks. These results not only highlight the need to increase the cybersecurity maturity level of the station but also become applicable to similar architectures.

Index Terms—Cybersecurity, Multi-Mission, MQTT, VPN, TT&C.

I. INTRODUCTION

The Natal Multi-Mission Station (EMMN) plays a crucial role in the control, tracking, and monitoring of CubeSats and NanoSats, functioning as a ground segment [1]. Established with the purpose of modernizing the satellite tracking system of the National Institute for Space Research (INPE), the EMMN currently operates with an infrastructure based on distributed virtualized and networked systems, facilitating secure and effective communication between operators and satellites in orbit. Remote access is ensured via a VPN (Virtual Private Network), allowing operators to perform TT&C. Additionally, the radio communication subsystem utilizes reconfigurable radio frequency (RF) channels, which are frequency bands used to transmit radio signals between the ground station and the satellites. These channels can be adjusted or modified as needed. Moreover, the Message Queuing Telemetry Transport (MQTT) protocol is employed for data sharing and synchronization of operations among the various subsystems of the station [2].

The use of a VPN at the station is justified by the need for secure external access by operators. Widely used virtual private networks create an encrypted connection that allows for the private sending and receiving of data. Technically, the VPN hides the user's IP address, redirecting the connection through a remote server configured by the provider, so that the IP address displayed during online browsing is that of the VPN server [3].

In turn, the MQTT protocol is widely used for message transport using the publish-subscribe model. Due to its lightweight nature, it becomes efficient for use in low-bandwidth and high-latency devices, such as the Internet of Things, sensors, and microcontrollers [4].

Within the scope of the EMMN, its lightweight nature and low overhead are essential for synchronizing operations and sharing TT&C data. Furthermore, the flexibility of MQTT allows for the reconfiguration of RF channels, facilitating real-time communication with orbiting satellites.

However, M. Manulis et al. [5] describe how the boom in new technologies has revolutionized the era of new satellites, expanding the space market and the security threats this has brought. Their work addresses some vulnerabilities and attacks targeting different architectures, such as the ground segment, space segment, and others. The authors concluded that, in previous studies, the ground segment and electronic warfare operations were the most affected by attacks.

Thus, this work aims to conduct a cybersecurity analysis in the context of the EMMN, aiming to strengthen its communication systems. The main focus is to identify the most critical vulnerabilities in related studies and, from them, build an attack tree that could compromise the VPN, the MQTT protocol, or both. The adopted methodology will be a systematic review, which will serve as a basis for creating the attack tree, supported by the MITRE ATT&CK framework. The branches of the tree will be organized into the stages of Reconnaissance, Resource Development, Execution, and Impact, allowing for the categorization of possible TTPs (Tactics, Techniques, and Procedures) of malicious actors. Each branch will include the respective

leaf nodes with the identified tactics and methods.

This article is organized into six sections. Section II addresses the methodology used, detailing the systematic literature review process. Section III discusses the theoretical foundations of cybersecurity, focusing on the MITRE ATT&CK framework and the identification of vulnerabilities in systems similar to the EMMN. Sections IV and V analyze and discuss the main results. Finally, Section VI presents the conclusions, discussing the limitations of the research and proposing directions for future work.

II. METHODOLOGY

In this section, the methodology employed in this study is presented, which is based on a systematic literature review of a qualitative nature. The main objective is to identify the key vulnerabilities to which ground segment stations are exposed. The review process was conducted using the Parsifal software, an online platform that provides a structured and systematic process, divided into detailed stages: Planning, Selection, and Evaluation.

A. Planning Phase

This phase was essential for the development of the remaining work, requiring extensive research and in-depth study to understand and complete the sub-phases, which are quite detailed. This phase includes the following steps: PICOC (Population, Intervention, Comparison, Outcome, Context), Research Questions, Keywords and Synonyms, Search String, Sources, Selection Criteria, Quality Assessment Checklist, and Data Extraction Form.

The developed search string was: "Natal Multi-Mission Station" OR "EMMN" OR "ground station" OR "satellite control station" OR "TT&C" OR "telemetry tracking command") AND ("attack tree methodology" OR "cybersecurity analysis" OR "vulnerability analysis" OR "threat modeling" OR "MITRE ATT&CK") AND ("cybersecurity framework" OR "risk assessment" OR "cyber defense techniques" OR "security methodologies") AND ("vulnerability identification" OR "TTP categorization" OR "risk mitigation" OR "incident response" OR "mitigation effectiveness") AND ("simulation of cyber attacks" OR "testing cyber defenses" OR "security improvement" OR "threat mitigation evaluation") NOT "UAVs".

The inclusion criteria covered publications from 2015 to 2024, written in English, that addressed cybersecurity in the context of ground segment stations and contained the established keywords. The exclusion

criteria eliminated duplicate articles, those outside the period of 2015 to 2024, those not written in English, those not addressing cybersecurity in the ground segment, or those that did not contain the search keywords.

B. Selection Phase

In the selection phase, the articles were imported from all the listed platforms. This phase included the importation of the pre-selected articles for a more rigorous evaluation, applying the established criteria.

C. Evaluation Phase

In the evaluation phase, two subphases were conducted: Quality Assessment and Data Extraction. The Quality Assessment involved evaluating the articles based on eight specific questions related to the cybersecurity methodology in the ground segment. Each question was answered with "yes," "partially," or "no," resulting in a final score for each article. During the Data Extraction, additional questions were raised to obtain more details from the articles and to verify whether they met the research objectives.

III. BACKGROUND

The following subsections form the essential basis for the cybersecurity analysis proposed in this study, aiming to provide the necessary context for a thorough understanding of the topic. The MITRE framework will be presented, and vulnerabilities detected in VPNs and the MQTT Protocol will be discussed, highlighting the relevance of evaluating these systems at the EMMN.

A. MITRE ATT&CK

The MITRE ATT&CK project, created by the MITRE Corporation, has become widely recognized and used in the information security sector as a valuable knowledge resource. Its aim is to serve as a continuously updated database validated by the industry to ensure the accuracy and trust that has been earned. The focus is on techniques, or specific methods identified by security professionals, such as reconnaissance, execution, and lateral movement [6]. For example, reconnaissance techniques include phishing and active scanning.

B. Vulnerabilities in the MQTT Protocol

Before discussing the vulnerabilities of the Message Queue Telemetry Transport (MQTT) protocol, it is important to understand how it works. MQTT is a protocol based on the publish/subscribe model, where the broker acts as the central server, receiving and distributing messages among clients [7].

At the EMMN, MQTT is crucial for the synchronization and coordination of operations, efficiently centralizing and distributing data [2]. However, the

security of MQTT requires attention, as it is vulnerable to cyberattacks, such as denial-of-service (DoS) attacks and Man-in-the-Middle (MitM) attacks [8].

In a Man-in-the-Middle (MitM) attack, an attacker intercepts and potentially alters the messages exchanged between the client and the MQTT broker, compromising information security. Even with bilateral authentication, the lack of proper encryption can expose the system to risks. In a Denial-of-Service (DoS) attack, the broker can be overwhelmed with an excessive volume of requests, preventing it from responding to legitimate requests [8].

Haripriya and Kulothungan also highlight MQTT's susceptibility to DoS attacks, where fake packets can impact communication and the system [9]. Additionally, the absence of an effective Intrusion Detection System (IDS) increases vulnerabilities.

In the context of the EMMN, the MQTT protocol serves as the central component in the communication system, coordinating the interaction between the different subsystems of the station. As illustrated in the following flow, all communication between the subsystems, necessary for the user to access the satellite's TT&C, is conducted through MQTT.

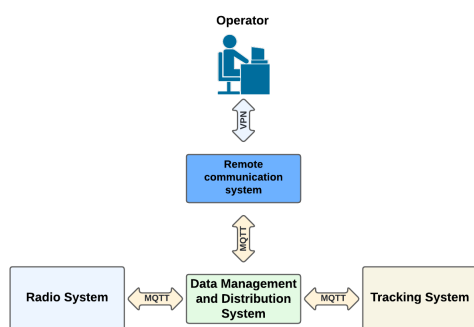


Fig. 1. Flow in the EMMN communication system. Adapted from [2].

Therefore, MQTT presents significant cybersecurity risks, particularly DoS attacks, highlighting the need to ensure the integrity and availability of data at EMMN.

C. Vulnerabilities in Virtual Private Networks - VPNs

A VPN acts as a gateway that allows external users to securely access a remote network, such as an organization's internal network or control stations. Security is ensured through the use of encryption algorithms during the data tunneling process, protecting the traffic between the two points of remote communication [10].

However, this method does not guarantee 100% effectiveness in protecting a system. It is essential to continuously check for potential vulnerabilities in communications conducted via VPN to enhance the cybersecurity of the environment and make cyberattacks more difficult [11].

As discussed by J. Pavur, many satellite clients turn to the use of VPNs to protect the privacy and integrity

of their data due to the vulnerability of interception in satellite communications [11].

Furthermore, the work highlights several vulnerabilities associated with the use of VPNs in satellite communications. Among these vulnerabilities are those related to satellite control, which are classified as threats to the direct control of satellites [11]. In ground stations, an attack that compromises communications via VPN could grant an attacker unauthorized access to satellite control systems, potentially resulting in the sending of malicious commands to the satellites, altering their trajectories or manipulating sensitive payloads, such as cameras or sensors. The article cites documented cases in which hackers temporarily gained control over satellites through compromises in ground control systems.

In the context of EMMN, this type of vulnerability can be classified as critical, as the VPN provides external users access to the station's TT&C system. If a malicious actor were to gain such control, mission security and satellite data could be compromised.

Therefore, it can be asserted that the VPN is one of the critical systems of the station that requires attention. Analyzing these vulnerabilities is essential to minimize the likelihood of cyberattacks.

IV. SYNTHESIS OF SELECTED WORKS

During the selection phase, articles were imported from all the listed platforms, with the following results:

- Google Scholar: Returned 63 articles, of which 27 were selected for detailed evaluation.
- ACM Digital Library and SBC-OpenLib: Did not present any relevant articles.
- IEEE Digital Library: Returned one article, which was not selected.
- Springer Link: Presented 463 articles, but 95% were unrelated to the topic or search keywords, and none were selected.

The methodology used in this work was effective, ensuring the selection of quality articles and providing solid evidence for the proposed objectives. Of the 27 selected articles, most focused on the analysis and development of strategies to identify, assess, and mitigate cyber threats directed at systems in the space sector, with an emphasis on ground segments and satellite control systems. Additionally, a significant portion of the studies adopted security frameworks or assessment methodologies. The most common approaches included:

- NIST: Used in 8 articles.
- SPARTA: Used in 2 articles.
- Attack Tree: Used in 2 articles.
- Risk Management Framework (RMF): Used in 2 articles.
- ISO Models: Used in 2 articles.
- SCADA: Used in 1 article.
- FDNA (Functional Dependency Network Analysis): Used in 1 article.

- No framework: 9 articles did not mention the use of specific frameworks.

A. Identified Vulnerabilities in Space Systems Based on the Literature

This section aims to present and discuss the vulnerabilities identified in the articles analyzed in the systematic review. The vulnerabilities have been categorized to provide a clear understanding of the critical points in satellite control systems and ground infrastructures.

1) *Communication Protocol Vulnerabilities:* The vulnerabilities associated with communication protocols have been extensively discussed in the literature. Zegeye W. et al.[12] highlight that the inherent security risks of the protocols used in telemetry and SCADA systems can be substantial, given the complexity of these systems and their stringent specifications. Pavur J. et al.[13] address the challenges of applying conventional encryption techniques, such as IPsec and VPNs, in space systems due to their technical peculiarities. Bailey B. et al.[14] note that weak or inadequate protocols can be exploited by attackers, resulting in data interception or denial of service (DoS) attacks. Furthermore, Bace B. and Dr. Tata U.[15], along with Bradbury M. et al.[16], emphasize that vulnerabilities in communication protocols pose a critical concern for space security. The increasing use of dual-use technologies and commercially off-the-shelf (COTS) components may introduce additional risks. These risks can be exploited by malicious actors, compromising the integrity of communications between space subsystems.

2) *Dependency on Third-Party Components:* The use of third-party components can significantly increase the complexity of satellite architecture, broadening the attack surface and making them more susceptible to threats. Moreover, the integration of IT and IoT technologies in the space environment can introduce additional risks that require greater attention, as discussed by Calabrese et al.[17]. The reliance on external vendors is a critical issue, as it can expose systems to vulnerabilities in the supply chain. An attack on a vendor can compromise the security of the final system, as emphasized by Pócsi B.[18]. Additionally, relying on third parties for software updates and maintenance can result in delays in applying security patches, increasing the susceptibility of systems to cyberattacks, a concern also raised by Bailey B.[19].

Bonnart, S. et al.[20] note that the use of COTS subsystems designed for terrestrial applications can introduce considerable risks. These risks include the potential for backdoors inserted by vendors, the need for frequent updates due to vulnerability to exploits, and the enlargement of the attack surface caused by activated but undocumented features. Akande A. et al.[21] discuss that this dependency can introduce cyber risks, as third-party components may not meet the same security standards or may be susceptible

to failures not directly controlled by the organization operating the satellite system. Furthermore, Carlo A.[22] highlights that third-party components may have hidden vulnerabilities that can be exploited by attackers, compromising the integrity of the system as a whole.

The lack of control over the security of these components represents a significant challenge, especially in Internet of Space Things (IoST) systems, which often rely on a variety of components developed by different companies and countries. This diversity of suppliers can introduce additional vulnerabilities, as the security of these components may not be adequately guaranteed or controlled. EAR E. et al.[23] mention that the effectiveness of Notional Risk Scores (NRS) depends on the analysts' ability to identify applicable attack techniques for a space system, which includes considering vulnerabilities introduced by third-party components.

3) *Lack of Updates and Patches:* One of the most frequently mentioned vulnerabilities in the space cybersecurity sector is inadequate encryption. The lack of robust encryption compromises both the confidentiality and integrity of data in space systems, exposing them to risks such as interception and data manipulation. Kavallieratos G. and Katsikas S.[24] emphasize that many systems use weak or outdated encryption methods, which do not provide adequate protection for transmitted data. This insufficiency in encryption practices can jeopardize the security of communications between space subsystems and ground stations. Furthermore, Diro A. et al.[25] highlight that the absence of updates and patches can be exploited by adversaries, exacerbating the insecurity of space systems.

The lack of updates and patches represents one of the most critical vulnerabilities in space cybersecurity. Due to challenging conditions and a lack of adequate support, space systems often remain outdated and exposed to attacks. The absence of updates can leave systems vulnerable to known and emerging threats, as noted by Calabrese M.[26] and Zachar BD.[27]. Specifically, Zachar BD mentions that system capabilities may be outdated by the end of a mission, increasing the likelihood of malicious malware insertion. Thangavel K. et al.[28] also discuss this concern, emphasizing that negligence in security measures such as authentication and encryption exacerbates the risk. Weber A. et al.[29] corroborate that the lack of updates exposes systems to threats, increasing their susceptibility to attacks.

4) *Inadequate Encryption:* Another frequently mentioned vulnerability is inadequate encryption, a widely recognized problem in the technology sector. The lack of robust encryption in space systems can seriously compromise the confidentiality and integrity of data. Thomas H. et al.[30] support this view, highlighting the criticality of this issue.

Pavur J. et al.[31] observe that many satellite sys-

tems still transmit sensitive data in clear text, which represents a significant vulnerability. Law Y. et al.[32] add that the security of ground systems is often treated as an extension of conventional IT security. This approach can lead to inadequate practices, such as using encryption that does not meet the necessary standards to protect communications and sensitive data in space environments. Furthermore, many systems still use weak or outdated encryption methods, providing inadequate protection for transmitted data.

Additionally, Bailey B.[33] highlights that the complexity of space systems and their supply chains can introduce additional vulnerabilities, including the improper implementation of encryption.

Driouch O. et al.[34] emphasize that although cryptographic solutions are implemented to secure command and control (TT&C) messages and payload data, the effectiveness of these solutions can be compromised by security vulnerabilities. Exploiting these vulnerabilities can lead to unauthorized access, malicious control, and unwanted connections, underscoring the importance of effective strategies to mitigate these risks without compromising system performance.

5) *Software and Firmware Vulnerabilities*: Lightman et al.[35], in their study of the ground segment of satellites, highlight the importance of considering the vulnerabilities associated with software and firmware, especially in command and control (C2) systems and Telemetry, Tracking, and Control (TTC) tools. Hanan et al.[36] reinforce that satellite subsystems are susceptible to cyberattacks that can exploit software vulnerabilities, demonstrating the need to protect not only the systems in orbit but also the ground equipment that supports them. It becomes evident that understanding and addressing software and firmware-related vulnerabilities is crucial for ensuring the protection of space systems and maintaining the integrity and availability of data and services.

In this context, Tsamis et al.[37] suggest considering the system architecture and adapting security solutions to space operations. They emphasize the importance of creating security protocols throughout the system's lifecycle. Furthermore, the growing relevance of cybersecurity in the space sector is discussed, illustrating the challenges and vulnerabilities in ground stations, communication networks, and satellite control systems. The main vulnerabilities identified include failures in communication protocols, inadequate encryption, and dependence on third-party components, highlighting the need for specific solutions tailored to the space environment.

Adopting a proactive risk analysis approach from the early stages of development is essential. This includes implementing robust encryption and utilizing protocols such as HTTPS and CCSDS, as well as advanced techniques like public key cryptography and quantum key distribution.

Moreover, Johnson et al.[38] point out that Global

Navigation Satellite System (GNSS) infrastructures can be vulnerable to attacks that exploit software and firmware flaws, compromising the security and integrity of operations. Baker DZ. et al.[39] analyze how these vulnerabilities can impact the security of space communication networks, emphasizing that many systems rely on software and firmware that may contain security flaws. Such vulnerabilities can be exploited by attackers, resulting in significant security compromises.

V. DISCUSSION

This section aims to provide a discussion and comparison of the reviewed articles, and will be divided into the subsections of Theory vs. Practice, Contrast of Results, and Mitigation Proposals.

A. *Theory vs. Practice*

The articles "The Mission as a Tree" [20] and "Towards Principled Risk Scores for Space Cyber Risk Management" [23] adopt theoretical approaches, focusing on creating abstract frameworks and analyzing risk frameworks to categorize cyber threats and vulnerabilities. In contrast, studies such as "A Hosted Payload Cyber Attack Against Satellites" [17] and "Intrusion Detection System for CubeSats: A Survey" [34] apply these theories in practical scenarios, revealing specific vulnerabilities and suggesting technical solutions, such as intrusion detection systems.

The former works provide an overview of threats, while "Understanding and Investigating Adversary Threats and Countermeasures in the Context of Space Cybersecurity" [28] and "Space-Domain AI Applications Need Rigorous Security Risk Analysis" [29] present concrete analyses, addressing real threats and proposing practical mitigation strategies, such as Zero Trust frameworks and security controls for AI in the space context.

B. *Contrast of Results*

The articles are consistent in identifying critical vulnerabilities in the space sector, but they differ in the depth of analysis and proposed solutions. For example, "Intrusion Detection System for CubeSats: A Survey" [34] focuses on specific vulnerabilities of CubeSats, while "Understanding and Investigating Adversary Threats and Countermeasures in the Context of Space Cybersecurity" [28] addresses a wide range of threats. Additionally, "An Exploratory Analysis of the Last Frontier: A Systematic Literature Review of Cybersecurity in Space" [24] reveals gaps in the existing literature, highlighting areas that require further research and development.

C. *Attack Tree - EMMN*

Based on the vulnerabilities identified in the MQTT protocol and VPNs discussed in Section II, and the attacks analyzed in Section IV, an attack tree was

developed (Figure 2). This tree, available in the appendices of this work, focuses on the threats that could compromise these systems at the Estação Multimissão de Natal (EMMN). Its purpose is to visualize the possible paths an attacker could take to exploit vulnerabilities in the VPN or the MQTT protocol. The following subsections detail how these vulnerabilities may impact the security of the EMMN.

1) *Impacts on VPN*: VPNs are essential for establishing secure communication channels by encrypting and protecting data from interception or unauthorized access. However, when vulnerabilities arise, such as improper configurations or lack of updates, these networks can be exploited by attackers. For example, a man-in-the-middle (MitM) attack can intercept and alter data, compromising security.

Vulnerabilities in authentication protocols or the implementation of encryption can also allow intruders to gain unauthorized access to the internal network, compromising the entire connected infrastructure. In the case of space systems, where sensitive commands are transmitted via VPN to satellites or ground stations, this failure is even more critical.

Moreover, the use of weak or outdated encryption makes communications vulnerable to denial-of-service (DoS) attacks and the injection of malicious data, which can disrupt operations and prevent the sending or receiving of commands in space systems. These vulnerabilities can have consequences such as the loss of telemetry data, manipulation of orbital trajectories, and disruption of communications, which can delay missions and cause damage to equipment.

2) *Impacts on the MQTT Protocol*: MQTT (Message Queuing Telemetry Transport) is a crucial protocol for the EMMN, but it has vulnerabilities that, if exploited, can compromise its security. Improper configurations or the use of outdated versions make MQTT susceptible to attacks such as message interception, publisher spoofing, and denial of service (DoS).

One of the main vulnerabilities occurs when authentication in MQTT is weak or nonexistent, allowing an attacker to initiate communication sessions, intercept, or alter messages. Furthermore, the lack of encryption in MQTT messages can expose sensitive data during transmission, such as critical commands sent to a satellite, which can be captured and manipulated, jeopardizing the mission.

Exploiting communication flaws impacts the application layer of the MQTT protocol, enabling attackers to inject malicious commands or manipulate messages between devices and servers, which can lead to operational failures. Additionally, vulnerabilities in MQTT client software or firmware can allow intruders to execute arbitrary code or gain unauthorized access, threatening not only the affected device but the entire connected network.

The systematic review conducted provided a deep

understanding of the main vulnerabilities and challenges in the cybersecurity of space systems. Through the analysis of various articles, relevant patterns and frameworks were identified, along with concerns such as flaws in communication protocols, dependence on third-party components, and the need for robust encryption practices and software updates. This study was essential for the development of the attack tree, which clearly maps the possible exploitation vectors.

VI. CONCLUSIONS AND FUTURE WORK

The Multi-Mission Station of Natal is crucial for the control and monitoring of CubeSats and NanoSats, featuring modern infrastructure that includes virtualized systems, a distributed network, VPN for remote access, and the MQTT protocol for data synchronization. However, the complexity of the communication systems requires a detailed cybersecurity analysis to protect the integrity and availability of the data.

In this study, we focused on the security of the VPN and MQTT protocols through a systematic literature review, which served as the theoretical basis for creating an attack tree, mapping vulnerabilities and exploitation vectors. We identified that the EMMN systems could be vulnerable to attacks such as DoS and MITM if they exhibit the discussed flaws. Our analysis underscores the importance of not only using robust encryption and maintaining regular updates of patches and appropriate configurations but also strengthening the cyber resilience of the station. We recommend implementing intrusion detection systems (IDS) and enhancing the configurations of the VPN and MQTT protocol.

In summary, this work provides a detailed view of the cybersecurity challenges and solutions at the EMMN, identifying vulnerabilities in previous studies and proposing measures to strengthen the security of control and communication systems. The appendix includes an Attack Tree, which presents a comprehensive overview of the findings.

For future work, we suggest comparing the efficiency and security of different communication protocols beyond MQTT in space systems. This analysis could identify alternatives that reduce latency and increase robustness against cyberattacks.

REFERENCES

- [1] INPE, *Programa nanosat-br, desenvolvimento de cubesats*, Accessed: 2024-07-15, 2021. [Online]. Available: http://www.inpe.br/sul/nanosat/missao/nanosatc_br2.php.
- [2] H. Castro, M. Carvalho, M. Souto, J. da Silva, and L. Jotha, "Emmn-reports about a multi-mission ground station on cubesats tracking," Nov. 2022.
- [3] KASPERSKY, *O que é uma vpn e como funciona?* Accessed: 2024-07-02. [Online]. Available: <https://www.kaspersky.com.br/resource-center/definitions/what-is-a-vpn>.
- [4] E. MOSQUITTO, *Eclipse mosquito*, Accessed: 2024-07-03. [Online]. Available: <https://mosquito.org/>.
- [5] M. Manulis, C. P. Bridges, R. Harrison, V. Sekar, and A. Davis, "Cyber security in new space: Analysis of threats, key enabling technologies and challenges," *International Journal of Information Security*, vol. 20, pp. 287–311, 2021.
- [6] J. Hubbard, "Measuring and improving cyber defense using the mitre att & ck framework," *SANS Whitepaper*, 2020.

- [7] M. A. Prada, P. Reguera, S. Alonso, A. Morán, J. J. Fuertes, and M. Domínguez, "Communication with resource-constrained devices through mqtt for control education," *IFAC-PapersOnLine*, vol. 49, no. 6, pp. 150–155, 2016.
- [8] A. Singh, A. Kumar, and V. Kumar, "A study on mqtt protocol and its cyber attacks," *Int. Adv. Res. J. Sci. Eng. Technol.*, vol. 9, pp. 209–213, 2022.
- [9] H. Ap and K. K., "Secure-mqtt: An efficient fuzzy logic-based approach to detect dos attack in mqtt protocol for internet of things," *EURASIP Journal on Wireless Communications and Networking*, vol. 2019, no. 1, p. 90, 2019.
- [10] Z. Liu, *Application and security analysis of virtual private network (vpn) in network communication*, 2023. [Online]. Available: <https://api.semanticscholar.org/CorpusID:266102764>.
- [11] J. Pavur, *Securing new space: On satellite cyber-security*, 2021. [Online]. Available: <https://ora.ox.ac.uk/objects/uuid:11e1b32a-8117-46b1-a0ce-9c485221d112/files/d02870w18z>.
- [12] W. Zegeye, R. Dean, M. Dugda, F. Moazzami, and A. Bezabih, "Modeling networked telemetry," *Computers*, vol. 10, no. 4, p. 45, 2021.
- [13] J. Pavur, "Securing new space: On satellite cyber-security," Ph.D. dissertation, University of Oxford, 2021.
- [14] B. Bailey, "Cybersecurity protections for spacecraft: A threat based approach," *The Aerospace Corporation*, 2021.
- [15] B. Bace and U. Tatar, "Securing the void: Assessing the dynamic threat landscape of space," *Military Cyber Affairs*, vol. 7, no. 1, p. 2, 2024.
- [16] M. Bradbury, C. Maple, H. Yuan, U. I. Atmaca, and S. Cannizzaro, "Identifying attack surfaces in the evolving space industry using reference architectures," in *2020 IEEE Aerospace Conference*, IEEE, 2020, pp. 1–20.
- [17] M. Calabrese, G. Kavallieratos, and G. Falco, "A hosted payload cyber attack against satellites," in *AIAA SCITECH 2024 Forum*, 2024, p. 0270.
- [18] B. Batizi-Pocsi, "Cyber security in the space domain: Can traditional cyber methods be applied in the ground segment of space projects?," 2021.
- [19] B. Bailey, *Establishing space cybersecurity policy, standards, and risk management practices*. Aerospace Corporation El Segundo, CA, 2020.
- [20] S. Bonnart, A. Pickard, N. P. Manti, and D. Jha, "The mission as a tree: A novel approach to identifying cyber threats to satellites," *IAC-20 E*, vol. 9, no. 2, 2020.
- [21] A. J. Akande, E. Foo, Z. Hou, and Q. Li, "Cybersecurity for satellite smart critical infrastructure," in *Emerging Smart Technologies for Critical Infrastructure*, Springer, 2023, pp. 1–22.
- [22] A. Carlo, "The space-cyber nexus: Ensuring the resilience, security and defence of critical infrastructure,"
- [23] E. Ear, B. Bailey, and S. Xu, "Towards principled risk scores for space cyber risk management," *arXiv preprint arXiv:2402.02635*, 2024.
- [24] G. Kavallieratos and S. Katsikas, "An exploratory analysis of the last frontier: A systematic literature review of cybersecurity in space," *International Journal of Critical Infrastructure Protection*, p. 100640, 2023.
- [25] A. Diro, S. K. Khan, and A. Molla, "Leveraging system dynamic modelling for space cybersecurity conceptualisation and assessment," Available at SSRN 4671343.
- [26] M. Calabrese, "Space oddity: Space cybersecurity lessons from a simulated ops-sat attack," 2023.
- [27] B. Zachar, *Analysis and risk assessment of malicious cyber activity against space systems*, 2023.
- [28] K. Thangavel, J. J. Plotnek, A. Gardi, and R. Sabatini, "Understanding and investigating adversary threats and countermeasures in the context of space cybersecurity," in *2022 IEEE/AIAA 41st Digital Avionics Systems Conference (DASC)*, IEEE, 2022, pp. 1–10.
- [29] A. Weber and P. Franke, "Space-domain ai applications need rigorous security risk analysis,"
- [30] T. H. Llansó, D. A. Hedgecock, J. A. Pendergrass, and J. Hopkins, "The state of cyber resilience: Now and in the future," *Johns Hopkins APL Technical Digest*, vol. 35, no. 4, 2021.
- [31] J. Pavur and I. Martinovic, "Building a launchpad for satellite cybersecurity research: Lessons from 60 years of spaceflight," *Journal of Cybersecurity*, vol. 8, no. 1, tyac008, 2022.
- [32] Y. W. Law and J. Slay, "Siem4gs: Security information and event management for a virtual ground station testbed," in *ECCWS 2022 21st European Conference on Cyber Warfare and Security*, Academic Conferences and publishing limited, 2022.
- [33] B. Bailey, "Reducing the software risk in ground systems," in *Annual Ground System Architectures Workshop (GSAW)*, 2018.
- [34] O. Driouch, S. Bah, and Z. Guennoun, "Intrusion detection system for cubesats: A survey," in *2023 International Wireless Communications and Mobile Computing (IWCMC)*, IEEE, 2023, pp. 596–601.
- [35] S. Lightman, T. Suloway, and J. Brule, "Satellite ground segment: Applying the cybersecurity framework to assure satellite command and control," National Institute of Standards and Technology, Tech. Rep., 2022.
- [36] J. T. Hanan, E. Fowler, S. Hernandez, M. Niemczyk, U. Tatar, and O. F. Keskin, "Analysis of satellite systems' dependencies and their cascading impacts," in *2024 Systems and Information Engineering Design Symposium (SIEDS)*, IEEE, 2024, pp. 493–498.
- [37] M. N. Tsamis, H. Reed, and D. Vivanco, "Cybersecurity's role in supporting space situational awareness," in *Proceedings of the Advanced Maui Optical and Space Surveillance (AMOS) Technologies Conference*, 2023, p. 188.
- [38] C. Johnson and A. A. Yepez, "Cyber security threats to safety-critical space-based infrastructures," in *Proceedings of the Fifth Conference of the International Association for the Advancement of Space Safety*, Citeseer, 2011.
- [39] D. Z. Baker, H. Liu, and C. Roberts, "Ensuring flexibility and security in sdn-based spacecraft communication networks through risk assessment," in *2019 IEEE International Symposium on Technologies for Homeland Security (HST)*, IEEE, 2019, pp. 1–6.

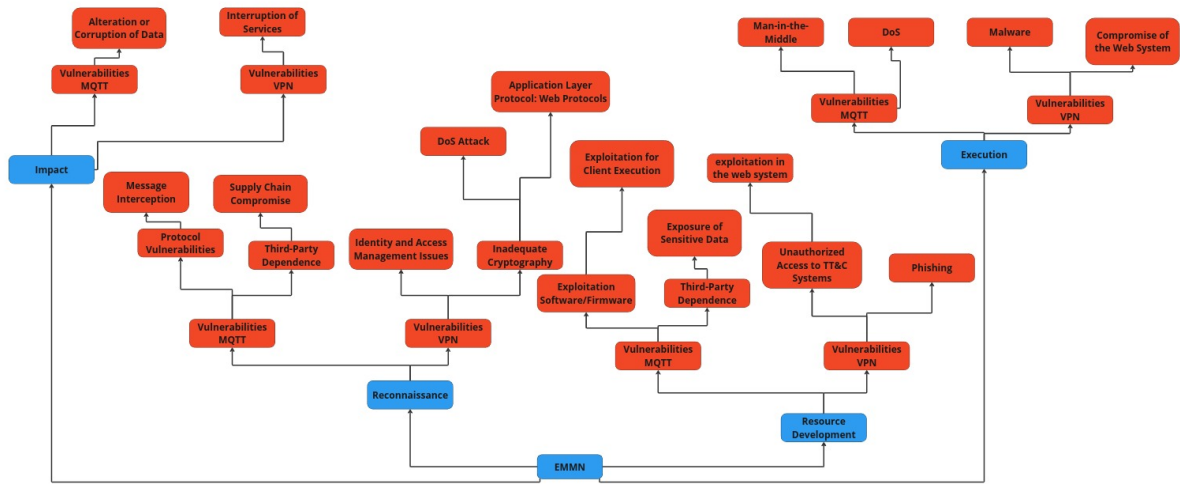


Fig. 2. Attack Tree EMMN - Source: Own elaboration

Review of the Application of CCSDS Telemetry and Telecommand Recommendations in CubeSat Missions

Ana Clara Melo de Araújo*, Moisés Cirilo Brito Souto*

*IFRN - Instituto Federal de Educação, Ciência e Tecnologia do Rio Grande do Norte
Campus Natal Central of Natal, CCSL - Centro de Competências em Soluções Livres of Natal
Email: meloanaclara299@gmail.com, moises.souto@ifrn.edu.br

Abstract—This study aims to exemplify the standards of the Consultative Committee for Space Data Systems (CCSDS) with regard to telemetry (TM) and telecommand (TC) protocols, as well as to investigate CubeSat missions that have applied these standards and their respective results.

In this way, it becomes possible to identify the particularities of each mission in the implementation of these standards, thus allowing us to conclude lessons for future missions involving the adoption of CCSDS TM/TC standards on CubeSats.

The results lead us to understand important elements in this integration, as well as the challenges that CubeSats missions tend to face or solve in this scenario, in addition to the advantages and disadvantages that different CubeSats missions encounter when implementing these protocols. The choice of some missions to adopt the CCSDS standard optimally, in conjunction with other standards such as the CubeSat Space Protocol (CSP) and the European Cooperation for Space Standardization (ECSS), is also addressed.

This study was based on the realization that the significant growth of small satellites in the context of space communications imposes the need to adhere to international standards, which aim to guarantee efficiency, robustness, interoperability, compatibility and support, such as those provided by CCSDS.

Index Terms—component, formatting, style, styling, insert

I. INTRODUCTION

This document is a model and instructions for L^AT_EX. Please observe the conference page limits.

II. EASE OF USE

A. Maintaining the Integrity of the Specifications

III. INTRODUCTION

Over the years, CubeSats have become essential to space missions [1], enabling small startups and academic institutions to plan their own missions [1]. With this growth, adhering to international standards for satellite-to-ground communication has become increasingly efficient. The CCSDS provides these standards freely through comprehensive documentation, covering various aspects of space missions, from onboard spacecraft data processing to ground-based operations [2].

However, these publications are exhaustive, as they must cover all the needs of the [3] partners, which is essential for the context. With this in mind, we have tried to exemplify them in a clear and objective way, offering a broader understanding

of their content. In this way, we will be able to present CubeSats and small satellite missions as lessons learned in the implementation of the CCSDS TM/TC standards for future missions.

The methodology adopted is based on a thorough analysis of the standards established by the CCSDS regarding TM/CT protocols, as well as a review of the existing literature, with the aim of identifying crucial information about the approaches, contributions and limitations pertinent to the context under investigation.

The literature reveals different approaches to implementing CCSDS standards. Missions such as CubeL indicate that the definition of the degree of compliance with the standards is flexible, with “adaptation” being a viable alternative, and in certain cases, a necessity [3]. On the other hand, missions such as ALE-1 point out that, in the context of small satellites, it is preferable to reduce system complexity, save development time and minimize data overload, favoring simplified implementations that use only a subset of the protocols, while still complying with the CCSDS [4]. On the other hand, the SEAM mission exemplifies the optimization of CCSDS standards with others, such as ECSS and the CSP protocol, to better meet the particularities of each mission.

Thus, this study contributes by demonstrating the application and optimization of CCSDS recommendations in CubeSat missions, highlighting challenges, solutions and lessons learned for future implementations.

This article is structured in four sections. Section IV presents examples of the analysis of the CCSDS TM/TC protocols, their structure and operation in conjunction with other protocols, such as ECSS and CSP, and the missions that implement them. Section V discusses the results and limitations of the methodological approach. Finally, section VI explores future perspectives.

IV. METHODOLOGICAL ANALYSIS

The research undertaken adopts a qualitative approach with the aim of examining the standards established by the CCSDS for TM/TC. The focus of the analysis is on missions that apply these standards and their particularities, in order to identify specific aspects related to the implementation of these standards in CubeSats systems.

Identify applicable funding agency here. If none, delete this.

As a theoretical basis, we used the most recent CCSDS publications on TM and TC protocols, specifically the blue cover books entitled TM Space Data Link Protocol 132.0-B-3 [5] and TC Space Data Link Protocol 232.0-B-4 [6]. These documents were the basis for a detailed understanding of the applicability of the standards in question. In addition, the selection of materials was guided by ideal criteria for this work, such as:

- **Contribution and Relevance:** Priority was given to articles that presented substantial contributions, such as a detailed description of the implementation, problems encountered, solutions adopted, or an analysis of the advantages and disadvantages of applying the CCSDS TM/TC standards.
- **Mission:** Priority was given to articles that showed the applicability of the standards in CubeSats for specific missions, ensuring a contextualized and focused analysis.
- **Simplicity:** Only articles related to missions that did not involve advanced technologies were included, as such complexities could make it impossible to apply the standards to missions with limited resources.
- **Mission Launch:** Missions with launches between 2017 and 2024 were filtered to ensure the relevance of the topic.

In addition, the following elements are highlighted in all missions:

- **approach:** Provides an understanding of how the CCSDS standards were implemented in each mission, highlighting the strategies used to meet specific needs.
- **contribution:** Highlights the impact each study has had on the field.
- **limitation:** Identifies the difficulties faced by the studies, pointing out challenges that can serve as lessons for future research and implementation in similar missions.

As a result, recommendations for future implementation are generated, providing a comprehensive perspective.

A. Explanation of CCSDS telecommand and telemetry protocols

The telecommand and telemetry process can be seen in Figure 17, where a user at a ground station sends a command to the satellite requesting data, and the satellite responds with telemetry, providing the requested information.

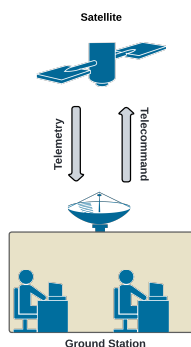


Fig. 1. Communication Between Satellite and Earth Station.

The CCSDS TM/TC standards are today being employed for a large number of scientific and commercial spacecraft [7]. using this standard allows reduced costs for on-board, ground and test equipment, as well as for spacecraft testing and in-orbit operation [7].

The CCSDS establishes the services, data units and procedures of the TM and TC protocols, deliberately not specifying individual implementations, service interfaces, methods, technologies or management activities in order to preserve the objectivity and flexibility of each mission.

To this end, the CCSDS layer can be represented in correspondence with the OSI reference model, as illustrated in Figure 2.

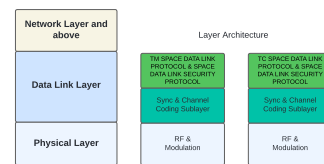


Fig. 2. CCSDS layer. Figure Adapted from [5].

Therefore, the CCSDS TM and TC protocol is positioned in the data link layer of the OSI reference model. In addition, there is the presence of the Space Data Link Security Protocol (SDLS) at the same layer, which is established as an option by CCSDS and provides additional security, authentication and confidentiality for the [6] transfer frames. This paper focuses on TM/TC standards without the inclusion of SDLS.

In addition, it can be understood that the main concepts covered in the books are based on elements such as:

- **Physical channel:** transfers data across the air-interface [8].
- **virtual channel (VC):** multiplexes the data transferred over the physical channel.
- **master channel (MCID):** coordinates the multiplexing of the Virtual Channel Transfer Frames.
- **transfer frame:** this is the protocol unit of the TM Space Data Link Protocol.

Consequently, the data standards are mainly based on these concepts and are essential to the structure and operation of the protocol.

1) *CCSDS Telemetry Protocol:* CCSDS defines a virtual channel as a data multiplexer with different requirements from a physical channel and establishes that each transfer frame transmitted over a physical channel belongs to one of the virtual channels of that physical channel [5].

Virtual and master channels can offer service types such as Asynchronous or Periodic. In addition, each type of service on a virtual or master channel has a Service Access Point (SAP address), which acts as an identifier for the type of service transmitted over that channel. The SAP address is used to identify the user of the service and ensure that the data is routed correctly through the specific channel, be it virtual or master [5].

For example, according to the CCSDS, the Virtual Channel Packet (VCP) service is asynchronous, and its data unit is packets. Its SAP address is called GVCID + Packet Version Number. The GVCID (Global Virtual Channel Identifier) indicates that the structuring of the data transmitted by a VCP is based on:

$$\text{GVCID} = \text{MCID} + \text{VCID} \quad (1)$$

Where, MCID = version number of the transfer frame (TFVN) + SCID (Spacecraft Identifier) and VCID = virtual channel identifier.

A VCP service user is a protocol entity identified by a Packet Version Number (PVN) and a GVCID, which sends or receives packets. Different users can share a Virtual Channel, and the provider multiplexes packets of different versions into a single flow on that channel.

This correspondence can be seen in Figure 17.

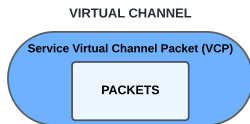


Fig. 3. Virtual Channel Packet Service.

Where packets are encapsulated in a VCP and transmitted over a virtual channel.

On master channels, all transfer frames with the same MCID on a physical channel constitute a Master Channel (MC). A Master Channel is made up of one or more Virtual Channels. In most cases, a Physical Channel only carries transfer frames from a single MCID, and the Master Channel will be identical to the Physical Channel [5].

The CCSDS which establishes various identifications, such as the Global Virtual Channel Identifier (GVCID) and the Spacecraft Identifier (SCID), which are used to manage and identify channels and spacecraft in space data communication systems. These identifications help ensure interoperability and the efficient organization of transmitted data.

For a master channel, one example is the Master Channel Frame Secondary Header (MC_FSH) service:

- service type: Asynchronous or periodic.
- service data unit: OFC_SDU.
- sap address: MCID. aonde, mcid = tfvn + scid.

In the MC_FSH service, only one user can use this service on a Master Channel, identified by the MCID of that channel. The service data units of different users are not multiplexed on a single Master Channel.

This correspondence can be seen in Figure 4.

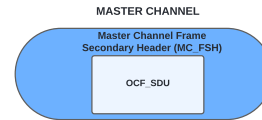


Fig. 4. Service Encapsulation MC_FSH.

where the OFC_SDU is encapsulated in an MC_FSH that is transferred over a master channel.

The relationship between the channels, in general, can be seen as in figure 5:

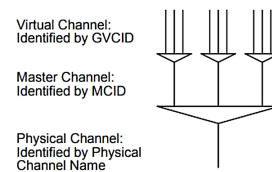


Fig. 5. Relationship Between Channels. Figure Adapted From [5].

Another concept that ccstd standardizes for this protocol is the tm transfer frame, its function is to be the data transfer unit from a satellite to a ground station.

The structure is defined in the following figure 6:

TM TRANSFER FRAME				
TRANSFER FRAME PRIMARY HEADER	TRANSFER FRAME SECONDARY HEADER (Optional)	TRANSFER FRAME DATA FIELD	TRANSFER FRAME TRAILER (Optional)	
6 octets	Up to 64 octets	Varies	4 octets	2 octets

Fig. 6. TM transfer Frame. Figure Adapted From [5].

Transfer Frame Primary Header:

TRANSFER FRAME PRIMARY HEADER (6 octets)						
MASTER CHANNEL ID		VIRTUAL CHANNEL ID	OFC FLAG	MASTER CHANNEL FRAME COUNT	VIRTUAL CHANNEL FRAME COUNT	TRANSFER FRAME DATA FIELD STATUS
TRANSFER FRAME VERSION NUMBER	SPACECRAFT ID					
2 bits	10 bits	3 bits	1 bit	1 octet	1 octet	2 octets

Fig. 7. Transfer Frame Primary Header [5].

Where according to [1], we can conclude:

- Master Channel Identifier (12 bits) : a) Transfer Frame Version Number(2 bits): it shall be set to '00' for TM packets. b) Spacecraft Identifier (10 bits): Assigned by: the Space Assigned Numbers Authority (SANA)
- Virtual Channel Identifier (3 bits): Identifies the virtual channel of the packet stream.
- Operational Control Field Flag (1 bit)

- Master Channel Frame Count (1 byte): Keeps track of packet primary sequence
- Virtual Channel Frame Count (1 byte): Keeps track of Virtual Channel stream packets
- Transfer Frame Data Field Status:

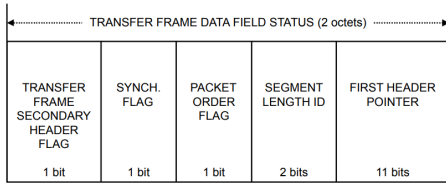


Fig. 8. Transfer Frame Data Field Status [5].

- Transfer Frame Secondary Header Flag (1 bit): Gives an indication of secondary header
- Synchronization Flag (1 bit): It signals the type of data which are inserted into the Transfer Frame Data Field
- Packet Order Flag (1 bit): Reserved for future use by CCSDS. Its value is set to '0'.
- Segment Length Identifier (2 bits): Contains segment length identifier. Its value is set to '11'.
- First Header Pointer (11 bits): Helps in keeping track of space packet (Network Layer) headers.

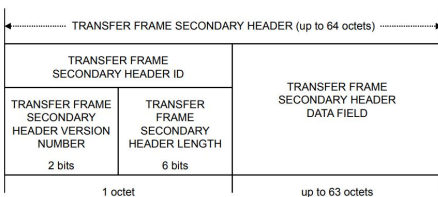


Fig. 9. Transfer Frame Secondary Header [5].

Where, according to [5]:

- Transfer Frame Secondary Header Version Number : bits 0-1 store the Header Version Number, encoded in binary, set to '00'.
- bits 2-7 shall contain the Transfer Frame Secondary Header Length.
- The Transfer Frame Secondary Header Data Field shall follow, without gap, the Transfer Frame Secondary Header Identification Field and data.

Finally, according to [5], the last fields in the frame have a transfer frame:

- Transfer Frame Data Field (variable) : The Data Field can contain Packets, a VCA_SDU or Idle Data(oids).
- Transfer Frame Trailer (Optional) : joins the OPERATIONAL CONTROL FIELD (Optional) + FRAME ERROR CONTROL FIELD (Optional) fields.

Virtual Channel Access Service Data Units (VCA_SDU) are privately formatted, fixed-length service data units [5].

About the fields, still according to [5], we can conclude that in their transfer, they must be:

- The Spacecraft Identifier shall be static throughout all Mission Phases.
- The Operational Control Field Flag shall be static within the associated Master or Virtual Channel throughout a Mission Phase.
- The Transfer Frame Secondary Header Flag shall be static within the associated Master or Virtual Channel throughout a Mission Phase.
- The Synchronization Flag shall be static within a specific Virtual Channel throughout a Mission Phase.
- If present, the Transfer Frame Secondary Header shall be associated with either a Master Channel or a Virtual Channel.
- The Transfer Frame Secondary Header Length shall be static within the associated Master or Virtual Channel throughout a Mission Phase.
- The Transfer Frame Secondary Header Data Field shall be of fixed length within the associated Master or Virtual Channel throughout a Mission Phase.
- If present, the Operational Control Field shall be associated with either a Master Channel or a Virtual Channel.

B. CCSDS Telecommand Protocol

The TC introduces a concept that is not present in the telemetry protocol: the MAP Channel (optional). The MAP Channel is identified by the Multiplexer Access Point Identifier (MAP ID) and consists of all transfer frames with the same GVCID and MAP ID [6].

Its representatives in relation to the other channels can be seen in the following figure:

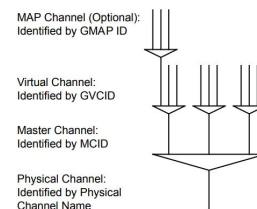


Fig. 10. Relationship between Channels [6].

The MAP Packet Service (MAPP) provides a service that transfers a sequence of variable, delimited and octet-aligned service data units, known as Packets, over a spatial link on a specified MAP Channel [6]. Both the Sequence Controlled Service (Type-A) and the Accelerated Service (Type-B) are available for the MAPP Service.

According to CCSDS:

- Type-A: Data transmitted by the Type-B Service is sent only once, with no guarantee of delivery to the recipient
- Type-B: The Type-A Service is a more reliable service that should be used only when available, as it offers retransmission mechanisms to guarantee data delivery.

Therefore, this protocol offers two types of data transmission services on virtual channels, typ-b and type-a.

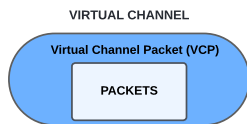


Fig. 12. servico virtual channel packet

We can also classify the MAP Packet Service (MAPP) as follows, according to the CCSDS:

- service type: Type-a and Type-b
- service data unit: Packet
- SAP address: GMAP ID + Packet Version Number, where GMAP ID = GVCID + MAP ID. The MAP ID indicates the MAP channel (within the Virtual Channel specified by GVCID) through which the packet will be transferred in the MAP Packet service.

We can visualize it as follows:

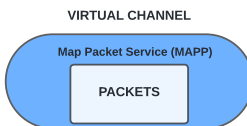


Fig. 11. Service Map Packet.

For a Virtual Channel Packet (VCP), we can classify:

- Service Type: Type-A and Type-B
- Service Data Unit : Packet
- SAP Address : GVCID + Packet Version Number

Seen as:

As well as the Master Channel Frame (MCF) service, and several more.

- Service Type: N/A
- Service Data Unit: Transfer Frame
- SAP Address : MCID

Where:

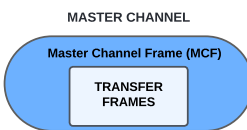


Fig. 13. Service Master Channel Frame

The tc transfer frame can be seen in the figure below:

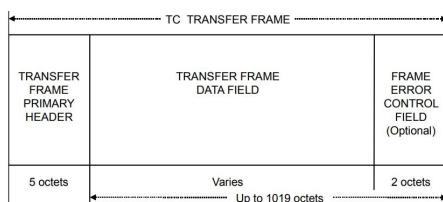


Fig. 14. Tc Transfer Frame [6].

Transfer frame primary header:

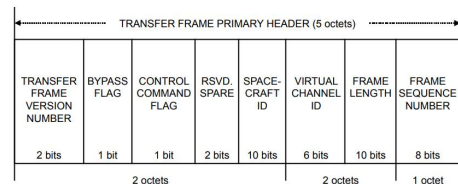


Fig. 15. TC Transfer Primary Header [6].

Where, according to [1], we can conclude:

- Transfer Frame Version Number (2 bits) : Set to '00'
- Bypass Flag (1 bit): Set to '0'
- Control Command Flag (1 bit): Set to '1' as all uplinks would contain control commands only.
- RSVD. SPARE (2 bits): Reserved for future application by CCSDS and shall be set to '00'
- Spacecraft Identifier (10 bits): Assigned by: the Space Assigned Numbers Authority (SANA).
- Virtual Channel Identifier (6 bits): Identifies the virtual channel of the packet stream.
- Frame Length (10 bits): This 10-bit contains a count of C. Where $C = (\text{Total Number of Octets in the Transfer Frame}) - 1$.
- Frame Sequence Number (8bits).

Finally, we have the TRANSFER FRAME fields DATA FIELD and FRAME ERROR CONTROL FIELD (Optional) of the tc transfer frame. where, according to CCSDS:

- TRANSFER FRAME DATA FIELD (variable): can carry two types of information, 1. An integral number of octets corresponding to a Frame Data Unit for a Type-D Transfer Frame (used to transport user data); 2. An integral number of octets of Control Command information for a Type-C Transfer Frame (used to transport control commands).
- FRAME ERROR CONTROL FIELD (Optional-16 bits): used to detect errors that may have been introduced into the Transfer Frame during the data transmission and manipulation process.

Regarding the fields, still according to [6], we can conclude that, during their transfer, they must be:

- The Spacecraft Identifier shall be static throughout all Mission Phases.
- If present, the Frame Error Control Field shall occur within every Transfer Frame transmitted within the same Physical Channel throughout a Mission Phase.

Additionally this standard introduces the communication operation procedure (COP) management service also referred to as COP-1, which ensures that frames are received sequentially by reporting back the current transfer frame acceptance status via the Communication Link Control Words (CLCW) as part of transfer frames for

TC and TM [9]. This mechanism can be used to issue automatic retransmissions.

C. CCSDS/ECSS and CSP Protocol

The CubeSat Space Protocol (CSP) is a network and transport protocol specially designed for embedded [9].

CSP functions as an interface between multiple nodes that may be either onboard or ground-based [9]. This protocol is highly functional for CubeSat constellations that require communication. Although CSP is somewhat contrary to CCSDS, it can be adapted to work in conjunction with CCSDS, as stipulated by the CubeL mission [9].

This process can be documented by the CubeL mission in the following manner:

- For uplink this means that the CCSDS/ECSS TC packet application data is a CSP TC packet. Once reaching the spacecraft, the CSP TC packets are extracted and processed like any other CSP TC packet.
- For downlink this means that each Source Data field from the CCSDS/ECSS TM source packet is a CSP TM packet. On ground, the CSP TM packets are extracted and sent to a CSP terminal system.

The ECSS (European Cooperation for Space Standardization) is an organization that develops standards for the European space industry. The ECSS PUS (Packet Utilization Standard) is a standard that defines various types and subtypes of packets, corresponding to specific aspects and capabilities of each application process, and allows flexibility in the implementation of onboard application software [9]. This standard is commonly used in conjunction with CCSDS without any interference.

The implementation of ECSS PUS regarding TM/TC frames can be simplified as follows:

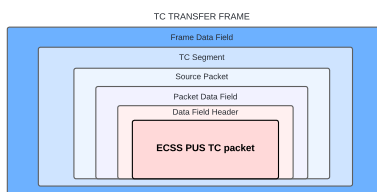


Fig. 16. TC with ECSS PUS. Adapted from [9].

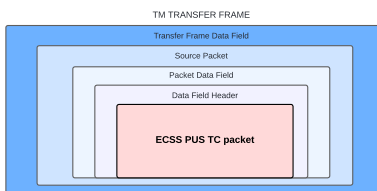


Fig. 17. TM with ECSS PUS, Adapted from [9].

Therefore, the PUS is indirectly encapsulated within the transfer frames. The PUS source packets are inserted into the transfer frames, which are then transmitted.

D. Critical Analysis and Systematic Review of the Literature

This study conducted a systematic review of the literature, selecting studies based on essential criteria, with the aim of evaluating the experiences of CubeSat missions in integrating this standard and understanding more suitable implementation alternatives for various scenarios, drawing on lessons learned.

1) *Team Anant Mission*: According to [1], we can conclude:

- Approach: The CCSDS standard was chosen for its suitability for S-band communications, robust space heritage, extensive documentation, and reliability. The use of open-source CCSDS protocols facilitated the implementation of TM/TC, providing access to online resources and ground station support, resulting in efficient communication. Additionally, the open-source software simplified both implementation and testing.
- Contribution: The importance of optimizing packet size to meet the requirements for transmitting multi-spectral images with minimal loss in S-band communications using the CCSDS TM/TC protocol.
- Limitation: This implementation significantly increased power consumption, which must be considered in the design of small satellites, especially in the context of simpler missions.

2) *CubeL Mission*: According to [3], we can conclude:

- Approach: The work explains that the primary idea is to create a simple wrapper in the CCSDS standard to encapsulate CSP packets. It adheres to the CCSDS TM/TC standard but employs the ECSS standard for the secondary header, complementing CCSDS by ensuring interoperability and proper data formatting. However, the CubeL mission encountered challenges with data overhead when integrating CSP packets as fixed-length CCSDS packets, necessitating bandwidth expansion as an effective solution.
- Contribution: Demonstrates that although the CSP protocol is contrary to CCSDS/ECSS, it can be used efficiently with CCSDS/ECSS when properly optimized.
- Limitation: Implementing CSP over CCSDS/ECSS results in significant overhead and a loss of payload capacity due to the encapsulation of smaller CSP packets within TM packets.

3) *Floriposat Mission*: According to [10], we can conclude:

- Approach: Describes the development of a communication module for CubeSat based on CCSDS recommendations, implemented on a radiation-tolerant FPGA. The system includes a TM/TC unit, as well as a data handling component (OBDAH) compatible with CCSDS. The proposed architecture aims to balance the demands of the case study.
- Contribution: The application can be generalized and easily adapted for other missions.
- Limitation: The implementation of an on-chip communication bus and the application of services proposed by the ECSS PUS standard were not fully developed or tested.

4) *AcubeSat Mission*: According to [11], we can conclude:

- Approach: The ACubeSat mission is open-source, providing publicly available software, hardware, and documentation that can be utilized in other projects. On the mission's GitHub repository, you can find the implementation of the CCSDS TM and TC standards (232.0-B-4, 232.1-B-2, 132.0-B-3), covering transfer frame formats and data encoding/decoding, primarily in C++. The primary CCSDS header is fully compliant with the standards, while the secondary PUS header has been adjusted to ensure header sizes are multiples of a byte, with some fields modified or removed.
- Contribution: Provides libraries and source code to the community for the implementation of the CCSDS TM/TC standard.
- Limitation: The context of the application of the CCSDS TM/TC standards for the AcubeSat mission is not provided, which could be valuable for offering important insights for similar missions.

5) *Aalto-2 Mission*: According to [12], we can conclude:

- Approach: The adopted approach is innovative, combining various libraries and features of concatenative languages. However, it is noted that maintaining system simplicity and reliability requires careful design and precise derivation of requirements and constraints.
- Contribution: It does not define mission-specific concepts, such as payload application functions, making it adaptable for any spacecraft mission regardless of payload objectives, orbit characteristics, or ground station requirements.
- Limitation: The study is limited by its lack of sufficient information on the implementation and structuring of the CCSDS TM/TC protocol within the mission.

6) *AlfaCrux Mission*: According to [13], we can conclude:

- Approach: The communication system of the AlfaCrux satellite employs the CubeSat CSP and adapts CCSDS standards for data and telemetry transfer. Commands are categorized into three types: EPS, PAYLOAD (as per CCSDS), and FLAGS (one byte). Communication is effectively achieved using the 'cosmos' software, ensuring that transmitted and received data are identical and free from interference..
- Contribution: It contributes by detailing the mission and presenting initial results, highlighting the use of the CSP for data packet transmission.
- Limitation: The study does not provide a satisfactory explanation of how the implementation of CCSDS/ECSS protocols with CSP occurs.

7) *Seam Mission*: According to [2], we can conclude:

- Approach: The Small Explorer for Advanced Mission (SEAM) utilizes a communication link compatible with CCSDS and commercial ground station equipment. The mass memory manages the network layer in software, adhering to the CCSDS/ECSS standard. Data transmission between the satellite and the ground station is divided into

Telemetry and Telecommand. For instance, Telemetry includes onboard computer beacon messages sent as CSP packets and collected by the radio transceiver.

- Contribution: Demonstrates the solution implemented for integrating CCSDS TM/TC standards in a constrained CubeSat environment.
- Limitation: The study is conducted broadly and does not provide sufficient data for implementation in other missions.

8) *Ale-1 Mission*: According to [4], we can conclude:

- Approach: The primary challenge was to implement the CCSDS protocols while preserving the functionality of the custom communication protocol with minimal alterations to the original design. A simplified implementation of CCSDS was developed, integrating a commercial CCSDS controller into the existing system. This approach resulted in a balance between advantages and disadvantages: while there was a potential increase in data overhead due to additional headers and control fields, communication reliability was enhanced, which was the mission's priority.
- Contribution: Highlights the importance of adhering to CCSDS standards for TM/TC in a simplified manner for legacy systems.
- Limitation: Fails to provide sufficient information regarding the challenge of overhead and how to manage it effectively.

9) *Flying Laptop Mission*: According to [14], we can conclude:

- Approach: The requirement to adhere to industry standards whenever feasible led to the adoption of CCSDS standards for satellite communications, ensuring compatibility with professional ground stations. The TM/TC standard was developed, and modular software in JavaScript was implemented to provide CCSDS-compatible command transfer frames from any mission control system to the designated base band equipment of the antenna, and telemetry transfer frames from the spacecraft to its designated data collector.
- Contribution: The implementation of a ground segment compliant with industry standards such as ECSS and CCSDS facilitates integration with commercial tools and collaboration with other institutions.
- Limitation: The need to restart the mission control system when installing a new Mission Information Base (MIB) can be inconvenient during testing and operations.

V. DISCUSSION OF RESULTS

It is possible to summarize the key points of each mission for a comprehensive analysis:

TABLE I
SUMMARIZING EXISTING REVIEWS

Work	Implementation	Model	Launch
Team anant	CCSDS	3U	Expected in 2024 [15]
CubeL	CCSDS/ECSS and CSP Protocol	3U CubeSat	2021 [3]
Floripasat	CCSDS/ECSS	1U CubeSat	2019 [16]
AcubeSat	CCSDS/ECSS	3U CubeSat	2021 [11]
Aalto-2	CCSDS	2U CubeSat	2017 [17]
Alfacrux	CCSDS/ECSS and CSP Protocol	1U CubeSat	2022 [18]
Seam	CCSDS/ECSS and CSP Protocol	3U CubeSat	2017 [19]
Ale-1	CCSDS	Micro-satellite	2019 [4]
Flying laptop	CCSDS	Small Satellite	2017 [20]

Based on this summary, it is possible to discuss the following:

- The approach of using CCSDS standards in conjunction with ECSS is a prevailing trend.
- Even small CubeSats are adopting these standards, and it is important to explore their results. Given that these systems are constrained, the robustness of these standards could impact communication. Therefore, investigating this scenario is crucial.
- The flexibility of CCSDS in working alongside other protocols allows for a broad range of optimizations. However, it is important to assess the impact of adopting CCSDS in conjunction with other protocols. What are the advantages and disadvantages of this approach?

However, this work becomes limiting in terms of discussing these issues, presenting a general implementation of these standards, which may restrict more specific conclusions.

Regarding missions, it is generally possible to discuss that each mission has its own specifics, and CCSDS offers a degree of flexibility that can and should be explored by missions. However, to be compatible with the simplicity of many CubeSats and legacy systems, the simplicity of these standards, as discussed in the ALE-1 mission [4], can be a good choice for constrained missions.

On the other hand, if robustness, reliability, integrity, and other benefits provided by international space data standards are a priority, the use of the CCSDS TM/TC protocol is more attractive. Additionally, if the mission requires optimization or customization with other particularities, using CCSDS in conjunction with ECSS or CSP protocols can help achieve these objectives.

VI. CONCLUSION AND FUTURE WORK

This paper has presented a comprehensive and practical overview of the application of the extensive CCSDS telemetry and telecommand (TM/TC) standards at the link layer, highlighting how these standards are implemented in CubeSat missions. Given the increasing use of CubeSats and small satellites in a wide range of space missions, the adoption of space data standards becomes essential to ensure interoperability, efficiency and reliability in communications.

For future work, we recommend testing the efficiency of communication between a CubeSat and ground station using

the TM/TC protocol, comparing this scenario with the joint application of CCSDS/ECSS standards and the CSP protocol. This analysis will make it possible to identify the advantages and disadvantages of each approach, providing a solid basis for strategic choices in future CubeSat missions.

REFERENCES

- [1] S. Majumder, H. Tambi, K. Mathur, P. Putrevu, and H. Venkat, "Design and development of a high-speed communication system for a leo nano satellite," Oct. 2021.
- [2] P. Hyvönen, N. Ivchenko, and M. Tsamsakizoglou, "Small explorer for advanced missions (seam), a ccstds compatible cubesat supported on a global commercial ground network," May 2016. DOI: 10.2514/6.2016-2626.
- [3] P.-A. Lagadrillière, T. Brüggel, and K. Müller, *Confronting or linking csp and ccstds? a view on how to operate small satellites today*, 2023. [Online]. Available: <https://digitalcommons.usu.edu/cgi/viewcontent.cgi?article=5699&context=smallsat> (visited on 09/15/2024).
- [4] H. Tomio, Y. Shibuya, T. Kuwahara, S. Fujita, Y. Sato, and K. Kamachi, "Development and evaluation of a ccstds-based communication system on microsatellite ale-1," *TRANSACTIONS OF THE JAPAN SOCIETY FOR AERONAUTICAL AND SPACE SCIENCES, AEROSPACE TECHNOLOGY JAPAN*, vol. 19, no. 2, pp. 368–376, May 2021. DOI: 10.2322/tastj.19.368.
- [5] *Recommendation for space data system standards tm space data link protocol recommended standard*, CCSDS, Oct. 2021. [Online]. Available: <https://public.ccsds.org/Publications/BlueBooks.aspx>.
- [6] *Recommendation for space data system standards tc space data link protocol recommended standard*, CCSDS, Oct. 2021. [Online]. Available: <https://public.ccsds.org/Pubs/232x0b4c1.pdf> (visited on 09/15/2024).
- [7] P. Sinarrow and S. Habinc, *Telecommand and telemetry components for today and tomorrow*, 1998. [Online]. Available: <http://microelectronics.esa.int/vhdl/doc/TmTe98.pdf> (visited on 09/15/2024).
- [8] L. with Examples, *Channel mapping*, Nrexplained.com, 2024. [Online]. Available: <https://www.nrexplained.com/chmap> (visited on 09/15/2024).
- [9] L. Grillmayer and S. Arnold, *Integrating the cubesat space protocol into gsoc's multi-mission environment*, DigitalCommons@USU, 2020. [Online]. Available: <https://digitalcommons.usu.edu/smallsat/2020/all2020/181/> (visited on 09/15/2024).
- [10] L. Matana Luza, "A contribution to the in-orbit validation of a radiation-hardened communication platform to be used in small satellites," Ph.D. dissertation, Jan. 2019.
- [11] P. Bountzioukas, G. Kikas, C. Tsiolkas, *et al.*, "The evolution from design to verification of the antenna system and mechanisms in the acubesat mission," Oct. 2023. DOI: 10.48550/arXiv.2310.16134.
- [12] M. Mayoral, *Telecommand and telemetry implementation of aalto-2 cubesat project*, 2016. [Online]. Available: <https://upcommons.upc.edu/bitstream/handle/2117/97427/1/5BMarc%20Justicia%205D%20Telecommand%20and%20Telemetry%20Implementation%20of%20Aalto-2.pdf> (visited on 09/15/2024).
- [13] R. A. Borges, A. C. dos Santos, W. R. Silva, *et al.*, "The alfacrux cubesat mission description and early results," *Applied Sciences*, vol. 12, no. 19, 2022. ISSN: 2076-3417. DOI: 10.3390/app12199764. [Online]. Available: <https://www.mdpi.com/2076-3417/12/19/9764>.
- [14] K. Klemich, N. Bucher, M. Boettcher, *et al.*, "A ground segment for small satellite operations in a university context combining professional and custom software tools," May 2016. DOI: 10.2514/6.2016-2545.
- [15] E. Kulu, *Anant - nanosats database*, Nanosats Database, 2024. [Online]. Available: <https://www.nanosats.eu/sat/anant> (visited on 09/15/2024).
- [16] *Satélites cbers-4a e floripasat já estão em órbita a 628 km da terra*, Agência Espacial Brasileira, Nov. 2019. [Online]. Available: <https://www.gov.br/aeb/pt-br/assuntos/noticias/satelites-cbers-4a-e-floripasat-ja-estao-em-orbita-a-628-km-da-terra> (visited on 09/15/2024).
- [17] *Aalto-2: Satellite for qb50 constellation — aalto university*, Aalto.fi, May 2018. [Online]. Available: <https://www.aalto.fi/en/spacecraft/aalto-2-satellite-for-qb50-constellation> (visited on 09/15/2024).
- [18] *Lodestar unb*, Lodestar UnB, 2022. [Online]. Available: <https://lodestar.aerospace.unb.br/projects/alfacrux> (visited on 09/15/2024).
- [19] *Seam*, Gunter's Space Page, 2017. [Online]. Available: https://space.skyrocket.de/doc_sdat/seam.htm#:~:text=The%20satellite%20was%20launched%20on%2028%20November%202017 (visited on 09/15/2024).
- [20] *Flying laptop - eoportal*, Eoportal.org, 2017. [Online]. Available: <https://www.eoportal.org/satellite-missions/flying-laptop> (visited on 09/15/2024).

Quadrupole Antennas for Cubesats: Radiation Characteristics in Different Configurations and Initial Results

1st Yunior Alcantara Guevara
Dept. of Electrical and Electronics Engineering
UFSC
Florianópolis, Brazil
yunior.alcantarag@gmail.com

2nd Prof. Xisto Lucas Travassos Junior
Dept. of Electrical and Electronics engineering
UFSC
Florianópolis, Brazil
lucas.travassos@ufsc.br

3rd Prof. Eduardo Augusto Bezerra
Dept. of Electrical and Electronics Engineering
UFSC
Florianópolis, Brazil
bezerra.rs@gmail.com

Abstract—In a CubeSat design, analyzing the antenna radiation diagram is vital for the study of the link budget and the pointing budget. Quadrupole antennas are widely used in CubeSats, and their radiation patterns change depending on the array configuration and CubeSat structure variations. Although manufacturers adjust antennas relative to the CubeSat structure, understanding the radiation characteristics of quadrupole arrays can facilitate initial mission planning. This paper describes initial studies of radiation characteristics in CubeSats with quadrupole antennas, including monopole, dipole, v-dipole, and turnstile configurations. Simulations were performed using HFSS software, and measurements were made in an anechoic chamber. A 2U CubeSat structure was used for the study, as it was the one available for testing. All quadrupole configurations were simulated, from which radiation patterns were obtained. Initially, the simulation results were compared with real measurements of the antenna when it was in a monopole configuration, and both methods showed a correlation. Future tests will extend this to other quadrupole configurations and CubeSat structures of varying sizes.

Index Terms—CubeSat, Quadrupole Antenna, Radiation Diagram

I. INTRODUCTION

CubeSats have revolutionized space exploration by offering compact and low-cost satellite solutions. Among the main subsystems of a CubeSat, the communication module is essential to ensure data transmission and reception, which is directly related to the radiation characteristics of the antenna. Quadrupole antennas, in particular, can be arranged in different configurations, mainly monopole, dipole, v-dipole and turnstile, and are adopted due to their simplicity and efficiency [1]. However, the radiation pattern can vary significantly depending on the array configuration and the CubeSat design [1] [2].

Understanding radiation properties is crucial for effective mission planning, specifically for optimizing link and pointing

parameters. Although antenna manufacturers often adapt their designs to fit CubeSat form factors, more knowledge about radiation characteristics in various configurations would be very useful in preliminary mission planning. In this sense, this work presents a preliminary study of the radiation of the quadrupole antenna in various configurations, both by simulation and by measurement in an anechoic chamber.

A. Quadrupole Antenna for CubeSats

Quadrupole antennas, especially in monopole, dipole, v-dipole and turnstile configurations, are the majority in applications in CubeSats for operation in the VHF and UHF frequency regions; this can be attributed to their simple design characteristics, cost-effective nature and operational efficiency [1]. These types of antennas are considered particularly suitable for communication missions initiated in low Earth orbit (LEO), which is an area with the highest demand for durable long-range communication capabilities. According to sources such as [3], it is evident that the majority of CubeSat missions operate within the VHF and UHF frequency bands, a finding that is corroborated by a comprehensive review of the state of the art in 2023 [4], which highlights the dominance of these antennas in CubeSat applications. Some CubeSats utilize an orthogonal dipole (v-dipole) configuration that demonstrates characteristics similar to the turnstile and circularly polarized configuration, although with certain modifications in the radiation pattern predominantly attributed to the CubeSat structure [6].

The interaction between the antenna and the CubeSat structure has a major influence on the radiation characteristics. Previous studies, such as [2] and [6], have identified that the structural arrangement in the CubeSat influences the radiation pattern, and this sensitivity to the structure is one of the main drawbacks related to quadrupole antennas.

In addition, the antenna positioning on the CubeSat significantly influences its radiation pattern and coverage area. Investigating multiple antenna positioning configurations on different CubeSat designs may be impractical due to the vast number of possibilities, most of which rarely occur in reality. Therefore, this study focuses on a quadrupole antenna mounted on top of the standard 2U CubeSat structure. The goal of this approach is to provide detailed radiation performance of the antenna and provide input data that can be useful for a wider range of CubeSat missions.

II. ANTENNA CONFIGURATIONS

This study, focus on one quadrupole with four diferents configurations, resulting in four different radiation characteristics:

- 1) Monopole Antenna Configuration: A monopole antenna consists of a single radiating element that is perpendicular to the CubeSat structure.
- 2) Dipole Antenna Configuration: The dipole antenna comprises two opposing monopoles.
- 3) V-Dipole Array Configuration: In this configuration, two monopoles are arranged orthogonally on the CubeSat body.
- 4) Turnstile Antenna Configuration: The turnstile antenna is formed by crossing two dipoles, providing circular polarization.

III. SIMULATION SETUP AND RESULTS

The simulation setup utilized a simplified model of a 2U CubeSat structure and an antenna, as shown in Figure 1.

The material chosen for the structure and some parts of the antenna was aluminum, for the PCB it was copper, for the monopole supports it was nylon, and for the monopoles it was steel.

The software selected for the simulations was HFSS, to generate radiation patterns for each quadrupole configuration, maintaining a standard in the presentation of the results to avoid perspective errors.

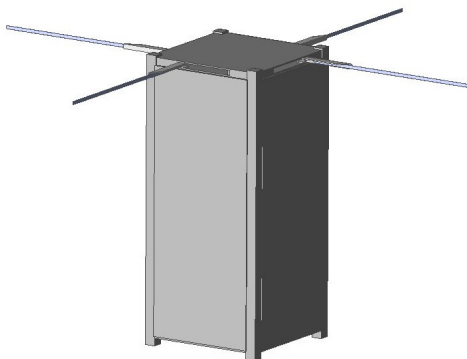


Fig. 1. Simulation model of the antenna and 2U cubesat

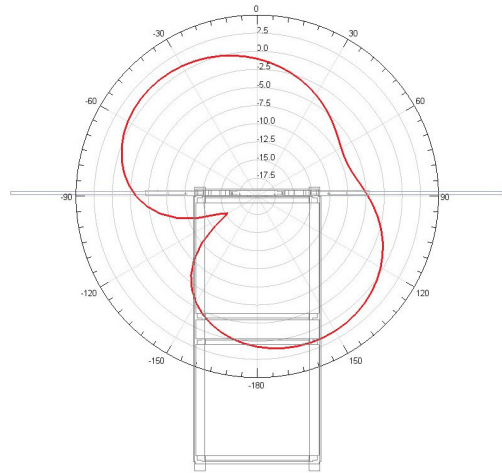


Fig. 2. Gain diagram of the antenna in monopole configuration for the 2U CubeSat simulation model in the x plane

In the context of HFSS, the Driven Solution Setup was created for an automatic configuration, while the frequency was set at 402 MHz and with a maximum of 20 steps. Furthermore, there was a *Maximum Delta D* set at 0.02. This therefore enabled the optimization of the four monopoles to operate at 402 MHz. For each of the monopoles, a *Wave Port* was assigned coupled with *Dembed* and impedance of 50 ohms. To replicate the four configurations, HFSS offers the functionality to independently activate or deactivate the feed for every port.

A. Simulation Results monopole configuration

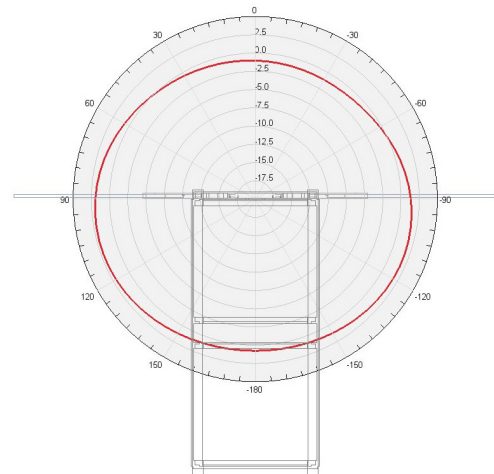


Fig. 3. Gain diagram of the antenna in monopole configuration for the 2U CubeSat simulation model in the y plane

In this subsection, the simulation results for the monopole configuration are presented. The antenna was analyzed in different planes to evaluate its performance in a 2U CubeSat simulation model. The gain diagrams illustrate the radiation

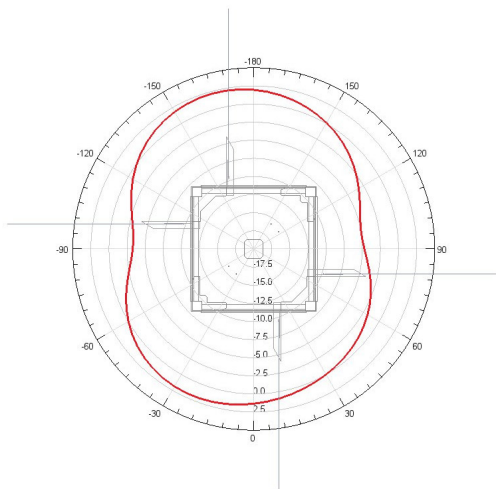


Fig. 4. Gain diagram of the antenna in monopole configuration for the 2U CubeSat simulation model in the z plane

pattern and the behavior of the antenna in the x, y, and z planes.

Figure 2 shows the gain diagram for the x plane. This antenna configuration shows a maximum gain of 3.5 dB. It is important to note the low gain part that shows the antenna at 120 degrees, where its -15 dB.

The antenna gain diagrams shown in Figure 3 and Figure 4 show a maximum gain of 3.5 dB, with the radiation being quite homogeneous at all angles, with the exception of the -90 and 90 degree angles in plane z, where the gain can reach -5 dB.

B. Simulation Results dipole configuration

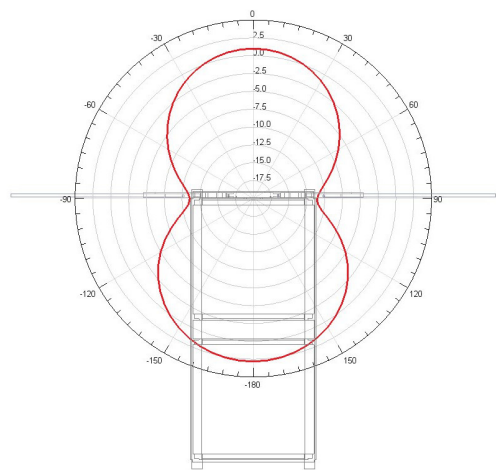


Fig. 5. Gain diagram of the antenna in dipole configuration for the 2U CubeSat simulation model in the x plane

The following figures show the simulation results for the dipole configuration, where the antenna's radiation patterns are evaluated in the x, y, and z planes.

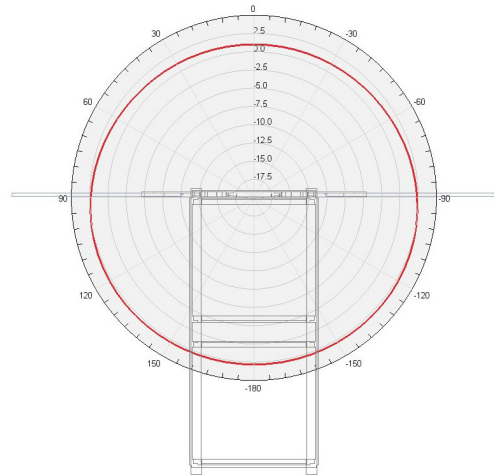


Fig. 6. Gain diagram of the antenna in dipole configuration for the 2U CubeSat simulation model in the y plane

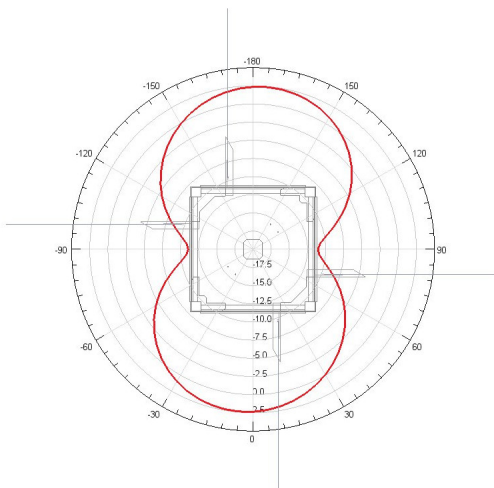


Fig. 7. Gain diagram of the antenna in dipole configuration for the 2U CubeSat simulation model in the z plane

Figure 5 illustrates the gain in the x plane. Here we can see that at angles -90 and 90 degrees the gain drops below -10 dB. The maximum gain is found at angles of 0 and 180 degrees, where it is approximately 2.5 dB.

Figure 6 shows the gain in the y plane. A homogeneous radiation diagram with a gain of approximately 2.5 dB is observed.

Finally, Figure 7 provides the gain diagram for the z plane. Similar to the x plane here we observe a radiation diagram with -10 dB gain for angles -90 and 90 degrees, and maximum gain is found at angles of 0 and 180 degrees, where it is approximately 2.5 dB.

C. Simulation Results V-dipole configuration

In the V-dipole configuration, the antenna's radiation pattern in the x, y, and z planes is analyzed and illustrated in the following figures.

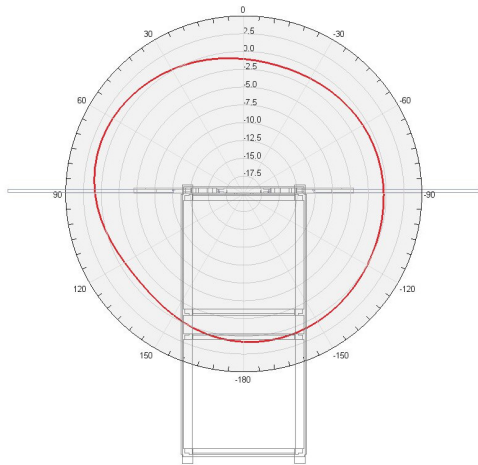


Fig. 8. Gain diagram of the antenna in V-dipole configuration for the 2U CubeSat simulation model in the x plane

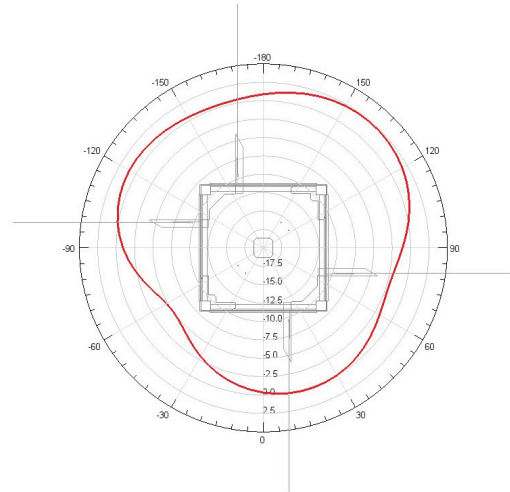


Fig. 10. Gain diagram of the antenna in V-dipole configuration for the 2U CubeSat simulation model in the z plane

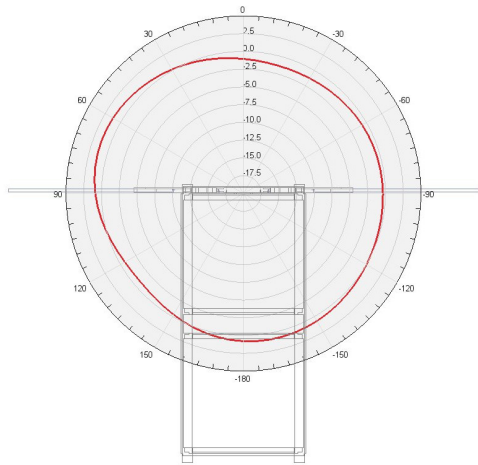


Fig. 9. Gain diagram of the antenna in V-dipole configuration for the 2U CubeSat simulation model in the y plane

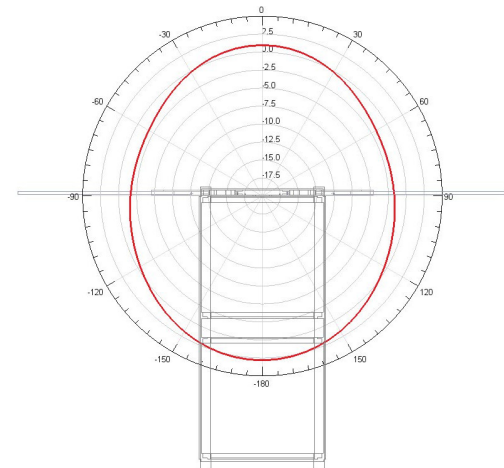


Fig. 11. Gain diagram of the antenna in turnstile configuration for the 2U CubeSat simulation model in the x plane

As can be seen in Figure 8, Figure 9 and Figure 10, the v-dipole configuration shows a radiation diagram with a homogeneous gain in all planes. The maximum gain is found between the angles of 120 and 150 degrees in the z plane, being approximately 2.5 dB, and the minimum gain is found in the same plane at the angle between the angles -30 and -60 degrees.

D. Simulation Results turnstile configuration

The turnstile configuration is analyzed in the x, y, and z planes, with the corresponding gain diagrams displayed below.

As observed in Figure 8, Figure 9 and Figure 10, the turnstile configuration shows a radiation diagram with a very homogeneous gain in all planes. The maximum gain is found at the 180 degree angle in the x and y planes, being approximately 2.5 dB, and the minimum gain in this case is the lowest of all the analyzed configurations, being -2.5 dB and is found in the same z plane at the angles 60 and -120 degrees.

IV. ANECHOIC CHAMBER SETUP AND RESULTS

Due to its simple design and frequent use in CubeSats, the monopole antenna configuration was selected for preliminary experimental verification. A semi-anechoic chamber, which has walls with high absorbance properties, reducing reflections and making the configuration controlled for accurate radiation pattern measurements, was used.

A. Experimental Setup

The cubesat model and antenna were fixed to a rotating platform inside the anechoic chamber, shown in Figure 14. For the monopole, two separate measurement series were made, placing the antenna in y and z panes in the current reference frame, and 72 measurements were made per measurement series, providing a resolution of 5 degrees for each plane. The

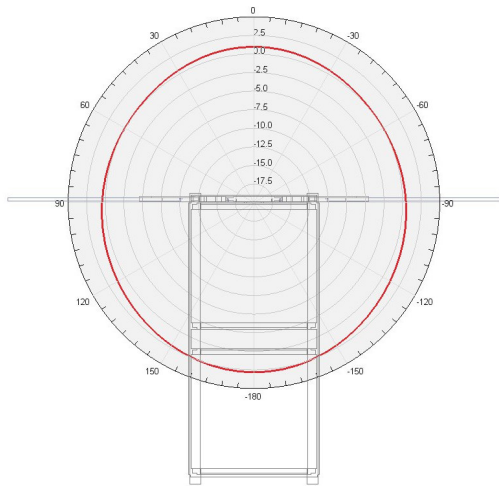


Fig. 12. Gain diagram of the antenna in turnstile configuration for the 2U CubeSat simulation model in the y plane

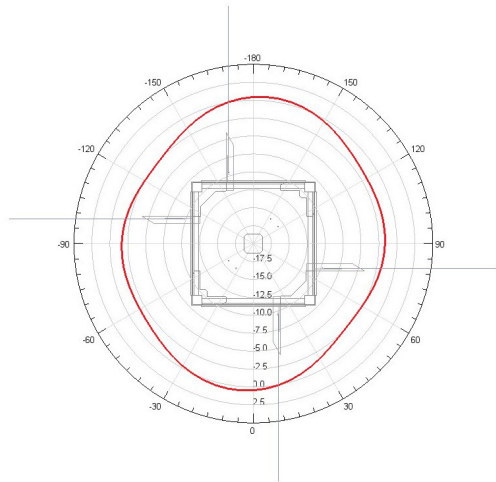


Fig. 13. Gain diagram of the antenna in turnstile configuration for the 2U CubeSat simulation model in the z plane

receiving antenna used was a herringbone antenna located 1 meter away from the satellite and at an altitude of 1.6 meters.

During the test, a signal at a frequency of 402 MHz and 30 dBm of power was placed on the CubeSat antenna, in transmitter function, combined with a 30 dB attenuator. To minimize the measurement error, the configuration was calibrated before the tests. This calibration allows the loss in the coaxial cable and the properties of the receiving antenna to be disregarded during the measurement execution, thus ensuring greater accuracy of the results.

B. Preliminary Experimental Results

The received signal was measured using the *ESU EMI Test Receiver*, and the values were recorded in tables. These values were then normalized and plotted on the polar plots shown in Figure in the figures below 15 and Figure 16. The polar plots

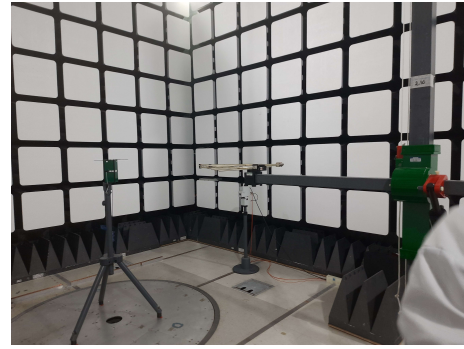


Fig. 14. Anechoic chamber setup for monopole antenna measurement

provide a visual representation of the antenna gain distribution over 360 degrees, allowing an analysis of the antenna radiation characteristics.

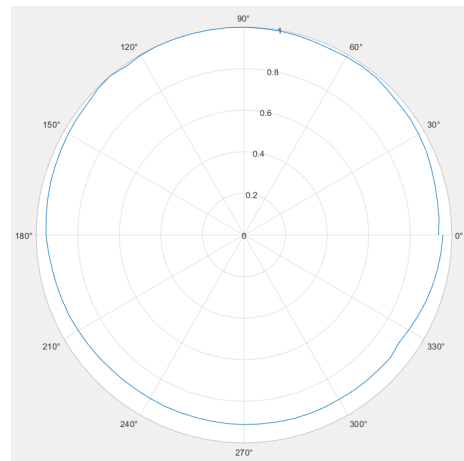


Fig. 15. Normalized radiation diagram obtained in the tests for the y plane.

Figure 15 shows the measurements made on the antenna in the y plane. The measured values indicate a homogeneous distribution along the 360 degrees, showing a similarity with the result obtained with the y plane of the simulated monopole.

Finally, Figure 16 presents the measurements made for the z plane, illustrating the antenna performance in 360 degrees. In this case, some points of minimum gain are observed that stand out in relation to the maximum gain, similar to what happens with the simulated monopole z plane.

V. CONCLUSION

This paper presents a first study of radiation characteristics for quadrupole antennas on CubeSats in monopole, dipole, V-dipole, and turnstile configurations.

The distinctive trait in the design of the monopole is its simplicity, having only a coaxial cable feed for each monopole.

Dipoles and V-dipoles present similar complexity, needing a previous circuit. However, for a CubeSat application, the V-dipole would be preferable due to its circular polarization, with a more uniform radiation pattern.

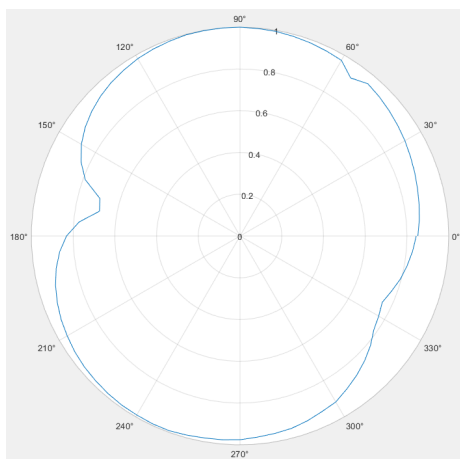


Fig. 16. Normalized radiation diagram obtained in the tests for the z plane.

The turnstile configuration is very desirable for CubeSats without attitude control, as it provides circular polarization and a highly uniform radiation pattern. However, this is at the expense of increased implementation complexity: whereas the linear antenna only requires two monopoles, the turnstile requires four, which reduces the number of radios that can be directly connected.

The monopole configuration is thus the easiest to realize. From dipole and V-dipole, V-dipole would, hence, become the most desirable configuration once circular polarization and absence of attitude control are favored. Finally, the turnstile antenna, due to its highly uniform radiation pattern, offers more reliable communications for a CubeSat with no attitude control, thus becoming the best choice for more stable links.

A. Future Work

A hardware will be designed for dipole, V-dipole and turnstile configurations to further this research. Experiments will then be performed in the anechoic chamber to verify the radiation patterns for these configurations using CubeSat arrays of various sizes.

REFERENCES

- [1] S. Abulgasm, "Antenna Designs for CubeSats: A Review," *IEEE Access*, 2021. [Online]. Available: <https://ieeexplore.ieee.org/document/9380228>
- [2] J. Coll Ortega, "Study and Simulation of CubeSats Communication Systems for ISARA Mission," 2014. [Online]. Available: https://upcommons.upc.edu/bitstream/handle/2117/102916/REPORT_268.pdf
- [3] Nanosat Database, "Nanosatellites Database," Nanosat.eu, [Online]. Available: <https://www.nanosat.eu>. [Accessed: Sept. 10, 2024].
- [4] NASA, "State of the Art: Communications," NASA, 2023. [Online]. Available: <https://www.nasa.gov/smallsat-institute/sst-soa/soa-communications/>
- [5] SpaceLab, "GOLDS-UFSC Design and Mission Overview," GitHub repository, 2020. [Online]. Available: <https://github.com/spacelab-ufsc/floripasat2-doc/blob/master/slb-fsat2-doc-v0.2.pdf>
- [6] M. Lankinen, "Design and Testing of Antenna Deployment System for Aalto-1 Satellite," Aalto University repository, 2015. [Online]. Available: <https://core.ac.uk/reader/80718000>
- [7] L. I. Buzas, "Design of a Deployable Tape Spring Half Wavelength Dipole Antenna for the ORCASat Nanosatellite," UVicSpace, University of Victoria, 2022. [Online]. Available: <https://dspace.library.uvic.ca/handle/1828/13717>
- [8] T. Dolapçı, "Design, Simulation, and Fabrication of CubeSat Antenna Systems," Middle East Technical University, 2020. [Online]. Available: <http://etd.lib.metu.edu.tr/upload/12625832/index.pdf>

Analysis of dielectric material for S-band microstrip antenna aimed at space applications

1st Lucas Ryan Carneiro

Dept. of Electrical and Electronics engineering
UFSC

Florianópolis, Brazil
lucasryan9999@gmail.com

2nd Yuniur Alcântara Guevara

dept. of Electrical and Electronics Engineering
UFSC

Florianópolis, Brazil
yuniur.alcantarag@gmail.com

3rd Eduardo Augusto Bezerra

dept. of Electrical and Electronics Engineering
UFSC

Florianópolis, Brazil
bezerra.rs@gmail.com

Abstract—This paper describes the work performed in order to choose the most suitable material to be used as dielectric substrate for patch antennas, operating on the S-band and designed for space applications. The study involved an extensive literature review on several antenna designs in order to obtain the most commonly used dielectric materials for this specific niche. As result of this study a table was generated, providing information about the dielectrics found in the reviewed literature, their frequency of use, dielectric constant value, their respective reference and the stage of development of the antenna design in which they were found. The analysis revealed a preference for lower permittivity (low dielectric constant). However, there were cases where it was employed materials with higher permittivity values, usually in association with other dielectrics. Two materials emerged as the most utilized substrates: Rogers RT Duroid 5880 and FR4. This study highlights the importance of choosing the correct dielectric based on the requirements and characteristics of each mission. The database created in this study, serves as a valuable reference for future projects of patch antenna designs, presenting a comparison between the dielectric materials used in today space technologies.

Index Terms—cubesat, dielectric, patch antenna, space applications.

I. INTRODUCTION

Satellites have historically been expensive and inaccessible to developing and emerging economies, but since the Cubesat's introduction, the scenario has shifted towards the increasing presence of space technology on those countries through government, industry and mainly academic institutions initiative. What once were big satellites, complex, inevitably expensive and only the main wealthy nations could afford to develop, launch and operate, are today much easier to develop, as it is possible nowadays to build a complete cubesat from components off the shelf, which facilitates the development by emerging economies [1].

Over the last decades, there has been a significant growth on the amount of Cubesats that have been launched into space. Only in the period of 2000 to 2016, it was seen a sharped

increase of almost 100% on the amount of launched satellites. And that significant growth is mainly due to the insertion of the Cubesat in the space segment. Cubesats are characterized as being small Cubes, measuring 10x10x10 cm per unit (1U) and with very modular components within it, in addition to very limited resources. Additionally, from 2016 to 2023 the amount of satellites launched into space grew from around 1090 satellites to 6468, showing the ever growing necessity for satellite's generated information and products [2] [3].

Satellites are composed of several subsystems for its correct functionality, such as: the electrical system, responsible for managing the energy in the satellite, and assuring the basic energy for its operation; the communication module, that is responsible for exchanging information with the ground station and/or other satellites; the attitude control and determination, that maintains the satellite in its correct orientation in space, among others. The communication module stands out as being one of the most crucial parts of the satellite, both for its survival, allowing monitorization of its health and status, but also as primary payloads, mainly in missions with transmission of data or providing communication services [1].

Such importance of the communication module is seen in [3], where from all the 7560 satellites present in their dataset, 73% of them had as primary mission, communication, being led by Starlink constellation of satellites. With this percentage, it is shown the growing necessity of satellite communication in current societies, covering a big range of applicability, such as in internet access, telecommunication services and data transmission. Following this trend, it is evident the need and importance of antenna development, once that antennas are the main component of the communication system, both for transmitting and receiving signals.

In this paper patch antennas were analyzed focused for S-band frequencies. Microstrip type of antennas have become one of the most popular types in the modern space industry. Accounting for approximately 18% of all the different types of antennas used in cubesats during the period of 2003 -

Identify applicable funding agency here. If none, delete this.

2012 as shown in [4]. Their popularity stems from their lightweight, low profile structure and cost-effectiveness, which makes them the ideal choice for compact satellite missions, such as Cubesat, which have strict limitations in physical size, power consumption and weight.

There are several ways to improve the bandwidth of a microstrip antenna, as obtaining a broader frequency range is very useful for applications that require high data rates or operations across multiple frequency bands. Normally the most common ways of increasing the bandwidth consists of utilizing a thicker dielectric substrate alongside with a material with a low dielectric constant [5].

II. CONSIDERATIONS

In order to choose the dielectric material for a patch antenna design, it is needed to take into account more than performance characteristics such as gain and bandwidth, but also physical constrains and specifications of the mission for the antenna. Antenna for a Cubesat mission impose several restrictions on the antenna, such as: limited size, power budget, and weight; as well as the need to resist harsh environmental situations, as high radiation exposure, temperature fluctuations and mechanical stress [62]. Therefore, to obtain an appropriate dielectric material, the choice has to consider several trade-offs between mechanical and electrical constrains.

For example, in the case of Cubesats, where the antenna has a very limited size, materials with a higher dielectric constant (such as FR4) might be chosen, in order to minimize the physical size of the antenna to be able to fit within the nanosatellite, even if that results in obtaining a lower gain. If the mission specifications require a strong signal, then a substrate with a lower dielectric material might be preferable (such as RT Duroid 5880), given its ability to minimize the signal loss and increase the gain of the signal.

III. ANALYSIS OF DIELECTRICS

For the present work, it was analyzed a total of 54 scientific papers regarding patch antenna designs operable on the S-band frequency range. All of them which were utilized for space applications, showing their flying heritage and constant utilization. This study aimed at investigating material properties of these antenna designs, particularly focusing on their used dielectric substrate. The dielectric material has a crucial role in the microstrip antenna design, once it directly affects signal propagation speed, antenna efficiency and bandwidth [60]. In this study it was sought to create a comprehensive database for future utilization on patch antenna design projects, particularly for space applications, which also requires light weight, durability and good performance.

The dielectric material has a direct impact on the antenna performance, once it is responsible for how the electromagnetic waves travels through the substrate, also having influence in both the size of antenna and its efficiency. Therefore, having information about the materials that were used in previous designs helps to make a choice with foundation about the already used materials for future utilization. Additionally, having

information about the level of development of these antennas, such as if the antenna was fabricated, launched into space, or only simulated in software, prepares the antenna designer about the practical applicability and maturity of the materials and designs in real antenna, aimed at space environments.

Following the analysis of the papers, table I was generated, where it comprises some useful information about the substrates and the designs of the examined antennas. In the first column it is presented the dielectric material used in each of the designs, which are included in the table the most commonly used substrates for S-band patch antenna projects, this knowledge can often be essential when selecting materials for such applications. In the second column it is indicated how many times the dielectric has appeared in the analyzed papers, offering information about the popularity and reliability of the materials in space applications. The materials that have appeared more frequently, are more likely to have their properties validated by several projects and as consequence they might be able to be more trustworthy and reliable.

The third column dispose the references of the paper of each of the antenna design analyzed in the study. This column is organized according to the state of development of the antenna, which is described in the fifth column. The states of development are divided in three groups: Fabricated Prototype, Launched and Simulation. This differentiation helps identify whether the antenna design has successfully deployed in space, or if it was only tested in a laboratory on Earth, or if it was a case, where the design was only explored through simulation in software. Understanding the degree of reliability the material has, as well as its position in relation to real-world applications are extremely important for engineers to replicate or build a project upon these designs.

The fourth column lists the dielectric constants of the substrates of the first column. The dielectric constant is a fundamental property, once it affects how the electromagnetic waves propagates through the material. Lower values of the constant generally results in larger antennas, but also offers a wider bandwidth, whereas a higher value for the dielectric constant normally results in a smaller size of antenna, but with a more limited bandwidth. The professional who is responsible for an antenna project, must take this trade-off into account for its personal project limitations and characteristics. For Cubesat missions in specific, it might be reasonable to choose a substrate with a higher value of dielectric constant, once it results in a smaller antenna, to be most adequate for the limited size and space within a Cubesat. Unless that a wide bandwidth and higher data rate is an important aspect of the mission, in this case the trade-off mentioned must be more thoroughly analyzed.

As there are different types of antennas, some of them utilized more than one type of substrate for their design, as result of a combination of dielectrics. This combination of dielectrics or substrate layers affects the overall performance of the antenna. The use of combination of different materials is often done in order to obtain specific performance character-

Table of dielectrics obtained in the study				
Dielectric	N°	Reference	Dielectric constant value	Stage of development
Rogers RT/duroid 5880 material (2 layers) / Rogers RT/duroid 6010	1	[6]	2.2 / 10.2	Fabricated Prototype
Rogers RT Duroid 5880	11	[11] [17] [25] [29] [10] [8] [16] [24] [43] [?] [50]	2.2	4 - Fabricated Prototype 1 - Launched 6 - Simulation
Rogers RO3210	1	[7]	10.2	Fabricated Prototype
Rogers RT5870	6	[32] [9] [28] [34] [47] [53]	2.33	1 - Fabricated Prototype 5 - Simulation
Double-sided Glass Epoxy Sheet FR-4	1	[12]	4.3	Fabricated Prototype
pyralux FR 9111	1	[13]	3	Fabricated Prototype
Rogers RO4003C	1	[14]	3.38	Fabricated Prototype
3D printed polyethylene terephthalate glycol (PETG)	1	[15]	2.5	Fabricated Prototype
FR4	11	[18] [20] [21] [30] [33] [36] [44] [51] [52] [56] [57]	4.3/4.4 /4.6	6 - Fabricated Prototype 5 - Simulation
Rogers RT Duroid-5880 (Dielectric substrate for radiating patch) / FR4 (Dielectric substrate for RIS metallic patches)	1	[19]	2.2/4.4	Simulation
polylactic acid (PLA)	3	[41] [48] [22]	2.1/2.55/3.1	2 - Fabricated Prototype 1 - Simulation
Rogers Arlon DiClad 880	1	[23]	2.2	Fabricated Prototype
AF32/Solar cell/Kapton/FR4epoxy(RIS)	1	[26]	4.5/16/3/4.4	Simulation
NPC-H220A	1	[27]	2.17	Simulation
Rogers RT Duroid 5880, Rogers RT Duroid 5880, Rogers RT duroid 6010	1	[31]	2.2/2.2/10.2	Simulation
Soda lime glass	1	[35]	7.75	Simulation
Rogers TMM10	1	[37]	9.2	Fabricated Prototype
F4B	1	[38]	2.65	Fabricated Prototype
glass epoxy	1	[39]	4.4	Fabricated Prototype
Y36 ferrite	1	[40]	13.7	Fabricated Prototype
Taconic TLP-3	1	[42]	2.33	Fabricated Prototype
glass epoxy / RO3003	1	[46]	4.4/3.0	Fabricated Prototype
R04003C / RO4360G2 / Fast Rise 27 (FR27)	1	[49]	3.49/6.15/2.75	Fabricated Prototype
Taconic Cer-10	1	[54]	10.2	Fabricated Prototype
Taconic RF-35	1	[55]	3.5	Fabricated Prototype
R4350B	1	[59]	3.48	Fabricated Prototype
Roger 4350 / Roger 5880	1	[58]	3.48/2.2	Fabricated Prototype
Total	54			

TABLE I
DIELECTRIC MATERIALS OBTAINED IN THE STUDY

istics. In cases where it was utilized more than one dielectric, the materials were listed in the first column of I separated by slashes.

The use of multiple substrates can significantly impact the dielectric constant of the antenna structure. Each dielectric material has its own constant value, and the combination of different materials can alter the effective value of the dielectric constant of the antenna. Therefore in the fourth column of the I, when utilized more than one substrate, the different dielectric constants are listed separated by slashes, corresponding to their respective dielectric in the first column.

Analyzing the results obtained with table I, the most used dielectric material for patch antennas aimed at space applications were equally Rogers RT Duroid 5880 and Flame Retardant 4 (FR4), where they were both utilized a total of 11 times in the reviewed papers. Both of the main materials were also combined with several other dielectrics, even with each other, in order to experiment different substrates configurations.

These configurations are frequently used to test antenna and optimize them into specific project requirements and various frequency ranges.

1) *Comparison: Rogers RT Duroid 5880 x FR4:* Rogers RT Duroid 5880, known for its low dielectric loss and low dielectric constant, its valued in high-frequency applications for its excellent properties. FR4, is an ideal solution for cost-effectiveness applications, once it presents good general performance and it is cheaper for implementation.

As shown in [5], the dielectric constant of a material has a crucial role in the antenna performance. Specifically, the lower the value of the dielectric constant for the same design of a patch antenna, the higher the gain of the antenna, concomitantly, the bandwidth also increases with the constant value, from that it is clear that for the same patch antenna design, the RT Duroid 5880 leads to a better performance. Nevertheless, the appropriate material to be chosen for a design has to fit the conditions proposed on the specific project of the antenna.

IV. CONCLUSION

After analyzing table I, it was obtained two materials which appeared a total of 11 times each, being the most used dielectrics in the reviewed papers, these materials were: Rogers RT Duroid 5880 and Flame Retardant 4 (FR4), being equally the most used materials for S-band microstrip antennas aimed at space applications, with dielectric constants respectively of 2.2 and 4.4 (primarily). Rogers RT Duroid 5880 is a known substrate by having characteristics such as its low dielectric loss and superior performance at high frequencies, what makes it a popular choice for missions where high gain and efficiency are important factors. On the other hand, the FR4 material its an excellent cost-effective option, where it presents a decent performance while still meeting budgetary and manufacturing constrains, which is particularly common in Cubesat missions, where cost is a significant factor.

It is also observable that the majority of the materials on I were present on projects that were tested on fabricated prototypes of antennas, a total of 31 of the 54 materials analyzed, emphasizing the importance of the validation of antenna designs in the physical world. Fabricating prototypes are important for validating parameters, such as: radiation pattern, gain and bandwidth in real-world conditions. These tests are vital to guarantee that the antenna performs as expected in the physical world. Following the 'Fabricated Prototype' stage of development, the 'Simulation' followed with 22 design out of the total 54. Although the simulation stage is very important in the beginning of a design, it does not replicate the physical reality of an antenna's performance, they fail to account for problems that could arise during fabrication, integration or deployment, evidencing the necessity of the prototyping afterwards. For last, it is possible to observe that only one of the designs analyzed were launched into space, one microstrip antenna design utilizing Rogers RT Duroid 5880, emphasizing the high performance and reliability of the material for space applications.

The table generated in this study serves as a valuable tool for engineers and antenna designers when choosing a dielectric material for future projects. This study provides a comparative analysis of the materials used currently in the space industry and helps to guide decisions through I based on specific needs of a project by providing an informed reference. Furthermore, the inclusion of the state of development of the antenna ('Simulation', 'Fabricated prototype' or 'Launched'), gives a better understanding for the antenna designer about the validation of the material, giving information about the materials that have successfully been launched into space, and which are still in an experimental phase.

REFERENCES

- [1] K. Woellert, P. Ehrenfreund, A. J. Ricco, and H. Hertzfeld, "Cubesats: Cost-effective science and technology platforms for emerging and developing nations," *Advances in space Research*, vol. 47, no. 4, pp. 663–684, 2011
- [2] J. R. Kopacz, R. Herschitz, and J. Roney, "Small satellites an overview and assessment," *Acta Astronautica*, vol. 170, pp. 93–105, 2020.
- [3] U. of Concerned Scientists, "UCS satellite database 5-1-2023, [online]." <https://www.ucsusa.org/resources/satellite-database>, accessed 2024-05-29.
- [4] S. Liu, P. I. Theoharis, R. Raad, F. Tubbal, A. Theoharis, S. Iranmanesh, S. Abulgasem, M. U. A. Khan, and L. Matekovits, "A survey on cubesat missions and their antenna designs," *Electronics*, vol. 11, no. 13, 2022.
- [5] K. Rop and D. Konditi, "Performance analysis of a rectangular microstrip patch antenna on different dielectric substrates," *Innovative Systems Design and Engineering*, vol. 3, no. 8, pp. 1727–1729, 2012.
- [6] S. S. Kabir, M. H. Khan, and S. I. Latif, "A multi-band circularly polarized shared aperture antenna for space applications at s and x bands," *Electronics*, vol. 12, no. 21, 2023.
- [7] S. G. Dave, "Design and prototype of a phased-array antenna for nanosatellite radar and communication applications," 2018.
- [8] M. A. Zafrane, M. A. Mebrek, H. Souillah, Z. B. Madouri, and B. Abes, "Novel design and optimization of s band patch antenna for space application by using a gravitational search algorithm," *International Journal on Interactive Design and Manufacturing (IJIDeM)*, vol. 17, no. 3, pp. 1131–1148, 2023.
- [9] M. S. Hossen and S. Noman, "Antenna design for university low cost student-built cubesat missions," in *2021 IEEE International Conference on Signal Processing, Information, Communication & Systems (SPIC-SCON)*, pp. 32–35, IEEE, 2021.
- [10] M. T. Islam, M. Cho, M. Samsuzzaman, and S. Kibria, "Compact antenna for small satellite applications [antenna applications corner]," *IEEE Antennas and Propagation magazine*, vol. 57, no. 2, pp. 30–36, 2015.
- [11] A. Kaur and P. K. Malik, "Multiband elliptical patch fractal and defected ground structures microstrip patch antenna for wireless applications," *Progress In Electromagnetics Research B*, vol. 91, 2021.
- [12] N. Meirambekuly, A. A. Temirbayev, Z. Z. Zhanabaev, B. A. Karibayev, T. A. Namazbayev, B. A. Khaniyev, and A. K. Khaniyeva, "Dual-band optical imaging system-integrated patch antenna based on anisotropic fractal for earth-observation cubesats," *Ain Shams Engineering Journal*, vol. 13, no. 2, p. 101560, 2022.
- [13] T. Praludi, Y. Taryana, K. Paramayudha, B. Prawara, Y. Rahayu, C. B. A. Wael, Y. Sulaeman, B. E. Sukoco, R. Sariningrum, H. Kurniadin, et al., "Design of flexible 3.2 ghz rectangular microstrip patch antenna for s-band communication," *Jurnal Elektronika dan Telekomunikasi*, vol. 21, no. 2, pp. 140–145, 2021.
- [14] A. H. Lokman, P. J. Soh, S. N. Azemi, M. F. Jamlos, H. Lago, and A. Abdulllah Al-Hadi, "Gain enhanced circularly polarized antenna integrated with artificial magnetic conductor for s-band pico-satellites," *International Journal of RF and Microwave Computer-Aided Engineering*, vol. 28, no. 7, p. e21462, 2018.
- [15] G. Montisci, G. Mura, G. Muntoni, G. A. Casula, F. P. Chietera, and M. Aburish-Hmidat, "A curved microstrip patch antenna designed from transparent conductive films," *IEEE Access*, vol. 11, pp. 839–848, 2022.
- [16] M. K. Kumar, P. P. Sai, and J. Pushpa, "Design and analysis of microstrip square patch antenna at 2.4 ghz frequency," *International journal of multidisciplinary advanced research trends*, vol. 4, no. 1, p. 1, 2017.
- [17] S. Pandav, G. Sadhukhan, T. K. Das, S. K. Behera, and M. Mohanty, "Circularly polarized high gain koch fractal antenna for space applications," *Sādhanā*, vol. 47, no. 4, p. 276, 2022.
- [18] N. A. H. Putra, E. Edwar, et al., "Design of multiband microstrip antenna on cubesat for ads-b communication," *eProceedings of Engineering*, vol. 10, no. 5, 2023.
- [19] Z. Patel and A. Sarvaiya, "A novel compact rhcp antenna with wide 3 db ar bandwidth for s-band irnss application," in *2023 International Conference on Device Intelligence, Computing and Communication Technologies (DICCT)*, pp. 416–421, IEEE, 2023.
- [20] W. N. Saputra, B. Prasetya, and Y. Wahyu, "Design and realization of two array triangle patch of microstrip antenna with gold plat at frequency 2400–2450 mhz for hexagonal nanosatellite," in *2013 International Conference of Information and Communication Technology (ICoICT)*, pp. 322–327, IEEE, 2013.
- [21] S. O. Benyamin, H. Wijanto, V. S. W. Prabowo, H. Prananditya, S. M. Oktaviani, et al., "Design and characterization of rectangular array microstrip antenna for cubesat s-band transmitter," in *2020 3rd International Conference on Information and Communications Technology (ICOIACT)*, pp. 476–481, IEEE, 2020.
- [22] E. Pittella, L. D'Alvia, and E. Piuze, "Cubesat satellite patch antenna designed with 3d printable materials: a numerical analysis," in *Journal*

- of Physics: Conference Series, vol. 2526, p. 012042, IOP Publishing, 2023.
- [23] A. D. Johnson, V. Manohar, S. B. Venkatakrishnan, and J. L. Volakis, "Low-cost s-band reconfigurable monopole/patch antenna for cubesats," *IEEE Open Journal of Antennas and Propagation*, vol. 1, pp. 598–603, 2020.
- [24] N. Thunyakaset, S. Ratanacharoen, A. Namsang, R. Lerdwanittip, P. Chomtong, and P. Akkaraekthalin, "Design of s-band cubesat antenna," in *2021 9th International Electrical Engineering Congress (iEECON)*, pp. 543–546, IEEE, 2021.
- [25] S. M. Hasan, M. Samsuzzaman, M. Rana, T. Islam, and T. Islam, "Circularly polarized s band patch antenna for small satellite application," in *2017 IEEE International Conference on Telecommunications and Photon-ics (ICTP)*, pp. 200–204, IEEE, 2017.
- [26] A. Ygnacio-Espinoza, D. Penalzoza-Aponte, J. Alvarez-Montoya, A. Mesco-Quispe, and M. Clemente-Arenas, "Quasi-transparent meshed and circularly polarized patch antenna with metamaterials integrated to a solar cell for s-band cubesat applications," in *2018 International Conference on Electromagnetics in Advanced Applications (ICEAA)*, pp. 605–608, IEEE, 2018.
- [27] P. P. Sitompul, J. T. S. Sumantyo, F. Kurniawan, C. E. Santosa, T. Manik, A. Awaludin, and M. Y. Chua, "Dual-band circularly-polarized microstrip antenna for nano satellite," in *2018 Progress in Electromagnetics Research Symposium (PIERS-Toyama)*, pp. 864–867, IEEE, 2018.
- [28] M. J. C. Barbosa, P. L. R. Casilao, R. A. O. Fernando, R. M. M. Beato, M. J. V. De La Rosa, and R. A. Inojosa, "A new modification approach to enhance the em performance of an s-band patch antenna for nanosatellite application," in *2022 IEEE Asia-Pacific Conference on Geoscience, Electronics and Remote Sensing Technology (AGERS)*, pp. 99–103, IEEE, 2022.
- [29] M. Prajapati and A. Rawat, "Performance analysis of irnss using compact microstrip patch antenna for s band application," *Acta Geophysica*, vol. 68, no. 4, pp. 1223–1228, 2020.
- [30] H. M. Tun, Z. T. T. Lin, D. Pradhan, and P. K. Sahu, "Slotted design of rectangular single/dual feed planar microstrip patch antenna for siso and mimo system," in *2021 International Conference on Electrical, Computer and Energy Technologies (ICECET)*, pp. 1–6, IEEE, 2021.
- [31] S. S. Kabir and S. I. Latif, "Dual band high gain shared aperture antenna for cubesat application," in *SoutheastCon 2022*, pp. 441–442, IEEE, 2022.
- [32] M. Samsuzzaman, M. Islam, H. Arshad, J. Mandeep, and N. Misran, "Circularly polarized s band dual frequency square patch antenna using glass microfiber reinforced ptfе composite," *The Scientific World Journal*, vol. 2014, no. 1, p. 345190, 2014.
- [33] R. Azim, M. Samsuzzaman, T. Alam, M. Islam, M. Faruque, M. Zaman, and M. Islam, "Circularly polarized patch antenna for s-band satellite applications," in *2015 International Conference on Space Science and Communication (IconSpace)*, pp. 402–405, IEEE, 2015.
- [34] H. Chaabane, W. Jaballah, and N. Rokbani, "Fpa based design of 2 l microstrip antenna array for cubesat communications," in *2018 15th International Multi-Conference on Systems, Signals & Devices (SSD)*, pp. 1055–1060, IEEE, 2018.
- [35] J. Shinde, P. Shinde, and N. Gondane, "Circularly polarized transparent equilateral triangular shaped antenna with defected ground," in *2016 International Conference on Computing Communication Control and Automation (ICCUBEA)*, pp. 1–6, IEEE, 2016.
- [36] S. Dash, S. Rout, V. Gupta, et al., "Design of a s band circularly polarized microstrip patch antenna using ferrite disk," *Microwave Review*, vol. 23, no. 1, 2017.
- [37] D. A. Jiménez, A. Reyna, L. I. Balderas, and M. A. Panduro, "Design of 4x4 low-profile antenna array for cubesat applications," *Micromachines*, vol. 14, no. 1, p. 180, 2023.
- [38] M. Gao, P. Yang, and J. Nan, "Sixteen-element broadband circularly polarized microstrip antenna array for s-band," *Progress in Electromagnetics Research C*, vol. 128, pp. 195–205, 2023.
- [39] R. K. Kanth, W. Ahmad, Y. Amin, P. Liljeberg, L.-R. Zheng, and H. Tenhunen, "Analysis, design and development of novel, low profile 2.487 ghz microstrip antenna," in *2010 14th International Symposium on Antenna Technology and Applied Electromagnetics & the American Electromagnetics Conference*, pp. 1–4, IEEE, 2010.
- [40] E. Arnaud, L. Huitema, R. Chantalat, A. Bellion, and T. Monediere, "Circularly polarized ferrite patch antenna for leo satellite applications," *International Journal of Microwave and Wireless Technologies*, vol. 12, no. 4, pp. 332–338, 2020.
- [41] A. E. Ahmed and W. A. Ali, "Analysis and design of 3-d printed fractal triangular antenna for wireless communications applications," in *2020 International Conference on Electrical, Communication, and Computer Engineering (ICECCE)*, pp. 1–5, IEEE, 2020.
- [42] M. K. Ray, K. Mandal, N. Nasimuddin, A. Lalbakhsh, R. Raad, and F. Tubbal, "Two-pair slots inserted cp patch antenna for wide axial ratio beamwidth," *IEEE Access*, vol. 8, pp. 223316–223324, 2020.
- [43] S. Shankarappa and V. S. Rao, "S-band circularly polarized transceiver antenna for leo satellites," in *2019 IEEE 5th International Conference for Convergence in Technology (I2CT)*, pp. 1–4, IEEE, 2019.
- [44] N. El hassinate, A. O. Said, and Z. Guennoun, "Dual-band circularly polarized slotted patch antenna for s-band cubesat communication system," *CEAS Space Journal*, pp. 1–12, 2024.
- [45] S. Shankarappa and V. S. Rao, "Transceiver antenna for telemetry and telecommand applications," in *2019 International conference on communication and signal processing (ICCS)*, pp. 0511–0513, IEEE, 2019.
- [46] R. K. Kanth, P. Liljeberg, H. Tenhunen, W. Ahmad, S. Shakya, and L. R. Zheng, "Autonomous use of fractal structure in low cost, multiband and compact navigational antenna," in *2010 10th Mediterranean Microwave Symposium*, pp. 135–138, IEEE, 2010.
- [47] L. H. Abderrahmane and A. Brahimi, "A new design of dual band fractal antenna for leo applications," in *The Eighth International Conference on Systems and Networks Communications*, 2013.
- [48] G. Muntoni, G. A. Casula, and G. Montisci, "The 3d-printed non-radiating edge gap-coupled curved patch antenna," *IEEE Open Journal of Antennas and Propagation*, vol. 4, pp. 229–236, 2023.
- [49] F. Ferreira, J. M. Vieira, D. Fumagalli, L. S. Pereira, and M. V. Heckler, "Circularly polarized aperture-coupled microstrip antenna for nanosatellites," *XXXV Simpósio Brasileiro de Telecomunicações e Processamento de Sinais (SBRT 2017)*, pp. 57–61, 2017.
- [50] N. N. Rather and S. Suganthi, "Electrically small s-band antenna for cubesat applications," in *2017 International Conference on Wireless Communications, Signal Processing and Networking (WiSPNET)*, pp. 1687–1691, IEEE, 2017.
- [51] N. K. S. Wah and H. Tun, "Development of microstrip patch antenna design for s-band application," *American Journal of Electromagnetics and Applications*, vol. 6, no. 1, pp. 17–23, 2018.
- [52] M. Pushpalatha, N. Namana, T. Navadagi, and D. Varun, "Design of wide-band microstrip antenna for s-band telemetry applications," *Advanced Electromagnetics*, vol. 12, no. 1, pp. 70–76, 2023.
- [53] S. Gunaseelan and M. Murugan, "High gain patch antenna for cubesat," in *2016 International Conference on Wireless Communications, Signal Processing and Networking (WiSPNET)*, pp. 52–54, IEEE, 2016.
- [54] Y. Yao, S. Liao, J. Wang, K. Xue, E. A. Balfour, and Y. Luo, "A new patch antenna designed for cubesat: Dual feed, ls dual-band stacked, and circularly polarized," *IEEE Antennas and Propagation Magazine*, vol. 58, no. 3, pp. 16–21, 2016.
- [55] S. Xu-bao, "A design of microstrip antenna for s-band," in *2020 IEEE 3rd International Conference on Computer and Communication Engineering Technology (CCET)*, pp. 299–302, IEEE, 2020.
- [56] Parul Shrivastava and Sunil Kumar Singh, "Triangular Patch Antenna with Defected Ground Plane," *International Journal for Scientific Research and Development* 5.10 (2017): 409-411.
- [57] F. Armin, A. Noer, S. Prasetya, et al., "Modification of 2.2 ghz s-band rectangular patch microstrip antenna using truncated corner method for satellite applications," in *2020 3rd International Seminar on Research of Information Technology and Intelligent Systems (ISRITI)*, pp. 284–288, IEEE, 2020.
- [58] A. Akbar, E. T. Rahardjo, F. Y. Zulkifli, and Z. Rainaldy, "Design of microstrip antenna with dgs slot for satellite applications," in *2021 IEEE International Conference on Aerospace Electronics and Remote Sensing Technology (ICARES)*, pp. 1–5, IEEE, 2021.
- [59] R. S. Goopa, M. A. Hossain, and Q. D. Hossain, "Design and fabrication of a circular polarization microstrip patch antenna for s band applications,"
- [60] V. Hanumante and S. Roy, "Comparative study of microstrip patch antenna using different dielectric materials," in *9th International Conference on Microwaves, Antenna, Propagation and Remote Sensing (ICMARS-2013)*, pp. 56–60, 2013.
- [61] R. K. Raj, V. Sharma, P. Joshi, H. Choudhary, A. Tripathi, et al., "Comparative analysis of dielectric substrate materials (fr-4 & rt/duriod 5880) for antenna array (8* 1) designing," *Materials Today: Proceedings*, vol. 74, pp. 172–178, 2023.

- [62] S. Abulgasem, F. Tubbal, R. Raad, P. I. Theoharis, S. Lu, and S. Iranmanesh, "Antenna designs for cubesats: A review," *IEEE Access*, vol. 9, pp. 45289–45324, 2021.
- [63] K. Tharun, V. Vivekanand, T. Ravi, and M. Sugadev, "Design and fabrication of micro strip antenna for cubesat applications," in *IOP Conference Series: Materials Science and Engineering*, vol. 590, p. 012052, IOP Publishing, 2019.

ROCUS-1: The Preliminary Design Overview

1st Lucas Ryan Carneiro

Dept. of Electrical and Electronics Engineering
UFSC

Florianópolis, Brazil
lucasryan9999@gmail.com

4th Alec Oliveira Coelho

Dept. of Electrical and Electronics Engineering
UFSC

Florianópolis, Brazil
aleccoelho50@gmail.com

4th Felipe Costa Juliano

Dept. of Electrical and Electronics Engineering
UFSC

Florianópolis, Brazil
felipecostajuliano@live.com

5th Yunior Alcantara Guevara

Dept. of Electrical and Electronics Engineering
UFSC

Florianópolis, Brazil
yunior.alcantarag@gmail.com

3rd Eduardo Augusto Bezerra

Dept. of Electrical and Electronics Engineering
UFSC

Florianópolis, Brazil
bezerra.rs@gmail.com

Abstract—ROCUS-1 Mission will develop atmospheric profiling, especially in South America and over Brazil, using GNSS Radio Occultation techniques. The program is presently being funded by the Government of Brazil through CNPQ. In addition, the aims are to enhance meteorological weather forecasting based on highly accurate data concerning temperature, pressure, humidity, and air density. It is a detailed design review of the PDR mission requirements, communication links, mass considerations, and power allocations. The ROCUS-1 satellite is bound to extend the current meteorological capability by a significant factor and hence higher accuracy even at the most adverse atmospheric conditions.

Index Terms—Radio Occultation in CubeSat, GNSS, Preliminary Design Review

I. INTRODUCTION

The Radio Occultation (RO) technique was first introduced in the 1960s during NASA's Mars missions. Since then, RO has been used extensively to probe planetary atmospheres across the solar system. In the late 1980s, researchers at JPL proposed using GPS signals to profile the Earth's atmosphere, leveraging the refraction of GNSS signals as they pass through atmospheric layers [1]. This approach enables precise measurements of atmospheric variables such as temperature, pressure, humidity, and density, making RO one of the most reliable techniques for atmospheric profiling today.

For obtaining profiles of the Earth, is based at the refraction property of the GNSS signal from space. Once the signal passes through the atmosphere of a planet, it is refracted due to the composition of the atmosphere, generating a bending angle from the ray path and consequently a perturbation on it's phase, derivative from the Doppler Effect. From that, it is possible to retrieve precise information about temperature,

Identify applicable funding agency here. If none, delete this.

pressure, atmospheric density, humidity and winds in the neutral atmosphere, as well as electron density in the ionosphere [1] [2].

The Radio Occultation approach for analyzing and generating atmospheric profiles is one of the most accurate means available in the world today, complementing microwave and infrared sounders with its precise information even in cloudy conditions. It can also contribute with the identification of bias in both the IR and microwave sounding systems for weather forecasts [3].

Forecast of meteorological conditions is overall enhanced when taken RO measurements into account. Looking at brazilian context, it might improve the length of the useful forecasts up to 28.4% within the tropical region, which contemplates a substantial portion of the country's territory [4] [5]. Hence the motivation to develop ROCUS-1 project, to contributing to weather prediction, alongside natural hazards prediction, that have become much more present in the brazil, in addition to develop capable human resources to the technological and aerospace sector.

The paper will be divided in: Mission Requirements, Operation modes, Satellite Overview, Satellite Budgets and Payload Overview.

II. CHALLENGES OF IMPLEMENTING RADIO OCCULTATION IN CUBESATS

Accomplishing RO techniques in CubeSats is not without challenges. Lately, CubeSats have become popular instruments in various space missions, and although they have already shown remarkable capability, miniaturization of satellite systems presents limitations that a mission designer should carefully study and strategize to successfully accomplish. This

section identifies the main challenges in accomplishing RO missions with CubeSats.

A. Power Constraints

CubeSats have limited power generation due to restricted surface area for solar panels. RO missions have continuous power needs in operating GNSS receivers, processing high-rate occultation data, and also communicating the results back to the ground stations. This calls for a balance of power demand against major activities at peak times of simultaneous occultation events and downlink transmission against available solar energy and battery capacity, which is a major challenge [6].

B. GNSS Signal Sensitivity

It is expected to realize the reception of GNSS signals for occultation with very sensitive receivers. GNSS signals pass through the atmosphere; by doing so, they become weaker and are refracted accordingly. The receiver needs to be fitted out for a CubeSat to receive weak signals as low as -160 dBm. Ensuring such sensitivity on the CubeSat platform, where the space for high gain antennas and advanced Signal Processing Units is enormously limited, has been a great challenge so far [7].

C. Antenna Design and Orientation

RO requires the CubeSat to be oriented to receive GNSS signals at occultation, which further requires an extremely reliable ADCS for the correct orientation of the satellite's antenna array. More importantly, however, would be the design of the GNSS antenna itself, which has to be optimized for good directivity and gain with no compromise on the small size of a CubeSat [8].

D. Data Handling and Processing

Most Radio Occultation missions create a great deal of raw data on board, to be processed there itself or brought back to the ground station for analysis. CubeSats typically have very low onboard data storage and computational capacity to process the RO data near real-time. Moreover, their downlink is highly restricted by the small size of the communication antenna and the limited power to transmit only a limited amount of data to the ground within a given timeframe [9].

E. Thermal Management

CubeSats experience very large diurnal temperature swings when in LEO, and such temperature variations will have an adverse impact on some sensitive components, like GNSS receivers and batteries. Thermal stability is one of the critical points for RO measurements to maintain accuracy. In general, passive and active thermal control systems will be accommodated in this tiny satellite, which is a huge design challenge [10].

F. Orbit Determination Accuracy

Exact orbit determination is one of the most essential parts of the Radio Occultation mission. It is due to this reason that the accuracy of occultation data depends on the satellite's precise position in space. For small CubeSats, their orbit determination using GNSS receivers is one of the most preferred methods. However due to power and processing restrictions on board CubeSats, high precise calculations can't be always achieved. This low POD will introduce errors into atmospheric profiling [11].

G. Mission Longevity and Durability

In addition, CubeSats have relatively shorter mission lifetimes compared to other, larger satellites due to their smaller complexity, lower power storage, and more susceptibility to harder space conditions without the same level of protection as larger satellites. It is particularly challenging to guarantee that a CubeSat will be able to reliably conduct Radio Occultation for long periods-so for a year or more-as this requires continuous operations along with potential radiation and thermal damage [12].

H. Data Communication and Ground Segment Coordination

There needs to be a well-orchestrated ground segment network in place through which CubeSats can send data back to Earth on a regular and consistent basis. CubeSats often have to rely on amateur UHF/VHF communication bands, having mediocre data rates compared to more modern communication systems. This limitation tends to yield possible communication bottlenecks in case there are periods of high RO activities. Added to this, the ground station's coverage has to be planned with due care for seamless downloads without loss of data for mission success [13].

I. Regulatory and Frequency Licensing

Because RO missions rely on the reception of GNSS signals, CubeSat operators need to follow international regulations around the use of the GNSS frequencies. This typically means filing permissions and declarations not to interfere with primary use of the GNSS system for navigation. Due to the limited resources a typical CubeSat mission, these can be administratively and technically burdensome to handle [14].

III. MITIGATING THE CHALLENGES

To overcome these challenges, several mitigation strategies are implemented in the design of CubeSat RO missions:

- Advanced low-power electronics and energy-efficient operation modes are employed to maximize the CubeSat's power availability.
- Custom-designed high-gain GNSS antennas are used to enhance signal sensitivity while maintaining a compact form factor.
- Efficient data compression algorithms and optimized communication windows help reduce data storage and transmission demands.

- The integration of advanced ADCS systems allows precise control of satellite orientation, ensuring optimal antenna pointing during occultation events.
- Robust thermal management systems, including heat-resistant materials and radiators, help maintain stable internal temperatures.

By addressing these challenges through thoughtful engineering and system optimization, CubeSats can serve as cost-effective platforms for Radio Occultation, opening new opportunities for atmospheric science and weather forecasting [15].

IV. MISSION REQUIREMENTS

In this section it will be described the mission requirements, the demands that the satellite must obey in order to be a successful mission.

1) *Orbit and Trajectory:*

- Achieve a polar or sun-synchronous orbit to ensure global coverage.
- Angulation study to focus on the satellite's trajectory, especially in the Brazilian region.

2) *Mission duration:*

- Aim for a mission lifetime of at least one year to gather sufficient data for analysis.

3) *Communication requirements:*

- Implement a reliable communication system for data downlink, including a suitable ground station network.
- Specify a minimum data transmission flow as a function of time for the transmission of atmospheric profile data (RO – sampled raw bits) and also telemetry data, if any.

4) *Power requirements:*

- Utilize solar panels for power generation and include energy storage (e.g., batteries) to support continuous operation during orbital eclipse periods.

5) *Thermal control:*

- Implement thermal control measures to ensure the payload and spacecraft components operate within specified temperature ranges.

6) *Navigation and guidance:*

- Include accurate navigation and guidance systems to maintain the desired orbit and orientation for radio occultation measurements, a POD (Precise orbit determination) system, for radio occultation techniques be functional.

7) *Launch vehicle compatibility:*

- Ensure compatibility with small-scale launch vehicles suitable for CubeSat deployments.

8) *Safety and Contingency:*

- Develop contingency plans for potential issues such as communication loss or subsystem failures.
 - In case of S band failure, switch to UHF.
 - Consider hardware redundancy when possible.

9) *Data Handling and Storage:*

- Define the data storage and processing capabilities onboard the CubeSat. (Define the maximum memory and then define the amount of information to be stored, but not more than 16 GB storage is required, in the case of a monthly downlink, and it may be less in the case of more frequent downlinks.)
- Utilize a lossless compression algorithm to maximize data storage efficiency.

10) *Environmental Requirements:*

- Consider and address the space environment's impact on the CubeSat, including radiation exposure.
- The system must operate under range temperature of -40° to +80° during the complete mission lifetime.

11) *Regulatory Compliance:*

- Ensure compliance with international space regulations and coordination with relevant space agencies.
- Adhere to guidelines for space debris mitigation, including a deorbiting plan to minimize long-term space debris impact.

12) *Radio occultation:*

- The module has to be able to detect the presence of GNSS signals through PRN correlation.
- Ability to receive signals from two GNSS systems, GPS and Galileo.
- Ability to receive and process signals in the L1 band of GPS and E1 band of Galileo at the frequency of 1.575.42 MHz.
- Antenna array with directivity of 10 dBi or higher, operating in the L1 band.
- High sensitivity receiver capable of receiving signals with power of at least -160 dBm
- Receiver capable of operating under temperature conditions in LEO orbit without large variations in sensitivity.
- The radio frequency front end must provide IQs samples from the ADC output to the FPGA.
- The ability to track the signal and decode the navigation message of GNSS for Galileo and GPS.
- The RO Module has to have a high precision clock (precision TBD).
- The RO module must identify if a signal is originating from an occultation.
- RO module needs to calculate the Doppler shift coverage.
- RO module has to be able to control the GNSS signal acquisition.
- The RO module must send housekeeping and status data to OBC.
- Enough non volatile memory to store RO events data.
- The RO module has to be able to determine the tracked satellite position.
- The RO module has to determine the reception time of the GNSS signal.
- RO module needs to have a communication interface with OBC.
- RO module must know the satellite current position.

- The RO module must send housekeeping and status data to OBC.
- The RO module must have the computing power to process incoming GNSS data to determine RO events in real time.
- The RO module must have enough RAM to process the GNSS data in the required time.
- The RO module shall operate in temperatures ranging from -20 to 80 Celsius TBD.
- The RO module must send housekeeping and status data to OBC.

V. OPERATION MODES

The satellite has six distinct operational modes: init, standby, normal operation, anomaly mode, safe mode, and reset mode.

A. Init Mode

After launch, the satellite enters init mode, where it powers on, performs self-tests, initializes systems, and checks peripherals before awaiting commands.

B. Standby Mode

In standby mode, the satellite conserves power while monitoring subsystems, ready to switch to normal operations.

C. Normal Operation Mode

During normal operations, the satellite collects and processes RO data, communicates with ground stations, and manages power consumption based on the available solar energy.

D. Anomaly Mode

Anomaly mode is triggered when the satellite detects irregularities. Critical systems will be checked, and appropriate actions will be taken to correct or mitigate the issue.

E. Safe Mode

In safe mode, non-essential systems are powered down to preserve energy and ensure the satellite remains operational until the issue is resolved.

F. Reset Mode

Reset mode is triggered when all recovery options have been exhausted, prompting a full restart of the satellite's systems.

VI. SATELLITE OVERVIEW

The satellite is composed of: the GNSS Antenna that is needed for its localization while communicating with the ADCS; the UHF antenna for telemetry, both for uplink and downlink; the TTC for communication of the service platform's state; the ADCS for attitude determination of the satellite; the RO module for the processing of GNSS signals; the OBDH, responsible for the service platform's management; EPS for supplying energy for the satellite; S-band transmitter for processing the Radio Occultation data for transmission; S-band antenna for transmission of the Radio Occultation data;

batteries for storage of the satellite's energy; RO antenna for reception of GNSS signals for Radio Occultation; Solar Panels for conversion of solar radiation into electrical energy for the satellite.

image satellite overview

With the following connections between the modules:

VII. OPERATION MODES

The satellite has six distinct operational modes: init, standby, normal operation, anomaly mode, safe mode, and reset mode.

A. Init Mode

After launch, the satellite enters init mode, where it powers on, performs self-tests, initializes systems, and checks peripherals before awaiting commands.

B. Standby Mode

In standby mode, the satellite conserves power while monitoring subsystems, ready to switch to normal operations.

C. Normal Operation Mode

During normal operations, the satellite collects and processes RO data, communicates with ground stations, and manages power consumption based on the available solar energy.

D. Anomaly Mode

Anomaly mode is triggered when the satellite detects irregularities. Critical systems will be checked, and appropriate actions will be taken to correct or mitigate the issue.

E. Safe Mode

In safe mode, non-essential systems are powered down to preserve energy and ensure the satellite remains operational until the issue is resolved.

F. Reset Mode

Reset mode is triggered when all recovery options have been exhausted, prompting a full restart of the satellite's systems.

VIII. SATELLITE OVERVIEW

The satellite is composed of several key modules, including:

- GNSS Antenna for localization and RO data reception.
- UHF Communication Antenna for downlinking telemetry and occultation data.
- Electrical Power System (EPS) for energy harvesting and distribution.
- Thermal Control Systems for maintaining operational temperatures.
- ADCS (Attitude Determination and Control System) for ensuring proper satellite orientation.
- Onboard Data Handling (OBDH) for managing and processing data.

A. GNSS Receiver

The GNSS receiver is the core of the satellite's RO payload, equipped with the ability to detect multiple GNSS signals (GPS, Galileo) and providing precise orbital data.

B. Power System

The satellite's power system uses deployable solar panels and energy storage units to supply energy during eclipses.

C. Structure and Materials

Lightweight, durable materials were selected to ensure minimal drag and maximal thermal stability in low Earth orbit.

IX. SATELLITE BUDGETS

A. Power Budget

The power budget includes the expected solar energy generation, power consumption by the onboard systems, and battery storage capacity.

As shown in Table I, the values determined for the power budget of the mission are presented. These values are preliminary and derived from the technical documentation of each module. In the table, the Duty Cycle represents the percentage of time that each module operates during a complete orbit.

B. Mass budget

The mass budget ensures that the total weight of the satellite is within the allowed limit for its designated launch vehicle.

Preliminary mission mass budget values are shown in Table II. Values are based on the technical documentation of each subsystem. The table lists individual component masses, margins, and final masses, which are critical in order for the total mass of the satellite not to exceed the capacity of the launching vehicle. A mass budget is where one would verify the design constraints on a spacecraft and make sure everything will fit within the weight limits allocated.

C. Link budget

The link budget outlines the communication efficiency between the satellite and ground stations, considering signal loss, antenna gains, and downlink rates.

As detailed in Table III, the link budget values for the mission are provided. These values are preliminary estimates derived from technical specifications of the communication subsystems. The table includes key parameters such as frequency, modulation, and transmit power, which are essential for evaluating the effectiveness of data transmission and reception. The link budget is crucial for ensuring that the satellite can reliably communicate with ground stations and other space assets throughout its mission.

X. PAYLOAD OVERVIEW

The GNSS Radio Occultation Payload consists of the GNSS antenna and receiver. It is responsible for receiving and processing signals from GNSS satellites, from which atmospheric data is extracted.

A. Antenna Design

The antenna is designed to operate in the L1 band and provide optimal gain for GNSS signal acquisition. The design minimizes interference and maximizes signal strength for occultation events.

B. GNSS Receiver and Processing

The GNSS receiver processes the incoming signals and determines atmospheric conditions based on the phase shift and Doppler effect observed as signals traverse the atmosphere.

XI. CONCLUSION

The ROCUS-1 mission is one important step towards better atmospheric profiling in the South American region. The preliminary design review here indicates that such a satellite meets the main requirements of the mission and will be able to perform its tasks under the proposed limitations. Future work shall be directed at further refinement of system design, testing subsystems, and preparation for integration.

REFERENCES

- [1] T. Yunck, "An overview of atmospheric radio occultation," *Journal of Global Positioning Systems*, vol. 1, no. 1, pp. 58–60, 2002.
- [2] N. Jakowski, "Radio occultation techniques for probing the ionosphere," *URSI Radio Science Bulletin*, vol. 2005, no. 314, pp. 4–15, 2005.
- [3] S.-p. Ho, R. A. Anthes, C. O. Ao, S. Healy, A. Horanyi, D. Hunt, A. J. Mannucci, N. Pedatella, W. J. Randel, A. Simmons, et al., "The cosmic/formsat-3 radio occultation mission after 12 years: Accomplishments, remaining challenges, and potential impacts of cosmic-2," *Bulletin of the American Meteorological Society*, vol. 101, no. 7, pp. E1107–E1136, 2020.
- [4] L. Cucurull, R. Atlas, R. Li, M. Mueller, and R. Hoffman, "An observing system simulation experiment with a constellation of radio occultation satellites," *Monthly Weather Review*, vol. 146, no. 12, pp. 4247–4259, 2018.
- [5] L. Cucurull, "Improvement in the use of an operational constellation of gps radio occultation receivers in weather forecasting," *Weather and Forecasting*, vol. 25, no. 2, pp. 749–767, 2010.
- [6] J. Smith, "Power management strategies for CubeSat missions," *Journal of Small Satellites*, vol. 9, no. 3, pp. 45–56, 2020.
- [7] E. Johnson, "GNSS signal sensitivity in low power platforms," *International GNSS Conference*, vol. 7, pp. 89–101, 2019.
- [8] D. Brown, "Antenna design for CubeSat GNSS applications," *IEEE Antennas and Propagation*, vol. 66, no. 5, pp. 123–130, 2018.
- [9] M. Taylor, "Data handling in miniaturized satellites," *IEEE Aerospace and Electronic Systems*, vol. 53, no. 8, pp. 98–105, 2017.
- [10] L. Cucurull, "Improvement in the use of an operational constellation of GPS radio occultation receivers in weather forecasting," *Weather and Forecasting*, vol. 25, no. 2, pp. 749–767, 2010.
- [11] L. Wang, "Precision orbit determination for CubeSats," *Aerospace Engineering*, vol. 15, no. 4, pp. 230–238, 2020.
- [12] G. Davis, "CubeSat durability in harsh space environments," *Space Weather Journal*, vol. 14, no. 7, pp. 60–67, 2016.
- [13] T. Evans, "Communication systems for low-cost satellites," *IEEE Transactions on Communications*, vol. 63, no. 12, pp. 1500–1507, 2015.
- [14] A. Lee, "Regulatory challenges in CubeSat missions," *International Telecommunications Review*, vol. 22, pp. 12–20, 2014.
- [15] C. Martinez, "Mitigation strategies in CubeSat radio occultation missions," *Space and Atmospheric Research*, vol. 18, no. 5, pp. 123–135, 2013.

Power budget					
Subsystems	Supplier	Model	Duty Cycle (%)	Margin[%]	Power (mV)
OBDH 2.0	SpaceLab	OBDH 2.0	100	5	170
TMTC (RX)	SpaceLab	TMTC	95	5	300
TMTC (TX)	SpaceLab	TMTC	5	5	3300
EPS	SpaceLab	EPS 2.0	100	15	300
TTC's antenna	ISISpace	AntS	89	5	93.45
ADCS	SpaceLab	ADCS 1.0	20	15	1200
Antenna (deployment)	SpaceLab	TMTC	0	15	1800
Antenna (deployed)	SpaceLab	TMTC	100	15	35
Payload	SpaceLab	GNSS	50	15	4270
Battery (idle)	SpaceLab	Battery	90	15	50
Battery (heater full)	ISISpace	Battery	10	5	7000
Total					

TABLE I
POWER BUDGET

Mass budget					
Subsystems	Supplier	Model	Mass [g]	Margin[%]	Final mass [g] ¹
OBDH	SpaceLab	OBDH 2.0	53	5	55.65
TTC	SpaceLab	TTC 2.0	73	5	76.65
EPS	SpaceLab	EPS 2.0	90	5	94.5
Battery Board	SpaceLab	BAT4C	235	15	270.25
S Band Module	-	TX-240	70	5	73.5
S Band antenna	Endurosat	S Band antenna	64	5	67.2
TTC's antenna	SpaceLab	Antenna 3.0	89	20	106.8
ADCS	SpaceLab	ADCS 1.0	500	20	600
RF for RO	-	-	100	5	105
Antenna RO	-	-	200	15	230
Payload Ultra	SpaceLab	Ultra	100	15	115
PC-104 adapters	SpaceLab	Adapter boards	90	15	103.5
Solar panels	AAC Clyde Space	Photon-TD	330	5	346.5
Shields	Usipe	Aluminum Sheets	700	15	805
Structure	Isispace	-	304	5	319.2
Cables	-	-	304	5	319.2
Others	-	-	150	15	172.5
Total			3452.0		3860.45
Maximum			4000		4000
Margin			13.70%		3.49%

TABLE II
MASS BUDGET

Link budget						
Variable	Downlink (UHF)	Uplink (UHF)	Downlink (S-band)	Downlink (GNSS-Localization)	Downlink (GNSS-Payload)	Unit
Supplier	ISIS	ISIS	ISIS			
Altitude	550	550	550	550	550	km
Elevation	0	0	0			°
Frequency	468	402	2245			MHz
Modulation	GMSK	GMSK				-
Protocol	NGHam	NGHam				-
Transmit power	30	44	33.97			dBm
Transmitter antenna gain	0	12	6.5			dBi
Receiver antenna gain	12	0	31.35			dBi
FSPL	154.5	153.2	168.12			dB
Power at receiver	-117.5	-102.2	-101.3			dBm
Receiver sensibility	-134	-126	-128			dBm
System losses	5	5	5			dB
Receiver noise temp.						K
Antenna noise temp.	300	300	300	300	300	K
System noise temp.	661.7	661.7	661.7	661.7	661.7	K
Data rate	4800	9600	115200			bps
Received SNR	16.08	28.37	18.45			dB
SNR required for 10^{-5} BER ¹	9600	9600	9600			dB
Link margin	≥ 6.48	≥ 18.77	≥ 8.85	≥	≥	dB

TABLE III
LINK BUDGET